(11.47)

where K for round channels is 16, and for square cross-section channels is 14.2 for Reynold's numbers (Re) < 2100, the laminar flow regime. The contraction and expansion flows into and out of the monolith channels can be transitional or turbulent. Friction coefficients for these flows can be estimated from the following correlations:

$$K_{\text{in}} = 1.08 - 0.415\left(A_F/A\right)$$

(11.48)

and

$$K_{\text{out}} = \left(1 - A_F/A\right)^2$$

(11.49)

where A_F/A is the ratio of the substrate (open) flow area to the total substrate cross-sectional area. Combining Eqs. (11.45) to (11.49) gives the total catalyst substrate pressure drop:

$$\Delta p_c = \left[4f\left(L/d_{\text{ch}}\right) + K_{\text{in}} + K_{\text{out}}\right]\left(\rho v^2/2\right)$$

(11.50)

This pressure drop is comparable in magnitude to the exhaust pipe pressure drop, and to the muffler pressure drop.

11.6.3. Catalytic Converters

The catalytic converters used to clean up the engine's exhaust gases, as explained in the previous section, consist of active catalytic material on the surface of a ceramic monolith in a specially designed metal casing which directs the exhaust gas flow through the catalyst bed. The active material employed for CO and HC oxidation or NO reduction (normally noble metals, though base metals oxides can be used) must be distributed uniformly over a large surface area so that the mass-transfer characteristics between the gas phase and the active catalyst surface are sufficiently fast to enable close to 100% conversion efficiency. The converter configuration commonly used is shown in Fig. 11.55. The active noble metal catalyst material is impregnated into a highly porous alumina washcoat about 20 μm thick that is applied to the passageway walls. The typical monolith has square-cross-section passageways with inside dimensions of ~1 mm separated by thin (0.15 to 0.3 mm) porous walls. The number of passageways per square centimeter varies between about 60 and 100 (400 to 700 passageways/in^2). The washcoat, 5 to 15% of the weight of the monolith, has a highly porous surface area of area 100 to 200 m^2/g. The gas flow is directed down through the bed as shown to provide a large flow area and catalytic surface area, and low-pressure drop. While the exhaust gas flow is turbulent, in the monolith catalyst passageways, it is laminar.

Air Esscentials – Exhibit 2007
Aroma 360 v. Air Esscentials
IPR No. 2025-00706

11.6.3.1. Oxidation Catalysts

Oxidation catalysts were the first type of catalytic converter widely used to reduce engine-out HC and CO emissions with gasoline engines in the 1970s. Their use declined in the 1980s as strict control of NO_x emissions became mandatory and three-way catalysts which, with stoichiometric engine operation removed all three pollutants, became the dominant SI engine

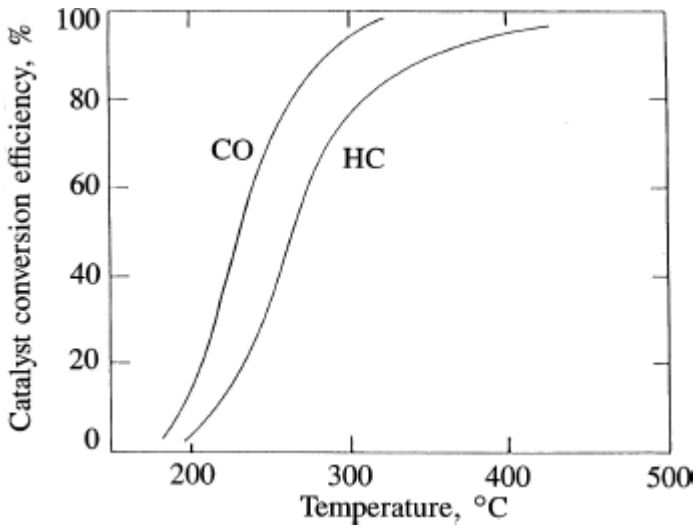
© McGraw-Hill Education. All rights reserved. Any use is subject to the Terms of Use, Privacy Notice and copyright information.

catalyst technology (see below). The function of an oxidation catalyst engine is to oxidize CO to CO_2, and hydrocarbons to CO_2 and water, in the exhaust gas stream which typically contains about 10% CO_2, 12% H_2O, 100 to 2000 ppm NO, SO_2 at the ppm level, 1 to 2% O_2, 0.2 to 2% CO, and 1000 to 5000 ppm C_1 HC. About half the hydrocarbons emitted by the SI engine are unburned fuel compounds. The saturated hydrocarbons (which comprise some 20 to 30%) are the most difficult to oxidize. The ease of oxidation increases with increasing molecular weight. Sufficient oxygen must be present to oxidize the CO and HC. This may be supplied by the engine running slightly lean of stoichiometric or with a secondary air pump that introduces air into the exhaust ports just downstream of the valve (see secondary air discussion on p. 648).

Because of their high intrinsic activity, noble metals are the most effective catalytic materials. They show higher specific activity for HC oxidation, are more thermally resistant to loss of low-temperature activity, and are much less deactivated by the sulfur in the fuel than base metal oxides. A mixture of platinum (Pt) and palladium (Pd) is commonly used. For the oxidation of CO, olefins, and methane, the specific activity of Pd is higher than that of Pt. For the oxidation of aromatic compounds, Pt and Pd have similar activity. For oxidation of paraffin hydrocarbons (with molecular size greater than C_3), Pt is more active than Pd. Pure noble metals sinter rapidly in the 500 to 900°C temperature range experienced by exhaust catalysts. Since catalytic behavior is manifested exclusively by surface atoms, the noble metals are dispersed as finely as possible on an inert support such as γ-A_2O_3 which prevents particle-to-particle metal contact and suppresses sintering. The size of the noble metal particles in a fresh catalyst is less than 50 nm. This can increase to ~100 nm when the catalyst is exposed to the high temperatures of the exhaust in vehicle operation. Typical noble metal concentrations in a commercial monolith catalyst are between 1 g/liter and 2 g/liter of monolith volume, with Pt/Pd ≈ 2 on a weight basis. As a rough rule of thumb, the ceramic honeycomb volume required is about half the engine displaced volume. This gives a space velocity through the converter (volume flow rate of exhaust divided by converter volume, Eq. 11.44) over the normal engine operating range of 5 to 20 per second (20,000 to 70,000 h^{-1}).

The *conversion efficiency* of a catalyst is the ratio of the rate of mass removal in the catalyst of the particular pollutant of interest to the mass flow rate of that pollutant into the catalyst, Eq. (11.43). The variation of conversion efficiency of a typical oxidizing catalytic converter with temperature is shown in Fig. 11.60. At high enough temperatures, the steady-state conversion efficiency of a new oxidation catalyst is typically 98 to 99% for CO and above 95% for HC. However, the catalyst is ineffective until its temperature has risen above the *light-off temperature* (about 250°C) at which point the catalyst becomes more than 50% effective.

Figure 11.60 Conversion efficiency for CO and HC as a function of temperature for typical oxidizing catalytic converter.[35]



The above numbers apply to new noble-metal oxidation catalysts: as catalysts spend time in service their effectiveness deteriorates. Catalysis involves the adsorption of the reactants onto surface sites of high activity, followed by chemical reaction, then desorption of the products. As explained in Sec. 11.6.2, catalyst degradation involves both the deactivation of

© McGraw-Hill Education. All rights reserved. Any use is subject to the Terms of Use, Privacy Notice and copyright information.

these sites by catalyst poisons and a reduction in the effective number of these sites through sintering. Poisoning affects both the warm-up and steady-state performance of the catalyst. When poisoning occurs, catalytic activity is impeded through prolonged contact with interfering elements that either physically block the active sites or interact chemically with the active material.

A material balance across the catalyst monolith, assuming steady-state, one-dimensional plug flow operation gives

$$\frac{d(vC)}{dz} = -R$$

(11.51)

where *v* is the exhaust flow velocity, *C* the concentration of the reactant of interest (g-moles/cm^3), *z* is the axial distance, and *R* the rate of reaction (g-moles/cm^3 · s). If the reactant concentration is low, the chemical energy release is modest, so the flow can be treated as isothermal and Eq. (11.51) simplifies to

$$v\frac{dC}{dz} = -R$$

(11.52)

Since
$C_{\mathrm{HC}} \ll C_{\mathrm{O}_2}$, there is an excess of O_2 so the reaction rate depends to first order on the hydrocarbon concentration: for example, for ethane oxidation

$$\mathrm{C_2H_6} + \frac{7}{2}\mathrm{O_2} \rightarrow 2\mathrm{CO_2} + 3\mathrm{H_2O}$$

the reaction rate equation is

$$v\frac{dC_{\mathrm{C_2H_6}}}{dz} = -k'C_{\mathrm{C_2H_6}}$$

which integrates to

$$\ln\frac{C_o}{C_i} = \frac{k'z}{v} = -k't$$

(11.53)

where subscripts *o* and *i* denote catalyst-out and -in concentrations, and *t* is the residence time of C_2H_6 in the catalyst bed (the reciprocal of the space velocity, Eq. 11.44). Rate constants, such as *k'*, are determined experimentally.[79] Similar relationships can be written for the oxidation rates of the more reactive olefinic and aromatic hydrocarbon.

The oxidation kinetics of CO over Pt and Pd noble metal catalysts can be described by

© McGraw-Hill Education. All rights reserved. Any use is subject to the Terms of Use, Privacy Notice and copyright information.

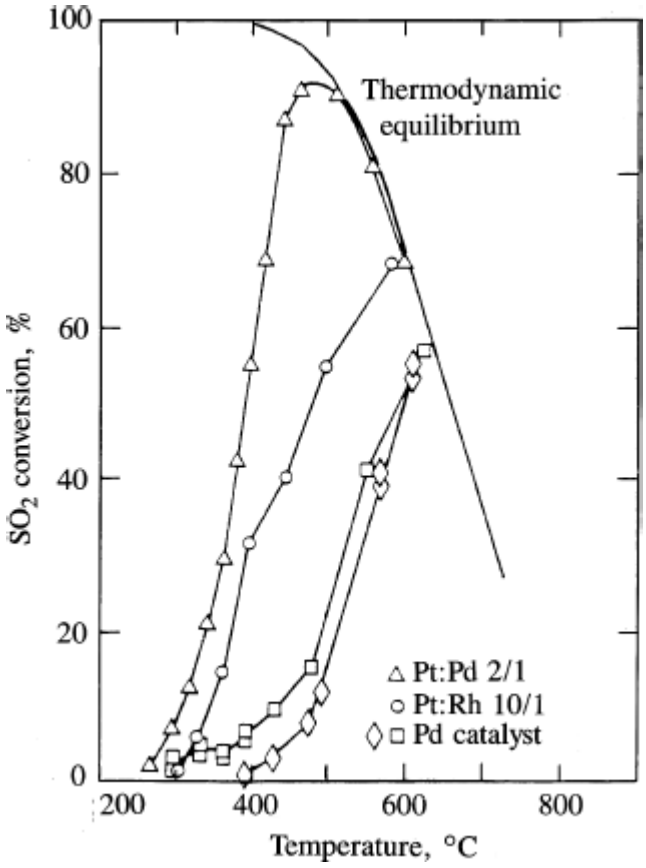
$$\frac{d[\mathrm{CO}]}{dt} = \frac{K_1 p_{\mathrm{CO}} p_{O_2}}{(1 + K_2 p_{\mathrm{CO}} + K_3 p_{\mathrm{HC}})^2 (1 + K_4 p_{\mathrm{NO}}^n)}$$

(11.54)

where K_1 to K_4 and n are constants at any given temperature, and p_{CO}, p_{O_2}, p_{HC}, and p_{NO} are the partial pressures of carbon monoxide, oxygen, hydrocarbons, and nitric oxide, respectively. These relationships incorporate the fact that the rates of HC and CO oxidation are inhibited by high CO and reactive HC concentrations, and that NO concentrations in the range of 0 to 1000 ppm inhibit HC and CO oxidation also.[81]

Oxidation-catalyst equipped vehicles may emit sulfuric acid aerosol. Gasolines contain between about 10 and several hundred ppm by weight S (depending on fuel specifications), which leaves the combustion chamber as SO_2. This SO_2 can be oxidized by the catalyst to SO_3, which combines with water at ambient conditions to form an H_2SO_4 aerosol. The SO_3 can be chemisorbed on the alumina catalyst surface. SO_3 production can be controlled by lowering or raising the catalyst temperature. Figure 11.61 shows that at low temperatures, SO_3 production is kinetically limited; at high temperatures SO_3 production is thermodynamically limited. Palladium and rhodium catalysts produce less SO_3 than Pt and have comparable HC and CO catalytic activity. By decreasing oxygen concentrations leaving the catalyst to ~1%, SO_3 production can be substantially reduced.[81]

Figure 11.61 SO_2 conversion to SO_3 within an oxidizing catalytic converter, as a function of temperature, with 5% O_2 concentration and no reducing gases present. Space velocity (volume flow of exhaust per unit catalyst volume) ~10 s^{-1}. Results for Pt–Pd, Pt–Rh, and Pd catalysts.[82]



Oxidation catalysts, no longer widely used in gasoline SI engines, have come back as an important component of diesel aftertreatment systems. Oxidation of diesel HC emissions became important from a regulatory point of view, and because high-molecular-weight hydrocarbons condense and contribute to particulate emissions (termed the soluble organic fraction,

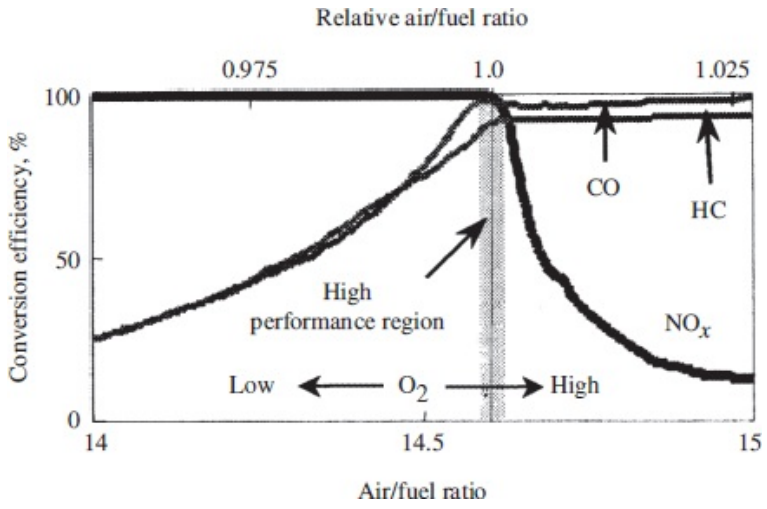
© McGraw-Hill Education. All rights reserved. Any use is subject to the Terms of Use, Privacy Notice and copyright information.

SOF, of the total particulate matter). Data suggest that this SOF of the diesel particulate matter varies significantly with engine design details and operating conditions, but can be some one-third of the total particulate matter.[83] An oxidation catalyst is able to remove much of this SOF, but exhaust gas temperatures are usually too low to oxidize the insoluble soot fraction of PM. Diesel exhaust gas is inherently lean of stoichiometric so there is always excess oxygen. While that lowers the effective HC and CO oxidation catalyst light-off temperatures, the diesel exhaust gases are significantly cooler than in stoichiometric-operating gasoline engines so overall catalyst efficiencies are lower than is achieved in gasoline-engine oxidation catalysts, rising to about 70% for HC and approached 90% for CO. However, DOCs do remove a significant fraction of the aldehydes and ketones responsible for diesel exhaust odor, and the polycyclic aromatic hydrocarbons, an especially toxic component of diesel exhaust.[79,83]

11.6.3.2. Three-Way Catalysts

When a gasoline engine is operated at the stoichiometric air/fuel ratio, then both NO reduction and CO and HC oxidation can be effected in a single catalyst bed. The catalyst brings the exhaust gas composition to a near-equilibrium state at these exhaust conditions; i.e., a composition of CO_2, H_2O, and N_2. Enough reducing gases will be present to reduce NO and enough O_2 to oxidize the CO and hydrocarbons. Such a catalyst is called a*three-way catalyst* since it removes all three pollutants simultaneously. Figure 11.62 shows the conversion efficiency for NO, CO, and HC as a function of the actual and relative air/fuel ratio. There is a narrow range of air/fuel ratios close to stoichiometric in which high conversion efficiencies for all three pollutants are achieved. The width of this window is narrow, about 0.1 air/fuel ratios (7×10^{-3} in relative air/fuel or equivalence ratio units), and depends on catalyst formulation details and engine operating conditions.

Figure 11.62 Conversion efficiency for NO, CO, and HC for a three-way catalyst as a function of exhaust gas air/fuel ratio.[84]



The overall chemical conversions that remove the three pollutants under stoichiometric exhaust conditions are these:

Oxidation:

$$\mathrm{CO} + \mathrm{oxygen} \rightarrow \mathrm{CO_2}$$
$$\mathrm{HC} + \mathrm{oxygen} \rightarrow \mathrm{CO_2\ and\ H_2O}$$

Reduction:

$$\mathrm{NO} + \mathrm{CO,\ HC,\ or\ H_2} \rightarrow \mathrm{N_2} + \mathrm{CO_2,\ H_2O}$$

© McGraw-Hill Education. All rights reserved. Any use is subject to the Terms of Use, Privacy Notice and copyright information.

Usually the catalyzed CO reactions begin first, followed by the HC and NO reactions. With hot exhaust gases in a warmed-up gasoline engine, the chemical reaction rates are fast, and the overall conversion rates are controlled by pore diffusion and/or bulk mass transfer.[78]

The relative air/fuel ratio window for achieving both oxidation and reduction simultaneously is too narrow to be realized in an operating engine without *closed-loop* relative air/fuel ratio control. An oxygen sensor in the exhaust is used to indicate whether the engine is operating on the rich or lean side of stoichiometric, and provide a signal for adjusting the fuel system to achieve the desired air-fuel mixture (see Sec. 7.4). Holding the equivalence ratio precisely on the chosen close-to-stoichiometric value is not a practical expectation of such a feedback system, so oxygen storage capacity (OSC) is built into the washcoat. Ceria (CeO_2) is the most commonly used oxygen storage component. It can release oxygen (forming Ce_2O_3) when the exhaust gas at the surface of the catalyst is slightly rich: then Ce_2O_3 can absorb and store oxygen from the exhaust gas on the catalyst surface when the gas is lean, by transitioning to CeO_2: that is,

$$2CeO_2 \rightleftarrows Ce_2O_3 + O$$

Ceria constitutes some 10 to 20% of the γ–Al_2O_3 washcoat material.[83] It has been found that addition of zirconia to the ceria (in roughly comparable amounts) in the washcoat improves the stability of the ceria and promotes oxygen ion mobility.

To maintain this OSC in a state where oxygen can always be released or absorbed in response to random relative *A/F* fluctuations in the engine's exhaust gases, the engine air/fuel ratio control system is oscillated about stoichiometric, rich and lean at a given amplitude and frequency, to maintain the desired storage level. Amplitudes of ± about 0.5 *A/F* ratio at between 0.5 Hz and 1 Hz frequency provide optimum performance. Thus the actual exhaust gas relative air/fuel ratio window within which all three pollutants are effectively removed, is widened substantially. Note that while the engine-out exhaust gas composition varies around the stoichiometric composition (due to both this deliberate oscillation and through more random engine variations), the oxygen storage capability ensures that the gas composition at the three-way catalyst surface remains within the narrow high-efficiency close-to-stoichiometric band shown in Fig. 11.62.

The noble metal catalysts utilized in TWCs are combinations of platinum, rhodium, and palladium. Rhodium is the principal ingredient used in commercial Pt-Rh catalysts to remove NO. It is very active for NO reduction, is much less inhibited by CO and sulfur compounds, and produces less NH_3 than Pt. To remove NO under slightly lean-of-stoichiometric conditions, the catalyst must react the CO, H_2, or HC with NO rather than with O_2, as the exhaust gas passes through the catalyst bed. Rhodium shows some NO reduction activity slightly lean of stoichiometric. On the rich side, the three-way catalyst window is determined by hydrocarbon and CO removal. Platinum is commonly used for HC and CO oxidation; it has good activity under stoichiometric and slightly lean conditions. When sufficient rhodium is present, the participation of Pt in NO removal is minimal. In the rich regime, the three-way catalyst consumes all the oxygen that is present in the exhaust, and as a consequence removes an equivalent amount of CO, H_2, and hydrocarbons; it is thought that the H_2 is removed first. In addition, the water-gas shift reaction

$$CO + H_2O \rightleftarrows H_2 + CO_2$$

and the steam-reforming reaction

$$\text{Hydrocarbon} + H_2O \rightarrow CO, CO_2, H_2$$

can consume CO and HC. (Ceria also promotes these reactions.) The exhaust contains an H_2/CO molar ratio of about one-third (see Sec. 4.9.1): the equilibrium ratio at 500°C is about 4. Considerable CO removal can be expected if the water-gas shift equilibrium is approached. Platinum is active in promoting this equilibrium. For large molecular weight paraffin hydrocarbons, and for olefins and aromatic hydrocarbons, the equilibrium for the steam-reforming reactions lies to the right. This reaction can therefore lead to considerable hydrocarbon removal. Rhodium is particularly active in the steam-reforming

© McGraw-Hill Education. All rights reserved. Any use is subject to the Terms of Use, Privacy Notice and copyright information.

reaction; platinum is also active. Commercial three-way catalysts contain platinum and rhodium (the ratio Pt/Rh being around 5). The amounts used are a few grams of Pt-Rh per liter. Alumina is the preferred support material. Ceria is the oxygen storage component.[80] Palladium is also used in three-way catalysts, alone or with rhodium. It is used in greater amounts (several times that of Pt-Rh—some 10g/liter). It has a lower light-off temperature than Pt-Rh catalysts. Its performance is comparable to that of Pt-Rh catalysts.[83]

The effectiveness of the catalyst depends on its operating temperature, the availability of excess oxygen mixed throughout the reacting gases, and the monolith surface area. The operating temperature depends on the inlet gas temperature, heat losses, and the amount of HC, CO, and H_2 burned up in the reactor. This latter factor is important: 1.5% CO removal results in a 220 K temperature rise. As a consequence, catalytic converters with fuel-rich cylinder-exhaust gas and secondary air give greater fractional reductions in HC and CO emissions than reactors with fuel-lean cylinder exhaust (which do not require any secondary air).

A practical limitation to catalyst effectiveness with fuel-rich engine operation is adequate mixing of secondary air and engine exhaust gases in the exhaust ports and manifold. The secondary airflow with a conventional air pump is effectively shut off by the exhaust blowdown process, and little oxidation occurs in the exhaust port because the air and exhaust gases are effectively segregated. Mixing can be promoted by suitably arranging the catalyst inlet and exit ports and by using baffles.

11.6.3.3. DeNO$_x$ Catalysis

NO is removed by reduction using the CO, hydrocarbons, and H_2 in the exhaust. No catalyst is available for the decomposition of NO to O_2 and N_2 (thermodynamically favored at exhaust gas temperatures) that is sufficiently active for use in engines. NO reduction can be carried out under rich conditions where there is an excess of reducing species over oxidizing species. The catalyst is then referred to as an *NO reduction catalyst*. Such an approach is used to regenerate a lean NO_x trap (LNT; see below) when its NO_x storage capacity reaches its limit. However, the rich operation necessary for NO reduction results in a fuel consumption penalty and constrains the performance of the NO catalyst since a fraction of the NO removed can be converted to ammonia NH_3 rather than N_2. NH_3 formation under rich operation must be small because the ammonia can be oxidized back to NO. Reduction of NO by CO, HC, or H_2 can be accomplished by base metal catalysts (e.g., CuO, NiO) in an appropriate temperature range (350 to 600°C). This "passive deNO$_x$" approach has not proved that attractive.

However, catalytic reduction of NO in lean operating engines, whether lean-at-light-load gasoline engines (e.g., stratified charge DI spark-ignition engines) or diesel engines, is an import emissions control need. Two approaches have been extensively explored and developed over the past several years, and are now in production. One is the lean NO_x trap (LNT), which stores the NO_x as nitrate when the engine is operating lean and then operates fuel-rich for a short period when the nitrogen oxides are released and then reduced to N_2. The second approach (used with light- and heavy-duty diesel engines) is selective catalytic reduction (SCR) of NO_x. In the predominant version of this approach, urea (stored on the vehicle) is titrated into the exhaust gases, converted to the reducing agent (ammonia), which then effects the NO_x reduction in a quasi-steady manner. A second SCR strategy is to add and use hydrocarbons as the "titrated" reducing agent. These approaches will now be reviewed.

11.6.3.4. Lean NO$_x$ Trap

This catalyst system absorbs and stores NO_x when an oxidizing exhaust gas flows through it and, since the storage capacity is limited, is periodically regenerated by a reducing purge. During this purge the engine is operated fuel-rich so exhaust gas constitutes can reduce the stored NO_x to N_2.

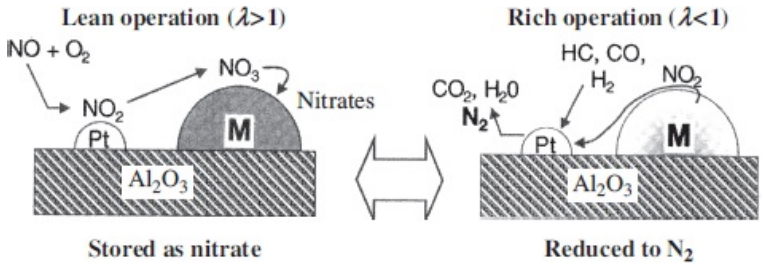
Figure 11.63 illustrates this operation. Under lean operating conditions, the platinum catalyst oxidizes the NO in the exhaust gases to NO_2. This is then absorbed and stored as an alkaline-earth (base metal, M) nitrate on the catalyst surface. Barium is usually the absorbant: Ca, Sr, and Mg are other alkaline earths that are also effective.

© McGraw-Hill Education. All rights reserved. Any use is subject to the Terms of Use, Privacy Notice and copyright information.

$$\mathrm{Ba} + 2\mathrm{NO_2} + \frac{1}{2}\mathrm{O_2} = \mathrm{Ba(NO_3)_2}$$

(11.55)

Figure 11.63 *Schematic of NO_x storage-reduction mechanism of lean NO_x trap (LNT).*[85]



The noble metal catalyst sites (Pt and Rh) must be in close proximity to the base nitrate-storage material. Alkali metal absorbers (Cs, K, Na) are added to the barium to improve catalyst efficiency, nitrate stability, and resistance to sulfur poisoning: see below.

When the nitrate storage capacity is essentially full, the trap is regenerated by rapidly transitioning the engine to rich operation (*A/F* 11.5 to 12.5) so the barium nitrate decomposes and the NO_2 released is reduced by the CO, HC, and H_2 in the now-rich exhaust gases. The decomposition of the barium nitrate occurs through the reverse of reaction (11.55) or its equivalent

$$\mathrm{Ba(NO_3)_2} = \mathrm{BaO} + 2\mathrm{NO} + 1\frac{1}{2}\mathrm{O_2}$$

(11.56)

followed by NO (and NO_2) reduction: for example,

$$\mathrm{NO} + \mathrm{CO} = \frac{1}{2}\mathrm{N_2} + \mathrm{CO_2}$$

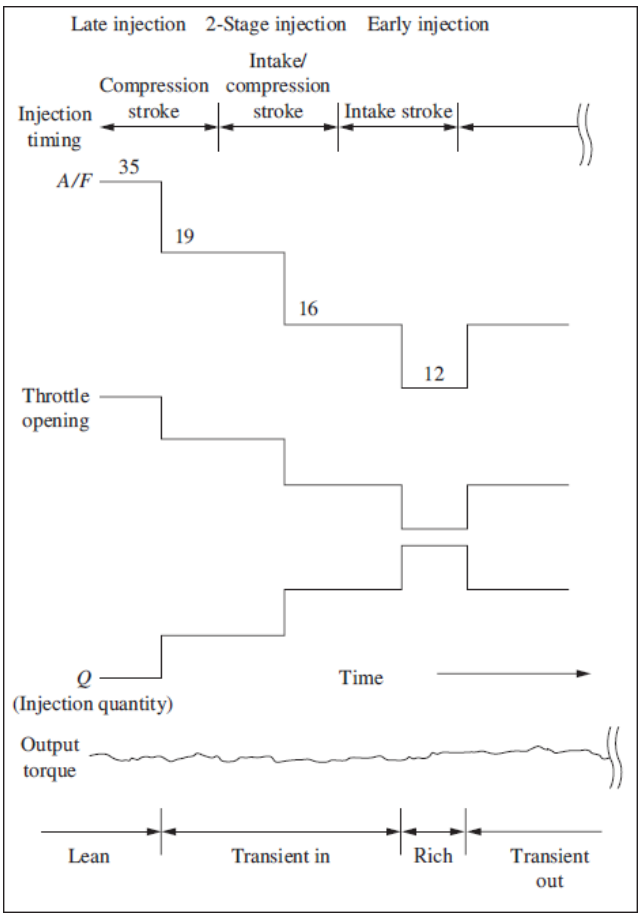
(11.57)

Under these fuel-rich conditions at elevated temperatures, the nitrate species become thermodynamically unstable and decompose to NO and NO_2 [Eqs. (11.55) and (11.56)], and the HC, CO, and H_2 reduce these oxides of nitrogen on the noble metal catalyst to N_2, CO_2, and H_2O. Once the storage capacity has been regenerated, the engine returns to its (normal) lean operating mode.

Figure 11.64 illustrates how this regeneration process is controlled. The stoichiometry of the engine, when the regeneration process is initiated, transitions from its normal light-load lean operation, in stages, to well rich of stoichiometric (*A/F* about 12). To maintain constant torque, the throttle opening is reduced and the quantity of fuel injected per cycle is increased.[2] The rich-operation regeneration period is short (1 to 3 seconds). Once regeneration is complete, the return transient takes the engine back to its normal lean operating conditions. With these LNTs, regeneration occurs roughly every 60 s. There is therefore a fuel economy penalty of a few percent due to this frequent periodic regeneration process.

© McGraw-Hill Education. All rights reserved. Any use is subject to the Terms of Use, Privacy Notice and copyright information.

Figure 11.64 *Regeneration control strategy of lean NO_x trap: steady-state lean operation (NO_x storage); transition to fuel-rich operation; fuel-rich regeneration and NO_x reduction; transition back to lean operation.*[85]



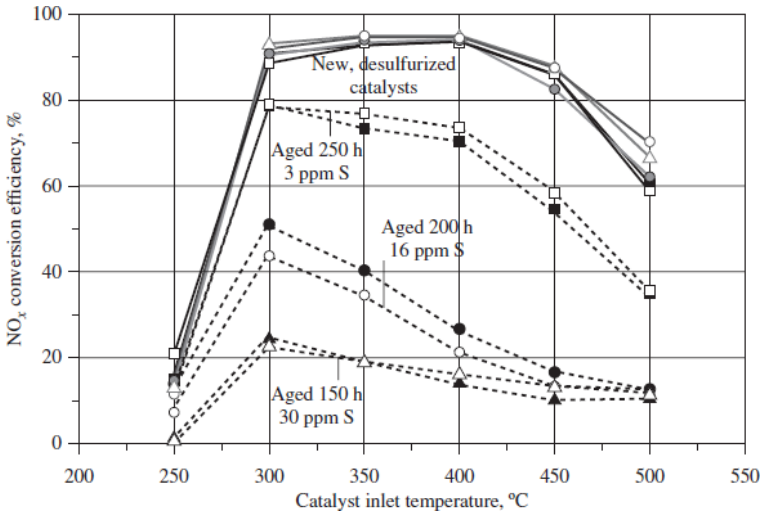
An issue with LNTs is their susceptibility to sulfur poisoning. Just as barium and other alkaline bases store NO_x as nitrates, they can store sulfur oxides as sulfates. To maintain high catalyst efficiency over long periods of operation, the sulfur content of the fuel must be very low (a few ppm S). Some regions of the world have gasoline's and diesel fuels approaching these low levels. Many areas do not. In general sulfur poisoning of LNTs is reversible and catalytic site activity can be restored by a desulfation process which involves decomposition of the sulfate. This requires temperatures between about 500°C and 700°C accompanied by mixture enrichment. However, desulfation of LNTs does not quite restore the full nitrate storage capacity, so there is a requirement for extremely low S fuels to maintain high catalyst efficiency over extended operation.[79]

Various desulfation approaches are possible. For diesel engine LNT use, exhaust gas temperatures can be increased by additional late injections of fuel. With lean-operating gasoline engines, rapid large amplitude modulation of the (*A/F*) to enable exothermic reactions increases catalyst temperature (and minimizes the production of H_2S rather than SO_x). Another possibility is a sulfur trap ahead of the LNT.

The catalyst efficiencies achievable in LNTs, and the impact of sulfur and desulfation, are illustrated in Fig. 11.65. NO_x conversion efficiencies of more than 90% are realizable over the 300 to 400°C range with new catalyst systems (top set of curves). Additional developments are extending this high efficiency temperature range to 600°C.[86] When aged for 250 hours with 3 ppm S fuel, about a 20% loss in conversion efficiency occurs (next two lower curves). Higher levels of fuel sulfur (16 ppm S for 200 hours), and higher levels still (30 ppm S for 150 hours), further degrade efficiency as indicated in the third and fourth pairs of curves. Desulfurization of all these catalysts restores their NO_x conversion efficiency to close to their efficiencies before aging and exposure to fuel sulfur. Successive desulfurizations show modest loss in efficiency from the clean catalyst levels. Note 200 hours of "aging" corresponds to about 13,000 km (8,000 miles) of driving in an automobile.

© McGraw-Hill Education. All rights reserved. Any use is subject to the Terms of Use, Privacy Notice and copyright information.

Figure 11.65 Conversion efficiencies for two lean NO_x storage catalysts as a function of temperature: curves are for new catalysts, aged catalysts (with 3 to 30 ppm S fuels), and after desulfurization.[86] Two hundred hours of aging corresponds to about 13,000 km of driving.

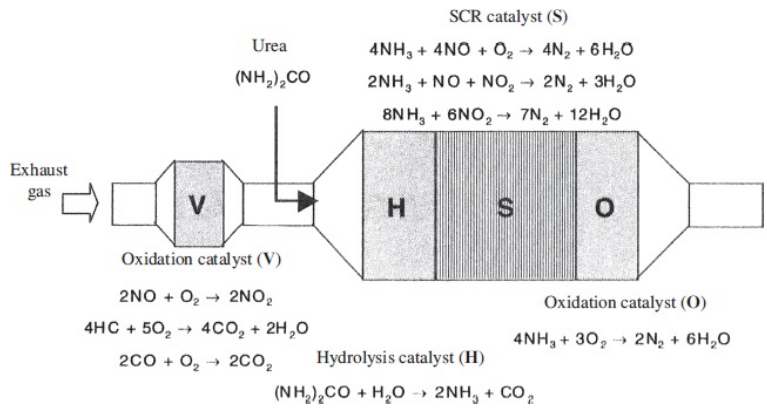


11.6.3.5. Selective Catalytic NO_x Reduction

The established NO_x catalytic reduction approach for diesels in passenger cars and for most heavy-duty and off-road applications is selective catalytic reduction (SCR). Urea is generally the source of the ammonia (NH_3) used as the reducing agent in this catalyst system. SCR catalysts have a higher efficiency than LNT technology, though ongoing developments may change that ranking.

The overall system is complex and a typical layout is shown in Fig. 11.66.[87] The exhaust first passes through an oxidation catalyst (V) where the NO is largely oxidized to NO_2. A high NO_2/NO_x ratio entering the SCR catalyst (S) is important. The HC and CO in the exhaust as are also oxidized to CO_2 and H_2O. Urea $(NH_2)_2CO$ is injected into and mixes with the exhaust gases, and that mixture then passes through a hydrolysis catalyst (H)—the first part of the SCR system—where water in the exhaust reacts with the urea releasing ammonia (NH_3). The figure shows the overall chemical reactions that occur in each stage of the total process. The ammonia is the reducing agent in the SCR catalyst (S), which converts the NO_2 and NO in the mixture exiting the oxidation catalyst to N_2. The amount of NH_3 supplied via control of the urea flow is adjusted to provide a modest excess (up to 20%) above the amount required for the NO_2 and NO to be reduced to N_2. A final oxidation catalyst (O) then removes any excess NH_3 by oxidizing it to N_2.

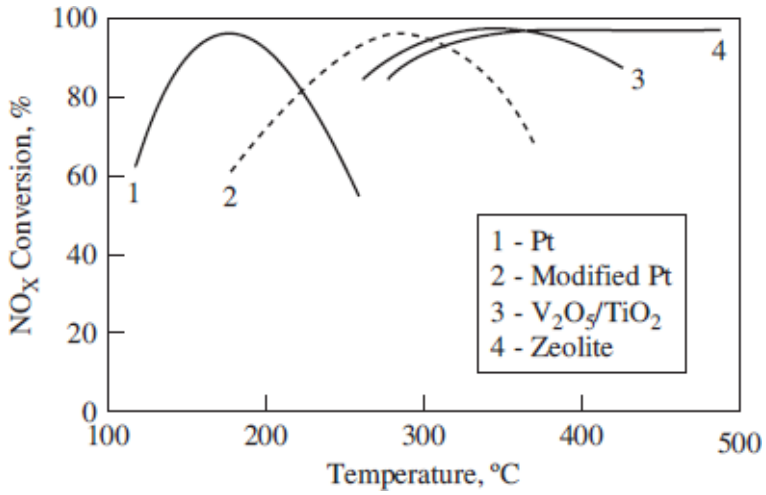
Figure 11.66 Layout of multi-component selective catalyst reduction system for NO_x reduction in a lean-operating diesel engine: oxidation catalyst (V); urea hydrolysis catalyst (H); SCR catalyst (S); oxidation catalyst (O). The overall chemical reactions are shown.[87]



© McGraw-Hill Education. All rights reserved. Any use is subject to the Terms of Use, Privacy Notice and copyright information.

The overall NO_x conversion efficiency is high over a specific operating temperature window that depends on the catalyst used, as is illustrated in Fig. 11.67. Platinum catalyst technology can only be used at temperatures below about 250°C due to its poor selectivity for NO_x reduction at higher temperatures. A vanadium catalyst with a titanium oxide carrier shows good efficiency up to above 500°C. These catalyst materials are resistant to sulfur and HC poisoning. Copper zeolite catalysts have been developed to the point where they show high efficiency (>95%) over a wide temperature range up to about 650°C. Iron zeolites are also used as an SCR catalyst, as are copper/iron combination zeolites. The results in Fig. 11.67 are illustrative, and development of this SCR catalyst technology is expanding their high-efficiency temperature windows.

Figure 11.67 Operating temperature windows for different SCR catalysts: NO_x conversion efficiencies as a function of catalyst temperature.[79]



Other factors of importance are the impact of the NH_3: NO_x ratio, the fraction of the NO_x that is NO_2, ammonia "slip" through the SCR system, the production of N_2O (a greenhouse gas of significance) and poisoning by sulfur and hydrocarbons. At temperatures above 300°C the NO_x conversion efficiency increases linearly with increasing NH_3: NO_x molar ratio, as expected, for the stoichiometric reaction between NO and NH_3. At lower temperatures, above a critical value of this ratio, the conversion efficiency increases little, and ammonia slip then occurs. Also, to achieve a high SCR catalyst deNO_x efficiency, it is desirable to over-inject urea. The excess NH_3 then needs to be oxidized to N_2 to prevent slip. Ammonia slip catalysts may be needed to convert this ammonia to N_2 (rather than NO_x and N_2O).

The effect of increasing NO_2 as a fraction of total NO_x depends on SCR catalyst temperature and space velocity. Increasing the NO_2/NO_x molar ratio to about 0.5 increases the low-temperature NO_x conversion activity and efficiency. At higher ratios, the high-temperature activity and the achievable NO_x conversion efficiency are significantly reduced. The higher NH_3 stoichiometry needed to convert NO_2 (1.33) compared to converting NO (1.0), and the slower reaction of NO_2 with NH_3 results in ammonia slip which must then be controlled.[87] A Pt upstream oxidation catalyst can increase the NO_2/NO_x ratio in the exhaust (which is typically 10 to 15% in diesel exhaust, as shown in Fig. 11.16) to over 80%, depending on the catalyst temperature.

Vanadia-based SCR catalysts are more tolerant to sulfur poisoning, and are used in world regions where fuel sulfur levels are higher. The sulfur accumulates in the top layer of the catalyst washcoat as ammonium sulfate. When heated to 500°C the SCR catalyst performance is recovered. Hydrocarbons can be absorbed on the catalyst surface at lower temperatures and then ignite at higher catalyst temperatures and, through the energy that releases, cause thermal deterioration of the catalyst surface.[88]

11.6.4. Particulate Filters or Traps

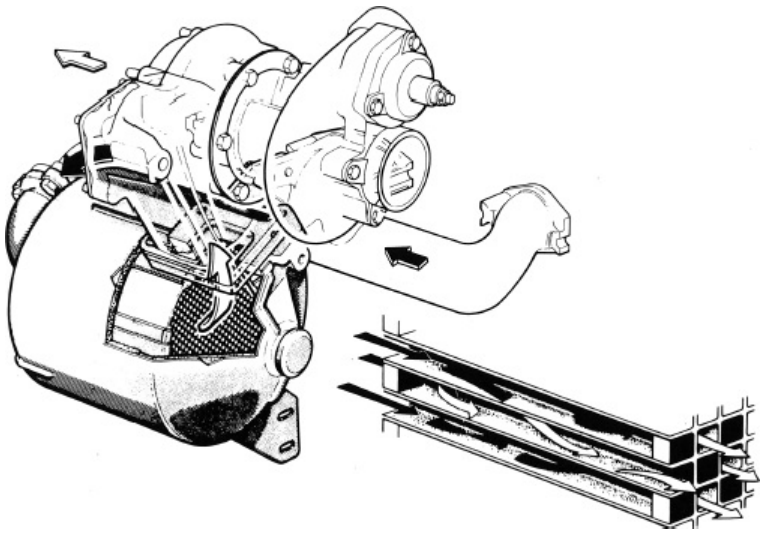
© McGraw-Hill Education. All rights reserved. Any use is subject to the Terms of Use, Privacy Notice and copyright information.

An exhaust treatment technology that substantially reduces engine particulate emissions is particulate filters or traps. A temperature-tolerant filter or trap removes the particulate material from the exhaust gas: the filter is then "cleaned off" by oxidizing the accumulated particulates—the regeneration process. Diesel particulate filters (DPF) are in common use. The technology can also be used on gasoline engines and may be needed on direct-injection gasoline engines since their particulate emissions are significantly higher than equivalent port-fuel-injected gasoline engine emissions, though lower than diesel engine-out levels.

The challenges to implementing particulate filter technology are many: (1) the filter, even when clean, increases the pressure in the engine exhaust manifold; (2) this pressure increase steadily rises as the filter collects particulate matter; (3) under normal diesel engine operating conditions, the collected particulate matter is not hot enough to spontaneously ignite and oxidize; and (4) once ignition of the filtered particulate matter occurs, the burn-up process must be controlled to prevent excessively high temperatures and trap damage or destruction. Particulate filters are now in production for light-duty automobile diesel engines as well as heavy-duty diesel engines.

Types of particulate filters include: wall-flow ceramic monoliths, sintered metal on stainless steel wire mesh, ceramic fiber woven (wound and knitted) silica. Each of these has different inherent pressure drop and filtering efficiency.[79] The majority of filters are ceramic wall-flow or fiber based, and most of these are wall-flow filters of the type shown in Fig. 11.68. Such wall-flow filters are based on monolith catalyst substrates where half the cells are plugged at the inlet end and the other half at the outlet end. Thus the exhaust gas is forced to flow through the porous ceramic walls. The thickness of these walls and their porosity are carefully controlled to provide good particulate filtration with a low enough pressure drop. The particle separation is effected by depositing the particles in the exhaust gases onto the filter surface. This generally occurs initially within the porous ceramic wall as various force fields hold the particles on the surfaces of the pores (depth filtration). Then, as the amount of filtered particulate builds up, a layer of particulate may collect on the channel wall surface which then acts as a sieve, further filtering out the particulate ("cake" filtration).

Figure 11.68 Ceramic monolith particulate filter mounted in the exhaust of a turbocharged automobile diesel engine.[89]

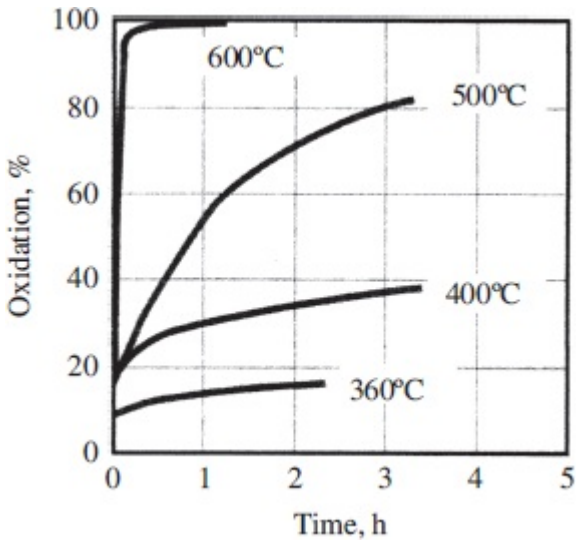


Due to the low packing density of diesel particulate (about 0.1 g/cm^3) such filters quickly accumulate considerable volumes of soot. The pressure drop across the DPF steadily increases as particulate matter accumulates, and to avoid excessively high pressures in the engine's exhaust manifold the filter must be regenerated. There are several approaches to filter regeneration. Thermal regeneration is the primary method: the solid particulates largely (soot) in the DPF are oxidized to CO_2 (and some H_2O). The rate of oxidation of soot is significantly lower than oxidation of gaseous emissions such as HC and CO: the reason that solid particulates are not oxidized in flow-through oxidation catalysts designed to remove gaseous pollutants is that they provide relatively short residence times (see Sec. 11.6.3). Diesel soot oxidation rates (under controlled conditions) are shown as a function of temperature in Fig. 11.69: temperatures above 500°C are required in the absence of catalysts. The

© McGraw-Hill Education. All rights reserved. Any use is subject to the Terms of Use, Privacy Notice and copyright information.

temperature of diesel exhaust gas is normally well below this level. So means for raising the exhaust gas temperature, or use of a catalyst to reduce the activation energy and achieve adequate oxidation rates at lower temperature, must be employed. The former is categorized as active regeneration and the latter as passive.

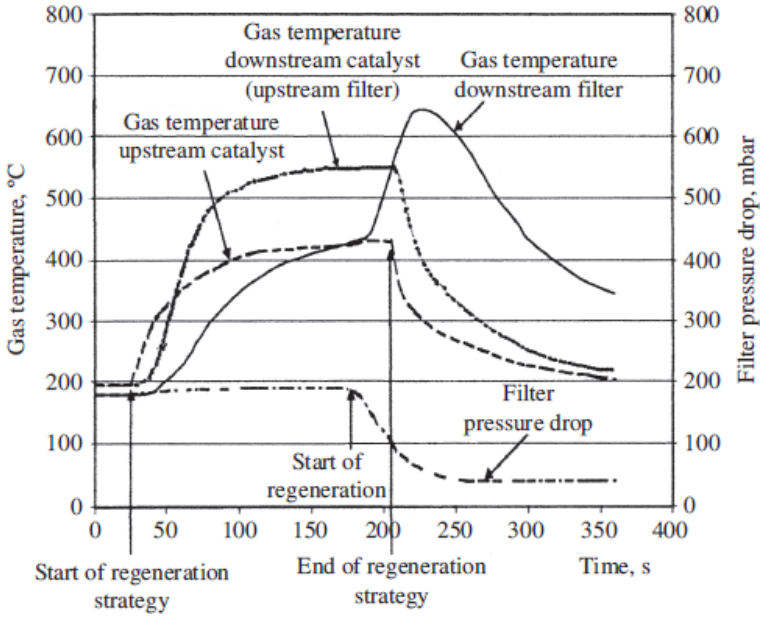
Figure 11.69 Diesel soot oxidation rates, as a function of temperature.[79]



Combinations of active and passive approaches have been explored and are being deployed. One such combination approach to regeneration is illustrated in Fig. 11.70 which shows a particulate filter regeneration process lasting about 200 s. The DPF system in this light-duty diesel vehicle consists of a filter (like that shown in Fig. 11.68) with a DOC in the exhaust system ahead of the DPF. The engine's common- rail fuel-injection system can provide three injection pulses: a pilot or pre-injection (to achieve a shorter ignition delay), a main injection (primarily responsible for generating bmep/torque), and a late or after injection well into the expansion process primarily to raise the exhaust gas temperature to initiate the particulate filter regeneration process. Figure 11.70 shows the start of regeneration at 25 seconds where late fuel injection occurs and the energy release from that fuel burning starts to raise the exhaust temperature above about 200°C. The DOC through additional oxidation of this third injected fuel pulse further raises the exhaust gas temperature downstream of the DOC and upstream of the filter. At 175 seconds, the soot in the filter starts oxidizing and releasing its chemical energy causing the filter exit gas temperature to rise sharply. As the soot within the DPF burns (following the start of regeneration), the filter pressure drop falls (bottom curve).

© McGraw-Hill Education. All rights reserved. Any use is subject to the Terms of Use, Privacy Notice and copyright information.

Figure 11.70 Example of exhaust gas temperature variation during particulate filter regeneration, passenger car diesel engine, under steady-state conditions.[90] Late injection increases exhaust gas temperature, lighting off the catalyst: soot burns and back pressure drops. Cerium, added to the fuel, is used to drop the regeneration temperature, catalytically.



In this DPF system, a cerium-based fuel additive is injected into the fuel tank in modest amounts: the ceria acts as a catalyst in the soot oxidation process within the filter allowing regeneration initiation to occur at about 400°C rather than at the higher temperatures (some 600°C; see Fig. 11.69) needed in the absence of a catalyst. Metal-based fuel additives, however, must be controlled for many reasons: stable catalytic activity, cost, environmental and health impacts, degradation of catalytic activity in the exhaust treatment system. A more permanent alternative to catalytic fuel additives is to build the catalyst into the filter surface, creating a more "passive" catalyzed particulate filter. These usually utilize platinum or base-metal catalyst materials. As in the DPF example described above, a thermal regeneration strategy is often employed as well to raise the exhaust gas temperature to the level at which the catalyzed filter initiates the soot oxidation process to achieve the required degree of control of trap or filter regeneration process.[79]

An alternative to using oxygen to oxidize the soot is to use NO_2 in a platinum-catalyzed DPF. The NO_2 is generated through use of an upstream oxidation catalyst from the nitric oxide (NO) which constitutes most (some 90%) of the NO_x in diesel exhaust gases. The NO_2 fraction, with an appropriate oxidation catalyst, can be increased to about three-quarters of the NO_x at temperatures of about 300°C. NO_2 is a sufficiently active soot oxidizing agent that the filter need not be catalyzed. However, the NO_2 is reduced to NO and not to N_2, so a deNO_x catalyst would have to follow the DPF in the total exhaust treatment system.

Control of the regeneration process is critical to the durability of filter systems. Whatever process is used for regeneration must be reliable and robust. The soot holding capacity of filter systems is typically several hours. While some DPF systems are designed to continuously regenerate (e.g., a catalyzed filter in an application where exhaust gas temperatures are relatively high), an active regeneration process once a day, or more often, may be the needed approach. The filtration efficiency[3] of DPFs (based on particulate mass) is 95 to close to 100% for soot (predominantly elemental carbon) and 50 to 90% for the absorbed SOF with the lower values for non-catalyzed filters. The overall efficiency for total PM is in the 70 to 95% range. Ash from the inorganic material in the lubricating oil and fuel is also trapped in the filter and is not burned-off in the regeneration process. Thus ash accumulates in the filter incrementally over time, causing a gradual increase in the filter pressure drop. Periodic "cleaning" of the filter of ash, every year or so, is required through washing with water or reverse gas flow through the filter walls to "unblock" the pores.[79]

Controlling the particulate and filter temperature during regeneration is a critical challenge. To start the regeneration process,

© McGraw-Hill Education. All rights reserved. Any use is subject to the Terms of Use, Privacy Notice and copyright information.

the temperature must be high enough to initiate the soot oxidation process. As explained above, for non-catalyzed filters this temperature is higher; for catalyzed filters it is lower. The PM oxidation process converts its chemical energy (soot, SOF, HCs) to thermal energy (these are exothermic reactions), which heats up the exhaust gases, the particulate matter, and the filter monolith structure. The change in within-filter temperatures depends on the rate of PM burning (which is strongly dependent on the exhaust gas and soot temperature), and the partitioning of the thermal energy thereby released between heating the exhaust gases, and the soot and the filter material. Thus, as shown in Fig. 11.70, the gas temperature downstream of the filter rises as the PM oxidation rate increases, reaches a maximum and then falls, as the soot is increasingly consumed and the rate of energy release falls. The filter pressure loss curve at the bottom of the figure indicates what the rate of PM burn-up actually is: it first increases and then decreases. Peak temperatures within the ceramic filter structure during regeneration must be limited to below about 1200°C due to ash sintering and reactions of the cordierite with the ash in the filter. At higher temperatures the cordierite itself may sinter and melt.

The high particulate trapping efficiencies of wall-flow DPFs have as a consequence a high-pressure drop. And, as the trapped PM builds up, that pressure drop increases substantially. The pressure drop has several components: the loss of pressure at the entrance and exit of the filter monolith due to the significant contraction and expansion that occurs; the pressure loss due to channel-wall flow friction; the pressure drop across the channel walls; and, of course, the additional channel wall pressure drop due to the steadily increasing particulate loading. The increase in pressure drop above that of a clean wall-flow filter initially rises rapidly as particulate is deposited in the ceramic wall pores, then rises steadily over time as particulate builds up as a layer on the wall surface. This building soot deposit layer constitutes the largest part of the pressure drop. The pressure drop across the channel walls with a clean filter is in the 1 to 2 kPa range; a moderately loaded filter has a pressure drop of some 10 kPa.[4] This pressure drop can be modeled quite accurately, and used as a signal that defines the extent of the DPFs particulate loading to trigger trap regeneration.

Particulate filters are now a practical and effective control technology that significantly reduces particulate emissions. In diesel engines almost two orders of magnitude reduction in particulate number density emissions can be achieved using a trap. The most important issues with such exhaust treatment devices are reliable filter regeneration with minimum impact on engine operation (especially any fuel consumption penalty), and their cost. Particulate filters could also be used effectively with DI gasoline engines (especially if these are stratified DI SI engines), but again, the additional cost of using this particulate emissions control technology, relative to in-cylinder particulate reduction is a critical factor.

11.6.5. Exhaust Treatment Systems

These specific catalyst and particulate trap devices need to be combined into an exhaust aftertreatment system since there are several different pollutants in engine exhaust gases whose concentrations need to be substantially reduced. In spark-ignition (gasoline) engines, the three main strictly-regulated air pollutants (especially in vehicles) are CO, hydrocarbons, and NO_x. To these have been added fine particulates which, while low in port-fuel-injection SI engines, are much higher in direct-injection gasoline engines. In diesel engines, the primary engine-out emissions needing major reduction are particulates and NO_x. Note also that the exhaust gas composition (relative *A/F* or fuel-air equivalence ratio) and exhaust gas temperature ranges for these two types of engines are substantially different. So we discuss each type of engine in turn.

11.6.5.1. Gasoline SI Engines

The predominant aftertreatment system incorporates three-way catalyst technology with stoichiometric engine operation, and oxygen (λ) exhaust-gas sensors for closed-loop fuel feedback control (see Sec. 7.8). Figure 11.71 illustrates, with schematics, the historical development of exhaust aftertreatment systems. First, Fig. 11.71a shows an early 1970s system with an oxidation catalyst to remove CO and HC. An option was to pump secondary air into the exhaust port to ensure sufficient oxygen was available when the engine operated fuel-rich to achieve complete CO and HC burn up. Then came three-way catalysts with a lambda sensor in the exhaust manifold to control the engine's relative air/fuel ratio to close to stoichiometric. For effective removal of the three pollutants CO, HC, and NO_x together, ceria was built into the TWC washcoat to ensure

© McGraw-Hill Education. All rights reserved. Any use is subject to the Terms of Use, Privacy Notice and copyright information.

sufficient oxygen storage so that the gas at the catalyst active surface sites was always at stoichiometric despite air-fuel ratio fluctuations within the engine itself.

Figure 11.71 Development of gasoline SI engine exhaust aftertreatment systems: (a) oxidation catalyst for CO and HC removal, late 1970s; (b) three-way catalyst system with exhaust oxygen sensor and fuel metering feedback control, 1980s; (c) close-coupled fast light-off catalyst (largely for cold engine HC control) and under-floor three-way catalyst for further HC, CO, and NO_x reduction, with close-mounted and downstream exhaust oxygen (λ) sensors for feedback engine control, and as a catalyst oxygen storage diagnostic.

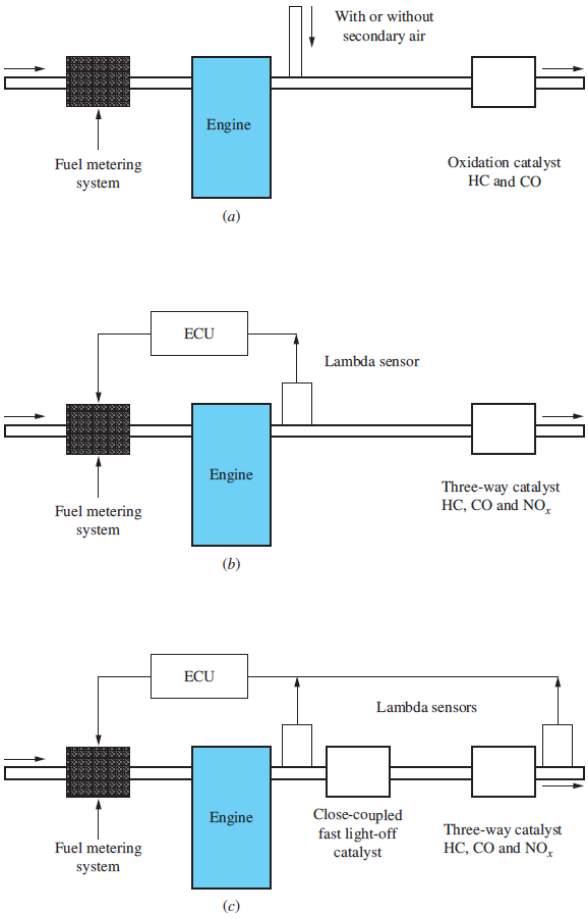


Figure 11.71c shows a more complex system with a close-coupled fast-light-off version of the three-way catalyst designed to heat up quickly following a cold start,. To limit HC emissions during starting and early warm up (see Fig. 11.33). Then a larger TWC (under the floor of a light-duty vehicle) completes the catalyst's HC, CO, NO_x clean up task. Some systems now use a larger, single, close-coupled fast-light-off three-way catalyst. As noted previously, very high catalyst efficiencies (about 98%) are now achieved with such systems. The two lambda sensors check whether the oxygen storage capability in the TWC is operating effectively. The upstream sensor follows the low-frequency (1-Hz) lambda oscillations (fuel-rich, then lean) that the engine fuel control system implements to maintain oxygen storage capacity so oxygen can be released or absorbed at the catalyst surface. The downstream sensor gives a steady non-oscillating signal when oxygen release or storage within the catalyst maintains the exhaust gases at stoichiometric.

Rapid light off of the close coupled catalyst during the early stages of engine warm up is usually achieved through low thermal inertia design, and use of substantial spark (i.e., combustion) retard for some 10 to 100 seconds following engine start up. Use of a fuel-rich mixture during engine starting, with secondary air added to the exhaust gases, with this spark retard, can be used to achieve a hotter exhaust through burning up the extra CO and HC emissions in the exhaust gases, in the exhaust port and manifold, prior to the catalyst location.

© McGraw-Hill Education. All rights reserved. Any use is subject to the Terms of Use, Privacy Notice and copyright information.

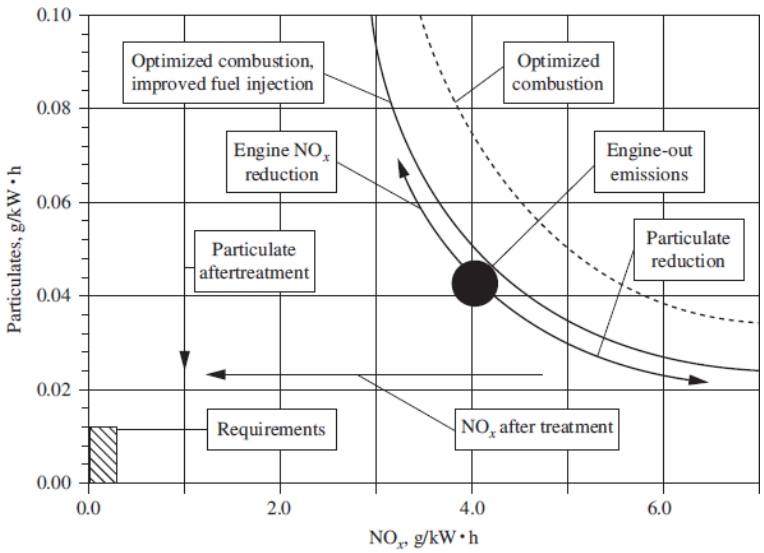
With turbocharged SI engines, the turbine is normally mounted close to the exhaust manifold exit to minimize loss of exhaust gas enthalpy prior to turbine entry, and shorten the turbocharger response time to increases in engine load. The insertion of the turbine into the exhaust system upstream of the close-coupled catalytic converter can lengthen the catalyst light-off time and thus worsen emissions. However, the turbine can withstand higher exhaust gas temperatures than can the three-way catalyst, so the negative impact can be partly offset by permitting higher exhaust gas enthalpy fluxes into the exhaust system.

11.6.5.2. Diesel Engines

Diesels always operate fuel lean: thus their exhaust gas temperatures are significantly lower than in gasoline SI engines. As a consequence of these factors, and that the primary pollutants of concern are NO_x (a gas which has to be reduced to N_2) and particulate matter (small particles with absorbed condensed hydrocarbons), the aftertreatment systems are more complex and require periodic regeneration.

The task of significantly reducing these two major diesel-engine air pollutants is spelled out in Fig. 11.72 where average test-cycle particulate emissions are plotted as a function of NO_x emissions, for a heavy-duty diesel engine. Implementation of engine emission control technologies (optimized combustion, low sulfur fuels, and EGR) reduces engine-out emissions to about 0.04 g/kW · h particulates and 4 g/kW · h NO_x. The emissions requirements in many parts of the world require additional reductions by a factor of 5 to 10 or so. Thus use of particulate traps and NO_x catalysts is essential.

Figure 11.72 Trade-off curves between particulates and NO_x emissions for a typical heavy-duty diesel engine (average test cycle values in g/kWh). Dark circle indicates typical engine-out levels with engine emission controls. Cross-hatched low PM and NO_x region indicates levels required to meet emissions regulations in the United States and Europe. Source: Ref. 87.



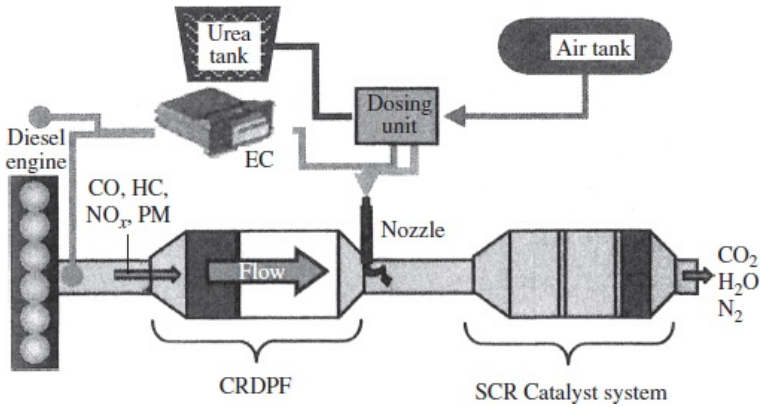
Diesel engines now require particulate traps which must be regenerated—the filtered particulate must be burned up. This can be done by raising the engine's exhaust gas temperature to initiate trap regeneration by injecting additional fuel late in the expansion stroke (see Fig. 11.70, and accompanying text) to raise the exhaust gas and trapped particulate temperatures so the particulate matter is burned up. (In the example shown, a fuel additive, ceria, was used to catalyze the particulate oxidation reactions.) Or the particulate filter surface may have embedded catalyst sites.

In both heavy-duty and many light-duty diesel engines, the principal NO_x aftertreatment control strategy is selective catalytic reduction (SCR), which adds urea, the source of the reducing agent ammonia, to the exhaust gases. Figure 11.73 shows an example of an aftertreatment system that reduces HC, CO, particulates, and NO_x emissions for a heavy-duty engine. The continuously regenerating diesel particulate filter (CRDPF) comprises an oxidation catalyst followed by a wall-flow particulate

© McGraw-Hill Education. All rights reserved. Any use is subject to the Terms of Use, Privacy Notice and copyright information.

filter. The oxidation catalyst oxidizes the engine-out HC and CO, and a portion of the NO to NO_2. NO_2 oxidizes the particulate in the filter at a much lower temperature (250°C). This lower temperature particulate oxidation by NO_2 allows passive and continuous particulate removal from the trap/filter surface.[91]

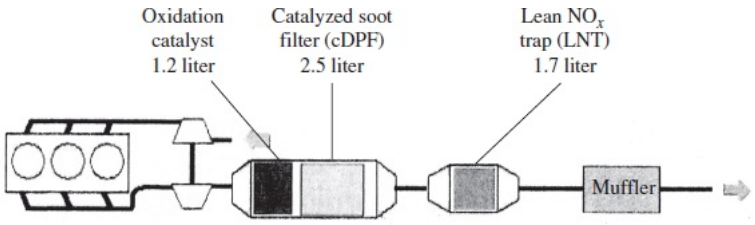
Figure 11.73 Layout of engine aftertreatment system embodying a continuously regenerating diesel particulate filter (CRDPF) and selective catalytic reduction (SCR) system, where the urea dispensing system shown provides the NO_x reducing agent, ammonia.[91]



The SCR system uses NH_3 derived from a urea solution via rapid hydrolysis in the "hydrolysis catalyst" section of the SCR device: see Fig. 11.66, and accompanying text.[87] Successful implementation requires matching the amount of urea injected to the amount of NO_x emitted from the engine. Two approaches are used: (1) a urea injection map based on engine operating information (essentially a map-based estimation of engine-out NO_x emissions) or (2) an NO_x sensor to give real time measurements of exhaust gas NO_x concentrations. The middle section of the SCR catalyst does the reduction of NO and NO_2 to N_2 with ammonia as the reducing agent. The final section (shown dark gray in Fig. 11.73) is an oxidation catalyst that oxidizes any excess NH_3 to N_2 (see Fig. 11.66). The layout of the urea tank, dosing control unit, air tank to provide the air stream that transports the urea through the injection nozzle into the engine's exhaust downstream of the CRDPF unit are also shown.

An alternative diesel exhaust aftertreatment approach is shown in Fig. 11.74 where a LNT is used for NO_x reduction in the diesel's fuel-lean exhaust gases.[92] The operation of the LNT is illustrated in Fig. 11.63 and discussed in the accompanying text. A catalyzed particulate filter, preceded by a DOC, is the first aftertreatment system device, followed by the LNT. The oxidation catalyst converts some of the NO to NO_2: the NO_2 is more effective at trap regeneration since it oxidizes the particulate (soot) at lower temperatures than does oxygen. Details of the engine enrichment strategy to regenerate the LNT, desulfurization challenges because of the difficulty in attaining high enough temperatures due to the significant thermal capacity in the catalyzed particulate filter upstream of the LNT, and the need to control component temperatures throughout the aftertreatment system, can be found in Ref. 92. An alternative to the layout shown is to place the LNT first, followed by the catalyzed particulate filter.

Figure 11.74 Layout of light-duty high-speed diesel aftertreatment system incorporating a catalyzed soot filter (cDPF) followed by a lean NO_x trap (LNT). The cDPF and the LNT both need to be periodically regenerated.[92]



© McGraw-Hill Education. All rights reserved. Any use is subject to the Terms of Use, Privacy Notice and copyright information.

Lean NO_x traps need to be regenerated (releasing the NO_2 and reducing the NO_x to N_2) about every 60 seconds: the duration of the rich regeneration phase is some 3 to 5 seconds. There is thus an engine fuel consumption penalty of several percent. The above approach is better suited to smaller high-speed DI diesels than to larger engines.

[1] While this choice of volume is not strictly correct, since it does not account for cell density or catalyst loading, it is straightforward to apply and is widely used.

[2] The engine efficiency decreases as the air/fuel ratio is reduced from very lean values to rich of stoichiometric.

[3] Filtration efficiency is the mass ratio of particulate collected in the filter to particulate entering the filter.

[4] 1 atmosphere is close to 100 kPa (1 bar).

© McGraw-Hill Education. All rights reserved. Any use is subject to the Terms of Use, Privacy Notice and copyright information.

11.7. PROBLEMS

11.1. Figure 11.2 shows concentrations of NO, CO, and HC in a spark-ignition engine exhaust as a function of the relative air/fuel ratio. Assume the concentration scale is parts per million. Explain the trends shown as the mixture is first made richer and then leaner than stoichiometric.

11.2. Figure 11.2 is for a spark-ignition engine. Construct a similar qualitative graph of NO, CO, and HC concentrations versus equivalence ratio for a direct-injection four-stroke cycle diesel engine. Explain your graphs.

11.3. A spark-ignition engine driving a car uses, on average, 120 grams of gasoline per mile traveled. The average emissions from the engine (upstream of the catalyst) are 1.5, 2, and 20 grams per mile of NO_x (as NO_2), HC, and CO, respectively. The engine operates with a stoichiometric gasoline-air mixture. Find the average concentrations in parts per million of NO, HC (as ppm C_1), and CO in the engine exhaust.

11.4. Calculate the average combustion inefficiency corresponding to the spark-ignition engine engine-out emissions levels given in Prob. 11.3. Include any hydrogen you estimate would be present in the exhaust stream.

11.5. A three-way catalytic converter is used with the spark-ignition engine in Prob. 11.3. For 10% of the driving time, the catalyst is cold and ineffective, and does not reduce the engine's emissions. For 90% of the time, the catalyst is hot and has conversion efficiencies as given in Fig. 11.62. Estimate for a cold catalyst and a hot catalyst, the average *vehicle* emissions of NO_x, HC, and CO in grams per mile.

11.6. Figure 15.18 shows the variation in NO and HC emissions as concentrations (ppm) in the exhaust of a spark-ignition engine as a function of speed and load. Convert these data to graphs of indicated specific NO and HC emissions (g/kW · h) versus speed and imep. Assume η_v (based on atmospheric air density) = imep (kPa) × 10^{-3}.

11.7. Use the data in the figure to estimate:

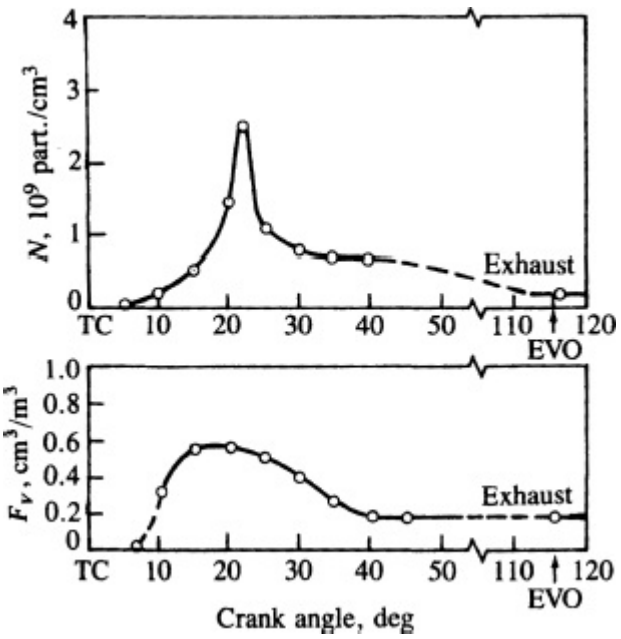
a. The exhaust particulate emissions as a fraction of the maximum particulate loading during the cycle.

b. The maximum measured soot loading and the exhaust soot loading as fractions of the fuel carbon.

c. The equivalent sphere size of each soot particle at the number density peak (22° ATC) and in the exhaust.

Assume a particulate density of 2 g/cm^3. Note that the gas volumes in the figure are determined at standard temperature and pressure.

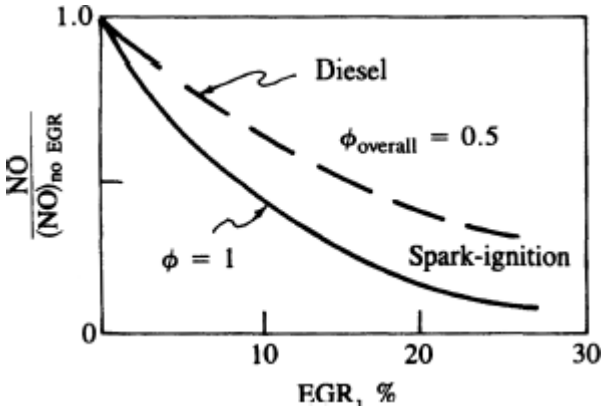
© McGraw-Hill Education. All rights reserved. Any use is subject to the Terms of Use, Privacy Notice and copyright information.



11.8. Explain the following emissions trends. Highest marks will be given for succinct summaries of the *important* technical issues.

a. Nitric oxide (NO) emissions from diesels and spark-ignition engines as the relative air/fuel ratio, or fuel/air equivalence ratio ϕ, is varied show significantly different behavior (see Figs. 11.8 and 11.16). Redraw these graphs on the same plot and explain the different trends for these two types of engines as ϕ decreases on the lean side of stoichiometric.

b. Recirculation of a fraction of the exhaust gases to the intake is used to control engine nitric oxide emissions at part load. Exhaust gas recycle is usually more effective with spark-ignition engines than with diesels, as shown in the figure. Explain why these trends are different.



c. Brake-specific particulate emissions from diesels are a major problem. Particulate emissions from port fuel injected spark-ignition engines are not that important. Briefly explain why the particulate emission levels from these two types of engines are so different in magnitude.

d. Diesels have low carbon monoxide (CO) emissions. Spark-ignition engine CO emissions when *averaged* over a typical urban automobile trip (cold engine start, warm-up, cruise, idle, acceleration, etc.) are substantial and require an oxidation catalyst for effective control. Explain this difference in average CO emissions (upstream of any catalyst) from these two types of engines.

11.9. The following questions refer to an engine with these geometric and operating characteristics: ϕ = 1.0, compression ratio = 8:1, bore = 85 mm, stroke = 85 mm, piston diameter above top ring = 84.4 mm, distance from piston crown top to top ring = 10 mm, volumetric efficiency = 0.8, temperature in cylinder at the start of compression = 333 K,

© McGraw-Hill Education. All rights reserved. Any use is subject to the Terms of Use, Privacy Notice and copyright information.

pressure in cylinder at start of compression = 1 bar, mixture temperature before entering cylinder = 30°C, brake-specific fuel consumption = 300 g/kW · h.

A substantial fraction of spark-ignition engine hydrocarbon emissions comes from the crevice between the piston crown and cylinder wall. Gas is forced into this crevice as the cylinder pressure increases and flows out of this crevice as the cylinder pressure decreases. The gas in the crevice can be assumed to be at the wall temperature, 400 K. The gas pushed into the crevice ahead of the flame is unburned mixture; the gas pushed in behind the flame is burned mixture. About two-thirds of the crevice gas is unburned. The maximum cylinder pressure is 3 MPa (see sketch below).

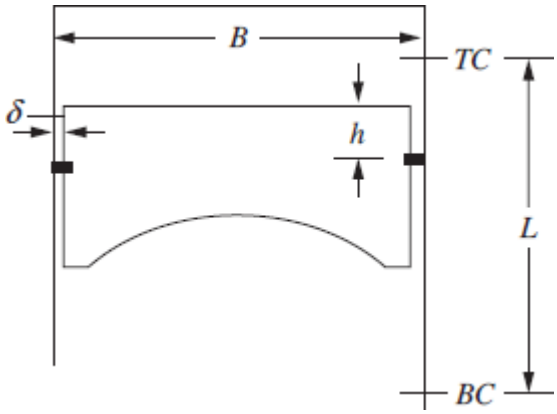
a. Derive an expression for the fraction of the cylinder charge which is contained in this piston crevice region at crank angle of maximum cylinder pressure ($\theta_{p\ \max}$) in terms of (δ/B), (h/L), the cylinder volume $p_{\max}$, V_{cyl} ($\theta_{p\ \max}$), the clearance volume V_c, $T_{-\text{cyl}}$ ($\theta_{p\ \max}$) the mean cylinder-gas temperature at $\theta_{p\ \max}$, and wall temperature T_w. Assume that the pressure in the crevice equals the pressure in the cylinder and that the temperature of the gas in the crevice equals the wall temperature T_w.

b. Calculate the mass fraction of the cylinder gas which is in the crevice between the piston and cylinder wall and above the first piston ring, at the time of peak pressure when the average in-cylinder gas temperature is 2400 K.

c. Assuming that half of the unburned fuel in this region is oxidized within the cylinder and a further one-third is oxidized in the exhaust port, calculate the engine-out HC emissions from this source in parts per million (ppm C_1) by volume.

d. Estimate the ratio of brake-specific hydrocarbon emissions to brake-specific fuel consumption.

e. The vehicle exhaust HC emissions with this engine are 0.1 g/mile; the gasoline consumption is 25 miles per gallon. The catalyst efficiency for HC is 0.96. What percentage of the engine HC emissions is from the crevice?



11.10. Nitric oxide, NO, forms via reactions (11.1) to (11.3). Reaction (11.1) is "slow" and reactions (11.2) and (11.3) are "fast," so the initial rate of formation of NO is given by Eq. (11.8):

$$\frac{d[\mathrm{NO}]}{dt} = 2k_1^+[\mathrm{N_2}]_e[\mathrm{O}]_e$$

where [ ] denote concentrations in gram-moles per cubic centimeter,
k_1^+ is the rate constant for reaction (11.1), and the factor of 2 enters because the N atom formed in (11.1) immediately reacts via (11.2) or (11.3) to give an additional NO molecule:

$$k_1^+ = 7.6 \times 10^{13} \exp\left(\frac{-38{,}000}{T}\right) \mathrm{cm^3/gmol \cdot s}$$

where T is in kelvins.

© McGraw-Hill Education. All rights reserved. Any use is subject to the Terms of Use, Privacy Notice and copyright information.

Using the equilibrium composition data provided for mole fraction atomic oxygen (O), molecular nitrogen (N_2), and nitric oxide (NO):

a. Plot the formation rate of NO as a function of the equivalence ratio at 3000 K and 5.5 MPa, and as a function of temperature for a stoichiometric mixture at 5.5 MPa pressure.

b. Estimate approximately the time taken to reach equilibrium NO levels at ϕ = 1, 2750 K and 3000 K, 5.5 MPa pressure.

c. If the stoichiometric mixture inducted into the engine reaches 3000 K and 5.5 MPa after combustion, in the absence of any exhaust gas recirculation, estimate the percentage of the exhaust that must be recycled to the intake (at the initial intake temperature) to reduce the NO formation rate by a factor of 4 (assume the final pressure 5.5 MPa stays the same; of course, the final temperature decreases as the exhaust gas is recycled).

	p = 5.5 MPa			ϕ = 1.0, p = 5.5 MPa			
		Mole fraction			Mole fraction		
ϕ	T (K)	O	N_2	T (K)	O	N_2	NO
0.9	3000	2.1×10^{-3}	0.73	2500	6×10^{-5}	0.73	–
1.0	3000	1.5×10^{-3}	0.73	2750	5×10^{-4}	0.73	4×10^{-3}
1.11	3000	1×10^{-3}	0.73	3000	1.5×10^{-3}	0.73	8×10^{-3}

11.11. The following data relate to a 2-liter gasoline engine operating at stoichiometric conditions at wide-open throttle and 2500 rev/min.

$$\dot{m}_{\text{air}} = 42\,\text{g/s};\ \dot{m}_{\text{fuel}} = 2.8\,\text{g/s}$$

and the exhaust gas composition was:

$$x_{CO_2} = 0.114;\ x_{CO} = 0.0114;\ x_{H_2O} = 0.120;\ x_{H_2} = 0.0057;\ x_{O_2} = 0.0142;\ x_{CH_2} = 0.0038;\ x_{N_2} = 0.731$$

This exhaust then flows steadily through an oxidizing catalyst system where the species in the engine exhaust that are not fully oxidized then oxidize completely. The exhaust gas temperature entering the catalyst is 700 K. The extensive surface area of the catalyst maintains the local catalyst and gas temperatures essentially the same as the exhaust flows through the catalyst, and its remaining chemical energy is released. Show that there is enough oxygen for complete oxidation of the exhaust gases, and calculate the temperature of the exhaust gas as it leaves the catalyst, neglecting any heat losses to the outside environment. The specific heat, c_p, of the exhaust gas is 1.28 kJ/kg·K.

© McGraw-Hill Education. All rights reserved. Any use is subject to the Terms of Use, Privacy Notice and copyright information.

11.8. REFERENCES

1. Bowman, C. T.: "Kinetics of Pollutant Formation and Destruction in Combustion," *Prog. Energy Combust. Sci.,* vol. 1, pp. 33–45, 1975.
2. Lavoie, G. A., Heywood, J. B., and Keck, J. G: "Experimental and Theoretical Investigation of Nitric Oxide Formation in Internal Combustion Engines," *Combust. Sci. Technol.,* vol. 1, pp. 313–326, 1970.
3. Heywood, J. B., Fay, J. A., and Linden, L. H.: "Jet Aircraft Air Pollutant Production and Dispersion,"*AIAA J.,* vol. 9, no. 5, pp. 841–850, 1971.
4. Newhall, H. K., and Shahed, S. M.: "Kinetics of Nitric Oxide Formation in High-Pressure Flames," in*Proceedings of Thirteenth International Symposium on Combustion,* pp. 381–390, The Combustion Institute, Pittsburgh, 1971.
5. Hilliard, J. C, and Wheeler, R. W.: "Nitrogen Dioxide in Engine Exhaust," SAE paper 790691,*SAE Trans.,* vol. 88, 1979.
6. Merryman, E. L., and Levy, A.: "Nitrogen Oxide Formation in Flames: The Roles of NO_2 and Fuel Nitrogen," in *Proceedings of Fifteenth International Symposium on Combustion,* p. 1073, The Combustion Institute, Pittsburgh, 1975.
7. Komiyama, K., and Heywood, J. B.: "Predicting NO_x Emissions and Effects of Exhaust Gas Recirculation in Spark-Ignition Engines," SAE paper 730475, *SAE Trans.,* vol. 82, 1973.
8. Alperstein, M., and Bradow, R. L.: "Exhaust Emissions Related to Engine Combustion Reactions," SAE paper 660781,*SAE Trans.,* vol. 75, 1966.
9. Starkman, E. S., Stewart, H. E., and Zvonow, V. A.: "Investigation into Formation and Modification of Exhaust Emission Precursors," SAE paper 690020, 1969.
10. Lavoie, G. A.: "Spectroscopic Measurement of Nitric Oxide in Spark-Ignition Engines," *Combust. Flame,* vol. 15, pp. 97–108, 1970.
11. Blumberg, P., and Kummer, J. K.: "Prediction of NO Formation in Spark-Ignition Engines—An Analysis of Methods of Control," *Combust. Sci. Technol.,* vol. 4, pp. 73–96, 1971.
12. Sakai, Y., Miyazaki, H., and Mukai, K.: "The Effect of Combustion Chamber Shape on Nitrogen Oxides," SAE paper 730154, 1973.
13. Quader, A. A.: "Why Intake Charge Dilution Decreases Nitric Oxide Emission from Spark Ignition Engines," SAE paper 710009, *SAE Trans.,* vol. 80, 1971.
14. Benson, J. D., and Stebar, R. F.: "Effects of Charge Dilution on Nitric Oxide Emission from a Single-Cylinder Engine," SAE paper 710008, *SAE Trans.,* vol. 80, 1971.
15. Toda, T., Nohira, H., and Kobashi, K.: "Evaluation of Burned Gas Ratio (BGR) as a Predominant Factor to NO_x," SAE paper 760765, *SAE Trans.,* vol. 85, 1976.
16. Lavoie, G. A., and Blumberg, P. N.: "A Fundamental Model for Predicting Fuel Consumption, NO_x and HC Emissions of the Conventional Spark-Ignited Engine," *Combust. Sci. Technol,* vol. 21, pp. 225–258, 1980.
17. Lavoie, G. A., and Blumberg, P. N.: "Measurements of NO Emissions from a Stratified Charge Engine: Comparison of Theory and Experiment," *Combust. Sci. Technol,* vol. 8, p. 25, 1973.
18. Akinyemi, O. E., and Cheng, W. K., "A Flame Sheet Model for NO Production in Diesel Combustion Simulation," SAE paper 982586, 1998.

© McGraw-Hill Education. All rights reserved. Any use is subject to the Terms of Use, Privacy Notice and copyright information.

19. Vioculescu, I. A., and Borman, G. L.: "An Experimental Study of Diesel Engine Cylinder-Averaged NO_x Histories," SAE paper 780228, *SAE Trans.,* vol. 87, 1978.
20. Aoyagi, Y., Kamimoto, T., Matsui, Y., and Matsuoka, S.: "A Gas Sampling Study on the Formation Processes of Soot and NO in a DI Diesel Engine," SAE paper 800254, *SAE Trans.*, vol. 89, 1980.
21. Yu, R. C., and Shahed, S. M.: "Effects of Injection Timing and Exhaust Gas Recirculation on Emissions from a D.I. Diesel Engine," SAE paper 811234, *SAE Trans.,* vol. 90, 1981.
22. Dickey, D. W., Ryan III, T. W., and Matheaus, A. C., "NO_x Control in Heavy-Duty Diesel Engines—What is the Limit?" SAE paper 980174, 1998.
23. Plee, S. L., Ahmad, T., and Myers, J. P.: "Diesel NO_x Emissions—A Simple Correlation Technique for Intake Air Effects," in *Proceedings of Nineteenth International Symposium on Combustion,* pp. 1495–1502, The Combustion Institute, Pittsburgh, 1983.
24. Ahmad, T., and Plee, S. L.: "Application of Flame Temperature Correlations to Emissions from a Direct-Injection Diesel Engine," SAE paper 831734, *SAE Trans.,* vol. 92, 1983.
25. Harrington, J. A., and Shishu, R. C: "A Single-Cylinder Engine Study of the Effects of Fuel Type, Fuel Stoichiometry, and Hydrogen-to-Carbon Ratio and CO, NO, and HC Exhaust Emissions," SAE paper 730476, 1973.
26. Newhall, H. K.: "Kinetics of Engine-Generated Nitrogen Oxides and Carbon Monoxide," in *Proceedings of Twelfth International Symposium on Combustion,* pp. 603–613, Mono of Maryland, 1968.
27. Delichatsios, M. M.: "The Kinetics of CO Emissions from an Internal Combustion Engine," S.M. Thesis, Department of Mechanical Engineering, MIT, Cambridge, MA, June 1972.
28. Jackson, M. W.: "Analysis for Exhaust Gas Hydrocarbons—Nondispersive Infrared Versus Flame-Ionization,"*J. Air Pollution Control Ass.,* vol. 16, p. 697–702, 1966.
29. Jackson, M. W.: "Effect of Catalytic Emission Control on Exhaust Hydrocarbon Composition and Reactivity," SAE paper 780624, *SAE Trans.,* vol. 87, 1978.
30. Carter, W. P. L.: *Updated Maximum Incremental Reactivity Scale and Hydrocarbon Bin Reactivities for Regulatory Applications,* Report to California Air Resources Board (Contract 07-339), University of California, Riverside, CA, January 28, 2010.
31. Lavoie, G. A.: "Correlations of Combustion Data for S.I. Engine Calculations—Laminar Flame Speed, Quench Distance and Global Reaction Rates," SAE paper 780229, *SAE Trans.,* vol. 87, 1978.
32. Smith, P., Cheng, W. K., and Heywood, J. B.: "Crevice Volume Effect on Spark Ignition Engine Efficiency," SAE paper 2014-01-2602, 2014.
33. Kaiser, E. W., Adamczyk, A. A., and Lavoie, G. A.: "The Effect of Oil Layers on the Hydrocarbon Emissions Generated During Closed Vessel Combustion," in *Proceedings of Eighteenth International Symposium on Combustion,* pp. 1881–1890, The Combustion Institute, Pittsburgh, 1981.
34. Cheng, W. K., Hamrin, D., Heywood, J. B., Hochgreb, S., Min, K., and Norris, M.: "An Overview of Hydrocarbon Emissions Mechanisms in Spark-Ignition Engines," SAE paper 932708, *SAE Trans.,* vol. 102, 1993.
35. Amann, C. A.: "Control of the Homogeneous-Charge Passenger-Car Engine—Defining the Problem," SAE paper 801440, 1980.
36. Tabaczynski, R. J., Heywood, J. B., and Keck, J. C: "Time-Resolved Measurements of Hydrocarbon Mass Flow Rate in the Exhaust of a Spark-Ignition Engine," SAE paper 720112, *SAE Trans.,* vol. 81, 1972.
37. LoRusso, J. A., Lavoie, G. A., and Kaiser, E. W.: "An Electrohydraulic Gas Sampling Valve with Application to Hydrocarbon Emissions Studies," SAE paper 800045, *SAE Trans.,* vol. 89, 1980.

© McGraw-Hill Education. All rights reserved. Any use is subject to the Terms of Use, Privacy Notice and copyright information.

38. Namazian, M., and Heywood, J. B.: "Flow in the Piston-Cylinder-Ring Crevices of a Spark-Ignition Engine: Effect on Hydrocarbon Emissions, Efficiency and Power," SAE paper 820088, *SAE Trans.,* vol. 91, 1982.

39. Furuhama, S., and Tateishi, Y.: "Gases in Piston Top-Land Space of Gasoline Engine," *Trans. SAE J.,* no. 4, 1972.

40. Bignion, E., and Spicher, U.: "Investigation of the Influence of Top Land Crevice Geometry on Hydrocarbon Emissions from SI Engines," SAE paper 982560, 1998.

41. Adamczyk, A. A., Kaiser, E. W., and Lavoie, G. A.: "A Combustion Bomb Study of the Hydrocarbon Emissions from Engine Crevices," *Combust. Sci. Technol.,* vol. 33, pp. 261–277, 1983.

42. Wentworth, J. T.: "Piston and Ring Variables Affect Exhaust Hydrocarbon Emissions," SAE paper 680109,*SAE Trans.,* vol. 77, 1968.

43. Kaiser, E. W., LoRusso, J. A., Lavoie, G. A., and Adamczyk, A. A.: "The Effect of Oil Layers on the Hydrocarbon Emissions from Spark-Ignited Engines," *Combust. Sci. TechnoL,* vol. 28, pp. 69–73, 1982.

44. McGeehan, J. A.: "A Literature Review of the Effects of Piston and Ring Friction and Lubricating Oil Viscosity on Fuel Economy," SAE paper 780673, *SAE Trans.,* vol. 87, 1978.

45. Shin, K., Tateishi, Y., and Furuhama, S.: "Measurement of Oil-Film-Thickness between Piston Ring and Cylinder," SAE paper 830068, *SAE Trans.,* vol. 92, 1983.

46. Ishizawa, S., and Takagi, Y.: "A Sudy of HC Emission from a Spark-Ignition Engine (the Influence of Fuel Absorbed into Cylinder Lubricating Oil Film), *JSME Int. J.*, vol. 30, no. 260, pp. 310–317, 1987.

47. Gatellier, B., Trapy, J., Herrier, D., and Quelin, J.: "Hydrocarbon Emissions of SI Engines as Influenced by Fuel Absorption-Desorption in Oil Films," SAE paper 920095, 1992.

48. Kaiser, E., Siegl, N., and Russ, S.: "Fuel Composition Effects on Hydrocarbon Emissions from a Spark-Ignited Engine," SAE paper 952542, 1995.

49. Frottier, V., Heywood, J. B., and Hochgreb, S.: "Measurement of Gasoline Absorption into Engine Lubricating Oil," SAE paper 961229, in *Engine and Gear Lubricants (SP-1183).*

50. Tondelli, G., Carriero, M., and Pedicillo, A.: "Combustion Chamber Deposits: Fuel and Lubricant Effects on Exhaust Hydrocarbon Emissions Measured by Fast FID Analyzer," SAE paper 2000-01-2024, 2000.

51. Valtadoros, T. H., Wong, V. W., and Heywood, J. B.: "Fuel Additive Effects on Deposit Build-Up and Engine Operating Characteristics," ACS Preprints, Vol. 36, No. 1, Symposium on Fuel Composition/Deposit Formation Tendencies, Division of Petroleum Chemistry, American Chemical Society, 1991.

52. Cheng, C.-O., Cheng, W. K., Heywood, J. B., Maroteaux, D., and Collings, N.: "Intake Port Phenomena in a Spark-Ignition Engine at Part Load," SAE paper 912401, *SAE Trans.*, vol. 100, 1991.

53. Landsberg, G. B., Heywood, J. B., and Cheng, W. K.: "Contribution of Liquid Fuel to Hydrocarbon Emissions in Spark Ignition Engines," SAE paper 2001-01-3587, *SAE Trans.*, vol. 110, 2001.

54. Fox, J. W., Min, K.-D., Cheng, W. K., and Heywood, J. B.: "Mixture Preparation in a SI Engine with Port Fuel Injection During Starting and Warm-Up," SAE paper 922170, *SAE Trans.*, vol. 101, 1992.

55. Costanzo, V., and Heywood, J. B.: "Effect of In-Cylinder Liquid Fuel Films on Engine-Out Unburned Hydrocarbon Emissions for an SI Engine," SAE paper 2012-01-1712, 2012.

56. Zhao, F., Harrington, D. L., and Lai, M.-C.: *Automotive Gasoline Direct-Injection Engines,* SAE, 2002.

57. Daniel, W. A.: "Why Engine Variables Affect Exhaust Hydrocarbon Emission," SAE paper 700108,*SAE Trans.,* vol. 79, 1970.

© McGraw-Hill Education. All rights reserved. Any use is subject to the Terms of Use, Privacy Notice and copyright information.

58. Ekchian, A., Heywood, J. B., and Rife, J. M.: "Time Resolved Measurements of the Exhaust from a Jet Ignition Prechamber Stratified Charge Engine," SAE paper 770043, *SAE Trans.,* vol. 86, 1977.

59. Lee, D., and Heywood, J. B.: "Effects of Secondary Air Injection During Cold Start of SI Engines," SAE paper 2010-01-2124, *SAE Journal of Engines*, V119-3EJ, December 2010.

60. Greeves, G., Khan, I. M., Wang, C. H. T., and Fenne, I.: "Origins of Hydrocarbon Emissions from Diesel Engines," SAE paper 770259, *SAE Trans.,* vol. 86, 1977.

61. Schaberg, P., Zarling, D. D., Waytulonis, R. W., and Kittleson, D. B.: "Exhaust Particle Number and Size Distributions with Conventional and Fischer-Tropsch Diesel Fuels," SAE paper 2002-01-2727, 2002.

62. Cadle, S. H., Nebel, G. J., and Williams, R. L.: "Measurements of Unregulated Emissions from General Motors' Light-Duty Vehicles," SAE paper 790694, *SAE Trans.,* vol. 88, 1979.

63. Bosch, R.: *Automotive Handbook*, 8th edition, Robert Bosch GmbH, SAE, 2011.

64. Baumgard, K. J., and Johnson, J. H.: "The Effect of Fuel and Engine Design on Diesel Exhaust Particle Size Distributions," SAE paper 960131, 1996.

65. Ladommatos, N., Balian, R., Horrocks, R., and Cooper, L.: "The Effect of Exhaust Gas Recirculation on Soot Formation in a High-Speed Direct-Injection Diesel Engine," SAE paper 960841, 1996.

66. Miller, A., Ahlstrand, G., Kittleson, D., and Jachanah, M.: "The Fate of Metal (Fe) during Diesel Combustion: Morphology, Chemistry, and Formation Pathways of Nanoparticles," *Combust. Flame, vol.* 149, pp. 129–143, 2007.

67. Amann, C. A., and Siegla, D. C.: "Diesel Particulates—What They Are and Why,"*Aerosol Sci. Technol.,* vol. 1, pp. 73–101, 1982.

68. Lahaye, J., and Prado, G.: "Morphology and Internal Structure of Soot and Carbon Blacks," in *Particulate Carbon Formation during Combustion,* D. C. Siegla and G. W. Smith (eds), pp. 33–55, Plenum Press, New York, 1981.

69. Smith, O. I.: "Fundamentals of Soot Formation in Flames with Application to Diesel Engine Particulate Emissions,"*Prog. Energy Combust. Sci.,* vol. 7, pp. 275–291, 1981.

70. Heywood, J. B., and Sher, E.: *The Two-Stroke Cycle Engine,* Taylor & Francis, Philadelphia, and SAE, 1999.

71. Flynn, P., Durrett, R., Hunter, G., zur Loye, A., Akinyemi, O., Dec, J., and Westbrook, C., et al.: "Diesel Combustion: An Integrated View Combining Laser Diagnostics, Chemical Kinetics, and Empirical Validation," SAE paper 1999-01-0509, 1999.

72. Haynes, B. S., and Wagner, H. G.: "Soot Formation,"*Prog. Energy Combust. Sci.,* vol. 7, pp. 229–273, 1981.

73. Park, C., and Appleton, J. P.: "Shock-Tube Measurements of Soot Oxidation Rates,"*Combust. Flame,* vol. 20, pp. 369–379, 1973.

74. Amann, C. A., Stivender, D. L., Plee, S. L., and MacDonald, J. S.: "Some Rudiments of Diesel Particulate Emissions," SAE paper 800251, *SAE Trans.,* vol. 89, 1980.

75. Otto, K., Sieg, M. H., Zinbo, M., and Bartosiewicz, L.: "The Oxidation of Soot Deposits from Diesel Engines," SAE paper 800336, *SAE Trans.,* vol. 89, 1980.

76. Fenimore, C.P., and Jones, G.W.: "Oxidation of Soot by Hydroxy Radicals," *The Journal of Physical Chemistry*, vol. 71, no. 3, 1967.

77. Kittleson, D. B., Sun, R., Blackshear, Jr., P. L., and Brehob, D. D.: "Oxidation of Soot Agglomerates in a Direct Injection Diesel Engine," SAE paper 920111, 1992.

78. Heck, R. M., and Farrauto, R. J.: *Catalytic Air Pollution Control,* Van Nostrand Reinhold, New York, 1995.

© McGraw-Hill Education. All rights reserved. Any use is subject to the Terms of Use, Privacy Notice and copyright information.

79. Majewski, W. A., and Khair, M. K.: *Diesel Emissions and their Control,* SAE International, 2006.

80. Takada, T., Itoh, H., and Yaegashi, T.: "Study of Divided Converter Catalytic System Satisfying Quick Warm Up and High Heat Resistance," SAE paper 960797, 1996.

81. Kummer, J. T.: "Catalysts for Automobile Emission Control," *Prog. Energy Combust. Sci.,* vol. 6, pp. 177–199, 1981.

82. Hammerle, R., and Truex, T.: "The Kinetics of SO_2 Oxidation for Various Catalyst Compositions," SAE paper 760090, 1976.

83. Eastwood, P.: *Critical Topics in Exhaust Gas Aftertreatment,* Research Studies Press Ltd., England, 2000.

84. Yoshida, T., Sato, A., Suzuki, H., Tanabe, T., and Takahashi, N.: "Development of High Performance Three-Way-Catalyst," SAE paper 2006-01-1061, 2006.

85. Harada, J., Tomita, T., Mizuno, H., Mashiki, Z., and Ito, Y.: "Development of Direct Injection Gasoline Engine," SAE paper 970540, 1997.

86. Johnson, T.V., "Vehicular Emissions in Review," SAE paper 2012-01-0368, *SAE Int., J. Engines*, vol. 5, pp. 216–234, 2012.

87. Gieshoff, J., Schafer-Sindinger, A., Spurk, P. C., van den Tillaart, A. A., and Garr, G.: "Improved SCR Systems for Heavy Duty Applications," SAE paper 2001-01-0189, in *Diesel Exhaust Aftertreatment 2000-2007*, M. Khair and F. Millo (eds), *SAE Int.*, 2008.

88. Johnson, T. V.: "Vehicular Emissions in Review," SAE paper 2013-01-0538, *SAE Int.*, *J. Engines*, vol. 6, no. 2, pp. 699–715, 2013.

89. Abthoff, J., Schuster, H., Langer, H., and Loose, G.: "The Regenerable Trap Oxidizer—An Emission Control Technique for Diesel Engines," SAE paper 850015, 1985.

90. Salvat, O., Marez, P., and Belot, G.: "Passenger Car Serial Application of a Particulate Filter System on a Common Rail Direct Injection Diesel Engine," SAE paper 2000-01-0473, 2000.

91. Conway, R., Chatterjee, S., Beavan, A., Goersmann, C., and Walker, A.: "NO_x and PM Reduction Using Combined SCR and DPF Technology in Heavy Duty Diesel Applications," SAE paper 2005-01-3548, in *Diesel Exhaust Aftertreatment 2000-2007,* J. Khair and F. Millo (eds), SAE, 2008.

92. Herrmuth, H., Cartus, T., Ducellari, R., and Derschmidt, O.: "Combined NO_x and PM Exhaust Gas Aftertreatment Approaches for HSDI Diesel Engines," SAE paper 2004-01-1425, in *Diesel Exhaust Aftertreatment 2000-2007,* M. Khair and F. Millo (eds), SAE, 2008.

© McGraw-Hill Education. All rights reserved. Any use is subject to the Terms of Use, Privacy Notice and copyright information.

12.0. CHAPTER PRELIMINARIES

IMPORTANCE OF HEAT TRANSFER

MODES OF HEAT TRANSFER

HEAT TRANSFER AND ENGINE ENERGY BALANCE

CONVECTIVE HEAT TRANSFER

RADIATIVE HEAT TRANSFER

MEASUREMENTS OF INSTANTANEOUS HEAT-TRANSFER RATES

THERMAL LOADING AND COMPONENT TEMPERATURES

PROBLEMS

REFERENCES

© McGraw-Hill Education. All rights reserved. Any use is subject to the Terms of Use, Privacy Notice and copyright information.

12.1. IMPORTANCE OF HEAT TRANSFER

Heat transfer is a parasitic process that removes from the engine's cylinder, as thermal energy, a significant fraction of the fuel's chemical energy. It results in a loss in efficiency. It is an inherent loss because the peak burned gas temperature in the cylinder of an internal combustion engine is of order 2500 K. Maximum metal temperatures for the inside of the combustion chamber space are limited to much lower values by a number of considerations, and cooling for the cylinder head, cylinder, and piston must therefore be provided. These conditions lead to heat fluxes to the chamber walls that can reach as high as 10 MW/m^2 during the combustion period. However, during other parts of the engine's operating cycle, the heat flux is close to zero. The flux varies substantially with location and is periodic: regions of the chamber that are contacted by rapidly moving high-temperature burned gases generally experience the highest fluxes. In regions of high heat flux, thermal stresses must be kept below levels that would cause fatigue cracking (so temperatures must be less than about 400°C for cast iron and 300°C for aluminum alloys). The gas-side surface of the cylinder liner must be kept below about 180°C to prevent deterioration of the lubricating oil film. Spark plug and valves must be kept cool enough to avoid knock and preignition problems, which can result from overheated spark plug electrodes or exhaust valves. Solving these engine heat-transfer problems is obviously a major design task.

Heat transfer affects engine performance, efficiency, and emissions. For a given mass of fuel within the cylinder, higher heat transfer to the combustion chamber walls will lower the average combustion gas temperature and pressure, and reduce the work per cycle transferred to the piston. Thus specific power and efficiency are affected by the magnitude of engine heat transfer. Heat transfer between the unburned charge and the chamber walls in spark-ignition engines affects the onset of knock which, by limiting the compression ratio, also influences power and efficiency. Especially critical is heat transfer from the hot exhaust valve and piston crown to the unburned mixture. Changes in gas temperature due to heat-transfer can impact the emission formation processes both within the engine's cylinder and in the exhaust system where afterburning of CO and HC occurs. The exhaust temperature also governs the power that can be obtained from exhaust energy driven devices such as a turbocharger turbine. The exhaust gas temperature has a significant impact on the effectiveness of emissions after treatment devices such as catalysts and particulate traps. Engine friction is both affected by engine heat transfer and contributes to the coolant load. The cylinder liner temperature governs the piston and ring lubricating oil film temperature, and hence its viscosity. Piston and liner distortion due to temperature nonuniformities have a significant impact on the piston-ring component of engine friction. Much of the mechanical energy dissipated due to friction must be rejected to the atmosphere via the cooling system. The fan and water pump power requirements are determined by the magnitude of the heat rejected. The importance of engine heat transfer is clear.

To examine heat transfer more fully, it is helpful to consider the engine's subsystems. The intake system consists of intake manifold and inlet ports and valves. Heat transfer to the inflowing charge reduces volumetric efficiency (see Sec. 6.2.1). However, higher intake port and valve surface temperatures aid in vaporizing the fuel. Within the engine cylinder, the temperature of the charge relative to the wall temperature, and the flow field, vary substantially throughout the cycle. Both of these have a major influence on heat transfer. During the intake process, the incoming charge is usually cooler than the walls and flow velocities are high. During compression the charge temperature rises above the wall temperatures, and gas velocities decrease (see Sec. 8.2.2). Heat transfer thus changes direction, and is now from the cylinder gases to the chamber walls. During combustion, gas temperatures increase to very high values, and the local gas expansion that occurs as the fuel-air mixture burns increases gas motion. This is the period when heat-transfer rates to the walls are highest. Also, as the cylinder pressure rises, a small fraction of the cylinder charge is forced into crevice regions, resulting in additional heat losses (see Sec. 8.6). During expansion, gas temperatures decrease so heat-transfer rates decrease. When the exhaust valve opens, however, the blowdown process (Sec. 6.5) produces high velocities within the cylinder, and past the exhaust valve and in the exhaust port. Substantial heat transfer from the exhausting gases to the exhaust valve, port, and (to a lesser extent) manifold, occurs during the exhaust process. An ability to predict the magnitude of the heat transfer between the working fluid, the walls of the intake system, combustion chamber, and exhaust system, and to the coolant is of obvious importance to the engine designer. Sitkei provides a useful overview of engine heat transfer.[1]

© McGraw-Hill Education. All rights reserved. Any use is subject to the Terms of Use, Privacy Notice and copyright information.

12.2. MODES OF HEAT TRANSFER

The following modes of heat transfer are important.

12.2.1. Conduction

Heat is transferred by molecular motion, through solids and through fluids at rest, due to a temperature gradient. The heat transfer by conduction, per unit area per unit time,
$\dot{q}$, in a steady situation is given by Fourier's law:

$$\dot{q} = k\nabla T$$

(12.1)

where *k* is the thermal conductivity. For a steady one-dimensional temperature variation

$$\dot{q} = \frac{\dot{Q}}{A} = -k\frac{dT}{dx}$$

Heat is transferred by conduction through the cylinder head, cylinder liner, and piston; through the piston rings to the cylinder wall; through the engine block and manifolds.

12.2.2. Convection

Heat is transferred through fluids in motion, and between a fluid and a solid surface. When the fluid motion is produced by forces other than gravity, the term *forced convection* is used. In engines, the fluid motions are turbulent (see Chap. 8).

Heat (more accurately, thermal energy) is transferred by forced convection between the in-cylinder gases and the cylinder head, valves, cylinder walls, and piston during the induction, compression, expansion, and exhaust processes. Heat is transferred by forced convection from the cylinder walls and head to the coolant (which may be liquid or gas), and from the piston when lubricant is used as a piston coolant. Substantial convective heat transfer occurs to the exhaust valve, exhaust port, and exhaust manifold during the exhaust process. Heat transfer by convection from the intake port and valve surfaces raises the temperature of the incoming charge. Heat is also transferred by convection from the engine block to the surrounding environment by convection.

In steady-flow forced-convection heat-transfer problems, the heat flux
$\dot{q}$ transferred to a solid surface at temperature T_w from a flowing fluid stream at temperature T is determined from the relation

$$\dot{q} = h_c(T - T_w)$$

(12.2)

where h_c is the heat-transfer coefficient.[1] For many flow geometries (such as flow through pipes or over a plate)h_c is given by relations of the form

© McGraw-Hill Education. All rights reserved. Any use is subject to the Terms of Use, Privacy Notice and copyright information.

$$\left(\frac{h_c L}{k}\right) = \text{constant} \times \left(\frac{\rho v L}{\mu}\right)^m \left(\frac{c_p \mu}{k}\right)^n$$

(12.3)

where L and v are a characteristic length and velocity of the fluid flow. The terms in brackets from left to right are the Nusselt, Reynolds, and Prandtl dimensionless numbers, respectively. For gases, the Prandtl number ($c_p\mu/k$) varies little and is about 0.7 (see Sec. 4.8). Values for m and n are typically 0.8 and 0.3.

When nucleate boiling occurs at the surface (i.e., vapor bubbles are formed in the liquid at a hot wall), as may be the case in high heat flux areas on the coolant side in a water-cooled cylinder head, then h_c is increased and different relationships for h_c must be used.

12.2.3. Radiation

Heat exchange by radiation occurs through the emission and absorption of electromagnetic waves. The wavelengths at which significant thermal energy is transferred are in the visible range (0.4 to 0.7 μm) and the infrared (0.7 to 100 μm). Heat transfer by radiation occurs from the high-temperature combustion gases and the flame region to the combustion chamber walls (although the magnitude of this radiation heat transfer relative to convective heat transfer is only significant in diesel engines). Heat transfer by radiation to the environment occurs from all the hot external surfaces of the engine.

The theory of radiant heat transfer starts from the concept of a "black body," that is, a body that has a surface that emits or absorbs equally well radiation of all wavelengths and that reflects none of the radiation falling on it. The heat flux from one plane black body at temperature T_1 to another at temperature T_2 parallel to it across a space containing no absorbing material is given by

$$\dot{q} = \sigma\left(T_1^4 - T_2^4\right)$$

(12.4)

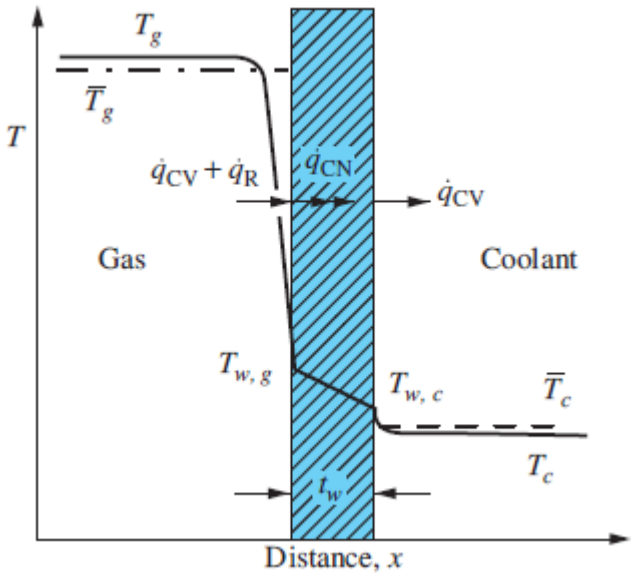
where σ is the Stefan-Boltzmann constant 5.67×10^{-8} W/m$^2 \cdot$ K^4. Real surfaces are not "black" but reflect radiation to an extent, which depends on wavelength. Gases are far from this black-body idealization. They absorb and emit radiation almost exclusively within certain wavelength bands characteristic of each molecular species. These departures from black-body behavior are usually dealt with by applying a scaling factor (an *emissivity*, ε) to Eq. (12.4). Similarly, a shape factor is applied to account for the fact that the angle of incidence of the radiation usually varies over any actual surface. These factors can be calculated for simple cases.

12.2.4. Overall Heat-Transfer Process

Figure 12.1 shows, schematically, the overall heat-transfer process driven by hot gases within the cylinder through the combustion chamber wall to the coolant flow. The heat flux into the wall has in general both a convective and a radiation component. The heat flux is conducted through the wall, and then convected from the wall to the coolant. A schematic temperature profile, and mean gas and coolant temperatures,
$\overline{T}_g$ and
$\overline{T}_c$, are shown.

© McGraw-Hill Education. All rights reserved. Any use is subject to the Terms of Use, Privacy Notice and copyright information.

Figure 12.1 Schematic of temperature distribution and heat flow across the combustion chamber wall.



In internal combustion engines, throughout each engine operating cycle, the heat transfer takes place under conditions of varying gas pressure and temperature, and with local velocities which vary more or less rapidly depending on intake port and combustion chamber configuration (see Chap. 8). In addition, the surface area of the combustion chamber varies through the cycle. The heat flux into the containing walls changes continuously from a small negative value during the intake process to a positive value of order several megawatts per square meter during combustion, early in the expansion process. While the flux variation lags slightly behind the change in gas temperature, investigators have concluded that the assumption that the heat-transfer process is *quasi steady* is sufficiently accurate for most purposes. However, gas temperature and gas velocities vary significantly across the combustion chamber, so the heat flux distribution over the combustion chamber walls is nonuniform.

For a steady one-dimensional heat flow through a wall as indicated in Fig. 12.1, the following equations relate the heat flux $\dot{q} = \dot{Q}/A$ and the temperatures indicated:

$$\text{Gas side:} \quad \dot{q} = \dot{q}_{\text{CV}} + \dot{q}_{\text{R}} = h_{c,g}\left(\overline{T}_g - T_{w,g}\right) + \sigma\varepsilon\left(\overline{T}_g^4 - \overline{T}_{w,g}^4\right)$$

(12.5)

where ε is the emissivity. The radiation term is usually negligible for SI engines.

$$\text{Wall:} \quad \dot{q} = \dot{q}_{\text{CN}} = \frac{k\left(T_{w,g} - T_{w,c}\right)}{t_w}$$

(12.6)

$$\text{Coolant side:} \quad \dot{q} = \dot{q}_{\text{CV}} = h_{c,c}\left(T_{w,c} - \overline{T}_c\right)$$

(12.7)

If $h_{c,g}$ and $h_{c,c}$ are known, the temperatures

© McGraw-Hill Education. All rights reserved. Any use is subject to the Terms of Use, Privacy Notice and copyright information.

$\overline{T}_g$, $T_{w,g}$, $T_{w,c}$, and $\overline{T}_c$ can be related to each other.

Equations (12.5), (12.6), and (12.7) show that the heat flux per unit area for these different heat transfer modes scale with the temperature difference [e.g., between the hot fluid and wall, Eq. (12.5), for gas-side convection, and hotter and cooler sides of the cylinder head for conduction]. The analogy with electrical circuit behavior is clear: The heat flux term $\left(\dot{q} \text{ or } \dot{Q} = \dot{q}A\right)$ is effectively the electrical current, and the driving temperature difference is the voltage difference, *V*. Since *I* = *V*/*R*, these equations define the three thermal resistances involved in this sequence of heat transfers (illustrated in Fig. 12.1) as

$$R_{\mathrm{CV},g} = \frac{1}{h_{c,g}A}, R_{\mathrm{CN}} = \frac{t_w}{kA}, R_{\mathrm{CV},c} = \frac{1}{h_{c,c}A}$$

(12.8*a*, *b*, *c*)

Note that if the "current" is $\dot{q}$ rather than $\dot{Q}$, then the surface area *A* drops out. Also, the radiation term in Eq. 12.5 has been omitted: it is negligible for spark-ignition engines. The radiation term, important in the diesel gas-to-wall heat transfer process, can be linearized in $\left(\overline{T}_g - \overline{T}_w\right)$.[2]

Since the thermal inertia of the metal combustion chamber walls and the coolant are large, this sequence of heat transfer processes is effectively quasi-steady. Thus the thermal "circuit" acts as three resistances in series, and the overall resistance (defined by an overall heat transfer coefficient *h*) is thus

$$\frac{1}{hA} = \frac{1}{h_g A} + \frac{t_w}{kA} + \frac{1}{h_c A}$$

(12.9)

Again, *A* can be removed from each term in Eq. (12.9) if the heat flux per unit area $\dot{q}$ is used instead of $\dot{Q}$. The temperature profile sketched in Fig. 12.1 (which is roughly to scale) indicates that the gas-to-metal thermal resistance [first term on the right-hand side in Eq. (12.9)] is by far the largest during the portion of the cycle when the in-cylinder gas temperature is much higher than the wall temperature. Note that *k* for an aluminum wall is three times *k* for cast iron (180 and 60 W/m · K), respectively.

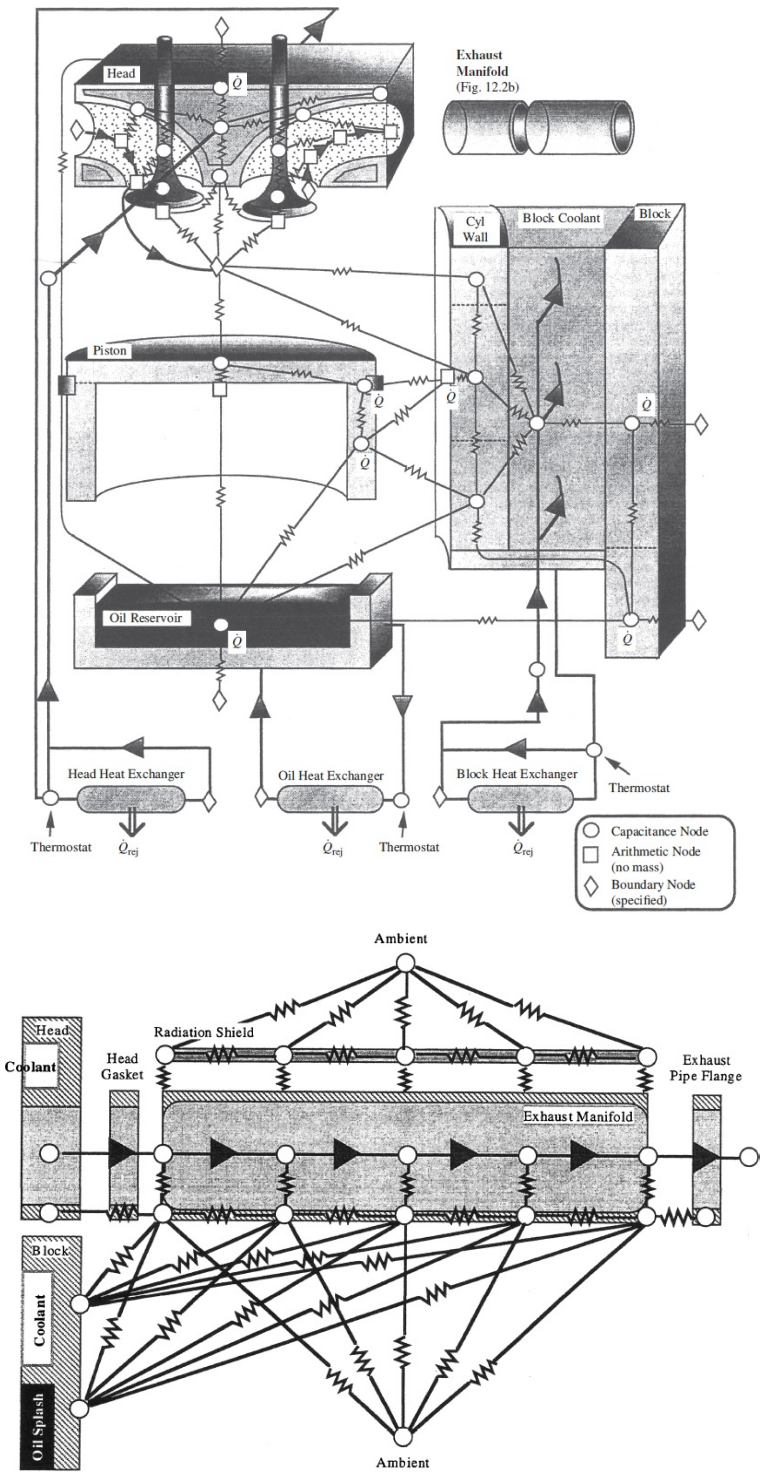
This *thermal resistance* approach, analogous to an electrical resistance network, is commonly used to analyze more complex heat transfer problems. It can, of course, be coupled with thermal capacitances, analogous to electrical capacitance, to analyze unsteady engine heat transfer situations.

An example of a resistor-capacitor network model of one cylinder of an engine (piston, block, cylinder head, exhaust manifold) is shown in Fig. 12.2.[2] Such a model can simulate engine heat fluxes and component temperatures for steady-state and transient engine operating conditions (such as engine warm-up). Lumped capacitances are used to model the thermal capacity transients: heat-transfer submodels (e.g., conduction, convection) provide the resistive linkages. This lumped parameter method applies energy conservation to each node of the system. Here, three types of nodes are included. Capacitance nodes possess thermal capacity and thus provide the dynamic elements of the simulation. Arithmetic nodes have no mass or thermal capacity so respond instantaneously to changes in temperature of the surrounding nodes. These are

© McGraw-Hill Education. All rights reserved. Any use is subject to the Terms of Use, Privacy Notice and copyright information.

appropriate when the time constant of a node's response is much shorter than that of the rest of the model. The third type of node is a boundary node, which has a specified temperature and is a boundary condition. Each node connects only with its adjacent nodes through conductive, convective, and radiative heat flows modeled, and shown, as resistors. The engine's fluids (intake flow—air and fuel, in–cylinder gases—which burn, exhaust flow, coolant flow, oil flow) drive or respond to this network. Reference 2 gives further details and results.

Figure 12.2 (a) Resistor-capacitor network model for analyzing heat flows and the resulting component temperatures in an internal combustion engine: piston, cylinder liner, cylinder head and valves, with coolant and oil systems. (b) Resistor-capacitor network model of the exhaust manifold that connects with the engine block network in (a).[2]



© McGraw-Hill Education. All rights reserved. Any use is subject to the Terms of Use, Privacy Notice and copyright information.

[1] h_c is an empirical constant, usually determined through correlation with experimental data: see Sec. 12.4.

[2] The term $\left(\overline{T}_g^4 - \overline{T}_{w,g}^4\right)$ in Eq. (12.5) can be rearranged as $\left(\overline{T}_g^2 + \overline{T}_w^2\right)\left(\overline{T}_g + \overline{T}_w\right)\left(\overline{T}_g - T_w\right)$ which, to a reasonable approximation, can be scaled linearly with $\left(\overline{T}_g - T_{w,g}\right)$.

© McGraw-Hill Education. All rights reserved. Any use is subject to the Terms of Use, Privacy Notice and copyright information.

12.3. HEAT TRANSFER AND ENGINE ENERGY BALANCE

An overall first law energy balance for an engine provides useful information on the disposition of the initial fuel energy. For a control volume which surrounds the engine (see Fig. 3.8), the steady-flow energy-conservation equation is

$$\dot{m}_f h_f + \dot{m}_a h_a = P_b + \dot{Q}_{\text{cool}} + \dot{Q}_{\text{misc}} + \left(\dot{m}_f + \dot{m}_a\right) h_e$$

(12.10)

where P_b is the brake power,
$\dot{Q}_{\text{cool}}$ is the heat-transfer rate to the cooling medium,
$\dot{Q}_{\text{misc}}$ is the heat rejection rate to the oil (if separately cooled) plus convection and radiation from the engine's external surface. It proves convenient to divide the exhaust enthalpy h_e into a sensible part $h_{e,s} = h_e(T) - h_e(298\ \text{K})$, plus the exhaust reference state enthalpy (see Sec. 4.5). Then Eq. (12.10) can be written:

$$P_b + \dot{Q}_{\text{cool}} + \dot{Q}_{\text{misc}} + \dot{H}_{e,\text{ic}} + \dot{m} h_{e,s} = \dot{m}_f Q_{\text{LHV}}$$

(12.11)

where
$\dot{H}_{e,\text{ic}}$ represents the exhaust enthalpy loss due to incomplete combustion of the fuel. Typical values of each of these terms relative to the fuel flow rate × heating value are given in Table 12.1.

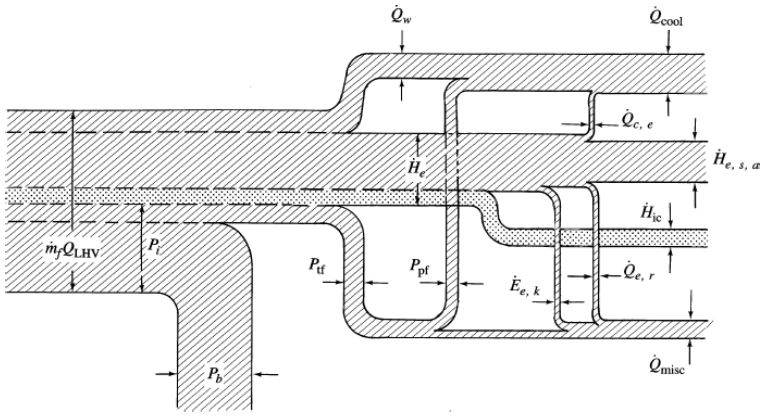
Table 12.1 Energy balance for automotive engines at maximum power

	P_b	$\dot{Q}_{\text{cool}}$	$\dot{Q}_{\text{misc}}$	$\dot{H}_{e,\text{ic}}$	$\dot{m} h_{e,s}$
(percentage of fuel heating value)					
SI engine	25–30	17–25	5–10	6–15	25–35
Diesel	35–40	20–35	2–6	1–2	22–35
Sources: From Sitkei,[1] Khovakh,[3] Burke et al.,[4] and Gruden et al.[5]					

The energy balance within an engine is more complicated and is illustrated in the energy flow diagram shown inFig. 12.3. The indicated power is the sum of the brake power and the friction power. A substantial part of the friction power is dissipated between the piston skirt and rings, and the cylinder wall, and is transferred as thermal energy to the cooling medium. The remainder of the friction power is dissipated in the bearings, valve mechanism, or drives auxiliary devices, and is transferred as thermal energy to the coolant, oil, or surrounding environment (in $\dot{Q}_{\text{misc}}$). The enthalpy in the exhaust gases exiting the cylinder can be subdivided into the following components: a sensible enthalpy (70%), an exhaust kinetic energy (7%), an incomplete combustion term (10%), and a heat transfer to the exhaust system (12%) (part of which is radiated to the environment, with the remainder ending up in the cooling medium).[1]

© McGraw-Hill Education. All rights reserved. Any use is subject to the Terms of Use, Privacy Notice and copyright information.

Figure 12.3 *Energy flow diagram for a gasoline SI engine.*
$\left(\dot{m}_f \dot{Q}_{\mathrm{LHV}}\right)$ *= fuel flow rate × lower heating value,*
$\dot{Q}_w$ *= heat-transfer rate to combustion chamber wall,*
$\dot{H}_e$ *= exhaust gas enthalpy flux,* P_b *= brake power,* P_{tf} *= total friction power,* P_i *= indicated power,* P_{pf} *= piston friction power,*
$\dot{Q}_{\mathrm{cool}}$ *= heat-rejection rate to coolant,*
$\dot{Q}_{c,e}$ *= heat-transfer rate to coolant in exhaust ports,*
$\dot{Q}_{\mathrm{oil}}$ *heat rejection to oil,*
$\dot{H}_{e,s,a}$ *= exhaust sensible enthalpy flux entering atmosphere,*
$\dot{H}_{e,ic}$ *= exhaust chemical enthalpy flux due to incomplete combustion,*
$\dot{Q}_{e,r}$ *= heat flux radiated from exhaust system,*
$\dot{E}_{e,k}$ *= exhaust kinetic energy flux,*
$\dot{Q}_{\mathrm{misc}}$ *= sum of remaining energy fluxes and transfers such as radiation and convection from the outside surface of the engine.*

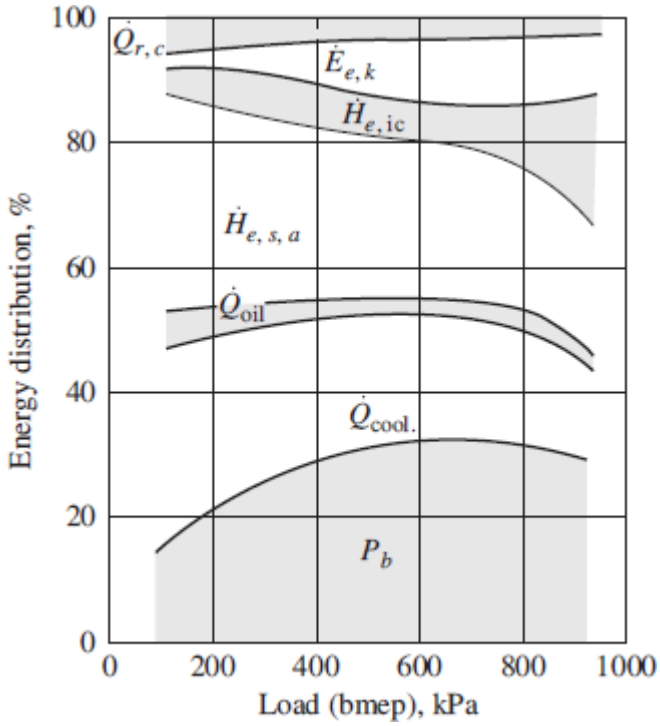


Thus the heat carried away by the coolant medium consists of heat transferred to the combustion chamber walls from the gases in the cylinder, heat transferred to the exhaust valve and port in the exhaust process, and a substantial fraction of the friction work. The heat (thermal energy) transferred to the combustion chamber walls $(\dot{Q}_w)$ and the thermal energy that ends up in the coolant are not equal (though they are connected as illustrated in Fig. 12.3). This distinction is significant. First, $\dot{Q}_w$, is important primarily because it impacts the processes that take place inside the combustion chamber: second, $\dot{Q}_{\mathrm{cool}}$, is important because it determines the design of the engine cooling system. The heat loss to the walls of the combustion chamber is only about two-thirds of the coolant thermal load; thermal energy generated by engine friction is the remaining one third.

Figure 12.4 shows an energy balance for a water-cooled spark-ignition engine, as a function of load (bmep), where the total initial fuel chemical energy is the normalizing factor. The brake power P_b expressed as a percent of fuel chemical energy is the engine's brake fuel conversion efficiency and rises from about 15% at low load to 34% at higher load (until enriching the mixture above stoichiometric to increase torque and avoid knock causes efficiency to level off and decline). At part-load, a greater fraction of the fuel chemical energy is absorbed into the coolant and oil, and leaves the cylinder as thermal energy in the exhaust. At low speeds and loads, the total coolant heat-transfer rate is about two times the brake power. Note also that at about three-quarters load, the exhaust kinetic energy $(\dot{E}_{e,k})$ has become significant as the engine's mass flow rate increases. The exhaust unreleased chemical energy (CO, H_2, and HC) also increases above about three-quarters load in this SI engine example because the mixture fuel-air equivalence ratio is enriched (steadily increased above stoichiometric) above this load to increase maximum power and prevent knock.

© McGraw-Hill Education. All rights reserved. Any use is subject to the Terms of Use, Privacy Notice and copyright information.

Figure 12.4 Energy balance for a gasoline spark-ignition engine as a function of load: brake power, coolant and oil thermal load, sensible exhaust enthalpy, exhaust chemical and kinetic energy, and radiation and convection heat transfer from the block and head to the surrounding air; energy transfers as percent of fuel flow rate × heating value. Operating conditions: 2000 rev/min, bmep from 100 to 920 kPa.[5]



Although the heat losses are such a substantial part of the fuel energy input, elimination of heat losses would only allow a fraction of the heat transferred to the combustion chamber and exhaust port walls to be converted to useful work. The remainder would leave the engine as sensible exhaust enthalpy. Consider an example of an automotive naturally-aspirated high-speed CI engine with a compression ratio of 15. The indicated efficiency is 45%, and 25% of the fuel energy is carried away by the cooling water. Of this 25%, about 2 percentage points is due to friction. Of the remaining 23%, about 8% is heat loss during combustion, 6% heat loss during expansion, and 9% heat loss during exhaust. Of the 8 percentage points lost during combustion about, half (or 4% of the fuel energy) could be converted into useful work on the piston (see Fig. 5.9). Of the 6% heat loss during expansion, about one-third (or 2% of the fuel energy) could have been utilized. Thus, of the 25% lost to the cooling system, only about 6% (one-quarter) could have been converted to useful work on the piston. This upper bound (zero heat loss) would only increase the indicated efficiency of the engine from 45 to 51%.

For a spark-ignition engine, the conversion to useful work will be lower, because the compression ratio is lower. However, as shown in Fig. 12.4, the heat losses at part-load (an important operating regime for automobile use) are a substantially larger fraction of the fuel heating value. Studies with computer simulations of the SI engine operating cycle indicate that at typical part-load operating conditions a proportional reduction in combustion-chamber-wall heat losses of 10% results in a relative increase (an improvement) in brake fuel conversion efficiency of about 3%.[6]

[1] The percentages are approximate. Note that, for a diesel engine, the exhaust chemical energy is significantly lower.

© McGraw-Hill Education. All rights reserved. Any use is subject to the Terms of Use, Privacy Notice and copyright information.

12.4. CONVECTIVE HEAT TRANSFER

12.4.1. Dimensional Analysis

While the overall time-averaged heat transfer to the coolant medium is adequate for some design purposes, the instantaneous heat flux during the engine cycle, between the in-cylinder gases and combustion chamber walls, is a necessary input for realistic cycle calculations (see Sec. 14.4) and provides the fundamental input for obtaining the heat flux distribution to the various parts of an operating engine. Equations (12.5), (12.6), and (12.7) provide the framework for calculating the heat flux $\dot{q}$ based on the assumption that at each point in the cycle the heat-transfer process is quasi steady. For example, neglecting radiation, if
$\overline{T}_g$,
$\overline{T}_{w,g}$, and $h_{c,g}$ can be calculated at each point in the cycle,
$\dot{q}\,(\theta)$ is obtained. Alternatively, if
$\overline{T}_c$, $h_{c,c}$,
$\overline{T}_g$, and $h_{c,g}$ are known,
$\dot{q}$ $T_{w,g}$, and $T_{w,c}$ can be computed.

Dimensional analysis can be used to develop the functional form of relationships which govern the gas-side heat-transfer coefficient.[7] The engine convective heat-transfer process can be characterized geometrically by a length dimension—say the bore B—and a number of length ratios y_1, y_2, y_3, etc. (of which one will be the axial cylinder length z divided by the bore z/B), which define the cylinder and combustion chamber geometry. The flow pattern, similarly, may be characterized by one chosen velocity v and a set of velocity ratios u_1, u_2, u_3, etc. The gas properties of importance are the thermal conductivity k, the dynamic viscosity μ, the specific heat c_p, and the density ρ. If there is combustion, then the chemical energy release rate per unit volume
$\dot{q}_{\text{ch}}$ may be important. The engine speed N and relative position in the cycle denoted by crank angle θ introduce the cyclical nature of the process. Thus

$$f(h_c, B, z, y_1, y_2, \ldots y_m, v, u_1, u_2, \ldots, u_n, k, \mu, c_p, \rho, \dot{q}_{\text{ch}}, N, \theta) = 0$$

Applying dimensional analysis, with mass, length, time, and temperature as the independent dimensions, reduces this set of actual variables to four-fewer nondimensional groups:

$$F\left(\frac{h_c B}{k}, \frac{\rho v B}{\mu}, \frac{c_p \mu}{k}, \frac{c_p T}{v^2}, \frac{NB}{v}\frac{\dot{q}_{\text{ch}}}{\rho c_p N T}, \frac{z}{B}, y_1, \ldots, y_m, u_1, \ldots, u_n, \theta\right) = 0$$

The first three groups are the familiar Nusselt, Reynolds, and Prandtl numbers. The next has the form of a Mach number since c_pT is proportional to the square of the sound speed. For Mach numbers much less than 1, the Mach number dependence is known to be small and can be omitted. It is usual to take for v the mean piston speed
$\overline{S}_p = 2LN$. Then, by introducing the bore/stroke ratio B/L, the term NB/v is eliminated. z/B is a function of the compression ratio r_c, the ratio of connecting rod to crank radius $R = l/a$, and θ. Thus

$$F\left(\frac{h_c B}{k}, \frac{\rho \overline{S}_p B}{\mu}, \frac{c_p \mu}{k}, \frac{B}{L}, \frac{\dot{q}_{ch}}{\rho c_p N T}, r_c, R, y_1, \ldots, y_m, \theta, u_1, \ldots, u_n\right) = 0$$

© McGraw-Hill Education. All rights reserved. Any use is subject to the Terms of Use, Privacy Notice and copyright information.

(12.12)

The dimensionless groups may be varied (but not reduced in number) by combination. While Eq. (12.12) reveals nothing about the functional form of the relationship between the groups, it provides a basis for evaluating the correlations which have been proposed.

Many formulas for calculating instantaneous engine heat-transfer coefficients have been developed (see Ref. 8 for a review). Only those with a functional form that fits Eq. (12.12) will be summarized here. The basis of these correlations is the assumption that the Nusselt, Reynolds, and Prandtl number relationship will have the same form as that used for turbulent flow in pipes and over flat plates:

$$\mathrm{Nu} = a\mathrm{Re}^{m}\mathrm{Pr}^{n}$$

(12.13)

Distinctions should be made between correlations intended to predict the *time-averaged* heat flux to the combustion chamber walls, the *instantaneous spatially averaged* heat flux to the chamber walls (which is required for engine performance analysis), and the *instantaneous local* heat fluxes (which are not uniform over the combustion chamber and may be required for thermal stress calculations). In using these heat-transfer correlations, the critical choices to be made are (1) the velocity to be used in the Reynolds number; (2) the gas temperature at which the gas properties in Eq. (12.13) are evaluated; and (3) the gas temperature used in the convective heat-transfer equation, Eq. (12.2).

The most widely used correlations and the basis of their derivation will now be summarized. Because the experimental data for evaluating these correlations in CI engines includes both convective and radiative heat fluxes, comparison of these correlations with data is deferred to Sec. 12.6.4.

12.4.2. Correlations for Time-Averaged Heat Flux

Taylor and Toong[9] have correlated overall heat-transfer data from 19 different engines. It was assumed that coolant and wall temperatures varied little between designs and that the effects of geometrical differences were small. Thus, at a given fuel/air ratio, the convective part of the heat flux should correlate with Reynolds number. To allow for variations in fuel/air ratio, Taylor and Toong defined an average effective gas temperature $T_{g,a}$ such that

$$\int A h_c \left(T - T_{g,a}\right) d\theta = 0$$

over the engine cycle. $T_{g,a}$ is the temperature at which the wall would stabilize if no heat was removed from the outside of the wall. $T_{g,a}$ was obtained by extrapolating average heat-transfer data plotted versus gas-side combustion chamber surface temperature back to the zero heat-transfer axis. The Nusselt number, defined as

$$\mathrm{Nu} = \frac{\overline{Q}\,B}{\left(\pi B^2/4\right)\left(T_{g/a} - T_c\right)k_g} = \frac{4\overline{Q}}{\pi B k_g \left(T_{g,a} - T_c\right)}$$

(12.14)

plotted against Reynolds number, defined as

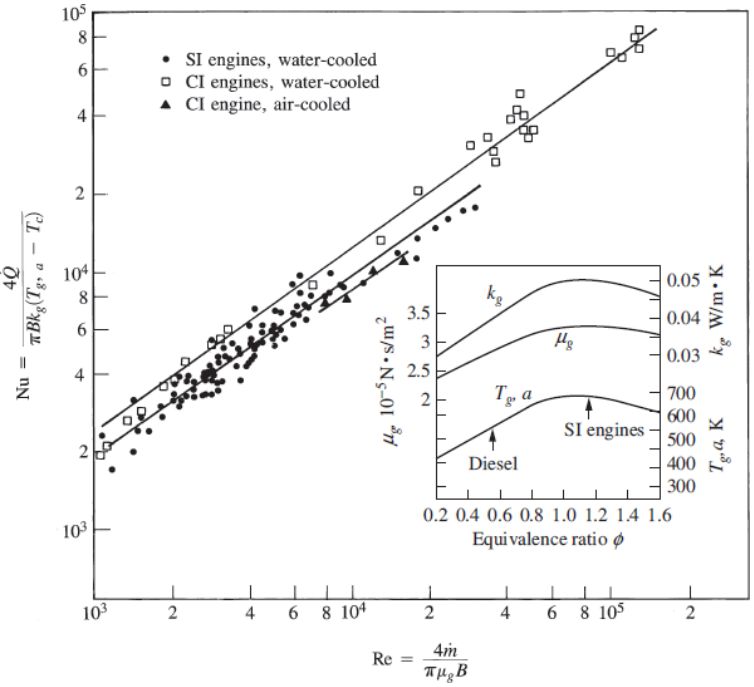
© McGraw-Hill Education. All rights reserved. Any use is subject to the Terms of Use, Privacy Notice and copyright information.

$$R_e = \frac{\dot{m}B}{\mu_g(\pi B^2/4)} = \frac{4\dot{m}}{\pi\mu_g B}$$

(12.15)

where
$\dot{m}$ is the charge mass flow rate, is shown in Fig. 12.5. Taylor and Toong proposed a Reynold's number power law with *m* in Eq. (12.13) equal to 0.75.[1] Annand[7] suggests three separate lines for the three different types of engines covered, with slope 0.7. The diesel line is about 25% higher than the spark-ignition engine line (which corresponds in part to the radiative heat flux component present in diesels). The air-cooled engine line is lower than the liquid-cooled line presumably because surface temperatures are higher. The average gas temperature values developed by Taylor and Toong are shown in the insert in Fig. 12.5.

Figure 12.5 Overall engine heat-transfer correlation: gas-side Nusselt number versus Reynolds number for different types of IC engines. See text for definition of symbols. Insert gives effective gas temperature (wall temperature for adiabatic operation), gas viscosity μ_g and thermal conductivity k_g. Lines have slope 0.7.[7, 9]



12.4.3. Correlations for Instantaneous Spatial Average Coefficients

Annand[7] developed the following convective heat-transfer correlation to match previously published experimental data on instantaneous heat fluxes to selected cylinder head locations:

$$\left(\frac{h_c B}{k}\right) = a\left(\frac{\rho \overline{S}_p B}{\mu}\right)^b$$

© McGraw-Hill Education. All rights reserved. Any use is subject to the Terms of Use, Privacy Notice and copyright information.

(12.16)

The value of a varied with intensity of charge motion and engine design. With normal combustion, $0.35 \le a \le 0.8$ with $b = 0.7$; a increases with increasing intensity of charge motion. Gas properties are evaluated at the cylinder-average charge temperature $\overline{T}_g$:

$$\overline{T}_g = \frac{pVM}{m\tilde{R}}$$

(12.17)

The same temperature is used in Eq. (12.2) to obtain the convective heat flux.

Note that in developing this correlation, the effects of differences in geometry and flow pattern between engines [the ratios $y_1, \ldots, y_m$ and $u_1, \ldots, u_n$ in Eq. (12.12)] have been incorporated in the proportionality constant a, and the effect of chemical energy release is omitted. While only data from cylinder head thermocouple locations were used as a basis for this correlation, it has often been used to estimate instantaneous spatial average heat fluxes for the entire combustion chamber.

Woschni[10] assumed a correlation of the form

$$\mathrm{Nu} = 0.035\mathrm{Re}^m$$

(12.18)

With the cylinder bore B taken as the characteristic length, with w as a local average gas velocity in the cylinder, and assuming $k \propto T^{0.75}$, $\mu \propto T^{0.62}$, and $p = \rho RT$, the above correlation can be written

$$h_c = CB^{m-1}p^m w^m T^{0.75-1.62m}$$

(12.19)

During intake, compression, and exhaust, Woschni argued that the average gas velocity should be proportional to the mean piston speed. During combustion and expansion, he attempted to account directly for the gas velocities induced by the change in density that results from combustion, which are comparable to mean piston speeds (~10 m/s). Thus a term proportional to the pressure rise due to combustion ($p - p_m$) was added (p_m is the motored cylinder pressure). The coefficients relating the local average gas velocity w to the mean piston speed and ($p - p_m$) were determined by fitting the correlation, integrated over the engine cycle, to time-averaged measurements of heat transfer to the coolant for a wide range of engine operating conditions for a direct-injection four-valve diesel without swirl. T in Eq. (12.19) is the mean cylinder gas temperature defined by Eq. (12.17); the same temperature is used to obtain the heat flux from the heat-transfer coefficient h_c. Thus this correlation represents *spatially averaged* combustion chamber heat fluxes.

The average cylinder gas velocity w (meters per second) determined for a four-stroke, water-cooled, four-valve direct-injection CI engine without swirl was expressed as follows:

$$w = \left[C_1 \overline{S}_p + C_2 \frac{V_d T_r}{p_r V_r}(p - p_m)\right]$$

(12.20)

© McGraw-Hill Education. All rights reserved. Any use is subject to the Terms of Use, Privacy Notice and copyright information.

where V_d is the displaced volume, p is the instantaneous cylinder pressure, p_r, V_r, T_r are the working-fluid pressure, volume, and temperature at some reference state (say inlet valve closing or start of combustion), and p_m is the motored cylinder pressure at the same crank angle as p, with:

For the gas exchange period:	C_1 = 6.18,	C_2 = 0
For the compression period:	C_1 = 2.28,	C_2 = 0
For the combustion and expansion period:	C_1 = 2.28,	$C_2 = 3.24 \times 10^{-3}$

Subsequent studies in higher-speed engines with swirl indicated higher heat transfer than these velocities predicted. For engines with swirl, cylinder averaged gas velocities were given by Eq. (12.20) with:

For the gas exchange period:	$C_1 = 6.18 + 0.417\frac{v_s}{S_p}$
For the rest of cycle:	$C_1 = 2.28 + 0.308\frac{v_s}{S_p}$

where
v_s, the swirl velocity, is $B\omega_p/2$ and ω_p is the rotation speed of the paddle wheel used to measure the swirl velocity (see Sec. 8.3.1).[11] Spark-ignition engine tests showed that the above velocities gave acceptable predictions for this type of engine also.[12]

Woschni's correlation, with the exponent m in Eq. (12.19) equal to 0.8, has been widely used, and can be summarized as:

$$h_c\left(\mathrm{W/m^2 \cdot K}\right) = 3.26B(\mathrm{m})^{-0.2}p(\mathrm{kPa})^{0.8}T(\mathrm{K})^{-0.55}w(\mathrm{m/s})^{0.8}$$

(12.21)

with w defined above, Eq. (12.20).

Hohenberg[13] examined Woschni's formula and made changes to give better predictions of time-averaged heat fluxes measured with probes in a direct-injection diesel engine with swirl. The modifications include use of a length based on instantaneous cylinder volume instead of bore, changes in the effective gas velocity, and in the exponent of the temperature term. Han et al.[14] have proposed as empirically based correlation of similar form to Eq. (12.21) with the same variables (B, p, T, and w) but modified exponents, and with a different method of calculating the representative in-cylinder gas velocity through compression, combustion, and expansion. They showed acceptable agreement with the heat transfer coefficients they determined from time-resolved surface temperature measurements in a gasoline-fueled SI engine.

12.4.4. Correlations for Instantaneous Local Coefficients

LeFeuvre et al.[15] and Dent and Sulaiman[16] have proposed the use of the flat-plate forced convection heat-transfer correlation formula

$$\left(\frac{h_c l}{k}\right) = 0.036\left(\frac{\rho v l}{\mu}\right)^{0.8}\left(\frac{\mu c_p}{k}\right)^{0.333}$$

© McGraw-Hill Education. All rights reserved. Any use is subject to the Terms of Use, Privacy Notice and copyright information.

(12.22)

where *l* is the length of the plate and *v* the flow velocity over the plate. This formula has been applied to DI diesel engines with swirl, with *l* and *v* evaluated at a radius *r* as

$$l = 2\pi r \quad v = r\omega$$

ω being the solid-body angular velocity of the charge. The heat flux at any radius *r* (with Pr = 0.73) is then given by

$$\dot{q}\,(r) = 0.023\frac{k}{r}\left(\frac{\omega r^2}{v}\right)^{0.8}\left[\overline{T}_g(r) - T_w(r)\right]$$

(12.23)

This equation can be used if the swirl variation with crank angle is known (see Sec. 8.3) and an appropriate local gas temperature can be determined. It would not be consistent to use the cylinder average gas temperature given by Eq. (12.17) because during combustion substantial temperature non-uniformities exist between burned gases and air or mixture which has yet to burn or mix with already burned gas.

An alternative approach is zonal modeling, where the combustion chamber is divided into a relatively small number of zones each with its own temperature, heat-transfer coefficient, and heat-transfer surface area history. This approach has been applied to spark-ignition engines (e.g., Ref. 17), where the division of the in-cylinder gases during combustion into a higher-temperature burned gas region behind the flame and lower-temperature unburned gas region ahead of the flame is clear (see Fig. 9.6). The heat transfer to the combustion chamber surfaces in contact with the unburned and burned gas zones [analogous to Eq. (12.2)] is given by

$$\dot{Q}_u = A_{u,w}h_{c,u}(T_u - T_w) \quad \dot{Q}_b = A_{b,w}h_{c,b}(T_b - T_w)$$

(12.24*a*, *b*)

respectively. Since h_c depends on local gas properties and velocities, $h_{c,u}$ and $h_{c,b}$ are not necessarily the same. Examples of how the burned-gas wetted areas on the piston, cylinder head, and liner vary during the combustion process are given in Fig. 14.8. Since the burned gas temperature T_b is much larger than the unburned gas temperature, the heat flux from the burned gas zone dominates.

One useful development of this two-zone approach is the division of the burned gas zone into an adiabatic core and a thermal boundary layer. The advantages are: (1) this corresponds more closely to the actual temperature distribution (see Sec. 12.6.5); and (2) a model for the boundary-layer flow provides a more fundamental basis for evaluating the heat-transfer coefficient. The local heat flux is then given by[18]

$$\dot{q} = \frac{k_e(T_{\text{ac}} - T_w)}{\delta}$$

(12.25)

where k_e is the effective thermal conductivity in the boundary layer, T_{ac} is the adiabatic core temperature, and δ the boundary-layer thickness. In the laminar regime δ would grow as $t^{1/2}$; in the turbulent regime δ would grow as $t^{0.8}$. Both growth regimes are observed.

© McGraw-Hill Education. All rights reserved. Any use is subject to the Terms of Use, Privacy Notice and copyright information.

Zonal models have also been used to describe DI diesel engine heat transfer.[19] A bowl-in-piston chamber was divided into three flow regions and two gas-temperature zones during combustion. An effective velocity

$$w = \left(U_x^2 + U_y^2 + 2k\right)^{1/2}$$

was used to obtain the heat-transfer coefficient, where U_x and U_y are the two velocity components parallel to the surface outside the boundary layer and k is the turbulent kinetic energy. Zonal models would be expected to be more accurate than global models. However, only limited validation has been carried out.

12.4.5. Exhaust and Intake System Heat Transfer

Convective heat transfer in the intake and exhaust systems is driven by higher flow velocities than in-cylinder heat transfer. Intake system heat transfer is usually described by steady, turbulent pipe-low correlations.[7] With liquid fuel present in the intake, the heat-transfer phenomena become more complicated (see Sec. 7.6). Exhaust flow heat-transfer rates are the largest in the entire cycle due to the very high gas velocities developed during the exhaust blowdown process and the high gas temperature (see Sec. 6.5). Exhaust system heat transfer is especially important since it affects emissions burn-up in the exhaust port, catalyst, or particulate trap: it also influences turbocharger performance, and contributes significantly to engine cooling requirements.

The highest heat-transfer rates occur during the exhaust blowdown, to the exhaust valve and port. Detailed exhaust port convective heat-transfer correlations have been developed and tested. These are based on Nusselt-Reynolds number correlations. For the valve open period, relations of the form

$$\mathrm{Nu} = K\mathrm{Re}_j^n$$

(12.26)

have been proposed and evaluated.[20] For
$L_v/D_v \lesssim 0.2$, the flow exits the valve as a jet, and
$\mathrm{Re}_j = v_j D_v/\nu$, where D_v is the valve diameter, v_j the velocity of the exhaust gases through the valve opening, and v the kinematic viscosity. For
$L_v/D_v \lesssim 0.2$, the port is the limiting flow area and a pipe flow model with
$\mathrm{Re} = v_p D_p/\nu$ is more appropriate. v_p is the gas velocity in the port and D_p is the port diameter.

For the valve closed period, the correlation

$$\mathrm{Nu} = 0.022\overline{\mathrm{Re}}_D^{0.8}$$

(12.27)

was developed. Here
$\overline{\mathrm{Re}}_D = \bar{v}_p D_p/\nu$, where
$\bar{v}_p$ is the time-averaged exhaust port gas velocity and D_p is the port diameter.

For straight sections of exhaust pipe downstream of the port, an empirical correlation based on measurements of average heat-transfer rates to the pipe has been derived:[21]

© McGraw-Hill Education. All rights reserved. Any use is subject to the Terms of Use, Privacy Notice and copyright information.

$$\mathrm{Nu} = 0.0483\mathrm{Re}^{0.783}$$

(12.28)

The Reynolds number is based on pipe diameter and gas velocity. Heat-transfer correlations for steady developing turbulent flow in pipes predict values about half that given by Eq. (12.28), in part because the exhaust gas flow is pulsating. Detailed analysis of exhaust system heat transfer in a gasoline engine can be found in Ref. 21. Included are measurements of wall temperature and heat flux measurements, and water condensation effects, during the engine warm-up process.

Heat transfer between the intake system walls and the intake airflow (plus fuel flow into the intake port with port fuel injection) is much less in magnitude than exhaust flow heat transfer, but does impact the engine's volumetric efficiency, propensity to knock at higher loads, and NO_x emissions, due to heating of the air on its way into the engine cylinder. Intake port wall and valve surface temperatures rise during warm-up from ambient levels in a cold engine to the quasi-steady levels of a warmed-up engine (intake port walls are close to the coolant temperature: intake valve head surface temperatures are 150 to 250°C, depending on operating conditions). While most of the intake flow is toward the cylinder, during the valve overlap period initiated by the intake valve opening, especially with throttled engine operation, there is a strong backflow of hot burned gases from the cylinder into the intake port. Under these throttled operating conditions, the intake pressure is significantly lower than the exhaust pressure so this backflow occurs with high gas velocities, exiting the valve seat region as a conical jet that impacts the valve head and port walls close to the valve, significantly. For a short time period (20 to 40 crank-angle degrees, some 2 to 4 ms), this hot gas backflow results in some heating of the intake valve and upstream port surfaces. With port fuel injection systems, the intake port and valve surface temperatures are high enough to affect the fuel vaporization process that results from these several intake thermal phenomena. The fraction of the injected gasoline that vaporizes is small (~10%) with a cold (~20°C) engine, rises increasingly rapidly with rising surface temperatures to close to 100% for a fully warmed-up engine.[22]

Additional details of intake system heat transfer rates (per cycle, and cycle resolved), on intake valve surface temperatures, and effects on fuel vaporization in port fuel injected engines, can be found in Refs. 23 to 26. Typically, as a result of heat transfer from the intake valve and port walls, the temperature of the intake mixture entering the cylinder of a gasoline or diesel engine is 20 to 30°C higher than the air temperature in the intake manifold.

[1] Taylor and Toong also found $a = 10$ a good fit. Note $n \approx 0.3$, so for gases Pr^n is close to unity.

© McGraw-Hill Education. All rights reserved. Any use is subject to the Terms of Use, Privacy Notice and copyright information.

12.5. RADIATIVE HEAT TRANSFER

There are two sources of radiative heat transfer within the cylinder: the high-temperature burned gases and the soot particles which burn up in the diesel engine flame. In a spark-ignition engine, the flame propagates across the combustion chamber from the point of ignition through previously mixed fuel and air. Although the flame front is slightly luminous (see Fig. 9.1), all the chemical intermediaries in the reaction process are gaseous. Combustion is essentially complete within the first third of the expansion stroke. In the compression-ignition engine the fuel partially burns in a rich reaction region within each spray: combustion then continues in a turbulent diffusion flame as this partially reacted fuel and air mix together and burn up. That diffusion flame separates the fuel sprays from the surrounding air (see Figs. 10.4 and 10.5). The flame is highly luminous because soot particles (which are mostly carbon) form within the fuel sprays, enter the diffusion flame, burn, become hot and radiate.

The radiation from soot particles in the diesel engine flame is about five times the radiation from the high-temperature gaseous combustion products. Radiative heat transfer in conventional spark-ignition engines is small in comparison with convective heat transfer from the hot burned gases. However, radiative heat transfer in diesel engines is not negligible; it contributes 20 to 35% of the total heat transfer and a higher fraction of the maximum heat-transfer rate.

12.5.1. Radiation from Gases

Gases absorb and emit radiation in narrow wavelength bands rather than in a continuous spectrum as do solid surfaces. The simpler gas molecules such as H_2, O_2, and N_2 are essentially transparent to radiation. Of the gases important in combustion, CO, CO_2, and H_2O emit sufficient energy to warrant consideration. In gases, emission and absorption of radiation will occur throughout the gas volume. These processes will be governed by the temperature, and the number of molecules, along the radiation path. For each species, the latter will be proportional to the product of the species partial pressure p_i and the path length l. Also, the radiative capacity depends on gas temperature T_g. Thus the emissivity of the gas ε_g can be expressed as

$$\varepsilon_g = f\left(T_g, p_1 l, \ldots, p_n l\right)$$

(12.29)

The mean path length for a volume V with surface area A is given with sufficient accuracy by

$$l = 0.9 \times \frac{4V}{A}$$

(12.30)

$4V/A$ is the mean path length for a hemispherical enclosure.

Standard methods have been developed for estimating ε_g for mixtures of CO_2 and H_2O by Hottel and others (see Ref. 27). Charts based on experimental data give
ε_{CO_2} and
ε_{H_2O} as functions of $p_i l$ and T_g. Correction factors are applied for total pressures above one atmosphere and for the overlapping of spectral bands of CO_2 and H_2O. Estimates for engine combustion gases at peak conditions give $\varepsilon_g \approx 0.1$ and peak heat fluxes due to gas radiation of order 0.2 MW/m^2. This amounts to some 5% of the peak convective heat transfer.

© McGraw-Hill Education. All rights reserved. Any use is subject to the Terms of Use, Privacy Notice and copyright information.

Since gas radiation is proportional to T_g^4, this radiative flux falls off more rapidly from peak values than convective heat flux as gas temperatures fall and, when integrated over the cycle, can be neglected.

12.5.2. Flame Radiation

Flame radiation in diesel engines is a much more complex process because the detailed geometry and chemical composition of the radiating region are not well defined. Since the radiation from the optically transparent nonluminous flames of spark-ignition engines is small, we will deal only with luminous nontransparent flames where the radiation comes from incandescent soot particles and has a continuous spectrum. Because the particle size distribution, number density, temperature, and flame geometry in a diesel are not easily quantified, flame emissivities cannot be calculated from first principles. Direct measurements of flame emissivities are required. A number of measurements of the magnitude and spectral distribution of radiation from a diesel engine combustion chamber have been made (see Ref. 8 for a summary). Flynn et al.[28] in a direct-injection diesel engine used a monochromator to measure intensity of radiation at seven wavelengths. The viewing path cut through the piston crown into the central region of the bowl-in-piston combustion chamber. Fuel was injected through a five-hole nozzle and some air swirl was provided. At any given crank angle, the distribution of energy over the seven wavelengths was used to reconstruct the complete energy spectrum and to calculate the apparent radiation temperature and optical thickness. This approach has been used by others.[29]

The radiant energy distribution is skewed from that of a gray-body model (for which emissivity is independent of wavelength). The monochromatic emissivity is well fitted by an equation of the form

$$\varepsilon_\lambda = 1 - \exp\left(\frac{-kl}{\lambda^\alpha}\right)$$

(12.31)

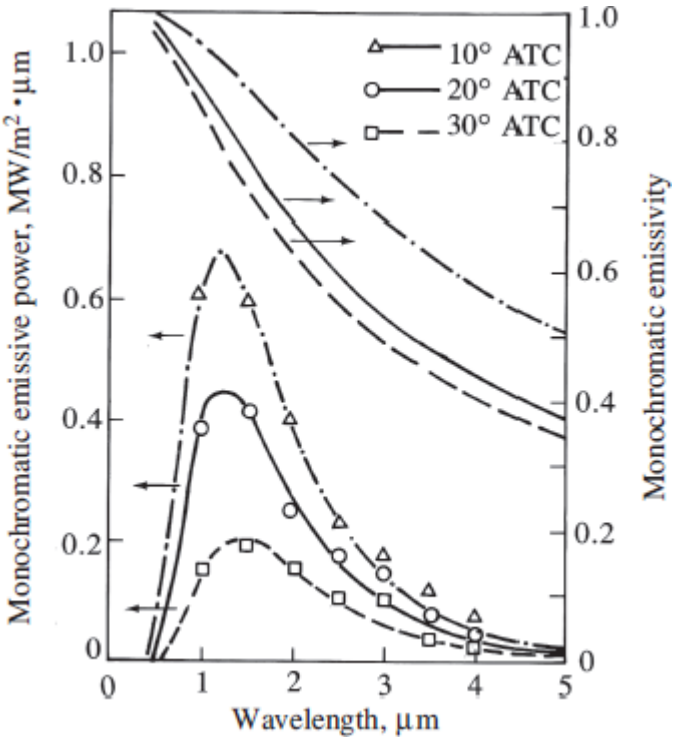
used by Hottel and Broughton[30] and others to describe the emissivity of clouds of soot particles in flames. There is much discussion as to the appropriate value of α. A value of 0.95 is often used. Figure 12.6 shows sample results for the monochromatic emissive power and monochromatic emissivity. Equation (12.31), combined with Planck's equation for black-body monochromatic emissive power

$$e_{b,\lambda} = \frac{2\pi K_1}{\lambda^5\left(e^{K_2/\lambda T_R} - 1\right)}$$

(12.32)

© McGraw-Hill Education. All rights reserved. Any use is subject to the Terms of Use, Privacy Notice and copyright information.

Figure 12.6 Variation in monochromatic emissive power and emissivity, with wavelength, at three different crank angles. DI diesel engine with 114-mm bore, 1995 rev/min, overall equivalence ratio 0.46. Radiation from piston bowl measured through cutout in piston crown.[28]



where $K_1 = 0.59548 \times 10^{-16}$ W · m^2 and $K_2 = 1.43879$ cm · K, defines an apparent radiation temperature T_R and optical thickness kl for the radiating medium. An apparent gray-body emissivity ε_a can then be calculated from the standard definition of ε_a,

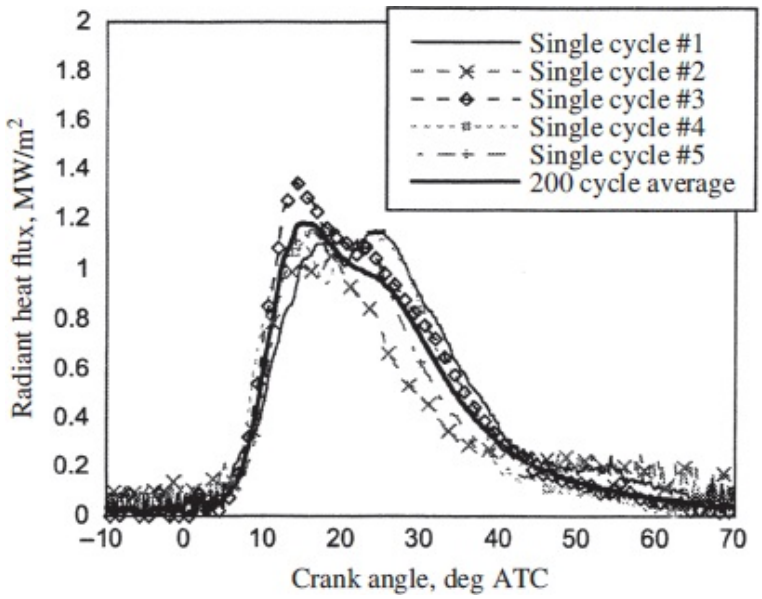
$$\varepsilon_a = \frac{\int \varepsilon_\lambda e_{b,\lambda} d\lambda}{\int e_{b,\lambda} d\lambda}$$

Additional details of the methodology can be found in Ref. 29.

Figure 12.7 shows the radiant heat flux rate (MW/m^2) measured in the cylinder head of a single-cylinder version of the Cummins N14 turbocharged six-cylinder in-line DI diesel engine, which has a low-swirl Mexican-hat-shaped combustion chamber. Five different individual cycles and an average over 200 cycles are shown. There is significant cycle-to-cycle variation in the profile, presumably due to differences between the development of each individual diffusion flame.

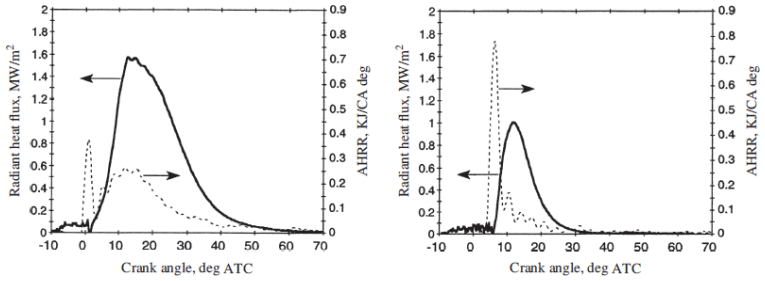
© McGraw-Hill Education. All rights reserved. Any use is subject to the Terms of Use, Privacy Notice and copyright information.

Figure 12.7 Radiant heat flux, for five individual cycles and 200-cycle average, as function of crank angle for DI diesel engine at high loads. Engine and measurement details in reference: fuel/air equivalence ratio 0.635, 1200 rev/min.[29]



The shapes of these radiant heat flux profiles follow that of the second, mixing-controlled diffusion-flame, apparent heat release rate (AHRR) profiles (see Fig. 12.8, and Sec. 10.3.3). This would be expected since the AHRR scales with fuel burning rate, and thus the surface area of the diffusion flame surrounding each fuel spray. This approximate scaling is evident in the two radiant flux and AHRR profiles a high (on left) and low load (on right) shown in Fig. 12.8.

Figure 12.8 Radiant heat flux and apparent heat release rate (AHRR) profiles at 100% load (on left) and 50% load (on right): start of injection 14.5° CA before TC, 1500 rev/min; single-cylinder version of Cummins N14 turbocharged DI diesel engine.[29]

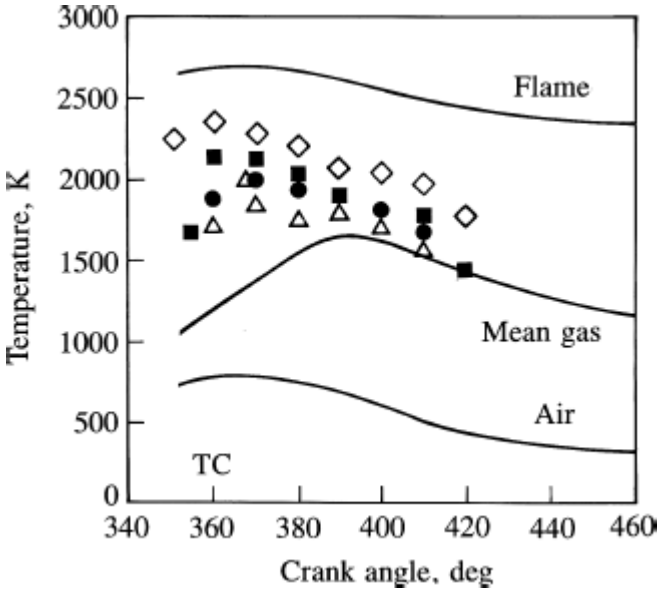


During the period of maximum radiation, the apparent emissivity is 0.8 to 0.9; it then decreases as the expansion process proceeds.[28] A comparison of radiant and total heat fluxes (both peak and average) shows that the radiation heat flux can be a substantial fraction of the peak heat flux. The average radiant heat flux is about 20% of the average total flux: the percentage varies with load.

The radiation and the apparent flame temperatures measured in diesels by several investigators show consistent results (see Fig. 12.9). Also included in the figure during the combustion and expansion process are typical values of: (1) the temperature of any air not yet mixed with fuel or burned gases; (2) the average temperature of the cylinder contents; and (3) the maximum possible flame temperature [corresponding to combustion of a slightly rich mixture (ϕ = 1.1) with air at the temperature shown]. The measured radiation temperatures fall between the maximum flame temperatures and the bulk temperature. Models for obtaining the relevant temperatures have been proposed (e.g., the diffusion flame reaction zone is stoichiometric[16, 19]) to fit the available data, and have been used to define an appropriate flame temperature.[31]

© McGraw-Hill Education. All rights reserved. Any use is subject to the Terms of Use, Privacy Notice and copyright information.

Figure 12.9 Apparent radiation temperatures measured in diesel engines, compared to calculated maximum adiabatic flame, cylinder-mean, and air temperatures, during the combustion period. Adiabatic flame temperature is temperature attained by burning air at the air temperature with fuel for an equivalence ratio of 1.1. (Data from Dent and Sulaiman,[16] Flynnet al.,[28] Lyn,[32] Kamimotoet al.,[33] calculated curves from Assanis and Heywood.[31])



The emissivity of an incandescent soot-burning flame can be calculated from a knowledge of the monochromatic absorption coefficient, which is given by

$$k_\lambda = 36\pi \frac{c_s}{\rho_s} \frac{n^2\kappa}{\lambda\left[\left(n^2+n^2\kappa^2\right)^2+4\left(n^2-n^2\kappa^2+1\right)\right]} = 36\pi \frac{c_s}{\rho_s} f(\lambda, T)$$

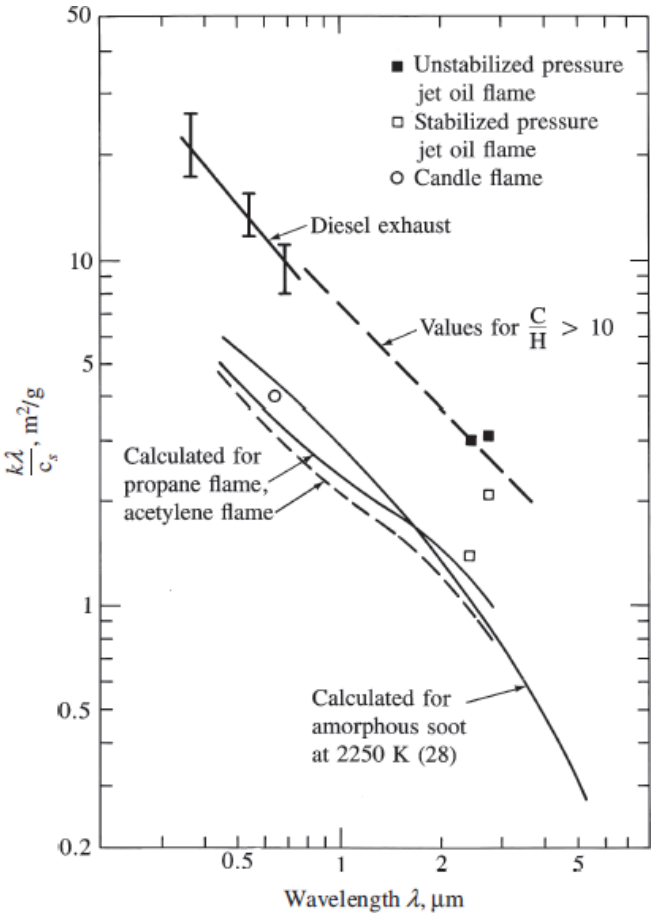
(12.33)

where n is the refractive index, κ is the absorption term in the complex refractive index, c_s is the soot concentration in kilograms per cubic meter, and ρ_s is the density of the soot particles (≈2 g/m^3).[34] The absorption coefficient depends on wavelength and temperature, is independent of particle size, and depends only on the soot mass loading. Figure 12.10 shows several estimates of k_λ/c_s as a function of λ. The strong dependence on λ shows that clouds of soot particles are markedly not gray. There is a considerable spread in the different estimates shown. This could be the result of different soot compositions (the C/H ratio affects the optical properties) and temperatures. To find a mean value for the absorption coefficient of a wide spectrum of radiation, the expression

$$k_a = \frac{\int k_\lambda e_{b,\lambda} d\lambda}{\int e_{b,\lambda} d\lambda}$$

© McGraw-Hill Education. All rights reserved. Any use is subject to the Terms of Use, Privacy Notice and copyright information.

Figure 12.10 Measured and calculated values of k_λ/c_s as a function of wavelength λ. k_λ is monochromatic absorption coefficient, c_s is the soot concentration. (From Fieldet al.[34] and Greeves and Meehan.[35])



must be evaluated. For example, for radiation from a black body at temperature 1800 K, the mean absorption coefficient is about $1300c_s$ per meter, where c_s is in kilograms per cubic meter. At higher black-body temperatures, the value of k_a would be higher.

Annand[36] has applied this approach to a diesel engine. The apparent flame emissivity was related to the apparent mean absorptivity by

$$\varepsilon_a = 1 - \exp(-k_a l)$$

(12.34)

For Flynn's data, the peak emissivity is 0.8 which gives $k_a l = 1.6$. Since $l \approx 0.07$ m, this gives $k_a \approx 22$ m^{-1} and $c_s \approx 16$ g/m^3 (≈1 g/m^3 at NTP), which is a soot loading comparable with values measured in diesel engines during combustion (see Sec. 11.5.2).

Well-accepted prediction formulas for radiant heat flux in diesel engines are not available. Annand has proposed a radiation term of the form

$$\dot{q}_R = \beta\sigma(\overline{T}_g^4 - T_w^4)$$

© McGraw-Hill Education. All rights reserved. Any use is subject to the Terms of Use, Privacy Notice and copyright information.

(12.35)

where σ a is the Stefan-Boltzmann constant,
$\overline{T}_g$ is the mean gas temperature, and T_w is the wall temperature. This term was coupled with a convective heat flux term to give a correlation for predicting total heat flux. In a first evaluation, when coupled with Eq. (12.14), β = 0.6 was proposed.[8] In a later study with a modified convective heat-transfer correlation,[37] $\beta \approx 1.6$ was proposed.

© McGraw-Hill Education. All rights reserved. Any use is subject to the Terms of Use, Privacy Notice and copyright information.

12.6. MEASUREMENTS OF INSTANTANEOUS HEAT-TRANSFER RATES

12.6.1. Measurement Methods

Values of instantaneous heat flux into the combustion chamber walls can be obtained from measurements of the instantaneous surface temperature. The temperature variation in the wall is a result of the time-varying boundary condition at the gas/wall interface. It is damped out within a small distance (~1 mm) from the wall surface, so measurements must be made at the surface. Various types of thermocouple or thermistor have been used.[8] One-dimensional unsteady heat conduction into the wall is then assumed:

$$\frac{\partial T}{\partial t} = \frac{1}{\rho c}\frac{\partial}{\partial x}\left(k\frac{\partial T}{\partial x}\right)$$

(12.36)

A sinusoidal variation with time of heat flux into a semi-infinite solid can be shown to produce a sinusoidal variation of surface temperature of the same frequency displaced in phase by 90°. The surface temperature T_w can be expressed as a Fourier series:

$$T_w = T_m + \sum_{n=1}^{N} \left[A_n \cos(n\omega) + B_n \sin(n\omega)\right]$$

(12.37)

where T_m is the time-averaged value of T_w, A_n and B_n are Fourier coefficients, n is a harmonic number, and ω is the angular frequency (radians per second). The boundary conditions are $T = T_w(t)$ at $x = 0$ and $T = T_l$ (constant) at $x = l$. The solution of Eq. (12.37) is[38]

$$T(x,t) = T_m - (T_m - T_l)\frac{x}{l} + \sum_{n=1}^{N} \exp(-\phi_n x) F_n(x,t)$$

(12.38)

where

$$F_n = A_n \cos(n\omega - \phi_n x) + B_n \sin(n\omega - \phi_n x)$$

and $\phi_n = (n\omega/2\alpha)^{1/2}$, where α is the thermal diffusivity of the wall material $k/(\rho c)$.

The heat flux components at each frequency that caused that variation with time can be calculated via Fourier's law [Eq. (12.1)], and summed to give the total fluctuation of heat flux with time:

© McGraw-Hill Education. All rights reserved. Any use is subject to the Terms of Use, Privacy Notice and copyright information.

$$\dot{q} = \frac{k}{l}(T_m - T_l) + k\sum_{n=1}^{N} \phi_n \left[(A_n + B_n)\cos(n\omega) - (A_n - B_n)\sin(n\omega)\right]$$

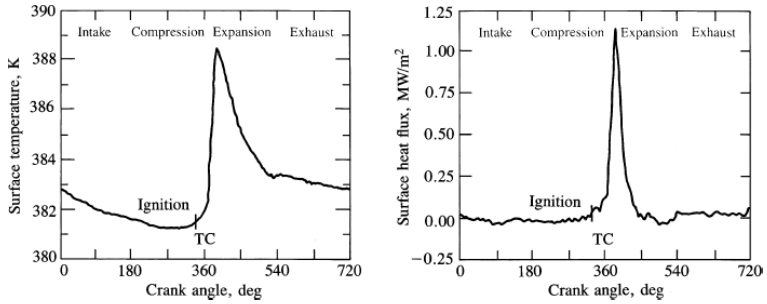
(12.39)

Alternative approaches for solving Eq. (12.36) are through use of an electrical analog to heat flow and by numerical methods. The latter become necessary if wall material properties depend significantly on temperature, as do combustion chamber deposits and some insulating ceramic materials. Several measurements of this type in spark-ignition and diesel engines have been made. A summary of these measurements can be found in Ref. 8. Radiant heat fluxes can be determined directly by several techniques: for example, photo-detector and infrared monochromator; thermocouple shielded by a sapphire window; pyroelectric thermal detector.

12.6.2. Spark-Ignition Engine Measurements

Figure 12.11 shows the surface temperature variation with crank angle, and the heat flux variation calculated from it, on the cylinder head of a spark-ignition engine at a part-load low-speed operating condition. The swing in surface temperature at this point (about halfway from the on-cylinder-axis spark plug to the cylinder wall) is 7 K. The heat flux rises rapidly when the flame arrives at the measurement location, has its maximum at about the time of peak cylinder pressure when burned gas temperatures peak (see Sec. 9.2.1), and then decays to relatively low levels by 60° ATC as expansion cools the burned gases. Peak heat fluxes on the cylinder head of 1 to 3 MW/m^2 were measured over the normal engine speed and load range.[39,41]

Figure 12.11 Surface temperature measured with thermocouple in cylinder head, and surface heat flux calculated from that surface temperature, as a function of crank angle. Spark-ignition engine operated at part-load.[39]



The heat flux profiles vary with location in a given engine, and also from one cycle to the next. (Figure 12.7 showed typical cycle-to-cycle variations for a DI diesel.) The rapid rise in heat flux depends on the flame arrival time at the measurement location. As a consequence, the heat fluxes determined from surface temperature data averaged over many cycles usually show a less rapid rise rate. Figure 12.12 also shows the effect of spark retard at a given location. The later arrival of the flame at the measurement location delays the start of the rapid rise in heat flux. Also, the magnitude of the peak heat flux rate is reduced as combustion is retarded since peak pressure is later and lower, and the peak burned gas temperature is consequently lower, too.

© McGraw-Hill Education. All rights reserved. Any use is subject to the Terms of Use, Privacy Notice and copyright information.

Figure 12.12 (a) Variation of surface heat flux with crank angle at four temperature measurement locations in the cylinder head of a naturally-aspirated spark-ignition engine: speed 1000 rev/min, stoichiometric operation, volumetric efficiency 0.8, spark advance 40°BTC. (b) Effect of retarding spark timing from 40° BTC to TC in 10° CA intervals on heat flux profile, location 1, same spark-ignition engine operating conditions as in (a).[40]

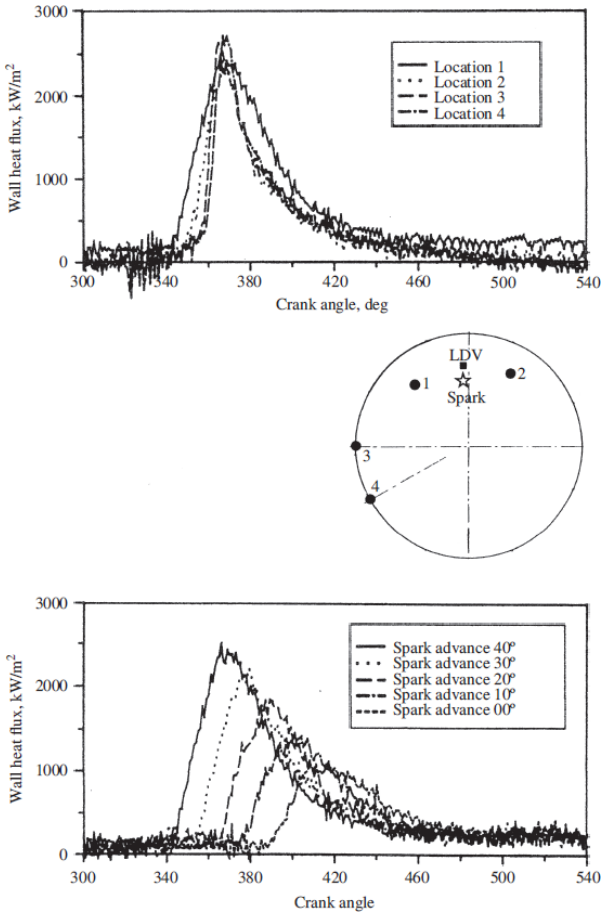
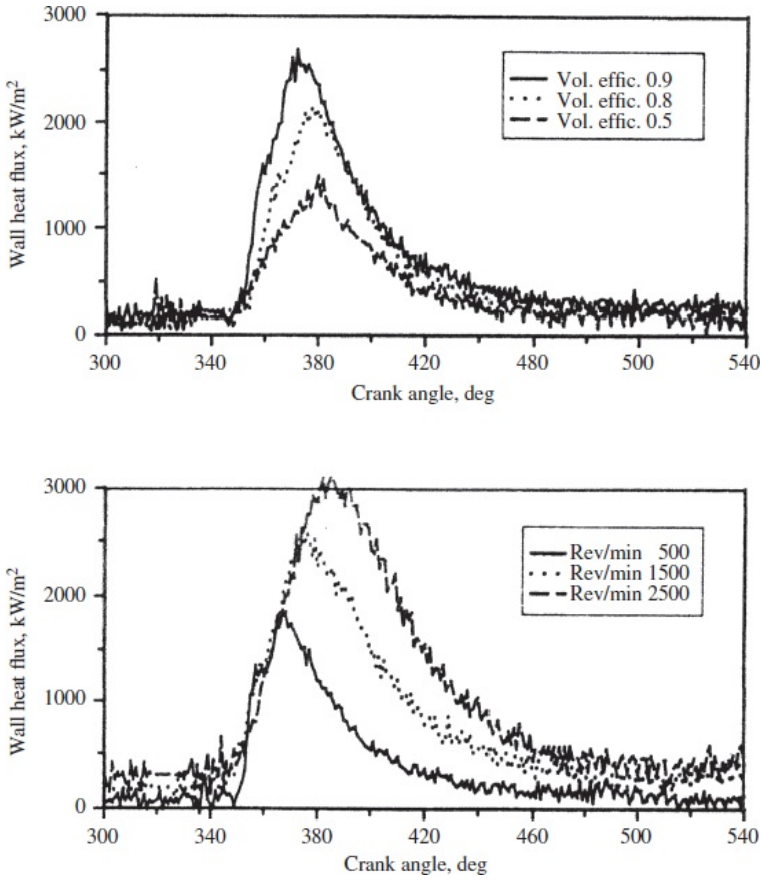


Figure 12.13 shows the effects of engine load (defined by the engine's volumetric efficiency) and speed on heat flux profile. Such measurements show that increasing engine load and increasing engine speed increase the surface heat flux. Maximum heat fluxes occur with close-to-stoichiometric mixtures.[39–41] All these trends would be expected from the variations in burned gas temperature that result from these changes in engine operation.

© McGraw-Hill Education. All rights reserved. Any use is subject to the Terms of Use, Privacy Notice and copyright information.

Figure 12.13 Variation of surface heat flux with engine load (volumetric efficiency) and speed: η_v = 0.5 (mid-load), 0.8, and 0.9 (high-load); speed (rev/min), 500, 1500, 2500, location 1. Same spark-ignition engine as in Fig. 12.12, and same base operating conditions.[40]

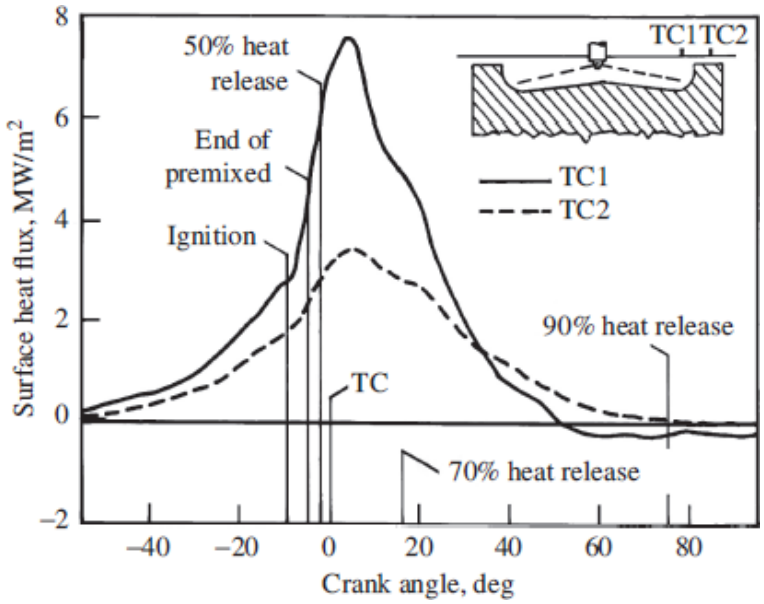


12.6.3. Diesel Engine Measurements

Measurements of instantaneous heat fluxes in diesel engines show similar features. The heat flux distribution over the combustion chamber walls is usually highly nonuniform. There are also variations between the heat flux profiles from individual cycles. Figure 12.14 shows surface heat fluxes at two locations in a medium-swirl DI diesel, one over the piston bowl (higher heat flux) and the other over the piston squish area, in relation to the heat-release profile. The heat flux increases rapidly once combustion starts, reaches a maximum at close to the time of maximum cylinder pressure, and decreases to a low value by 40 to 60° ATC. Peak heat fluxes to the primary combustion chamber surfaces (the piston bowl and head directly above the bowl) are of order 10 MW/m^2.

© McGraw-Hill Education. All rights reserved. Any use is subject to the Terms of Use, Privacy Notice and copyright information.

Figure 12.14 Measured surface heat flux at two locations in the cylinder head of a medium-swirl DI diesel engine. TC1 above the piston bowl, TC2 above the piston squish area, as shown. Percentages of heat release are indicated. Bore = stroke = 114 mm, r_c = 16, 2000 rev/min, overall equivalence ratio = 0.5, intake pressure = 1.5 arm.[42]



In smaller diesel engines with swirl, the mean heat flux to the piston within the piston bowl is usually higher than the mean heat fluxes to the cylinder head and the annular squish portion of the piston crown (by about a factor of two).[16,37] This would be expected since the piston bowl is the zone where most of the combustion takes place and gas velocities are highest. There are, in addition, substantial variations in heat flux at different locations within the piston bowl, on the head, and on the annular region of the piston crown.

In contrast to the above results obtained on smaller high-speed (7- to 9-cm bore) diesels with swirl with deep bowl-in-piston combustion chambers of diameter about half the piston diameter, results from tests on a medium-speed 30-cm bore quiescent shallow-bowl piston direct-injection supercharged diesel showed a much more uniform heat flux distribution over the combustion chamber walls.[43]

Heat fluxes to the cylinder liner are much lower still (an order of magnitude less than the peak flux to the combustion chamber surface) and are also nonuniform. Figure 12.15 compares heat fluxes to the cylinder head with three locations along the liner. Even at the top of the liner, the peak heat flux is only 15 to 20% of the flux to the primary combustion chamber surfaces. Again this would be expected, since the combustion gases do not contact the lower parts of the cylinder wall until later in the expansion stroke when their temperature is much below their peak value.

© McGraw-Hill Education. All rights reserved. Any use is subject to the Terms of Use, Privacy Notice and copyright information.

Figure 12.15 Measured surface heat fluxes at different locations in cylinder head and liner of naturally-aspirated four-stroke cycle DI diesel engine. Bore = stroke = 114 mm, 2000 rev/min, overall equivalence ratio = 0.45.[15]

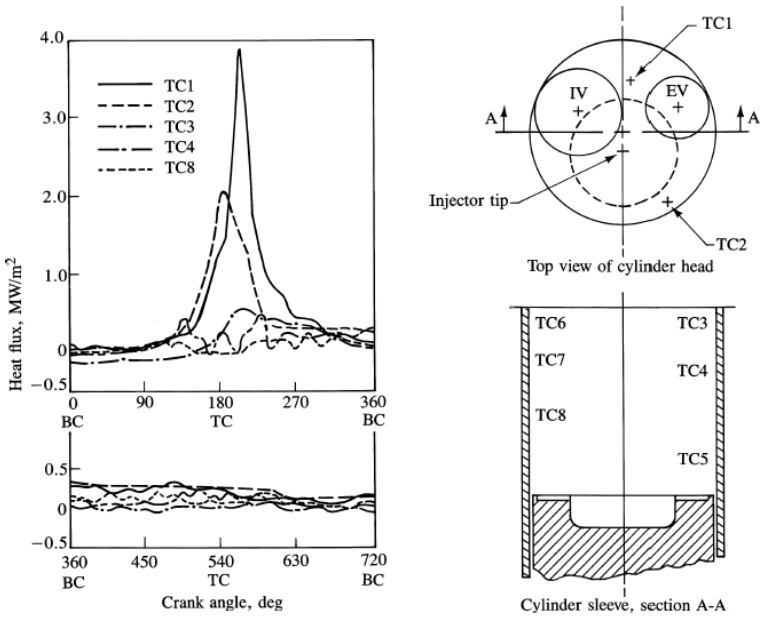
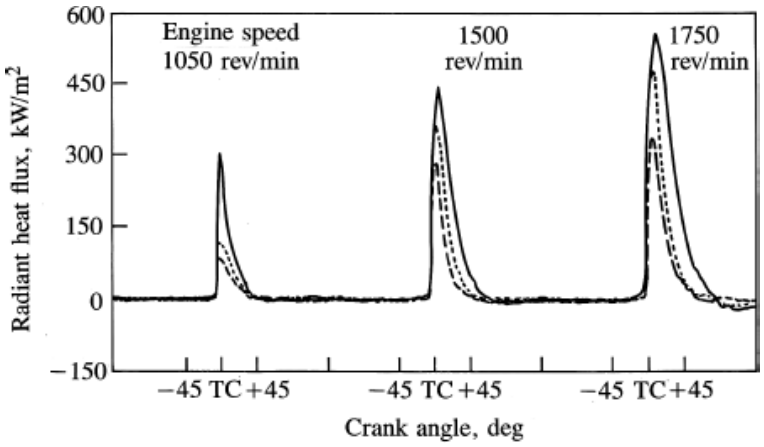


Figure 12.16 shows examples of radiant heat flux measured above the piston bowl of a medium-swirl DI diesel engine as a function of engine speed and load.[16] The limited radiant heat flux data available exhibit the following trends. The rapid increase in radiant heat flux following combustion is delayed relative to the start of pressure rise due to combustion by about 5°; this delay increases with increasing speed. This delay occurs because the radiation results from soot burn up in the second diffusion-flame phase of the diesel combustion process. The peak radiant flux remains approximately constant with increasing equivalence ratios up to $\phi \approx 0.5$. Further increases in the equivalence ratio produce a drop in level of radiant flux. The time-averaged radiant heat flux increased approximately linearly with increasing manifold pressure; however, peak radiative flux levels remained essentially unchanged. Peak and time-averaged values of the radiant heat flux decreased as injection timing was retarded due to lower flame temperatures.

Figure 12.16 Measured radiant heat flux to cylinder head above the piston bowl in a high-swirl DI diesel engine when load and speed are varied. Solid curve: 80% load. Dotted curve: 40% load. Dashed curve: no load.[16]

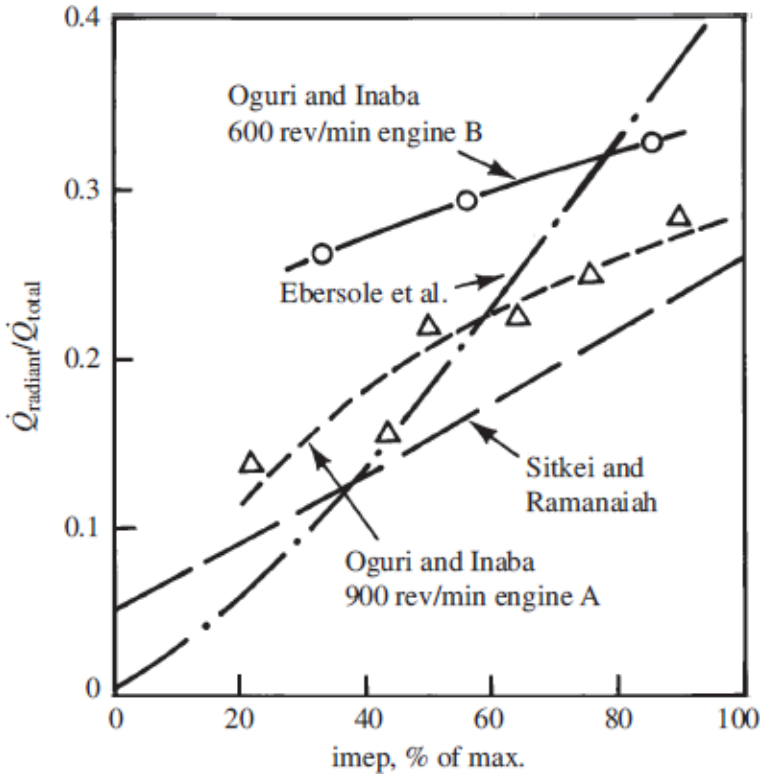


In diesel engines, the relative importance of radiant heat transfer (as a percentage of the total heat flux) depends on the location on the combustion chamber surface, crank angle, engine load, engine size, and engine design details. The time-

© McGraw-Hill Education. All rights reserved. Any use is subject to the Terms of Use, Privacy Notice and copyright information.

averaged radiant heat transfer increases as a proportion of the total heat transfer, with increasing load, as indicated in Fig. 12.17.[8] At high load, the radiant heat flux is between 25 and 40% of the total time-averaged heat flux.

Figure 12.17 Radiant heat flux as fraction of total heat flux over the load range of several different diesel engines. See Ref. 8 for sources of engine data.



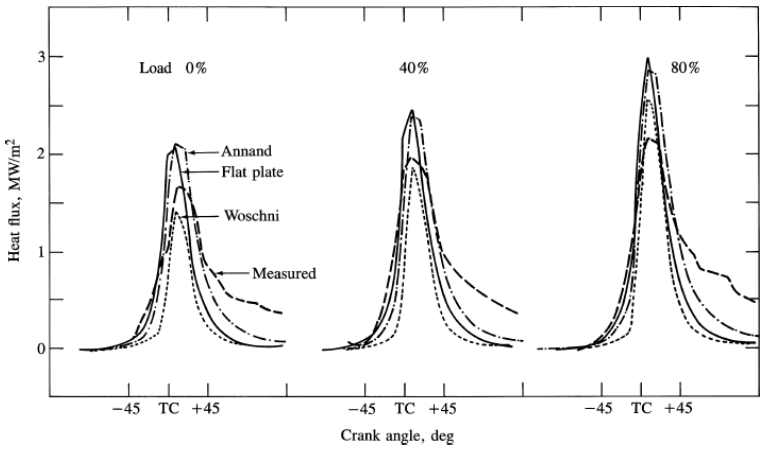
12.6.4. Evaluation of Heat-Transfer Correlations

The available convective (or combined convective plus radiative) heat flux correlations have been compared with instantaneous engine heat-transfer measurements. One difficulty in such evaluations is the determination of spatially-averaged combustion-chamber heat fluxes from the experimental data for comparison with correlations intended to predict the mean chamber heat flux as a function of crank angle. Area-averaged instantaneous heat flux prediction using Woschni's equation (12.19) for the spark-ignition engine conditions have generally been found to be similar in magnitude to measured heat fluxes to the cylinder head (e.g., Ref. 44).

Comparisons have been made of predictions with data for diesel engines. Annand's correlations, Eqs. (12.14) and (12.35) with $a = 0.06$, $b = 0.85$, and β (for the combustion phase only) = 0.57, gave reasonable agreement with instantaneous cylinder head heat fluxes, and overall time-averaged heat fluxes for a medium-speed quiescent DI engine design.[43] In a small high-speed diesel with swirl, values of $a = 0.13$, $b = 0.7$, and $\beta = 1.6$ gave a reasonable fit to estimates of the instantaneous area-mean heat flux[37] and time-averaged heat flux to the piston.[45] Comparisons of the Annand and Woschni correlations generally show that the Annand correlation predicts somewhat higher heat fluxes at the same crank angle.[10] The most careful comparison of all three correlations summarized in Secs. 12.4.3 and 12.4.4 with experimental data has been made by Dent and Sulaiman in a small high-speed diesel engine with swirl.[16] The mean experimental heat flux was estimated from a number of thermocouple measurements located at different points around the combustion chamber surface. Figure 12.18 shows the comparison. The Woschni correlation is lower than the others at light load because the combustion-induced velocity term is smaller. Expansion stroke heat fluxes are underpredicted by all three correlations. Given the uncertainty in converting the measurements to an average heat flux value, the agreement is reasonably good.

© McGraw-Hill Education. All rights reserved. Any use is subject to the Terms of Use, Privacy Notice and copyright information.

Figure 12.18 Comparison of measured mean heat fluxes on the cylinder head at 1050 rev/min in a fired high-swirl DI diesel engine with various prediction equations: Annand, Eq. (12.14); Woschni, Eq. (12.19); flat plate, Eq. (12.20) using measured gas motion.[16]



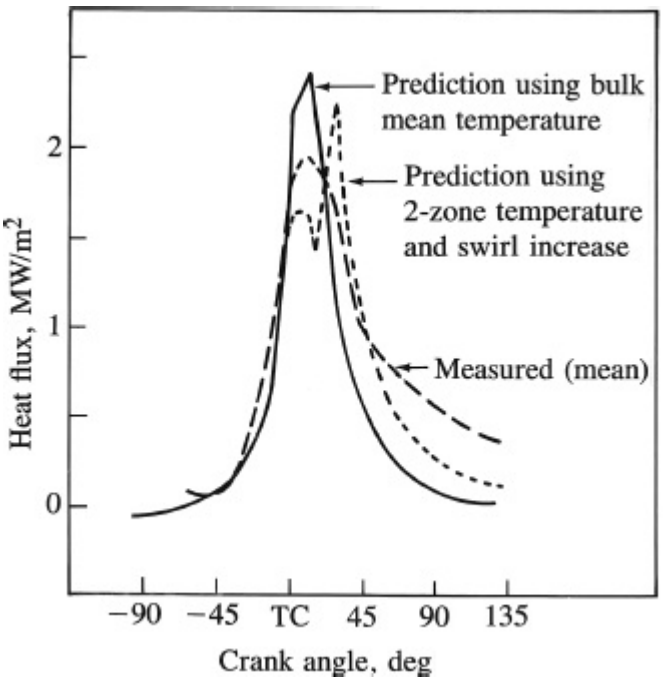
Dent examined additional modifications to the flat plate formula [Eq. (12.20)], which was based on the cylinder-mean gas temperature. During combustion a two-zone model is more appropriate. Assuming an equivalence ratio for the burned gas (Dent assumed stoichiometric), a combustion zone temperature can be determined from the relation

$$\overline{T}_b = \frac{m\overline{T}_g - m_a T_a}{m_b}$$

where m_a is the mass of air, T_a is the air temperature, and m_b is the burned gas mass, $m_b = m - m_a$. In addition, the observed swirl enhancement which occurs due to the combustion was included by multiplying the swirl velocity used in the heat-transfer correlation by the square root of the ratio (density of air in the motored case)/(density of burned gas in fired case). The combination of both effects (see Fig. 12.19) improves the shape of the predictions by broadening and lowering the peak.

© McGraw-Hill Education. All rights reserved. Any use is subject to the Terms of Use, Privacy Notice and copyright information.

Figure 12.19 Measured heat fluxes on cylinder head in fired high-swirl DI diesel engine at 1050 rev/min and 40% load compared with predictions based on bulk mean gas temperature and using temperatures based on two-zone (air and burned gas) model.[16]



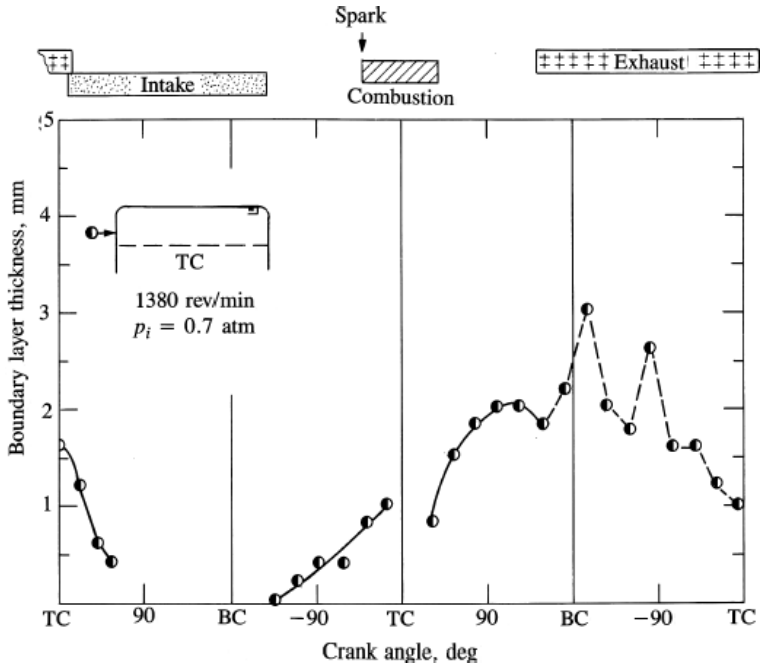
Each of the convective-heat-transfer correlations described has experimental support. However, under engine design and operating conditions different from those under which they were derived, the predictions should be viewed with caution. Woschni's correlation is the correlation used most extensively for predicting spatially averaged instantaneous convective heat fluxes. It has been shown that average heat transfer rates calculated using Woschni's correlation compare well in an SI engine with heat loss values estimated from an engine energy balance.[46] However, the empirical constants which relate the mean piston speed and combustion-induced gas motion to the velocity used in the Reynolds number, determined by Woschni, will not necessarily apply to all the different types of engine. If local velocities are known, the flat-plate-based correlations provide the best available approach. Annand's correlation has the advantage of being the simplest correlation to use. Since the radiation component in diesel engine heat transfer is normally 20 to 40% of the total, an approximate estimate of its value may suffice. A more extensive review of these heat transfer correlations and comparisons with experimental data on heat transfer to the engine's combustion chamber walls[44] reaches similar conclusions. While the functional forms of these correlations (based on the relevant dimensionless numbers) are well grounded, they are inherently empirical and conceptually over simplified. The combustion, thermal, and fluid flow phenomena occurring inside the engine's cylinders are extremely complex, creating significant modeling and measurement challenges.

12.6.5. Boundary-Layer Behavior

Measurements of thermal boundary-layer thickness in an operating spark-ignition engine have been made using schlieren photography in a flow-visualization engine. Figure 12.20 shows one set of measurements on the cylinder wall in the clearance volume opposite the spark plug. The boundary-layer thickness decreases during intake and increases steadily during compression and expansion to about 2 mm. It stops growing and becomes unstable during the exhaust process, separating from the cylinder wall and becoming entrained into the bulk gas leaving the cylinder. The thickness of the thermal boundary layer varies substantially at different locations throughout the chamber. While the trends with crank angle were similar, the layers on the cylinder head and piston crown were significantly (up to two to three times) thicker during compression and expansion in the simple disc-shaped chamber studied.[47] This different behavior probably results because there is no bulk flow adjacent to the head and piston crown.

© McGraw-Hill Education. All rights reserved. Any use is subject to the Terms of Use, Privacy Notice and copyright information.

Figure 12.20 Thermal boundary-layer thickness, at the top of the cylinder wall in the clearance volume, determined from schlieren photographic measurements in a special visualization square-piston spark-ignition engine.[47]



Estimates of thermal boundary-layer thickness in spark-ignition engines, based on convective-heat-transfer correlations and thermal energy conservation for the growing layer give thicknesses comparable to these measurements. Note that a substantial fraction of the cylinder mass is contained within the thermal boundary layer. For example, for an average thickness of 3 mm at 90° ATC during expansion, the volume of the boundary layer is 20% of the combustion chamber volume for typical engine dimensions. Since the average density in the boundary layer is about twice that in the bulk gases, some 30 to 40% of the cylinder mass would be contained within this boundary layer.

© McGraw-Hill Education. All rights reserved. Any use is subject to the Terms of Use, Privacy Notice and copyright information.

12.7. THERMAL LOADING AND COMPONENT TEMPERATURES

The heat flux to the combustion chamber walls varies with engine design and operating conditions. Also, the heat flux to the various surfaces that bound the combustion chamber is not uniform. This nonuniform heat flux, combined with the different thermal impedances between locations on the combustion chamber surface and the cooling fluid, results in different surface temperatures and temperature distributions within the engine's components. This section reviews the variation in heat flow into the components that comprise the combustion chamber, and the temperature distribution in these components.

12.7.1. Effect of Engine Variables

The following variables affect the magnitude of the heat flux to the different surfaces of the engine combustion chamber and thus the temperature distribution in the components that bound the chamber: engine speed; engine load; overall equivalence ratio; compression ratio; spark or injection timing; swirl and squish motion; mixture inlet temperature; coolant temperature and composition; wall material; wall deposits. Of these variables, speed and load have the greatest effect. Equation (12.19), derived from the Nusselt-Reynolds number relation,

$$h_c = \text{constant} \times B^{-0.2} p^{0.8} T^{-0.55} w^{0.8}$$

and the relation for heat-transfer rate per unit area, Eq. (12.2),

$$\dot{q} = h_c (T - T_w)$$

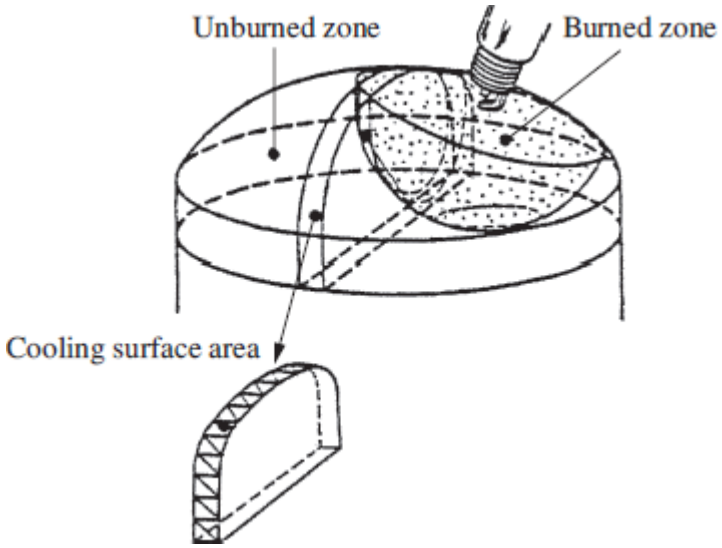
are useful for predicting these thermal trends as engine operating and design variables change. The temperature *T* in the above two equations is the average temperature of the in-cylinder gases. This choice is made for pragmatic reasons: the average gas temperature is readily obtained from the cylinder pressure (which can be measured or calculated), the ideal gas law $\left(pV = mR\overline{T}\right)$, and the mass in the cylinder. However, heat transfer to the combustion chamber walls is most significant when the hot burned gases contact or "wet" these walls. Figure 12.21 illustrates the situation in a spark-ignition engine where, during combustion, the burned gases behind the propagating flame contact only part of the cylinder head and piston crown. The heat transfer from the burned gas zone is given by:

$$\dot{Q}_b = \sum_i A_{ci,b} h_b (T_b - T_{w,i})$$

(12.40)

© McGraw-Hill Education. All rights reserved. Any use is subject to the Terms of Use, Privacy Notice and copyright information.

Figure 12.21 Illustration of heat transfer process during combustion in a spark-ignition engine. The burned gases are hot (~2500 K); the unburned gases are significantly cooler (400 to 800 K). The area wetted by the burned gases and unburned gases are shown, and can be calculated as indicated to obtain the burned zone and unburned zone heat fluxes [see Eqs. (12.40) and (12.41)].



where $A_{ci,b}$ is the area of the combustion chamber surface i wetted by the hot burned gases at temperature T_b. The heat transfer from the unburned gas zone is

$$\dot{Q}_u = \sum_i A_{ci,u} h_u (T_u - T_{w,i})$$

(12.41)

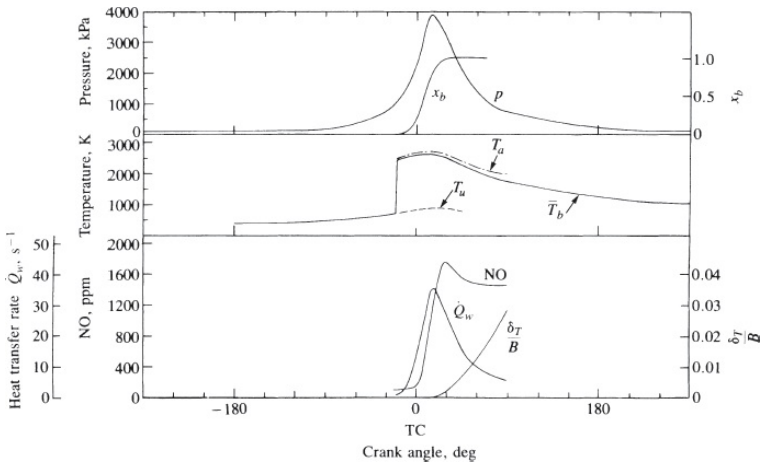
where
$\dot{Q}_u$ is the heat transfer from the unburned zone, $A_{ci,u}$ is the area of the combustion chamber wetted by the unburned gas, denoted by the subscript u. Other symbols have similar definitions to those in Eq. (12.40) but for the unburned gas zone. Because T_b is some four times higher than T_u (in K), the burned zone heat flux is much larger than the unburned zone heat flux.

This fundamentally-based description of the engine heat transfer process is the appropriate model to use to assess heat transfer effects of changes in engine design and operating variables. Figure 12.22 shows a set of results obtained with this two-zone combustion and heat transfer model in a cycle simulation of a spark-ignition engine at mid-speed and high load. As combustion proceeds, the mass fraction burned x_b, rises from zero at time of spark to approach unity at about 30° CA ATC, the cylinder pressure rises, as do the gas temperatures in the unburned and burned gas zones. The heat transfer rate rises from a low value before the spark discharge (unburned mixtures are at relatively low temperatures, less than about 600 K) to a peak value (more than an order of magnitude higher) at time of peak pressure and burned gas temperature (some 2500 K) at about 15° CA ATC, and then decays to about one-quarter of the peak rate by about 60° CA ATC. During the early stages of combustion, the total unburned gas wetted area is much larger than the burned gas wetted area; see Fig. 12.21. During combustion, the burned gas density is one-fourth that of the unburned (much lower temperature) gas: this wetted area ratio (unburned/burned) transitions through unity to values much less than one. Thus the changing relative size of $A_{c,u}$ and $A_{c,b}$ offsets the substantial difference between ($T_b - T_w$) and ($T_u - T_w$) in Eqs. (12.40 and 12.41). This is a major reason why heat transfer estimates based on the average temperature of the in-cylinder gases, and the total combustion chamber surface area, do not differ that much from the two-zone model estimates such as the one shown in Fig. 12.22. (Note that the boundary

© McGraw-Hill Education. All rights reserved. Any use is subject to the Terms of Use, Privacy Notice and copyright information.

layer thickness grows to some 3% of the cylinder bore of 80 to 90 mm, i.e. a few mm, which is consistent with the measurements shown in Fig. 12.20.)[1]

Figure 12.22 Cylinder pressure p, mass fraction burned x_b, unburned and burned gas temperatures (T_u = unburned, T_a = adiabatic burned core, $\overline{T}_b$ = mean burned gas temperatures), heat-transfer rate $\dot{Q}_w$ (normalized by fuel flow rate × heating value), thermal boundary-layer thickness δ_T and mean nitric oxide concentration in the burned gases, through a four-stroke engine operating cycle, predicted by thermodynamic-based cycle simulation. 5.7-dm^3 displacement eight-cylinder engine operating at wide-open throttle, 2500 rev/min, with equivalence ratio = 1.1. Gross indicated mean effective pressure is 918 kPa and specific fuel consumption is 254 g/kW · h.[48]



With this fundamental description of the of the loss of thermal energy from the hot burned gases to the combustion chamber walls, the effect of changes in the above listed variables on engine and component heat flux will now be summarized. The comments which follow apply primarily to spark-ignition engines. In compression-ignition engines, the basic geometry of the hot burned gas zones and the air are different, and distribution of heat flux and temperature varies greatly with the size of cylinder and thus its combustion chamber, and with the in-cylinder flow.

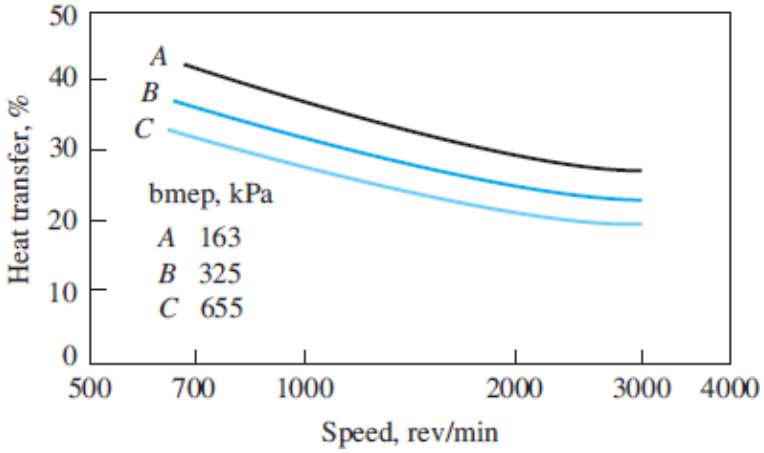
12.7.1.1. Speed, Load, and Equivalence Ratio

The convective wall heat flux varies significantly with engine speed and load. Measured time-resolved values (in kW/m^2) taken in a gasoline spark-ignition engine are shown in Figs. 12.12 and 12.13.[40] The heat flux profiles at the four measuring locations show comparable peak values though this is not always the case. The load scaling (based on volumetric efficiency: 90% corresponds to full-load; 50% would be about half load) and the speed scaling, in terms of heat transfer rate, are significant, as Eq. (12.19) indicates. The gas pressure (load) and speed scaling have exponents of 0.8.

Cycle simulation predictions of spark-ignition engine combustion chamber heat transfer (per cycle) as a function of speed and load are shown in Fig. 12.23. The cycle heat transfer is expressed as a percent of the fuel's chemical energy (mass of fuel × Q_{LHV}). The heat transfer to the total combustion chamber surface (excluding the exhaust port) was calculated using a thermodynamic-based cycle simulation (see Sec. 14.4). The relative importance of heat losses *per cycle* decreases as speed and load increase (Fig. 12.23): the *average* heat transfer *per unit time*, however, increases as speed and load increase (Fig. 12.13).

© McGraw-Hill Education. All rights reserved. Any use is subject to the Terms of Use, Privacy Notice and copyright information.

Figure 12.23 Predicted average heat-transfer rate (as percent of fuel flow rate ×Q_{LHV}) to combustion chamber walls of an eight-cylinder 5.7-dm^3 spark-ignition engine as a function of speed and load. Stoichiometric operation; MBT timing.[48]



Since speed and load affect p, T, and w in Eq. (12.19), simpler correlations have been developed to predict component heat fluxes directly from experimental data. Time-averaged heat fluxes at several combustion chamber locations, determined from measurements of the temperature gradient in the chamber walls, have been fitted with the empirical expression

$$\dot{q} = \text{constant} \times \left(\frac{\dot{m}_f}{A_p} \right)$$

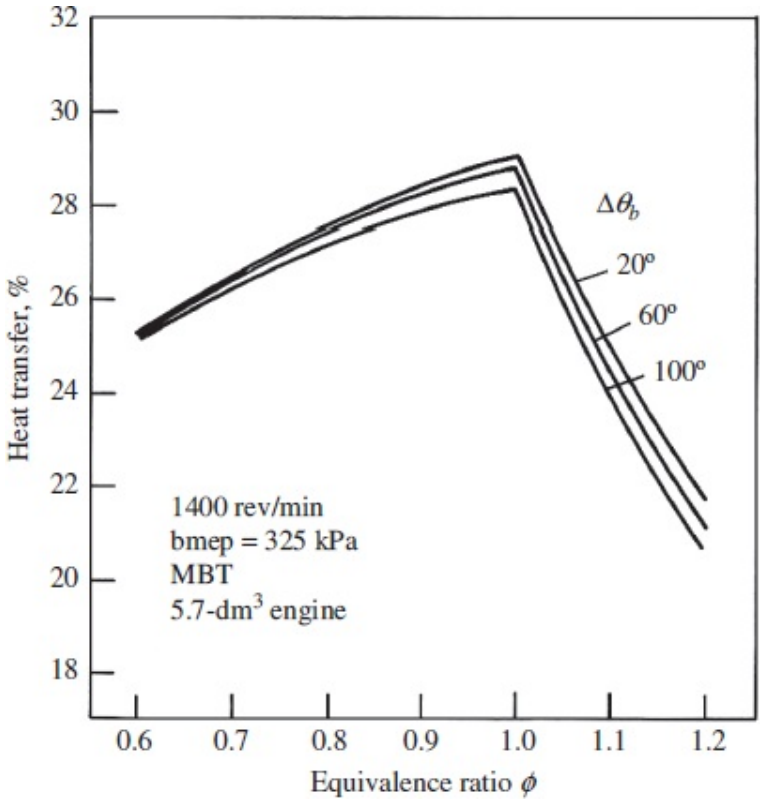
(12.42)

with n between 0.5 and 0.75 (the value of n depending on engine type and location within the combustion chamber and A_p the piston crown area). Results for several spark-ignition and diesel engine designs, with appropriate values of n, can be found in Refs. 49 to 51. While this correlation is not dimensionless and is different from Eq. (12.19), it provides a convenient method for scaling experimental heat flux data. The heat flux to the cylinder head and liner for a spark-ignition engine were well correlated by Eq. (12.42) with n = 0.6. The heat flux distributions over the cylinder head at a fuel flow rate per unit piston area of 0.195 kg/s · m^2 for several different DI diesel engines were comparable in magnitude. The effect of speed at wide-open throttle on component temperatures for a spark-ignition engine can also be found in Ref. 51. Exhaust valve, piston crown and top ring groove, and nozzle throat temperatures for a Comet prechamber diesel as a function of fuel flow rate can be found in Ref. 49.

The peak heat flux in an SI engine occurs at the mixture equivalence ratio for maximum power, $\phi \approx 1.1$, and decreases as ϕ is leaned out or enriched from this value. The major effect is through the gas temperature in Eqs. (12.2) and (12.19). However, as a fraction of the fuel's chemical energy, the heat transfer per cycle is a maximum at ϕ = 1.0 and decreases for richer and leaner mixtures as shown by the thermodynamic-based cycle-simulation predictions in Fig. 12.24.

© McGraw-Hill Education. All rights reserved. Any use is subject to the Terms of Use, Privacy Notice and copyright information.

Figure 12.24 Predicted average heat-transfer rate (as percent of fuel flow rate ×Q_{LHV}) to combustion chamber walls of an eight-cylinder 5.7-dm^3 spark-ignition engine as a function of equivalence ratio and burn rate ($\Delta\theta_b$ = combustion duration).[48]



Measurements and predictions of the effects of variations in engine speed and load in a DI diesel (with a 2.3ℓ cylinder size) show similar trends to SI engines. Significant variations with combustion chamber surface location were observed, with the piston bowl and cylinder head above the bowl showing higher peak heat fluxes do to the proximity of these surfaces to the hot combustion gases with these surfaces. One expects higher convective and radiative heat transfer rates in these locations. In CI engines, the overall air/fuel ratio variation is incorporated directly in the load variation effects.[52]

12.7.1.2. Compression Ratio

Increasing the compression ratio in an SI engine decreases the total heat flux to the coolant until $r_c \approx 10$; thereafter heat flux increases slightly as r_c increases.[53] The magnitude of the change is modest; for example, a 10% decrease in the maximum heat flux (at the valve bridge) occurs for an increase in r_c from 7.1 to 9.4.[49] Several gas properties change with increasing compression ratio (at fixed throttle setting): cylinder gas pressures and peak burned gas temperatures increase; gas motion increases; combustion is faster; the surface/volume ratio close to TC increases; the gas temperature late in the expansion stroke and during the exhaust stroke is reduced. Measured mean exhaust gas temperatures confirm the last point, which probably dominates the trend at lower compression ratios. As the compression ratio increases further, the other factors (which all increase heat transfer) become important.

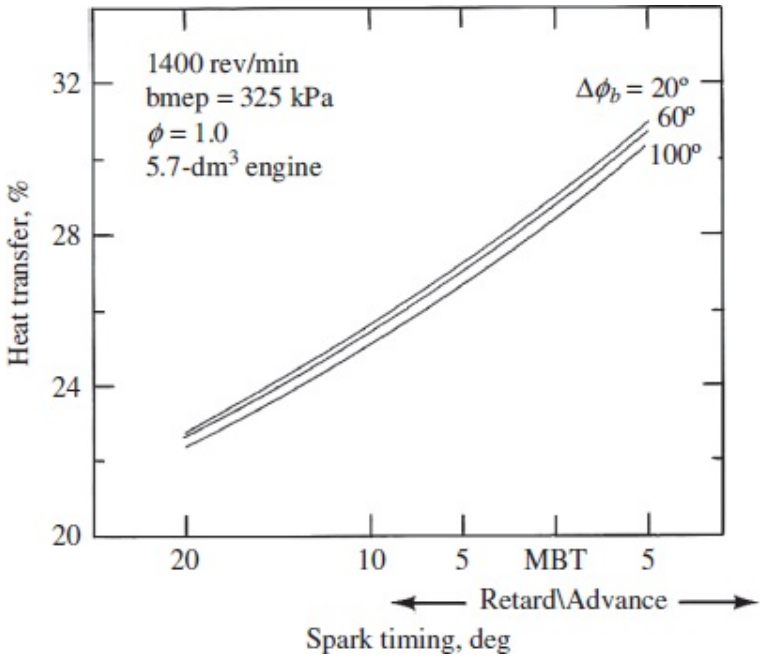
The effect of changes in compression ratio on component temperatures depends on location. Generally, head and exhaust valve temperatures decrease with increasing compression ratio, due to lower late-expansion and exhaust stroke temperatures. The piston and spark plug electrode temperatures increase, at constant throttle setting, due to the higher peak combustion temperatures at higher compression ratios. If knock occurs (see Sec. 9.6), increases in heat flux and component temperatures result; see below.

© McGraw-Hill Education. All rights reserved. Any use is subject to the Terms of Use, Privacy Notice and copyright information.

12.7.1.3. Spark Timing

In a naturally-aspirated SI engine, retarding the spark timing decreases the heat flux as shown in Figs. 12.12*b* and 12.25. A similar trend in CI engines with retarding injection timing would be expected. The burned gas temperatures are decreased as timing is retarded because combustion occurs later when the cylinder volume is larger. Surface temperature trends vary with component. Piston and spark plug electrode temperatures change most with timing variations; exhaust valve temperature increases as timing is retarded due to higher exhausting gas temperatures.[49] In turbocharged SI engines, the impact of retarding combustion is more complex because the engine's exhaust gas temperature increases, thus driving the turbocharger faster. Depending on how the engine is being controlled, this could increase the compressor boost level and airflow. Depending on the intercooler performance, the engine intake air temperature may then increase, resulting in an increase in burned gas temperature. However, the convective heat transfer to the combustion chamber walls is driven by the difference between the in-cylinder gas temperature and the wall temperatures. Most important, therefore, are the higher burned gas temperatures attained. These temperatures are not that strongly influenced by engine operating condition charges.

Figure 12.25 Predicted average heat-transfer rate (as percentage of fuel flow rate ×Q_{LHV}) to combustion chamber walls of an eight-cylinder 5.7-dm^3 spark-ignition engine as a function of spark timing and burn rate ($\Delta\theta_b$ = combustion duration).[48]



12.7.1.4. Swirl and Squish

Increased gas velocities, due to swirl or squish motion, will result in higher heat fluxes. Equation (12.19) indicates that the effect on local heat flux, relative to quiescent engine designs, should be proportional to local gas velocity raised to the 0.8 power. Experimental evidence supports this trend.[41]

12.7.1.5. Inlet Temperature

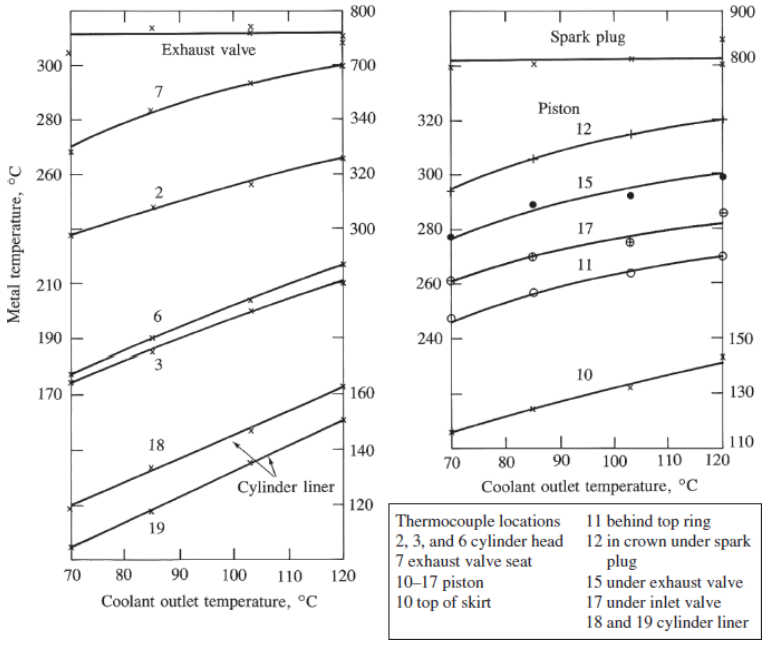
The heat flux increases with increasing inlet temperature since the gas temperatures throughout the cycle are increased. An increase of 100 K gives a 13% increase in heat flux.[40]

© McGraw-Hill Education. All rights reserved. Any use is subject to the Terms of Use, Privacy Notice and copyright information.

12.7.1.6. Coolant Temperature and Composition

Increasing coolant temperature increases the temperature of components directly cooled by the liquid coolant. Figure 12.26 shows the result of a 50-K rise in coolant temperature in a spark-ignition engine. The exhaust valve and spark plug temperatures are unchanged. The smaller response of the metal temperatures to coolant temperature change occurs at higher heat flux locations (such as the valve bridge), and indicates that heat transfer to the coolant has entered the nucleate-boiling regime in that region. The response is greater where heat fluxes are lower (e.g., the cylinder liner), indicating that there heat transfer to the coolant is largely by forced convection. When nucleate boiling occurs (i.e., when steam bubbles are formed in the liquid at the metal surface, although the bulk temperature of the coolant is below the saturation temperature), the metal temperature is almost independent of coolant temperature and velocity.

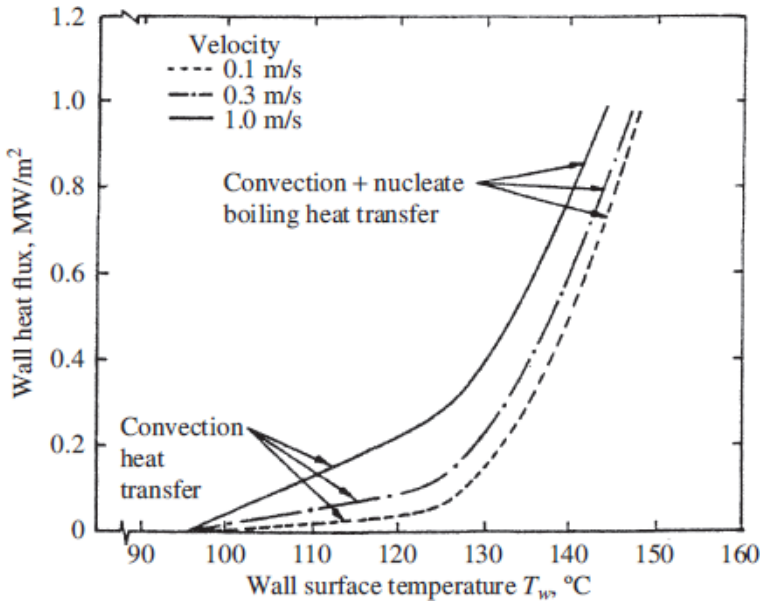
Figure 12.26 Effect of coolant temperature on cylinder head, liner, exhaust valve, valve seat, piston, and spark plug metal temperatures. Spark-ignition engine at 5520 rev/min and wide-open throttle. r_c = 8.5.[49]



The impact of adding nucleate boiling heat transfer to forced-convection heat transfer where coolant passage surface temperatures are high (e.g., between adjacent exhaust valve seats in the cylinder head) are illustrated in Fig. 12.27.[54] The heat flux measurements shows the influence of cooling water flowing at a given velocity (0.1 to 1 m/s) over a wall with various heat fluxes flowing through the wall surface. The resulting surface temperature was measured. The coolant water temperature was 95°C. As the heat flux rises, the wall temperature rises linearly at each flow velocity until about 125°C: the rate of increase in wall temperature with increasing heat flux then roughly halves. Higher heat fluxes can be accommodated with significantly lower increases in wall surface temperatures. The occurrence of nucleate boiling this moderates the impact of higher heat fluxes. However at much higher heat fluxes, nucleate boiling can produce so much steam that it forms a vapor film which then acts as an insulating layer adjacent to the wall surface and forces the surface temperature to much higher and potentially damaging values.

© McGraw-Hill Education. All rights reserved. Any use is subject to the Terms of Use, Privacy Notice and copyright information.

Figure 12.27 Impact of nucleate boiling heat transfer on forced-convection engine cooling: influence of cooling water velocity on relationship between heat flux and wall surface temperature (cooling water temperature 95°C, and pressure 2 bar).[54]



Automotive liquid coolants are mixtures of ethylene glycol (or propylene glycol) with water usually in about equal mass proportions. Water with its high specific heat and density is a very good cooling fluid, but its freezing temperature (of 0°C) makes it unsuitable for many applications in colder regions. Glycol (usually ethanol glycol) is added as an "anti-freeze": with glycol, the water no longer freezes but forms ice crystals that, though they are precipitated—the so-called ice flaking point, can still be pumped through the engine's cooling circuit. The coolant's boiling point is also raised. Table 12.2 shows the effect that adding various levels of glycol to water has on the ice flaking point and the boiling point. Coolants also contain additives to protect metallic cooling-system components against corrosion, to prevent foaming, and protect glycol from oxidation.

Table 12.2 Ice flaking and boiling points for water-glycol mixtures[55]

Glycol, % by vol.	Ice flaking point, °C	Boiling point, °C
10	−4	101
20	−9	102
30	−17	104
40	−26	106
50	−39	108

Mixtures of glycol and water are not as effective coolants as water due to their different physical properties. Values of the physical properties of automotive coolants can be found in standard references (e.g., Ref. 56). Equations for the variation of the relevant physical properties of automotive coolants, with temperature, for 50% glycol aqueous mixtures have been developed by Alshamani.[57]

12.7.1.7. Wall Material

© McGraw-Hill Education. All rights reserved. Any use is subject to the Terms of Use, Privacy Notice and copyright information.

While the common metallic component materials of cast iron and aluminum have substantially different thermal properties, they both operate with combustion chamber surface temperatures (200 to 400°C) that are low relative to burned gas temperatures. Interest continues in exploring materials that could operate at much higher temperatures so that the heat losses from the working fluid would be reduced. Ceramic materials, such as silicon nitride and zirconia, have much lower thermal conductivity than cast iron, would operate at higher temperatures, and thereby insulate the engine. The thermal properties of some of these materials are listed in Table 12.3. With these thermally insulating materials, it is possible to reduce the heat transfer through the wall by a substantial amount.

Table 12.3 Thermal properties of wall materials

Material	Thermal conductivity k, W/m · K	Density ρ, kg/m^3	Specific heat c, J/kg · K	Thermal diffusivity α, m^2/s	$k\rho c$	Skin depth δ, mm	Peak temperature swing, K
Cast iron	54	7.2×10^3	480	1.57×10^{-5}	1.8×10^8	2.8	18
Aluminum	155	2.8×10^3	915	6.2×10^{-5}	3.9×10^8	5.4	12
Silicon nitride	5–10	2.5×10^3	710	2.8×10^{-6}	1.3×10^7	1.2	70
Sprayed zirconia	1.2	5.2×10^3	732	3.2×10^{-7}	4.6×10^6	0.39	95

This approach has been considered for diesel engines where there is the possibility of eliminating the conventional engine coolant system. Since the coolant-side heat transfer is essentially steady during each cycle, a high-enough thermal resistance in the wall material can bring the net heat transfer for the cycle to close to zero. However, there is still substantial heat transfer between the working fluid in the cylinder and the combustion chamber walls. Thermodynamic simulations of a turbocompounded diesel engine operating cycle, with the ceramic material at about 800 K surface temperature, show that the *net* heat transfer is much reduced compared with the normal metal wall case. However, there is substantial heat transfer to the gas from the ceramic walls during intake (which reduces volumetric efficiency) and compression (which increases compression stroke work), and still significant heat transfer from the gas during combustion and expansion. These negative effects of high combustion chamber surface temperatures reduce the efficiency benefits to only modest gains.[31] For spark-ignition engines, the heat transfer from the hot walls to the incoming charge makes thermally insulating materials more unattractive still. Such charge-heating heat transfer would increase the unburned mixture temperature leading to earlier onset of knock, the autoignition of the end gas fuel-air mixture (see Sec. 9.6).

The inherently unsteady nature of the heat-transfer interaction with the wall leads to time-varying combustion chamber surface temperatures. During combustion and expansion, the thermal energy transferred from the gas to the wall is stored in a thin layer of wall material adjacent to the surface. While some of this thermal energy diffuses through the wall, during intake and compression much of it is transferred back to the now low-temperature cylinder contents. The depth of penetration of the thermal wave into the material, the skin depth δ, is proportional to $\sqrt{\alpha}/\omega$ where $\alpha = k/(\rho c)$ is the thermal diffusivity and ω the frequency of the wave (proportional to engine speed). Values of α and δ are given in Table 12.3 for an engine speed of 1900 rev/min: $\sqrt{\alpha}/\delta \approx 1.4$ (units: s$^{-1/2}$), a constant. The magnitude of the temperature fluctuation (important because it is a source of fluctuating thermal stress) is proportional to $(\delta\rho c)^{-1}$: this varies as $(k\rho c)^{-1/2}$. Estimated peak surface temperature swings for the materials in Table 12.3 are tabulated.

12.7.1.8. Knock

© McGraw-Hill Education. All rights reserved. Any use is subject to the Terms of Use, Privacy Notice and copyright information.

Knock in an SI engine is the spontaneous ignition of the unburned "end-gas" ahead of the flame as the flame propagates across the combustion chamber. It results in an increase in gas pressure and temperature above the normal combustion levels (see Sec. 9.6). Knock results in increased local heat fluxes to regions of the piston, the cylinder head, and liner in contact with the autoignited end-gas. Increases to between twice and three times the normal heat flux in the end-gas region have been measured.[59, 60] It is thought that the primary knock damage to the piston crown in this region is due to metal fatigue resulting from the combination of high local pressure oscillations, and higher material temperatures.

12.7.2. Component Temperature Distributions

Here, we show illustrative examples of measured temperature distributions in various engine components. Normally, the heat flux to the combustion chamber surfaces is highest in the central region of each cylinder head, in the exhaust valve seat region, and to the center of the piston crown. It is lowest to the cylinder liner. Cast-iron pistons run about 40 to 80°C hotter than aluminum pistons. With flat-topped pistons (typical of spark-ignition engines) the center of the crown is hottest and the outer edge cooler by 20 to 50°C. Diesel engine piston crown surface temperatures are about 50°C higher than SI engine equivalent temperatures. As shown in Fig. 12.28, the maximum piston temperatures with DI diesel engine pistons are at the lip of the bowl. In prechamber diesel engines, maximum piston temperatures occur where the hot jet exiting the pre-chamber impinges on the piston crown.

Figure 12.28 Isothermal contours (solid lines) and heat flow paths (dashed lines) determined from measured temperature distribution in piston of high-speed DI diesel engine. Bore 125 mm, stroke 110 mm, r_c = 17, 3000 rev/min, and full load.[58]

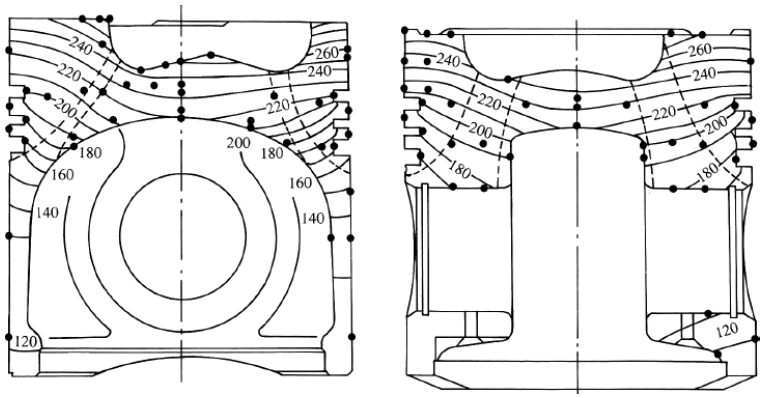


Figure 12.29 shows the temperatures at various locations on a four-cylinder SI engine cylinder head. The maximum temperatures occur where the heat flux is high and access for cooling is limited. Such locations are the bridge between the valves and the region between the exhaust valves of adjacent cylinders. Figure 12.30 shows how the average heat flux and temperature vary along the length of a DI diesel engine liner. Because the lower regions of the liner are only exposed to combustion products for part of the cycle after substantial gas expansion has occurred, the heat flux and temperature decrease significantly with distance from the cylinder head. Note that the heat generated by friction between the piston and the liner, the difference between
$\dot{q}_{GL}$ (the gas to liner heat flux) and
$\dot{q}_{L}$ (the total heat flux into the liner), is a significant fraction of the liner thermal loading.

© McGraw-Hill Education. All rights reserved. Any use is subject to the Terms of Use, Privacy Notice and copyright information.

Figure 12.29 Variation of cylinder head temperature with measurement location in a spark-ignition engine operating at 2000 rev/min, wide-open throttle, with coolant water at 95°C and 2 atm.[54]

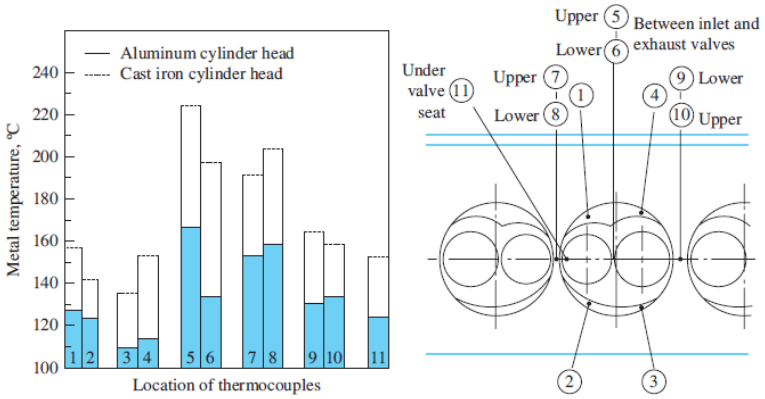
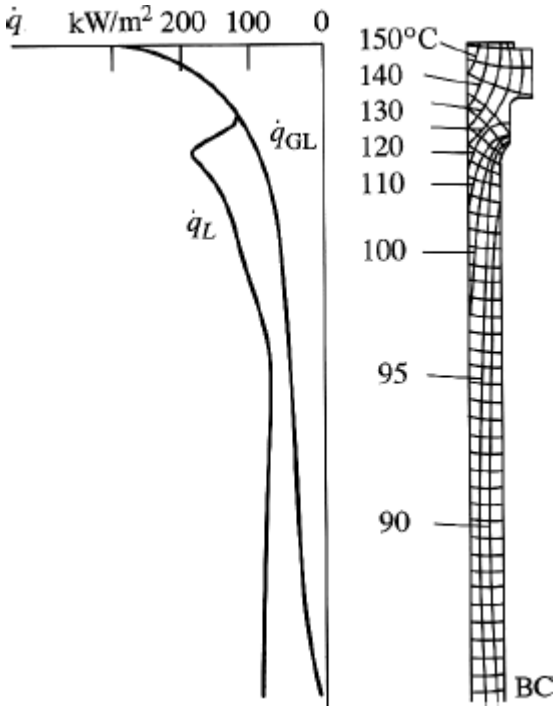


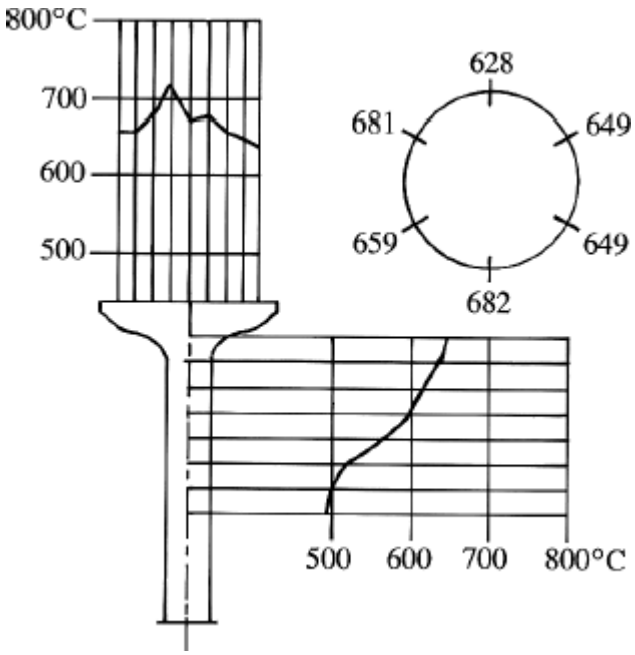
Figure 12.30 Temperature and heat flux distribution in the cylinder liner of a high-speed DI diesel engine at 1500 rev/min and bmep = 11 bar.
$\dot{q}_L$ is heat flux into the liner;
$\dot{q}_{GL}$ is heat flux from the gas to the liner: difference is friction-generated heat flux.[61]



The exhaust valve is cooled through the stem and the guide, and the valve seat. In small-size valves the greater part of the heat transfer occurs through the stem; with large-size valves, the valve seat carries the higher thermal load. Figure 12.31 shows the temperature distribution in an exhaust valve (one of two) in a two-stroke DI diesel at high load. Such peak exhaust valve temperatures of 650 to 700°C are typical of highly loaded engine operation. When additional exhaust valve head cooling is required, under extreme conditions, sodium-cooled valves can be used. Here the valve stem is hollow and is filled with sodium: the melting and thermally driven convective motion of the sodium in the stem transfers thermal energy from the valve head region to that portion of the stem within the valve guide.

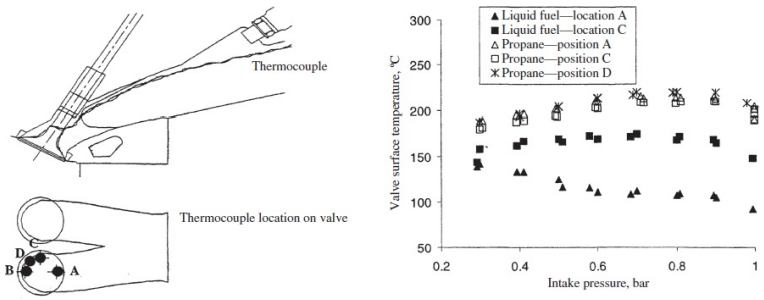
© McGraw-Hill Education. All rights reserved. Any use is subject to the Terms of Use, Privacy Notice and copyright information.

Figure 12.31 Temperature distribution in one of the four exhaust valves of a two-stroke cycle uniflow DDA 4-53 DI diesel engine. Bore = 98 mm, stroke = 114 mm.[62]



Intake valve temperatures in a warmed-up engine are higher than the coolant temperature (≈ 90°C) but significantly lower than exhaust valve temperatures. The valve head is heated by heat transfer from the high-temperature in-cylinder burned gases (and by the backflow of hot residual into the intake when the intake valve opens). It is cooled by the intake airflow and, with port fuel-injection, by the evaporation of liquid fuel off the valve head and stem surface. Figure 12.32 shows valve surface temperatures over the load range of a 2-liter four-cylinder spark-ignition engine with port fuel injection, with gasoline and propane fueling. The valve surface temperatures (at several locations on the valve head) rise modestly with increasing load—except where fuel spray impingements are direct and substantial (thermocouple location A). The head temperatures are about 40 deg. C higher with propane fuel, where there is no liquid evaporation. Fuel evaporation with gasoline cools the entire valve head. At locations with direct impingement, local evaporation of the impinging liquid steadily reduces the surface temperature (location A), as increasing amounts of liquid fuel are deposited as load increases. Under typical gasoline engine operating conditions, intake valve head temperatures are in the 150 to 200°C range.[24, 26]

Figure 12.32 Intake valve-head surface temperatures at several locations in an operating spark-ignition engine fueled with gasoline and propane, as a function of load (range of intake manifold pressures), at 1500 rev/min.[26]

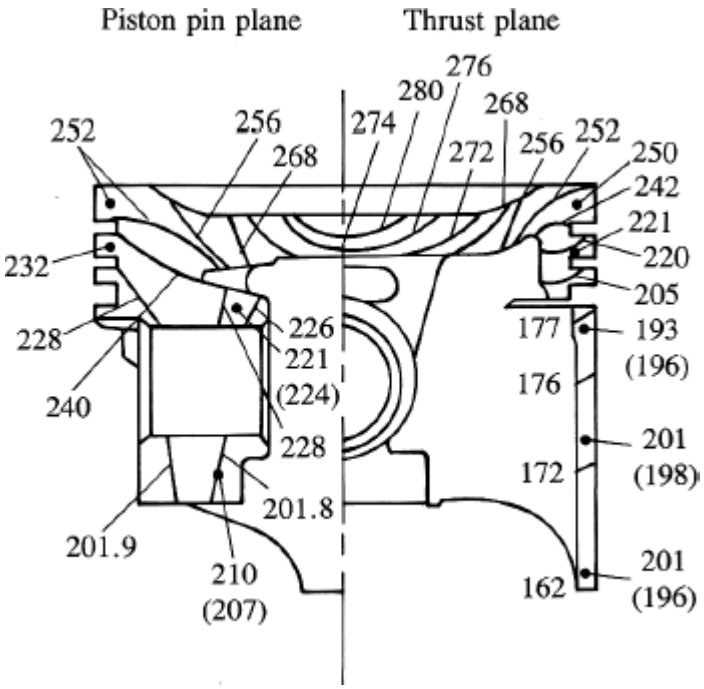


Temperature distributions in engine components can be calculated from a knowledge of the heat fluxes across the component surface using finite element analysis techniques. For steady-state engine operation, the depth within a component to which the unsteady temperature fluctuations (caused by the variations in heat flux during the cycle) penetrate is small, so a quasi-steady solution is satisfactory. Results from such calculations for a spark-ignition engine piston illustrate the method.[63] A

© McGraw-Hill Education. All rights reserved. Any use is subject to the Terms of Use, Privacy Notice and copyright information.

mean heat-transfer coefficient from the combustion chamber gases to the piston crown, and a mean chamber gas temperature, were defined (using the input from a cycle simulation of the type described in Sec. 14.4). These define the time-averaged heat flux into the piston. Heat-transfer coefficients for the different surfaces of the piston (underside of dome, ring-land areas, ring regions, skirt outer and inner surfaces, wrist pin bearings, etc.) were estimated. The actual piston shape was approximated with a three-dimensional grid for one quadrant of the piston. A standard finite-element analysis of the heat flow through the piston yields the temperature distribution within the piston. The thermal stresses can then be calculated and added to the mechanical stress field to determine the total stress distribution. Such results can be used to define the potential fatigue regions in the actual piston design. Figure 12.33 shows the temperature distribution calculated with this approach, compared with measurements (indicated by dots). The agreement is acceptable, except in the piston skirt where the heat-transfer rate between the skirt and cylinder liner has been overestimated.

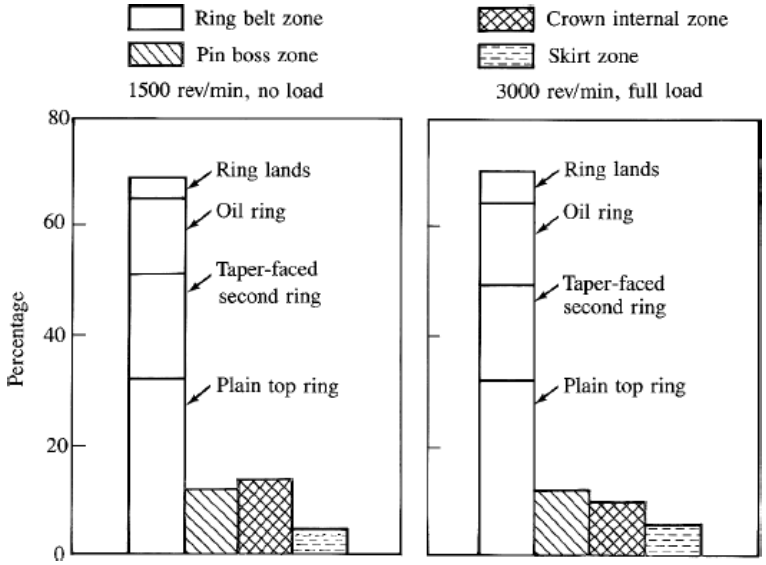
Figure 12.33 Measured (dots) and calculated temperature (°C) distributions in piston pin and thrust planes of the piston of a four-cylinder 2.5-liter spark-ignition engine at 4600 rev/min and wide-open throttle.[63]



Detailed measurements of the temperature distribution in the piston allow the relative amounts of heat which flow out of the different piston surfaces to be estimated. Figure 12.34 shows such estimates for a DI diesel engine at no-load and full-load. About 70% of the heat flows out through the ring zone, and much smaller amounts through the pin boss zone, underside of the crown and skirt. In larger diesel engines and highly loaded diesel engines, one or more cooling channels are usually incorporated into the piston crown. This reduces the heat flow out through the ring area significantly.[64]

© McGraw-Hill Education. All rights reserved. Any use is subject to the Terms of Use, Privacy Notice and copyright information.

Figure 12.34 Heat outflow from various zones of a piston as percentage of heat flow in from combustion chamber. High-speed DI diesel engine, 125-mm bore, 110-mm stroke, r_c = 17.[58]



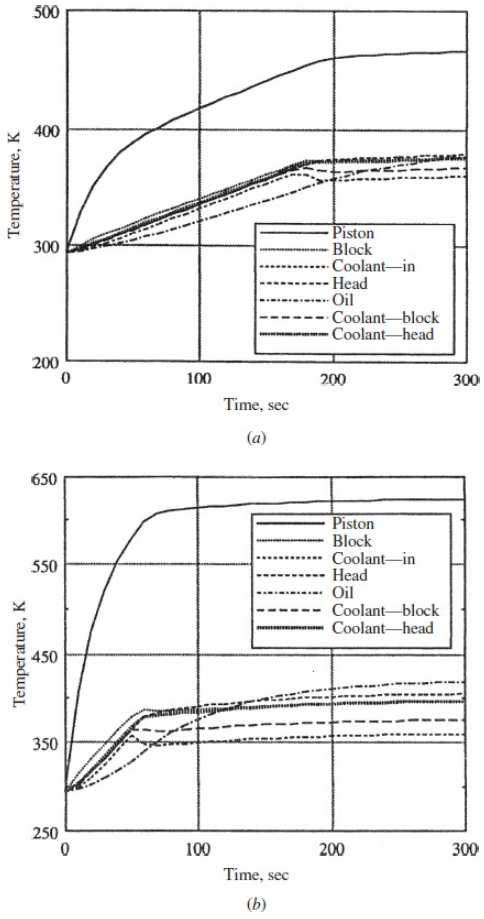
12.7.3. Engine Warm-Up

So far we have focused primarily on heat transfer processes in a warmed-up engine. When an engine is started after a substantial shut down period. The components are at close-to-ambient temperatures. Thus the wall temperature T_w in Eq. (12.2) is well below the warmed-up values discussed in the previous section, so the wall heat transfers (driven by $T_g - T_w$) are higher. It takes from one to ten or so minutes for the engine's components to reach their steady state temperatures, depending on operating conditions. The engine's performance, efficiency, and emissions depend on component (and exhaust-gas) temperatures. These are all affected by the engine's heat transfer process: an engine's warm-up behavior is important.

The engine warm-up process can be studied through measurement of component surface and coolant temperatures and through the analysis of heat flows through the components that make up the total engine structure. Figure 12.2 illustrates the layout of models used to do this type of analysis, with heat flows through thermal resistance networks, and thermal capacitances at the nodes to capture the changing thermal state (temperature) of each major component and the fluids involved. Results from such analysis are shown in Fig. 12.35,[65] which shows temperature versus time plots for the major components of a gasoline SI engine at light load, and at wide-open throttle. [Note each component in the block diagram of the engine structure is characterized by its mean temperature since the Biot number (hd/k), the ratio of the resistance to conduction within a solid to the convection heat flux resistance across the thermal boundary layer at the fluid/solid surface boundary, is less than 0.1.]

© McGraw-Hill Education. All rights reserved. Any use is subject to the Terms of Use, Privacy Notice and copyright information.

Figure 12.35 Predicted temperatures of key components as a function of time following a cold (20°C) engine start. 1.9-liter four-cylinder SI engine; coolant 50% ethylene glycol, flow rate 0.57 kg/s; oil flow rate, 0.08 kg/s. (a) 1500 rev/min, 260-kPa bmep; (b) 2500 rev/min, wide-open throttle. Convective heat transfer coefficients, W/m^2 · K: head, 10; block, 25; oil pan, 70.[65]



Engine operating conditions have significant effects on component temperatures, as discussed in the previous section. Figure 12.35*a* shows light-load low-speed behavior (typical of normal passenger vehicle driving): temperatures rise over some 200 seconds. The piston (since it is not directly cooled by the coolant) has a temperature about 100 K hotter than the other components. Its temperature rises rapidly over the first 50 seconds, and then more slowly, paralleling the block, head, and coolant temperatures. The coolant circuit thermostat opens, allowing coolant flow to the radiator, at about 175 seconds. The oil temperature lags because its thermal energy is received through secondary processes. The rate of heat transfer to the oil is small until the rest of the components reach higher temperatures. At the higher load and speed, component temperatures rise more rapidly, and to higher values: the thermostat opens at about 60 seconds after start up. This accelerated behavior results from the significantly higher heat fluxes (W/m^2) at the wide-open-throttle condition, primarily due to the higher engine speed.[65] Characteristic times for component warm up are not as strongly influenced by load since, while heat fluxes are higher (see Fig. 12.23), the steady-state warmed-up temperatures are higher too.[66]

The complexity of the warm-up process in the major engine components is indicated by the results shown in Fig. 12.36, where the heat flow rates into and out of the engine's block and cylinder head, and the increase in these component's stored thermal energy, are plotted as a function of time. Figure 12.36*a* shows the heat flow through the block. The largest heat transfer is to the coolant. The rapid increase in heat flux to the coolant at 165 seconds occurs because the thermostat has opened, admitting cool water. The heat flux form the piston to the liner plays an important role in heating this component, adding almost 40% to the direct heat flux from the hot in-cylinder combustion gases. At this point, the rate at which the thermal energy stored in the block increases, drops to close to zero. Note that in the quasi-steady-state situation beyond this point, the heat transfer driven by the in-cylinder hot gases resulting from combustion, levels off at about 70% of the heat flux into the

© McGraw-Hill Education. All rights reserved. Any use is subject to the Terms of Use, Privacy Notice and copyright information.

coolant: the additional coolant thermal load is the heat flux from the pistons through the cylinder liners to the coolant, augmented by thermal energy from the lubricating oil generated by frictional dissipation.[65]

Figure 12.36 (a) Predictions of heat flow rates into and out of engine block of a four-cylinder spark-ignition engine, and rate of thermal energy storage in the block. (b) Predictions of heat flow rates and storage for the cylinder head. 1.9-liter four-cylinder gasoline engine operating at stoichiometric air/fuel ratio, MBT spark timing, 1500 rev/min, bmep 260 kPa.[65]

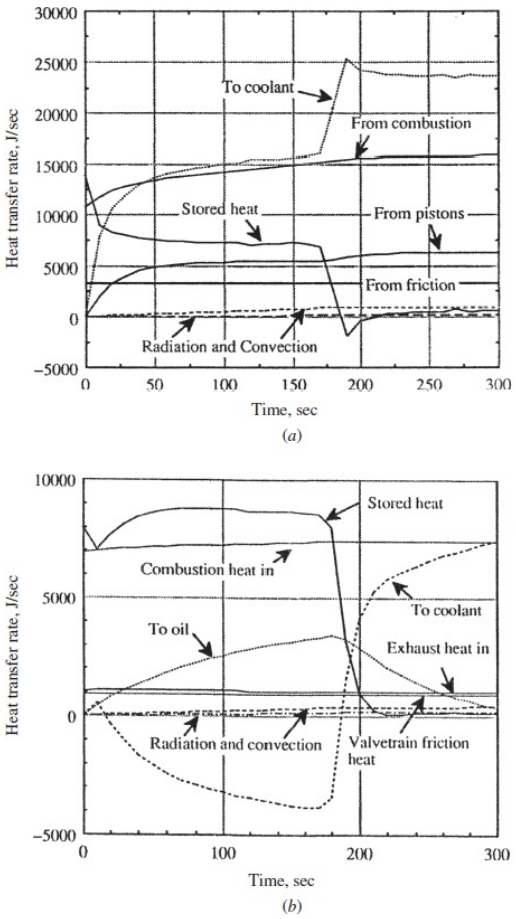


Figure 12.36*b* shows similar results for the engine's cylinder head. The simulation results indicate that the coolant initially picks up thermal energy from the block and actually heats the head. The oil removes heat form the head until the radiator thermostat opens: shortly thereafter (see Fig. 12.35*a*) it reaches a higher temperature than the head and becomes a source of thermal energy for this component.[65]

These discussions indicate the complexity of this transient engine warm-up process. Many of these details and trends are confirmed by experimental data (e.g., Ref. 67). Quantifying the component and gas temperatures during the engine warn-up is important for many reasons. The lower than steady-state temperature values increases engine friction: at 20°C the mechanical friction power loss is almost twice the warmed-up value.[67] The exhaust gas temperature is lower during warm-up which negatively impacts the turbine performance in the turbocharger. The fast light-off of the exhaust system catalyst and particulate traps is affected by the thermal energy flux in the engine exhaust. This is lower during warm-up.

[1] The model calculates the boundary layer thickness using a quasi-steady balance between the thermal energy flux to the wall and the additional adiabatic-core burned gas that enters the thickening thermal boundary layer region and experiences the decrease in gas temperature—adiabatic-core gas temperature to average of the wall temperature and that core temperature.

© McGraw-Hill Education. All rights reserved. Any use is subject to the Terms of Use, Privacy Notice and copyright information.

12.8. PROBLEMS

12.1. If radiation in the combustion chamber is negligible, Eqs. (12.5), (12.6), and (12.7) can be combined into the following overall equation approximating the time-averaged heat transfer from the engine:

$$\dot{q} = h_{c,o}\left(\overline{T}_g - \overline{T}_c\right)$$

Derive the expression for the overall heat transfer coefficient, $h_{c,o}$, for the flow of thermal energy from the hot gases in the cylinder, through the wall, into the coolant.

12.2. Given that the average heat flux through a particular zone in a cast iron liner 1 cm thick is 0.2 MW/m^2, the coolant temperature is 85°C, and the coolant side heat-transfer coefficient is 7500 W/m^2 · K, find the average surface temperature on the combustion chamber and coolant sides of the liner at that zone.

12.3. Figure 12.1 shows a schematic of the temperature profile from the gas inside the combustion chamber out to the coolant. Draw an equivalent figure showing schematically the temperature profiles at the following points in the engine cycle: (*a*) late in the intake stroke; (*b*) just prior to combustion; (*c*) just after combustion; (*d*) during the exhaust stroke. Your sketch should be carefully proportioned.

12.4. Using dimensional analysis, compare the relative heat losses of two geometrically similar SI engines (same bore/stroke ratio, same connecting rod/stroke ratio) operating at the same imep and power. Engine A has twice the displacement per cylinder of engine B. Assume that the wall temperature and the gas temperature for both engines are the same.

12.5

a. Using Woschni's in-cylinder heat transfer correlation, evaluate the percentage increase in heat transfer expected in an engine with a mean piston speed of 10 m/s when the swirl ratio is raised from 0 to 5. Do your comparison for the intake process only. The engine bore is 0.15 m and the engine speed is 2000 rev/min.

b. Explain how both the generation of swirl and the change in heat transfer that results affect the volumetric efficiency of the engine.

12.6

a. Explain how you would estimate the thermal boundary-layer thickness on the combustion chamber wall of an internal combustion engine.

b. Using representative data, make a rough estimate of the thickness of the thermal boundary layer in the combustion chamber of an SI engine just after the completion of combustion, and the fraction of the cylinder mass contained within the boundary layer. $B \approx 100$ mm. Transport properties given in Sec. 4.8.

12.7

a. Using the analysis found in Sec. 12.6.1, calculate the depth below the surface where the amplitude of the temperature oscillations has attenuated to 1% of the amplitude at the surface. The wall material is aluminum and the four-stroke cycle engine is operating at 2500 rev/min. For this estimate, consider only the temperature oscillations which have a frequency equal to the engine firing frequency ($\omega = 2\pi N/n_R$).

b. Repeat the calculation for the engine operating at 5000 rev/min.

c. What is the dependence of the penetration depth on the amplitude of surface temperature fluctuations?

© McGraw-Hill Education. All rights reserved. Any use is subject to the Terms of Use, Privacy Notice and copyright information.

12.8. The instantaneous heat-transfer rate $\dot{Q}$ from the cylinder gases to the combustion chamber walls in a spark-ignition gasoline engine may be estimated approximately from the equation

$$\dot{Q} = h_c A \left(\overline{T}_g - \overline{T}_w\right)$$

where h_c is the heat-transfer coefficient, A is the surface area, $\overline{T}_g$ is the average temperature of the gas in the cylinder, and $\overline{T}_w$ is the average wall temperature. The heat-transfer coefficient can be obtained from the Nusselt, Reynolds, and Prandtl number relationship:

$$\mathrm{Nu} = C(\mathrm{Re})^m(\mathrm{Pr})^n$$

where $C = 0.4$, $m = 0.75$, $n = 0.4$. The characteristic velocity and length scales used in this relation are the mean piston speed and the cylinder bore.

Assuming appropriate values for the engine geometry and operating conditions at wide-open throttle with the wall temperature at 400 K, at an engine speed of 2500 rev/min, and using the cylinder pressure versus crank angle curve of Fig. 12.22, calculate the following:

a. The *average* temperature of the gas in the cylinder at $\theta = -180°, -90°, 0°, 20°, 40°, 90°, 150°$.

b. The instantaneous heat-transfer coefficient h_c and heat-transfer rate $\dot{Q}$ from the gas to the combustion chamber walls of one cylinder at these crank angles. Plot these results versus θ.

c. Estimate the fraction of the fuel energy that is transferred to the cylinder walls during compression and during expansion.

Assume for the gas that the viscosity $\mu = 7 \times 10^{-5}$ kg/m · s, the thermal conductivity $k = 1.5 \times 10^{-1}$ J/m · s · K, the molecular weight = 28, and the Prandtl number is 0.8. Assume that the combustion chamber is disc shaped with $B = 102$ mm, $L = 88$ mm, and $r_c = 9$. (The calculations required for this problem are straightforward; do not attempt anything elaborate.)

© McGraw-Hill Education. All rights reserved. Any use is subject to the Terms of Use, Privacy Notice and copyright information.

12.9. REFERENCES

1. Sitkei, G.: *Heat Transfer and Thermal Loading in Internal Combustion Engines*, Akademiai Kiado, Budapest, 1974.
2. Bohac, S. V., Baker, D. M., and Assanis, D. N., "A Global Model for Steady State and Transient S.I. Engine Heat Transfer Studies," SAE paper 960073, SP-1168 Modeling of SI and CI Engines, SAE, 1996.
3. Khovakh, M. (ed.): *Motor Vehicle Engines*, Ch. 12, Mir Publishers, Moscow, 1971.
4. Burke, C. E., Nagler, L. H., Campbell, E. C., et al.: "Where Does All the Power Go,"*SAE Trans.*, vol. 65, pp. 713–738, 1957.
5. Gruden, D., Kuper, P. F., and Porsche, F.: "Heat Balance of Modern Passenger Car SI Engines," in *Heat and Mass Transfer in Gasoline and Diesel Engines,* D. Spalding and N. H. Afgan (eds), Hemisphere Publishing Corp., New York, 1989.
6. Novak, J. M., and Blumberg, P. N.: "Parametric Simulation of Significant Design and Operating Alternatives Affecting the Fuel Economy and Emissions of Spark-Ignited Engines," SAE paper 780943, *SAE Trans.*, vol. 87, 1978.
7. Annand, W. J. D.: "Heat Transfer in the Cylinders of Reciprocating Internal Combustion Engines," *Proc. Instn Mech. Engrs*, vol. 177, no. 36, pp. 973–990, 1963.
8. Borman, G., and Nishiwaki, K.: "A Review of Internal Combustion Engine Heat Transfer,"*Prog. Energy Combust. Sci.*, vol. 13, pp. 1–46, 1987.
9. Taylor, C. F., and Toong, T. Y.: "Heat Transfer in Internal Combustion Engines," ASME paper 57-HT-17, 1957.
10. Woschni, G.: "Universally Applicable Equation for the Instantaneous Heat Transfer Coefficient in the Internal Combustion Engine," SAE paper 670931, *SAE Trans.*, vol. 76, 1967.
11. Sihling, K., and Woschni, G.: "Experimental Investigation of the Instantaneous Heat Transfer in the Cylinder of a High Speed Diesel Engine," SAE paper 790833, 1979.
12. Woschni, G., and Fieger, J.: "Experimental Investigation of the Heat Transfer at Normal and Knocking Combustion in Spark Ignition Engines," *MTZ*, vol. 43, pp. 63–67, 1982.
13. Hohenberg, G. F.: "Advanced Approaches for Heat Transfer Calculations," SAE paper 790825,*SAE Trans.*, vol. 88, 1979.
14. Han, S. B., Chung, Y. J., Kwon, Y. J., and Lee, S.: "Empirical Formula for Instantaneous Heat Transfer Coefficient in Spark Ignition Engine," SAE paper 972995, SP-1306 Diesel and SI Engine Modeling, SAE, 1997.
15. LeFeuvre, T., Myers, P. S., and Uyehara, O. A.: "Experimental Instantaneous Heat Fluxes in a Diesel Engine and Their Correlation," SAE paper 690464, *SAE Trans.*, vol. 78, 1969.
16. Dent, J. C., and Sulaiman, S. J.: "Convective and Radiative Heat Transfer in a High Swirl Direct Injection Diesel Engine," SAE paper 770407, *SAE Trans.*, vol. 86, 1977.
17. Krieger, R. B., and Borman, G. L.: "The Computation of Apparent Heat Release for Internal Combustion Engines," ASME paper 66-WA/DGP-4, in *Proceedings of Diesel Gas Power*, ASME, 1966.
18. Borgnakke, C., Arpaci, V. S., and Tabaczynski, R. J.: "A Model for the Instantaneous Heat Transfer and Turbulence in a Spark Ignition Engine," SAE paper 800287, 1980.
19. Morel, T., and Keribar, R.: "A Model for Predicting Spatially and Time Resolved Convective Heat Transfer in Bowl-in-Piston Combustion Chambers," SAE paper 850204, 1985.
20. Caton, J. A., and Heywood, J. B.: "An Experimental and Analytical Study of Heat Transfer in an Engine Exhaust Port,"*Int. J. Heat Mass Transfer*, vol. 24, no. 4, pp. 581–595, 1981.

© McGraw-Hill Education. All rights reserved. Any use is subject to the Terms of Use, Privacy Notice and copyright information.

21. Heller, S., and Wachtmeister, G.: "Analysis and Modeling of Heat Transfer in the SI Engine Exhaust System During Warm-Up," SAE paper 2007-01-1092, in SP-2079 *Modeling of SI and Diesel Engines*, SAE, 2007.
22. Shayler, P. J., Colechin, M. J. F., and Scarisbrick, A.: "Fuel Film Evaporation and Heat Transfer in the Intake Port of an S.I. Engines," SAE paper 961120, 1996.
23. Shayler, P. J., Colechin, M. J. F., and Scarisbrick, A.: "Heat Transfer Measurements in the Intake Port of a Spark Ignition Engine," SAE paper 960273, 1996.
24. Alkidas, A. C.: "Intake-Valve Temperature and the Factors Affecting It," SAE paper 971729, in SP-1280*Mixture Preparation in SI and Diesel Engines*, SAE, 1997.
25. Bauer, W., Balun, P., Heywood, J. B., and Gronniger, S.: "Heat Transfer and Mixture Vaporization in the Intake Port of a Spark-Ignition Engine," SAE paper 972983, in SP-1305 *Preparing Mixtures for Diesels and SI Engines*, SAE, 1997.
26. Cowart, J., and Cheng, W.: "Intake Valve Thermal Behavior During Steady-State and Transient Engine Operation," SAE paper 1999-01-3643, 1999.
27. Hottel, H. C., and Sarofim, A. F.: *Radiative Transfer*, McGraw-Hill, New York, 1967.
28. Flynn, P., Mizuszwa, M., Uyehara, O. A., and Myers, P. S.: "Experimental Determination of Instantaneous Potential Radiant Heat Transfer within an Operating Diesel Engine," SAE paper 720022, *SAE Trans.*, vol. 81, 1972.
29. Struwe, F. J., and Foster, D. E.: "In-Cylinder Measurement of Particulate Radiant Heat Transfer in a Direct Injection Diesel Engine," SAE paper 2003-01-0072, in *CI Engine Combustion Processes & Performance with Alternative Fuels,* SP-1737, SAE, 2003.
30. Hottel, H. G., and Broughton, F. P.: "Determination of True Flame Temperature and Total Radiation From Luminous Gas Flame," Industrial and Engineering Chemistry, Analytical Edition, vol. 4, 1932.
31. Assanis, D. N., and Heywood, J. B.: "Development and Use of Computer Simulation of the Turbocompounded Diesel System for Engine Performance and Components Heat Transfer Studies," SAE Paper 860329, 1986.
32. Lyn, W. T.: "Diesel Combustion Study by Infra Red Emission Spectroscopy,"*J. Instn Petroleum*, vol. 43, 1957.
33. Kamimoto, T., Matsuoka, S., Matsui, Y., and Aoyagi, Y.: "The Measurement of Flame Temperature and Thermodynamic Analysis of the Combustion Process in a Direct Injection Diesel Engine," paper C96/75, in *Proceedings of Conference on Combustion in Engines*, Cranfield, Institution of Mechanical Engineers, 1975.
34. Field, M. A., Gill, D. W., Morgan, B. B., and Hawksley, P. G. W.: *Combustion of Pulverised Coal*, British Coal Utility Research Association, Leatherhead, U.K., 1967.
35. Greeves, G., and Meehan, J. O.: "Measurements of Instantaneous Soot Concentration in a Diesel Combustion Chamber," paper C88/75, in *Proceedings of Conference on Combustion in Engines*, Cranfield, England, Institution of Mechanical Engineers, London, 1975.
36. Annand, W. J. D.: "Heat Transfer from Flames in Internal Combustion Engines," in *Heat Transfer from Flames*, N. Afgan and J. M. Beer (eds), Ch. 24, John Wiley, New York, 1974.
37. Annand, W. J. D., and Ma, T. H.: "Instantaneous Heat Transfer Rates to the Cylinder Head Surface of a Small Compression-Ignition Engine," *Proc. Instn Mech. Engrs*, vol. 185, no. 72/71, pp. 976–987, 1970–1971.
38. Overbye, V. D., Bennethum, J. E., Uyehara, O. A., and Myers, P. S.: "Unsteady Heat Transfer in Engines," SAE paper 201C, *SAE Trans.*, vol. 69, pp. 461–494, 1961.
39. Alkidas, A. C.: "Heat Transfer Characteristics of a Spark-Ignition Engine," *Trans. ASME, J. Heat Transfer*, vol. 102, pp. 189–193, 1980.

© McGraw-Hill Education. All rights reserved. Any use is subject to the Terms of Use, Privacy Notice and copyright information.

40. Gilaber, P., and Pinchon, P.: "Measurements and Multidimensional Modeling of Gas-Wall Heat Transfer in a S.I. Engine," SAE paper 880516, 1988.
41. Alkidas, A. C., and Myers, J. P.: "Transient Heat-Flux Measurements in the Combustion Chamber of a Spark-Ignition Engine," *Trans. ASME, J. Heat Transfer*, vol. 104, pp. 62–67, 1982.
42. Van Gerpen, J. H., Huang, C.-W., and Borman, G. L.: "The Effects of Swirl and Injection Parameters on Diesel Combustion and Heat Transfer," SAE paper 850265, 1965.
43. Whitehouse, N. D.: "Heat Transfer in a Quiescent Chamber Diesel Engine," *Proc. Instn Mech. Engrs*, vol. 185, no. 72/71, pp. 963–975, 1970–1971.:
44. Finol, C. A., and Robinson, K.: "Thermal Modeling of Model Engines: A Review of Empirical Correlations to Estimate In-cylinder Heat Transfer Coefficient," *Proc. I. Mech. E.: J. Automobile Engineering, Part D*, vol. 220, no. 12, pp. 1765–1781, 2006.
45. Ramchandani, M., and Whitehouse, N. D.: "Heat Transfer in a Piston of a Four Stroke Diesel Engine," SAE paper 760007, 1976.
46. Shayler, P. J., May, S. A., and Ma, T.: "Heat Transfer to the Combustion Chamber Walls in Spark Ignition Engines," SAE paper 950686, 1995.
47. Lyford-Pike, E. J., and Heywood, J. B.: "Thermal Boundary Layer Thickness in the Cylinder of a Spark-Ignition Engine," *Int. J. Heat Mass Transfer*, vol. 27, no. 10, pp. 1873–1878, 1984.
48. Watts, P. A., and Heywood, J. B.: "Simulation Studies of the Effects of Turbocharging and Reduced Heat Transfer on Spark-Ignition Engine Operation," SAE paper 800289, 1980.
49. French, C. C. J., and Atkins, K. A.: "Thermal Loading of a Petrol Engine," *Proc. Instn Mech. Engrs*, vol. 187, 49/73, pp. 561–573, 1973.
50. Brock, E. K., and Glasspoole, A. J.: "The Thermal Loading of Cylinder Heads and Pistons on Medium-Speed Oil Engines," in *Proceedings of Symposium on Thermal Loading of Diesel Engines*, vol. 179, part 3C, pp. 3–18, Institution of Mechanical Engineers, 1964–1965.
51. French, C. C. J., and Hartles, E. R.: "Engine Temperatures and Heat Flows under High Load Conditions," in *Proceedings of Symposium on Thermal Loading of Diesel Engines*, vol. 179, part 3C, pp. 126–135, Institution of Mechanical Engineers, 1964–1965.
52. Morel, T., Wahiduzzaman, S., Tree, D. R., and DeWitt, D. P., "Effect of Speed, Load, and Location on Heat Transfer in a Diesel Engine—Measurements and Predictions," in SP-700, *Adiabatic Engines and Systems,* SAE, 1987.
53. Kerley, R. V., and Thurston, K. W.: "The Indicated Performance of Otto-Cycle Engines," *SAE Trans.*, vol. 70, pp. 5–30, 1962.
54. Finlay, I. C., Harris, D., Boam, D. J., and Parks, B. I.: "Factors Influencing Combustion Chamber Wall Temperatures in a Liquid-Cooled, Automotive, Spark-Ignition Engine," *Proc. Instn Mech. Engrs*, vol. 199, no. D3, pp. 207–214, 1985.
55. Bosch, R.: *Automotive Handbook*, 8th edition, Robert Bosch GmbH, SAE, 2011.
56. American Society of Heating, Refrigerating and Air Conditioning Engineers (ASHRAE), *Fundamentals Handbook,* Ch. 20, pp. 20.1–20.13, Atlanta, GA, 1997.
57. Alshamani, K., "Equations for Physical Properties of Automotive Coolants," SAE paper 2003-01-0532, 2003.
58. Furuhama, S., and Suzuki, H.: "Temperature Distribution of Piston Rings and Piston in High Speed Diesel Engine," *Bull. JSME*, vol. 22, no. 174, pp. 1788–1795, 1979.
59. Lee, W., and Schaefer, H. J.: "Analysis of Local Pressures, Surface Temperatures and Engine Damages Under Knock Conditions," SAE paper 830508, *SAE Trans.*, vol. 92, 1983.

© McGraw-Hill Education. All rights reserved. Any use is subject to the Terms of Use, Privacy Notice and copyright information.

60. Syrimis, M., and Assanis, D. N.: "Piston Heat Transfer Measurements Under Varying Knock Intensity in a Spark-Ignition Engine," SAE paper 971667, 1997.

61. Woschni, G.: "Prediction of Thermal Loading of Supercharged Diesel Engines," SAE paper 790821, 1979.

62. Worthen, R. P., and Raven, D. G.: "Measurements of Valve Temperatures and Strain in a Firing Engine," SAE paper 860356, 1986.

63. Li, C-H.: "Piston Thermal Deformation and Friction Considerations," SAE paper 820086, 1982.

64. Woschni, G., and Fieger, J.: "Determination of Local Heat Transfer Coefficients at the Piston of a High Speed Diesel Engine by Evaluation of Measured Temperature Distribution," SAE paper 790834, *SAE Trans.*, vol. 88, 1979.

65. Kaplan, J. A., and Heywood, J. B.: "Modeling the Spark Ignition Engine Warm-Up Process to Predict Component Temperatures and Hydrocarbon Emissions," SAE paper 910302, 1991.

66. Morel, T., and Keribar, R.: "Warm-Up Characteristics of a Spark-Ignition Engine as a Function of Speed and Load," SAE paper 900683, 1990.

67. Shayler, P. J., Christian, S. J., and Ma, T.: "A Model for the Investigation of Temperature, Heat Flow and Friction Characteristics During Engine Warm-Up," SAE paper 931153, 1993.

© McGraw-Hill Education. All rights reserved. Any use is subject to the Terms of Use, Privacy Notice and copyright information.

13.0. CHAPTER PRELIMINARIES

BACKGROUND

DEFINITIONS

FRICTION FUNDAMENTALS

MEASUREMENT METHODS

ENGINE FRICTION DATA

MECHANICAL FRICTION COMPONENTS

PUMPING FRICTION

ACCESSORY POWER REQUIREMENTS

ENGINE FRICTION MODELING

OIL CONSUMPTION

LUBRICANTS

PROBLEMS

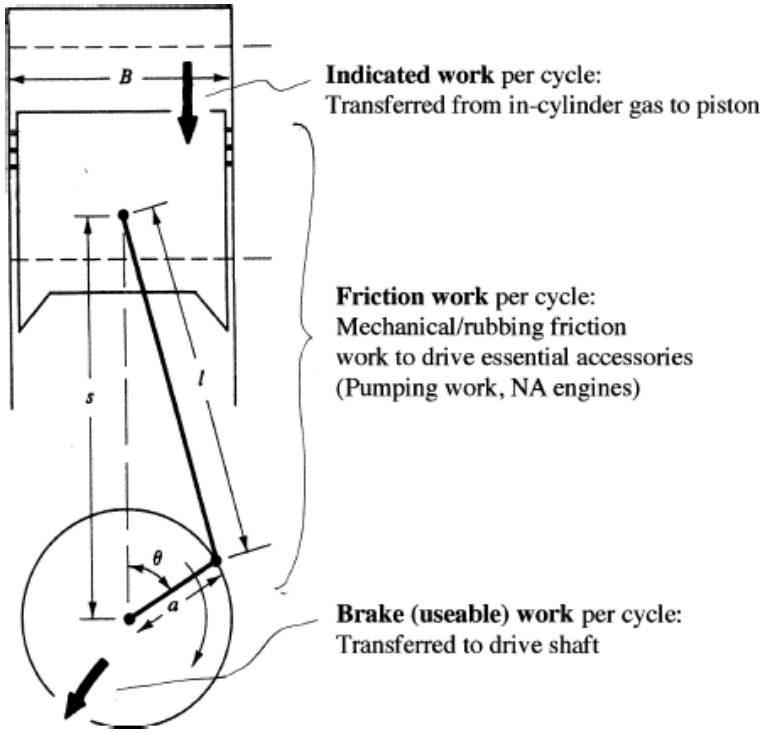
REFERENCES

© McGraw-Hill Education. All rights reserved. Any use is subject to the Terms of Use, Privacy Notice and copyright information.

13.1. BACKGROUND

Not all the work transferred to the piston from the high-pressure gases contained inside the cylinder—the indicated work—is available at the drive shaft for actual use. That portion of the work transferred, which is not available, is usually termed friction work. It is dissipated in a variety of ways within the engine and engine auxiliaries. The friction work or power is a sufficiently large fraction of the indicated work or power—varying between about 10% at full load and lower speeds, through 50% at light load, to 100% at idle or no-load—for the topic to be of great practical importance. Friction losses affect the maximum brake torque and minimum brake specific fuel consumption directly. A large part of the friction losses appear as thermal energy in the coolant and oil which must be removed in the radiator and oil cooler system. Thus, friction losses influence the size of the engine coolant systems. A knowledge of friction power is required to relate the combustion characteristics of an engine—which influence the indicated power—and the useful output—the brake power, as illustrated in Fig. 13.1.

Figure 13.1 Work flow within the engine: Indicated work is transferred from the in-cylinder gases to the piston; a portion of this, the friction work, is dissipated; the brake work is then available at the drive shaft.



The friction work, defined as the difference between the work delivered to the piston from the working fluid within the cylinder, and the useable work delivered to the drive shaft, is expended as follows:

- To draw the fresh mixture through the intake system and into the cylinder, and to expel the burned gases from the cylinder and out of the exhaust system. This is usually called the pumping work.
- To overcome the resistance to relative motion of all the moving parts of the engine. This includes the friction between the piston rings, piston skirt, and cylinder wall; friction in the piston pin, connecting rod small and big ends, crankshaft and camshaft bearings and seals; friction in the valve actuation mechanism; friction in the gears, or pulleys and belts, which drive the camshaft and engine accessories.
- To drive the engine accessories. These usually include: the water pump, the oil pump, the fuel pump, a secondary air pump (if used) for emission control, the fan, and the generator. The various pumps are defined as the *essential* engine

© McGraw-Hill Education. All rights reserved. Any use is subject to the Terms of Use, Privacy Notice and copyright information.

accessories.

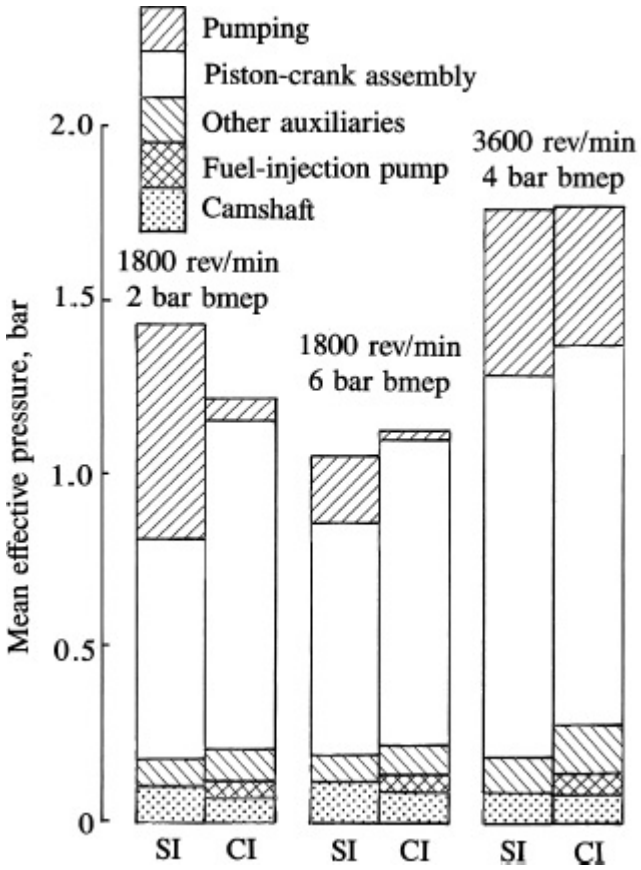
Pumping work is treated differently in naturally-aspirated and turbocharged engines. In naturally-aspirated engines, the pressure in the cylinder during the intake stroke is below atmospheric pressure due to flow resistances in the total intake system, and is higher than atmospheric pressure during the exhaust stroke. The pumping work per cycle (the $\int pdV$ over the exhaust and intake strokes) is therefore negative and thus dissipates part of the gross indicated work (see Fig. 6.1). In turbocharged engines the same intake and exhaust system flow resistances and pressure drops are present, but the in-cylinder intake and exhaust stroke pressures are primarily controlled by the turbocharger compressor and turbine behavior. The air pressure rise the compressor produced at higher engine loads is significantly larger than the intake flow resistance-induced pressure losses. And at higher engine loads, the pressure difference needed to drive the turbine (which then drives the compressor) is higher than the exhaust flow resistance pressure drops (see Fig. 6.2). Note that at lighter loads and lower turbocharged engine speeds, the flow-resistance pressure drops, and the impact of the turbocharger on intake and exhaust stroke in-cylinder pressures, are small. As load and speed increase, the flow resistances increase (see Sec. 6.2.3) but the compressor outlet and turbine inlet pressures increase much more. Under these more highly loaded conditions, the pumping work over the exhaust and intake strokes becomes positive and *adds* to the gross indicated work. Note that the exhaust gas temperature in spark-ignition engines is significantly higher than in diesel engines. Thus, the exhaust manifold pressures required to drive the turbines in diesel engines are higher than in spark-ignition engines. As a consequence, in diesels this higher-load (positive) pumping work is smaller.

All this work is eventually dissipated into thermal energy: the term friction work or power is therefore appropriate. In this chapter we will explore the relative importance of these components in typical automotive SI and diesel engines at different loads and speeds. The absolute value of the total friction work varies with load, and increases as speed increases. The piston and connecting rod assembly contributes the largest friction component.

The relative importance of the friction components in a naturally-aspirated gasoline SI engine at light load and low-to-mid speed is illustrated in Fig. 13.2. Typical ranges are crankshaft 10 to 15%, reciprocating (piston and con rod) 25 to 30%, valvetrain 10 to 15%, auxiliaries 10 to 15%, and pumping 30 to 45%. In a small turbocharged diesel engine at equivalent operating conditions, the pumping work is much lower (only a few percent) and the reciprocating component is significantly larger due to higher in-cylinder pressures. The high-pressure fuel pump drive requirement (small in a gasoline engine) becomes comparable to the water and oil pump requirements.

© McGraw-Hill Education. All rights reserved. Any use is subject to the Terms of Use, Privacy Notice and copyright information.

Figure 13.2 Comparison of major categories of friction losses: friction mean effective pressure at different loads and speeds for 1.6-liter four-cylinder overhead-cam automotive spark-ignition (SI) and compression-ignition (CI) engines.[1]



Note that the *magnitude* of engine friction is important, and has been steadily reduced over the years through engineering research, development, and design improvements. The *relative* importance of friction relative to the indicated engine output is also important. As the specific output of engines has steadily increased, the relative (negative) impact of friction has been reduced. The pumping work for naturally-aspirated SI engines is larger than for equivalent CI engines and becomes comparable to rubbing friction at light loads as the engine is increasingly throttled.

© McGraw-Hill Education. All rights reserved. Any use is subject to the Terms of Use, Privacy Notice and copyright information.

13.2. DEFINITIONS

The following terminology will be used in discussing engine friction.

Pumping work W_p. The net work per cycle done by the piston on the in-cylinder gases during the inlet and exhaust strokes. W_p is only defined for four-stroke cycle engines. It is the area ($B + C$) in Fig. 2.6*b* for a naturally-aspirated gasoline SI engine.[1]

Mechanical friction work W_{mf}. The work per cycle dissipated in overcoming the friction due to relative motion of adjacent components within the engine. This includes all the items listed in the second category of engine friction enumerated above. This is also referred to as *rubbing friction work*.

Accessory work W_a. The work per cycle required to drive the essential engine accessories; for example, water, oil, and fuel pumps, fan, generator, etc. Normally, only those accessories essential to engine operation are included.

Total friction work W_{tf}. The total friction work is the sum of these three components, that is,

$$W_{\mathrm{tf}} = W_p + W_{\mathrm{mf}} + W_a$$

(13.1)

It is often useful to discuss the difference between indicated and brake output in terms of *mean effective pressure*, mep, the work per cycle per unit displaced volume:

$$\mathrm{mep} = \frac{W_c}{V_d}$$

and also power. Power and mep are related by

$$P = \mathrm{mep} \times V_d \times \frac{N}{n_R}$$

where n_R (the number of revolutions per cycle) = 1 or 2 for the two-stroke or four-stroke cycles, respectively. Hence, from W_p, W_{mf}, W_a, and W_{tf} we can define pumping mean effective pressure and power (pmep and P_p), mechanical friction mean effective pressure and power (mfmep and P_{mf}), accessory mean effective pressure and power (amep and P_a), and total friction mean effective pressure and power (tfmep and P_{tf}), respectively.

Brake mean effective pressure and power (bmep and P_b), indicated mean effective pressure and power (imep and P_i), and mechanical efficiency have already been defined in Secs. 2.3, 2.4, 2.5, and 2.7. Note that for four-stroke cycle engines, two definitions of indicated output are in common use. These have been designated as:

Gross indicated mean effective pressure, imep_g. The work delivered to the piston over the compression and expansion strokes, per cycle per unit displaced volume.

Net indicated mean effective pressure, imep_n. The work delivered to the piston over the entire four strokes of the cycle, per unit displaced volume.

From the above definitions it follows that for naturally-aspirated four-stroke cycle engines:

© McGraw-Hill Education. All rights reserved. Any use is subject to the Terms of Use, Privacy Notice and copyright information.

$$\text{imep}_g = \text{imep}_n + \text{pmep}$$

(13.2*a*)

$$\text{tfmep} = \text{pmep} + \text{mfmep} + \text{amep}$$

(13.2*b*)

and

$$\text{bmep} = \text{imep}_g - \text{tfmep}$$

(13.2*c*)

For turbocharged four-stroke cycle engines:

$$\text{imep}_n = \text{imep}_g + \text{pmep}$$

(13.2*d*)

$$\text{tfmep} = \text{mfmep} + \text{amep}$$

(13.2*e*)

and

$$\text{bmep} = \text{imep}_n - \text{tfmep}$$

(13.2*f*)

Note that for both types of engines, pmep in these equations is a *positive* quantity: thermodynamically, the pumping work per cycle ($\int p dV$) for a naturally-aspirated engine is *negative*, and for higher loads in a turbocharged engine where $p_i > p_e$, it is *positive* (and will approach zero at mid-load and become negative at the lighter engine loads).

That two different definitions of indicated output are in common use follows from two different approaches to determining friction work or power. In the standard engine test code procedures friction power is measured in a hot *motoring test*: the engine is motored with water and oil temperatures held at the firing engine values, with the throttle setting unchanged from its firing engine position (in an SI engine). This measures (approximately) the sum of pumping, mechanical or rubbing friction, and auxiliary power requirements. The sum of brake power, and friction power determined in this way, is the gross indicated power. Alternatively, when an accurate record of cylinder pressure throughout the whole cycle is available, pumping power can be determined directly: the sum of mechanical friction and accessory power is then the difference between the net indicated power—determined from $\int p dV$ over the whole cycle—and the brake power.

[1] This definition gives $W_p > 0$ for naturally-aspirated engines. This is then added to the other friction components (and thus subtracted from the work transferred to the piston). For supercharged and turbocharged engines at high loads, where p_i is greater than p_e, this definition gives $W_p < 0$; thus it adds to the work transferred to the piston. (Different sign conventions for pumping work are sometimes used in order to maintain W_p as a positive quantity.)

© McGraw-Hill Education. All rights reserved. Any use is subject to the Terms of Use, Privacy Notice and copyright information.

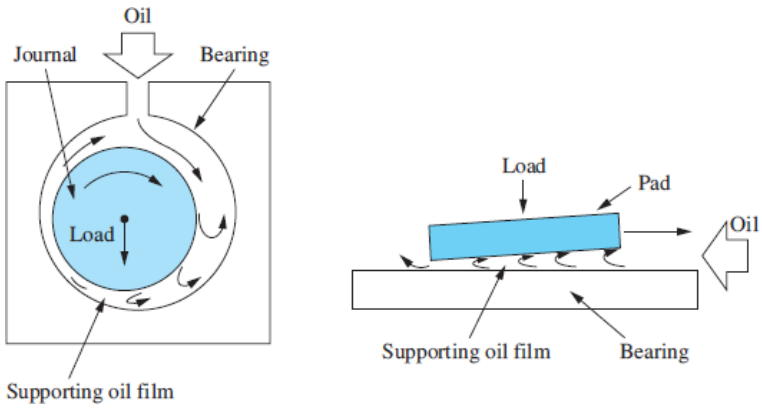
13.3. FRICTION FUNDAMENTALS

The friction losses outlined in Sec. 13.1 can be classified into two groups, depending on the type of dissipation which occurs. One type is friction between two metal surfaces in relative motion, with a lubricant in between. The other type is dissipation in turbulent flows.

13.3.1. Lubricated Friction

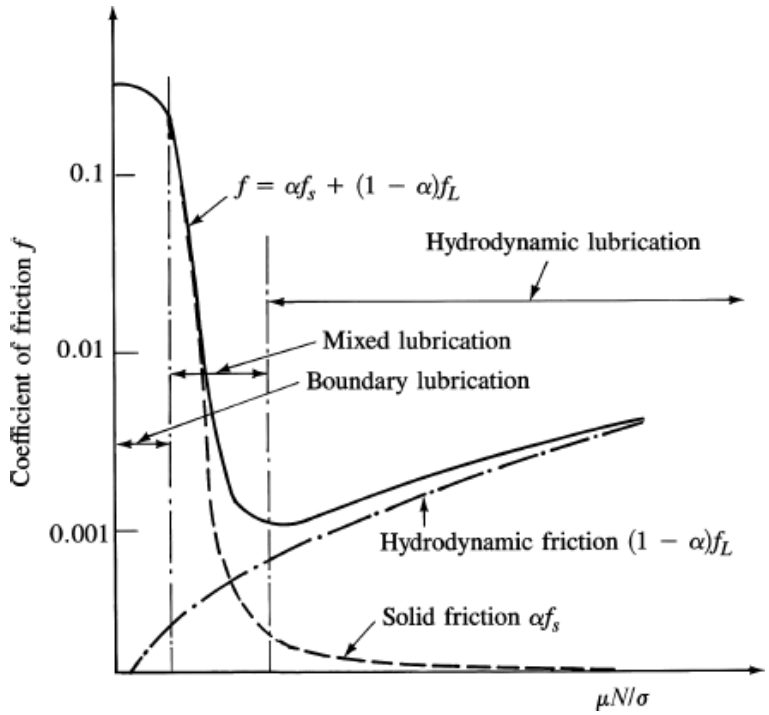
A primary problem in understanding friction between lubricated surfaces in engines is the wide variation in the magnitude of the forces involved. Thus various regimes of lubrication can occur. Figure 13.3 shows two common geometries for lubricated parts: a journal bearing and a slider bearing. The different regimes of lubricated friction are illustrated by the Stribeck diagram shown in Fig. 13.4, where the coefficient of friction f (ratio of tangential force to normal force) for a journal bearing is plotted against a dimensionless duty parameter $\mu N/\sigma$, where μ is the dynamic viscosity of the lubricant, N is the rotational speed of the shaft, and σ is the loading force per unit area. For sliding surfaces the dimensionless duty parameter becomes $\mu U/(\sigma b)$, where U is the relative velocity of the two surfaces and b is the length of the sliding pad in the direction of motion.

Figure 13.3 Schematic of a lubricated journal bearing, and a sliding bearing.



© McGraw-Hill Education. All rights reserved. Any use is subject to the Terms of Use, Privacy Notice and copyright information.

Figure 13.4 Stribeck diagram for journal bearing: coefficient of friction f versus dimensionless duty parameter μN/σ, where μ is the lubricant dynamic viscosity, N is rotational speed of shaft, and σ is the loading force per unit area.



The coefficient of friction can be expressed as

$$f = \alpha f_s + (1 - \alpha) f_L$$

(13.3)

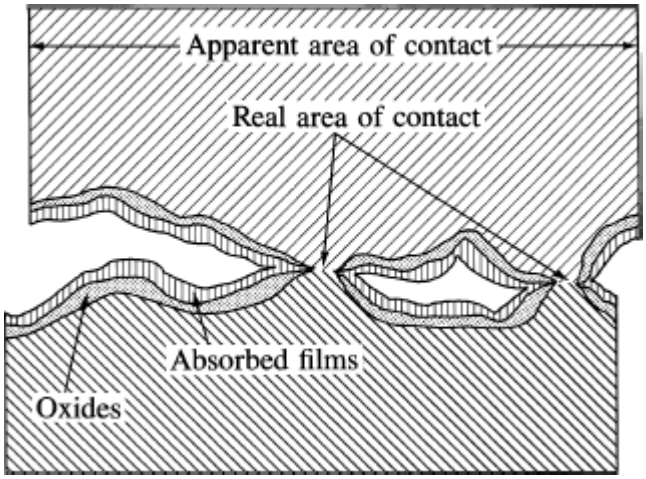
where f_s is the metal-to-metal coefficient of dry friction, f_L is the hydrodynamic coefficient of friction, and α is the metal-to-metal contact constant, varying between 0 and 1. As $\alpha \to 1$, $f \to f_s$, and the friction is called *boundary friction*; that is, close to solid friction. The lubricating film is then sufficiently thin that it cannot prevent metal-to-metal contact between surface asperities. As $\alpha \to 0$, $f \to f_L$ and the friction is called *hydrodynamic* or *viscous* or *thick film* lubrication. The lubricant film is sufficiently thick that it separates completely the surfaces in relative motion. In between these regimes, there is a *mixed* or *partial* lubrication regime where the transition from boundary to hydrodynamic lubrication occurs. WhileFig. 13.4 applies to journal bearings, this discussion holds for any pair of engine parts in relative motion with lubricant in between.

Under boundary lubrication conditions, the friction between the two surfaces in relative motion is determined by surface properties as well as by lubricant properties. The important surface properties are roughness, hardness, elasticity, plasticity, shearing strength, thermal conductivity, and wettability with respect to the lubricant. The important lubricant properties are mainly surface ones or chemical ones, which govern the ability of lubricant (and additive) molecules to attach themselves to the solid surfaces. Figure 13.5 shows two surfaces under boundary lubrication conditions. Due to the surface asperities, the real contact area is much less than the apparent contact area. The real contact area A_r is equal to the normal load F_n divided by the yield stress of the material σ_m:

$$A_r = F_n/\sigma_m$$

© McGraw-Hill Education. All rights reserved. Any use is subject to the Terms of Use, Privacy Notice and copyright information.

Figure 13.5 *Schematic of two surfaces in relative motion under boundary lubrication conditions.*[2]



The force required to cause tangential motion is the product of the real contact area and the shear strength of the material τ_m:

$$F_t = A_r \tau_m$$

Thus the coefficient of friction *f* is

$$f = F_t / F_m = \tau_m / \sigma_m$$

(13.4)

For dissimilar materials, the properties of the weaker material dominate the friction behavior. Since, as shown in Fig. 13.5, the surfaces are covered by oxide films and adsorbed lubricant films, the shear strength of the material in Eq. (13.4) is effectively the shear strength of the surface film. Under boundary lubrication conditions, the coefficient of friction is essentially independent of speed. Boundary lubrication occurs between engine parts during starting and stopping, and during normal running at the piston ring/ cylinder interface at top and bottom center crank positions, between heavily loaded parts, between slow moving parts such as valve stems and rocker arms, and crankshaft timing gears and chains.

Hydrodynamic lubrication conditions occur when the shape and relative motion of the (lubricated) sliding surfaces form a liquid film in which there is sufficient pressure to keep the surfaces separated. Resistance to motion results from the vicious shear forces within the liquid film, and not from the interaction between surface irregularities, as was the case under boundary lubrication. The shear stress τ in a liquid film between two surfaces in relative motion is given by

$$\tau = \mu \left(\frac{dv}{dy} \right)$$

where μ is the fluid viscosity and (dv/dy) the velocity gradient across the film. Hence, the friction coefficient (shear stress/normal load stress) in this regime will be proportional to viscosity × speed ÷ loading, essentially a straight line on the Stribeck diagram. Full hydrodynamic lubrication or viscous friction is independent of the material or roughness of the parts, and the only property of the lubricant involved is its viscosity. Hydrodynamic lubrication is present between two converging surfaces, moving at relatively high speed in relation to each other and withstanding a limited load, whenever an oil film can be formed. This type of lubrication is encountered in engine bearings, between piston skirt and cylinder liner, and between piston rings and liners for high sliding velocities.

© McGraw-Hill Education. All rights reserved. Any use is subject to the Terms of Use, Privacy Notice and copyright information.

Hydrodynamic lubrication breaks down when the thickness of the fluid film becomes about the same as the height of the surface asperities. To the viscous friction is then added metal-to-metal solid friction at the peaks of the asperities. Both hydrodynamic and boundary lubrication conditions coexist. The surface texture controls this transition from hydrodynamic to mixed lubrication: rougher surfaces make the transition at lower loads. Abrupt load or speed variations or mechanical vibration may cause this transition to occur. This phenomenon occurs in connecting rod and crankshaft bearings where periodic metal-to-metal contact results from breaks in the oil film. The contact area between rings and cylinders is a region where, due to sudden variations in speed, load, and temperature, lubrication is of the mixed type. Intermittent metal-to-metal contacts occur as the result of breaks in the oil film.[3]

13.3.2. Turbulent Dissipation

Part of the total friction work is spent on pumping fluids through flow restrictions. The cylinder gases, cooling water, and oil are pumped through the engine; the fan pumps air through the engine's radiator. Work is dissipated driving these turbulent viscous fluid flows. The pressure difference required to pump these fluids around their flow paths is proportional to ρv^2, where v is a representative fluid velocity. The proportionality constant depends primarily on the details of the flow-path geometry. Hence the friction forces associated with fluid pumping will be proportional to N^2 (or $\overline{S}_p^2$ if the piston motion forces the flow).

13.3.3. Total Friction

The work per cycle for each component i of the total friction is given by integrating the friction force $F_{f,i}$ times its displacement dx around the cycle:

$$W_{f,i} = \int F_{f,i}(\theta)\, dx$$

The friction force components are either independent of speed (boundary friction), proportional to speed (hydrodynamic friction) or to speed squared (turbulent dissipation), or some combination of these. It follows that the total friction work per cycle (and thus the friction mean effective pressure) for a given engine geometry engine will vary with speed according to

$$W_{\mathrm{tf}}(\text{or tfmep}) = C_1 + C_2 N + C_3 N^2$$

(13.5)

Some of the components of hydrodynamic lubrication friction and turbulent dissipation will be dependent on mean piston speed rather than crankshaft rotational speed N. Examples are piston skirt and ring friction, and the pressure losses associated with gas flow through the inlet and exhaust valves. For conventional engine geometries, crankshaft rotational speed is usually used to scale the total friction data rather than mean piston speed.[4, 5]

© McGraw-Hill Education. All rights reserved. Any use is subject to the Terms of Use, Privacy Notice and copyright information.

13.4. MEASUREMENT METHODS

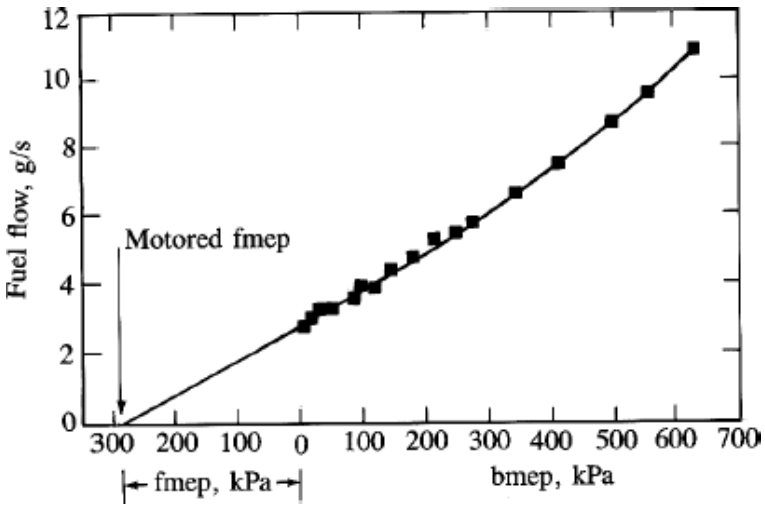
A true measurement of friction in a firing engine can only be obtained by subtracting the brake power from the indicated power determined from accurate measurements of cylinder pressure throughout the cycle. However, this method is not easy to use on multi-cylinder engines, both because of cylinder-to-cylinder differences in indicated power and due to the difficulties in obtaining sufficiently accurate cylinder pressure data from each cylinder. As a result, friction is often measured in a motored engine. Friction components in a firing and a motored engine are different for the reasons outlined below. First, the common measurement methods will be described.

1. *Measurement of fmep from imep.* The gross indicated mean effective pressure is obtained from $\int pdV$ over the compression and expansion strokes for a four-stroke engine, and over the whole cycle for a two-stroke engine. This requires accurate and in-phase pressure and volume data. Accurate pressure versus crank angle data must be obtained from each cylinder with a pressure transducer and crank angle indicator. Volume versus crank angle values can be calculated. Great care must be exercised if accurate imep data are to be obtained.[4] Both $imep_g$ and pmep are obtained from the *p-V* data. By subtracting the brake mean effective pressure, the combined mechanical/rubbing friction plus auxiliary requirements, mfmep + amep, are obtained.

2. *Direct motoring tests.* Direct motoring of the engine, under conditions as close as possible to firing, is another method used for estimating friction losses. Engine temperatures should be maintained as close to normal operating temperatures as possible. This can be done either by heating the water and oil flows or by conducting a "grab" motoring test where the engine is switched rapidly from firing to motored operation. The power required to motor the engine includes the pumping power. In tests on SI engines at part-load, the throttle setting is left unchanged. "Motoring" tests on a progressively disassembled engine can be used to identify the contribution that each major component of the engine makes to the total friction losses.

3. *Willans line.* An approximate equivalent of the direct motoring test for diesel engines is the Willans line method. A plot of fuel consumption versus brake output obtained from engine tests at a fixed speed is extrapolated back to zero fuel consumption. An example is shown in Fig. 13.6. Generally, the plot has a slight curve, making accurate extrapolation difficult. Agreement with a motored test result is shown.

Figure 13.6 Willans line method for determining friction mean effective pressure.[6]



4. *Morse test*. In the Morse test, individual cylinders in a multi-cylinder engine are cut out from firing, and the reduction in brake torque is determined while maintaining the same engine speed. The remaining cylinders drive the cylinder cut out.

© McGraw-Hill Education. All rights reserved. Any use is subject to the Terms of Use, Privacy Notice and copyright information.

Care must be taken to determine that the action of cutting out one cylinder does not significantly disturb the fuel or mixture flow to the others.

Only the first of these four methods has the potential for measuring the true friction of an operating engine. The last three methods measure the power requirements to motor the engine. The motoring losses are different from the firing losses for the following reasons:

- Only the compression pressure and not the full firing pressure acts on the piston, piston rings, and bearings. The lower gas loadings during motoring lower the rubbing friction.
- Piston and cylinder bore temperatures are lower in motored operation. This results in higher lubricant viscosity and therefore increased viscous friction. In addition, piston-cylinder clearances are greater during motoring operation, which tends to make friction lower. However, in firing operation, the lubrication of the top ring near the top of the stroke is inadequate to maintain normal hydrodynamic lubrication with the higher gas pressures behind the ring. The resulting boundary friction in this region makes friction in the firing engine higher. Overall, the net effect of lower piston and cylinder temperatures during motoring is unclear.
- In motored operation, the exhaust blowdown phase is missing and the gases discharged in the latter part of the exhaust stroke have a higher density than under firing conditions. These effects can result in different pumping work.
- When motoring, net work is done during the compression and expansion strokes because of heat loss from the gas to the walls, and because of gas loss through blowby. This work is not part of the true total friction work in a firing engine and should not be deducted from the indicated work of the firing engine to obtain the brake work; heat losses and blowby are additional energy transfers to the indicated work, friction work, and brake work.

Overall, there are both positive and negative differences between firing and motoring engine friction and the net difference is surprisingly small. Thus motoring tests are widely used to estimate total and also individual components of friction. Note, however, that reasonable agreement for total engine friction does not imply equally good agreement for each of the friction components.

© McGraw-Hill Education. All rights reserved. Any use is subject to the Terms of Use, Privacy Notice and copyright information.

13.5. ENGINE FRICTION DATA

13.5.1. SI Engines

Figure 13.7 shows total motored friction mep for several four-stroke cycle four-cylinder SI engines between 845 and 2000 cm^3 displacement, at wide-open throttle, as a function of engine speed. These data (from older engines) indicate that, for a range of cylinder sizes and geometries, friction mean effective pressure is an appropriate normalized measure of engine friction.[7]

Figure 13.7 Friction mean effective pressure under motored conditions at wide-open throttle for several four-cylinder spark-ignition engines.[7]

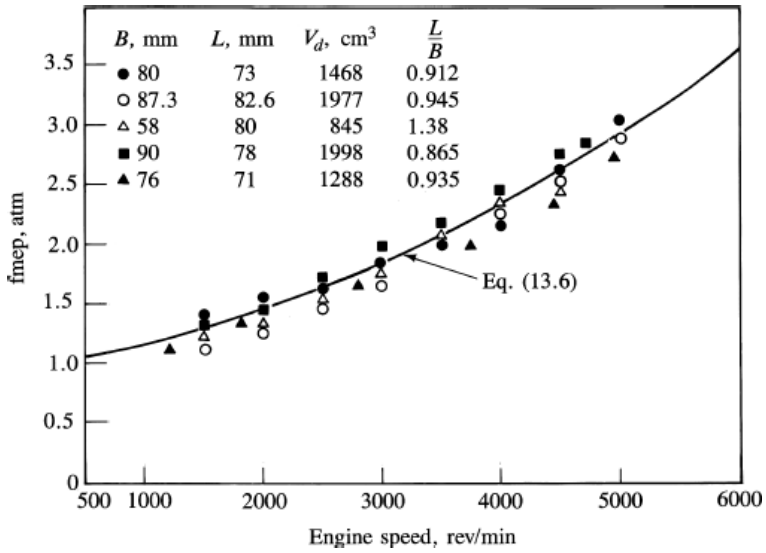
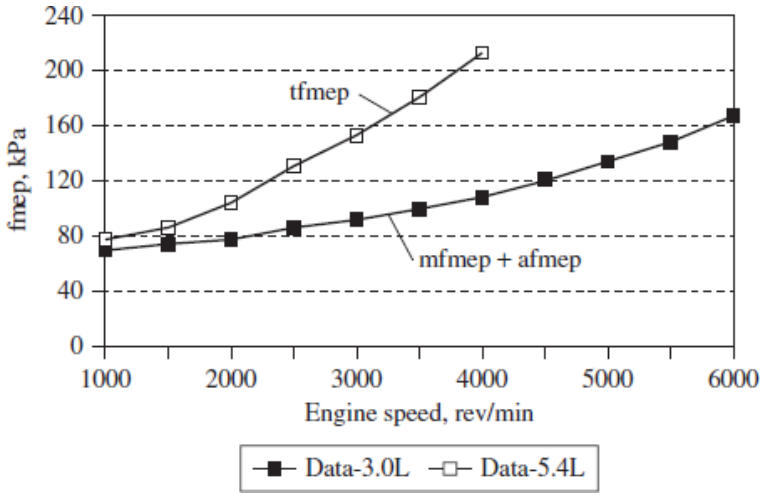


Figure 13.8 shows total friction mean effective pressure for a more recent 5.4-liter V-8 naturally-aspirated gasoline engine (with a single-overhead-cam 2-valve-per-cylinder valvetrain) as a function of engine speed at wide-open throttle. It also shows the mechanical plus accessory friction for a similar 3.0-liter V-6 engine (four valves per cylinder, with dual-overhead-cam roller finger follower). The markedly different slopes of these two curves is due to the increasing pumping gas-exchange losses with rising engine speed at WOT. At low engine speeds, WOT pumping losses are small and the two fmep curves have similar magnitude. However, pmep rises rapidly with the square of piston (and thus engine) speed as speed increases. The importance of avoiding high engine speeds in the interests of good mechanical efficiency is evident. Under normal automobile engine operating conditions, a reduction in total friction mean effective pressure by about 10 kPa results in about a 2% improvement in vehicle fuel consumption.[7]

© McGraw-Hill Education. All rights reserved. Any use is subject to the Terms of Use, Privacy Notice and copyright information.

Figure 13.8 Friction mean effective pressure for two naturally-aspirated spark-ignition engines, illustrating the importance of pumping friction: 5.4-liter, V-8, two-valve-per-cylinder engine (tfmep); 3.0-liter, V-6, four-valve-per-cylinder, valvetrain roller-follower engine.[8]



The WOT total friction mean effective pressure data in Fig. 13.8 (for the 5.4-liter engine) is well fitted by the correlation.

$$\text{tfmep(kPa)} = 57 + 15\left(\frac{N}{1000}\right) + 5.5\left(\frac{N}{1000}\right)^2$$

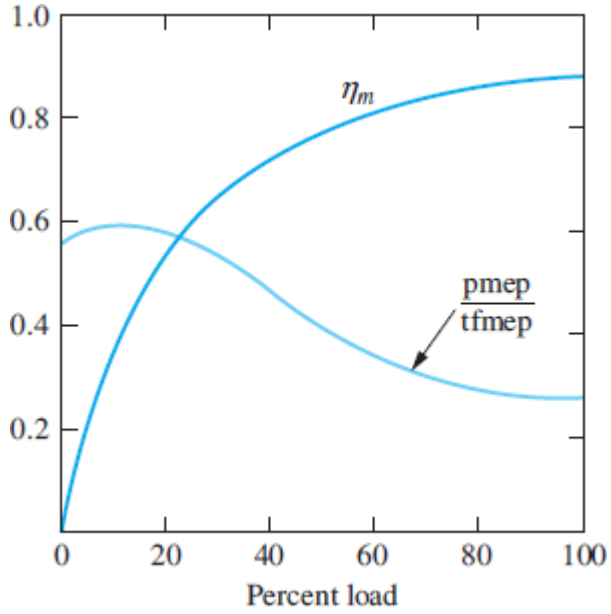
(13.6)

where N is in revolutions per minute. A comparison of this correction with an equivalent correlation from the 1980s indicates that total friction mean effective pressure has decreased substantially over the past 20 years: by 30 to 40% at low engine speeds, 20 to 25% at mid-speeds, and 10 to 15% at higher speeds. At lower speeds, valvetrain friction has been halved; at high speeds, flow resistances have been significantly reduced.

The relative importance of friction is quantified by the mechanical efficiency (η_m = bmep/imep). In SI engines, this increases from zero when the engine is idling, to a value close to 0.9 (at low to mid-engine speeds) at high loads. This behavior, and the decreasing relative importance of pumping friction (pmep) as load increases, are shown in Fig. 13.9 for a spark-ignition engine operating at a fixed (mid) speed.

© McGraw-Hill Education. All rights reserved. Any use is subject to the Terms of Use, Privacy Notice and copyright information.

Figure 13.9 Mechanical efficiency η_m and ratio of pumping mep to total friction mep as a function of load for a typical spark-ignition engine at fixed (mid) speed.[2]



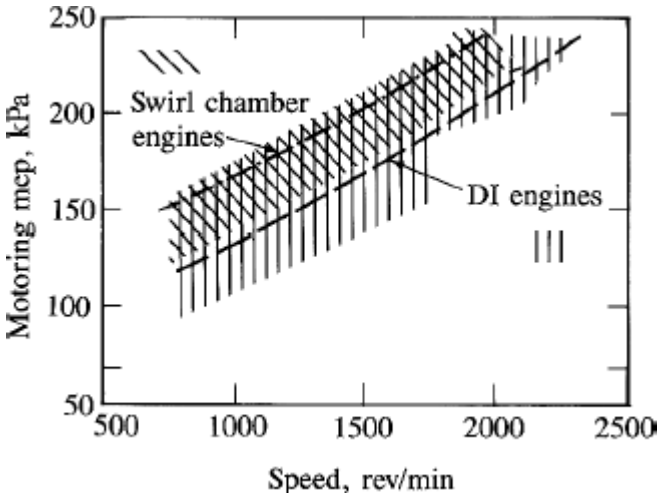
13.5.2. Diesel Engines

Figure 13.10 shows total friction as determined from motoring tests for direct-injection CI engines. Correlations for a typical diesel of each type are shown, of the form:

$$\text{Motoring mep (kPa)} = C_1 + 48\left(\frac{N}{1000}\right) + 0.4\overline{S}_p^2$$

(13.7)

Figure 13.10 Motored total friction mean effective pressure as a function of speed for several DI diesels (bores in range 100 to 137 mm) and IDI swirl-chamber diesels (bores in range 100 to 121 mm). Correlations for r_c = 15 and L = 142 mm (DI engine) and r_c = 16 and L = 142 mm (IDI engine).[6]

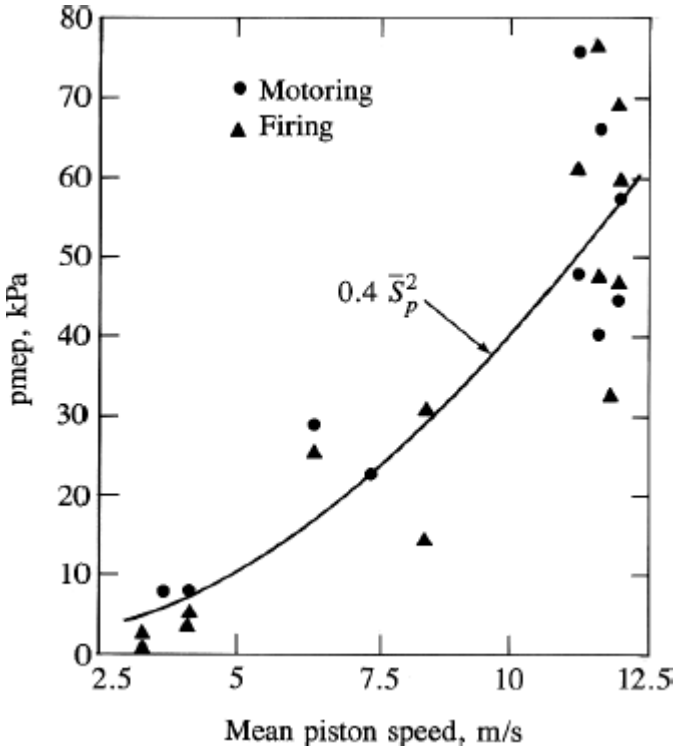


© McGraw-Hill Education. All rights reserved. Any use is subject to the Terms of Use, Privacy Notice and copyright information.

where N is in revolutions per minute and $\overline{S}_p$ in meters per second. For the direct-injection engine C_1 = 75 kPa. Mean piston speed was found to give a better correlation than does engine speed (N) for the last term in Eq. (13.7) which is mainly pumping mep.

Pumping mean effective pressure data for several naturally-aspirated diesel engines under both firing and motored conditions is shown in Fig. 13.11. The solid curve is the term $0.4\overline{S}_p^2$ in Eq. (13.7), with $\overline{S}_p$ in m/s which fits the data.

Figure 13.11 Pumping mean effective pressure as a function of mean piston speed for several naturally-aspirated diesel engines.[6]



© McGraw-Hill Education. All rights reserved. Any use is subject to the Terms of Use, Privacy Notice and copyright information.

13.6. MECHANICAL FRICTION COMPONENTS

In this section, a more detailed analysis of the major components of mechanical engine friction is presented, along with an overview of the engine's lubrication system. Pumping work and engine accessory friction are then discussed in Secs. 13.7 and 13.8.

13.6.1. Motored Engine Breakdown Tests

Motored engine tests, where the engine is disassembled or broken down in stages, can be used to determine the friction associated with each major engine assembly. While this test procedure does not duplicate the combustion-generated forces of actual engine operation, such tests are useful for assessing the relative importance of individual friction components. The results of breakdown tests on various spark-ignition engines, separating out the contribution to mechanical friction from the piston assembly (piston, rings, connecting rod, the valvetrain, crankshaft bearings and seals), indicate a breakdown of the overall mechanical friction as: piston assembly 60%; valvetrain 25%; crankshaft 15%. Note, however, that their relative importance does vary over the engine's speed range. A typical distribution (at light load and low engine speed) of total engine friction into its various categories for an automobile gasoline naturally-aspirated engine is shown in Table 13.1. The percentage breakdown is shown for mechanical plus accessory friction, and also with pumping work included. At this light load typical of passenger car urban driving, the pumping work losses (due primarily to throttling the engine intake flow) with a manifold pressure of about 0.5 bar is some 30%. At these operating conditions, the engine brake fuel conversion efficiency would be about 20%.

Table 13.1 Typical friction distribution: gasoline engine at light load[9]

Crankshaft	15	11
Piston, connecting rods	33	23
Valvetrain	28	20
Oil pump	15	11
Water pump	9	6
Subtotal	100	
Pumping work		~30
Total		100

More detailed motoring friction breakdowns for a gasoline SI engine and a diesel engine are shown in Figs. 13.12 and 13.13, respectively. For the four-cylinder gasoline engine, the largest components are the (motored) pumping work, which rises significantly as speed increases, and the mechanical (rubbing) friction components of the piston, rings, connecting rod assembly.

© McGraw-Hill Education. All rights reserved. Any use is subject to the Terms of Use, Privacy Notice and copyright information.

Figure 13.12 Motored friction breakdown (mfmep) for a 1.6-liter four-cylinder four-valve spark-ignition engine as a function of speed; oil and coolant temperature 88°C.[10]

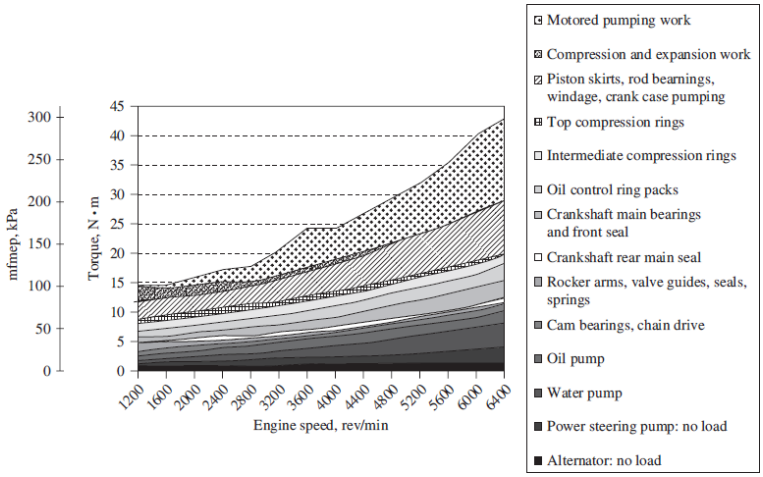


Figure 13.13 Pumping, mechanical friction, and accessory losses from a motoring tear-down test of a heavy-duty diesel engine.[11]

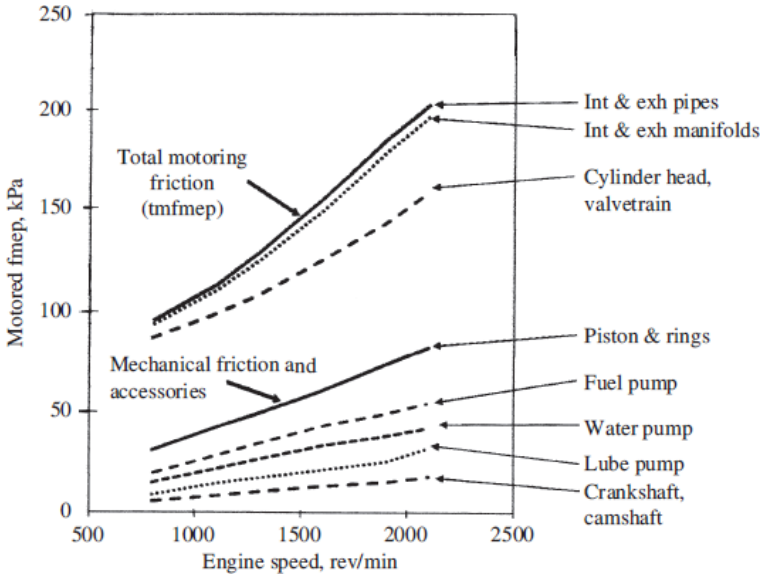


Figure 13.13 shows friction mean effective pressure data from a motored tear-down test of a heavy-duty diesel engine, as a function of speed. Flow losses in the total intake and exhaust systems are significant at the higher engine speeds, especially across the ports and valves in the cylinder heads, as are the mechanical friction losses in the piston, rings, and con rods.

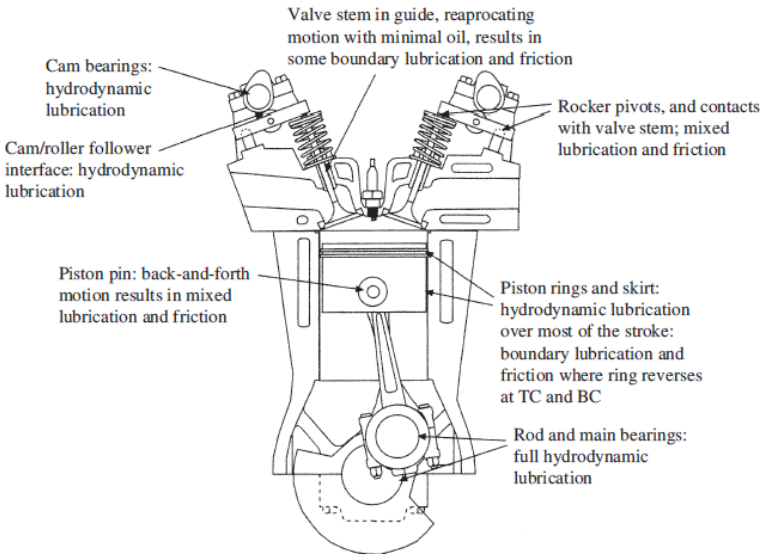
13.6.2. Engine Lubrication System

The lubrication of the sliding surfaces in the moving components of the engine is an essential factor in determining its mechanical friction. Figure 13.14 shows the various lubricated mechanical components of the engine and identifies the sliding contact lubrication regimes under which they operate—boundary, mixed, and hydrodynamic (see Sec. 13.3.1). Boundary lubrication friction, which is much higher than fully hydrodynamic friction, occurs when rotating and sliding components come to rest, and when the (normal) forces become high. Where shafts rotate continuously in journal bearings, a fully supporting oil layer (hydrodynamic lubrication) can normally be maintained except when the engine starts or stops: examples are crankshaft, camshaft, and con rod big-end bearings, cam roller followers driven by cam lobes, teeth contact in gear-drive systems. The

© McGraw-Hill Education. All rights reserved. Any use is subject to the Terms of Use, Privacy Notice and copyright information.

potential for boundary lubrication and thus surface-to-surface contact exists between piston rings, piston skirt, and the cylinder liner; also in various parts of the valve drive system. Whether or not surface contact (and thus boundary friction) occurs depends on whether a supporting oil film exists (as, say, when the piston comes to rest at TC or BC) and whether that film is squeezed out of the thin surface-to-surface gap under the loads being applied.[12]

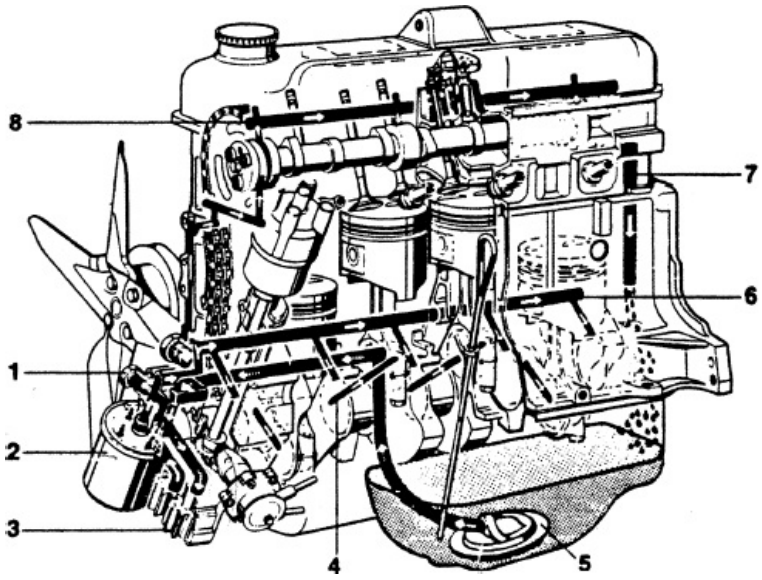
Figure 13.14 Engine components where relative motion between two surfaces occurs, and the lubrication and friction regimes which then prevail: boundary, mixed, and hydrodynamic.[12]



The principle moving parts of an engine, identified in Fig. 13.14, are positively lubricated by introducing a supply of oil from a pressurized system. An example of an engine lubrication system is shown in Fig. 13.15. The oil pump draws oil from the engine sump through a suction strainer and then delivers it through a control valve to the oil cooler (not shown in figure). The oil then passes through the filter to the main oil gallery. From the main oil gallery, it is branched to the main crankshaft bearings to the con rod big end bearings. In parallel, oil is directed to the camshaft bearings. Through a passage in these bearings, the oil flows to the valve tappets. As the oil passages of tappets and tappet bridges line up during tappet motion, rocker arms and valve stems are pulse-lubricated through the tappets (and pushrods, if present). For cooling pistons and lubricating cylinders, oil is thrown against the underside of the piston either through oil splashing from the crank or (for greater cooling) through nozzles connected to the main bearings. The gears of the main timing train are splash-lubricated. Oil, from these lubricated engine regions, is then returned to the sump. Lubricant properties are reviewed in Sec. 13.10.2.

© McGraw-Hill Education. All rights reserved. Any use is subject to the Terms of Use, Privacy Notice and copyright information.

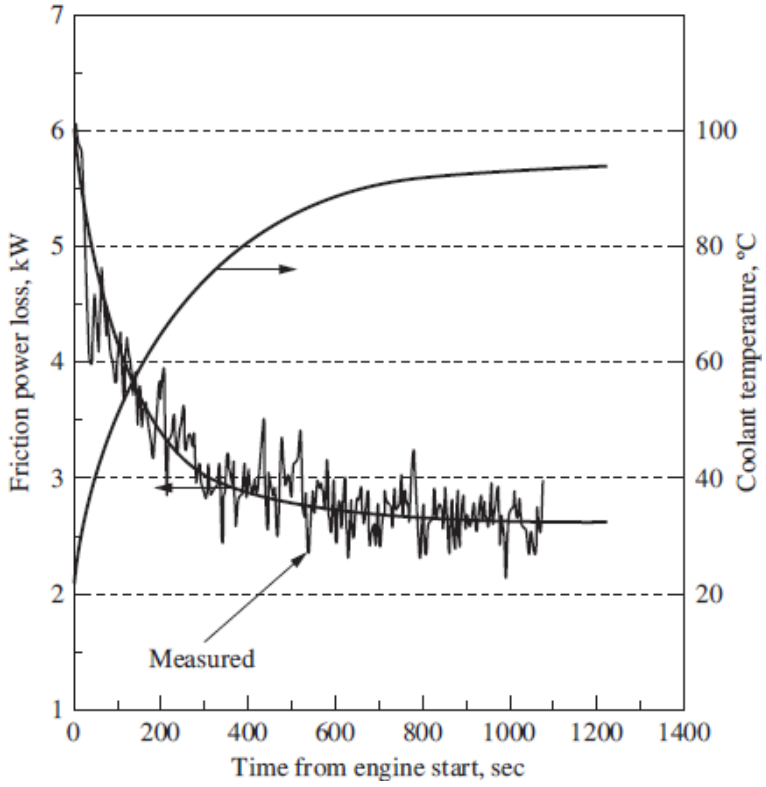
Figure 13.15 Layout for a forced-feed engine lubrication system: (1) Pressure relief valve; (2) Oil filter; (3) Gear pump; (4) Connection from main bearing to connecting-rod bearing; (5) Suction strainer; (6) Main pressurized oil line to crankshaft bearings; (7) Return flow from timing-gear case to crankcase; (8) Oil passage to camshaft bearings.[13] (Courtesy Robert Bosch GmbH and SAE.)



Mechanical engine friction depends on the temperature of the lubricating oil in the various lubricated regions of the engine, since the oil's viscosity is a function of temperature. When an engine is started cold, that viscosity will be significantly higher because the component and oil temperature will be close to ambient air temperature. As the engine then warms up, component, coolant, and oil temperatures rise to their steady-state values (which depend to a degree on engine load and speed). The impact of oil temperature on the engine's mechanical friction is substantial. As shown in Fig. 13.16, the total friction power loss decreases by a factor of two as the engine coolant temperature increases from 20 to about 90°C, where it then stabilizes. Fmep was determined from the difference between imep (obtained from cylinder pressure data) and the measured bmep.[14] The coolant temperature (used as an indicator for the local lubricant temperature) is estimated from a friction model.[8] During warm-up, the engine was operated at light load and low speed. Engine warm-up at these lightly loaded (normal driving) conditions takes some 10 minutes.

© McGraw-Hill Education. All rights reserved. Any use is subject to the Terms of Use, Privacy Notice and copyright information.

Figure 13.16 Measured coolant temperature and friction power loss as a function of time from engine start up. 1.1-liter four-cylinder gasoline engine.[14]



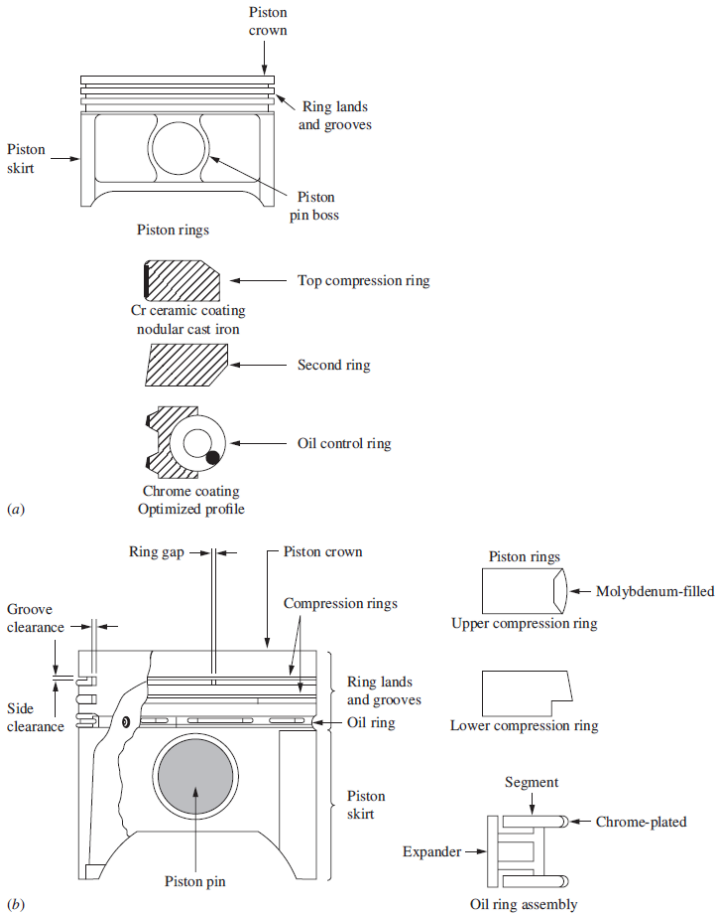
In the sections that follow, total engine friction will be discussed under the following headings: piston assembly friction, valvetrain friction, crankshaft bearing friction, pumping friction (in Sec. 13.7), and accessory power requirements (in Sec. 13.8).

13.6.3. Piston Assembly Friction and Lubrication

The construction and nomenclature of the piston and ring assembly for a typical automobile gasoline and truck diesel engine are shown in Fig. 13.17. The piston skirt is the load-bearing surface, which keeps the piston properly aligned within the cylinder bore. The piston skirt carries the side load, which is present when the connecting rod is at an angle to the cylinder axis. The rings control the behavior of the lubricant between the piston and ring surfaces and the liner. Automotive engines normally use three rings. These rings perform the following tasks: (1) The top ring seals the clearance between the piston and cylinder to retain in-cylinder gas pressure and minimize blowby; (2) the second ring (often called the oil scraper ring) controls the amount of oil on the liner above it so the top ring is adequately (but not excessively) lubricated; and (3) the bottom, oil control, ring controls the oil flow from the region below the ring pack into the third land region above this bottom ring. Effectively, the oil control ring does the gross oil flow management (there is plenty of oil below this ring) and the oil scraper ring does the fine control of oil left on the liner as the piston and its rings move down the cylinder. The back of the oil control ring groove has holes in it so excess oil can be returned to the crankcase.

© McGraw-Hill Education. All rights reserved. Any use is subject to the Terms of Use, Privacy Notice and copyright information.

Figure 13.17 Construction and nomenclature of typical piston and ring assemblies: (a) spark-ignition gasoline engine; (b) diesel engine (various sources).



Many designs of compression ring are employed, the differences between them being in the cross-sectional shapes (and hence relative flexibility) and in their use of wear-resistant surface treatments. Top compression rings are usually made of nodular cast iron (or steel). The ring profiles are chosen to facilitate hydrodynamic lubrication. Common shapes are a rectangular cross-section with inner and outer edges chamfered to prevent sticking in the groove, with a barrel-shaped working surface which can accommodate the rotation of the piston which occurs with short piston skirts (such as that shown in Fig. 13.17*a*). Wear-resistant coatings (either a hard chromium-plated overlay or a molybdenum-filled inlay) are usually applied to the outer ring surface. The rings are forced outward onto the liner surface through the ring tension produced in the ring as the ring gap is largely closed when the ring is inserted into the circular cross-section liner. The cut-off corner in the automobile top and second ring profiles in Fig. 13.17*a* causes the ring to *twist*. For the top compression ring shown, the chamfer at the top right-hand corner reduces the radial width of the top of this ring and thus makes its *stiffness* at the top less than at the bottom. A positive (anti-clockwise for the top ring profile in Fig. 13.17*a*) ring twist results. The second ring serves principally to fine tune the amount of oil left on the liner (though it also provides additional pressure sealing). Since the operating environment is less arduous, the second ring can be made more flexible to give better oil control through its "oil scraping" profile, and its chamfer that produces negative twist. Note these ring twists are small—fractions of a degree. Ring bottom-edge contact provides the desired oil scraping action on the down-stroke. The oil control ring meters and distributes the oil directed onto the cylinder liner by the crankshaft system, returning excess oil to the crankcase sump. It must exert sufficient pressure against the cylinder liner, possess suitably shaped wiping edges (usually two thin steel rings), and provide adequate oil drainage. Slotted or composite rings are normally used.

The tension in all the piston rings holds them out against the cylinder wall, and cylinder bore deformations require high ring conformability. The gas pressure behind the compression rings increases this radial force. All these factors contribute to piston assembly friction. The gas pressures behind the second ring are substantially lower than behind the first ring. The gas

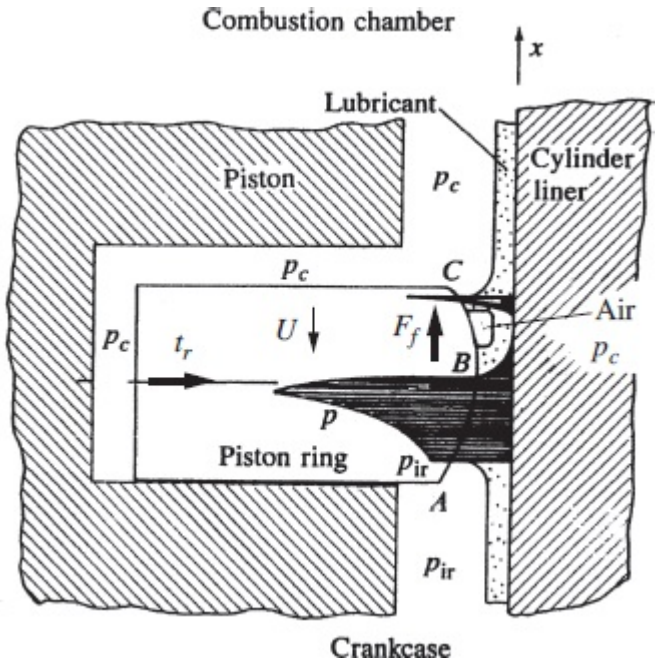
© McGraw-Hill Education. All rights reserved. Any use is subject to the Terms of Use, Privacy Notice and copyright information.

pressures behind the rings are a function of engine load. All three rings contribute significantly to piston assembly friction. The oil control ring, due to its two rail design and higher ring tension, may operate partly under boundary lubrication and contribute about twice the friction of each compression ring.[15] Ring pack friction mep is in the range of 4 to 12 kPa.

The piston assembly is the dominant source of engine rubbing friction. The components that contribute to friction are: the rings (as noted above), piston skirt, and piston pin. The forces acting on the piston assembly include: static ring tension (which depends on ring design and materials); the gas pressure forces (which depend on engine load); the inertia forces (which are related to component mass and engine speed). The major design factors which influence piston assembly friction are the following: ring width, ring face profile, ring tension, ring gap (which governs inter-ring gas pressure), liner temperature, ring-land width and clearances, skirt geometry, skirt-bore clearance.

Piston assembly friction is dominated by the ring friction. The forces acting on a compression ring, lubricated by a thin oil film, as it moves down the cylinder liner during the expansion stroke are indicated in Fig. 13.18. The analysis of this hydrodynamic contact is complex because the forces acting on the ring vary with time and slight changes in ring face geometry can have large effects on the computed results. Cylinder pressure p_c normally acts on the top and back of the ring. The inter-ring gas pressure p_{ir}, which depends on cylinder pressure and the geometry of the lands, ring grooves, and ring (especially the ring gap), acts on the oil film and bottom part of the ring. The character of the gas flow into and out of the inter-ring regions and its effect on ring motion were discussed in Sec. 8.6. Late in the expansion stroke, pressure reversals can occur which may cause the ring to move to the upper surface of the groove or to flutter in between. Ring tension t_r acts to force the ring against the liner. The pressure in the lubricating oil film generated by the downward ring motion is as shown by the surface *A-B*. The oil film can cavitate between *B* and *C*; if so, the pressure decreases to a low value and then increases to p_c. When the direction of motion is reversed, *C-B* becomes the pressure-generating surface. The pressure generated in the lubricant film holds the ring surface away from the liner.

Figure 13.18 Schematic of pressure distribution in the lubricating oil film and around a compression ring during expansion stroke. Pressure profile in the oil film indicated by horizontal shading.[2]



Models for the ring and oil film behavior have been developed. For the practical case where the oil film thickness*h* is much less than the ring width, the Navier-Stokes equation for the liquid film motion reduces to a one-dimensional Reynolds equation of the form:

© McGraw-Hill Education. All rights reserved. Any use is subject to the Terms of Use, Privacy Notice and copyright information.

$$\frac{\partial}{\partial x}\left(h^3\frac{\partial p}{\partial x}\right) = 6U\mu\frac{\partial h}{\partial x} + 12\mu\frac{\partial h}{\partial t}$$

(13.8)

where *h* is the local film thickness, *μ* the liquid viscosity, and *U* the relative velocity between the two surfaces. This equation, along with the appropriate force balances on the ring, can then be solved for the coupled film and ring behavior.

Oil film thickness measurements within the piston assembly illustrate many of the above-described phenomena. Figure 13.19 shows results obtained with a point laser-induced-fluorescence (LIF) measurement technique (where a fluorescing dye is added to the lubricating oil) of the oil film thickness between the piston rings and the liner, and of the oil accumulation on the piston lands and skirt, in an automobile gasoline engine. The piston profile is shown along the bottom of the graph, with the locations of the top ring groove, the scraper ring groove, and the oil control ring groove marked. The piston skirt is on the left-hand side. Two 25-μm-deep grooves used for measurement calibration are positioned just above the piston skirt. Oil film thicknesses of 1 to 2 μm are observed above the top of the piston (between 0 and +5 mm on the right-hand end of the horizontal axis). This film, left on the liner by the descending piston, lubricates the top rings on the piston upstroke. Oil film thicknesses between the liner and the two top rings have a minimum of some 1.5 μm. Elsewhere, primarily on the piston lands, the descending two rails of the oil control ring carry substantial oil from the piston skirt region downward, as does the second oil scraper ring. The liner surface temperature, and thus the oil temperature, does not affect this oil distribution pattern significantly. These oil distributions within the piston and ring assembly have a major impact on oil consumption (Sec. 13.10.1).[16]

Figure 13.19 Oil film thickness measurements between the piston, piston rings, and the liner made using a laser-induced fluorescence technique illustrated at top. Piston profile is along the bottom. Curves show the oil film thickness in microns at different liner temperatures in an operating gasoline spark-ignition engine.[16]

© McGraw-Hill Education. All rights reserved. Any use is subject to the Terms of Use, Privacy Notice and copyright information.

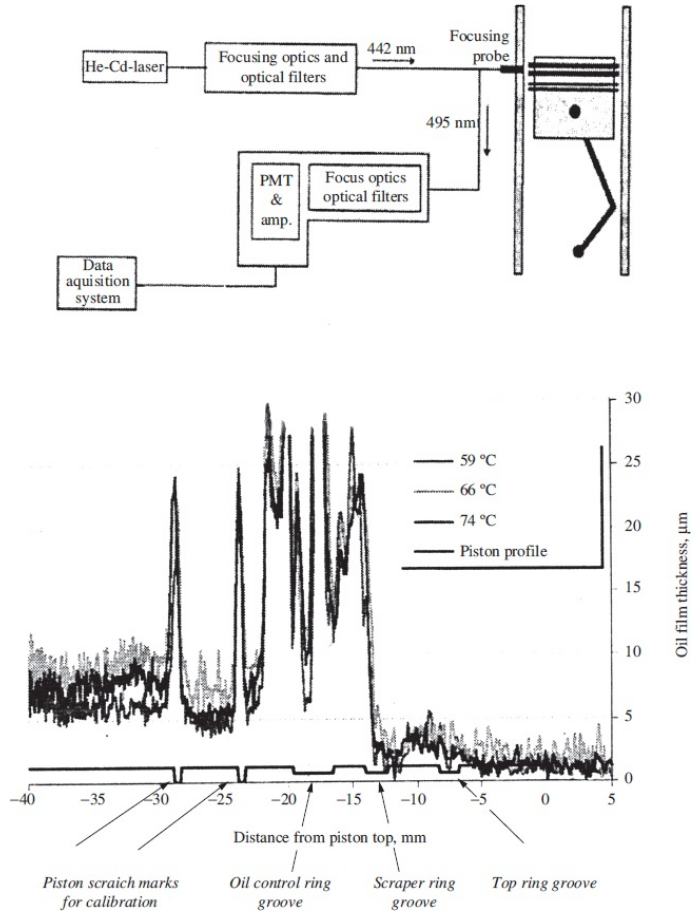
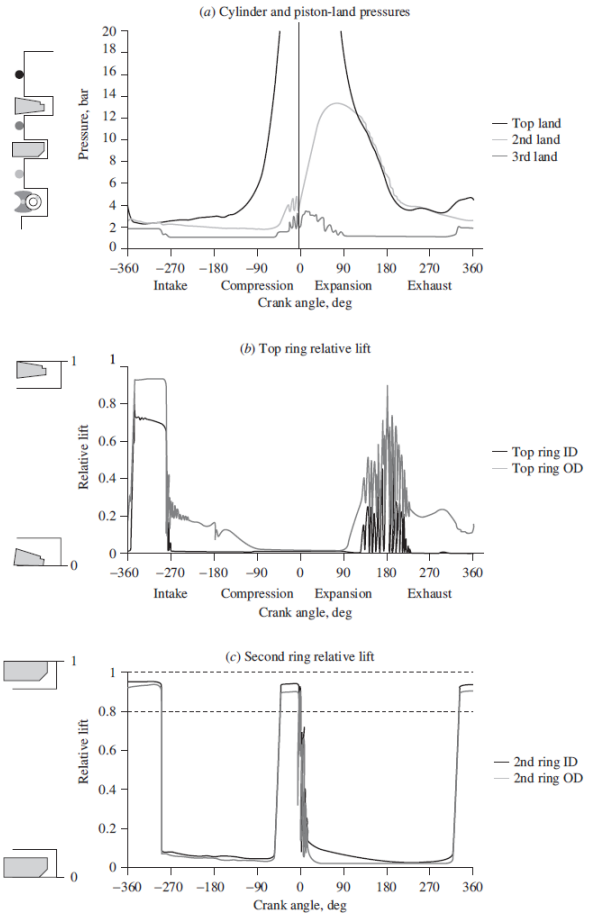


Figure 13.20 illustrates key aspects of piston ring behavior during the engine's operating cycle. The engine is a heavy-duty 8.9-liter diesel with a bore of 114 mm, stroke 144.5 mm, and compression ratio of 16.6 operating at its rated power.[17] The top graph (Fig. 13.20) shows the gas pressures above the top ring (which equals the cylinder pressure), between the top and second rings, and below the second ring. Note that during the latter half of the expansion stroke, the second land pressure is essentially the same as the pressure above the top ring. This is generally undesirable since there is no longer a significant pressure force holding the top ring on the bottom of its groove (see Fig. 13.18). During this period, as shown in Fig. 13.20, the top ring can oscillate up and down in its groove as the sketches and the simulation results for relative ring lift indicate. A consequence of this top ring *flutter* and the higher gas pressure below the ring is an oscillating (reverse) gas flow around the ring which can carry any oil available below the ring upward toward the combustion chamber, contributing to oil consumption (Sec. 13.10.1).

© McGraw-Hill Education. All rights reserved. Any use is subject to the Terms of Use, Privacy Notice and copyright information.

Figure 13.20 Piston ring motion, within the ring grooves, during the operating cycle in one cylinder of a 8.9-liter heavy-duty diesel engine: (a) cylinder and piston land pressures; (b) top ring relative lift; (c) second ring relative lift.[17]



The second ring lift behavior shows upward axial movement in its groove around the top center firing piston location. This can be helpful in reducing the second land pressure by enabling downward gas flow behind the second ring. Note that this gas flow resulting from top and second ring motion and flutter in their respective grooves, is significantly larger than the flows through the (relatively small area) ring gaps.[17]

The piston rings also rotate, circumferentially, within their grooves. The top and second rings usually move independently of each other, and arbitrarily. Changing engine operating conditions generally alters the location of the ring gap. The rotation speed of the rings is in the 0.2 to 0.4 rev/min range for the top ring, and can be twice that for the second ring. Ring rotation is easier at low engine speeds. Note that usually the ring gaps of the top two rings are in different circumferential positions: the blowby gases that pass that flow axially downward through the top ring gap must therefore flow circumferentially around the second land region before they can flow through the second ring gap. When the ring gaps line up (as they at times may) the blowby flow path is more direct. See Sec. 8.8 for additional discussion of ring-pack gas flows. Flow through the ring gaps impacts oil consumption (Sec. 13.10.1).[18]

The desired ring behavior as the piston moves up and down the cylinder during the four-stroke operating cycle can be summarized as follows.[12] As the piston accelerates down the cylinder during the intake stroke, ring friction and inertia forces move the rings to the top of their grooves. During this downward stroke, the oil control and oil scraper rings "scrape" oil which has accumulated on the liner back into the crankcase. As the piston decelerates approaching BC, the inertia of the rings dominates: rings move to the bottom of their grooves. As the piston moves up during the compression, friction and inertia forces on the rings hold the rings on the bottom of their grooves. As the piston approaches TC, the increasing gas pressure above the top ring keeps it on the bottom of its groove: lower inter-ring pressures allow the second ring, in the latter part of the compression stroke, to move to the top of its groove as it decelerates. During this upward stroke, the rings are lubricated

© McGraw-Hill Education. All rights reserved. Any use is subject to the Terms of Use, Privacy Notice and copyright information.

by the oil left on the liner during the last downward stroke. During the expansion (power) stroke, the high cylinder gas pressure holds the top ring on the bottom of its groove: rising inter-ring gas pressure part way into the stroke forces the second ring to the bottom of its groove. Again, on downward strokes, the descending oil control and scraper rings "scrape" excess oil off the liner and direct it back to the crankcase. Early in the exhaust stroke the ring friction dominates, and the top and second rings ride on the bottom of their grooves. As the piston slows in the latter part of the stroke and gas pressure are low, inertia moves both rings to the top of their grooves.[12]

The cylinder liner and piston ring surface finish impacts the piston assembly oil behavior and friction. The liner is *honed* to improve the liner surface's capacity to retain oil: that is, a closely spaced cross-hatched pattern of grooves some 1.5 to 3 μm deep are machined into the liner to retain oil and also wear debris. A finer honing operation smooths the surface. Combined, these surface modifications reduce piston assembly friction, especially during engine wear-in operation.

An analysis of the forces involved in the piston, connecting rod, crankshaft mechanism of Fig. 2.1 leads to the following. An axial force balance relates the piston mass *m* and acceleration to the net axial force:

$$m\frac{dS_p}{dt} = F_r \cos\phi - \frac{\pi B^2}{4} p \mp F_f$$

(13.9)

where ϕ is the angle between the cylinder axis and connecting rod, and *p* is the cylinder *gauge* pressure. The piston acceleration $a_p (= dS_p/dt)$ is given by Eq. (2.14).

A transverse force balance gives

$$F_t = F_r \sin\phi \left(-m\frac{dS_p}{dt} + \frac{\pi B^2}{4} p \mp F_f \right) \tan\phi$$

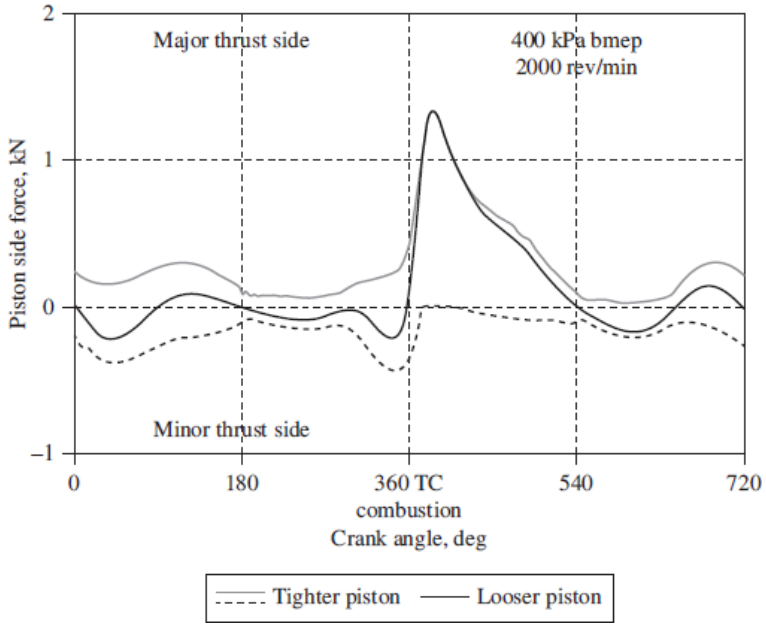
(13.10)

Here F_r is the force in the connecting rod (positive when in compression) and F_f is the friction force on the piston assembly (− when piston is moving toward the crank shaft; + when piston moves away from the crank shaft).

The side thrust F_t given by Eq. (13.10) is transmitted to the liner largely via the piston skirt. It changes direction as the piston passes through top- and bottom-center positions. Since the friction force changes sign at these locations, and the gas pressure during expansion is greater than during compression, the side thrust during the expansion or power stroke is greater. The side of the liner resisting that greater force (the left side in Fig. 2.1) is termed the *major thrust side*. The other (right) side is termed the *minor thrust side*. The variation of this piston side force through the operating cycle in a turbocharged gasoline engine (peak cylinder pressure 115 bar, specific output 87 kW/liter) is shown in Fig. 13.21.[19] Data for a standard looser fitting piston are shown, as well as for a tighter-fitting low-friction lighter piston where both piston skirts exert some side force on the two sides of the liner. The high side skirt loading due to the combustion-generated high in-cylinder gas pressures starting at (firing) TC piston position are apparent.

© McGraw-Hill Education. All rights reserved. Any use is subject to the Terms of Use, Privacy Notice and copyright information.

Figure 13.21 Piston side force through the operating cycle of a turbocharged gasoline engine: 400-kPa bmep, 2000 rev/min.[19]



The piston skirt carries most of this side thrust so it contributes to piston assembly friction. The large contact area between the skirt and liner, relative to the ring contact area, results in lighter loading (force/area) and promotes hydrodynamic lubrication. Piston skirt areas have been reduced substantially in recent years to reduce piston height and mass (which reduces side thrust) and contact area. An additional reduction in side thrust leading to reduced skirt friction has been standard design practice through use of an offset wrist-pin. By offsetting the pin axis by about 1 mm toward the major thrust side without changing its vertical location, the crank angle at which the piston traverses the bore and "slaps" the other side of the cylinder is advanced to before TC, so it occurs before combustion has increased the cylinder gas pressure significantly.

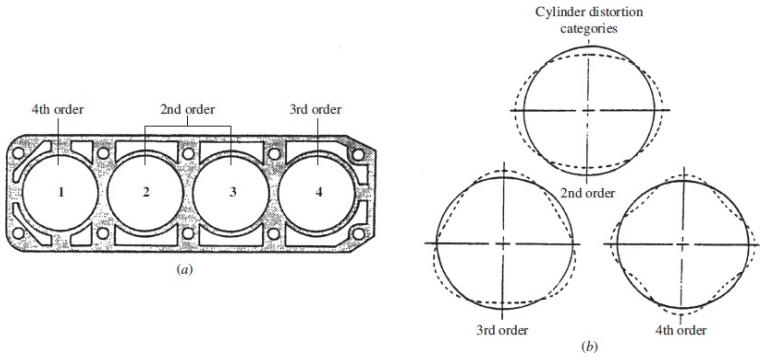
Offsetting the crankshaft axis from the cylinder axis toward the major thrust side of the cylinder by some 15% of the bore can modestly reduce the piston side force and thus piston friction. This is done in some production gasoline engines. Also, changes in R (the crank ratio, $R = a/\ell$; see Sec. 2.2) change the piston side force, and friction. It has been noted that if the piston side force is below a certain level, then piston assembly friction is not significantly affected by the side force. So while decreasing the crank ratio below about 3.5 increases expansion stroke friction due to the increased side force, increasing R above 3.5 has little impact. Crankshaft axis offset does reduce piston fmep during the first portion of the expansion stroke (from about 30° to 90° ATC). A crank offset of about the optimum (0.1 to 0.15, crankshaft offset: connecting rod length) which is about 15 mm with a stroke of 80 mm, resulted in a 10% reduction in piston assembly friction. This reduction occurs not only from the reduced piston side force, but also from the changed timing of the piston movement from the minor thrust side to major thrust side of the liner, relative to TC.[20]

An additional factor in piston assembly friction and oil consumption is cylinder bore distortion. Mechanical forces, gas pressures, and acting on the engine block and cylinder head, and thermal expansion, can cause the cylinder liner to be "out of round." Various block design and manufacturing approaches are used to minimize the mechanical distortions that occur during engine assembly. The previous discussion of the intended ring function and behavior makes clear that significant distortion of the liners in multi-cylinder engines will increase friction and oil consumption.

Figure 13.22 illustrates how cylinder distortion is categorized: whether it is primarily second, third, or fourth order.Figure 13.22*a* shows the block layout of a hypothetical engine where the cylinder liners are secured in different ways. Cylinder liners 2 and 3 are constrained on either side, and thus are prone to second-order distortion. Cylinder 4 is effectively attached to the block at three circumferential locations and is susceptible to third-order distortions. Cylinder 1 has four clamping points and thus fourth-order distortions are possible. Figure 13.22*b* shows these three orders of bore distortion.[21]

© McGraw-Hill Education. All rights reserved. Any use is subject to the Terms of Use, Privacy Notice and copyright information.

Figure 13.22 Definition of second-, third-, and fourth-order bore distortion, and illustration of block designs that are susceptible to these distortions.[21]



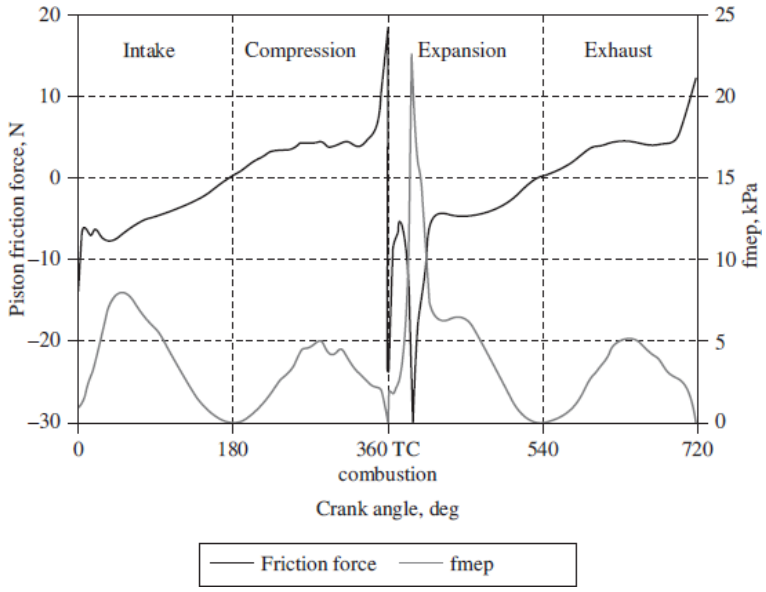
Maximum radial bore distortions in practice can be up to some ±30 μm Piston rings are designed to be flexible, and with adequate ring tension, to conform to liner distortions to a degree. Note second-order distortions are likely to be largest in amplitude; fourth-order distortions are significantly smaller. Since piston rings have a ring gap, their conformity to distorted bores is not circumferentially uniform.

A consequence of bore distortion and incomplete ring conformity is that the oil film thickness between the top ring (with its barrel-shaped outer surface) and the liner varies around the ring. Liner distortions can occur along the length of the liner. Ring conformity would be expected to vary with load (higher gas pressures force better conformity). Limited measurements of oil film thickness between the top ring and the liner show it can vary substantially (e.g., from less than 1 μm to 10, even 20, μm, depending on where the piston is in the 720° engine operating cycle). The oil film can vary from normal behavior (covering the majority but not all the top ring surface) to "fully flooded" behavior, or to significantly "starved" behavior.[22]

Measurements of the friction force associated with the piston assembly have been made. The most common technique involves the use of a special engine where the axial force on the cylinder liner is measured directly with a load transducer. Piston assembly friction can also be determined from cylinder pressure and connecting rod reaction force variations (see Fig. 13.1). Figure 13.23 shows the friction force (fmep) measured in small-displacement turbocharged gasoline engine through the engine's operating cycle. This data is from a lightly loaded lower speed operating point. Friction forces are highest just before and after top-center at the end of the compression stroke. The high values at the start of the expansion stroke under firing conditions are caused by the piston slap impulse,[21] and then by the piston skirt high side-thrust force as well as the combustion gas pressure loading on the rings, due to the high cylinder gas pressure (which peaks at 15 to 20° ATC). The figure also shows the piston friction mean effective pressure (friction work per cycle/displaced volume). When fmep is multiplied by N/2 (cycles per second) this gives friction power. When the piston comes to rest at TC and BC positions, the power lost (rate of doing work to overcome friction) goes to zero. The first half of the expansion stroke with its higher friction forces consumes more power than do the other strokes.[19]

© McGraw-Hill Education. All rights reserved. Any use is subject to the Terms of Use, Privacy Notice and copyright information.

Figure 13.23 Variation in piston friction force, and resulting fmep, through the operating cycle of a gasoline spark-ignition engine. Lightweight low-friction piston design: 400- kPa bmep, 2000 rev/min.[19]



13.6.4. Crankshaft Friction

Crankshaft friction contributions come from journal bearings (connecting-rod big end, main and accessory or balance shaft) bearings, and their associated seals. A schematic of a journal bearing operating under hydrodynamic lubrication is shown in Fig. 13.24. Large loads can be carried by journal bearings with low energy losses under normal operating conditions due to the complete separation of the two surfaces in relative motion by the lubricant film. Loads on crankshaft journal bearings vary in magnitude and direction because they result primarily from the inertial loads of the piston/connecting rod mechanism and the cylinder gas loads [see Eq. (13.15)]. Typical loads and the resulting journal eccentricity diagram for a connecting rod big-end bearing are shown in Fig. 13.25. From the journal eccentricity diagram, the minimum oil film thickness can be determined. This quantity, the minimum separation distance between the journal and bearing surfaces, is a critical bearing design parameter. If the film thickness is too low, asperities will break through the oil film and substantially increase the friction and wear. Journal bearings are usually designed to provide minimum film thicknesses of about 2 μm.

© McGraw-Hill Education. All rights reserved. Any use is subject to the Terms of Use, Privacy Notice and copyright information.

Figure 13.24 *Schematic of hydrodynamically lubricated journal bearing.*[3]

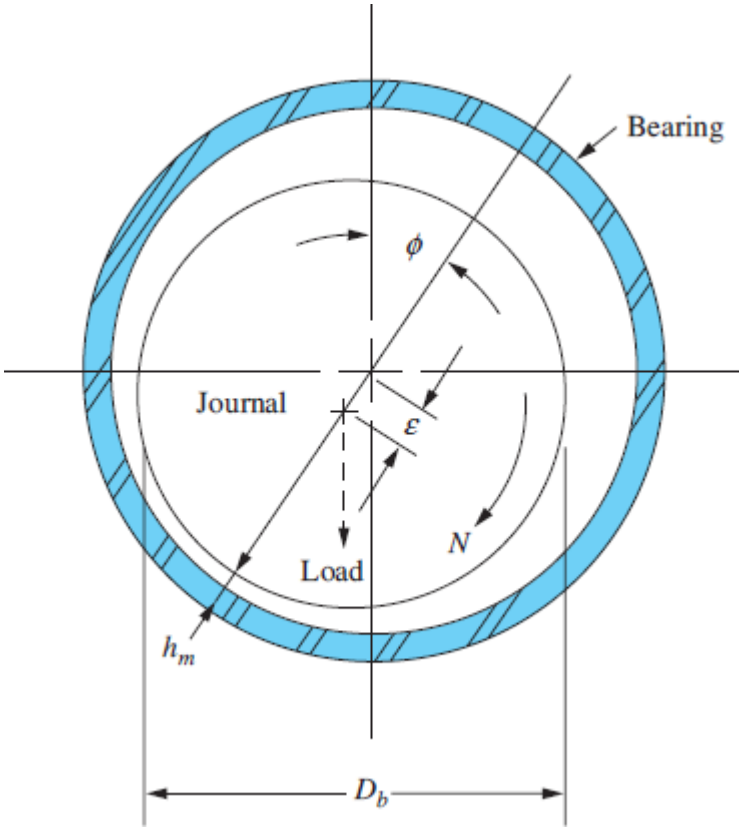
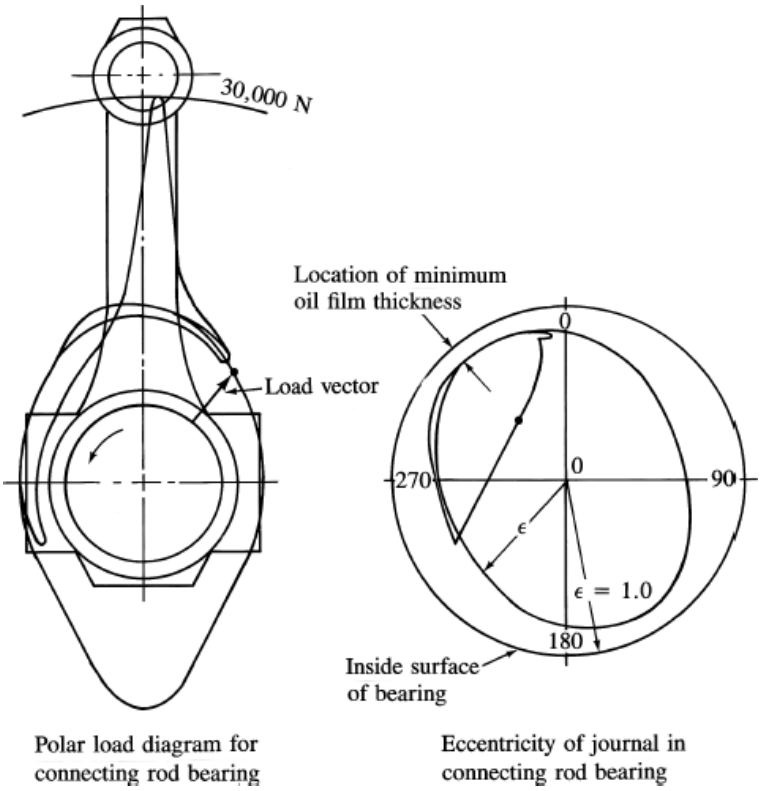


Figure 13.25 *Typical engine journal bearing load and eccentricity diagrams.*[3]



© McGraw-Hill Education. All rights reserved. Any use is subject to the Terms of Use, Privacy Notice and copyright information.

The friction force F_f in a bearing is given approximately by the product of the bearing area, the oil viscosity, and the mean velocity gradient in the oil:

$$F_f \approx (\pi D_b L_b)\,\mu\left(\frac{\pi D_b N}{\bar{h}}\right) = \frac{\pi^2 \mu D_b^2 L_b N}{\bar{h}}$$

(13.11)

where D_b and L_b are the bearing diameter and length,
$\bar{h}$ is the mean radial clearance, and N is the shaft rotational speed. A more sophisticated analysis of the friction in a hydrodynamically lubricated bearing yields the relation[20]

$$F_f = \frac{\pi^2 \mu D_b^2 L_b N}{(1-\varepsilon^2)^{1/2}\bar{h}} + \frac{\bar{h}\varepsilon W}{D_b}\sin\phi$$

(13.12)

where ε is the eccentricity ratio
$(\bar{h} - h_m)/\bar{h}$ and h_m is the minimum clearance. The first term closely matches the approximation given in Eq. (13.11). The factor $1/(1 - \varepsilon^2)^{1/2}$ and the second term correct for the offset of the journal center relative to the bearing center: W is the bearing load and ϕ the attitude angle. To first order, with hydrodynamic lubrication, the friction power does not depend significantly on the bearing load. If σ is the loading per unit projected area of the bearing $[W/(L_b D_b)]$ then the coefficient of friction/is given by

$$f = \frac{F_f}{W} \approx \frac{\pi^2 \mu D_b^2 L_b N}{\sigma L_b D_b \bar{h}} = \frac{\pi^2 D_b}{\bar{h}}\frac{\mu N}{\sigma}$$

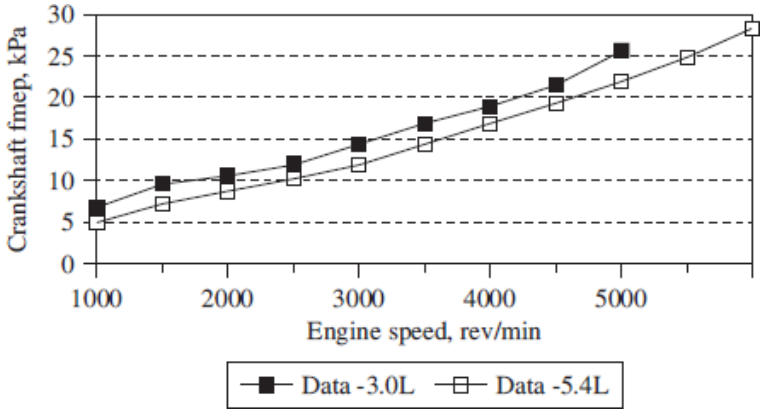
(13.13)

For a given bearing, or series of geometrically similar bearings, the friction coefficient is proportional to $\mu N/\sigma$. However, at low values of $\mu N/\sigma$ the hydrodynamic pressure in an actual bearing will be insufficient to support the shaft load and the oil film becomes incomplete. The friction coefficient increases rapidly as mixed lubrication then occurs.

Figure 13.26 shows two examples of crankshaft friction measurements, for a 3.0-liter and 5.4-liter naturally-aspirated gasoline engines.[8] The two engines show comparable crankshaft friction mep values which rise steadily with increasing engine speed. Note that the front and rear main bearing seals also contribute to crankshaft assembly friction. At 1500 rev/min, they are responsible for about 20% of the friction attributable to the crankshaft. Hoag[12] provides a useful summary of bearing and crankshaft design requirements.

© McGraw-Hill Education. All rights reserved. Any use is subject to the Terms of Use, Privacy Notice and copyright information.

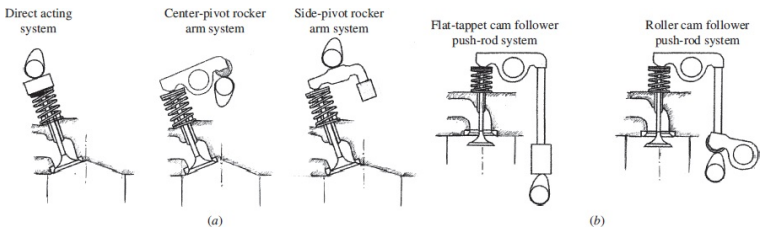
Figure 13.26 Crankshaft friction mean effective pressure data from a 3.0-liter V-6 and a 5.4-liter V-8 naturally-aspirated gasoline spark-ignition engine; from motored engine teardown tests.[8]



13.6.5. Valvetrain Friction

The valve train carries high loads over the entire speed range of the engine. Loads acting on the valve train at lower speeds are due primarily to the spring forces, while at higher speeds the inertia forces of the component masses dominate. Valve train designs can be classified by type of configuration. Examples of common valvetrain configurations are shown in Fig. 13.27. The objectives are to provide a compact, sufficiently "stiff," low mass, valve opening and closing mechanism at low cost. (Valve airflow and exhaust flow characteristics are discussed in Sec. 6.3.) The arrangements shown in Fig. 13.27*a* have overhead cam drives; those in (*b*) have cam-driven push-rod arrangements. The latter are the traditional valvetrain design for larger engines, where the camshaft can be positioned in the "vee" of the engine block: they have lower cost but higher mass and are less stiff. Overhead cam systems act more directly on the valves, have lower mass, and are preferred in smaller higher-speed engines. The direct-acting system shown is the simplest configuration, but since the cam lobe must provide the full valve lift, requires a larger cam and camshaft. Center- and side-pivot systems provide valve lift greater than the cam lobe height (by some 1.2 to 1.5 times). The direct-acting system thus increases engine height the most. Valvetrain friction can be broken down by critical contact regions: camshaft journal bearings, rocker-arm fulcrum, and cam/tappet interface. A flat tappet in sliding contact with a cam mostly experiences hydrodynamic lubrication. The contact between rocker arm and valve stem, and in the rocker arm fulcrum/pivot, experiences mixed-film lubrication. The use of roller cam followers (shown in the center pivot and roller-follower push rod drawings in Fig. 13.27) allows the load at this interface to be about twice that with a flat sliding tappet. If hydrodynamic lubrication between the roller and cam surface is maintained, use of roller followers significantly reduces valvetrain friction—especially at lower engine speeds.[12]

Figure 13.27 Different valve train arrangements: (a) overhead cam configurations; (b) push-rod configurations: roller cam-follower also illustrated.[12]

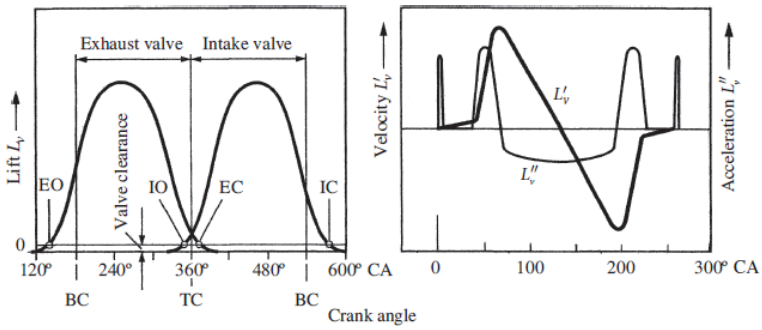


As the valves are opened and closed, the inertia force (effective mass × valve acceleration) as well as the valvetrain friction, determines the required driving force. Valve lift, velocity, and acceleration profiles through an engine operating cycle are shown in Fig. 13.28. Typical exhaust and intake valve lift profiles are shown on the left of the figure. The valve velocity profile, L'_v, is obtained by differentiating the valve lift with respect to time. A second time differentiation yields the valve acceleration,

© McGraw-Hill Education. All rights reserved. Any use is subject to the Terms of Use, Privacy Notice and copyright information.

L_v''. As the valves lift off (and later) close onto the seat, the velocity increases (or decreases) slowly to minimize the acceleration from impact to rest. The velocity then increases rapidly (on opening) to reach a large valve open area quickly. At maximum lift, the valve comes to rest, and the process reverses. Maximum accelerations occur as the valve velocity increases (later, decreases) rapidly as the valve reaches about half its maximum lift.

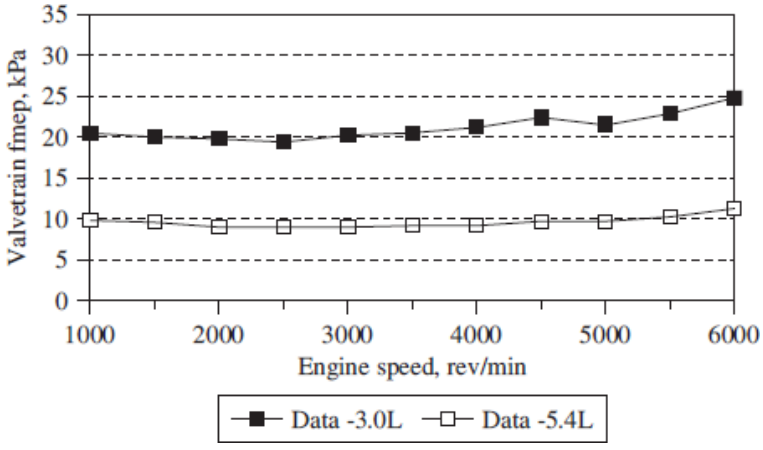
Figure 13.28 Left: Exhaust and intake valve lift L_v profiles versus crank angle; opening and closing angles (EO, IO, EC, and IC) are defined at a modest lift about equal to the slack in the valvetrain system. Right figure shows valve velocity L_v' and acceleration L_v'' during the valve open period.[13]



Friction differences between these systems are difficult to quantify. Generally, measurements of valvetrain friction for each of these valve train types show significant variations, especially at mid- and high-engine speeds.

Figure 13.29 shows two examples of valvetrain friction mean effective pressure for naturally-aspirated gasoline engine. The 5.4-liter V-8 engine had a two valve per cylinder, single overhead cam, with direct acting valve mechanism. The 3.0-liter V-6 engine had four valves per cylinder, double overhead cam with roller finger followers. The fmep values are significantly different. Older engines typically showed valvetrain fmep *decreasing* with increasing engine speed, believed due to the occurrence of boundary friction at low speed and the extent of that boundary friction period decreasing as speed increases. Significant reductions in valvetrain friction have been realized, and the valvetrain fmep is now almost independent of speed. The amount of boundary friction occurring has been substantially decreased.[8]

Figure 13.29 Valvetrain friction mean effective pressure (motored engine teardown tests) of two naturally-aspirated gasoline engines: a 3.0-liter (four-valve) V-6 and a 5.4-liter (two-valve) V-8.[8]



Effective methods of decreasing valve train friction are: (1) spring load and valve mass reduction; (2) use of tappet roller cam followers; (3) use of rocker arm fulcrum needle bearings. Studies of low-friction valve train designs indicate that roller cam-followers provide the largest benefit: reductions of order 50% in valve train friction can be achieved. Reducing valve, spring,

© McGraw-Hill Education. All rights reserved. Any use is subject to the Terms of Use, Privacy Notice and copyright information.

and tappet mass also reduces valvetrain friction: for example, reducing this mass by 30% reduced valvetrain friction torque by 40% at speeds of 2000 rev/min and above.[23]

© McGraw-Hill Education. All rights reserved. Any use is subject to the Terms of Use, Privacy Notice and copyright information.

13.7. PUMPING FRICTION

Pumping air into the engine during the intake process, and burned gases out during the exhaust process, during the gas exchange process (in the four-stroke engine cycle), requires a work transfer between the in-cylinder gases and the piston. Several flow restrictions outside the cylinder head, in the inlet and exhaust systems—air filter, ducting, throttle, intake manifold (on the inlet side), exhaust manifold and tail pipe, catalytic converter, and muffler (on the exhaust side)—cause pressure drops which require work to overcome. Equally important are pressure losses in the inlet and exhaust ports and valves. As load is reduced in a spark-ignition engine, the airflow is reduced by partly closing the throttle increasing its flow restriction. The increase in throttling work is more rapid than the decrease in flow work. Both throttling work and flow work increase as engine speed increases at constant load.

The above summary applies to both naturally-aspirated engines and turbocharged engines, and gasoline and diesel engines (though the latter do not normally embody a throttle). However, incorporating a turbocharger significantly changes the intake and exhaust pressures at mid and higher loads. Section 13.2 explains the different ways that pumping work is defined in naturally-aspirated and turbocharged engines. The primary reason for this difference is that in naturally-aspirated engines, the pumping work is always negative—a work loss—so is counted as an engine friction component. In turbocharged engines at high outputs, pumping work is positive and adds to the engine's output. It is not then counted as an engine friction component. But at light loads, when the impact of the turbocharger is modest, pumping work becomes a loss. Thus in assessing pumping work as a loss or gain, these three factors—the innate flow resistances, the extent the engine is throttled, and engine boosting via a turbocharger—must be considered.

The classical definition of pumping work, and pumping mean effective pressure, is given inSec. 2.5 (Fig. 2.6) and Sec. 5.3 [Eqs. (5.22) and (5.23)]. It is the $\int pdV$ over the expansion and exhaust strokes, which in simple terms is

$$\text{pmep} = \frac{W_p}{V_d} = p_e - p_i$$

(13.14)

where
p_e is the average in-cylinder pressure during the exhaust stroke, and
p_i the average in-cylinder pressure during the intake stroke. In naturally-aspirated (and throttled turbocharged) engines,
p_i is less than
p_e and W_p and pmep constitute a loss. When
p_i is greater than
p_e (i.e., when the engine is boosted), the pumping work is a gain. In a highly throttled naturally-aspirated gasoline engine,
$p_e - p_i$ might be 0.6 bar when the brake mep is 2 bar. At high loads and lower speeds,
$p_e - p_i$ would be 0.2 to 0.3 bar and bmep 10 bar. In a turbocharged engine at high load,
$p_i - p_e$ could be up to about 1 bar with a bmep of some 20 bar. With turbocharged diesel engines under boost conditions,
p_i is usually higher than with SI engines, but so also is
p_e due to the lower diesel exhaust gas temperatures and energy.

Pumping losses have been correlated in various studies with variables such as cylinder-head valve geometries, engine mass flow, and engine speed (usually squared). The pumping mep equation below comes from an overall engine friction model for naturally-aspirated gasoline engines which adds together sub-models for each friction component, each based on fundamental scaling laws and empirical data:[8]

© McGraw-Hill Education. All rights reserved. Any use is subject to the Terms of Use, Privacy Notice and copyright information.

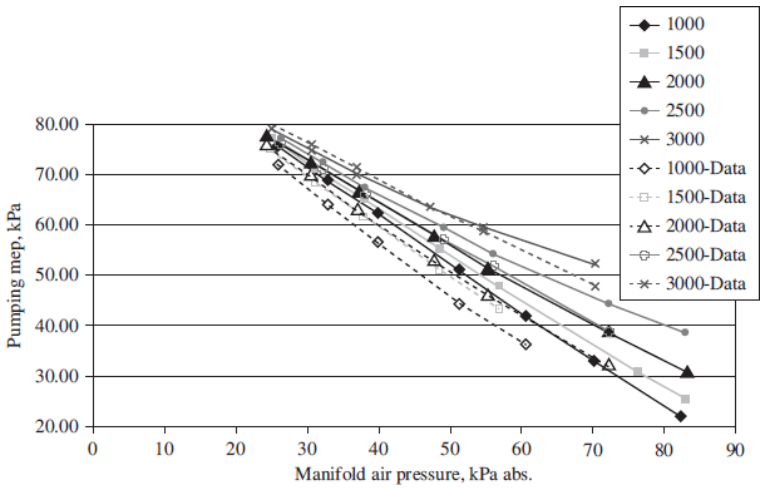
$$\text{pmep (kPa)} = (p_a - p_i) + 3.0 \times 10^{-3}\left(\frac{p_i}{p_a}\right)^2\left(\frac{\overline{S}_p^2}{n_v^2 r_i^4}\right) + 0.178\left(\overline{S}_p^2 \frac{p_i}{p_a}\right) + 3.0 \times 10^{-3}\left(\frac{p_i}{p_a}\right)^2\left(\frac{\overline{S}_p^2}{n_v^2 r_e^4}\right)$$

(13.15)

Here, p_a is atmospheric pressure, p_i the intake manifold pressure, $\overline{S}_p$ the mean piston (m/s) speed, n_v number of valves per cylinder, r_i the intake valve diameter/bore, r_e the exhaust valve diameter/bore; all pressures are in kPa. The first term represents the intake system pressure losses (including any throttling), the second term is the intake port and valve losses, the third term the exhaust system losses, and the fourth term the exhaust valve and port losses.[8]

Figure 13.30 shows pumping mep data and model [Eq. (13.15)] results for a naturally-aspirated 6.4-liter V-10 gasoline engine, as a function of engine speed and load (manifold air pressure, MAP). At typical light-load engine operation (MAP = 0.5 bar, 50 kPa), the pmep is about 0.5 bar and modestly dependent on engine speed. Even at high MAP values (above 0.8 bar) pmep is not negligible, and increases significantly with increasing engine speed.

Figure 13.30 Pumping mean effective pressure (pmep) as a function of (absolute) manifold air pressure (MAP): engine speeds, 1000–3000 rev/min. 6.4-liter V-10 NA gasoline engine. Data, open symbols and dashed lines; model results, Eq. (13.15), fitted symbols, and solid lines.[8]

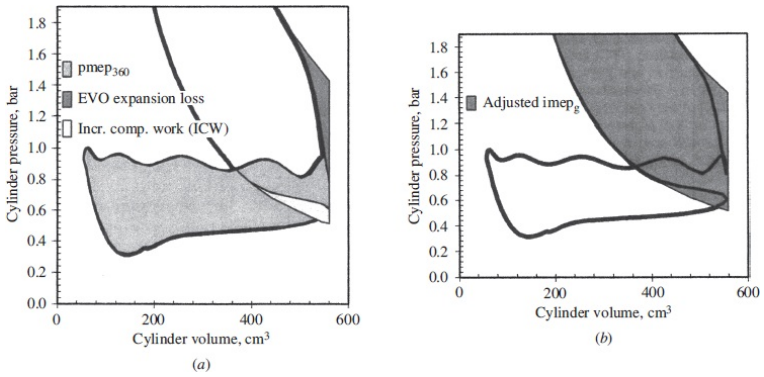


The advent of variable valve control has led to the introduction of a modified approach to pumping and indicated work. The classical approach discussed above neglects valve-timing impacts that occur during the expansion and compression strokes. With variable valve timing, the valve events can have a significant effect on all four strokes of the engine's operating cycle. As a consequence, changes in the net indicated performance cannot readily be separated into energy conversion efficiency effects and pumping work changes. The following approach calculates the work associated with the gas exchange process more completely by making adjustments to the pumping mep and gross indicated mep classical definitions.[24]

For an engine with fixed valve timing, the exhaust valve opening angle (EVO) is a trade-off between high-speed pumping work and low-speed expansion work.[25] This results in some loss of expansion stroke work at lower speeds as indicated on the *p-V* diagram (Fig. 13.31a, upper right). The amount of expansion work lost can be calculated by extrapolating the expansion stroke prior to EVO using the pV^n = constant relationship and integrating the area between that extrapolation and the measured in-cylinder pressure, as shown.

© McGraw-Hill Education. All rights reserved. Any use is subject to the Terms of Use, Privacy Notice and copyright information.

Figure 13.31 Cylinder pressure vs. cylinder volume diagram from EVO into the compression stroke: (a) Shaded areas represent all of the gas exchange work, defined as the adjusted pumping work; (b) shaded area represents the gross indicated work per cycle (Sec. 2.5) adjusted for valve timing effects. Engine data at 2.6-bar bmep, 1500 rev/min.[24]



With fixed intake cam timing, the intake valve is typically closed about 50° ABC of the compression stroke. Thus, as also shown in Fig. 13.27*a*, the compression stroke work is slightly higher due to the actual in-cylinder gas pressure being higher than the extrapolated pV^n = constant compression stroke line from IVC back to BC. The *adjusted* definitions for imep and pmep thus become:

$$\mathrm{imep(g)_{adj}} = \mathrm{imep(g)} + \mathrm{ICW} + \mathrm{EVO_{exp\ loss}} \tag{13.16}$$

$$\mathrm{pmep_{adj}} = \mathrm{pmep_{360}} + \mathrm{ICW} + \mathrm{EVO_{exp\ loss}} \tag{13.17}$$

Thus, the net imep (which is the 720° full cycle $\int pdV$) becomes

$$\mathrm{imep(n)} = \mathrm{imep(g)_{adj}} - \mathrm{pmep_{adj}} \tag{13.18}$$

which is an equivalent relationship to the classical approach equation

$$\mathrm{imep(n)} = \mathrm{imep(g)} - \mathrm{pmep_{360}} \tag{13.19}$$

The gross and net imep definitions are the standard ones based on gross and net indicated work per cycle (Sec. 2.5). ICW is *increased compression work*, $\mathrm{EVO_{exp\ loss}}$ is the expansion work lost due to early exhaust valve opening (both converted to mep by dividing by V_d), as described above: $\mathrm{pmep_{360}}$ is the standard exhaust plus intake stroke (360°) pumping work definition.

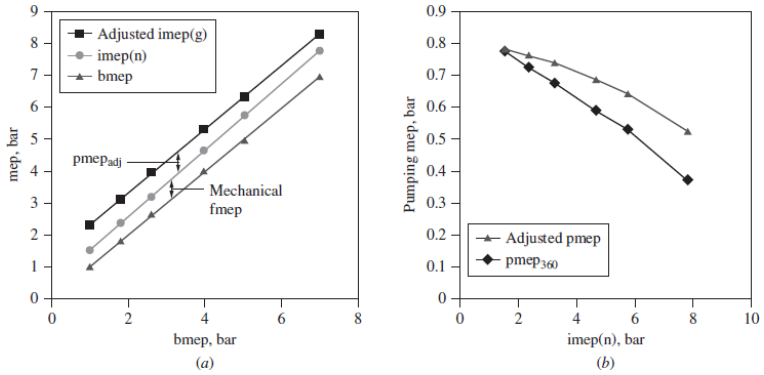
Note that Eqs. (13.18) and (13.19) give identical values for net imep (as they should). However, with the adjustments to imep and pmep summarized here, the valve timing effects on the gas exchange process work/losses, and the effects on the in-

© McGraw-Hill Education. All rights reserved. Any use is subject to the Terms of Use, Privacy Notice and copyright information.

cylinder fuel chemical energy to gas pressure energy to work transfer to-the-piston sequence, which determine the engine's inherent energy conversion effectiveness, have been more completely separated.

Figure 13.32 shows a load sweep for a standard naturally-aspirated gasoline engine, which illustrates the roles of this adjusted pmep approach (and that of mechanical friction mep) in the engine's imep and bmep at 1500 rev/min. Figure 13.32*a* shows how the adjusted pmep reduces the engine's imep(g), especially in relative terms at lower loads. It then shows the additional impact of mechanical friction mep, which increases with load due to higher component force levels due to higher cylinder pressures, decreasing imep(n) to the (usable) bmep. Figure 13.32*b* shows how that the adjusted pmep becomes steadily higher than pmep_{360} as load increases. At high load (in this NA engine) the real pumping mean effective pressure, even at this low speed, is significant.[24]

Figure 13.32 (a) Mean effective pressure parameters for a bmep sweep at 1500 rev/min; (b) comparison of pumping work mep parameters for a bmep sweep, plotted as imep(n), at 1500 rev/min.[24]



Variable valve control (see Sec. 6.3.3) allows the pumping work to be reduced. This is especially important at lighter loads and lower engine speeds, engine conditions important in automobile applications. Under these conditions, the objective is to increase
p_i so the pumping mep
$(p_e - p_i)$ is reduced. At IVC, under these quasi-static conditions,

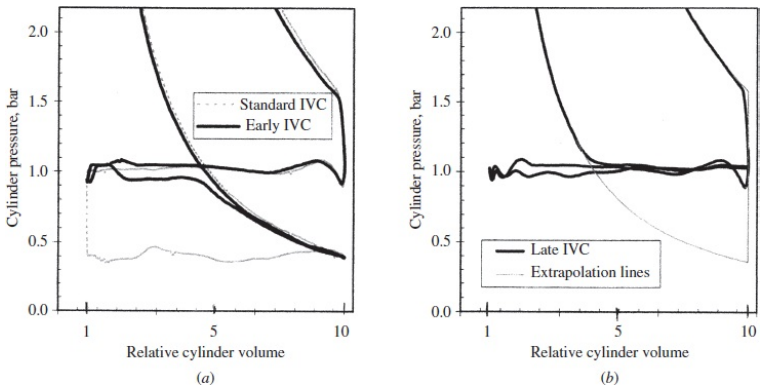
$$p_{\text{IVC}} V_{\text{IVC}} = mRT_{\text{IVC}} \tag{13.20}$$

A specific mass of air and fuel is needed to generate the required torque; thus m is essentially constant,[1] as also are R and T_{IVC} (in kelvins). Equation (13.20) thus indicates that closing the intake valve when the cylinder volume is smaller requires a higher intake manifold pressure.

The potential for pumping work reduction is illustrated in Fig. 13.33. Reduced V_{IVC} in Eq. (13.20) can be achieved by either closing the IV part way through the *intake* stroke; or closing it later in the compression stroke. These two strategies are shown on the *p-V* diagrams that result, Fig. 13.33*a* and *b*, respectively. The engine tested used a *camless valvetrain*—an electrical valve actuation (EVA) mechanism—to provide extensive valve control flexibility. Early valve closing (during the intake stroke) reduces the compression stroke work through gas expansion during the second half of the intake stroke followed by re-compression. The fixed-valve-timing engine pumping work is greatly reduced. With late IVC, more than halfway through the compression stoke, the pumping work is essentially eliminated, though the compression stroke work is increased.[24]

© McGraw-Hill Education. All rights reserved. Any use is subject to the Terms of Use, Privacy Notice and copyright information.

Figure 13.33 *Cylinder pressure vs. cylinder volume diagram from EVO into the compression stroke: (a) early intake valve closing (IVC) compared to standard IVC; (b) late IVC, with compression line extrapolated to BC. Engine data at 2.6-bar bmep, 1500 rev/min.*[24]



An alternative approach to reducing pumping used in some production gasoline engines is to reduce the number of firing cylinders (often called cylinder deactivation): for example, a V-8 engine firing only four cylinders; a V-6 firing only three or two cylinders. This is a part-load fuel consumption improvement strategy. Since, with reduced number of cylinders firing, the engine must still deliver the required torque, each firing cylinder must operate at higher bmep (half the cylinders firing, roughly twice the bmep). Thus the firing cylinders operate at significantly higher intake manifold pressure, and pumping work is reduced as is bsfc. Note that the mechanical and accessary friction of all the cylinders must be offset with part of the indicated work even when half (or one-third) of the cylinders are firing. Cylinder deactivation is implemented by decoupling the valve actuation mechanism of the cylinders that are not firing. In these cylinders, the mass of gas trapped is compressed and expanded, cycle after cycle.[26]

Finally, one of the benefits of turbocharging (*and* downsizing engines because the output for a given engine displacement goes up) is that pumping work is reduced. In automobile applications, typical vehicle driving is centered at a torque (or bmep) level that is about one-quarter of the maximum torque/bmep for that engine. Turbocharging increases the maximum bmep by some 50 to 100%. This typical part load bmep thus increases to 5 bar or more from a bmep of 2 to 3 bar in the corresponding naturally-aspirated engine. Pumping mep is correspondingly reduced.

The above discussion of pumping work (as well as of the other components of friction) emphasizes the two complementary paths available for reducing the impact of engine friction: (1) reducing the *absolute magnitude* of engine friction components and (2) reducing the *relative importance* of friction. This latter path is a major reason why turbocharging an engine not only increases its output per unit engine displacement, it also improves the engine's mechanical efficiency η_m [Eq. (2.24)], which quantifies the relative importance of engine friction.

[1] This neglects the second-order effect of the efficiency benefit that results from reduced pumping work.

© McGraw-Hill Education. All rights reserved. Any use is subject to the Terms of Use, Privacy Notice and copyright information.

13.8. ACCESSORY POWER REQUIREMENTS

The coolant/water pump, oil pump, and fuel pump are built-in accessories, essential to engine operation, and are normally considered part of the base engine. A fully-equipped engine usually includes additional accessories—for example, a fan and generator. In automobile use, it often includes a power-steering pump, an air conditioner, and even an air pump for emission control. These have been driven off the engine crankshaft, though some of these accessories may now be electrically driven to decouple their performance (and thus power dissipated) from scaling with engine speed. Friction belt drives (e.g., serpentine drives with ribbed V-belts and a tensioning pulley) are commonly used to drive the camshaft, water pump, alternator, power-steering pump, and air-conditioning compressor. Chain drives may be used to drive camshafts, oil pumps, and fuel pumps in diesel engines where (due to the high fuel-injection pressure) the fuel pump power requirements are significant,[27] since they provide more robust and maintenance free operation of these critical accessories.

The power requirements for the accessories fan, generator, and power-steering pump, are not normally included in the term "accessory friction" Of these, the fan requirement is the largest, and with a direct drive increases with the cube of the speed. Alternative couplings such as a viscous drive reduce the fan speed at high engine speed and thereby reduce its power significantly. The power-steering pump is only required to provide high pressures intermittently. With hydraulic power-assisted systems, only the fluid pumping losses are charged against the engine. Electric power-assisted steering systems are also used: these are driven by an electric motor powered by the electrical system.[13]

The power delivered by the fully equipped engine (the net power) is lower than the power delivered by the base engine due to the power requirements of these accessories. The friction mean effective pressures associated with driving the water pump, alternator, oil pump, and fuel pump (diesels) together comprise up to about 20% of total engine friction. The water pump fmep is typically less than about 7 kPa at 1500 rev/min; the oil pump 4 to 10 kPa at this speed; the alternator requires 7 to 10 kPa. These numbers vary significantly with component design details. The generator power depends on the electrical load to be met and the generator blower design. Average generator power is about two-thirds of the peak power.

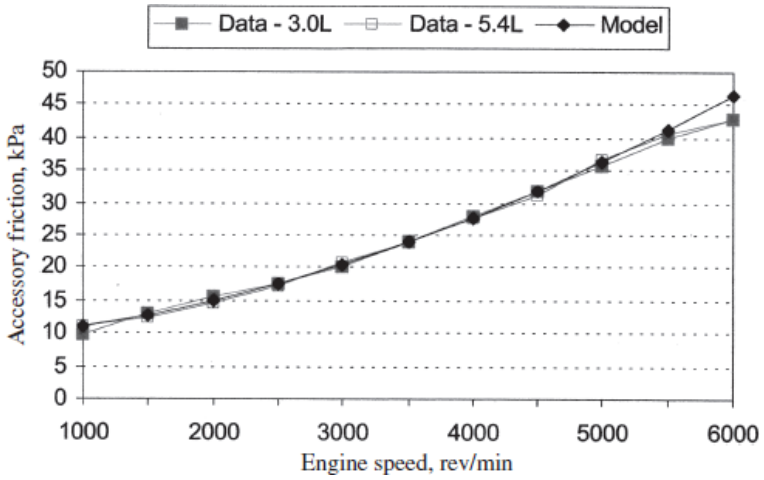
Air-conditioning is standard on a majority of U.S. cars; additional power is required for the air-conditioning compressor. Also, since the compressed refrigerant is condensed in a second radiator, a larger-than-standard fan is required to pull additional air through the combined radiator systems. An air pump which pumps air into the engine exhaust ports may be part of an SI engine emission control system (see Sec. 11.6). Its power requirements (~1 kW at normal engine speeds) must then be added to the accessory friction requirements.

The accessory friction mep as a function of speed for a 3.0-liter and a 5.4-liter naturally-aspirated gasoline engine is shown in Fig. 13.34. Both motored engine data and predictions from Eq. (13.21), below, are shown, and match well:

$$\text{afmep (kPa)} = 8.3 + 1.86\left(\frac{N}{1000}\right) + 0.75\left(\frac{N}{1000}\right)^2 \tag{13.21}$$

© McGraw-Hill Education. All rights reserved. Any use is subject to the Terms of Use, Privacy Notice and copyright information.

Figure 13.34 *Accessory friction mean effective pressure (motored engine teardown data) for 3.0-liter V-6 and 5.4-liter V-8 naturally-aspirated gasoline engines as a function of speed. Model is Eq. (13.21).*[8]



where *N* is engine speed in rev/min. Accessory friction mep here includes water pump, oil pump, and (unloaded) alternator. For diesels, the fuel pump drive requirements become significant. Note that accessory drive requirements are being reduced over time.[8]

© McGraw-Hill Education. All rights reserved. Any use is subject to the Terms of Use, Privacy Notice and copyright information.

13.9. ENGINE FRICTION MODELING

As this chapter has made clear, engine friction is a multi-component process with substantial and different details important in each friction component. Detailed models for these components, and models which combine these components, have been and continue to be developed. Integrated friction models are needed to convert from indicated engine performance and efficiency to brake values. They are a necessary component in widely used engine operating cycle simulations which though their flow, combustion, and heat transfer models essentially predict *indicated* engine operation. Detailed component models (e.g., for the piston ring pack) develop our understanding of critical friction and lubrication phenomena and identify from a fundamental perspective opportunities for improvement. Note that engine friction is steadily being reduced so friction models, which usually require some calibration against measured data, need to be periodically updated.

Integrated models are usually based on engine component friction data obtained from motored engine teardown tests (Sec. 13.4). Models for each major friction component (piston assembly, crankshaft, valvetrain, engine accessories, pumping work) are developed, sometimes at the subcomponent level, using terms based on the scaling laws for hydrodynamic and mixed (combined boundary and hydrodynamic modes) lubrication, and turbulent dissipation (see, for example, Patton et al.,[28] expanded and updated by Sandoval and Heywood[8]). These scaling law terms are then calibrated against engine teardown test data. Thus, total friction mean effective pressure is given by

$$\text{tfmep} = \sum_i (\text{component fmep})_i$$

(13.22)

where each component fmep term is the sum of sub-component terms with (as appropriate) hydrodynamic and mixed lubrication terms. These component models involve variables such as: lubricant viscosity (and its scaling with oil temperature); cylinder bore, stroke, compression ratio, number of cylinders; number of valves per cylinder, valve lift, valve diameter; engine speed, mean piston speed; ring tension; intake and exhaust manifold pressures relative to atmospheric; valvetrain constants for the different valve drive mechanisms; with, of course, several calibration constants.[1]

An important question is the effect of oil, coolant, and liner temperature on engine mechanical friction. The tribology literature shows that the oil viscosity scaling in the hydrodynamic friction terms should have the form:[29]

$$\mu_{\text{scaling}} = \sqrt{\frac{\mu(T)}{\mu_0(T_0)}}$$

(13.23)

where $\mu(T)$ is the viscosity of the oil in the engine for which friction predictions are being made, and $\mu_0(T_0)$ is the reference viscosity of the oil used in the engines that provided the data to calibrate the model. Viscosity values for several different oil grades can be obtained from Eq. (13.25) below, and Table 13.3 (in Sec. 13.11). Since the density of the oil is essentially constant, the dynamic viscosity μ is assumed to scale with the kinematic viscosity v. Thus

$$\mu_{\text{scaling}} = \sqrt{\frac{\nu(T)}{\nu_0(T_0)}}$$

© McGraw-Hill Education. All rights reserved. Any use is subject to the Terms of Use, Privacy Notice and copyright information.

(13.24)

where v_0 is the kinematic viscosity at reference temperature T_0.

The low shear rate viscosity v_0 of the oil (in centistokes) is related to temperature via the Vogel equation:

$$\nu_0 = k \exp\left(\frac{\theta_1}{\theta_2 + T}\right)$$

(13.25)

k is a correlation constant (in cSt), as are θ_1 and θ_2 (°C) for an oil, and T is the oil temperature (°C). This low-shear viscosity [Eq. (13.25)] is then converted to the high-shear-rate viscosity by multiplying by the ratio μ_∞/μ_0 (a standard ratio, of magnitude one or less, for a given oil) because most lubricated engine components operate in the high shear regime where multi-grade oils exhibit "shear thinning." (See Sec. 13.11, Table 13.3, for specific numbers.) Using Eqs. (13.23), (13.24), and (13.25), the effects of lubricant temperature on mechanical friction can be modeled.[8]

Figure 13.35*a* shows the effect of oil temperature (assumed to scale with the coolant temperature) on the components of mechanical friction for a 15W-40 oil for a 5.4-liter naturally-aspirated gasoline engine at 2000 rev/min. Note the substantial effect of oil temperature: friction in a just-started engine at 20°C is twice that in a warmed-up engine at 90 to 100°C coolant temperature (see Fig. 13.16 and accompanying text).

Figure 13.35 (a) Total mechanical friction mep as a function of lubricant (15W-40) temperature within the bearings and valvetrain, on the piston rings, and skirt (assumed to scale with coolant temperature). Also showing reciprocating fmep (without in-cylinder gas pressure, and the additional fmep impact from gas pressure), and crankshaft fmep. 5.4-liter V-8 naturally-aspirated engine at 2000 rev/min. (b) Total friction mep data (motored), with gas exchange losses added, and friction model results.[8]

© McGraw-Hill Education. All rights reserved. Any use is subject to the Terms of Use, Privacy Notice and copyright information.

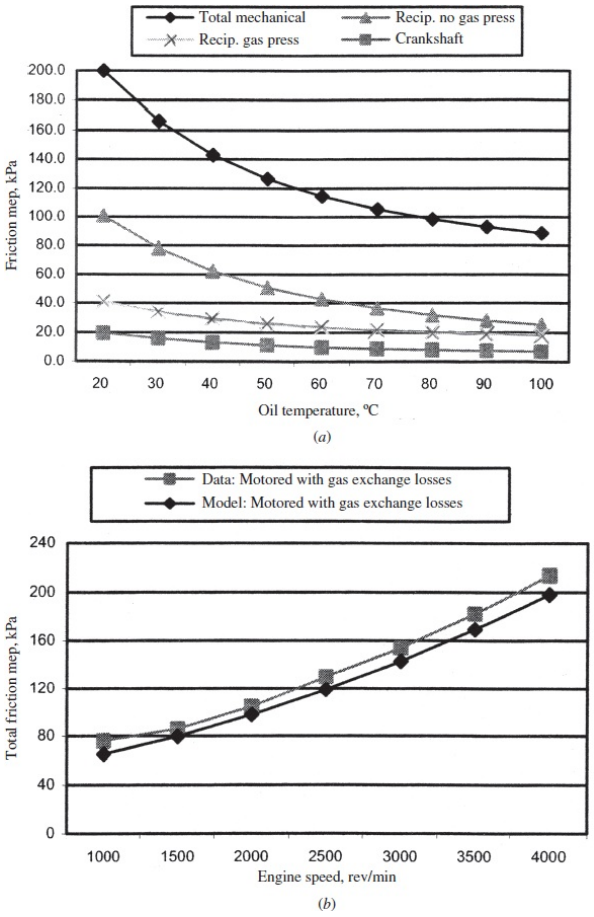


Figure 13.35*b* shows comparison of the Patton, Sandoval, and Heywood integrated friction model with total engine friction under motored conditions. The magnitude of motored friction and its dependence on engine speed are modeled accurately. Earlier figures in this chapter (Figs. 13.30 and 13.34) have compared results of pumping and accessory friction components from this model with measured data.[8]

[1] The fuel pump in a gasoline engine is electrically driven and its power requirements are small; the diesel fuel pump, which must deliver fuel at pressures of some 800 bar, needs to be included.[27]

© McGraw-Hill Education. All rights reserved. Any use is subject to the Terms of Use, Privacy Notice and copyright information.

13.10. OIL CONSUMPTION

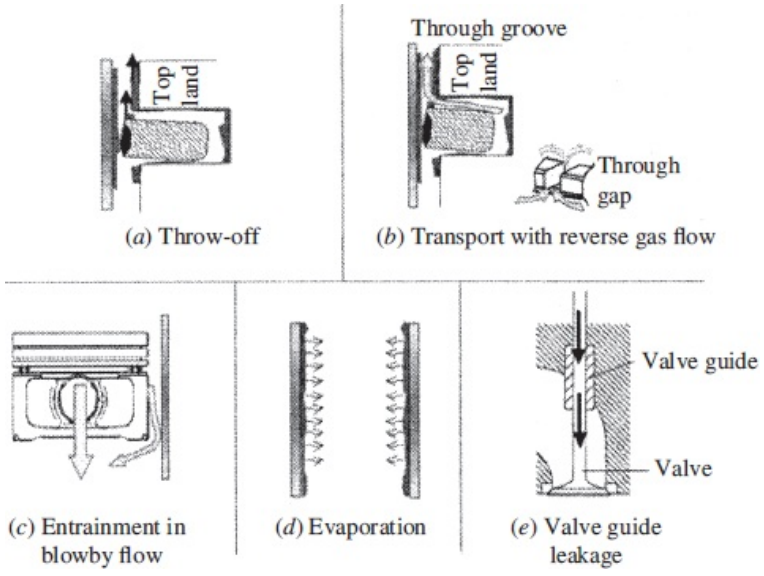
The engine's lubricating system and its functions are summarized in Sec. 13.6.2. Here, we discuss the processes that result in engine oil consumption, a critical combined engine and lubricant problem due to its impacts on operating costs, its contribution to engine emissions, and the role of ash from the lubricant that degrades exhaust catalyst and particulate trap performance (Secs. 11.6.3 and 11.6.4).

13.10.1. Oil Consumption Context

The magnitude of engine oil consumption is typically about 2 mg per second, per liter of engine displaced volume. This oil loss is roughly one-third of 1% of the fuel used in vehicular applications. Oil consumption rates vary substantially with type of engine, engine design, and with engine operating conditions (oil consumption is generally lowest at light load and low speed). Oil is consumed under both steady-state engine operating conditions and during rapid engine load transients when the oil distribution in the piston and ring assembly at the beginning of the transient is markedly different from the steady-state oil distribution at the end of the transient. As Sec. 13.6.3 indicates, the detailed behavior of the piston rings and the piston during the engine's operating cycle is complex. Oil transport processes within this region, which depend on the behavior of the piston rings, also affect the oil consumption mechanisms. Oil consumption is thus only partly understood.

The several sources of oil consumption are shown in Fig. 13.36:[30] each schematic illustrates a different oil transport process into the cylinder that leads to oil being consumed. Liquid oil can be thrown from the piston top land region into the combustion chamber due to the inertia forces generated by the acceleration and deceleration of the piston assembly (Fig. 13.36*a*). The ring-pack gas flows are known to transport oil within the piston and ring region (see Secs. 8.8 and 13.6.3). The gas pressure in the second land region can rise above the cylinder pressure at certain points in the engine's operating cycle (see Fig. 13.20). This causes a reverse gas flow through the top ring gap (Fig. 8.33), which can carry oil, in liquid or mist form, into the combustion chamber (Fig. 13.36*b*). This oil transport process requires oil build up on the second land below the first ring gap and is more likely to occur at lower engine loads.

Figure 13.36 Schematic illustrating the different oil transport and consumption mechanisms: see text.[30]



The in-cylinder gases which "blow by" the piston assembly into the engine's crankcase are also a source of oil consumption.

© McGraw-Hill Education. All rights reserved. Any use is subject to the Terms of Use, Privacy Notice and copyright information.

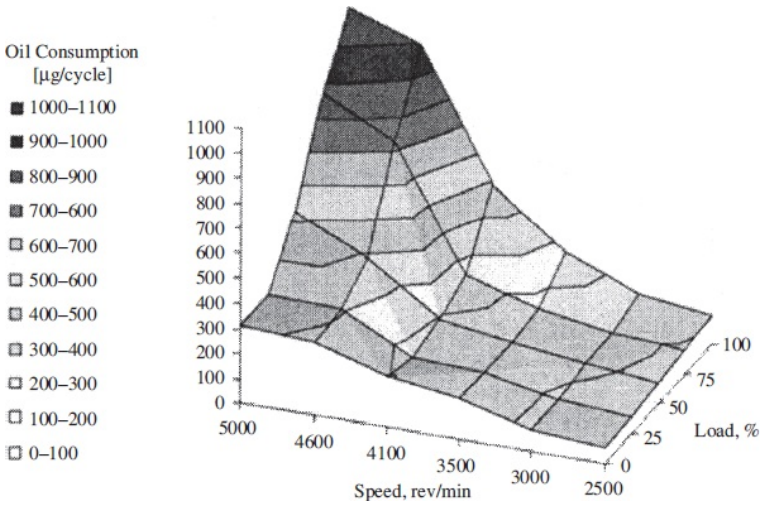
Blowby gases carry some oil back to the crankcase and oil sump. The rotating crank "splashes" oil, and through windage, can generate oil drops and oil mist. In higher-power engines (e.g., diesels), oil jets under the piston provide additional piston cooling. The gases flowing into the crankcase are recycled to the engine's cylinders through a positive crankcase ventilation (PCV) system which incorporates an oil separator at the crankcase exit. Despite the oil separator, the recycled blowby gases contain some oil which then enters the combustion chamber via the intake manifold and burns. In turbocharged engines, turbocharger blowby—leakage of air at high boost levels from the compressor to the turbine—driven past the turbocharger bearings by the higher compressor than turbine pressure, is also an oil consumption path.

Oil evaporation, primarily from the oil film on the cylinder liner, also contributes to oil consumption (Fig. 13.36*d*). The amount of oil evaporated depends on the oil film/liner temperature: higher engine thermal loadings at higher power levels lead to higher liner temperatures and thus greater oil evaporation.

In earlier spark-ignition engine designs, oil transport from the cylinder head through the valve guide into the intake port (Fig. 13.36*e*) contributed to oil consumption during part-load operation when the intake manifold pressure is well below atmospheric. This oil leakage path is largely prevented in modern engines by employing effective valve stem seals. Valve stem leakage contributes little to oil consumption in current engine designs.[30]

The oil consumption behavior in a typical four-cylinder 1.8-liter naturally-aspirated gasoline engine is illustrated by the oil consumption map in Fig. 13.37. The oil consumption data (in μg/cycle) show a clear dependence on engine speed and load increasing as these variables increase. Oil consumption was large at high speed (>4500 rev/min) and load (>75%) at least ten times (in μg/cycle) the oil consumption at low speed and load.[30]

Figure 13.37 Oil consumption map for a 1.8-liter four-cylinder naturally-aspirated gasoline engine, as a function of engine speed and load (%).[30]



13.10.2. Oil Transport into the Cylinder

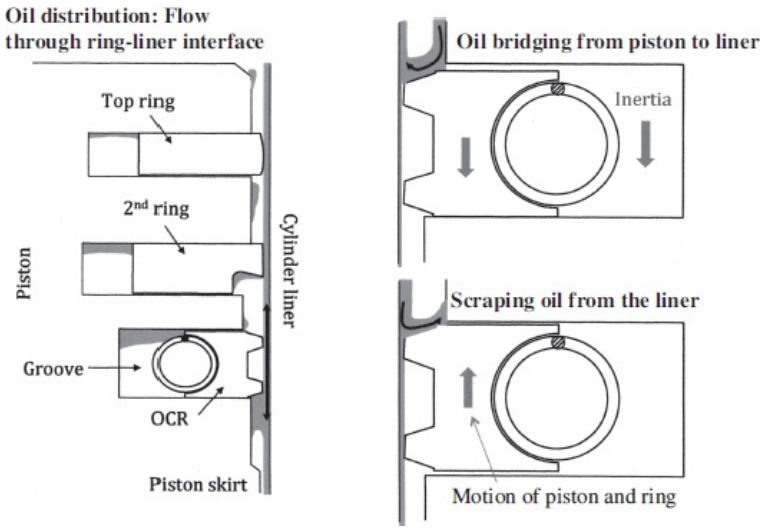
The question addressed here is how oil is transported from the piston skirt region below the oil control ring (where there is plenty of oil) up to the piston top-land region above the top (compression) ring. From there, inertia forces and reverse blowby gas flows could carry oil into the combustion chamber where it would burn.

Prior discussion (Secs. 8.8 and 13.6.3) has explained the behavior of the piston rings in their grooves and the gas flows into and out of these various piston land regions (Fig. 8.33). Here, we focus on the oil flows that occur in this piston ring and gas flow context.[1] Figure 13.38 shows schematically regions of the piston/ring/skirt system where oil could accumulate and from where it could be transported. The liner oil film does the primary ring and skirt lubrication task. Oil may be on the piston lands and within the ring grooves; oil is also "scraped" from the liner to the lands and vice-versa. Oil can flow through the ring

© McGraw-Hill Education. All rights reserved. Any use is subject to the Terms of Use, Privacy Notice and copyright information.

gaps, up or down, directly driven by pressure differences across the ring when oil accumulates below or above the ring gap location; or as oil mist carried by the ring-gap gas flows, up or down. If the ring gaps line up, the gas flows are increased. If they are not lined up, then circumferential oil flow on the piston lands may occur, dragged by the circumferential gas flows from one ring gap to the next. When the rings move up or down in their grooves, or flutter, then oil will be transported around the back of the ring if it has accumulated within the groove or at the groove entry.

Figure 13.38 Schematics showing oil distribution in the piston, piston ring, skirt, cylinder liner, region illustrating the major oil flow paths.[31]



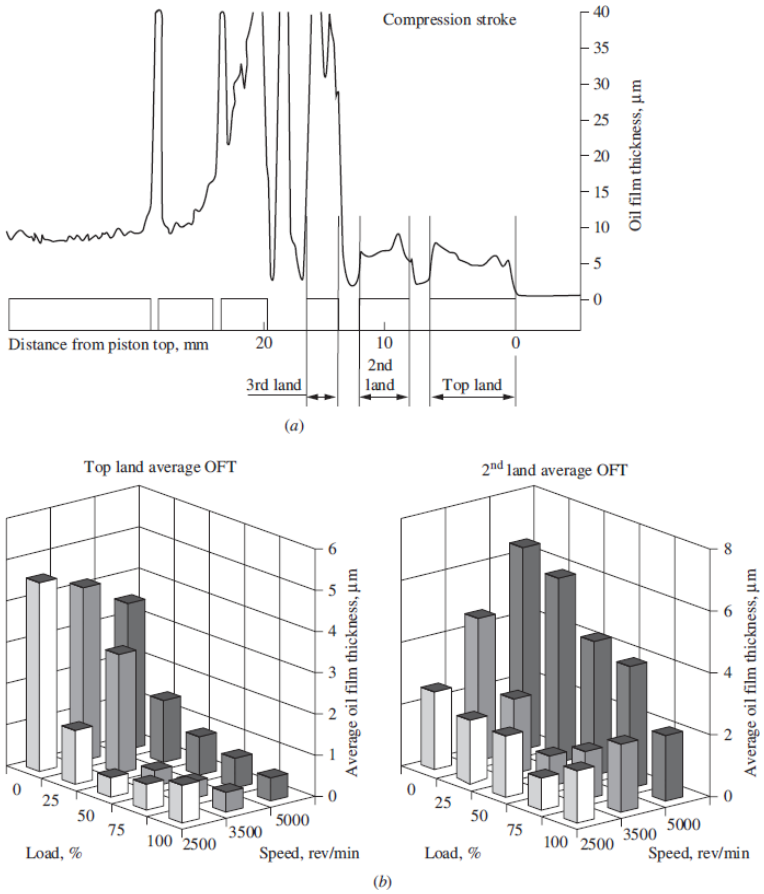
Cylinder bore distortion (Sec. 13.6.3) can increase the oil flow at the ring/liner interface (see Fig. 13.38*a*), depending on the magnitude of bore distortion and the extent to which the rings conform to that distortion. Larger ring-face to liner gaps will result in larger oil flows past the ring.

The several factors driving these oil transport flows in the piston and ring assembly are: pressure differences across the rings, ring-gap gas flows that entrain oil, shear forces between gas flows and oil films on the lands, inertia forces acting on the oil as the piston accelerates and decelerates.

Of greatest importance is the amount of oil on the upper part of the piston: the region above the second ring appears to be critical, and the reverse blowby top-ring gap flow is an important oil consumption contributor. Direct "throw off" of oil into the combustion chamber and evaporation of oil from any additional oil on the liner (see next section) are also major sources. Figure 13.39 shows measured oil film thicknesses on the top and second lands as a function of speed and load, along with an example of the oil film thickness distribution along the piston (Fig. 13.39*a*). The film thickness profile indicates oil film, some 2 μm thick between the ring and liner surfaces, and the substantial accumulation of oil on the lands in between.[32]

© McGraw-Hill Education. All rights reserved. Any use is subject to the Terms of Use, Privacy Notice and copyright information.

Figure 13.39 (a) Example of oil film thickness distribution between the piston and liner, along the piston and ring profile. (b) Average oil film thickness on the piston top land and second land, as a function of engine speed and load. Oil film thicknesses determined in a firing 1.8-liter four-cylinder gasoline engine using a laser-induced fluorescence optical measurement technique illustrated in Fig. 13.20.[30]

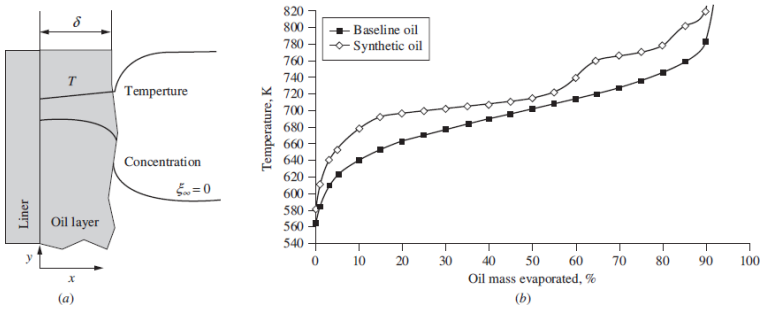


13.10.3. Oil Evaporation

Oil evaporating from the piston-ring-liner system is thought to contribute significantly to total oil consumption. The oil evaporation process is influenced by oil volatility, thermal conditions in the region where evaporation occurs, and gas convection from the oil film surface. The physical situation where evaporation occurs is shown in Fig. 13.40: the oil concentration (ξ) and temperature profiles between the oil layer (on the liner) and adjacent gas are indicated. Distillation curves for a standard 10W-40 oil (see Sec. 13.11) and a synthetic oil are also shown. The more volatile oil components obviously vaporize more easily.[32]

© McGraw-Hill Education. All rights reserved. Any use is subject to the Terms of Use, Privacy Notice and copyright information.

Figure 13.40 (a) Physical situation of oil film on the cylinder liner that leads to oil evaporation. (b) Distillation curves (percent oil evaporated versus temperature) for a standard 10W-40 oil and a synthetic oil.[30]

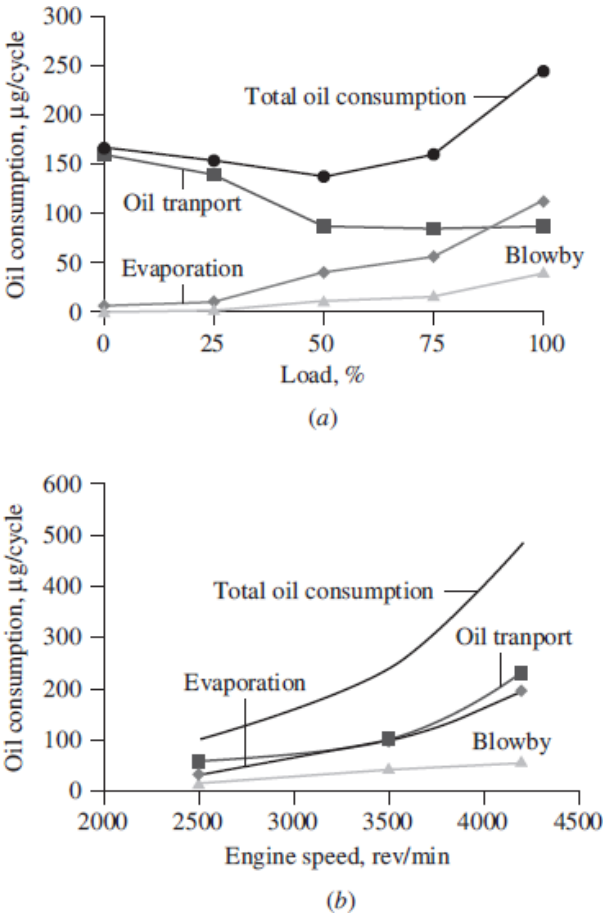


Evaporation primarily occurs from the oil film on the liner, and especially from above the TC location of the oil control ring. This portion of the liner is the hottest region, and it is well supplied with oil. Use of oils of different volatility changes the oil consumption in ways that support this upper-liner evaporative-oil-consumption source. Oil evaporation increases as engine load increases largely because of the increased thermal loading and thus higher liner temperatures. It also increases with increasing engine speed, again due to increasing liner temperatures, and also due to higher mass transfer convection rates.

Figure 13.41 shows the three major oil consumption sources as a function of load and speed in a 1.8-liter four-cylinder NA gasoline engine.[30] As summarized above, oil evaporation (largely from the exposed oil film on the liner) rises significantly with increasing load and speed. The oil transport oil-consumption source dominates at low engine loads and becomes comparable to the evaporative source at about 80% load. Evaporation and transport sources grow together with increasing engine speed. Blowby, as a mechanism for oil consumption, is much smaller: some 10% of the total oil consumption (see Sec. 13.10.4).

© McGraw-Hill Education. All rights reserved. Any use is subject to the Terms of Use, Privacy Notice and copyright information.

Figure 13.41 (a) Effect of engine load on the different oil consumption sources, and total oil consumption, at 3500 rev/min; (b) effect of engine speed on the different oil consumption sources, and total oil consumption, at 100% load for the baseline oil: four-cylinder 1.8-liter gasoline engine.[30]

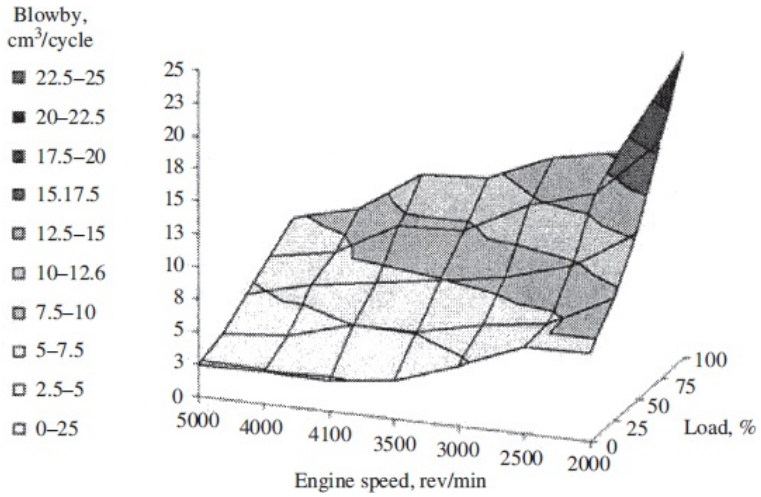


13.10.4. Blowby and Oil Entrainment

The gases that "blow by" the piston and rings enter the crankcase, and are recycled via the engine intake manifold to the combustion chamber. Any hydrocarbons in vapor form, and oil "mist" that passes through the inertial oil separator that is part of the positive crankcase ventilation system, will get burned. Oil thus consumed contributes about 10% to total oil consumption. The blowby flow is primary the flow through the ring gaps. Blowby oil consumption increases with increasing engine load and speed (see Fig. 13.41). Figure 13.42 indicates why: the blowby gas volume (cm^3/cycle)—in a 1.8-liter four-cylinder NA gasoline engine—increases at lower engine speeds with increasing load from about 7 to 23 cm^3/cycle (about 1% of the gas in the cylinder) due to the increasing in-cylinder pressures. Blowby decreases (in cm^3/cycle) with increasing speed at all loads primarily because, as speed rises, there is less time per cycle for blowby gas to flow through the ring gap flow restrictions. Blowby contributes little to oil consumption at the lighter loads where oil transport from below the piston which enters the combustion chamber is the dominant (more than 90%) mechanism. At high loads (and almost independent of speed) blowby is responsible for some 20%, and oil transport and oil evaporation contribute about 40%, each.[30]

© McGraw-Hill Education. All rights reserved. Any use is subject to the Terms of Use, Privacy Notice and copyright information.

Figure 13.42 *Blowby gas flow past the piston ring pack (at standard atmospheric pressure and temperature) into the crankcase: dependency on engine speed and load.*[30]



[1] These oil flows are discussed in an overview sense. The details of these flows are only partly understood.

© McGraw-Hill Education. All rights reserved. Any use is subject to the Terms of Use, Privacy Notice and copyright information.

13.11. LUBRICANTS

Lubricants separate two surfaces in relative motion. By forcing the surfaces apart through the pressure generated in this thin lubricant layer, direct contact between the two solid surfaces is prevented (or a least substantially reduced) thus minimizing wear and reducing friction. Lubricants also act as coolants, friction-surface sealants, and corrosion inhibitors.

The lubricant and the lubricating system perform the following functions:[3]

- Reduce the frictional resistance between moving parts of the engine to a minimum to ensure low friction and high mechanical efficiency.
- Protect the engine against wear in the above engine regions.
- Contribute to cooling the piston and regions of the engine where friction work is dissipated.
- Remove all injurious impurities and particles from lubricated regions.
- Hold gas and oil leakage (especially in the ring region) at an acceptable minimum level.

The base stock for engine lubricants (some 75 to 85% of the oil by volume) consists of a blend of higher molecular weight hydrocarbon compounds primarily selected for their viscosity characteristics. These hydrocarbons in the base stock may be refined from crude oil or, in synthetic lubricants, created through chemical processing. The remainder of the lubricant is the additive package containing a variety of chemical compounds selected to improve the lubricant's performance. Usually, these additive packages include dispersants and detergents, over-base (acid neutralizing) additives, anti-wear and anti-corrosion additives, viscosity improvers, and anti-oxidants.[12]

Note that during spark-ignition engine starting, especially in cold ambient conditions, gasoline fuel can flow past the piston rings and mix with the oil. As the engine and oil warm-up, the gasoline in the oil will vaporize. The presence of significant amounts of gasoline (or other liquid SI engine fuels) in the lubricant degrades many of its important characteristics.

Table 13.2 lists the qualities required of engine oils to perform the main lubrication system functions. These qualities can be summarized under the following headings.[33]

Table 13.2 Functions and qualities required of engine oils

Main functions required	Where and when	Qualities required
Reduce frictional resistance	During cold-starting Between con-rod/crankshaft bearings, and journals Between pistons, rings, and cylinders	Low enough viscosity to provide good pumping and avoid undue cranking resistance Minimum viscosity without risk of metal-to-metal contact under the varying conditions of temperature, speed, and load Sufficiently high viscosity at high temperatures; good lubrication property outside the hydrodynamic condition, especially at top-center Anti-seizure properties, especially during the run-in period

© McGraw-Hill Education. All rights reserved. Any use is subject to the Terms of Use, Privacy Notice and copyright information.

Main functions required	Where and when	Qualities required
Protect against corrosion and wear	During shut-down or when running at low temperature In normal running	Must protect metallic surfaces against corrosive action of fuel decomposition products (water, SO_2, HBr, HC1, etc.) Must resist degradation (resist oxidation, have good thermal stability) Must counteract action of fuel and lubricant decomposition products at high temperatures, especially on non-ferrous metals. By intervention in the friction mechanism must reduce the consequences of unavoidable metal-to-metal contact Must resist deposit formations which would affect lubrication (detergency or dispersive action). Must contribute to the elimination of dust and other contaminants (dispersive action)
Assist sealing	In the ring zone, especially at TC	Must have sufficient viscosity at high temperatures and low volatility Must limit ring and liner wear Must not contribute to formation of deposits in ring grooves and must prevent such formation
Contribute to cooling	Chiefly of pistons, rings, and connecting rod bearings	Must have good thermal stability and oxidation. Must have low volatility Viscosity must not be too high
Facilitate the elimination of undesirable materials	During oil drains to eliminate atmospheric dust, soot from diesel engines, salt, wear debris, organic products from burned fuel and lubricants, and other contaminants which promote deposits or accelerate wear	Must be able to maintain in fine suspension all solid material (dispersivity) whatever the temperature and physical and chemical conditions (water) Must be able to solubilize certain organic compounds, particularly heavy oxidation products
Source: From Schilling.[33]		

13.11.1.1. Oxidation Stability

The temperature of the oil and engine parts it contacts, the presence of oxygen, the nature of the metal surfaces and debris, and the products of the fuel combustion, all influence the oxidation of the hydrocarbon components in lubricating oil. High temperatures are the primary factor, and the top piston ring groove and the crankcase are the critical regions. The temperature of the top ring groove can easily reach 250°C. The lubricating oil when subject to these conditions must not, through oxidation, contribute to deposit formation, even after long periods of running. These deposits would eventually lead to ring sticking which results in excessive blowby. At high temperatures, deposits are related to the oxidized fraction of the oil.

The oil temperature in the crankcase is about 120 to 130°C, though oil can be exposed to higher temperatures. Oil at this temperature should neither form significant acid products capable of attacking the bearing alloys, nor form insoluble products which form deposits. However, to ensure that quality mineral oils stand up well over time to the range of temperatures the oil experiences, anti-oxidant and anti-corrosive additives are used. While anti-oxidants help to reduce deposit formation, detergent/dispersant additives are required to maintain any insoluble materials formed through oxidation in suspension.

13.11.1.2. Detergency/Dispersion

© McGraw-Hill Education. All rights reserved. Any use is subject to the Terms of Use, Privacy Notice and copyright information.

13.11.1.2. Detergency/Dispersion

Deposits in the oil are controlled by its detergency. The amount of deposits formed depends on the fuel used, the quality of combustion, the temperature of the lubricating oil and coolant, and on the effectiveness of gas sealing at the piston rings. The detergency property is given to straight mineral oils by additives; the function of the detergent additive is to reduce the amount of deposits formed and make their removal easier.

At low temperatures, deposits are mainly byproducts of fuel combustion, and the detergency function is to keep them in suspension or solution in the oil. At high temperatures, deposits come from the oxidized fractions of the oil. The detergency function here is both to keep these products in suspension and to inhibit the reactions that lead to the formation of varnishes and lacquers. In addition, in diesel engines, the detergency helps to neutralize the acidic reaction products from the sulfur compounds in the fuel.

13.11.1.3. Wear Reduction

Wear is due to the individual and combined effects of corrosion, adhesion (i.e., metal-to-metal contact), and abrasion.

Corrosive attack by acidic products of combustion is one of the chief causes of cylinder and ring wear. The effect is worst at low cylinder wall temperatures. In diesel engines, any sulfur in the fuel increases the corrosive wear. Corrosive wear is effectively prevented by the use of detergent oils which neutralize the corrosive acids as they form, and by designing the cooling system to control metal temperatures appropriately.

Adhesive wear affects certain parts of the engine. In the upper cylinder, metal-to-metal contact between piston, rings, and cylinder walls takes place each time the engine is started (most significant during cold-starts) because there is insufficient oil in the top portion of the engine. Oils with anti-wear additives and low viscosity at low temperatures provide a partial remedy. Adhesive wear also occurs on components such as cams, tappets, drive gears, rocker arm ends, and valve stems. A commonly used class of anti-wear inhibitors is zinc-dialkyl-dithio-phosphates (ZDDPs).

Abrasion results from the presence of atmospheric dust, and metallic debris from corrosive and adhesive wear, in the lubricating oil. Efficient air filtration is therefore most important (see Ref. 34 for a discussion of air filters). Elimination of abrasive particle impurities from the oil system by filtration and periodic oil change is essential.

13.11.1.4. Viscosity

For low resistance to cranking and ease of starting, and rapid distribution of the oil while the engine is cold, a low oil viscosity at low ambient temperatures is required. When the engine (and oil) is fully warmed up, viscosity in the proper range is important for adequate sealing of the piston, acceptable oil consumption, and low hydrodynamic friction losses. The viscosity of the oil at both low and normal engine temperatures (a spread of some 200 K) is, therefore, important. The viscosity of lubricating oils decreases with increasing temperature. The *pour point*, *viscosity*, and *viscosity index* are used to characterize the behavior of a lubricating oil for these aspects of engine operation.

The *pour point* is determined by cooling a sample of oil in a test jar until, when the jar is rotated from the vertical to the horizontal, no perceptible movement of the oil will occur within 5 seconds; 5°F above this temperature is the pour point.

The viscosity of lubricating oils is determined by measuring the time required for a specified volume of oil to flow through a capillary tube or orifice, contained in a constant temperature water bath. The *kinematic viscosity*, ν ($\nu = \mu/\rho$), is determined by this method. Use of a Saybolt tube with an orifice of specified diameter is the standard U.S. measurement practice. The viscosity is then given by the time t (in seconds) required to flow 60 cm^3 of oil, and is expressed as Saybolt universal seconds, SUS. Approximate conversion to centistokes (1 centistoke = 10^{-6} m^2/s) can be obtained via

© McGraw-Hill Education. All rights reserved. Any use is subject to the Terms of Use, Privacy Notice and copyright information.

$$\nu = at - \frac{b}{t}$$

where for 115 > t > 34 s, a = 0.224, and b = 185; for 215 > t > 115 s, a = 0.223, and b = 155; and for t > 215 s, a = 0.2158 and b = 0.[35]

The viscosity of lubricating oils decreases with increasing temperature. Since engine oils must operate over a range of temperatures, a measure of the rate of decrease is important. The *viscosity index*, an empirical number indicating the effect of temperature changes on viscosity, is used for this purpose;[36] a low viscosity index indicates a relatively large change of viscosity with temperature. To increase the viscosity index, lubricating oils incorporate additives called "viscosity-index improvers." These are high molecular weight compounds (molecular weight ≈ 10^3 to 10^4) whose primary function is to reduce the viscosity variation with temperature.

A discussion of lubricant viscosity, and its dependence on temperature can be found in Sec. 13.9. Equations (13.23) to (13.25) define the relationship between v and lubricant temperature T. Table 13.3 gives the constants for relating the low shear viscosity v_0 values and the scaling ratio (μ_∞/μ_0) to obtain values relevant to lubricants in engine operation.[33]

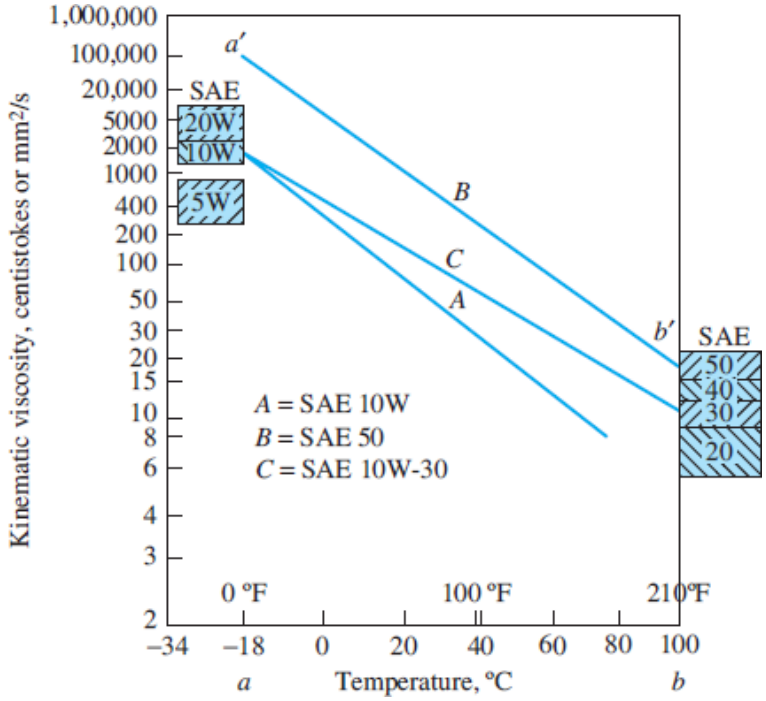
Table 13.3 Lubricant's viscosity data for various engine oil grades

Oil grade	k (cSt)	θ_1 (°C)	θ_2 (°C)	μ_∞/μ_0	Viscosity, v (cSt)	
					At 40°C	At 100°C
0W-40	0.01341	1986.4	189.7	0.67		
5W-20	0.4576	1224	134.1	0.94	49	8.6
5W-30					66	11
5W-40	0.15	1018.74	125.91	0.8		
10W-30	0.1403	869.72	104.4	0.76	75	10.8
10W-40					99	14.4
20W-50	0.0639	1255.46	117.7	0.84	174	19
SAE10	0.0258	1345.42	144.58	1		
SAE30	0.0246	1432.29	132.94	1		
SAE50	0.0384	1349.94	115.16	1		
Sources: Sandoval and Heywood,[8] Yilmaz,[32] Taylor et al.[37]						

The lubricating oil classification used most extensively is the SAE classification.[38] It depends solely on the viscosity of the oil. The seven different classification numbers 5W, 10W, 20W, 20, 30, 40, and 50 correspond to viscosity ranges; increasing numbers correspond to increasing viscosity, as shown in Fig. 13.43. SAE numbers followed by W (abbreviation for winter) refer to oils for use in cold climates, and viscosity is determined at −18°C (0°F). SAE numbers without W are applied to engine oils commonly used under warmer conditions; they are based on viscosity at 99°C (210°F). Multi-grade oils (e.g., 10W-40) satisfy service requirements at low as well as high temperatures in terms of the SAE classification. The first number indicates the viscosity at −18°C; the second number at 99°C. Examples are shown in Fig. 13.29. Multi-grade oils have a higher viscosity index than single-grade oils, which make them more attractive for engine use.

© McGraw-Hill Education. All rights reserved. Any use is subject to the Terms of Use, Privacy Notice and copyright information.

Figure 13.43 *Viscosity versus temperature curves illustrating SAE lubricating oil classification.*[33]



© McGraw-Hill Education. All rights reserved. Any use is subject to the Terms of Use, Privacy Notice and copyright information.

13.12. PROBLEMS

13.1

a. Show how friction mean effective pressure for a four-stroke cycle engine can be obtained from the brake power P_b, engine speed N, displaced volume V_d, and $\int pdV$ over the compression and expansion strokes ($W_{c,ig}$).

b. How is pumping mean effective pressure related to $\int pdV$ over the compression and expansion strokes and $\int pdV$ over the full four-stroke cycle?

c. Find the brake power, total friction power, total friction imep, and pumping imep for a four-stroke cycle SI engine operating at 1800 rev/min with a measured brake torque of 32 N · m, a gross imep of 933 kPa, and a net imep of 922 kPa. V_d = 0.496 liter.

13.2. Three categories of friction are described in Sec. 13.3: boundary friction, hydrodynamic (or fully-lubricated) friction, and turbulent dissipation. By means of Eq. (13.6), estimate the relative proportion of total friction work per cycle in each category for a four-cylinder automobile spark-ignition engine operating at 3000 rev/min.

13.3. For four-stroke cycle naturally-aspirated multi-cylinder spark-ignition and diesel automobile engines at full load and one-third full load, at mid speed (2000 rev/min), give approximate estimates of the percentages of total friction mep in these three categories: pumping mep, rubbing friction mep, and accessory friction mep. State explicitly how you develop these estimates and what you include as accessories.

13.4. All of the friction measurement procedures, except the difference between brake and gross indicated power or mep measured directly, assume that motored engine friction and firing engine friction are closely comparable. This is not an accurate assumption for the pumping component. Summarize the differences between the gas exchange processes under motoring and firing conditions for a spark-ignition engine at a fixed part-load throttle setting that will result in the pumping work being significantly different under these two conditions.

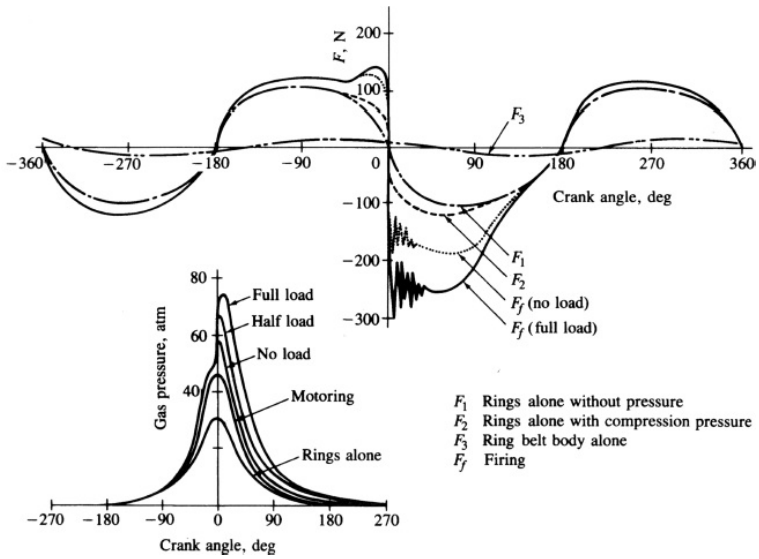
13.5. On separate accurately proportioned sketches of the piston, cylinder, connecting rod, and crank mechanism (similar to Fig. 2.1), during the intake stroke (at 120° ATC), compression stroke (at 60° BTC), expansion stroke (at 60° ATC), and exhaust stroke (at 120° BTC), draw an arrow for each of the forces acting on the piston (pressure forces, force from connecting rod, friction force, inertia force). Mark clearly the *positive* direction of each force. Express each force in terms of cylinder pressure p_c, crankcase pressure p_{cc}, friction force F_f, piston area A_p, effective piston (and part of connecting rod) mass m_p, piston acceleration a, connecting rod force F_{cr}.

13.6

a. For the DI diesel engine friction force data shown in Fig. P13.6, estimate the maximum pressure force on the piston (under full-load conditions) and the approximate magnitude of the inertia force [mass of piston plus part of the connecting rod $(7\ \text{kg}) \times \overline{S}_p \times (N/4)$]. Compare these forces with the piston friction force at time of peak pressure.

© McGraw-Hill Education. All rights reserved. Any use is subject to the Terms of Use, Privacy Notice and copyright information.

Figure P13.6 Measured frictional force on cylinder liner of 137 mm bore and 135 mm stroke single-cylinder DI diesel engine. 1200 rev/min, coolant temperature 80°C, cylinder liner inside temperature 90°C.[15]



b. The figure shows the variation in friction force acting on the piston of a DI diesel engine under no-load and full-load firing conditions. Carefully sketch the shape (indicating direction and rough magnitude) of the cylinder pressure force on the piston, the piston velocity, and the piston acceleration, as functions of crank angle on the same graph as these friction forces. Use these graphs to explain the variation of piston friction force throughout the four strokes of the cycle.

13.7. Show by dimensional analysis of the variables that govern the friction in a journal bearing (friction force F_f, oil viscosity μ, bearing diameter D_b, length L_b, mean clearance $\bar{h}$, shaft rotational speed N) that

$$\frac{F_f}{\mu D_b^2 N} = f\left(\frac{L_b}{D_b}, \frac{\bar{h}}{D_b}\right)$$

What additional physical assumptions are then required to obtain an equation of the form of Eq. (13.11)?

13.8. Explain whether each of the following components of engine friction would be expected to depend on (1) crankshaft rotational speed N, (2) mean piston speed S_p, (3) or both of these variables. Crankshaft journal bearings, connecting rod bearings, valve train, piston rings, piston skirt, water pump, fan, valve flow loss (resistance to flow through the inlet and exhaust valves).

© McGraw-Hill Education. All rights reserved. Any use is subject to the Terms of Use, Privacy Notice and copyright information.

13.13. REFERENCES

1. Ball, W. F., Jackson, N. S., Pilley, A. D., and Porter, B. C.: "The Friction of a 1.6 Litre Automotive Engine-Gasoline and Diesel," SAE paper 860418, 1986.
2. Rosenberg, R. C.: "General Friction Considerations for Engine Design," SAE paper 821576, 1982.
3. Schilling, A.: *Automobile Engine Lubrication*, Scientific Publications Ltd., Broseley, England, 1972.
4. Lancaster, D. R., Krieger, R. B., and Lienesch, J. H.: "Measurement and Analysis of Engine Pressure Data," SAE paper 750026, *SAE Trans.*, vol. 84, 1975.
5. Davis, R. S., and Patterson, G. J.: "Cylinder Pressure Data Quality Checks and Procedures to Maximize Data Accuracy," SAE paper 2006-01-1346, 2006.
6. Millington, B. W., and Hartles, E. R.: "Frictional Losses in Diesel Engines," SAE paper 680590,*SAE Trans.*, vol. 77, 1968.
7. Barnes-Moss, H. W.: "A Designer's Viewpoint," in *Passenger Car Engines, Conference Proceedings*, pp. 133–147, Institution of Mechanical Engineers, London, 1975.
8. Sandoval, D., and Heywood, J. B.: "An Improved Friction Model for Spark-Ignition Engines," SAE paper 2003-01-0725,*SAE Trans.*, vol. 112, *Journal of Engines*, 2003.
9. Fahl, E., and Haas, A.: "Potential for Friction Reduction on Passenger Car Engines," paper 940922, SIA Congress, Paris, Nov. 1994.
10. Regueiro, A.: "Dailmer-Chrylser's New 1.6 L, Multi-Valve 4-Cylinder Engine Series," SAE paper 2001-01-0330, 2001.
11. Stanton, D. W.: "Systematic Development of Highly Efficient and Clean Engines to Meet Future Commercial Vehicle Greenhouse Gas Regulations," SAE paper 2013-01-2421, L. Ray Buckendale Lecture, *SAE Int. J. Engines*, vol. 6, no. 3, pp. 1395–1480, 2013.
12. Hoag, K. L.: *Vehicular Engine Design*, SAE International, Warrendale, PA, Springer-Verlag, Vienna, 2006.
13. Bosch, R.: *Automotive Handbook*, 8th edition, Robert Bosch GmbH, SAE, 2011.
14. Shayler, P. J., Christian, S. J., and Ma, T.: "A Model for the Investigation of Temperature, Heat Flow and Friction Characteristics During Engine Warm-up," SAE paper 931153, *SAE Trans.*, vol. 102, 1993.
15. Furuhama, S., Takiguchi, M., and Tomizawa, K.: "Effect of Piston and Piston Ring Designs on the Piston Friction Forces in Diesel Engines," SAE paper 810977, *SAE Trans.*, vol. 90, 1981.
16. Yilmaz, E., Tian, T., Wong, V. W., and Heywood, J. B.: "An Experimental and Theoretical Study of the Contribution of Oil Evaporation to Oil Consumption," SAE paper 2002-01-2684, 2002.
17. Zottin, W., Bacchin, P. V., and Gracia, A. F.: "Numerical Simulation Study of Carbon Build-Up and Oil Consumption in a Heavy Duty Diesel Engine," SAE paper 2012, 01-1326, 2012.
18. Min, B. S., Kim, J.-S., Oh, D.-Y., Choi, J.-K., and Jin, J.-H.: "Dynamic Characteristics of Oil Consumption-Relationship Between the Instantaneous Oil Consumption and the Location of Piston Ring Gap," SAE paper 982442, 1998.
19. Hanke, W., Fahr, M., Rehl, A., Voigt, M., and Ando, H.: "Friction Reduction in Power Cylinder Systems for Downsize Gasoline Engines with Modern Surface Technologies of Aluminum Crankcases," SAE paper 2012-01-1332, 2012.
20. Wakakayhashi, R., Takiguchi, M., Shimada, T., Mizuno, Y., and Yamanchi, T.: "The Effects of Crank Ratio and Crankshaft Offset on Piston Friction Losses," SAE paper 2003-01-0983, *SAE Trans.*, vol. 112, 2003.

© McGraw-Hill Education. All rights reserved. Any use is subject to the Terms of Use, Privacy Notice and copyright information.

21. Amann, C.: "Engineering the Spark-Ignition Engine: The Piston-Ring-Cylinder Wall Interface," SAE paper 885056, 1988.
22. Yamada, T., Kobayashi, H., Kusama, K., Sagawa, J., Takiguchi, M., and Shikawa, T.: "Development of a Technique to Predict Oil Consumption with Consideration for Cylinder Deformation-Prediction of Ring Oil Film Thickness and Amount of Oil Passing Across Running Surface under Cylinder Deformation," SAE paper 2003-01-0982, *SAE Trans.*, vol. 112, 2003.
23. Fukuoka, W., Hara, X., Mori, Y., and Ohtsubo, Z.: "Friction Loss Reduction by New Lighter Valve Train System,"*JSAE Review*, vol. 16, pp. 107–111, 1997.
24. Shelby, M. H., Stein, R. A., and Warren, C. C.: "A New Analysis Method for Accurate Accounting of SI Engine Pumping and Indicated Work," SAE paper 2004-01-1262, 2004.
25. Asmus, T. W.: "Valve Events and Engine Operation," SAE paper 820749,*SAE Trans.*, vol. 91, 1982.
26. Leone, T. G., and Pozar, M.: "Fuel Economy Benefit of Cylinder Deactivation-Sensitivity to Vehicle Application and Operating Constraints," SAE paper 2001-01-3591, 2001.
27. Taraza, D., Henein, N. A., Ceausu, R., and Bryzik, W.: "Engine Friction Model for Transient Operation of Turbocharged, Common Rail Diesel Engines," SAE paper 2007-01-1460, 2007.
28. Patton, K. J., Nitschke, R. G., and Heywood, J. B.: "Development and Evaluation of a Performance and Efficiency Model for Spark-Ignition Engines," SAE paper 890836, *SAE Trans.*, vol. 98, pp. 1441–1461, 1989.
29. Williams, J. A.: *Engineering Tribology*, Oxford University Press, New York, 1994.
30. Yilmaz, E., Tian, T., Wong, V. W., and Heywood, J. B.: "The Contribution of Different Oil Consumption Sources to Total Oil Consumption in a Spark Ignition Engine," SAE paper 2004-01-2909, 2004.
31. Baelden, C.: "A Multi-Scale Model for Piston Ring Dynamics, Lubrication and Oil Transport in Internal Combustion Engines," Ph.D. Thesis, Department of Mechanical Engineering, MIT, Cambridge, MA, 2014.
32. Yilmaz, E.: "Sources and Characteristics of Oil Consumption in a Spark-Ignition Engine, Ph.D. Thesis, Department of Mechanical Engineering, MIT, Cambridge, MA, 2003.
33. Schilling, A.: *Motor Oils and Engine Lubrication*, Scientific Publications Ltd., Broseley, England, 1968.
34. Annand, W. J., and Roe, G. E.: *Gas Flow in the Internal Combustion Engine*, Haessner Publishing, Newfoundland, NJ, 1974.
35. ASTM Standards, Part 17, Petroleum Products, American Society for Testing and Materials.
36. ASTM D 2270-98, Standard Practice for Calculating Viscosity Index from Kinematic Viscosity at 40 and 100°C, American Society for Testing and materials, 1998.
37. Taylor, R. I., Brown, M. A., Thompson, D. M., and Bell, J. C.: "The Influence of Lubricant Rheology on Friction in the Piston Ring Pack," SAE paper 94981, 1994.
38. SAE J300a, Crankcase Oil Viscosity Specification, SAE International, Warrendale, PA.

© McGraw-Hill Education. All rights reserved. Any use is subject to the Terms of Use, Privacy Notice and copyright information.

14.0. CHAPTER PRELIMINARIES

PURPOSE AND CLASSIFICATION OF MODELS

GOVERNING EQUATIONS FOR AN OPEN THERMODYNAMIC SYSTEM

INTAKE AND EXHAUST FLOW MODELS

THERMODYNAMIC-BASED IN-CYLINDER MODELS

FLUID-MECHANIC-BASED MULTI-DIMENSIONAL MODELS

REFERENCES

© McGraw-Hill Education. All rights reserved. Any use is subject to the Terms of Use, Privacy Notice and copyright information.

14.1. PURPOSE AND CLASSIFICATION OF MODELS

In engineering, modeling a process means developing and using the appropriate combination of assumptions and equations that permit critical features of the process to be analyzed. The modeling of engine processes continues to evolve as our basic understanding of the physics and chemistry of the phenomena of interest steadily expands and as the capability of computers to solve complex equations continues to increase. Modeling activities can make major contributions to engine engineering at different levels of generality or detail by:

- Developing a more complete understanding of the process under study from the discipline involved in formulating the model;
- Identifying key controlling variables that provide guidelines for better structured and therefore less costly experimental development efforts;
- Predicting engine behavior over a wide range of design and operating variables to screen concepts prior to major hardware programs, to determine trends and tradeoffs, and, if the model is sufficiently accurate, to optimize design and control;
- Providing a rational basis for design innovation.

Each of these contributions is valuable. Whether a model is ready to pass from one stage to the next depends on the accuracy with which it represents the actual process, the extent to which it has been tested and validated, and the time and effort required to use the model for extensive sets of calculations and interpret the results.

This chapter reviews the types of models and their primary components that are used to describe engine performance, fuel consumption, and emissions characteristics. These models describe the thermodynamic, fluid-flow, heat-transfer, combustion, and pollutant-formation phenomena that govern these aspects of engine performance. Many of the building blocks for these models have been described in previous chapters. The purpose here is to show how fluid dynamics, heat-transfer, thermodynamics, and kinetics fundamentals can be combined at various levels of sophistication and complexity to predict, with varying degrees of completeness, internal combustion engine combustion and emissions processes, and engine operating characteristics.

For the processes that govern engine performance and emissions, two basic types of models have been developed. These can be categorized as *thermodynamic* or *fluid dynamic* in nature, depending on whether the equations which give the model its predominant structure are based on energy conservation or on a full analysis of the fluid motion. Other labels given to thermodynamic energy-conservation-based models are: zero-dimensional (since in the absence of any flow modeling, geometric features of the fluid motion cannot be predicted), phenomenological (since additional detail beyond the energy conservation equations is added for each phenomenon in turn), and quasi-dimensional (where specific geometric features, e.g., the spark-ignition engine flame or the diesel fuel spray shapes, are added to the basic thermodynamic approach). Fluid-dynamic-based models (referred to as computational fluid dynamics, CFD, models) are often called multi-dimensional, due to their inherent ability to provide detailed geometric information on the flow behavior, based on solution of the governing flow equations.

Some general observations about models of engine processes provide a context for the details that follow. The physical and chemical processes involved are extremely complex. While much is known about these processes, they are not fully understood at a fundamental level. At present, it is not possible to construct models that predict engine operation from the basic governing equations alone. Thus the objectives of any modeling effort should be clearly defined, and the structure and detailed content of the model should be appropriate to these objectives. It is not yet feasible to construct models that attempt to describe *all* important aspects of engine operation: more limited objectives are usually appropriate.

Due to this complexity of engine processes and our inadequate understanding at a fundamental level, most engine models are incomplete. Empirical relations and *ad hoc* approximations are often needed to bridge gaps in our understanding of critical

© McGraw-Hill Education. All rights reserved. Any use is subject to the Terms of Use, Privacy Notice and copyright information.

phenomena. Since models will continue to develop greater completeness and generality, the emphasis in this chapter is on the basic relationships used in engine process models rather than the current status of these models.

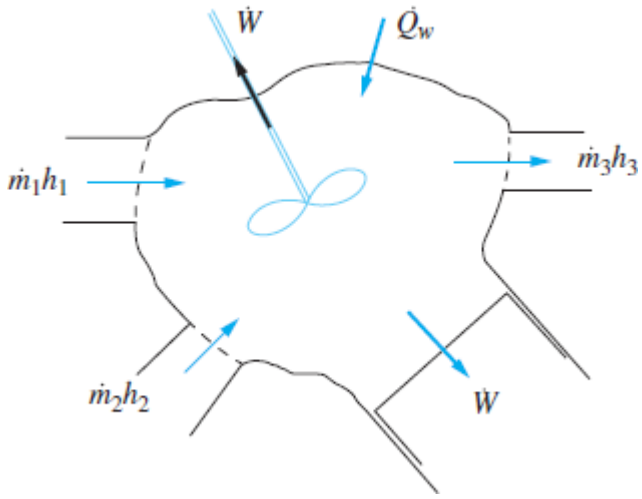
Finally, an important issue in any overall engine model is balance in complexity and detail amongst the process submodels. A model is no more accurate than its weakest link. Thus it makes sense to describe the key phenomena involved at comparable levels of sophistication.

© McGraw-Hill Education. All rights reserved. Any use is subject to the Terms of Use, Privacy Notice and copyright information.

14.2. GOVERNING EQUATIONS FOR AN OPEN THERMODYNAMIC SYSTEM

It is often required to model a region of the engine as an open thermodynamic system. Examples are the cylinder volume and the intake and exhaust manifolds (or portions of these volumes). Such an approach is appropriate when the gas inside the system boundary can be assumed uniform in composition and state at each point in time, and when that state and composition vary with time due to heat transfer, work transfer and mass flow across the boundary, and due to boundary displacement. Such an open system is illustrated in Fig. 14.1. The important equations are mass and energy conservation. These equations for an open system, with time or crank angle as the independent variable, are the building blocks for thermodynamic-based engine models.

Figure 14.1 Schematic of an open thermodynamic system.



14.2.1. Conservation of Mass

The rate of change of the total mass m of an open system is equal to the sum of the mass flows into and out of the system, $\dot{m}_j$:

$$\dot{m} = \sum_j \dot{m}_j$$

(14.1)

Mass flows into the system are taken as positive, mass flows out as negative. For conservation of the fuel chemical elements, it is convenient to use the fuel fraction f, which is defined as m_f/m, where m_f denotes the mass of fuel (or fuel elements in the combustion products) in the open system:

$$\dot{m}_f = \frac{d}{dt}(mf) = \sum_j \dot{m}_{f,j} = \sum_j \dot{m}_j f_j$$

© McGraw-Hill Education. All rights reserved. Any use is subject to the Terms of Use, Privacy Notice and copyright information.

(14.2)

Differentiation of Eq. (14.2) leads to an equation for the rate of change of fuel fraction:

$$\dot{f} = \sum_j \left(\frac{\dot{m}_j}{m}\right)(f_j - f)$$

(14.3)

The fuel/air equivalence ratio ϕ is related to f via $\phi = f/[(F/A)_s(1-f)]$. Hence the rate of change of equivalence ratio of the material in the open system is

$$\dot{\phi} = \frac{1}{(F/A)_s}\frac{\dot{f}}{(1-f)^2}$$

(14.4)

14.2.2. Conservation of Energy

The first law of thermodynamics for the open system in Fig. 14.1 can be written:

$$\dot{E} = \dot{Q}_w - \dot{W} + \sum_j \dot{m}_j h_j$$

(14.5)

$\dot{Q}_w$ is the total heat-transfer rate into the system, across the system boundary, and equals the sum of the heat-transfer rates across each part of the boundary, $\sum_i \dot{Q}_{w,i}$.
$\dot{W}$ is the work-transfer rate out of the system across the boundary: where the piston is displaced, the work-transfer rate equals $p\dot{V}$. Because all energies and enthalpies are expressed relative to the same datum (see Sec. 4.5.3), it is not necessary to explicitly identify the heat released by combustion in Eq. (14.5): this is already accounted for in the energy and enthalpy terms.

The goal here is to define the rate of change of state of the open system in terms of $\dot{T}$ and $\dot{p}$. Two approaches are commonly used, depending on whether the thermodynamic property routines provide values for internal energy u or enthalpy h. Thus $\dot{E}$ in Eq. (14.5) can be expressed as

$$\dot{E} = \frac{d}{dt}(mu) \quad \text{or} \quad \dot{E} = \frac{d}{dt}(mh) - \frac{d}{dt}(pV)$$

(14.6*a*,*b*)

© McGraw-Hill Education. All rights reserved. Any use is subject to the Terms of Use, Privacy Notice and copyright information.

It is assumed that the system can be characterized by *T*, *p*, and *ϕ*; thus

$$u = u(T,p,\phi) \quad h = h(T,p,\phi) \quad \rho = \rho(T,p,\phi)$$

(14.7)

and the rate of change of *u*, *h,* and *ρ* can be written in the form

$$\dot{\alpha} = \left(\frac{\partial \alpha}{\partial T}\right)\dot{T} + \left(\frac{\partial \alpha}{\partial p}\right)\dot{p} + \left(\frac{\partial \alpha}{\partial \phi}\right)\dot{\phi}$$

(14.8)

where *α* is *u*, *h*, or *ρ*. Using the ideal gas law in its two forms, *p* = *ρRT* and *pV* = *mRT*, and Eq. (14.8) for $\dot{\alpha}$, an equation for $\dot{p}$ can be derived:

$$\dot{p} = \frac{\rho}{\partial\rho/\partial p}\left(-\frac{\dot{V}}{V} - \frac{1}{\rho}\frac{\partial \rho}{\partial T}\dot{T} - \frac{1}{\rho}\frac{\partial \rho}{\partial \phi}\dot{\phi} + \frac{\dot{m}}{m}\right)$$

(14.9)

Returning now to the energy conservation equation, Eq. (14.5), expressing $\dot{E}$ in terms of $\dot{u}$ or $\dot{h}$, and $\dot{u}$ or $\dot{h}$ in terms of partial derivatives with respect to *T*, *p*, and *ϕ*, and substituting for $\dot{p}$ with Eq. (14.9), one can obtain equations for $\dot{T}$:

$$\dot{T} = \left[B - \frac{p}{D}\frac{\partial u}{\partial p}\left(\frac{\dot{m}}{m} - \frac{\dot{V}}{V} + \frac{\partial R}{\partial \phi}\frac{\dot{\phi}}{R}\right) - \frac{\partial u}{\partial \phi}\dot{\phi}\right] \Big/ \left(\frac{\partial u}{\partial T} + \frac{C}{D}\frac{p}{T}\right)$$

(14.10)

where

$$B = -RT\frac{\dot{V}}{V} + \frac{1}{m}\left(\dot{Q}_w + \sum_j \dot{m}_j h_j - \dot{m}u\right)$$

$$C = 1 + \frac{T}{R}\frac{\partial R}{\partial T}, \text{ and } D = 1 - \frac{p}{R}\frac{\partial R}{\partial p}$$

© McGraw-Hill Education. All rights reserved. Any use is subject to the Terms of Use, Privacy Notice and copyright information.

(see Ref. 1, for example). From Ref. 2,

$$\dot{T} = \frac{B'}{A'}\left[\frac{\dot{m}}{m}\left(1 - \frac{h}{B'}\right) - \frac{\dot{V}}{V} - \frac{C'}{B'}\dot{\phi} + \frac{1}{B'm}\left(\sum_j \dot{m}_j h_j - \dot{Q}_w\right)\right]$$

(14.11)

where

$$A' = \frac{\partial h}{\partial T} + \frac{\partial \rho / \partial T}{\partial \rho / \partial p}\left(\frac{1}{\rho} - \frac{\partial h}{\partial p}\right),$$
$$B' = \frac{1 - \rho\,(\partial h / \partial p)}{\partial \rho / \partial p}, \text{ and } C' = \frac{\partial h}{\partial \phi} + \frac{\partial \rho / \partial \phi}{\partial \rho / \partial p}\left(\frac{1}{\rho} - \frac{\partial h}{\partial p}\right)$$

Equations (14.1), (14.3), (14.4), (14.9), and (14.10) or (14.11) can now be used to obtain the state (defined by p and T) of the gases within the cylinder as a function of time.
$\dot{V}$ is obtained from Eq. (2.6), and the thermodynamic properties and their derivatives from the models described in Chap. 4.

Often, for specific applications, the above equations can be simplified substantially. For the intake and exhaust systems (or sections of these systems such as the manifold or plenum, etc.),
$\dot{V}$ is zero and effects of dissociation (the terms $\partial u/\partial p$, $\partial h/\partial p$, and $\partial R/\partial p$) can usually be neglected. For the cylinder during compression, dissociation can usually be neglected, also. Application of these equations during combustion must be related to the combustion model used. For the single-zone model often used in diesel engine simulations (see Sec. 10.4), the whole of the combustion chamber is treated as one system. For the two-zone model used for spark-ignition engine simulations, the unburned mixture zone and the burned mixture zone are each treated as separate open systems, with volumes V_u and V_b, respectively, where $V_u + V_b = V$. If a thermal boundary-layer region is included (see Sec. 12.6.5), an additional open system must be defined.

This open-system energy-balance approach is embedded in engine "cycle-simulation" codes such as GT-Power[3] and WAVE.[4]

© McGraw-Hill Education. All rights reserved. Any use is subject to the Terms of Use, Privacy Notice and copyright information.

14.3. INTAKE AND EXHAUST FLOW MODELS

14.3.1. Background

The behavior of the intake and exhaust systems is important because these systems govern the air flow into the engine's cylinders, and the outflow of burned gases. Inducting the maximum airflow at full load at any given speed and retaining that mass within the engine's cylinders is a primary design goal. The higher the airflow, the larger the amount of fuel that can be burned and the greater the power produced. The exhaust and intake behavior control the amount of hot residual burned gas left inside the cylinder. The important airflow parameters are volumetric efficiency (for four-stroke cycle engines) or scavenging and trapping efficiencies (for two-stroke cycle engines), along with equal air flows to each engine cylinder (see Secs. 6.2, 6.6, and 7.6.2).

The objectives for any manifold model have an important bearing on its complexity and structure. If the goal is to provide the input or boundary conditions to a detailed model of in-cylinder processes, then sophisticated intake and exhaust system models are not necessarily required. If the manifold flows are the primary focus, then models that adequately describe the unsteady gas-flow phenomena which occur are normally needed. Then simple models for the in-cylinder phenomena often suffice to connect the intake and exhaust processes. The valves and ports, which together provide the major restriction to the intake and exhaust flow, largely decouple the manifolds from the cylinders.

Three types of models for calculating details of intake and exhaust flows have been developed and used:

1. Quasi-steady models for flows through the restrictions which the valve and port (and other components) provide
2. Filling and emptying models which account for the finite volume of critical manifold components
3. Gas dynamic models which describe the spatial variations in flow and pressure throughout the manifolds

Each of these types of models can be useful for analyzing engine behavior. The appropriate choice depends on objectives, and the time and effort available. Each will now be reviewed.

14.3.2. Quasi-Steady Flow Models

Here the manifolds are considered as a series of interconnected components, which each constitute a significant flow restriction: for example, air cleaner, throttle, port, and valve for the intake system. The flow restriction each of these components represents is defined by their geometry and discharge coefficient, usually determined empirically under steady-state conditions. The gas flow rate through each component is computed using steady one-dimensional flow equations [see App. C, Eqs. (C.8) and (C.9)]: the actual flow is assumed to be quasi steady. These components are connected by the gas flow passing through them and the pressure ratios across them: mass accumulation between components is neglected.

In quasi-steady models, the assumption is made that any time-varying aspects of the processes involved are slow enough (have long-enough time constants) that the equilibrating process (with flows, usually pressure waves) is fast enough to maintain close to a quasi-equilibrium situation. Such models are often used to calculate the flows into and out of the cylinder through the inlet and exhaust valves (see Secs. 6.3 and 6.5 and Fig. 6.20). If the pressure variation with time upstream of the valve is known or is small, as usually occurs with large plenums and short manifold pipe lengths, such methods are accurate enough to be useful. This approach has been used extensively with engine cycle simulations, which predict engine performance characteristics from a thermodynamics-based analysis, to calculate the mass flow rates into and out of the cylinder (see Sec. 14.4). However, such methods are not able to accurately predict the variation of volumetric efficiency with

© McGraw-Hill Education. All rights reserved. Any use is subject to the Terms of Use, Privacy Notice and copyright information.

engine speed because some of the phenomena which govern this variation are omitted from this modeling approach (see Sec. 6.2 and Fig. 6.12).

14.3.3. Filling and Emptying Methods

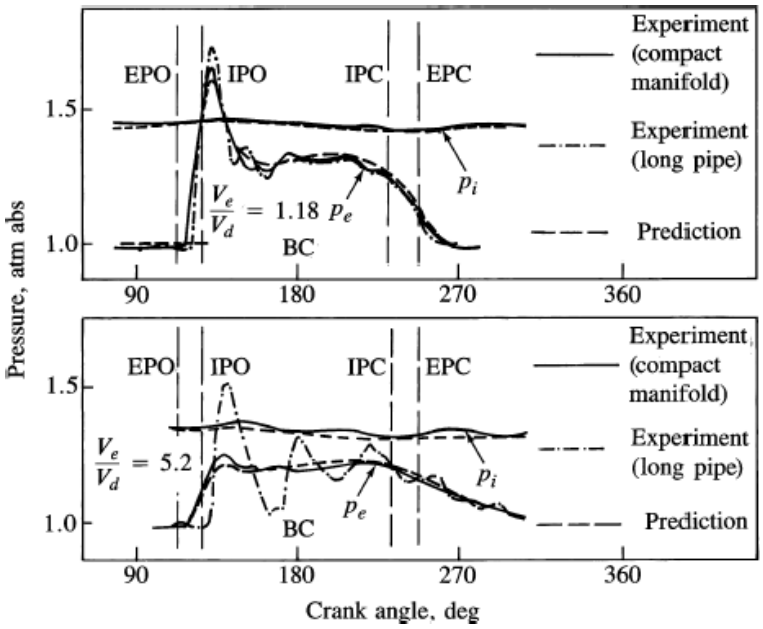
In "filling and emptying" models, the manifolds (or sections of manifolds) are represented by finite volumes where the mass of gas can increase or decrease with time. Such models can range from treating the whole intake or exhaust system as a single volume to dividing these systems into many sections, with flow restrictions such as the air cleaner, throttle valve, or inlet valve at the beginning, in between volumes, or at the end. Each volume is then treated as a control volume (an open system of fixed volume) which contains gas at a uniform state. The mass and energy conservation equations developed in Sec. 14.2 [Eqs. (14.1), (14.3), (14.9), and (14.10) or (14.11)], coupled with information on the mass flow rates into and out of each volume [e.g., determined by the equations for flow through a restriction, Eqs. (C.8) and (C.9)], are used to define the gas state in each control volume. For intake and exhaust flows, these equations can be simplified since the volumes are fixed $(\dot{V} = 0)$ and gas composition can be assumed frozen ($\partial u/\partial p$, $\partial h/\partial p$, and $\partial R/\partial p$ are then zero). Unless backflow occurs or recycled exhaust is used for emission control, changes in fuel fraction are not significant, and for intake systems it may be acceptable to omit heat transfer to the walls $\left(\dot{Q}_w\right)$. Such methods characterize the contents of the manifold (or a region thereof) with a single gas temperature, pressure, and composition. These vary periodically with time as each cylinder in turn draws on the intake system and discharges to the exhaust system. Also, under transient conditions when engine load and/or speed change with time, manifold conditions will vary until the new engine steady-state conditions are established. Watson and Janota[5] discuss the application of filling and emptying models to manifolds in more detail. Such models can characterize these time-varying phenomena, spatially averaged over each manifold region corresponding to each volume analyzed: however, they cannot describe the spatial variation of pressure (and other gas properties) due to unsteady gas dynamics in the manifolds.

An application of a filling and emptying model to the intake manifold of a spark-ignition engine was described inSec. 7.6.2. The manifold was analyzed as a single control volume with the throttle plate controlling mass flow into the manifold and the engine cylinders controlling mass flow out. An equation for the rate of change of manifold pressure [Eq. (7.9)] was derived and used to explain how the air flow past the throttle varied as the throttle open angle was increased, as would occur following the start of a vehicle acceleration at part-throttle conditions (see Fig. 7.24).

A second example will illustrate the conditions under which filling and emptying models give sufficiently accurate predictions to be useful. It concerns a single-cylinder two-stroke cycle loop-scavenged direct-injection diesel engine. The engine was modeled as three open systems (the intake system, the cylinder, and the exhaust system) connected by flow restrictions. Various exhaust manifold volumes and shapes were examined, using nozzles at the manifold exit to simulate the exhaust-driven turbine. The in-cylinder models were calibrated to match the measured engine performance. Figure 14.2 shows the predicted and measured pressure variation at the exhaust system exit for two exhaust system volumes (V_e). With the compact manifold, the measured and predicted pressures were in good agreement. With the larger exhaust system shown in the bottom of the figure (V_e/V_d = 5.2) and the compact manifold, good agreement is again obtained. Only with the larger volume and long pipe exhaust system, is there evidence in the measured pressure variation of substantial unsteady gas-dynamic effects. When used appropriately, filling and emptying models can be a useful predictive tool.

© McGraw-Hill Education. All rights reserved. Any use is subject to the Terms of Use, Privacy Notice and copyright information.

Figure 14.2 Comparison of intake and exhaust manifold pressures, p_i and p_e predicted by filling and emptying model, with experimental data. Single-cylinder two-stroke loop-scavenged direct-injection diesel engine. Top and bottom: Different ratios of exhaust system volume V_e to displaced volume V_d, and exhaust manifold shapes.[6] EPO, exhaust port opens; IPO, inlet port opens; IPC, inlet port closes; EPC, exhaust port closes.



14.3.4. Gas Dynamic Models

Many intake and exhaust system design variables determine their performance. These variables include the length and cross-sectional area of both primary and secondary runners, the volume and location of the plenums or junctions which join the various runners, the entrance or exit angles of the runners at a junction, the number of engine cylinders and their dimensions, intake and exhaust port and valve design, and valve lift and timing (see Secs. 6.2, 6.3, 6.7, and 7.6). Most of this geometric detail is beyond the level that can be incorporated into the models discussed above. Coupled with the pulsating nature of the flow into and out of each cylinder, these details create significant gas dynamic effects on intake and exhaust flows which require a more complete modeling approach.

Gas dynamic models have been used for many years to study engine gas exchange processes. These models utilize the mass, momentum, and energy conservation equations for the unsteady compressible flow in the intake and exhaust. Normally, the *one-dimensional* unsteady flow equations are used.[1] These models often use a thermodynamic analysis of the in-cylinder processes to link the intake and exhaust flows. In the past, the method of characteristics was used to solve the gas dynamic equations. Finite difference techniques are used in more recent intake and exhaust flow models. The basic equations and assumptions of these models will now be reviewed.[7]

14.3.4.1. Unsteady Flow Equations

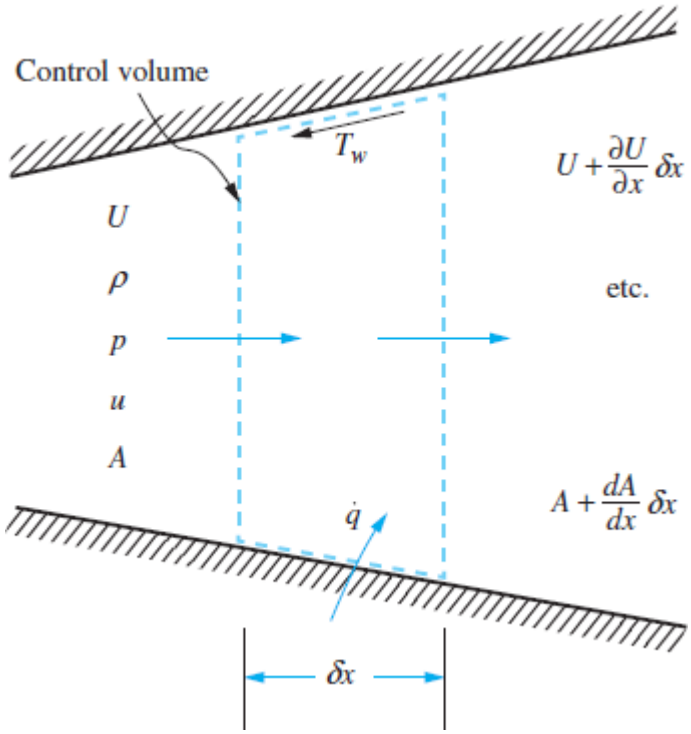
Consider the flow through the control volume within a straight duct shown in Fig. 14.3. It is assumed that the area change over the length δx of the control volume is small so the flow is essentially one dimensional. Mass conservation requires that the rate of change of mass within the control volume equals the net flow into the control volume: that is,

© McGraw-Hill Education. All rights reserved. Any use is subject to the Terms of Use, Privacy Notice and copyright information.

$$\frac{\partial}{\partial t}(\rho A \delta x) = \rho A U - \left[\rho A U + \frac{\partial}{\partial x}(\rho A U)\,\delta x\right]$$

(14.12)

Figure 14.3 Control volume for unsteady one-dimensional flow analysis.



Retaining only first-order quantities, this equation simplifies to

$$\frac{\partial \rho}{\partial t} + \frac{\partial}{\partial x}(\rho U) + \frac{\rho U}{A}\frac{dA}{dx} = 0$$

(14.13)

The momentum conservation equation states that the net pressure forces plus the wall shear force acting on the control volume surface equal the rate of change of momentum within the control volume plus the net flow of momentum out of the control volume. The net forces and momentum changes are given by:

Pressure forces:

$$pA - \left(p + \frac{\partial p}{\partial x}\delta x\right)\left(A + \frac{dA}{dx}\delta x\right) + p\frac{dA}{dx}\delta x = -A\frac{\partial p}{\partial x}\delta x$$

Shear forces:

$$-\tau_w \pi D \delta x = -\xi \frac{\rho U^2}{2}\pi D \delta x$$

© McGraw-Hill Education. All rights reserved. Any use is subject to the Terms of Use, Privacy Notice and copyright information.

where D is the equivalent diameter $(4A/\pi)^{1/2}$, and ξ is the friction coefficient given by $\tau_w/\left(\rho U^2/2\right)$.

The rate of change of momentum within the control volume is

$$\frac{\partial}{\partial t}\left(U\rho A\delta x\right)$$

and the net efflux of momentum across the control volume surface is

$$\left(\rho+\frac{\partial\rho}{\partial x}\delta x\right)\left(U+\frac{\partial U}{\partial x}\delta x\right)^2\left(A+\frac{dA}{dx}\delta x\right)-\rho U^2A=\frac{\partial}{\partial x}\left(\rho U^2A\right)\delta x$$

Combining these terms into the momentum conservation equation yields

$$-A\frac{\partial p}{\partial x}\delta x-\xi\frac{\rho U^2}{2}\pi D\delta x=\frac{\partial}{\partial t}\left(\rho UA\delta x\right)+\frac{\partial}{\partial x}\left(\rho U^2A\right)\delta x$$

(14.14)

This can be rearranged and combined with the mass conservation equation (14.13) to give

$$\frac{\partial U}{\partial t}+U\frac{\partial U}{\partial x}+\frac{1}{\rho}\frac{\partial p}{\partial x}+2\xi\frac{U^2}{D}=0$$

(14.15)

14.3.4.2. Energy Conservation

The first law of thermodynamics for a control volume states that the energy within the control volume changes due to heat and shear work transfers across the control volume surface and due to a net efflux of stagnation enthalpy resulting from flow across the control volume surface. The stagnation enthalpy h_0 is

$$h_0=h+\frac{U^2}{2}=u+\frac{p}{\rho}+\frac{U^2}{2}$$

where u is the specific internal energy of the fluid (often approximated by c_vT). The shear work transfer across the control volume surface is zero. The heat-transfer rate $\dot{Q}_w$ is given by

$$\delta\dot{Q}_w=\dot{q}\rho A\delta x$$

where $\dot{q}$ is the heat transfer per unit mass of fluid per unit time into the control volume.

© McGraw-Hill Education. All rights reserved. Any use is subject to the Terms of Use, Privacy Notice and copyright information.

The rate of change of energy within the control volume is

$$\frac{\partial E}{\partial t} = \frac{\partial}{\partial t}\left[(\rho A \delta x)\left(u + \frac{U^2}{2}\right)\right]$$

The net efflux of stagnation enthalpy is

$$\frac{\partial}{\partial x}\left[(\rho U A)\left(u + \frac{p}{\rho} + \frac{U^2}{2}\right)\right]\delta x$$

Hence, the equation for energy conservation becomes

$$\frac{\partial}{\partial t}\left[(\rho A \delta x)\left(u + \frac{p}{\rho} + \frac{U^2}{2}\right)\right] + \frac{\partial}{\partial x}\left[(\rho U A)\left(u + \frac{p}{\rho} + \frac{U^2}{2}\right)\right]\delta x - \dot{q}\rho A \delta x = 0$$

(14.16)

Additional simplifications are possible. Expanding Eq. (14.16) and using the mass and momentum conservation equations yield

$$\frac{\partial u}{\partial t} + U\frac{\partial u}{\partial x} = \dot{q} + 2\xi\frac{U^3}{D} - \frac{p}{\rho A}\frac{\partial (UA)}{\partial x}$$

(14.17)

If u can be represented by $c_v T$, and $R/c_v = \gamma - 1$ is constant, Eq. (14.17) can be rearranged and simplified to give

$$\frac{\partial p}{\partial t} + U\frac{\partial p}{\partial x} - a^2\left(\frac{\partial \rho}{\partial t} + U\frac{\partial \rho}{\partial x}\right) - (\gamma - 1)\rho\left(\dot{q} + 2\xi\frac{U^3}{D}\right) = 0$$

(14.18)

where the sound speed a for an ideal gas is given by

$$a^2 = \left(\frac{\partial p}{\partial \rho}\right)_s = \gamma\frac{p}{\rho}$$

(14.19)

If friction and heat-transfer effects are small enough to be neglected, Eqs. (14.15) and (14.18) can be considerably simplified. In the absence of these effects the flow is *isentropic;* it has uniform entropy which is constant with time and is often called *homentropic* flow. If the duct area can be neglected then the continuity equation, (14.13), can be simplified also.

These one-dimensional unsteady flow equations have been used for a number of years to study the flow in the intake and exhaust systems of spark-ignition and diesel engines, both naturally-aspirated and turbocharged. Two types of methods have been used to solve these equations: (1) the method of characteristics and (2) finite difference procedures. The characteristic

© McGraw-Hill Education. All rights reserved. Any use is subject to the Terms of Use, Privacy Notice and copyright information.

methods have a numerical accuracy that is first order in space and time, and require a large number of computational points if resolution of short-wavelength variations is important. Finite difference techniques are of higher order and more efficient:[8] this approach is now preferred. Methods for treating the boundary conditions will be described below.

14.3.4.3. Finite Difference Methods

Finite difference methods for solving the one-dimensional unsteady flow equations in intake and exhaust manifolds are more efficient and flexible than the method of characteristics. The conservation equations, (14.13), (14.14), and (14.16), can be rearranged and written in matrix form as

$$\frac{\partial}{\partial t}\begin{pmatrix}\rho\\ \rho U\\ \rho u\end{pmatrix}+\frac{\partial}{\partial x}\begin{pmatrix}\rho U\\ \rho U^2+p\\ p+\rho U u\end{pmatrix}=\begin{pmatrix}-\rho U\dfrac{dA}{dx}\\ -\rho\dfrac{U^2}{A}\dfrac{dA}{dx}-\rho\dfrac{2\xi U\left|U\right|}{D}\\ -\dfrac{4h_c\left(T-T_w\right)}{D\rho}-\dfrac{1}{A}\dfrac{dA}{dx}\left(\dfrac{1}{2}\rho U^3+\dfrac{\gamma}{\gamma-1}Up\right)\end{pmatrix}$$

(14.20)

The fluid viscous shear is small relative to friction at the wall in the momentum equation, and heat conduction and viscous dissipation prove negligible relative to convective heat transfer at the wall in the energy conservation equation. These equations have the vector form:

$$\frac{\partial F}{\partial t}+\frac{\partial G}{\partial x}=H$$

(14.21)

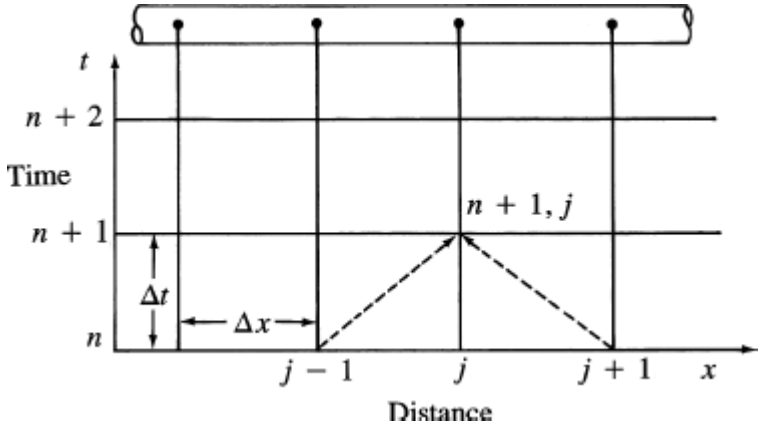
where *G* and *H* are functions of *F* only. Several finite difference methods have been used to solve Eq. (14.21) (e.g., see Refs. 7, 8, and 9). The one-step Lax-Wendroff method will be illustrated.[9] Equation (14.21) can be developed into a Taylor series with respect to time, and the time and space derivatives approximated by central differences around the mesh point, shown in Fig. 14.4, as

$$\begin{aligned}F_j^{n+1} &= F_j^n-\frac{1}{2}\frac{\Delta t}{\Delta x}\left(G_{j+1}^n-G_{j-1}^n\right)+\Delta t H_j^n\\ &\quad+\frac{1}{4}\left(\frac{\Delta t}{\Delta x}\right)^2\left[\left(G'^n_{j+1}+G'^n_j\right)\left(G_{j+1}^n-G_j^n\right)-\left(G'^n_j+G'^n_j\right)\left(G_j^n-G_{j-1}^n\right)\right]\end{aligned}$$

(14.22)

© McGraw-Hill Education. All rights reserved. Any use is subject to the Terms of Use, Privacy Notice and copyright information.

Figure 14.4 Mesh in time-distance plane for application of one-step Lax-Wendroff method to intake or exhaust pipe.



where G' = ∂G/∂F. This equation is first-order accurate, unless *H* is small. For stability in the integration process, the time step and mesh size must satisfy the requirement that

$$C = (|U| + a)\frac{\Delta t}{\Delta x} < 1$$

(14.23)

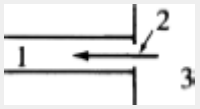
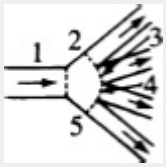
where *C* is the Courant number.

These finite difference solution methods usually require the introduction of some dissipation or damping to prevent instabilities and large non-physical oscillations from occurring with nonlinear problems with steep gradients. Amplification of the physical viscosity and the addition of artificial viscosity, damping, and smoothing terms to Eq. (14.22) are frequently used techniques.

The boundary conditions at pipe ends and junctions are obtained from the appropriate conservation equations and pressure relations, as illustrated in Table 14.1. Out-flows and in-flows obviously conserve mass and energy. For the flow out through a restriction, there is no pressure recovery downstream: for flow in through a restriction, the flow upstream of the restriction is isentropic. For pipe junctions, the conservation equations are applied to the control volume (*V*) contained within the dashed lines in the sketch in the table. The pressure boundary conditions are most easily estimated by modifying the simple constant-pressure assumption with pressure losses at each pipe exit or entry, calculated from experimentally determined loss coefficients (see Fig. 6.7).

© McGraw-Hill Education. All rights reserved. Any use is subject to the Terms of Use, Privacy Notice and copyright information.

Table 14.1 Boundary conditions for unsteady one-dimensional finite element analysis[10]

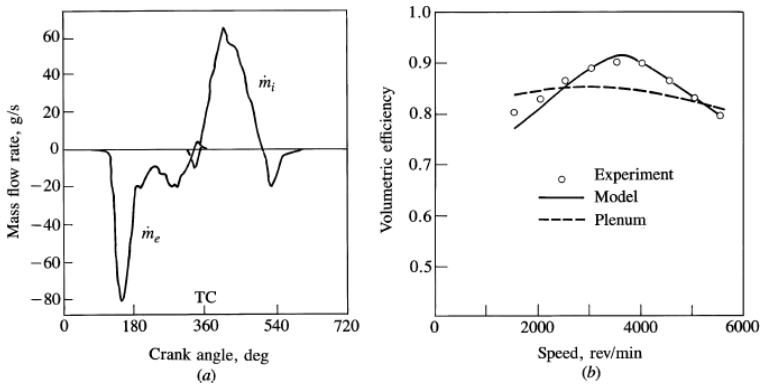
Pipe ends			
Out-flow	Mass	$\rho_1 U_1 A_1 = \rho_2 U_2 A_2$	
	Energy	$c_p T_1 + \frac{U_1^2}{2} = c_p T_2 + \frac{U_2^2}{2}$	
	Isobaric	$p_2 = p_3$	
In-flow	Mass	$\rho_1 U_1 A_1 = \rho_2 U_2 A_2$	
	Energy	$c_p T_3 = c_p T_2 + \frac{U_2^2}{2} = c_p T_1 + \frac{U_1^2}{2}$	
	Isentropic	$p_2/\rho_2^\gamma = p_3/\rho_3^\gamma$	
Pipe junctions			
	Mass	$V\frac{\partial \rho}{\partial t} = \sum_i \rho_i U_i A_i$	
	Energy	$\rho V \frac{\partial u}{\partial t} = \sum_i (\rho_i U_i A_i)\left(c_p T_i + \frac{U_i^2}{2}\right)$	
	Pressure	$p_1 + \Delta p_1 = p_2 + \Delta p_2 = p_3 + \Delta p_3 = \ldots$ $\Delta p_i / p_i = C_i (U_i / a_i)^2$	

Calculations of intake and exhaust flows using these techniques predict the variations in intake and exhaust manifold pressure with crank angle (as shown, for example, in Fig. 6.10), in single and multi-cylinder engines, with acceptable accuracy.[8,10] Measured volumetric efficiency variations with engine speed, manifold design, and valve dimensions and timing are adequately predicted also. Figure 14.5*a* shows the instantaneous exhaust and intake mass flow rates for cylinder number 1 of a four-cylinder spark-ignition engine at wide-open throttle at 1500 rev/min. Note how gas dynamic effects distort the exhaust flow. Note also the "reverse" flows into the cylinder past the exhaust valve and out of the cylinder past the intake valve at the end of the exhaust process, and the larger reverse flow at the end of the intake process at this low engine speed. Figure 14.5*b* shows the volumetric efficiency for this engine based on these predicted mass flow rates, as a function of speed. Experimental values and values predicted with quasi-steady flow equations and infinite plenums for manifolds are also shown. These results clearly demonstrate the important role that intake and exhaust system gas dynamics play in determining

© McGraw-Hill Education. All rights reserved. Any use is subject to the Terms of Use, Privacy Notice and copyright information.

both the engine speed at which peak breathing efficiency occurs and the air charging characteristics over the full engine speed range.[8]

Figure 14.5 (a) Predicted mass flow rate through the exhaust valve $\dot{m}_e$ and through the intake valve $\dot{m}_i$ in cylinder 1; four-cylinder four-stroke cycle spark-ignition engine at wide-open throttle and 1500 rev/min. Flows into cylinder are positive; flows out are negative. (b) Predicted and measured volumetric efficiency at wide-open throttle for four-cylinder spark-ignition engine. Solid line: one-dimensional unsteady flow model. Dashed line: quasi-steady flow calculation based on infinite plenums for manifolds.[8]



[1] Two- and three-dimensional effects are often important and are modeled with multi-dimensional flow models described in Sec. 14.5.

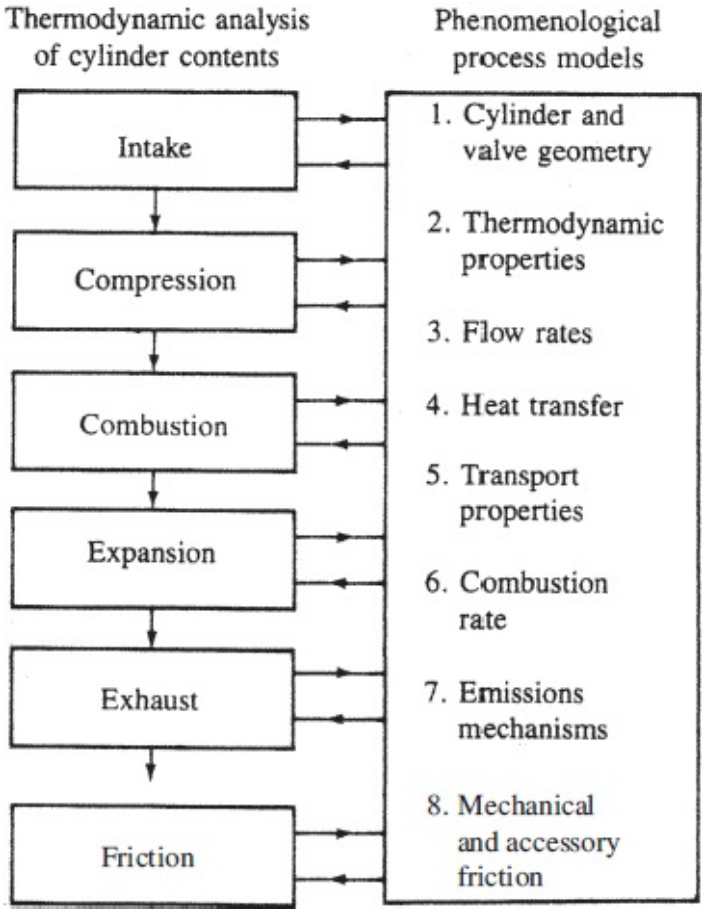
© McGraw-Hill Education. All rights reserved. Any use is subject to the Terms of Use, Privacy Notice and copyright information.

14.4. THERMODYNAMIC-BASED IN-CYLINDER MODELS

14.4.1. Background and Overall Model Structure

If the mass transfer into and out of the cylinder during intake and exhaust, the heat transfer between the in-cylinder gases and the cylinder head, piston, and cylinder liner, and the rate of charge burning (or rate of energy release from the fuel) are all known, the energy and mass conservation equations permit the cylinder pressure and the work transfer to the piston to be calculated. Engine models of this type have been developed and used extensively to predict engine operating characteristics (indicated power, mean effective pressure, specific fuel consumption, etc.) and to define the gas state for emission calculations. These models effectively follow the changing thermodynamic and chemical state of the working fluid through the engine's intake, compression, combustion, expansion, and exhaust processes. Then, once the indicated performance of the engine has been computed, friction work or losses are deducted. The pumping component is included in the intake and exhaust process analysis: so the needed phenomenological model here is of mechanical (rubbing) and accessary friction. The total model (as outlined in Fig. 14.6) is often called an engine *cycle simulation.*

Figure 14.6 Logic structure of thermodynamic-based simulation of internal combustion engine operating cycle.



The starting point for these cycle simulations is the first law of thermodynamics for an open system, developed in Sec. 14.2. This is applied to the cylinder volume for the intake, compression, combustion, expansion, and exhaust processes that in

© McGraw-Hill Education. All rights reserved. Any use is subject to the Terms of Use, Privacy Notice and copyright information.

sequence make up the engine's operating cycle. The structure of this type of engine simulation is indicated in Fig. 14.6. Then, during each process, submodels are used to describe geometric features of the cylinder and valves or ports, the thermodynamic properties of the unburned and burned gases, the mass and energy transfers across the system boundary, and the combustion process.

During intake and compression, the cylinder volume is modeled as a single open system. Application of the conservation equations in the form of Eqs. (14.1), (14.3), and (14.10) or (14.11) for the intake and then the compression process gives[2]

Intake:

$$\dot{m} = \dot{m}_i - \dot{m}_e$$

(14.24)

$$\dot{f} = \frac{\dot{m}_i}{m}(f_i - f) - \frac{\dot{m}_e}{m}(f_e - f)$$

(14.25)

$$\dot{T} = \frac{B}{A}\left[\frac{\dot{m}}{m}\left(1 - \frac{h}{B}\right) - \frac{\dot{V}}{V} - \frac{C}{B}\dot{\phi} + \frac{1}{Bm}\left(\dot{m}_i h_i - \dot{m}_e h_e - \dot{Q}_w\right)\right]$$

(14.26)

where m is the mass of gas in the cylinder,
$\dot{m}_i$ and
$\dot{m}_e$ are the mass flow rates through the intake valve and the exhaust valve, and f is the fuel fraction m_f/m. The subscripts i and e denote properties of the flow through the intake and exhaust valves, respectively. The thermodynamic properties for these flows are the values upstream of the valves and therefore depend on whether the flow is into or out of the cylinder.

Compression:

$$\dot{m} = 0 \quad \dot{f} = 0$$

(14.27*a*,*b*)

$$\dot{T} = \frac{B}{A}\left(-\frac{\dot{V}}{V} - \frac{\dot{Q}_w}{Bm}\right)$$

(14.28)

The pressure is then determined from Eq. (14.9).

During intake and compression, the working fluid composition is frozen. The composition and thermodynamic properties can be determined using the models described in Secs. 4.2 and 4.7. Mass flows through open valves are usually calculated using one-dimensional compressible flow equations for flow through a restriction (see App. C and Secs. 6.3.2 and 14.3.2) or filling and emptying models (Sec. 14.3.3). The more accurate unsteady gas-dynamic intake (and exhaust) flow models described in

© McGraw-Hill Education. All rights reserved. Any use is subject to the Terms of Use, Privacy Notice and copyright information.

Sec. 14.3.4 can be used to calculate the mass flow into the engine cylinder in complete engine cycle simulations when the variation in engine flow rate with speed is especially important: the disadvantage is increased computing time. Heat transfer during intake and compression is calculated using one of the Nusselt-Reynolds number relations for turbulent convective heat transfer described in Sec. 12.4.5. The transport properties, viscosity, and thermal conductivity used in these correlations can be obtained from relations such as Eqs. (4.52) to (4.55).

During combustion which starts with the spark discharge in spark-ignition engines and with spontaneous ignition of the developing fuel-air jets in compression-ignition engines, the actual processes to be modeled become more complex. Many approaches to predicting the burning or chemical energy release rate have been used successfully to meet different simulation objectives. The simplest approach has been to use a one-zone model where a single thermodynamic system represents the entire combustion chamber contents and the energy release rate is defined by empirically based functions specified as part of the simulation input. Or, in spark-ignition engines, quasi-geometric models of turbulent premixed flames are used with a two-zone analysis of the combustion chamber contents—an unburned and a burned gas region. In compression-ignition engines, multiple-zone models of the developing fuel-air jets have been used to provide more detailed predictions of the combustion process and the nonuniform cylinder composition and state. These combustion models will be reviewed in the following sections (14.4.2 and 14.4.3) and the appropriate conservation equations for the *combustion process* will be developed there. In diesels, radiation heat transfer becomes important during the combustion process (see Sec. 12.6.3).

The *expansion process* is either treated as a continuation of the combustion process or, once combustion is over, can use the form of the mass, fuel, and energy conservation equations which hold during compression [Eqs. (14.27) and (14.28)]. The exhaust process conservation equations for a one-zone open-system model of the cylinder contents are[2]

Exhaust:

$$\dot{m} = -m_e \quad \dot{f} = -\frac{\dot{m}_e}{m}(f_e - f)$$

(14.29*a*,*b*)

$$\dot{T} = \frac{B}{A}\left[-\frac{\dot{m}_e}{m}\left(1 - \frac{h}{B}\right) - \frac{\dot{V}}{V} - \frac{C}{B}\dot{\phi} + \frac{1}{Bm}\left(-\dot{m}_e h_e - \dot{Q}_w\right)\right]$$

(14.30)

where h_e, the enthalpy of the flow through the exhaust valve, is the cylinder average enthalpy at that point in time for flow *out* of the cylinder, or the exhaust system gas enthalpy if reverse flow back into the cylinder occurs.

The engine operating cycle should end with the working fluid at the same state that it started out in. For the first calculations of the sequence of processes in Fig. 14.6, property values defining the initial state of the fluid in the cylinder are assumed. If the values of these properties at the end of the first cycle differ from the assumed values, the cycle calculation is repeated with the appropriate new initial values until the discrepancy is sufficiently small. Convergence with these cycle simulations occurs within a few iterations.

The working fluid state is now defined throughout the operating cycle. The work transfer to the piston per cycle

$$W_c = \oint p dV$$

© McGraw-Hill Education. All rights reserved. Any use is subject to the Terms of Use, Privacy Notice and copyright information.

(14.31)

can now be obtained. From W_c, the masses of fuel and air inducted, m_f and m_a, and engine speed N, all the engine *indicated* performance parameters can be calculated: power, mean effective pressure, specific fuel consumption, fuel-conversion efficiency; as well as volumetric efficiency, residual gas fraction, total heat transfer, etc. With a friction model, the indicated quantities can be converted to brake quantities (including torque).

The more sophisticated of these thermodynamic-based engine cycle simulations define the working fluid state throughout the cycle in sufficient detail for predictions of engine emissions to be made. The discussion in Chap. 11 of emission-formation mechanisms indicates that our understanding of how some of these pollutants form (e.g., NO_x, CO) is reasonably complete, and thus can be modeled. The formation processes of the other pollutants (unburned hydrocarbons and particulates) are not yet adequately understood, though modeling activities continue to contribute to that understanding. The key features of models for predicting engine emissions are discussed in Chap. 11.

Cycle simulations and combustion models which have been developed for spark-ignition engines, where the fuel, air, residual gas mixture is essentially uniform, are discussed in Sec. 14.4.2. Compression-ignition engine simulations and their combustion models are then discussed in Sec. 14.4.3. The special features required for prechamber engine models are reviewed in Sec. 14.4.4. Finally, thermodynamic-based models for more complex engine systems—multi-cylinder, turbocharged, and turbocompounded engines—are discussed in Sec. 14.4.5.

14.4.2. Spark-Ignition Engine Models

These models have usually followed the conceptual structure indicated in Fig. 14.6. We focus here on the combustion submodels that have been developed and used successfully. Features of the spark-ignition engine combustion process that permit major simplifying assumptions for thermodynamic modeling are: (1) the fuel, air, residual-gas charge is essentially uniformly premixed; (2) the volume occupied by the reaction zone where the fuel-air oxidation process actually occurs is small compared with the clearance volume—the flame is a thin reaction sheet even though it becomes highly wrinkled and convoluted by the turbulent flow as it develops (see Sec. 9.3); and (3) for thermodynamic analysis, the contents of the combustion chamber during combustion can be analyzed as two zones—an unburned and a burned zone.

Useful combustion chamber design information can be generated with simple geometric models of the flame. In the absence of strong swirl, the surface which defines the flame location can be approximated by a portion of the surface of a sphere. The mean burned gas front can similarly be approximated. Thus, for a given combustion chamber shape and assumed flame center location (e.g., the spark plug electrodes), the spherical burning area A_b [see Eq. (9.43)], the burned gas volume V_b [see Eq. (9.42)], and the combustion chamber surface "wetted" by the burned gases can be calculated for a given flame radius r_b and piston position (defined by crank angle) from purely geometric considerations.[1] The practical importance of such "model" calculations is that (1) the mass burning rate for a given burning speed S_b (which depends on local turbulence and mixture composition) is proportional to the spherical burning area A_b as given by Eq. (9.47); (2) the heat transfer occurs largely between the burned gases and the walls and is proportional to the chamber surface area wetted by the burned gases $A_{b,w}$ (see Fig. 12.21). Using the fact that the density ratio across the flame ρ_u/ρ_b is approximately constant and equals about 4, the unburned and burned gas volumes V_u and V_b can be related to the unburned and burned mass fractions, $(1 - x_b)$ and x_b, respectively.

Examples of the results of such flame geometry calculations are shown in Figs. 14.7 and 14.8.[11] Figure 14.7*a* shows spherical flame areas A_b as a function of flame radius r_b for two different chambers and two plug locations and the TC piston position. The much larger flame area and shorter flame travel length of the central plug location are obvious. Such area data can be plotted as a function of burned gas volume V_b, as shown in Fig. 14.7*b*, so that comparisons of $A_b(r_b)$ for different chambers at the same mass fraction burned can be made. The advantage of a more compact chamber with higher central clearance height is apparent. Figure 14.8 shows burned-gas-wetted wall area on the cylinder head, cylinder wall, and piston as a function of

© McGraw-Hill Education. All rights reserved. Any use is subject to the Terms of Use, Privacy Notice and copyright information.

flame radius and crank angle for an open chamber with central ignition. The cylinder head and piston are the dominant areas early in the expansion stroke when the burned gas temperatures and heat fluxes are highest.

Figure 14.7 Calculated spark-ignition engine spherical flame surface area, scaled by cylinder bore squared: (a) as a function of flame radius for different combustion chamber shapes and spark plug locations; (b) as a function of enflamed volume, scaled by bore cubed. Piston in top center position.[11]

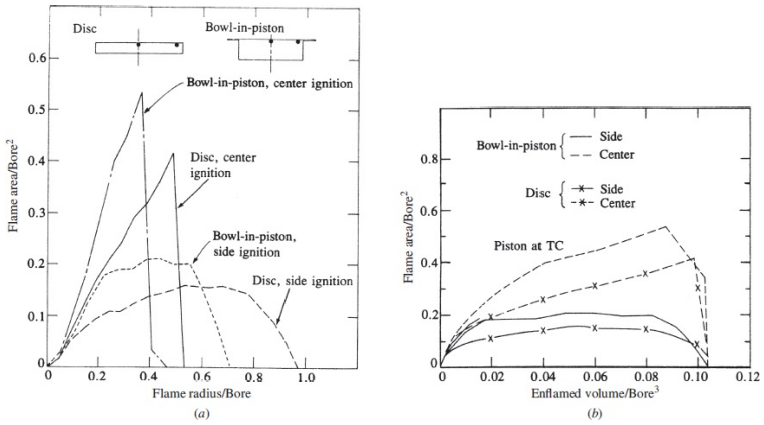
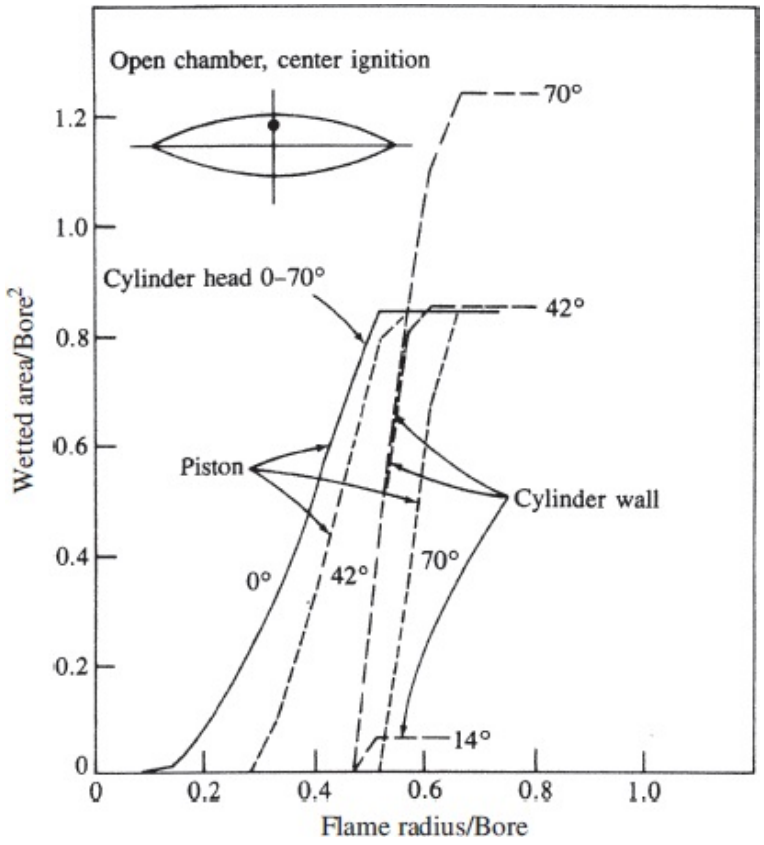


Figure 14.8 Calculated burned-gas-wetted wall area as a function of radius based on spherical flame model of an open-chamber SI engine with center plug location normalized by bore squared: for piston locations of 0°, 42°, and 7°.[11]



Mass fraction burned versus crank-angle profiles determined from a first-law analysis of cylinder pressure data, as shown in Figs. 9.4, 9.8, and 9.10 have an essentially universal dimensionless shape, as indicated in Fig. 9.15. Much useful analysis has

© McGraw-Hill Education. All rights reserved. Any use is subject to the Terms of Use, Privacy Notice and copyright information.

been done with engine simulations where this universal combustion profile has been used as a calculation input. The S-shaped mass fraction burned profile is often represented by the Wiebe function:

$$x_b = 1 - \exp\left[-a\left(\frac{\theta - \theta_0}{\Delta\theta}\right)^{m+1}\right]$$

(14.32)

where θ is the crank angle, θ_0 is the start of combustion, $\Delta\theta$ is the total combustion duration ($x_b = 0$ to $x_b \approx 1$), and a and m are adjustable parameters which fix the shape of the curve. Actual mass fraction burned curves have been fitted with $a = 5$ and $m = 2$.[12]

The conservation equations for an open system [Eqs. (14.1) and (14.10) or (14.11)] are now applied to the unburned gas zone ahead of the flame and to the burned zone behind the flame, in turn (see Fig. 9.4). For premixed engines,
$\dot{f}$ and
$\dot{\phi}$ are zero. During combustion,
$\dot{m}$ and
$\dot{m}_j$ in Eq. (14.10) or Eq. (14.11) are the mass flow rate across the flame sheet. This is
$-\dot{m}_b$ for the unburned zone system and
$+\dot{m}_b$ for the burned zone system;
$\dot{m}_b$ is given by
$m\dot{x}_b$, with
$\dot{x}_b$ obtained by differentiating Eq. (14.32).

To calculate the effect of heat transfer on the burned gas state more accurately, the burned gas zone in Fig. 9.6 can be modeled in two parts: an adiabatic core and a boundary-layer region. The intent here is to account for the fact that heat loss to the walls primarily cools the burned gas adjacent to the wall, and only indirectly affects the core gas through the change in pressure that results from heat loss. The open-system conservation equations, (14.1) and (14.10) or (14.11), are now applied to the core and boundary-layer region separately. The boundary-layer region covers that portion of the combustion chamber wall wetted by the burned gases, as shown in Fig. 12.21, and is of thickness δ_T, which increases with time. The temperature of the boundary-layer zone (assumed uniform) is usually taken to be the mean of the wall temperature and burned gas core temperature. Equation (14.10) or Eq. (14.11) is used to relate the enthalpy flux due to the mass flow across the edge of the boundary layer (which has an enthalpy equal to the core-gas enthalpy), the heat transfer to the wall, the changing energy within the boundary-layer system due to its increasing mass and changing state, and the work transfer due to its changing volume.

An example of predictions of cylinder pressure, unburned and burned gas temperatures, heat-transfer rate, and boundary-layer thickness, based on an assumed 50° total burn duration for a 5.7-liter eight-cylinder engine at wide-open throttle and 2500 rev/min, is shown in Fig. 14.9. Appropriately based predictions of overall engine performance parameters made with this type of thermodynamic model agree well with engine data. Figure 14.10 shows predictions of indicated specific fuel consumption and exhaust gas temperature as a function of the fuel/air equivalence ratio at fixed load and speed. The isfc predictions and data agree well (except for very lean mixtures with retarded timing where cycle-by-cycle combustion variations are sufficiently large so predictions based on the average cycle lose accuracy); the predicted curves for exhaust temperature show the same trends as the experimental data. However, they are higher due to underestimation of the heat losses during the exhaust process.[13]

© McGraw-Hill Education. All rights reserved. Any use is subject to the Terms of Use, Privacy Notice and copyright information.

Figure 14.9 *Cylinder pressure p, mass fraction burned x_b, unburned and burned gas temperatures (T_u = unburned, T_a = adiabatic burned core, $\overline{T}_b$ = mean burned gas temperatures), heat-transfer rate $\dot{Q}_w$ (normalized by fuel flow rate × heating value), thermal boundary-layer thickness δ_T, and mean nitric oxide concentration in the burned gases, through the four-stroke SI engine operating cycle, predicted by a thermodynamic-based cycle simulation. 5.7-liter displacement eight-cylinder engine operating at wide-open throttle, 2500 rev/min, with fuel/air equivalence ratio = 1.1. Gross indicated mean effective pressure is 918 kPa and specific fuel consumption is 254 g/kW · h.*[14]

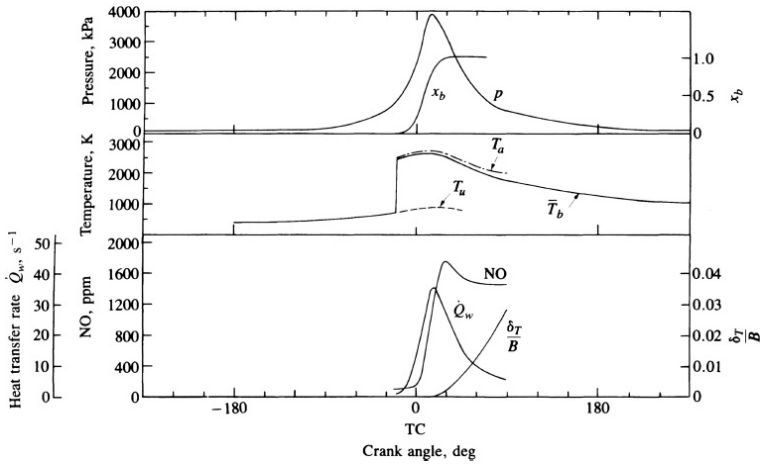
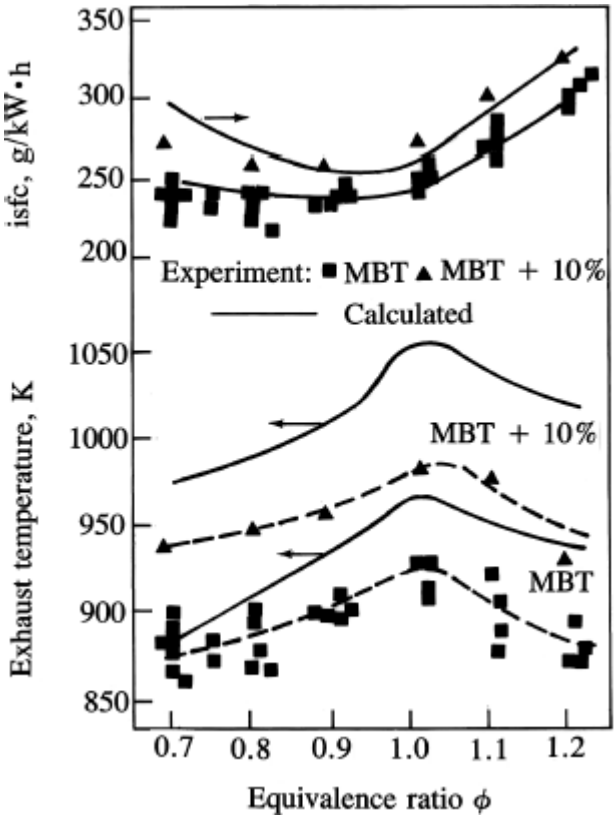


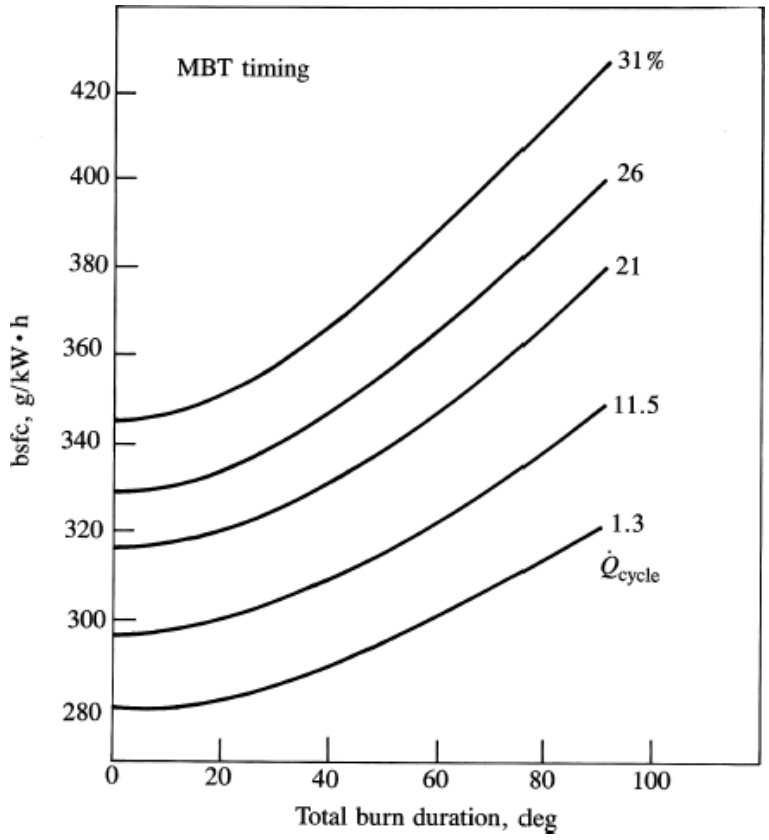
Figure 14.10 *Predicted and measured indicated specific fuel consumption and exhaust temperature as a function of the fuel/air equivalence ratio for a spark-ignition engine operated at 1250 rev/min and imep of 379 kPa. MBT, maximum brake torque timing. MBT + 10%: combustion timing was retarded to give a 10% fuel consumption penalty relative to MBT timing.*[13]



© McGraw-Hill Education. All rights reserved. Any use is subject to the Terms of Use, Privacy Notice and copyright information.

The output from such thermodynamic-based cycle simulations has replaced the fuel-air cycle as a predictor of effects of major variables on engine performance and efficiency. An instructive example of the value of such predictions is shown in Fig. 14.11, where fuel consumption at constant fuel/air equivalence ratio, load, and speed has been computed as a function of total burn duration and heat loss to the chamber walls: increasing burn duration and heat loss both worsen fuel consumption.[15] Such data can be used to assess the efficiency improvements that should result from reduced heat transfer (e.g., reduced chamber surface area) and increased burn rate. With 0–100% burned crank angle duration of about 60° (corresponding to $\Delta\theta_{0-90\%}$ of about 50°), the impact of heat losses on bsfc is about one-third: a 10% reduction (relative) in heat loss per cycle results in a 3 to 3.5% reduction in bsfc at about one-quarter the maximum load. Obviously the dependence of burn rate on engine design and operating parameters has not been modeled; the burn rate profile was a calculation input. Such models are most useful either: (1) when the burn rate profile is *not critical* to the problem under study; or (2) when predictions for a *range* of assumed burn rate profiles provide the required information.

Figure 14.11 Predicted brake specific fuel consumption as a function of heat transfer per cycle to the combustion chamber walls (as a percent of the fuel's heating value) and total burn duration [$\Delta\theta$ in Eq. (14.32)]. 1250 rev/min, 262 kPa bmep, relative air/fuel ratio = 1.1, maximum brake torque spark timing.[15]



So far we have discussed engine cycle simulations where details of the combustion process have been specified as input. The same thermodynamic-based simulation structure can be used in conjunction with a combustion model which *predicts* the rate of fuel burning. Various combustion models have been proposed and used for this purpose. Some of these are empirically based. The more useful are based on the wrinkled thin reaction-sheet flame model described in Sec. 9.3. These models assume that the overall flame shape approximates a portion of a sphere centered at or near the spark plug. It is important to describe the three phases of the combustion process—flame development, rapid burning, and termination—from the basic flow and chemistry principles. The critical flow feature is the level of in-cylinder turbulence (characterized by the local rms velocity fluctuation u' during combustion). The flame chemistry dependence on fuel-air mixture composition can be incorporated appropriately through the mixture's laminar flame speed.

© McGraw-Hill Education. All rights reserved. Any use is subject to the Terms of Use, Privacy Notice and copyright information.

Spark-ignition engine combustion models with such a fundamental framework have been developed and used extensively. Based on coupled analysis of flame front location and cylinder pressure data, Keck and coworkers[16–18] have derived the following entrainment-based burning law:

Rate of entrainment (laminar diffusion plus turbulent entrainment into the enflamed region):

$$\frac{dm_e}{dt} = \rho_u A_f S_L + \rho_u A_f u_T \left(1 - e^{-t/\tau_b}\right)$$

(14.33)

Rate of mixture burning (laminar flame propagation plus burn up of entrained yet-to-burn mass):

$$\frac{dm_b}{dt} = \rho_u A_f S_L + \frac{m_e - m_b}{\tau_b}$$

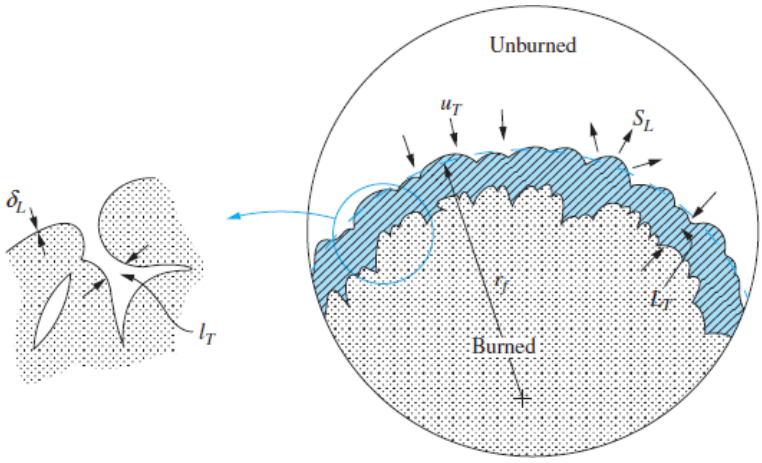
(14.34)

where A_f is the flame envelope area (portion of a sphere), S_L is the local laminar flame speed, u_T is the turbulent entrainment speed ($u_T \approx u'$), and $\tau_b = l_T/S_L$ is a characteristic burning time, where l_T is the characteristic length scale of the turbulent fluid motion. See Sec. 9.3.4.

Figure 14.12 illustrates the physical basis for this model. The first term in Eq. (14.33), the entrainment equation, represents the laminar diffusion of mixture across the approximately spherical front of the "thick" turbulent flame; the second term represents the entrainment of mixture into the flame due to the turbulent motion. In Eq. (14.34), which describes the rate of burning of the *unburned* mixture, the first term represents the burning due to the propagating laminar flame, and the second term the burn-up of unburned mixture within the turbulent flame "brush." This unburned mixture is the difference between the mass already entrained and the amount already burned, contained within the "wrinkles" and "islands" which the distorting and stretching of the thin reaction sheet by the turbulent flow produce. This is often called an "entrainment" or "eddy-burning "model for the above reasons. The exponential term in brackets in Eq. (14.33) allows for the fact that the flame sheet initially is spherical and "laminar-like": it requires a time of about τ_b to develop into a turbulent flame.[2]

© McGraw-Hill Education. All rights reserved. Any use is subject to the Terms of Use, Privacy Notice and copyright information.

Figure 14.12 Schematic of turbulent premixed spark-ignition engine flame illustrating the physical basis for the burning law of Eqs. (14.33) and (14.34). The approximately spherical front of the "thick" turbulent flame (dashed line) diffuses outward at the laminar flame speed S_L, and fresh mixture crosses this flame front at a characteristic velocity u_T due to turbulent convection. Schematic on left shows detailed flame structure: δ_L is the reaction-sheet thickness and l_T is the characteristic scale of wrinkles in the flame sheet.



The behavior of Eqs. (14.33) and (14.34) in four important limits is as follows:

1. For a quiescent mixture, $u_T \to 0$ or $l_T \to \infty$

$$S_b \to S_L \tag{14.35a}$$

2. Initially, as $t \to 0$,

$$S_b \to S_L \tag{14.35b}$$

3. Quasi-steady state, dm_b/dt equals dm_e/dt,

$$S_b \approx u_T + S_L \tag{14.35c}$$

4. Final burning stage after the flame front reaches the wall, $t \geq t_w$ (when $A_f \to 0$),

$$\dot{m}_b/\dot{m}_b(t_w) = e^{-(t-t_w)/\tau_b} \tag{14.35d}$$

To apply Eqs. (14.33) and (14.34), the quantities u_T and τ_b (or $l_T = \tau_b S_L$) must be evaluated. Two approaches have been taken: (1) use of empirical correlations for these variables, derived from engine flame data (such as that described in Sec. 9.3.4); (2) use of more fundamental models to predict these quantities.

© McGraw-Hill Education. All rights reserved. Any use is subject to the Terms of Use, Privacy Notice and copyright information.

Keck has derived the following correlations for u_T and l_T, based on the application of Eqs. (14.33) and (14.34) to several sets of engine combustion data:

$$u_T = 0.08 a_i \left(\frac{\rho_u}{\rho_i} \right)^{1/2}$$

(14.36)

$$l_T = 0.8 L_{\text{iv}} \left(\frac{\rho_i}{\rho_u} \right)^{3/4}$$

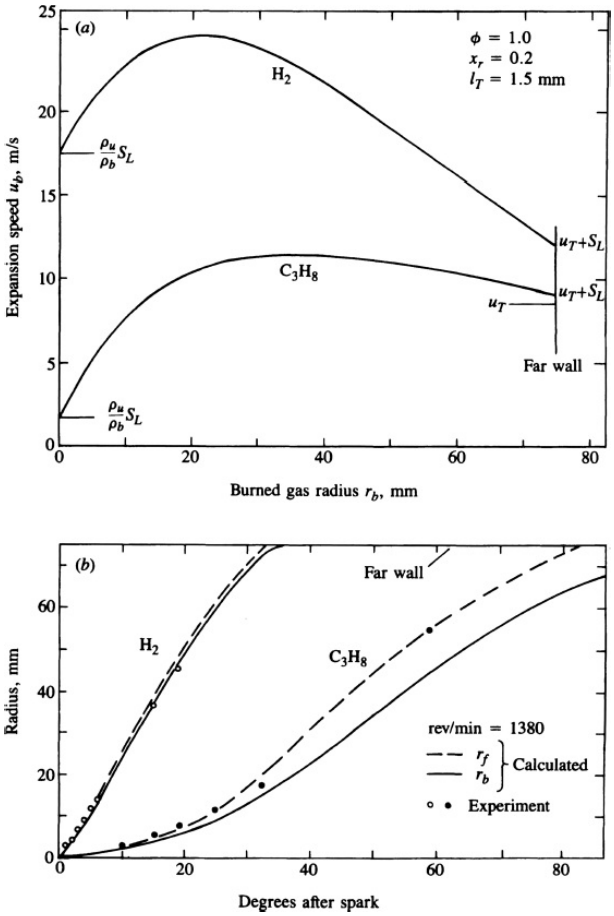
(14.37)

u_T was found to be proportional to $\sqrt{\rho_u}$ (at time of spark) and to correlate well with mean inlet gas speed $a_i = \eta_v (A_p / A_{\text{iv}}) \overline{S}_p$, where η_v is the volumetric efficiency, A_p is piston area, A_{iv} is the maximum open area of the inlet valve, $\overline{S}_p$ is mean piston speed. l_T appears to scale with valve lift, L_{iv}; it decreases with increasing density at a rate proportional to $\rho_u^{-3/4}$. While u_T and l_T are not constant during the combustion process, their variation is modest.[16]

A quantitative comparison of predicted and measured flame radius as a function of time is shown in Fig. 14.13 for propane and hydrogen fuel-air mixtures, which exhibit widely different behavior:[16] the figure indicates both the behavior and validity of the model. Predicted burned gas expansion speeds u_b [see Eq. (9.46)] are shown in Fig. 14.13*a* as a function of burned gas radius; the parameters u_T and l_T were chosen to fit the propane data. Figure 14.13*b* shows that the measured flame front radii, r_f, are in good agreement with the predicted flame and burned gas radii, r_f and r_b, for these two fuels. The initial expansion speed of hydrogen is about 10 times that of propane. Since $r_f \approx r_b$ for early times, and $S_b \approx S_L$, this ratio is expected. As r_b becomes large, $(r_f - r_b) \rightarrow u_T \tau_b$, which is several times smaller for hydrogen-air mixtures than for propane-air mixtures.

© McGraw-Hill Education. All rights reserved. Any use is subject to the Terms of Use, Privacy Notice and copyright information.

Figure 14.13 (a) Calculated burned gas expansion speed u_b for stoichiometric hydrogen-air and propane-air mixtures as a function of burned gas radius r_b. (b) Comparison of experimentally measured (points) and calculated (dashed curve) flame radii r_f for these mixtures as a function of crank angle. Also shown (solid curve) is the burned gas radius r_b.[16]



An adaption of this approach developed by Tabaczynski and coworkers[20,21] is based on the following model of turbulent flame propagation. The vorticity in the turbulent flow field is concentrated in vortex sheets which are of a size comparable to the Kolmogorov scale l_K [see Eq. (8.11)]. These vortex sheets are assumed to have a characteristic spacing which is of the order of the Taylor microscale l_M, which is a function of the integral length scale l_I and the turbulent Reynolds number as indicated by Eq. (8.15). From these turbulence assumptions, it is argued that ignition sites propagate along the vortex sheets with a velocity $u' + S_L$, where u' is the local turbulence intensity. The propagation of the reaction front between the vortex sheets is assumed to be a laminar process. Thus, in Eqs. (14.33) and (14.34), u_T and τ_b are given by

$$u_T \approx u' \quad \text{and} \quad \tau_b = \frac{l_T}{S_L} \approx \frac{l_M}{S_L}$$

(14.38)

where l_M, the microscale, is determined from the integral scale and the turbulent Reynolds number via Eq. (8.15), assuming that the turbulence is homogeneous and isentropic. The task therefore becomes one of evaluating u' and l_I.

One approach used is to relate the turbulence intensity at the start of the combustion process to the mean intake flow velocity through the valve: for example,[22]

© McGraw-Hill Education. All rights reserved. Any use is subject to the Terms of Use, Privacy Notice and copyright information.

$$u_0' = \frac{C\overline{S}_p B^2}{L_{\text{iv}} D_{\text{iv}}}$$

(14.39)

where
$\overline{S}_p$ is the mean piston speed, B the bore, and L_{iv} and D_{iv} the lift and diameter of the intake valve. It is assumed that the integral length scale at the start of combustion, $l_{I,0}$, is proportional to a characteristic flow dimension, usually the clearance height h. Then, during combustion, the unburned portion of the charge is assumed to undergo isentropic compression sufficiently rapidly that the angular momentum of the "eddies" is conserved and the length scale follows the eddy size: that is, a simple rapid-distortion process occurs:

$$u' = u_0'\left(\frac{\rho}{\rho_0}\right)^{1/3} \quad l_I = l_{I,0}\left(\frac{\rho_0}{\rho}\right)^{1/3}$$

(14.40)

This model predicts an increase in turbulence intensity and decrease in length scale with compression, which is only partly confirmed by experiment.

A more sophisticated approach is to describe the dynamic behavior of the turbulence with one or more rate equations for the key turbulence parameters: k the turbulent kinetic energy and ε the dissipation rate of k. Turbulence is generated, diffused, and dissipated by the flow field, so the rate of change of turbulent kinetic energy k can be written:

$$\frac{dk}{dt} = P_k + D_k - \rho\varepsilon$$

(14.41)

where the term P_k represents the volumetric production of turbulence and the diffusion term D_k can be modeled as a gradient diffusion with an effective turbulent viscosity which dominates the laminar diffusion process. In this application, Eq. (14.41) is integrated over the combustion chamber (or a region of the chamber) to provide spatially averaged turbulence predictions. Then the diffusion terms become boundary fluxes: for example, the transport of kinetic energy across the combustion chamber boundary due to flow through the inlet or exhaust valve. The dissipation rate ε is related to the integral length scale via

$$\varepsilon = C_D k^{3/2}/l_I, C_D = 0.09$$

(14.42)

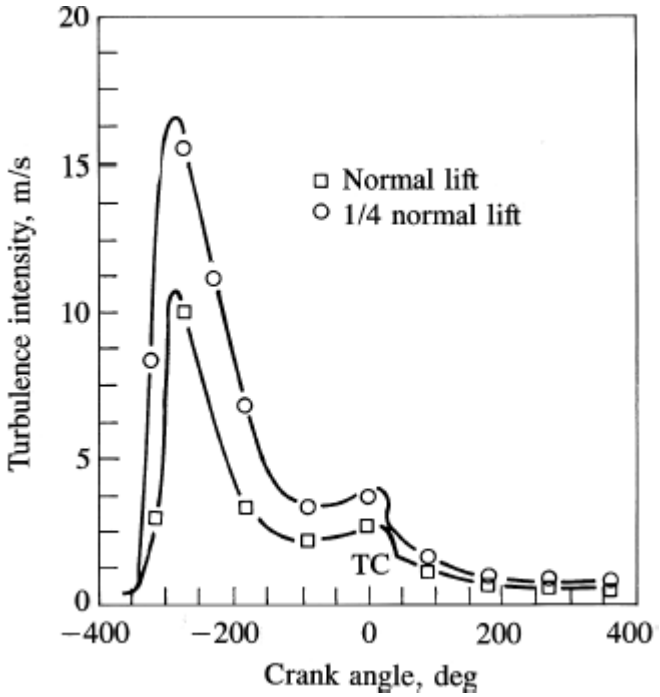
l_I can be taken as proportional to the clearance height ($l_I \approx 0.22\,h$), or an additional rate equation for the second turbulence parameter, the dissipation rate ε, can be used. In the more complete of these $k-\varepsilon$ turbulence models,[23] the ε equation is similar to the k equation with production, diffusion, and dissipation terms. These $k-\varepsilon$ turbulence models are discussed more fully in Sec. 14.5.2.

This turbulence model has been incorporated into spark-ignition engine combustion models: these references give the details.[24–27] Considerable success with predicting trends in mass burning rate has been achieved with this type of model. Design variables examined include: swirl, squish, valve lift, bore/stroke ratio. The advantage of such models is that they are straightforward computationally so that extensive parametric sets of calculations are feasible. Their disadvantage is the *ad*

© McGraw-Hill Education. All rights reserved. Any use is subject to the Terms of Use, Privacy Notice and copyright information.

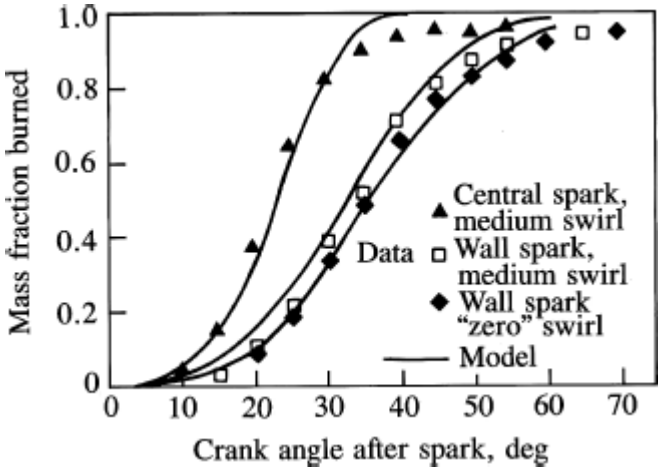
hoc nature of the turbulence and flame models which involve plausible but somewhat arbitrary assumptions. Sample predictions are shown in Fig. 14.14 which shows the variation in turbulence intensity *u'* in an engine with a disc-shaped combustion chamber, throughout the operating cycle. A normal valve-lift profile and reduced maximum valve-lift profile (one-quarter normal) are shown. The high levels of turbulence generated during the first half of the intake process decay substantially before the latter stages of the compression stroke produce some amplification. Reduced valve lift produces higher levels of turbulence intensity at combustion, as is well known. Predicted turbulence behavior during combustion indicates a moderate (some 10%) rise and fall. Swirl is shown to increase the turbulence intensity: low to high swirl increases *u'* by about 25%. Comparison of predicted and measured mass fraction burned profiles versus crank angle for different swirl levels and plug locations are shown in Fig. 14.15. The large flame area effects (shown here in the two limiting plug locations: side wall and center) and significant though lesser effect of swirl are correctly modeled. Such models are useful for relating changes in spark-ignition engine design and operating variables to changes in engine performance, via predictions of changes in flame development and propagation.

Figure 14.14 Predicted turbulence intensity u' as a function of crank angle and valve lift in a gasoline engine operating at 1500 rev/min, 414 kPa imep, with a compression ratio of 10.[26]



© McGraw-Hill Education. All rights reserved. Any use is subject to the Terms of Use, Privacy Notice and copyright information.

Figure 14.15 Comparisons of predicted and measured mass fraction burned versus crank-angle profiles for various swirl levels and plug locations.[27]



The above type of combustion model has been used to obtain explicit relations for the flame development and rapid burning angles as functions of engine design and operating variables.[28] The equations for the mass burning rate, (14.33 and 14.34), were effectively integrated over the relevant portion of the total combustion process; the turbulent characteristic velocity was assumed proportional to
$\overline{S}_p$, the mean piston speed. The flame development angle was found to vary as

$$\Delta\theta_d = C(\overline{S}_p\nu)^{1/3}\left(\frac{h}{S_L}\right)^{2/3}$$

(14.43)

where v is the kinematic viscosity ($v = \mu/\rho$) and h is the clearance height at ignition. C is a constant which depends on engine geometry and is determined by matching Eq. (14.43) with engine data. The rapid burn angle (here taken as the crank angle between x_b = 0.01 and 1.0) is given by

$$\Delta\theta_b = C'\left(\frac{B}{h^*}\right)\left(\frac{\rho_i}{\rho_u{}^*}\right)^{10/9}(\overline{S}_p\nu^*)^{1/3}\left(\frac{h_i}{S_L{}^*}\right)^{2/3}$$

(14.44)

where C' is a constant which depends on engine geometry, B is the bore, the subscript i denotes the value at ignition, and the superscript * denotes the value at cylinder conditions where x_b = 0.5. These expressions show reasonable agreement with observed trends in $\Delta\theta_d$ and $\Delta\theta_b$.

14.4.3. Direct-Injection Engine Models

In direct-injection diesel engines, the liquid fuel is injected into the cylinder as one or several jets just prior to ignition. In larger direct-injection compression-ignition engines, the airflow in the cylinder is essentially quiescent. However, in medium and smaller size DI engines, the air in the piston bowl during combustion is usually swirling about the cylinder axis at up to 10 times the crankshaft rotational speed; this swirling air-flow pattern increases the rate of entrainment of air into the fuel jet, increasing the fuel-air mixing rate. Thus modeling of the ignition and combustion processes (and thus performance) of direct-

© McGraw-Hill Education. All rights reserved. Any use is subject to the Terms of Use, Privacy Notice and copyright information.

injection diesel engines is much more complex than for premixed-charge spark-ignition engines. The unsteady liquid-fuel jet phenomena—atomization, liquid jet and droplet motion, fuel vaporization, air entrainment, fuel-air mixing, and the ignition chemistry—all play a role in the heat-release process (see Chap. 10). It is not yet possible to model all these phenomena from a fundamental basis, even with the most sophisticated fluid-dynamic-based codes now available (see Sec. 14.5), since many of these processes are not yet adequately understood. However, models at various levels of detail and empiricism have been developed and have proven useful in direct-injection diesel engine analysis.

The modeling of direct-injection gasoline SI engines also introduces additional complexity. As discussed inSec. 9.3.5, DI gasoline engines fall into two distinct categories depending on the nature of the in-cylinder fuel distribution during combustion: homogeneous charge, and stratified. While fuel injection into the cylinder adds some additional complexity, with early injection (during the intake stroke) the mixture becomes relatively homogeneous by start of combustion (though fuel injection into the intake port, vaporization off the intake valve and port surfaces, and mixing with air during flow past the valve head and seat, does produce a more uniform in-cylinder mixture). With stratified DI operation, where the fuel is injected into the cylinder during the middle or later portion of the compression stroke, spray behavior, fuel vaporization, and spray/air motion interactions all become important. But because of the different injection timing (to that in DI diesels), these processes are significantly different. We review stratified DI gasoline SI engine combustion modeling at the end of this section. Homogeneous DI gasoline SI engines are usually modeled, as are port-injected gasoline engines, as operating with close to a premixed essentially uniform fuel-vapor, air, and burned gas mixture. We approach this discussion of phenomenological models of DI engine combustion from a historical perspective since that helps prioritize the more important features of the overall combustion process. Additional details can be found in the references provided.

14.4.3.1. Diesels

This section reviews the important features of single-zone heat-release models and phenomenological spray-based combustion models for diesels. The relative simplicity and modest computer time requirements of these models make them especially useful for diesel cycle simulation and broader engine system studies.

Single-zone models assume that the cylinder contents can be adequately described by property values representing the average state, and use one or more algebraic formulas to define the heat-release rate. The functional forms of these formulas are chosen to match experimentally observed heat-release profiles (see Sec. 10.3.3). Coefficients in these formulas, which may vary with engine design details and operating conditions, are determined empirically by fitting with data. Earlier models used the phenomenological description of diesel combustion developed by Lyn (see Sec. 10.3.2) which comprised three primary phases: the ignition delay period, the premixed fuel-burning phase, and the mixing-controlled fuel-burning phase. Ignition delay correlations are reviewed in Sec. 10.5.6. Here models for the second and third phases, when the major heat release occurs, are summarized (see Ref. 29 for a more extensive review). The attraction of the one-zone heat-release approach is its simplicity; however, since it is a major simplification of the complex phenomena which comprise the combustion process, substantial empirical input must be used. One-zone heat-release models use simple equations to describe the rate of release of the fuel's chemical energy, sometimes modeled on the presumed controlling physical or chemical process and always calibrated by comparison with data.

One extensively used model of this type developed by Watson et al.[30] is especially appropriate for use in overall diesel engine system simulations where the combustion process details are not the primary focus. It is based on Lyn's description of compression--ignition combustion—a rapid premixed burning phase followed by a slower mixing-controlled burning phase. The fraction of the injected fuel that burns in each of these phases is empirically linked to the duration of the ignition delay. One algebraic function is used to describe the premixed heat-release phase and a second function to describe the mixing-controlled heat-release phase. These two functions are weighted with a phase proportionality factor, β, which is largely a function of the ignition delay. Thus:

© McGraw-Hill Education. All rights reserved. Any use is subject to the Terms of Use, Privacy Notice and copyright information.

$$\frac{m_{f,b}(t')}{m_{f,0}} = \beta f_1 + (1-\beta) f_2$$

(14.45)

where $m_{f,b}$ is the mass of fuel burned, $m_{f,0}$ is the total fuel mass injected per cycle per cylinder, and t' is time from ignition non-dimensionalized by total time allowed for combustion [= $(t - t_{ign})/\Delta t_{comb}$].[3] The premixed-burning function f_1 is

$$f_1 = 1 - \left(1 - t'^{K_1}\right)^{K_2}$$

(14.46)

and the mixing-controlled function f_2 is

$$f_2 = 1 - \exp\left(-K_3 t'^{K_4}\right)$$

(14.47)

where K_1, K_2, K_3, and K_4 are empirical coefficients. The proportionality factor β was given by

$$\beta = 1 - \frac{a\phi^b}{\tau_{\mathrm{id}}^c}$$

(14.48)

where ϕ is the overall fuel/air equivalence ratio and a, b, and c are empirical constants. Correlation with data from a typical turbocharged truck engine gave expressions for K_1 to K_4.[4]

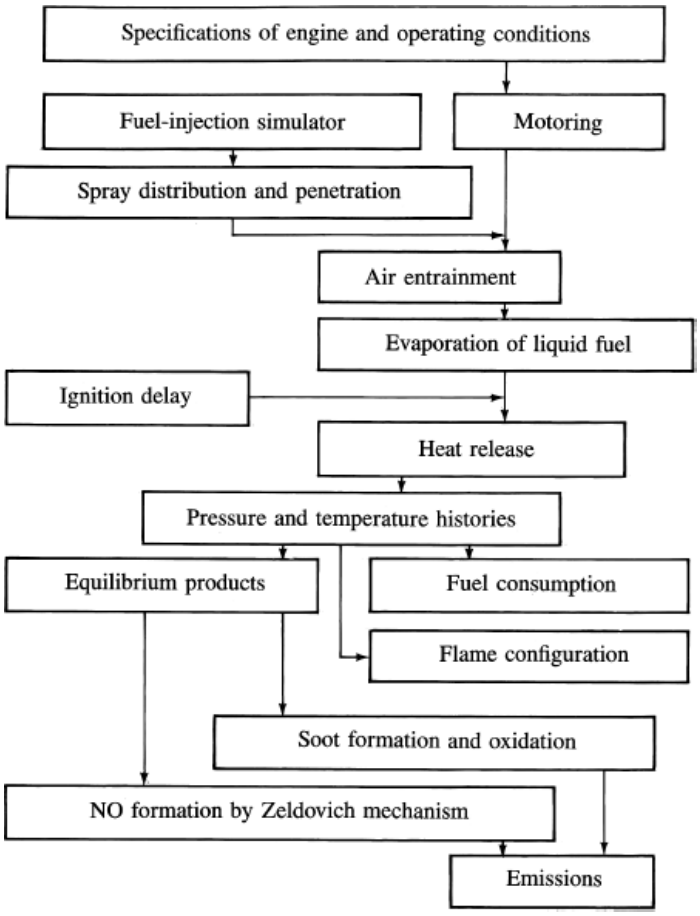
Such single-zone heat-release models can be useful because of their simplicity. They obviously cannot relate engine design and operating variables explicitly to the details of the combustion process. Experience indicates that one-zone combustion models with only one functional equation are not usually able to fit experimentally determined heat-release profiles with sufficient accuracy. Single-zone heat-release models should be checked against experimentally derived heat-release profiles and recalibrated, if necessary, before being used for predictions.

The overall structure of complete thermodynamic-based phenomenological models for predicting diesel engine performance and emissions requires much more than a combustion model. All the important processes (intake, compression, combustion, expansion, heat transfer, NO_x and particulate emissions formation mechanisms) must be included and connected. Figure 14.16 illustrates the major components and layout of such *engine cycle simulations*. As is clear, many different complex sub-models have to come together. An example of a diesel spray development and combustion model is shown in Fig. 14.17. It is based on a spray model with many small packets, each with the same fuel mass, from injection through combustion. The intent is to follow the spray development in a swirling airflow and the spray interaction with the combustion chamber walls. The liquid fuel which enters the chamber through the injector nozzle is divided into many small equal mass "elements." The spray motion is defined by an experimentally based correlation. Air entrainment is calculated from momentum conservation and the spray velocity decrease predicted by this correlation. The processes which occur within each element are also illustrated in Fig. 14.17. The fuel drops evaporate and fuel vapor mixes with entrained air. When ignition occurs, combustible mixture prepared before ignition burns rapidly. The continuation of the burning process may be limited by either the rate of production of fuel vapor by evaporation or the availability of air by the rate of entrainment (paths *A* and *B* in Fig. 14.17). The growth of the spray is determined from the air entrainment into each element and the combustion-produced expansion of

© McGraw-Hill Education. All rights reserved. Any use is subject to the Terms of Use, Privacy Notice and copyright information.

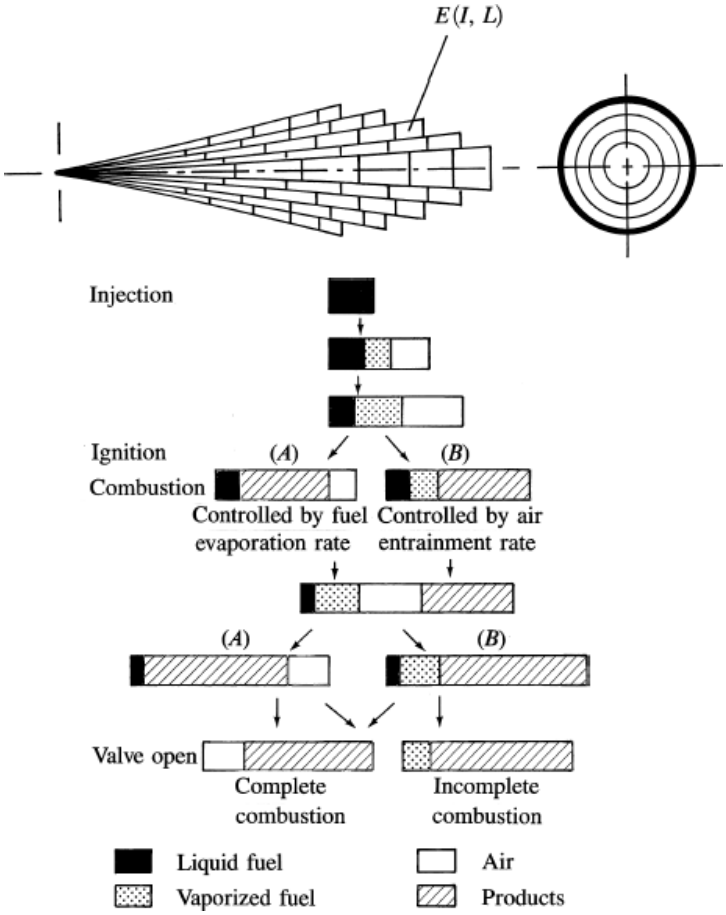
each element. When impingement on the wall occurs, the spray is assumed to spread along the wall. When the periphery of the spray reaches that of a neighboring spray, the sideways growth of the spray is then prevented and the thickness of the elements along the wall increases. Swirl effects are calculated from tangential momentum considerations.

Figure 14.16 Structure of thermodynamic-based DI diesel simulation for predicting engine performance and emissions.[31]



© McGraw-Hill Education. All rights reserved. Any use is subject to the Terms of Use, Privacy Notice and copyright information.

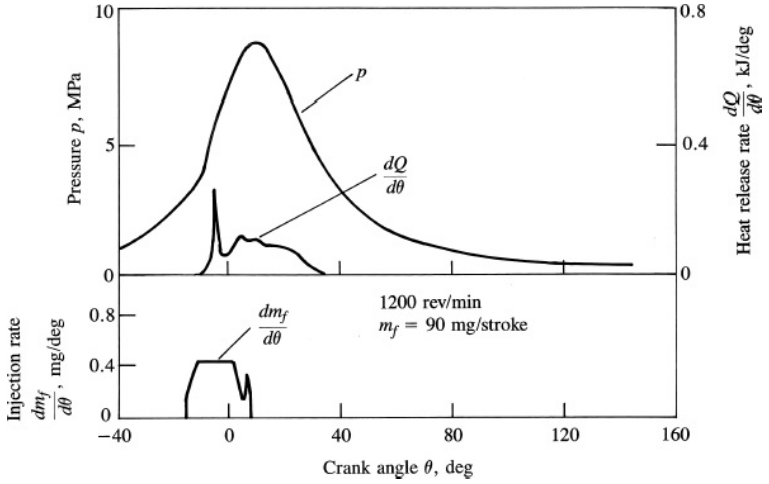
Figure 14.17 Schematic of spray model with many small packages, each with the same fuel mass, and of the processes that occur within each package, developed and used by Hiroyasu et al.[32]



The heat release rate in the combustion chamber is obtained by summing up the heat release in each element. Nitric oxide and soot formation calculations are based on the time histories of temperature, vaporized fuel, air and combustion products in each element. Figure 14.18 shows an example of the output from the above model. The injection rate diagram, the assumed Sauter mean drop size of the spray, and the air swirl determine the spray development, which leads to the heat-release rate predictions. This determines the cylinder pressure profile. Predicted engine performance results show reasonable agreement with data. A review of these types of jet models is given by Hiroyasu.[33]

© McGraw-Hill Education. All rights reserved. Any use is subject to the Terms of Use, Privacy Notice and copyright information.

Figure 14.18 Fuel injection rate, heat release rate profile, and cylinder pressure predicted with phenomenological DI diesel cycle simulation.[31]



Our understanding of diesel fuel spray behavior has advanced significantly from what these historical models assumed and could be included. Extensive correlations that describe the evolution of diesel fuel sprays are now available (see Secs. 10.4.2 to 10.4.6). The air entrainment process into each spray along the lift-off portion of the spray has been quantified. We now understand that the "rapid premixed" burning (second) phase occurs within each spray under fuel rich conditions, and the main burning phase occurs in the diffusion flame that rapidly envelops each developing fuel spray (see Sec. 10.3.4).

14.4.3.2. DI Gasoline Engines

Direct-injection gasoline-fueled spark-ignition engines can be operated in *homogeneous* or *stratified* mode. In homogeneous mode, the in-cylinder charge during combustion is usually well-enough mixed to be modeled as "uniform." However, direct injection into the in-cylinder charge does result in significant cooling of that charge as the fuel spray evaporates. With gasoline fuel, the maximum reduction in charge temperature is about 20° degrees C. Ethanol has a much higher heat of vaporization than gasoline: with 100% ethanol the maximum (potential) reduction is some 80 degrees C. Blends of ethanol with gasoline have evaporative cooling impacts that are linearly in between. Also, in homogeneous mode, especially when the engine has not fully warmed-up, the penetration and trajectory of the DI spray and consequent wall-wetting with liquid fuel can be important. Both these effects need to be modeled.

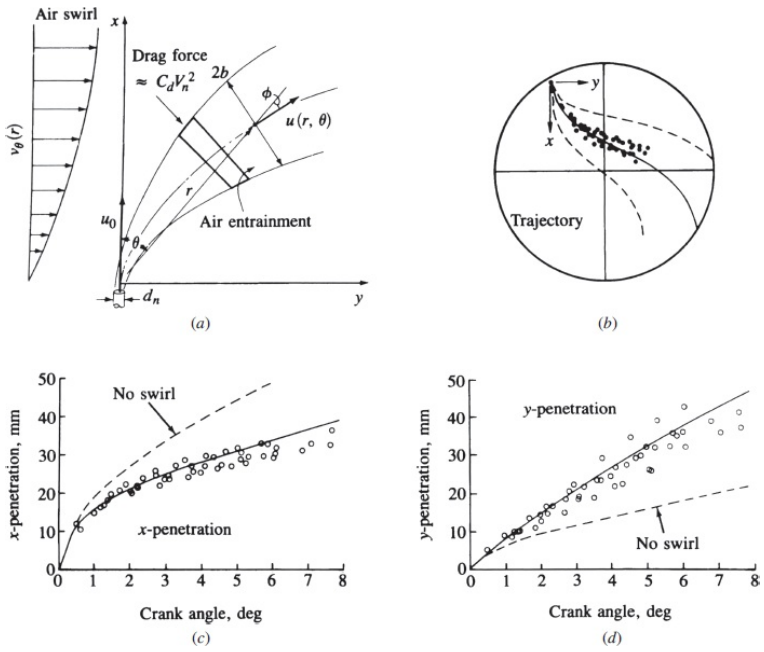
In stratified mode, usually at low- to mid-loads, a uniform in-cylinder mixture is not the objective. The injected fuel needs to mix with enough air yet stay confined within an evolving spray (or set of sprays) to form a "cloud" of close to stoichiometric mixture. Thus modeling the fuel spray trajectory and dispersion is an important task.

Figure 14.19 illustrates both the spray modeling approach, and an example of model results. The injected spray is analyzed as a quasi-steady one-dimensional turbulent gaseous jet.[34]. The intention is to describe the position of the jet as a function of time, as illustrated in Fig. 14.19*a*. Entrainment of air into the jet is assumed to take place at each point along the jet surface at a rate proportional to the velocity difference between the jet and surrounding air at that point. Two empirical entrainment coeffcients[35] are used for the proportionality constants for the relative motion in the jet axial and transverse directions. Conservation equations for fuel mass and total mass, and momentum (in two or three orthogonal directions) are used to determine the jet trajectory and size. The jet slows down due to air entrainment. Deflection of the jet results forms the entrainment of air with a momentum component normal to the jet axis, and forms drag forces due to the normal component of air flow past the jet. This approach does not define the velocity and concentration profiles across the jet: it only calculates the mean values at any jet axial position. Experimentally determined radial profiles for an axisymmetric turbulent jet[36] are often assumed. Although the fuel spray is initially mainly liquid, the fuel drops soon become a small fraction of the jet volume due to

© McGraw-Hill Education. All rights reserved. Any use is subject to the Terms of Use, Privacy Notice and copyright information.

vaporization and air entrainment. Downstream of the initial liquid breakup region, the velocity of the drops relative to that of the vaporized fuel and air is small, so the spray acts as a gaseous jet.

Figure 14.19 (a) Schematic of one-dimensional quasi-steady fuel spray model used to define spray centerline trajectory and width as the outward-moving spray interacts with the swirling airflow. (b) Spray trajectory and width calculated using a one-dimensional quasi-steady spray model of the type illustrated in (a), compared with experimental data taken in special visualization direct-injection stratified-charge engine. (c) and (d) Jet penetration as a function of time with and without swirl.[37]



In this comparison between a gaseous jet model and an experimental engine spray, shown in Fig. 14.19*b*, *c*, and *d*, a single fuel jet was injected into a disc-shaped chamber in the location shown, and Schlieren photography used to observe the spray trajectory. Good agreement was obtained for the spray center-line: note the significant effect of swirl. Reasonable agreement was also obtained between predicted and measured spray boundaries.

Combustion models for stratified operation of DI gasoline engines are more complex. Combustion of the stratified in-cylinder mixture usually occurs in two stages (see Sec. 9.3.5). The spray region or fuel vapor/air cloud where much of the fuel-air mixture will readily burn (since it is close to stoichiometric and has a high laminar flame speed) is ignited by the spark discharge, and a turbulent thin wrinkled-laminar flame propagates through this partially premixed region. This is followed by the still-rapid burnout of locally rich regions behind the flame front as oxygen from leaner regions and some of the surrounding air-mix into the hot post flame gases. Then a slower mixing-controlled combustion occurs of the remaining fuel-rich pockets, such as that resulting from the last-injected fuel, which enters the combustion chamber at lower velocity with poorer atomization and thus slower fuel-air mixing.

Models that analyze such a complex combustion process embedded in the fuel spray evolution and geometric detail (location of the spark plug and piston bowl in the context of the spray location and composition) are built into professional engine simulation software such as GT-Power.[3] (See Sec. 14.4.5.)

14.4.4. Prechamber Engine Models

Historically, small high-speed compression-ignition engines used an auxiliary combustion chamber, or prechamber, to achieve high fuel-air mixing rates. The prechamber was connected to the main combustion chamber above the piston via a nozzle,

© McGraw-Hill Education. All rights reserved. Any use is subject to the Terms of Use, Privacy Notice and copyright information.

passageway, or one or more orifices (see Secs. 1.9, 8.7, and 10.2.2). Auxiliary chambers have sometimes been used in spark-ignition engines, also. The plasma and flame-jet ignition systems described in Sec. 9.5.3 enclose the spark plug in a cavity or small prechamber which connects to the main chamber via one or more orifices. The function of the prechamber is to increase the initial growth rate of the flame. Combustion in the main chamber is initiated by one or more flame jets emanating from the prechamber created by the ignition process and subsequent energy release within the prechamber. If the mixture within the prechamber is richer than that in the main chamber (due to fuel injection or a separate prechamber intake valve—see Sec. 1.9), these are called stratified-charge engines.

The additional phenomena which these prechambers introduce beyond those already present in conventional chamber engines are: (1) gas flows through the nozzle or orifice between the main chamber and prechamber due to piston motion; (2) gas flows between these chambers due to the combustion-generated pressure rise; and (3) heat is transferred to the nozzle or passageway walls due to these flows. The first of these phenomena results in nonuniform composition and temperature distributions between the main and prechamber due to gas displacement primarily during compression, and determines the nature of the flow field within the prechamber toward the end of compression just prior to combustion. The second phenomenon controls the rate of energy release in the main chamber. The heat losses in the passageway and to the additional chamber surface area of the prechamber designs relative to conventional open chambers result in decreased engine performance and efficiency. Thus the prechamber concept adds additional complexity to the engine processes that must be modeled to predict engine behavior.

The following variables are important to prechamber engine performance and emissions characteristics, in addition to the design and operating variables which govern single-chamber engine behavior: prechamber geometry—size, shape, flow area, and shape of connecting passageway(s); prechamber location in relation to main chamber geometry; geometry and timing of any auxiliary prechamber valve; fuel metering strategy in prechamber compression-ignition or stratified-charge engines. Thermodynamic-based models have been developed and used to examine the overall impact of these variables (see Ref. 38). CFD models (see Sec. 14.5) have also been used to examine specific prechamber engine flow and combustion processes.

Useful predictions of fuel, air, and residual gas distributions and the corresponding temperature within the prechamber and main chamber can be obtained with simple gas displacement models. Only during combustion is the pressure difference across the nozzle or orifice sufficiently large in magnitude for its modeling to be essential; the assumption of uniform pressure during compression, the critical process for determining conditions just prior to combustion, introduces little error into calculations of the flows between the chambers. Section 8.5 develops the appropriate equations for these piston-motion driven gas displacements. Use of the conservation equations for an open system, for total mass, fuel mass, residual gas, and energy given in Sec. 14.2, for the main chamber and the prechamber, then give the mean composition and temperature variation in each chamber as a function of time due to this flow.

During combustion, the pressure difference across the connecting passageway or orifice is the driving force for the flow between chambers. Since combustion starts in the prechamber, the initial flow is into the main chamber; later, as the heat release in the main chamber becomes dominant, the flow may reverse direction and be into the prechamber. In thermodynamic-based models, the equations for one-dimensional quasi-steady ideal gas flow through a restriction given in App. C are used to relate these flows to the pressure difference between the two chambers. Open-system conservation equations are again used to calculate mean properties in each chamber.

Combustion models used are either empirically based [e.g., using specified heat-release or mass burning rates such as Eq. (14.32)[39]] or are developed from direct-injection compression-ignition engine models with spray evaporation, fuel-air mixing, and ignition delay processes explicitly included.[40] Because of the complexity of these processes in the prechamber engine geometry, substantial simplifying assumptions and empiricism must be used.

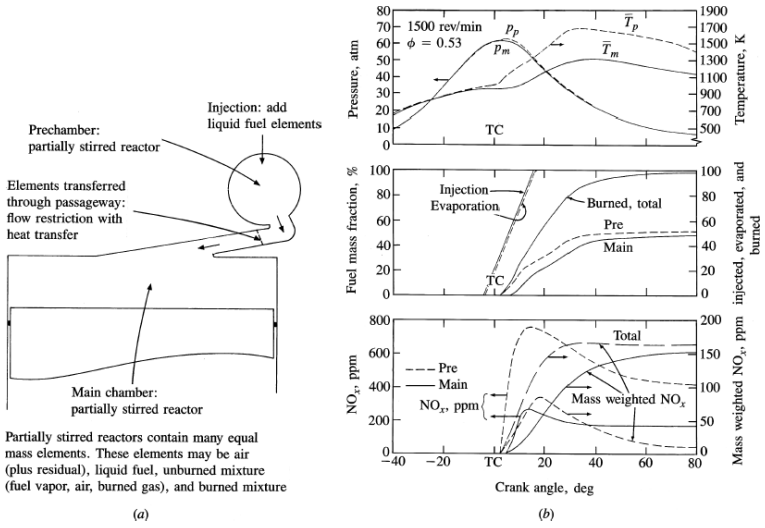
Heat transfer to the passageway and chamber walls is affected by the flows between the chambers: high velocities within the passageway result in high heat-transfer rates to the passageway walls, and the vigorous flows set by the passageway exit flow entering the prechamber or the main chamber increase heat-transfer rates to the walls of these chambers. The standard engine heat-transfer correlations which relate the heat-transfer coefficient to mean flow field variables via Nusselt-Reynolds number relationships (see Sec. 12.4) are normally used to describe these heat-transfer processes. The length scales are

© McGraw-Hill Education. All rights reserved. Any use is subject to the Terms of Use, Privacy Notice and copyright information.

chosen to match the prechamber or main chamber or passageway dimensions. The characteristic velocities in these relationships are equated with velocities which are representative of the flow in each of these regions at the relevant time in the engine operating cycle.[41,42]

The utility of the more sophisticated of these prechamber engine performance and emissions models is illustrated by the results shown in Fig. 14.20. This simulation of the indirect-injection compression-ignition engine's flow and combustion processes describes, through the use of stochastic mixing models, the development of the fuel/air ratio distribution and fuel-energy release distribution, and hence the development of the gas pressure and gas temperature distribution, within the prechamber and main chambers of the engine. With the (nonuniform) gas composition and state defined, the models for NO formation described in Sec. 11.2.1 was used to predict NO_x emissions. The approaches used to describe the evolution of the prechamber, main chamber, and passageway contents are summarized in Fig. 14.20*a*.

Figure 14.20 (a) Schematic of IDI diesel engine illustrating how stochastic mixing models are applied to the prechamber and main chamber, with a connecting passageway, to simulate turbulent mixing processes and pressure-driven flows; (b) example of simulation predictions through the engine's operating cycle. Shown are prechamber and main chamber pressures, prechamber and main chamber average gas temperatures; fuel mass injected, evaporated, and burned in prechamber and main chamber; average NO_x concentration in each chamber (and total) in ppm (by volume) and mass weighted ppm (mass in chamber × NO_x concentration in chamber/total mass in cylinder).[43]



The cylinder contents were divided up into a large number of elements. Pairs of elements are selected at random to undergo "turbulent mixing" interactions at a frequency related to the turbulence in each region. Rate processes—evaporation, ignition, NO formation, etc.—proceed within each element between these mixing interactions. Figure 14.20*b* shows sample results. At about TC, after some of the injected fuel has evaporated and the ignition delay is over, combustion starts in the prechamber and the prechamber pressure p_p rises above the main chamber pressure p_m. This forces air, fuel, and burned gases to flow from the prechamber into the main chamber; fuel and rich products can now mix with air and burn in the main chamber. NO starts to form in each mass element once it burns, at a rate dependent on each element's composition and state. Most of the NO forms within the prechamber and then flows into the main chamber as the expansion process proceeds. The attractive feature of this type of emission calculation is that the kinetically controlled NO formation calculations are based directly on local gas composition and temperature in a manner that approximates the mean and turbulent nonuniformities in these variables. Predictions of engine operation and emissions showed good agreement with data.[43]

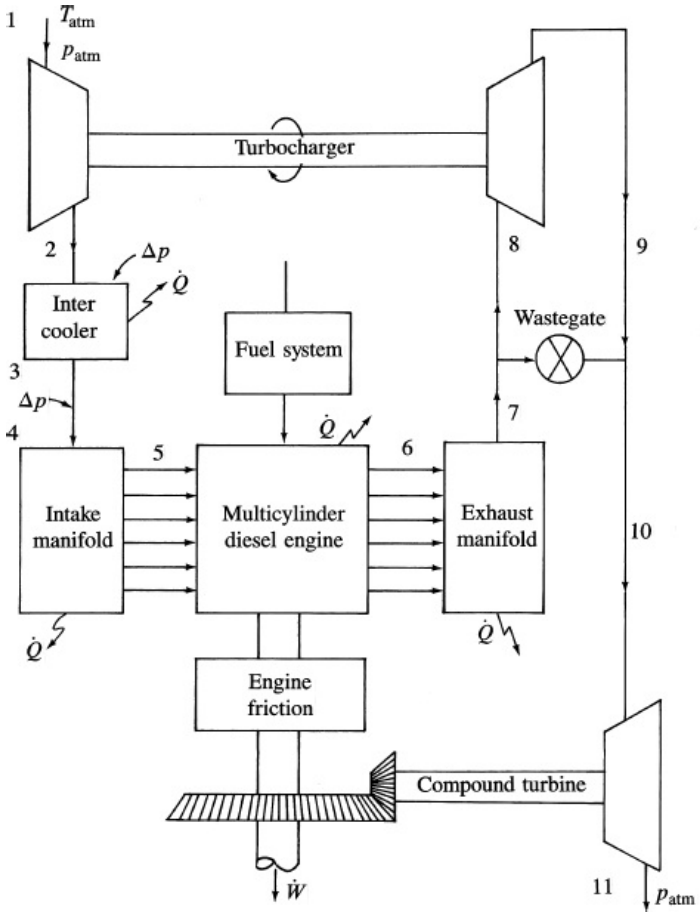
14.4.5. Multi-Cylinder and Complex Engine System Models

© McGraw-Hill Education. All rights reserved. Any use is subject to the Terms of Use, Privacy Notice and copyright information.

The models discussed in the previous parts of Sec. 14.4 focus on the processes occurring within *each* cylinder of an internal combustion engine. Most engines are multi--cylinder engines and the individual cylinders interact via the intake and exhaust manifolds. Also, many engine systems are more complex: internal combustion engines can be supercharged, turbocharged, or turbocompounded, and the manifolds then connect to the atmosphere via compressors or turbines (see Fig. 6.45 and Sec. 6.8). Thermodynamic-based simulations of the relevant engine processes, constructed from the types of model components already described, prove extremely useful for examining the behavior of these more complex engine systems. By describing the mass and energy flows between individual components and cylinders of such systems throughout the engine's operating cycle, the total system performance can be predicted. Such models have been used to examine steady-state engine operation at constant load and speed (e.g., where time-varying conditions in the manifolds due to individual cylinder filling and emptying events affect multi-cylinder engine behavior), and how the total system responds to changes in load and speed during engine transients.

The block diagram of a turbocharged and turbocompounded diesel engine system in Fig. 14.21 illustrates the interactions between the system components. By describing the mass and energy flows between components and the heat and work transfers within each component, total system behavior can be studied. In such engine simulations, the reciprocator cylinders, the intake manifold, and the various sections of the exhaust system are treated as connected open systems. The flows into and out of these volumes are usually analyzed using the quasi-steady emptying and filling approach described in Sec. 14.3.3, using the open-system conservation equations of Sec. 14.2. The reciprocator cycle is treated as a sequence of processes within each cylinder: intake, compression, combustion expansion, and exhaust. These are modeled using the approaches described previously in Secs. 14.4.1 to 14.4.4. Heat transfer has, of course, an important effect on the in-cylinder processes. It also is important in the exhaust system since the performance of the turbocharger turbine and of any compounded turbine depends on the gas state at turbine inlet. The performance of the turbomachinery components is normally defined by maps that interrelate efficiency, pressure ratio, mass flow rate, and shaft speed for each component (see Secs. 6.8.2 to 6.8.4).

Figure 14.21 Block diagram of turbocharged turbocompounded diesel engine system.[2]



© McGraw-Hill Education. All rights reserved. Any use is subject to the Terms of Use, Privacy Notice and copyright information.

When a reciprocating engine is coupled with turbomachinery, its manifolds no longer connect directly with the atmosphere: matching procedures are required to ensure that the pressure levels and mass flow rates of the compressor and turbines match with those of the engine. The following matching process is typical of those used for the simpler type of turbocharged engine (one compressor and one turbine). At a given time, the values of the variables describing the state of the various system components are known (from integration of the system governing equations over the previous time step). These include the intake and exhaust manifold pressures and the turbocharger rotor speed. The compressor inlet pressure is atmospheric pressure less the intake air-filter pressure drop. The turbine exit pressure is atmospheric plus the aftertreatment system, the exhaust system, and muffler pressure drops. By relating the compressor discharge pressure to the intake manifold pressure, and the turbine inlet pressure to the exhaust manifold pressure (incorporating suitable pressure drops), the pressure ratio across each machine is determined. Hence, the compressor and turbine maps can be entered using the calculated pressure ratios and the rotor speed as inputs (the latter the same for both the compressor and turbine). The output from the map interpolation routines determines the mass flow rate and efficiency of each component for the next time step. From these, the power required to drive the compressor $\left(-\dot{W}_C\right)$, and to drive the turbine $\left(\dot{W}_T\right)$ are determined from Eqs. (6.42) and (6.48), respectively. Any excess power (or power deficiency) will result in a change of rotor speed according to the turbocharger dynamics equation

$$\dot{W}_C + \dot{W}_T = I_{\mathrm{TC}}\omega\frac{d\omega}{dt} + B\omega^2$$

(14.49)

where I_{TC} is the rotational inertia of the turbocharger, ω is its angular velocity, and B is the rotational damping. The values of the other state variables for the next time step are determined from the solution of the mass and energy conservation equations for each open system, with the compressor and turbine mass flows taken from the output of the turbomachinery map interpolation routines.

This approach can be used to establish the steady-state engine operating characteristics from an assumed initial set of state variables. (Of course, due to the pulsating nature of the flows into and out of the cylinders, these state variables will vary in a periodic fashion throughout the engine cycle at a fixed engine load and speed.) This approach can also be used to follow transient engine behavior as load or speed is varied from such a steady-state condition. The additional inputs required are the fuel pump delivery characteristics as a function of fuel pump rack position and speed, with the latter evaluated from an appropriate model for dynamic behavior of the fuel system. From the brake torque of the engine T_B (determined by subtracting friction torque from the indicated torque), the torque required by the load T_L, the inertia of the engine and the load I_E and I_L, the dynamic response of the engine and load to changing fuel rate or engine speed can be obtained from

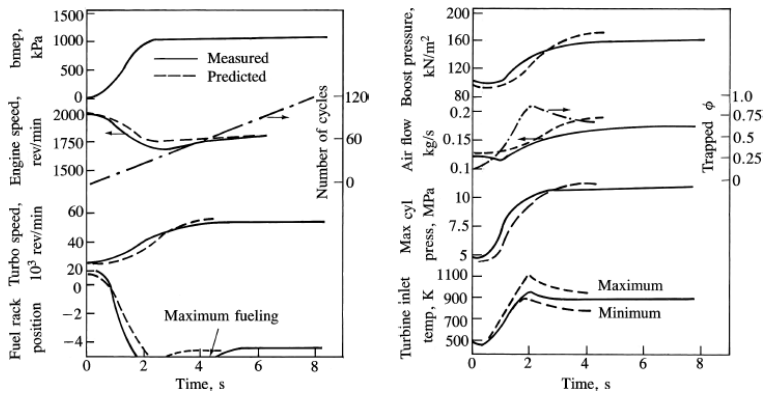
$$T_B - T_L = (I_E + I_L)\frac{d\omega}{dt}$$

(14.50)

An example of the output from this type of engine model is plotted in Fig. 14.22 where the response of a turbocharged DI diesel engine to an increase in load from 0 to 95% of full load is shown. The predictions come from a model of the type shown in Fig. 14.21, and engine details correspond to the experimental configuration.[44] The simulation follows the data through the engine transient with reasonable accuracy. Note that with the assumed fuel injection system response, during this transient the equivalence ratio of the trapped mixture rises to close to stoichiometric because the increase in air flow lags the increase in fuel flow. This would result in excessive smoke emissions. Such models prove extremely useful for exploring the effect of changes in engine system design on transient response.[45]

© McGraw-Hill Education. All rights reserved. Any use is subject to the Terms of Use, Privacy Notice and copyright information.

Figure 14.22 Predicted (– – –) and measured (—) response of a turbocharged direct-injection diesel engine to an increase in load.[44]



For two-staged turbocharged or turbocompounded systems the engine turbocharger matching process is more complicated. The division of the pressure ratio between the exhaust manifold and atmosphere between the two turbines in Fig. 14.21 is not known *a priori*. Nor, with two compressors, is the intake pressure ratio distribution known. Iterative procedures based on an assumed mass flow rate are used to determine the pressure level between the two turbines such that mass flow and pressure continuity through the exhaust system are satisfied (e.g., Ref. 2).

Commercial engine simulation software for analyzing the performance and emissions of internal combustion engines of many types and sizes are now available at high levels of sophistication and completeness. One such widely-used and comprehensive model is GT-Power.[3] It can be used to analyze naturally-aspirated, turbocharged, supercharged, turbocompounded, spark-ignition, diesel, homogeneous-charge compression-ignition (HCCI) engines, operating on a range of fuels. It can predict steady-state or transient engine behavior. It incorporates variable valve timing and lift. It calculates, from the basic principles reviewed in this section, airflow and volumetric efficiency, fuel consumption and fuel conversion efficiency, torque and power curves, and emissions. It does acoustic analysis of intake and exhaust systems, analysis of emissions reductions in exhaust aftertreatment systems (catalysts and filters), and finite-element thermal analysis of manifold and cylinder components.

14.4.6. Second-Law Analysis of Engine Processes

The first-law-based methods for evaluating power plant performances do not explicitly identify those processes within the engine system that cause unrecoverable degradation of the thermodynamic state of the working fluid. However, second-law-based analysis methods do provide the capability to identify and quantify this unrecoverable energy degradation. The cause and effect relationships that relate these losses to individual engine processes can, therefore, be determined. The first-law analysis approaches summarized in this section (14.4) are based on the fact that energy is conserved in every engine component and process. Thus, they take account of the conversion of energy from one form to another: for example, chemical, thermal, and mechanical. Although energy is conserved, second-law analysis indicates that various forms of energy have differing levels of ability to do useful work. This ability to perform useful work is defined as *availability*.

The availability of a system at a given state is defined as the amount of useful work that could be obtained from the combination of the system and its surrounding atmosphere, as the system goes through reversible processes to equilibrate with the atmosphere. It is a property of the system and the environment with which the system interacts, and its value depends on both the state of the system and the properties of the atmosphere. Availability is not a conserved property; availability is destroyed by irreversibilities in any process the system undergoes. When availability destruction occurs, the potential for the system to do useful work is permanently decreased. Thus to make a proper evaluation of the processes occurring within an engine system, both energy and availability must be considered concurrently.

© McGraw-Hill Education. All rights reserved. Any use is subject to the Terms of Use, Privacy Notice and copyright information.

The basis for an availability analysis of realistic models of internal combustion engine processes has already been developed in Sec. 5.7. The change in availability of any system undergoing any process where work, heat, and mass transfers across the system boundary occur (see Fig. 5.13) can be written as

$$\Delta A = A_{\text{in}} - A_{\text{out}} - A_{\text{destroyed}}$$

(14.51)

where A_{in} and A_{out} represent the availability transfers into and out of the system across the system boundary. Since availability is not a conserved quantity, this equation can only be used to solve for the availability destruction term, $A_{\text{destroyed}}$. Table 14.2 summarizes the equations for the availability change of the system and the availability transfers associated with work, heat and mass transfer across the system boundary, developed in Sec. 5.7.

Table 14.2 Available energy equations for various processes

Mechanism	Equation
Work transfer	$dA_w = dW$
Heat transfer	$dA_Q = dQ\,(1 - T_0/T)$
Gas transfer	$dA_g = dm_g\,[(h - h_0) - T_0\,(S - S_0)]$
Liquid fuel transfer*	$dA_f = dm_f(1.0338Q_{\text{LHV}})$
Control volume storage	$dA_{\text{cv}} = d\,\{m_{\text{cv}}\,[(u - u_0) - T_0\,(s - s_0) + p_0\,(v - v_0)]\}$
*The availability of the fuel is 1.0338 times its lower heating value; see Sec. 5.7.	
Note: Subscript zero denotes the property value at standard atmospheric conditions.	

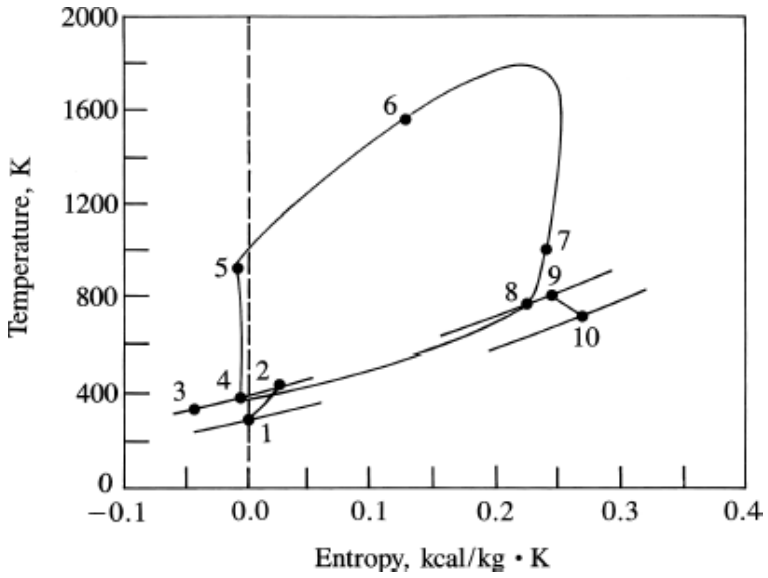
This availability balance is applied to the internal combustion engine operating cycle as follows. A first-law-based cycle analysis of the type described above in this section (14.4) is used to define the variation in working fluid thermodynamic state, and the work, heat, and mass transfers that occur in each of the processes that make up the total engine cycle. Integration of the availability balance over the duration of each process then defines the magnitude of the availability destruction that occurs during that process.

To illustrate this procedure, consider the operating cycle of a 10-liter six-cylinder turbocharged and aftercooled direct-injection four-stroke cycle diesel engine, operating at its rated power and speed of 224 kW and 2100 rev/min. The variations in temperature, energy, and entropy are determined with a first-law-based analysis. Figure 14.23 shows the *T-s* diagram for the working fluid as it goes through the sequence of processes from air inlet from the atmosphere (state 1) to exhaust gas exit to the atmosphere (state 10).[46] The incoming air is compressed (with some irreversibility) in the turbocompressor to state 2 and cooled with an aftercooler to state 3. The air at state 3 is drawn into the cylinder and mixed (irreversibly) with residual gases until, at the end of the intake process, the cylinder gases are represented by state 4. That mixture is subsequently compressed (with modest heat loss) to state 5. Fuel addition commences close to state 5; subsequent burning increases the combustion chamber pressure and temperature along the line 5-6. At 6 the heat release, heat transfer, and volume change rate are such that the maximum cylinder pressure is reached (a few degrees after TC). From 6 to 7, combustion continues to completion, the burned gases continue to expand doing work on the piston and losing heat to the walls. At state 7 the exhaust valve opens initiating a rapid pressure equilibration with the exhaust manifold to a pressure corresponding to point 8. Gases are expelled from the cylinder into the exhaust manifold. After the intake valve opens, in-cylinder residual gases mix with incoming air at

© McGraw-Hill Education. All rights reserved. Any use is subject to the Terms of Use, Privacy Notice and copyright information.

state 3 to yield gases at state 4 to complete the cycle. The exhaust gases that have been expelled from the cylinder experience additional thermodynamic losses and can be represented by state 9. These gases then pass through the turbocharger turbine to state 10 to provide the work needed to drive the compressor.

Figure 14.23 T-s diagram for the working fluid as it goes through the sequence of processes from intake to exhaust in a turbocharged aftercooled DI diesel engine. The 10-liter six-cylinder engine is operated at its rated power (224 kW) and speed (2100 rev/min). The text relates the processes occurring to the numbered end states.[46]



A first-law and second-law analysis of a naturally-aspirated diesel engine are compared in Table 14.3. Also shown is a second-law analysis of a turbocharged version of this engine. These results illustrate the value of defining the losses in availability that occur in each process.

© McGraw-Hill Education. All rights reserved. Any use is subject to the Terms of Use, Privacy Notice and copyright information.

Table 14.3 Comparison of first- and second-law analysis for six-cylinder 14-liter naturally-aspirated and turbocharged diesel engine at 2100 rev/min[47]

	First law, % fuel energy	Naturally-aspirated	Turbocharged
		Second law, % fuel availability	
Indicated work*	40.3	39.1	43.9
Combustion loss	—	15.9	19.2
Cylinder heat transfer	25.1	21.4	17.6
Intake valve throttling	—	0.7	0.7
Exhaust valve throttling	—	2.5	2.3
Loss in compressor	—	—	1.4
Loss in turbine	—	—	0.8
Exhaust to ambient	34.6	20.4	14.1
Total	100.0	100.0	100.0
Brake power, kW	185	185	220

*Note that the indicated work for the second-law balance is a lower percentage than for the first-law balance. This occurs because the availability of the fuel is 1.0317 times the fuel's heating value.

Consider the first- and second-law analysis results for the naturally-aspirated engine. While 25.1% of the fuel energy leaves the combustion chamber in the form of heat transfer, the availability transfer corresponds to 21.4% of the fuel's availability. It is this latter number that indicates the maximum amount of the heat transfer that can be converted to work. The table shows that 34.6% of the fuel energy is carried out of the engine in the exhaust gases. However, the second-law analysis shows that the exhaust contains only 20.4% of the available energy of the fuel. The ratio of these quantities shows that only about 60% of the exhaust energy can be converted to work using ideal thermodynamic devices.[5] The exhaust gas leaves the system in a high-temperature ambient-pressure state, and therefore has high entropy (relative to the p_0, T_0 reference state). This, via the gas-transfer equation in Table 14.2, reduces the available energy of the exhaust gas stream.

The quantity referred to as combustion loss in Table 14.3 is determined from an availability balance for the combustion chamber over the duration of the combustion period. The "availability destroyed" term in Eq. (14.51) then represents the deviation of the actual combustion process from a completely reversible process. The second-law analysis shows that the availability loss associated with the combustion irreversibilities is 16 or 19% of the fuel's availability. This loss depends on the overall equivalence ratio at which the engine is operating, as indicated in Fig. 5.17. Combustion of leaner air/fuel ratios would give a higher fractional availability loss due to mixing of the fuel-air combustion products with the increased amounts of excess air and the lower bulk temperature, as evidenced by the turbocharged engine value.

Overall, the most important point emerging from this comparison is that the work-producing potential of the heat loss to the combustion chamber walls and the exhaust mass flow out of the engine is not as large as the magnitude of the energy transferred out of the cylinder: some of these energy transfers, even with ideal thermodynamic work-producing devices, must ultimately be rejected to the environment as heat.

A comparison of the second and third columns in Table 14.3, both obtained with a combined first- and second-law analysis, illustrates how turbocharging improves the performance of a naturally-aspirated engine. The brake fuel conversion efficiency

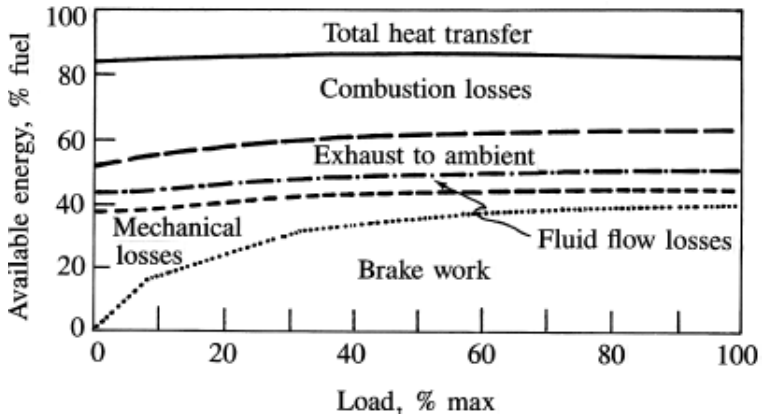
© McGraw-Hill Education. All rights reserved. Any use is subject to the Terms of Use, Privacy Notice and copyright information.

of the turbocharged engine is considerably improved—from 33.9 to 39.2%. The table indicates that through turbocharging, the availability transfers associated with the heat loss and exhaust gas flow are reduced from 41.8 to 31.7% (a difference of 10 percentage points), while the combustion and added turbomachinery availability losses increase from 15.9 to 21.4% (a difference of about 5 percentage points). By turbocharging, advantage has been taken of the following changes. While the leaner air/fuel ratio operation of the turbocharged engine increases the combustion availability losses due to the use of a greater portion of the chemical energy of the fuel to mix with and heat excess air, the lower burned gas temperature this produces results in reduced heat losses and lower cylinder exhaust temperature. In addition, the turbocharger transfers available energy from the cylinder exhaust to the inlet air. The reduced heat loss and lower final exhaust availability level give a substantial performance improvement.[47]

To interpret the second-law analysis results, one must remember that the desired output is brake work and increases in this quantity (for a given fuel flow) represent improved performance and efficiency. All other availability terms represent losses or undesirable transfers from the system; decreasing these terms constitutes an improvement. These undesirable available energy transfer and destruction terms fall into five categories: (1) heat transfer; (2) combustion; (3) fluid flow; (4) exhaust to ambient; and (5) mechanical friction. The available energy flows identified as heat transfer represent the summation of all availability transfers that occur due to heat transfers. The most significant of these are the in-cylinder and aftercooler heat rejection. The combustion loss represents the amount of available energy destroyed due to irreversibilities occurring in releasing the chemical potential of the fuel as thermal energy and mixing the combustion products with any excess air. The fluid flow losses include the available energy destroyed within the working fluid in the compressor, aftercooler, intake valve, exhaust valve, exhaust manifold, and turbine due to fluid shear and throttling. The availability destroyed due to lubricant shear and mechanical rubbing friction is separate from these working-fluid process availability losses.

Figure 14.24 shows the availability transfers or losses in each of these categories for a turbocharged six-cylinder 10-liter displacement direct-injection diesel engine, expressed as a percentage of the fuel availability, as a function of engine load. The percentage of fuel availability associated with the heat transfers varies little over the load range. The combustion loss increases from 22 to 33% as load is decreased due to the increasingly lean operation of the engine. Fluid friction losses, as a percentage, increase slightly as load increases due to larger mass flow rates. Since total engine friction is approximately constant in absolute magnitude, its relative importance increases drastically as the brake output goes to zero. Exhaust flow available energy decreases from 12 to 8% as load is decreased from 100 to 0%.

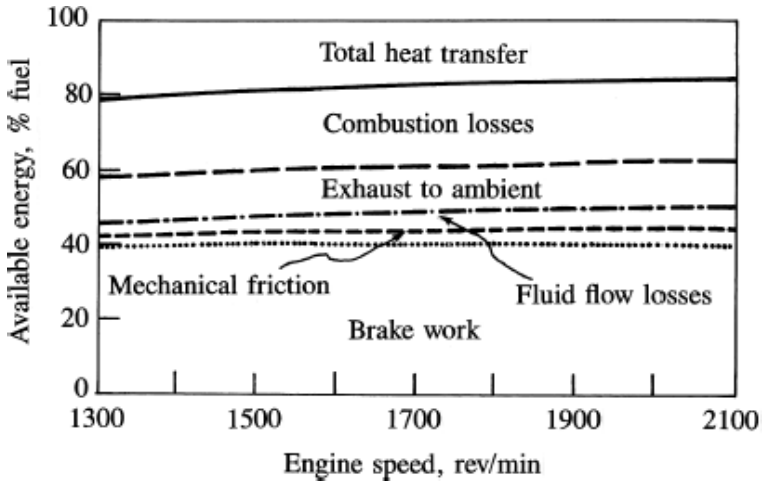
Figure 14.24 Distribution of available energy into major categories for the engine of Fig. 14.23 as a function of engine load.[46]



The effect of varying engine speed (at full load) is shown in Fig. 14.25. The availability associated with heat transfer changes over the speed range from 16 to 21%: more time during each cycle is available for heat transfer at lower speeds. Fluid flow and friction losses decrease slightly with decreasing speed. Other availability losses remain essentially constant as a percentage of the fuel's availability.[46]

© McGraw-Hill Education. All rights reserved. Any use is subject to the Terms of Use, Privacy Notice and copyright information.

Figure 14.25 *Distribution of available energy into major categories for the engine of Fig. 14.23 as a function of engine speed.*[46]



[1] Note that the center of this sphere may be convected away from the spark plug location, especially if some swirl is present. However, only strong swirling and squish flows produce major distortions to the flame surface shape.

[2] This initial laminar flame propagation process can be expressed in terms of a flame radius at which the transition to a turbulent flame occurs.[19]

[3] The combustion duration Δt_{comb} is an arbitrary period within which combustion must be completed. A value of 125 degrees CA was used above.

[4] $K_1 = 2 + 1.25 \times 10^{-8}(\tau_{id}N)^{2.4}$,
$K_2 = 5000$,
$K_3 = 14.2/\phi^{0.644}$,
$K_4 = 0.79K_3^{0.25}$ where τ_{id}, the ignition delay, is in milliseconds and *N*, engine speed, is in revolutions per minute. This study also gave 0.8 < *a* < 0.95; 0.25 < *b* < 0.45; and 0.25 < *c* < 0.5.[30]

[5] Of course, real thermodynamic devices will produce less work than ideal devices.

© McGraw-Hill Education. All rights reserved. Any use is subject to the Terms of Use, Privacy Notice and copyright information.

14.5. FLUID-MECHANIC-BASED MULTI-DIMENSIONAL MODELS

14.5.1. Basic Approach and Governing Equations

The prediction of the details of the flow field within engines, and the heat-transfer and combustion processes that depend on those flow fields, by numerical solution of the governing conservation equations has become an important engineering goal. Such computational-fluid-dynamic (CFD) based modeling approaches have been developing for several decades. They are now able to predict the complex fluid flow behavior in engine components with realistic geometries. While the overall dynamic behavior of intake and exhaust flows can usefully be studied with one-dimensional unsteady fluid-dynamic computer calculations (see Sec. 14.3.4), flows within the cylinder and in the intake and exhaust ports are usually inherently unsteady and three dimensional. Increases in computing power, and the development of better-grounded turbulence and combustion models now make realistic three-dimensional calculations feasible. Gas-flow patterns can be predicted best; predictions of fuel spray behavior are less complete, and fundamentally based combustion and emissions calculations still present some accuracy challenges.

These CFD-based engine analysis codes solve the partial differential equations for conservation of mass, momentum, energy, and species concentrations. To apply digital computers to the solution of a continuum problem (such as the flow field inside the cylinder), the continuum must be represented by a finite number of discrete elements. The usual method of discretization is to divide the region of interest into a large number of small zones or cells. These cells form a grid or mesh which serves as a framework for constructing finite volume approximations to the governing partial-differential equations. The time variable is similarly discretized into a sequence of small time steps, and the transient solution is "marched out" in time: the solution at time t_{n+1} is calculated from the known solution at time t_n. Three-dimensional formulations of the finite-difference equations are required for most practical engine calculations.

The principal components of these multi-dimensional engine flow models are the following:[48]

- The mathematical equations used to describe the flow processes. Especially important is the turbulence model, which describes the small-scale features of the flow which are not readily accessible to direct calculation.
- The discretization procedures used to transform the differential equations of the mathematical model into algebraic relations between discrete values of velocity, pressure, temperature, etc., located on a computing mesh which conforms to the geometry of the combustion chamber with its moving valves and piston.
- The solution algorithm whose function is to solve the algebraic equations.
- The computer codes which translate the numerical algorithm into computer language and also provide easy interfaces for the input and output of information.

The basic equations for in-cylinder flow calculation methods are the differential equations expressing the conservation laws of mass, momentum (the Navier-Stokes equations—a set of three), energy, and species concentrations. These equations, in the above order, may be written:

$$\frac{D}{Dt}\begin{pmatrix}1\\ u_i\\ e\\ Y_\alpha\end{pmatrix}=\begin{pmatrix}0\\ 0\\ Q\\ S_\alpha\end{pmatrix}-\frac{\partial}{\partial x_j}\begin{pmatrix}0\\ \tau_{ij}\\ q_j\\ J_{\alpha i}\end{pmatrix}$$

© McGraw-Hill Education. All rights reserved. Any use is subject to the Terms of Use, Privacy Notice and copyright information.

(14.52)

The first term (on the right of the equals sign) gives the source terms, the second term the diffusive transport. The *D/Dt* operator provides the convective transport terms, and is

$$\frac{Df}{Dt} \equiv \frac{\partial(\rho f)}{\partial t} + \frac{\partial}{\partial x_j}\left(\rho u_j f\right)$$

(14.53)

Here, ρ is the density, u_i the ith velocity component, e the internal energy per unit mass, and Y_α the concentration of species α per unit mass.

In the IC engine context, the thermal energy source term Q involves a viscous dissipation term and source terms arising from chemical reaction of the fuel-air mixture. Both Q and the species source term, S_α, will depend upon the chemical rate equations, which must be known to close the problem. Note that diffusion of the various species contributes to the diffusive flow of internal energy, q_j, in addition to conductive heat diffusion.

The fact that turbulent flows exhibit important spatial and temporal variations over a range of scales (dictated at the upper end by chamber dimensions and at the lower end by viscous dissipative processes; see Sec. 8.2.1) makes direct numerical solution of these governing equations impractical for complex engine flows. Recourse must therefore be made to some form of averaging or filtering which removes the need for direct calculation of the small-scale motions. Two approaches have been developed for dealing with this turbulence modeling problem: full-field modeling (FFM), sometimes called statistical flux modeling; and large-eddy simulation (LES) or subgrid-scale simulation. In FFM, one works with the partial differential equations describing suitably averaged quantities, using the same equations everywhere in the flow. For periodic engine flows, time averaging must be replaced by ensemble or phase averaging (see Sec. 8.2.1). The variables include the velocity field, thermodynamic state variables, and various mean turbulence parameters such as the turbulent kinetic energy, the turbulent stress tensor, etc. In FFM, models are needed for various averages of the turbulence quantities. These models must include the contributions of all scales of turbulent motion.

Large-eddy simulation (LES) is an approach in which one actually calculates the large-scale three-dimensional time-dependent turbulence structure in a single realization of the flow. Thus, only the small-scale turbulence need be modeled. Since the small-scale turbulence structure is more isotropic than the large-scale structure and responds rapidly to changes in the large-scale flow field, modeling of the statistical fluxes associated with the small-scale motions is a simpler task than that faced in FFM where the large-scale turbulence must be included.

An important difference between FFM and LES is their definition of "turbulence." In FFM the turbulence is the deviation of the flow at any instant from the average over many engine cycles of the flow at the same point in space and oscillation phase [i.e., the fluctuation velocity defined by Eq. (8.16) or (8.18)]. Thus, FFM "turbulence" contains some contribution from cycle-by-cycle flow variations. LES defines turbulence in terms of variations about a local average; hence in LES turbulence is related to events in the current cycle.[49]

14.5.2. Turbulence Models

In *full-field modeling* (FFM), equations for the averaged variables are formed from Eqs. (14.52). With periodic engine flows, phase or ensemble averaging must be used (see Secs. 8.2.1 and 8.2.2). Since the flow during the engine cycle is compressed and expanded, mass-weighted averaging (called Favre averaging) can be used to make the averaged compressible-flow equations look almost exactly like the averaged equations for incompressible flows. The combined ensemble-Favre averaging approach works as follows.[49]

© McGraw-Hill Education. All rights reserved. Any use is subject to the Terms of Use, Privacy Notice and copyright information.

We denote the phase-averaging process by { }, that is:

$$\{\rho(\mathrm{x},t)\} = \lim_{N\to\infty}\frac{1}{N}\sum_{n=1}^{N}\rho(\mathrm{x},t+n\tau)$$

(14.54)

where τ is the cycle period. We also write
$\{\rho\} = \tilde{\rho}$, and decompose ρ into
$\rho = \tilde{\rho} + \rho'$. The mass-weighted phase-averaged quantities (indicated by an overbar) are defined by

$$\rho(\mathrm{x},t)\,\bar{f}\,(\mathrm{x},t) = \lim_{N\to\infty}\sum_{n=1}^{N}\rho(\mathrm{x},t+n\tau)\,f(\mathrm{x},t+n\tau)$$

(14.55)

where all flow variables (except density and pressure) have been decomposed as
$f = \bar{f} + f'$. Note that {ρ'} is zero,
$\{\bar{f}\} = \bar{f}$, the mass-weighted phase average of f' is zero, but {f'} is not zero. With these definitions:

$$\begin{aligned}
&\{\rho f\} = \tilde{\rho}\bar{f}\\
&\{\rho f'\} = 0\\
&\{\rho fg\} = \tilde{\rho}\left(\bar{f}\,\bar{g} + \overline{f'g'}\right)\\
&\{\rho fgh\} = \tilde{\rho}\left(\bar{f}\,\bar{g}\bar{h} + \bar{f}\,\overline{g'h'} + \bar{g}\overline{f'h'} + \bar{h}\overline{f'g'} + \overline{f'g'h'}\right)
\end{aligned}$$

(14.56)

Phase-averaging Eq. (14.54), one obtains[49]

$$\frac{\overline{D}}{Dt}\begin{pmatrix}1\\ u_i\\ e\\ \overline{Y}_\alpha\end{pmatrix} = \begin{pmatrix}0\\ 0\\ \{Q\}\\ \{S_\alpha\}\end{pmatrix} - \frac{\partial}{\partial x_j}\begin{pmatrix}0\\ \{\tau_{ij}\}\\ \{q_j\}\\ J_{\alpha j}\end{pmatrix} - \frac{\partial}{\partial x_j}\begin{pmatrix}0\\ \tilde{\rho}\overline{u_i'u_j'}\\ \tilde{\rho}\overline{e'u_j'}\\ \tilde{\rho}\overline{Y_\alpha'u_j'}\end{pmatrix}$$

(14.57)

where

$$\frac{\overline{D}\bar{f}}{Dt} = \frac{\partial}{\partial t}\left(\tilde{\rho}\bar{f}\right) + \frac{\partial}{\partial x_j}\left(\tilde{\rho}u_j\bar{f}\right)$$

(14.58)

© McGraw-Hill Education. All rights reserved. Any use is subject to the Terms of Use, Privacy Notice and copyright information.

The terms on the left-hand side in Eq. (14.57) involve only the solution variables $\tilde{\rho}, \tilde{u}_i, \tilde{e}, \text{and} \widetilde{Y}_\alpha$, and hence require no modeling. However, all of the terms on the right, particularly the last terms that represent turbulent transport, involve turbulent fluctuation quantities and must be modeled in terms of the solution variables. The source terms {*Q*} and {S_α} present special difficulties to the engine modeler. Due to the exponential dependence of the heat release *Q* on temperature, {*Q*} will be strongly influenced by temperature fluctuations. These issues are discussed more fully in Secs. 14.5.5 and 14.5.6.

The momentum equations contain terms, $\tilde{\rho}\widetilde{u_i'u_j'}$, which represent turbulent stresses (often called the Reynolds stresses). These terms must be modeled with additional equations before the set of equations, (14.57), is "closed" and can be solved. The most widely used *turbulence model* or equation set is the *k-ε model*.[49–52] This assumes a Newtonian relationship between the turbulent stresses and mean strain rates, and computes the (fictitious) turbulent viscosity appearing in this relationship from the local turbulent kinetic energy *k* $(= u_i u_i/2)$ and its dissipation rate *ε*. An equation governing *k* can be developed by multiplying the u_i equation in Eq. (14.52) by u_i, subtracting from this the equation formed by multiplying the $\tilde{u}_i$ equation in Eq. (14.57) by $\tilde{u}_i$, and phase-averaging the result. The equation so obtained is

$$\frac{\overline{D}\tilde{k}}{Dt} = \tilde{\rho}\left(P - \varepsilon\right) - \frac{\partial}{\partial x_j} J_k$$

(14.59*a*)

where *P* is the rate of turbulence production per unit mass

$$P = \overline{u_i' u_j'} \frac{\partial u_i}{\partial x_j}$$

(14.59*b*)

and J_k represents diffusive transport.

In the most commonly used two-equation *k-ε* model, all the unknown turbulence quantities are modeled in terms of the turbulent velocity scale $k^{1/2}$ and the turbulence length scale $k^{3/2}/\varepsilon$ obtained from the definition of the energy dissipation rate, via

$$\varepsilon \propto \frac{k^{3/2}}{l}$$

(14.60)

The rationale is that the rate of energy dissipation is controlled by the rate at which the large eddies feed energy to the smaller dissipative scales which in turn adjust to handle this energy.[49]

A turbulent viscosity μ_T is defined:

$$\mu_T = \frac{C_0 \tilde{\rho} k^2}{\varepsilon}$$

© McGraw-Hill Education. All rights reserved. Any use is subject to the Terms of Use, Privacy Notice and copyright information.

(14.61)

where C_0 is a model constant. The turbulent stress terms appearing in Eqs. (14.57) and (14.59) are then modeled in a quasi-Newtonian manner:

$$\tilde{\rho}\overline{u_i'' u_j''} = \frac{2}{3}\tilde{\rho}k\delta_{ij} + \frac{2}{3}\mu_T \nabla \cdot \overline{\mathrm{u}}\,\delta_{ij} - 2\mu_T \overline{S}_{ij}$$

(14.62)

where
$\overline{S}_{ij}$ is the strain rate of the
u_i field:

$$\overline{S}_{ij} = \frac{1}{2}\left(\frac{\partial u_i}{\partial x_j} + \frac{\partial u_j}{\partial x_i}\right)$$

(14.63)

The viscous-stress terms in the momentum equations are evaluated using a Newtonian constitutive relation. The turbulent-diffusion terms in the various transport equations are modeled using the turbulent diffusivity. The diffusing flux of a quantity ϕ is given by

$$J_{\phi_i} = \frac{\mu_T}{\sigma_\phi}\frac{\partial \phi}{\partial x_i}$$

(14.64)

where σ_ϕ is the turbulent Prandtl number for ϕ.

The model is completed with a transport equation for ε. An exact equation can be developed by suitable manipulation of the Navier-Stokes equations. All ε equation models are of the form[49]

$$\frac{\overline{D}\varepsilon}{Dt} = W - \frac{\partial H_i}{\partial x_i}$$

(14.65)

where W is the source term and H_i is the diffusive flux of
$\tilde{\rho}\varepsilon$ which is modeled similarly to the other diffusion terms. The appropriate form of W is the subject of much debate. For an incompressible flow, W can be modeled adequately by

$$W = \left(C_1\frac{P}{\varepsilon} - C_2\right)\frac{\tilde{\rho}\varepsilon^2}{k}$$

(14.66)

C_1 and C_2 are constants: the C_2 term produces the proper behavior of homogeneous isotropic turbulence and the C_1 term

© McGraw-Hill Education. All rights reserved. Any use is subject to the Terms of Use, Privacy Notice and copyright information.

modifies this behavior for homogeneous shear. However, for a flow with compression and expansion, an additional term in Eq. (14.66) is needed to account for changes in ε produced by dilation. Several forms for this additional term have been proposed[49, 50, 53] (e.g., $C_3\tilde{\rho}\varepsilon\nabla\cdot\overline{\mathrm{u}}$) and compared.[51] The goal is to construct a W that predicts the appropriate physical behavior under the relevant engine conditions. While different choices for modeling these terms do affect the results (especially the behavior of the turbulence length scale during the cycle[50]), the predictions of mean flow and turbulence intensity do not differ significantly.[51]

One FFM that has been applied to engines is the *Reynolds stress model* (RSM) which, in its most general form, comprises seven simultaneous partial differential equations for the six stress components and the dissipation rate ε. This obviously imposes a much greater computing burden compared with the two-equation k-ε model. The results available indicate that RSM predictions of the flow field are closer to corresponding measured data than the simpler k-ε model predictions.[52]

The LES approach to turbulence modeling has also been applied to engines. Since here one calculates the large-scale three-dimensional time-dependent flow structure directly, only the turbulence smaller in scale than the grid size need be modeled. Hence these are often referred to as subgrid-scale models. A new dependent variable q, which represents the kinetic energy per unit mass of the turbulent length scales that are too small to be resolved in the mesh, is introduced. This variable satisfies a transport equation which contains terms for production and decay of q and for its convection and diffusion. This equation has the form:

$$\frac{\partial}{\partial t}(\rho q)+\nabla\cdot(\rho q\mathrm{u})=-\frac{2}{3}\rho q\nabla\cdot\mathrm{u}+\sigma:\nabla\mathrm{u}+\nabla\cdot(\mu\nabla q)-C\rho L^{-1}q^{3/2}+\dot{W}_s$$

(14.67)

where $\boldsymbol{\sigma}$ is the turbulent stress tensor, μ the turbulent viscosity, C a constant of order unity, and L a characteristic length on the order of twice the mesh spacing.
$\dot{W}_s$ is a source term representing the production of turbulence by the motion of fuel droplets in situations where fuel sprays are important.

The physical meaning of the terms in Eq. (14.67) are as follows. The term $\nabla\cdot(\rho q\mathrm{u})$ is the convection of the turbulence by the resolved (large-scale) velocity field. The term $-\frac{2}{3}\rho q\nabla\cdot\mathrm{u}$ is a compressibility term that is the turbulent analog of pdV work. The term $\boldsymbol{\sigma}$:$\nabla\mathbf{u}$ represents the production of turbulence by shear in the resolved velocity field; $\nabla\cdot(\mu\nabla q)$ is the self-diffusion of the turbulence with diffusivity μ/ρ. The term $-C\rho L^{-1}q^{3/2}$ represents the decay of turbulent energy into thermal energy. This term also appears, with opposite sign, as a source term in the thermal internal energy equation in place of $\boldsymbol{\sigma}$:$\nabla\mathbf{u}$, which can be thought of as the rate at which kinetic energy of the resolved motions is dissipated by the turbulence. Before it is dissipated, the kinetic energy of the resolved velocity field is first converted into subgrid-scale turbulent energy q, which is then converted into heat by the decay term $C\rho L^{-1}q^{3/2}$.[53]

Under most circumstances, the velocity and temperature boundary layers in an engine cylinder will be too thin to be resolved explicitly with a computing mesh that is practical. However, these layers are important because they determine the wall shear and heat flux which are essential boundary conditions for the numerical simulation, and are of practical importance (see Secs. 8.3 and 12.6.5). Special submodels for these boundary layers, referred to as wall functions, are used to connect the wall shear stresses, heat fluxes, wall temperatures, etc., to conditions at the outer edge of the boundary layer. This removes the need to place grid points within the layer. Since the boundary layers are usually turbulent, the logarithmic "turbulent law of the wall" is commonly used.

14.5.3. Numerical Methodology

© McGraw-Hill Education. All rights reserved. Any use is subject to the Terms of Use, Privacy Notice and copyright information.

The three important numerical features of multi-dimensional methods are: the computational grid arrangement which defines the number and positions of the locations at which the flow parameters are to be calculated; the discretization practices used to transform the differential equations of the mathematical model into algebraic equations; and the solution algorithms employed to obtain the flow parameters from the discrete equations.[54]

14.5.3.1. Computing Mesh

The requirements of the computing mesh are:

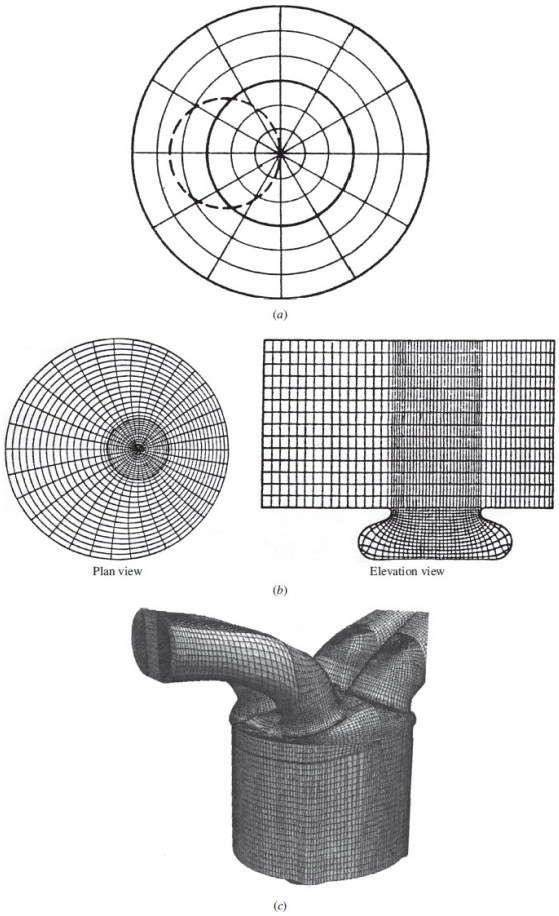
- It fits the topography of the combustion chamber and/or inlet port, including the moving components.
- It allows control of local resolution to obtain the maximum accuracy with a given number of grid points.
- It has the property that each interior grid point is connected to the same number of neighboring points.

The first requirement obviously follows from the need to simulate the effects of changes in engine geometry. The second requirement stems from the fact that computing time increases at least linearly with the number of mesh points. Thus it is desirable that the mesh allow concentration of grid points in regions where steep gradients exist such as jets and boundary layers. The third requirement comes from the need for the mesh to be topologically rectangular in some transformed space so that efficient equation solvers for such mesh systems can be utilized.

In the engine context the simplest grids are defined by the coordinate surfaces of a cylindrical-polar frame. Such an approach is only feasible if the combustion chamber walls coincide with the coordinate surfaces. This occurs for a restricted number of chamber geometries (e.g., disc and centered cylindrical bowl-in-piston shapes). Even for these, the inlet and exhaust valve circumferences would in general cut across the grid (see Fig. 14.26*a*). While procedures have been devised for modifying the difference equations for such grids to allow for noncoincident boundaries, the preferred approach is to employ some form of flexible "body-fitting" coordinate frame/grid whose surfaces can be shaped to the chamber geometry, as illustrated in Fig. 14.26*b* which shows a diesel engine combustion chamber fitted by a mesh which is orthogonal-curvilinear in the bowl. This enables the bowl shape to be accurately represented and the boundary layers on its surfaces to be resolved in greater detail. The region between the piston-crown and cylinder-head surfaces is fitted with a bipolar system which expands and contracts axially to accommodate the piston motion. The orthogonality constraint of this mesh limits its usefulness: the generation of orthogonal meshes for general three-dimensional geometries is time-consuming, and the resulting mesh often far from optimal. These problems can be largely surmounted by "arbitrary" nonorthogonal Lagrangian-Eulerian meshes like that used in KIVA.[54] This has the additional advantage that the mesh points in the swept volume are not constrained to move axially: their motion can be arbitrarily prescribed.[48] Figure 14.26*c* shows the full CFD mesh for a cylinder head and liner of a four-valve per cylinder gasoline direct-injection spark-ignition engine. The complexity of mesh generation is obvious.

© McGraw-Hill Education. All rights reserved. Any use is subject to the Terms of Use, Privacy Notice and copyright information.

Figure 14.26 Illustrations of the different types of computing mesh arrangements for engine combustion chambers. (a) Cylindrical polar mesh; dashed line shows intake valve head circumference.[55] (b) Body-fitted orthogonal curvilinear mesh fitted to DI diesel combustion chamber bowl.[56] (c) Cylinder head (with intake and exhaust ports), pent roof combustion chamber, and liner.[57]



14.5.3.2. Discretization Practices

These multi-dimensional engine flow models are time-marching programs that solve finite-difference approximations to the governing differential equations. The individual cells formed by the mesh or grid serve as the spatial framework for constructing these algebraic finite difference equations. The time variable is similarly discretized into a sequence of small time intervals called time steps: the solution at time t_{n+1} is calculated from the known solution at time t_n. The spatial differencing procedure used is to difference the basic equations in integral form, with the volume of a typical cell used as the control volume and the divergence terms transformed into surface integrals using the divergence theorem.[54]

The discretized equations for any dependent variable ϕ are of the general form:

$$A_p\phi_p^{i+1} = \sum_n A_n\phi_n^{i+1} + S_{\phi,p}V_p + A_p^i\phi_p^i$$

(14.68)

where the A's are coefficients expressing the combined influences of convection and diffusion, $S_{\phi,p}V_p$ is the source integral over the cell volume V_p, the subscript p denotes a typical node point in the mesh, the summation Σ is over its (six) nearest

© McGraw-Hill Education. All rights reserved. Any use is subject to the Terms of Use, Privacy Notice and copyright information.

neighbors, and the superscripts $i + 1$ and i denote "new" and "old" values, at times $t + \delta t$ and t, respectively, where δt is the size of the time step.[55]

Historically, all methods involved similar spatial approximations to calculate convective and diffusive transport, using a blend of first-order upwind differencing for the former and second-order central differencing for the latter. Unfortunately, all discretization practices introduce inaccuracies of some kind, and the standard first-order upwind scheme produces spatial diffusion errors which act in the same way as real diffusion to "smooth" the solutions. The magnitude of the numerical diffusion reduces as the mesh density is increased. A recent development has been the introduction of "higher order" spatial approximations which, in the past, had a tendency to produce spurious extrema. This problem has been overcome by the use of "flux blending" techniques. First-order upwind and higher-order approximations are blended in appropriate proportions to eliminate the overshoots of the latter.

14.5.3.3. Solution Algorithms

Numerical calculations of compressible flows are inefficient at low Mach numbers because of the wide disparity between the time scales associated with convection and with the propagation of sound waves. While all methods use first-order temporal discretization and are therefore of comparable accuracy, they differ in whether forward or backward differencing is employed in the transport equations leading to implicit or explicit discrete equations, respectively. In explicit schemes, this inefficiency occurs because the time steps needed to satisfy the sound-speed stability condition are much smaller than those needed to satisfy the convective stability condition alone. In implicit schemes, the inefficiency manifests itself in the additional computational labor needed to solve the implicit (simultaneous) system of equations at each time step. This solution is usually performed by iterative techniques.

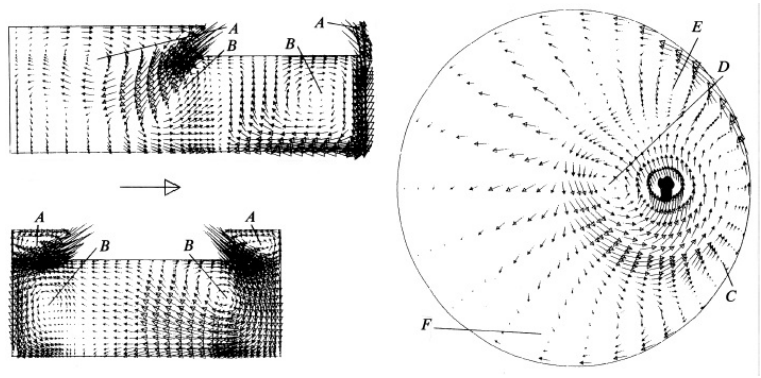
The computing time requirements of these two approaches scale with the number of equations n and the number of mesh points m, as follows. For explicit methods, computing time scales as nm, but the time step is limited by the stability condition as summarized above. For implicit methods, computing time scales as n^3m and Δt is only limited by accuracy considerations. The implicit equations that result from forward differencing consist of simultaneous sets for all variables and thus require more elaborate methods of solution. However, they contain no intrinsic stability constraints. Fully iterative solution algorithms for solution of these equation sets are being replaced with more efficient simultaneous linear equation solvers.[55]

14.5.4. Flow Field Predictions

To illustrate the capabilities of multi-dimensional modeling of IC engine flows, examples of such calculations will now be reviewed. A large amount of information on many fluid flow and state variables is generated with each calculation, and the processing, organization, and presentation of this information are tasks of comparable scope to its generation. Flow field results are usually presented in terms of the gas velocity vectors at each grid point of the mesh in appropriately selected planes. Arrows are usually used to indicate the direction and magnitude (by length) of each vector. Examples of such plots—of the flow pattern in the cylinder during the intake process—are shown in Fig. 14.27.[58] The flow field is shown 60° ATC during the intake stroke. A helical intake port is used to general swirl, and details of the flow through the valve curtain area (see Sec. 6.3.2)—the inlet boundary conditions for the calculation—were determined by measurement. The calculation used a curvilinear, axially expanding and contracting grid with about 16,000 mesh points of the type shown in Fig. 14.26*b*. It employed a fully iterative solution algorithm with standard upwind differencing and the k-ε turbulence model. Shown in Fig. 14.27 are the velocity components in the plane through the valve and cylinder axis (top left), the perpendicular plane through the valve axis (bottom left), and in a circumferential radial plane halfway between the cylinder head and the piston (right). Large-scale rotating flows are set up as the piston travels downward, created by the conical high velocity flow past the intake valve head.

© McGraw-Hill Education. All rights reserved. Any use is subject to the Terms of Use, Privacy Notice and copyright information.

Figure 14.27 Computed velocity field within the cylinder at 60° ATC during the intake stroke. Top left: plane through cylinder and inlet valve axes. Bottom left: orthogonal plane through valve axis. Right: circumferential-radial plane halfway between piston and cylinder head. Reference vector arrow corresponds to velocity of 132 m/s. Letters denote centers of toroidal flow structures.[58]

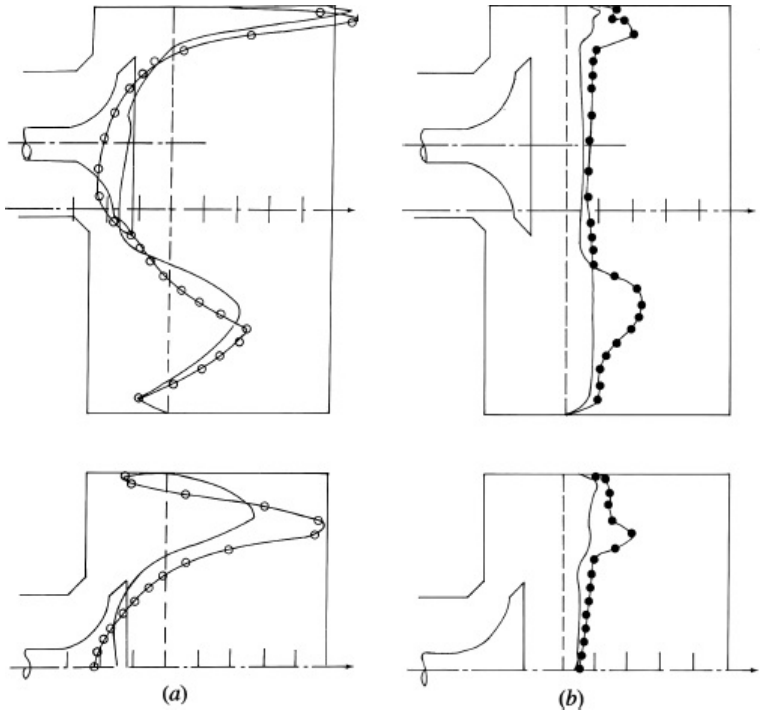


The major features of the conical jet flow through the inlet valve into the cylinder are apparent (see Sec. 8.1). However, the off-cylinder-axis valve and the swirl generated by the helical port produce substantial additional complexity. The letters on the figures show regions of local recirculation. Regions *A* and *B* correspond to the rotating flow structures observed in simpler geometries (see Fig. 8.3); however, regions *C* through *F* indicate that the swirling motion is far from a solid-body rotation.[58]

Figure 14.28 shows comparisons of three-dimensional predictions of in-cylinder flow fields with data. The computational and experimental geometries have been matched, as have the intake flow velocities through the valve open area, and engine speed. The figure shows predicted and measured mean flow velocities and turbulence intensities within the cylinder, with a conventional inlet port and valve configuration, at 68° ATC during the intake stroke.[59] The experimental values come from LDA measurements (see Sec. 8.2.2). The general features of the mean flow are reproduced by the model with reasonable accuracy, though some details such as the recirculating flow along the cylinder liner toward the head in the symmetry plane are not predicted. The approximate magnitude of the turbulence intensity levels is predicted, but the values within the conical intake jet are underestimated.

© McGraw-Hill Education. All rights reserved. Any use is subject to the Terms of Use, Privacy Notice and copyright information.

Figure 14.28 Comparison of (a) measured and predicted axial velocity profiles and (b) measured and predicted turbulence intensity profiles at 68° ATC during the intake stroke. Data: line with points. Predictions: line without points. Each interval on the scale on cylinder axes corresponds to two times the mean piston speed.[59]

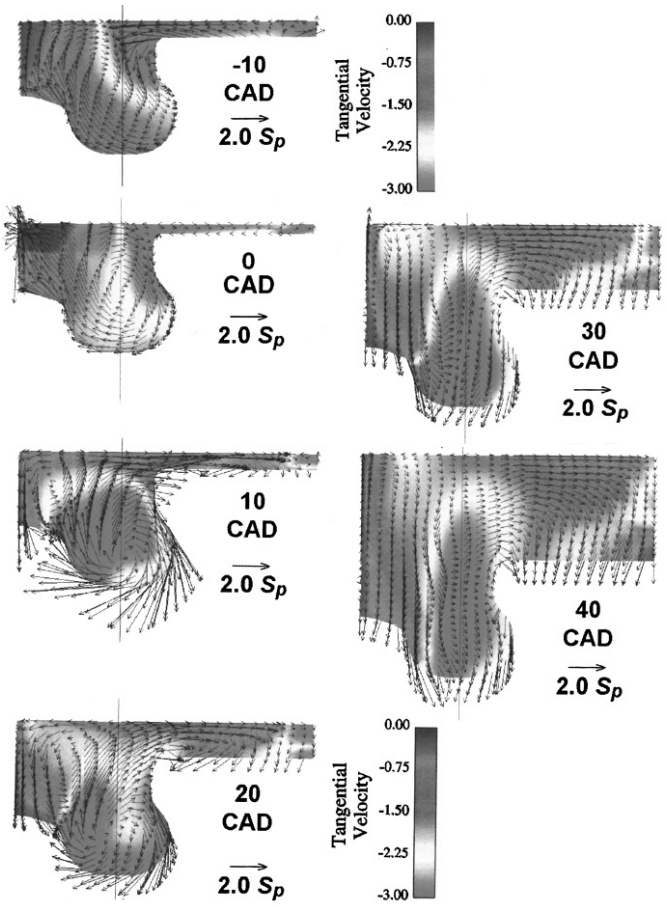


Comparative multi-dimensional modeling studies of different turbulence models,[51] differencing schemes,[48, 55] and number of grid points[48] indicate the following. Differences in the form and coefficients of the dilation term in the k-ε turbulence model have only modest effects on flow field predictions. Higher-order turbulence models do provide improved accuracy.[55] Both mesh refinement, more finely spaced grid points, and use of higher-order differencing schemes do improve the accuracy of the predictions, often of course with substantial increases in computing requirements.[48]

Examples of predictions of other types of engine flow processes are the following. Squish flows into bowl-in-piston combustion chambers with swirl have been extensively analyzed. Figure 14.29 shows the flow field into and within a bowl-in-piston high-speed direct-injection diesel. The figure shows the modeled velocity distributions in the radial-axial plane with the shading/color representing the tangential/azimuthal velocity component from the end of compression to end of combustion, −10 to 40 crank-angle degrees (CAD), relative to TC. Combustion commences about 2° ATC and heat release is three-quarters completed by about 15° ATC. The axes of the six fuel sprays are 17.5° downward directed (with piston at TC) into the farthest lower right side of the bowl. The r-z plane shown corresponds to the axis of one of the fuel sprays.

© McGraw-Hill Education. All rights reserved. Any use is subject to the Terms of Use, Privacy Notice and copyright information.

Figure 14.29 Flow velocity vectors in an r-z plane aligned with one (of six) fuel spray axis. The magnitude of the tangential/azimuthal velocity (in units of $\overline{S}_p$*) is shown by the grey scale). Start of fuel injection, 1.5 crank-angle degrees (CAD) before TC; end of injection, 2.5 CAD after TC; start of combustion, 2 CAD after TC; combustion three-quarters complete by 15 CAD after TC, and ends about 35 CAD after TC.*[60]



At −10 CAD, the strong radially inward squish motion is clear: at this crank angle, the upward piston-motion generated squish flow reaches its maximum (see Fig. 8.23). This inward flow does not penetrate to the cylinder/piston bowl axis, it is slowed and deflected down, then outward, by the pressure field generated by the high flow swirl within the bowl (some two to three times the mean piston speed). Within the bowl, a rotating flow (clockwise in this representation) in the *r-z* plane is created. With the radially inward squish flow decreasing rapidly as the piston approaches TC, the fuel injection spray supplements this *r-z* plane rotation within the bowl. The fuel spray entrains air and is seen to transport low angular momentum fluid outward from the upper center region of the piston bowl. The combustion-produced gas expansion within the bowl (0 to 10 CD) accelerates the gas rotation and increases the swirl. As the piston travels down the cylinder, the high swirl region within the bowl increases in size: the rotational velocity about cylinder axis of the gases that leave the bowl and move radially outward (the reverse squish flow) significantly decreases since, while their angular momentum is conserved, their radius increases.[60]

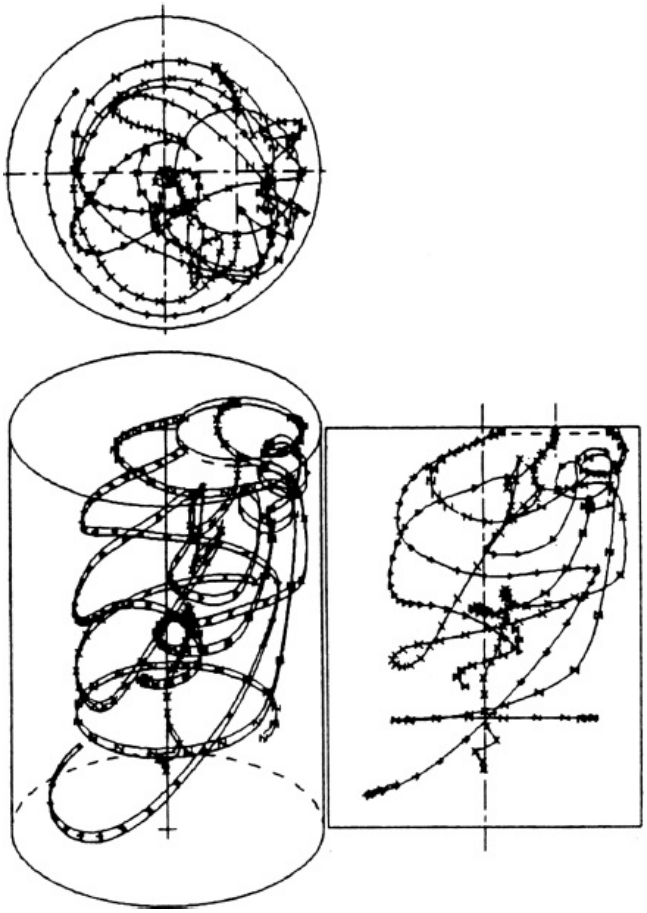
The turbulence intensity *u'* predicted by current CFD engine models generally shows moderate agreement with root-mean-square velocity measurements but with, at times, significant deviations. In the study shown in Fig. 14.29, the rms radial and tangential velocity components during injection and combustion, in the top portion of the bowl, were about 0.6 $\overline{S}_p$ and decreasing modestly. The turbulence was anisotropic. The measurements carried out in parallel with the modeling, showed some evidence of increased rms velocity fluctuations during and after combustion above and within the piston bowl possibly caused by the gas expansion on burning within the diesel diffusion flame.[60] These levels of turbulence intensity are significant, 2 to 3 m/s, would scale with engine speed, and obviously influence mixing rates between fuel and air, and combustion products with the excess air (post combustion) in the cylinder. Turbulence intensity results are often displayed

© McGraw-Hill Education. All rights reserved. Any use is subject to the Terms of Use, Privacy Notice and copyright information.

on contour plots. There is a correspondence between high-velocity regions generated by the squish flow (Fig. 14.29) and higher turbulence intensities. A substantial variation in intensity throughout the bowl is usually predicted. Computer-generated three-dimensional perspective views of the velocity field prove valuable.

An alternative method of displaying multi-dimensional model results, especially from three-dimensional calculations, is through particle traces. Infinitesimal particles are placed at key locations in the flow field at a given crank angle (e.g., at the start of the process of interest) and their trajectories are computed from the velocity field as a function of time. The particle traces illustrate the flow streamlines within the intake, port, valve, and cylinder. The example of particle traces (Fig. 14.30) within the cylinder during the intake stroke indicates the complexity of swirling flows with realistic intake port and valve geometries.[61] The figure shows the paths traced out by six particles, initially evenly spaced around the valve curtain area at TC at the start of the intake process, during the intake stroke with a tangentially directed inlet port. While all the particles follow a helical path within the cylinder, the steepness of these paths varies depending on the initial location of each particle.

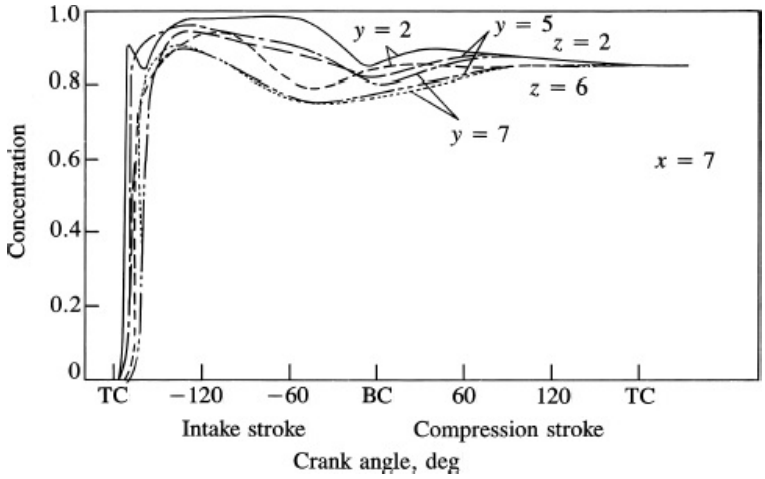
Figure 14.30 Computed trajectories traced out during the intake stroke by six gas particles initially evenly spaced around the valve curtain area at TC at the start of intake process, with a tangentially directed inlet port. Cylinder shown with piston at BC, at the end of the intake stroke.[61]



Multi-dimensional models also provide local mixture composition information. Studies have been done of the mixing of fuel with air in sprays, of two-stroke cycle scavenging flows (see Ref. 62), and of the mixing between fresh mixture and residual gases in four-stroke cycle engines (e.g., Ref. 63). Figure 14.31 shows how the mixing between fresh fuel and air, and residual gases, proceeds during the intake and compression strokes of a spark-ignition engine four-stroke cycle. Concentrations (defined as fresh mixture mass/ total mixture mass) at different locations within the cylinder are plotted against crank angle (z = 2 is near the head, z = 7 near the piston; y = 2 is near the cylinder axis, y = 7 near the cylinder liner). A relatively long time is required for the fresh and residual gases to mix and at 30° BTC there is still several percent nonuniformity. At part load with its higher residual fraction, one would expect these differences to be larger.[63]

© McGraw-Hill Education. All rights reserved. Any use is subject to the Terms of Use, Privacy Notice and copyright information.

Figure 14.31 Computed concentration distribution of fresh fuel-air mixture and residual gas within the cylinder during the intake and compression stroke of a spark-ignition engine. Concentration expressed as fresh mixture mass/total mixture mass, z = 2 is near the cylinder head,z = 7 near the piston; y = 2 near the cylinder axis,y = 7 near the cylinder liner;x = 7 along the radius passing beneath the inlet valve. 2000 rev/min and wide-open throttle.[63]



14.5.5. Fuel Spray Modeling

The physical behavior of liquid fuel sprays when injected into the engine cylinder, as occurs in DI stratified-charge spark-ignition and diesel engines, has already been described in Secs. 9.3.5 and 10.4. Here the current status of models for such spray behavior which are used with multi-dimensional models of gas motion within the cylinder is reviewed. Direct fuel-injected internal combustion engines present a particularly difficult problem for numerical simulation. The fuel spray produces an inhomogeneous fuel-air mixture: the spray interacts with and strongly affects the flow patterns and temperature distribution within the cylinder. The fuel is injected as liquid, it atomizes into a large number of small droplets with a wide spectrum of sizes, the droplets disperse and vaporize as the spray moves through the surrounding air, droplet coalescence and separation can occur, gaseous mixing of fuel vapor and air then takes place, followed finally by combustion. Models which explicitly treat the two-phase structure of this spray describe the spray behavior in terms of differential conservation equations for mass, momentum, and energy.

Two such classes of spray models exist, usually called the continuum droplet model (CDM) and the discrete droplet model (DDM). Both approaches average over flow processes occurring on a scale comparable to the droplet size, and thus require independent modeling of the interactions occurring at the gas droplet interface: typically this is done with correlations for droplet drag, and heat and mass transfer. The CDM attempts to represent the motion of all droplets via a Eulerian partial-differential spray probability equation containing, in its most general case, eight independent variables: time, three spatial coordinates, droplet radius and the three components of the droplet velocity vector. This approach imposes major computational requirements. The DDM uses a statistical approach; a representative sample of individual droplets, each droplet being a member of a group of identical non-interacting droplets termed a "parcel," is tracked in a Lagrangian fashion from its origin at the injector by solving ordinary-differential equations of motion which have time as the independent variable.

This latter type of model is used in engine spray analysis.[64] Droplet parcels are introduced continuously throughout the fuel-injection process, with specified initial conditions of position, size, velocity, number of droplets in the parcel prescribed at the "zone of atomization" according to an assumed or known size distribution, initial spray angle, fuel-injection rate, and fuel temperature at the nozzle exit. The values of these parameters are chosen to represent statistically all such values within the spray. They are then tracked in a Lagrangian fashion through the computational mesh used for solving the gas-phase partial differential conservation equations.

© McGraw-Hill Education. All rights reserved. Any use is subject to the Terms of Use, Privacy Notice and copyright information.

The equations describing the behavior of individual droplets are[65]

$$\frac{d}{dt}\mathrm{x_k} = \mathrm{u_k}$$

(14.69)

$$\frac{d}{dt}(m_k \mathrm{u_k}) = -\frac{m_k}{\rho_k}\nabla p + F_{D,k}(\mathrm{u} - \mathrm{u_k})$$

(14.70)

$$m_k \frac{dh_k}{dt} = \dot{q}_k + (h_v - h_k)\frac{dm_k}{dt}$$

(14.71)

where $\mathbf{x}_k$ is the position vector for droplet k and $\mathbf{u}_k$ its velocity, m_k is the droplet mass and ρ_k the droplet density, $\mathbf{u}$ is the gas velocity, h_k the droplet specific enthalpy, $\dot{q}_k$ the heat-transfer rate from the gas to the droplet, and h_v the specific enthalpy of fuel vapor. $F_{D,k}$ is the droplet drag function:

$$F_{D,k} = \frac{1}{2}\pi r_k^2 \rho C_D |\mathrm{u} - \mathrm{u_k}|$$

(14.72)

where r_k is the droplet radius, μ and ρ the gas viscosity and density, and C_D is the drag coefficient. $F_{D,k}$ is the sum of the Stokes drag and the form drag, and in the laminar limit where $C_D = 24/\mathrm{Re}$ with $\mathrm{Re} = 2r_k\rho|\mathrm{u} - \mathrm{u}_k|/\mu$ it goes to $6\pi r_k \mu$.

An equation for the evaporation rate completes this set: it is usually assumed that the droplet is in thermal equilibrium at its wet-bulb temperature, T_s. Then a balance between heat transfer to the droplet and the latent heat of vaporization carried away by the fuel vapor exists:

$$(h_v - h_k)\frac{dm_k}{dt} = -\dot{q}_k$$

(14.73)

While a large portion of the droplet lifetime is spent in this equilibrium, terms can be added to Eq. (14.73) so that it describes the heat-up phase where the droplet temperature increases from its initial value to T_s.[65] The heat and mass exchange rates are calculated from experimentally based correlations for droplet Nusselt and Sherwood numbers as functions of Reynolds, Prandtl, and Schmidt numbers.[66]

Account must now be taken of the two-way nature of the coupling between the gas and the liquid. The gas velocity, density, temperature, and fuel vapor concentration required for solving the droplet equations are taken from the values prevailing in the grid cell in which the droplet parcel resides. At the same time, a field of "sources" is assembled for the interphase mass,

© McGraw-Hill Education. All rights reserved. Any use is subject to the Terms of Use, Privacy Notice and copyright information.

momentum, and energy transfer, and these are subsequently fed back into the gas-phase solution preserving conservation between phases.[67] The gas-phase mass, momentum, and energy conservation equations require additional terms to account for the displacement effect of the particles, the density change associated with mixing with the fuel vapor, the drag of the droplets, the initial momentum difference, and enthalpy difference between evaporated fuel at the drop surface and the surrounding gas, and heat transfer to the droplet.[65]

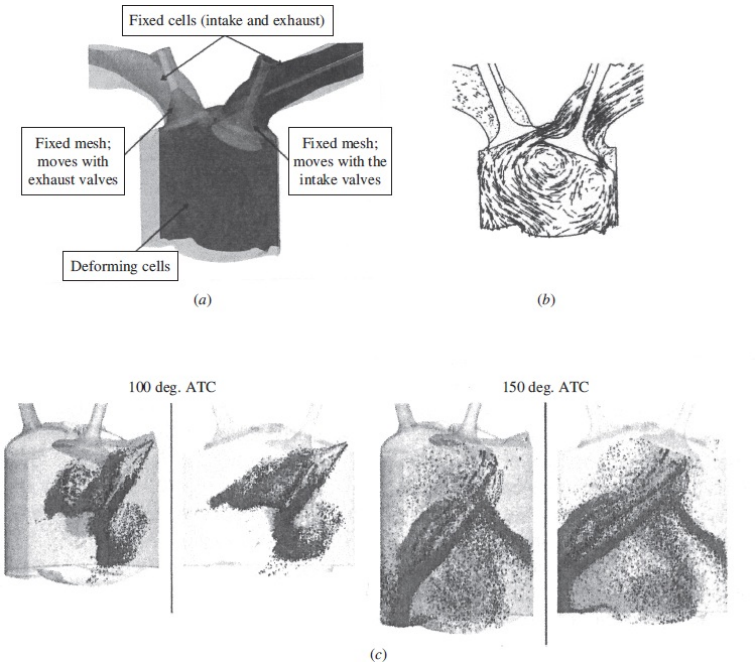
The above treatment is limited to "thin sprays" where the droplets are sufficiently far apart for interparticle interactions to be unimportant. This assumption is not valid in the immediate vicinity of the injector or in narrow cone sprays. In such "thick sprays" interparticle interactions—collisions which can result in coalescence or in reseparation of droplets—are important.

The most complete models of atomized fuel sprays represent the spray by a Monte Carlo-based discrete-particle technique.[54, 66] The spray is described by a droplet distribution function—a droplet number density in a phase space of droplet position, velocity, radius, and temperature. The development of this distribution function is determined by the so-called spray equation.[66] The distribution function is statistically sampled and the resulting discrete particles are followed as they locally interact and exchange mass, momentum, and energy with the gas, using the above Lagrangian droplet equations. Each discrete droplet represents a group or parcel of droplets. Droplet collisions are described by appropriate terms in the spray equation.

Figure 14.32 shows an example of the results such spray models can generate. The calculation involves fuel-air mixing in a direct-injection gasoline engine. The Eulerian-Lagrangian approach was used to model the fuel spray emerging from the multi-hole injector. Sub-models were developed and used for fuel injection, spray breakup, droplet-wall interaction and the liquid wall-film dynamics. Reference 67 gives details of these spray models. The DI engine was operated stoichiometric in homogeneous mode, at 1500 rev/min and 14.5 bar bmep. It had four valves per cylinder, displaced volume of 348 cm^3/cylinder, with bore and stroke close to 76 mm. Gasoline was injected into the cylinder at 80 bar injection pressure with injection commencing at 85° ATC of the intake stroke. Figure 14.32*a* shows the computational mesh set up: dynamic mesh layering is used to optimize cell size during piston motion. Much of the intake and exhaust use fixed cells. Around the valve seats and heads, fixed meshes move with the valves. Deforming cells in the cylinder follow the piston motion. Figure 14.32*b* shows the computed in-cylinder flow field in the plane of an intake and an exhaust valve stem at start of injection, about halfway down the intake stroke. The intake flow vortices generated by the flow past the intake valve head are apparent: see also Sec. 8.1. The maximum flow velocity shown is 30 m/s. Figure 14.32*c* shows paired views of the spray configuration at two crank angles, 100 and 150 degrees ATC of the intake stroke which indicate how the droplets in the spray spread and disperse.[67]

© McGraw-Hill Education. All rights reserved. Any use is subject to the Terms of Use, Privacy Notice and copyright information.

Figure 14.32 Predictions of key in-cylinder flows in a DI gasoline engine: (a) fixed mesh set-up which follows the motion of the valves and the piston; (b) computed flow field into and within the cylinder at start of fuel injection (maximum velocity is 30 m/s); (c) paired images showing the evolution of multi-hole-nozzle fuel sprays at 100 degrees ATC-intake (fuel injection starts at 85 deg. ATC), and at 150 degrees ATC-intake.[67]



14.5.6. Combustion Modeling

In numerical calculations of reacting flows, computer time and storage constraints have, in the past, limited the complexity of the reaction mechanisms that can be incorporated. It is now feasible to include detailed chemical mechanisms for combustion of hydrocarbon-air mixtures in CFD engine simulation codes. Detailed reaction schemes are available for the oxidation of the simpler hydrocarbon fuels such as, methane, n-heptane, isooctane, toluene, and for ethanol and methanol. For higher hydrocarbon compounds, and practical fuels which are blends of a large number of hydrocarbons, detailed mechanisms have yet to be developed. In the past, multi-dimensional engine calculations have used simplified chemical kinetic schemes, with one or at most a few reactions or empirical equations, to represent the combustion process. While such schemes can be calibrated with experimental data to give acceptable results over a limited range of engine conditions, they lack an adequate fundamental basis.

One common practice has been to assume the combustion process, fuel + oxidizer → products, is governed by a single rate equation of Arrhenius form:

$$R_f = A\rho^2 x_f^a x_{\text{ox}}^b \exp\left(-\frac{E_A}{\tilde{R}T}\right)$$

(14.74)

where R_f is the rate of disappearance of unburned fuel, x_f and x_{ox} are unburned fuel and oxidizer mass fractions, $\tilde{R}$ is the universal gas constant, and a, b, A, and E_A are constants (usually a and b are taken to be unity, or to be 0.5). Values for the pre-experimental factor A and activation energy E_A are obtained by matching such equations to experimentally determined rates of burning.

© McGraw-Hill Education. All rights reserved. Any use is subject to the Terms of Use, Privacy Notice and copyright information.

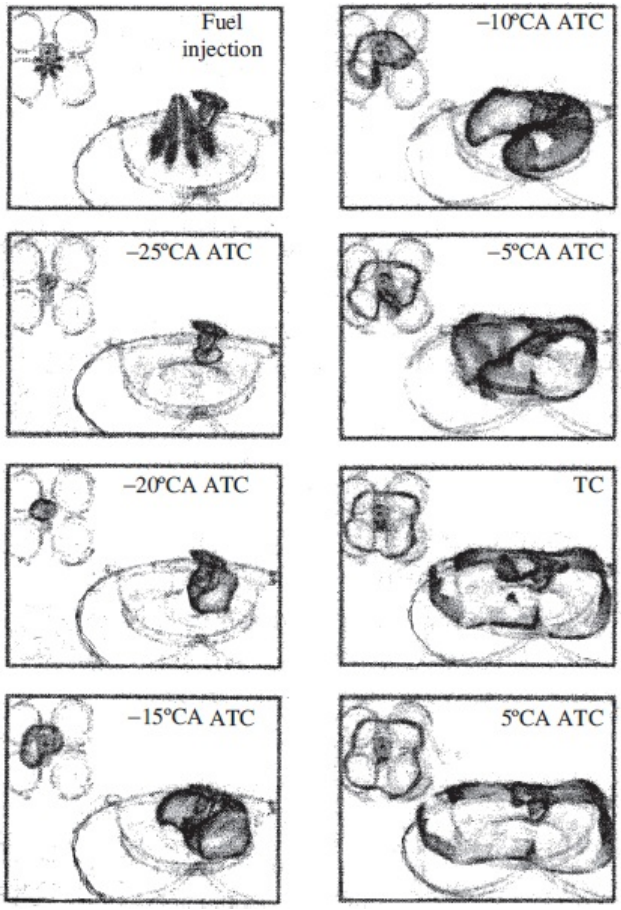
While this approach "works" in the sense that, when calibrated, its predictions can show reasonable agreement with data, it has three major problems. The first is the presumption that the complex hydrocarbon-fuel oxidation process can be adequately represented by a single (or limited number of) overall reaction(s). The fact that it is usually necessary to adjust the constants in Eq. (14.74) as engine design and operating parameters change is one indication of this problem. Second, Eq. (14.74) uses local *average* values of concentrations and temperatures to calculate the local reaction rate, whereas the *instantaneous* local values will determine the reaction rate. These two rates will only be equal if the time scale of the chemical reaction is significantly longer than that of the turbulent fluctuations, which is not the case in engine combustion. Third, the implied strong dependence of burning rate on chemical kinetics is at variance with the known experimental evidence on engine combustion (see Secs. 9.3.2 and 10.3). The effects of turbulence on the burning rate, apart from the augmentation of the thermal and mass diffusivities, are not represented by equations of the form of (14.74).

An alternative, also straightforward, approach assumes that turbulent mixing is the rate-controlling process: that is, the kinetics are sufficiently fast for chemical reaction modeling to be unimportant, and reactions proceed rapidly to completion once mixing occurs at a molecular level in the smaller-scale eddies of the turbulent flow: the rate-controlling process is then the communication between and decay of the large-scale eddies. Thus the reaction rate is inversely proportional to the turbulent mixing time
$\tau_T (= l_I/u')$ which is equated to k/ε. Whether the fuel or the oxygen concentration is limiting, and the need for sufficient hot products to ensure flame spreading, are also incorporated. For extremely lean (or rich) mixtures, the reaction may become kinetically controlled. A choice between Eq. (14.74) and the above mixing-controlled model can be made depending on whether the ratio of a chemical reaction time to the turbulent mixing time is greater or less than unity.

An example of a three-dimensional calculation of ignition and flame propagation in a spray-guided stratified, lean operating, gasoline DI spark-ignition engine in Fig. 14.33 indicates the sequence of individual process models (fuel spray development and evaporation, ignition, and turbulent flame propagation) as a function of crank angle from the latter part of the compression stroke into the main combustion process. A fuel spray model predicts the penetration and spread of the fuel droplets and vapor, and mixing with air, following the start of injection at 32° CA before TC. The ignition discharge (at 29° CA before TC), within the developing spray, is modeled as a spark channel. Flamelet equations incorporating autoignition are used to transition from the spark discharge to a flame kernel which, if conditions are right, develops into a turbulent premixed propagating flame. The turbulent flame incorporates the flame structure physics, and chemistry (via the laminar flame speed), as described in Ch. 9: see Fig. 9.22 and Sec. 9.3. In this example, the spray penetrates into the bowl-in-piston combustion chamber after start of injection.). Following ignition at 29° BTC, the turbulent flame model then takes over as the flame kernel grows. The figure shows the growing turbulent flame propagating outward from the spark location: its shape reflects the impact of the relatively high in-cylinder flow velocities induced by the bowl-in-piston combustion chamber geometry, the squish flows (into and out of the bowl), and the mixture stratification produced by the late-injection fuel spray evolution. This CFD model applied to this specific type of gasoline-fueled DI spark-ignition engine accurately predicted the engine's performance characteristics (such as cylinder pressure and burn rate profiles).

© McGraw-Hill Education. All rights reserved. Any use is subject to the Terms of Use, Privacy Notice and copyright information.

Figure 14.33 Illustration of the combustion process occurring in a spray-guided stratified DI gasoline engine modeled by a 3D CFD-based engine simulation code. The spray behavior is computed with a discrete droplet model using a multi-component fuel evaporation approach, and a model for spray impingement on the piston bowl. Ignition (29° BTC), early flame kernel growth, and fully developed turbulent flame front propagation are tracked by detailed fundamentally-based models. The first frame shows the fuel sprays. Subsequent frames show the growing flame boundary as the dark surface within the (outlined) bowl-in-piston combustion chamber, as the flame develops. In the upper left of each frame, the flame outer boundary is shown within a plan view of the full combustion chamber. Text and reference give additional details.[68]



Our final illustration of the use of 3D CFD numerical simulations of engine combustion is in a direct-injection diesel. As the discussion in Ch. 10 (Combustion in Compression-Ignition Engines) explains, the fuel spray development and the three phases of diesel combustion (autoignition, the rapid premixed fuel-rich combustion phase, and the main mixing-controlled diffusion-flame burning process) are individually complex, are linked, and (during combustion) couple turbulent convective processes with the complex HC oxidation chemistry. Models of NO_x formation and particulate formation and oxidation are then built upon the diesel combustion models utilized.

The choices for a diesel combustion model, a key component of any multi-dimensional engine model are between phenomenological models based on simplified descriptions of the underlying physics and chemistry (which are then calibrated against experimental data), or direct integration of the chemical kinetics of detailed (or reduced) chemical mechanisms. The latter approach offers better predictive accuracy and useful intermediate species information during combustion. However, it significantly extends the computational time involved.[1] More broadly, diesel combustion models used with CFD flow simulations require sub-models that predict the evolution of the fuel sprays, autoignition within the spray and the mixing controlled diffusion flames that completes the fuel burning process. Then, additional sub-models are required to connect the NO and soot formation processes to the combustion model.

© McGraw-Hill Education. All rights reserved. Any use is subject to the Terms of Use, Privacy Notice and copyright information.

An example of the overall results from such a diesel combustion model is shown in Fig. 14.34.[69] The engine involved was a 2-liter, four-cylinder (with bore and stroke both 86 mm), compression ratio 18.2:1, high-speed automobile direct-injection diesel engine with a deep re-entrant bowl-in-piston combustion chamber with swirl, and with pilot injection. A detailed fuel spray breakup, atomization, and evaporation model was used. A multi-step generic chemical model (the Shell model) was used to simulate the ignition delay. The combustion model deployed—the Coherent Flame Sheet model—embodies the autoignition process, and the premixed and diffusion-flame phases of the diesel's combustion process. A kinetic model of the NO formation process (see Sec. 11.2.1) was included, as were phenomenological models for particulate formation and oxidation.[69]

Figure 14.34 CFD engine simulation results of (a) cylinder pressure and heat release rate and (b) NO_x and soot emissions, compared with corresponding experimental data: 2-liter four-cylinder high-speed direct-injection diesel, with pilot injection and re-entrant bowl-in-piston combustion chamber, at 1600 rev/min. Details in text and reference.[69]

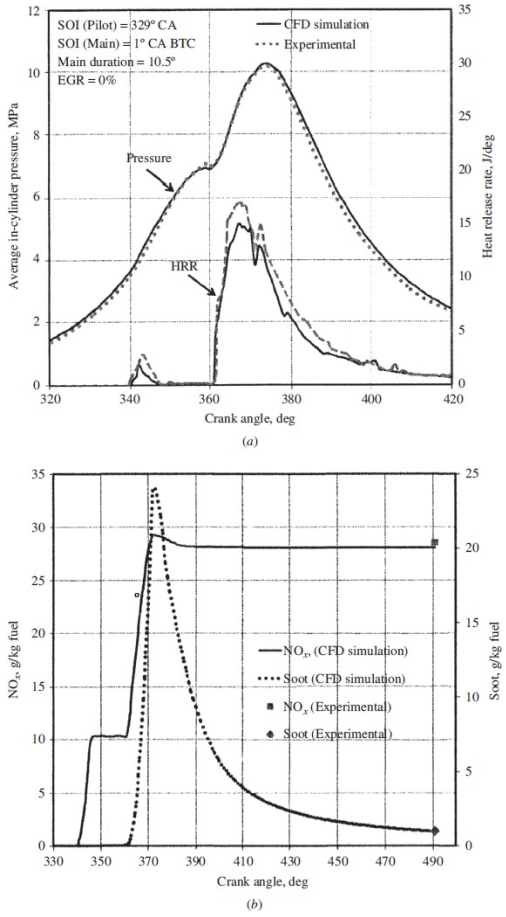


Figure 14.34*a* shows the computational results for cylinder pressure and (apparent) heat-release rate profiles with the corresponding experimentally determined profiles. Figure 14.34*b* shows the simulation's NO_x and soot predictions, along with the measured engine exhaust gas values. Note that combustion of the pilot-injection fuel (2.5% of the main-injection fuel), presumably due to its close-to-stoichiometric combustion process, produces some one-third of the peak NO_x levels formed inside the cylinder and, due to the temperature rise it produces, increases the main diffusion-flame NO formation rate. Soot forms rapidly within the fuel-rich sprays once the main-injection fuel starts to burn. Following the peak heat-release rate point, more than 90% of the soot formed within the diffusion-flame-surrounded fuel rich sprays burns up as the soot moves into the flame reaction zone. Good agreement between CFD-based simulation results and measurements is obtained. These results illustrate the value that detailed multi-dimensional CFD models can provide.

© McGraw-Hill Education. All rights reserved. Any use is subject to the Terms of Use, Privacy Notice and copyright information.

[1] A detailed discussion of these options, such as the KIVA-Characteristic-time Combustion (CTC) model and KIVA-Chemkin model, can be found in Ref. 53.

© McGraw-Hill Education. All rights reserved. Any use is subject to the Terms of Use, Privacy Notice and copyright information.

14.6. REFERENCES

1. Streit, E. E., and Borman, G. L.: "Mathematical Simulation of a Large Turbocharged Two-Stroke Diesel Engine," SAE paper 710176, *SAE Trans.*, vol. 80, 1971.
2. Assanis, D. N., and Heywood, J. B.: "Development and Use of Computer Simulation of the Turbocompounded Diesel System for Engine Performance and Component Heat Transfer Studies," SAE paper 860329, 1986.
3. GT-Power Engine Simulation Software (Engine Performance Analysis Modeling), Gamma Technologies: www.gtisoft.com.
4. WAVE: Engine Powertrain and Simulation Software. www.ricardo.com.
5. Watson, N., and Janota, M. S.: *Turbocharging the Internal Combustion Engine*, John Wiley, New York, 1982.
6. Janota, M. S., Hallam, A. J., Brock, E. K., and Dexter, S. G.: "The Prediction of Diesel Engine Performance and Combustion Chamber Component Temperatures Using Digital Computers," *Proc. Instn Mech. Engrs*, vol. 182, pt. 3L, pp. 58–70, 1967–1968.
7. Benson, R. S.: *The Thermodynamics and Gas Dynamics of Internal Combustion Engines*, in J. H. Horlock and D. E. Winterbone (eds.), vol. 1, Clarendon Press, Oxford, 1982.
8. Chapman, M., Novak, J. M., and Stein, R. A.: "Numerical Modeling of Inlet and Exhaust Flows in Multi-Cylinder Internal Combustion Engines," in T. Uzkan (ed.), *Flows in Internal Combustion Engines*, ASME, 1982.
9. Bulaty, T., and Niessner, H.: "Calculation of 1-D Unsteady Flows in Pipe Systems of I.C. Engines," ASME paper ASME-WA7, 1984.
10. Takizawa, M., Uno, T., Oue, T., and Yura, T.: "A Study of Gas Exchange Process Simulation of an Automotive Multi-Cylinder Internal Combustion Engine," SAE paper 820410, *SAE Trans.*, vol. 91, 1982.
11. Poulos, S. G., and Heywood, J. B.: "The Effect of Chamber Geometry on Spark-Ignition Engine Combustion," SAE paper 830334, *SAE Trans.*, vol. 92, 1983.
12. Heywood, J. B., Higgins, J. M., Watts, P. A., and Tabaczynski, R. J.: "Development and Use of a Cycle Simulation to Predict SI Engine Efficiency and NO_x Emissions," SAE paper 790291, 1979.
13. Lavoie, G. A., and Blumberg, P. N.: "A Fundamental Model for Predicting Fuel Consumption, NO_x and HC Emissions of the Conventional Spark-Ignited Engine," *Combust. Sci. and Technol*, vol. 21, pp. 225–258, 1980.
14. Watts, P. A., and Heywood, J. B.: "Simulation Studies of the Effects of Turbocharging and Reduced Heat Transfer on Spark-Ignition Engine Operation," SAE paper 800289, 1980.
15. Novak, J. M., and Blumberg, P. N.: "Parametric Simulation of Significant Design and Operating Alternatives Affecting the Fuel Economy and Emissions of Spark-Ignited Engines," SAE paper 780943, *SAE Trans.*, vol. 87, 1978.
16. Keck, J. C.: "Turbulent Flame Structure and Speed in Spark-Ignition Engines," *Proceedings of Nineteenth Symposium (International) on Combustion*, pp. 1451-1466, The Combustion Institute, Pittsburgh, 1982.
17. Beretta, G. P., Rashidi, M., and Keck, J. C.: "Turbulent Flame Propagation and Combustion in Spark Ignition Engines," *Combust. Flame*, vol. 52, pp. 217–245, 1983.
18. Keck, J. C., Heywood, J. B., and Noske, G.: "Early Flame Development and Burning Rates in Spark-Ignition Engines," SAE paper 870164, 1987.
19. Heywood, J. B.: "Combustion and Its Modeling in Spark-Ignition Engines," *Proceedings of Third International Symposium on Diagnostics and Modeling of Combustion in Internal Combustion Engines*, COMODIA 94, pp. 1-15, Yokohama, July 11–14,

© McGraw-Hill Education. All rights reserved. Any use is subject to the Terms of Use, Privacy Notice and copyright information.

1994.

20. Tabaczynski, R. J., Ferguson, C. R., and Radhakrishnan, K.: "A Turbulent Entrainment Model for Spark-Ignition Engine Combustion," SAE paper 770647, *SAE Trans.*, vol. 86, 1977.
21. Tabaczynski, R. J., Trinker, F. H., and Shannon, B. A. S.: "Further Refinement and Validation of a Turbulent Flame Propagation Model for Spark-Ignition Engines," *Combust. Flame*, vol. 39, pp. 111–121, 1980.
22. Borgnakke, C.: "Flame Propagation and Heat-Transfer Effects in Spark-Ignition Engines," in J. C. Hilliard and G. S. Springer (eds.), *Fuel Economy in Road Vehicles Powered by Spark Ignition Engines*, Ch. 5, pp. 183–224, Plenum Press, New York, 1984.
23. Launder, B. E., and Spalding, D. B.: *Lectures in Mathematical Models of Turbulence*, Academic Press, New York, 1972.
24. Borgnakke, C., Arpaci, V. S., and Tabaczynski, R. J.: "A Model for the Instantaneous Heat Transfer and Turbulence in a Spark Ignition Engine," SAE paper 800287, 1980.
25. Borgnakke, C., Davis, G. C., and Tabaczynski, R. J.: "Predictions of In-Cylinder Swirl Velocity and Turbulence Intensity for an Open Chamber Cup in Piston Engine," SAE paper 810224, *SAE Trans.*, vol. 90, 1981.
26. Davis, G. C., Tabaczynski, R. J., and Belaire, R. C.: "The Effect of Intake Valve Lift on Turbulence Intensity and Burnrate in S.I. Engines," SAE paper 840030, *SAE Trans.*, vol. 93, 1984.
27. Davis, G. C., Mikulec, A., Kent, J. C., and Tabaczynski, R. J.: "Modeling the Effect of Swirl on Turbulence Intensity and Burn Rate in S.I. Engines and Comparison with Experiment," SAE paper 860325, 1986.
28. Hires, S. D., Tabaczynski, R. J., and Novak, J. M.: "The Prediction of Ignition Delay and Combustion Intervals for a Homogeneous Charge, Spark Ignition Engine," SAE paper 780232, *SAE Trans.*, vol. 87, 1978.
29. Primus, R. J., and Wong, V. W.: "Performance and Combustion Modeling of Heterogeneous Charge Engines," SAE paper 850343, 1985.
30. Watson, N., Pilley, A. D., and Marzouk, M.: "A Combustion Correlation for Diesel Engine Simulation," SAE paper 800029, 1980.
31. Hiroyasu, H., Kadota, T., and Arai, M.: "Development and Use of a Spray Combustion Modeling to Predict Diesel Engine Efficiency and Pollutant Emissions (Part 2. Computational Procedure and Parametric Study)," paper 214–13, *Bull. JSME*, vol. 26, no. 214, pp. 576–583, 1983.
32. Hiroyasu, H., Kadota, T., and Arai, M.: "Development and Use of a Spray Combustion Modeling to Predict Diesel Engine Efficiency and Pollutant Emission (Part 1)," paper 214-12, *Bull. JSME*, vol. 26, no. 214, pp. 569–575, 1983.
33. Hiroyasu, H.: "Diesel Engine Combustion and Its Modeling," in *Proceedings of International Symposium on Diagnostics and Modeling of Combustion in Reciprocating Engines*, COMODIA 85, pp. 53-75, Tokyo, September 4–6, 1985.
34. Rife, J. M., and Heywood, J. B.: "Photographic and Performance Studies of Diesel Combustion with a Rapid Compression Machine," SAE paper 740948, *SAE Trans.*, vol. 83, 1974.
35. Ricou, F. P., and Spalding, D. B.: "Measurements of Entrainment by Axisymmetric Turbulent Jets," *J. Fluid Mech.*, vol. 9, pp. 21–32, 1961.
36. Abramovich, G. M.: *The Theory of Turbulent Jets*, MIT Press, Cambridge, MA, 1963.
37. Sinnamon, J. F., Lancaster, D. R., and Steiner, J. C.: "An Experimental and Analytical Study of Engine Fuel Spray Trajectories," SAE paper 800135, *SAE Trans.*, vol. 89, 1980.
38. Blumberg, P. N., Lavoie, G. A., and Tabaczynski, R. J.: "Phenomenological Models for Reciprocating Internal Combustion Engines," *Prog. Energy Combust. Sci.*, vol. 5, pp. 123–167, 1979.

© McGraw-Hill Education. All rights reserved. Any use is subject to the Terms of Use, Privacy Notice and copyright information.

39. Hires, S. D., Ekchian, A., Heywood, J. B., Tabaczynski, R. J., and Wall, J. C.: "Performance and NO_x Emissions Modeling of Jet Ignition Prechamber Stratified Charge Engine," SAE paper 760161, *SAE Trans.*, vol. 85, 1976.

40. Hiroyasu, H., Yoshimatsu, A., and Arai, M.: "Mathematical Model for Predicting the Rate of Heat Release and Exhaust Emissions in IDI Diesel Engines," paper C102/82, *Proceedings of Conference on Diesel Engines for Passenger Cars and Light Duty Vehicles*, Institution of Mechanical Engineers, London, 1982.

41. Watson, N., and Kamel, M.: "Thermodynamic Efficiency Evaluation of an Indirect Injection Diesel Engine," SAE paper 790039, *SAE Trans.*, vol. 88, 1979.

42. Mansouri, S. H., Heywood, J. B., and Radhakrishnan, K.: "Divided-Chamber Diesel Engine, Part I: A Cycle-Simulation which Predicts Performance and Emissions," SAE paper 820273, *SAE Trans.*, vol. 91, 1982.

43. Mansouri, S. H., Heywood, J. B., and Ekchian, J. A., "Studies of NO, and Soot Emissions from an IDI Diesel using an Engine Cycle Simulation," paper CI20/82, in *Diesel Engines for Passenger Cars and Light Duty Vehicles*, Institution of Mechanical Engineers Conference Publication 1982-8, pp. 215–227, 1982.

44. Watson, N., and Marzouk, M.: "A Non-Linear Digital Simulation of Turbocharged Diesel Engines under Transient Conditions," SAE paper 770123, *SAE Trans.*, vol. 86, 1977.

45. Marzouk, M., and Watson, N.: "Load Acceptance of Turbocharged Diesel Engines," paper C54/78,*Proceedings of Conference on Turbocharging and Turbochargers*, Institution of Mechanical Engineers, London, 1978.

46. Primus, R. J., and Flynn, P. F.: "Diagnosing the Real Performance Impact of Diesel Engine Design Parameter Variation (A Primer in the Use of Second Law Analysis)," in *Proceedings of International Symposium on Diagnostics and Modeling of Combustion in Reciprocating Engines*, COMODIA 85, pp. 529–538, Tokyo, September 4–6,1985.

47. Primus, R. J., Hoag, K. L., Flynn, P. F., and Brands, M. C.: "An Appraisal of Advanced Engine Concepts Using Second Law Analysis Techniques," SAE paper 841287, *SAE Trans.*, vol. 93, 1984.

48. Gosman, A. D.: "Computer Modeling of Flow and Heat Transfer in Engines, Progress and Prospects," in *Proceedings of International Symposium on Diagnostics and Modeling of Combustion in Reciprocating Engines*, COMODIA 85, pp. 15–26, Tokyo, September 4–6, 1985.

49. Reynolds, W. C.: "Modeling of Fluid Motions in Engines—An Introductory Overview," in J. N. Mattavi and C. A. Amann (eds.), *Combustion Modeling in Reciprocating Engines*, pp. 41–68, Plenum Press, New York, 1980.

50. Morel, T., and Mansour, N. N.: "Modeling of Turbulence in Internal Combustion Engines," SAE paper 820040, 1982.

51. Ahmadi-Befrui, B., Gosman, A. D., and Watkins, A. P.: "Prediction of In-Cylinder Flow and Turbulence with Three Versions of k-ε Turbulence Model and Comparison with Data," in T. Uzkan (ed.), *Flows in Internal Combustion Engines—II*, FED—vol. 20, p. 27, ASME, New York, 1984.

52. El Tahry, S. H.: "k-ε Equation for Compressible Reciprocating Engine Flows," *J. Energy*, vol. 7, no. 4, pp. 345–353, 1983.

53. Wang, H., Reitz, R. D., and Yao, M., "Comparison of Diesel Combustion CFD Models and Evaluation of the Effects of Model Constants," SAE paper 2012-01-0134, in *Multi-Dimensional Engine Modeling 2012*, SP-2331, SAE, 2012.

54. Amsden, A. A., Butler, T. D., O'Rourke, P. J., and Ramshaw, J. D.: "KIVA—A Comprehensive Model for 2-D and 3-D Engine Simulations," SAE paper 850554, 1985.

55. Gosman, A. D.: "Multidimensional Modeling of Cold Flows and Turbulence in Reciprocating Engines," SAE paper 850344, 1985.

56. Gosman, A. D., and Johns, R. J. R.: "Computer Analysis of Fuel-Air Mixing in Direct-Injection Engines," SAE paper 800091, *SAE Trans.*, vol. 89, 1980.

© McGraw-Hill Education. All rights reserved. Any use is subject to the Terms of Use, Privacy Notice and copyright information.

57. Benz, C., Nocke, J., and Hassel, E.: "Turbulence-Chemistry-Interaction Modeling in 3D-CFD for Study of Autoignition Phenomena," SAE paper 2012-01-0158, 2012.

58. Brandstatter, W., Johns, R. J. R., and Wigley, G.: "The Effect of Inlet Port Geometry on In-Cylinder Flow Structure," SAE paper 850499, 1985.

59. Gosman, A. D., Tsui, Y. Y., and Watkins, A. P.: "Calculation of Unsteady Three-Dimensional Flow in a Model Motored Reciprocating Engine and Comparison with Experiment," presented at Fifth International Turbulent Shear Flow Meeting, Cornell University, August 1985.

60. Miles, P., Megerle, M., Sick, V., Richards, K., Nagel, Z., and Reitz, R.: "The Evolution of Flow Structure and Turbulence in a Fired HSDI Diesel Engine," SAE paper 2001-01-3501, 2001.

61. Wakisaka, T., Shimamoto, Y., and Isshiki, Y.: "Three-Dimensional Numerical Analysis of In-Cylinder Flows in Reciprocating Engines," SAE paper 860464, 1986.

62. Heywood, J. B., and Sher, E.: *The Two-Stroke Cycle Engine: Its Development, Operation, and Design,* Taylor & Francis, Philadelphia, SAE, Warrendale, PA, 1999.

63. Yamada, T., Inoue, T., Yoshimatsu, A., Hiramatsu, T., and Konishi, M.: "In-Cylinder Gas Motion of Multivalve Engine—Three Dimensional Numerical Simulation," SAE paper 860465, 1986.

64. Watkins, A. P., Gosman, A. D., and Tabrizi, B. S.: "Calculation of Three Dimensional Spray Motion in Engines," SAE paper 860468, 1986.

65. Butler, T. D., Cloutman, L. D., Dukowicz, J. K., and Ramshaw, J. D.: "Toward a Comprehensive Model for Combustion in a Direct-Injection Stratified-Charge Engine," in J. N. Mattavi and C. A. Amann (eds.), *Combustion Modeling in Reciprocating Engines*, pp. 231–260, Plenum Press, New York, 1980.

66. Bracco, F. V.: "Modeling of Engine Sprays," SAE paper 850394, 1985.

67. Lucchini, T., D'Errico, G., Onorati, A., Bonandrini, G., Venturoli, L., and Gioia, R. D.: "Development of a CFD Approach to Model Fuel-Air Mixing in Gasoline Direct-Injection Engines," SAE paper 2012-01-0146, in *Multi-Dimensional Engine Modeling*, *2012*, SP-2331, SAE, 2012.

68. Dahms, R. N., Drake, M. C., Grover, R. O., Solomon, A. S., and Fansler, T. D.: "Detailed Simulations of Stratified Ignition and Combustion Processes in a Spray-Guided Gasoline Engine using the Spark CIMM/G-Equation Modeling Framework," SAE paper 2012-01-0132, in *Multi-Dimensional Engine Modeling*, *2012*, SAE, 2012.

69. Mobasheri, R., and Peng, Z.: "Analysis of the Effects of Re-Entrant Combustion Chamber Geometry on Combustion Process and Emission Formation in a HSDI Diesel Engine," SAE paper 2012-01-0144, in *Multi-Dimensional Engine Modeling, 2012*, SP-2331, SAE, 2012.

© McGraw-Hill Education. All rights reserved. Any use is subject to the Terms of Use, Privacy Notice and copyright information.

15.0. CHAPTER PRELIMINARIES

ENGINE DESIGN OBJECTIVES

ENGINE PERFORMANCE

OPERATING VARIABLES THAT AFFECT SI ENGINE PERFORMANCE, EFFICIENCY, AND EMISSIONS

SI ENGINE COMBUSTION SYSTEM DESIGN

VARIABLES THAT AFFECT DIESEL ENGINE PERFORMANCE, EFFICIENCY, AND EMISSIONS

TWO-STROKE CYCLE ENGINES

NOISE, VIBRATION, AND HARSHNESS

ENGINE PERFORMANCE AND FUELS SUMMARY

PROBLEMS

REFERENCES

This chapter reviews the operating characteristics of the common types of spark-ignition and compression-ignition engines. The performance, efficiency, and emissions of these engines, and the effect of changes in major design and operating variables, are related to the more fundamental material on engine combustion, thermodynamics, fluid flow, heat transfer, and friction developed in earlier chapters. The intent is to provide data on, and an explanation of, actual engine operating characteristics.

© McGraw-Hill Education. All rights reserved. Any use is subject to the Terms of Use, Privacy Notice and copyright information.

15.1. ENGINE DESIGN OBJECTIVES

Internal combustion engines are used in many different applications, though road transportation is the dominant one. The major engine design objectives and operating requirements are common to many of these applications: they are listed in Table 15.1[1]. These several objectives are important, and meeting them all involves trade-offs.

Table 15.1 Engine design objectives[1]

1. High performance (WOT torque, maximum power)
2. Excellent part-load fuel consumption
3. Meets air pollutant emission requirements
4. Good transient response (e.g., in a vehicle context)
5. Quiet operation, low vibration, good sound quality
6. Low weight, bulk volume (packaging)
7. High reliability, little maintenance, low oil consumption
8. Lowest possible cost

Items 1, 2, and 3 in Table 15.1 are obvious design requirements. Wide-open-throttle torque and power, as a function of engine speed, define the capabilities of the engine to produce the desired output under highly loaded operating conditions. In many applications, the time an engine spends at high outputs (and high speeds) is limited, so the engine's fuel consumption and emissions levels are often most critical at torque levels significantly below the maximum, under conditions where the engine operates for a large fraction of the time.[1] In light-duty vehicles, for example, engines operate for much of their "on time" at about one-quarter of the maximum torque, and at relatively low speeds (1500 to 2000 rev/min).

An engine's emissions of HC, CO, NO_x, and particulate matter are a result of the within-the-engine processes, and the effectiveness of the engine's exhaust aftertreatment system (if one is included). Normally, the aftertreatment system does more than 90% of the clean-up task. However, the engine-out emissions levels are still important (especially before the exhaust catalysts have warmed-up sufficiently to achieve light off). See Chap. 11 for a detailed discussion of emissions formation and controls.

While much of engine operation can be regarded as quasi-steady, depending on the engine's application area, transient behavior (item 4 in Table 15.1) is usually important also. Items 5, 6, and 7 are obviously critical practical engine design requirements.

Internal combustion engines (spark-ignition engines and diesel) steadily improve over time.[2,3] They do this as a result of many improvements and changes such as increased understanding of the opportunities and constraints, better integrated design, invention, more sophisticated controls, improved and new materials, and reductions in manufacturing costs. Strong competition in the engine market pushes these improvements; as also does pressure from alternatives to the petroleum-fueled IC engine.[4] Mainstream internal combustion engines continue to dominate the many application areas of widespread use, in large part due to this steady ongoing improvement in performance and operation. In the performance arena, these improvement in mainstream engine performance parameters are at rates of some 1 to 2% per year. Over decades, this adds up to substantial progress; year to year, average changes are more modest. Note that shifts in focus often occur in parallel (e.g., increasing emphasis on turbocharged and downsized gasoline spark-ignition engines).

In this chapter, our focus is on the operating characteristics of spark-ignition and diesel engines, largely using mainstream petroleum-based fuels, gasoline (petrol), or a distillate diesel fuel, respectively. Note that in many parts of the world, gasoline

© McGraw-Hill Education. All rights reserved. Any use is subject to the Terms of Use, Privacy Notice and copyright information.

now contains some 5 to 10% ethanol, and diesel fuel may contain a few percent biodiesel (see Sec. 10.5.5). At these blend levels, the changes in fuel properties are modest, though ethanol has good knock resistance and through E5 or E10 blends improves the octane rating of the base (hydrocarbon) gasoline stock. The future prospects for radically different engine fuels are unclear:[4] this is discussed at the end of the chapter. Natural gas is used as a spark-ignition engine fuel, and its impact on engine behavior will also be reviewed.

[1] *Load* is used here in the sense of relative torque: high load thus means close to wide-open-throttle or maximum torque.

© McGraw-Hill Education. All rights reserved. Any use is subject to the Terms of Use, Privacy Notice and copyright information.

15.2. ENGINE PERFORMANCE

15.2.1. Basic Characteristics of SI and Diesel Engines

As will by now be apparent, the ignition and combustion processes in gasoline-fueled spark-ignition engines, and in diesel-fueled diesel engines, are fundamentally different. Gasoline SI engines (unless in lean stratified mode) operate with a largely premixed fuel-vapor/air mixture (usually stoichiometric) that burns through a propagating turbulent wrinkled-laminar flame. The phasing of combustion relative to the piston's motion (determined by the crank angle of spark discharge) is usually close to that which gives the maximum brake torque (MBT) or minimum fuel consumption. Load (torque) is usually controlled by changing the intake system pressure through a throttle valve upstream of the intake manifold plenum: as the throttle is increasingly closed, the pressure drop across the throttle increases, less air is inducted into the cylinder, and less torque is generated. With turbocharged gasoline engines, with the throttle in its wide-open position, the airflow depends on the level of boost generated in the turbocharger compressor: increasing boost pressure above atmospheric increases the amount of air inducted, the amount of fuel burned can be increased, and thus the engine's torque rises.

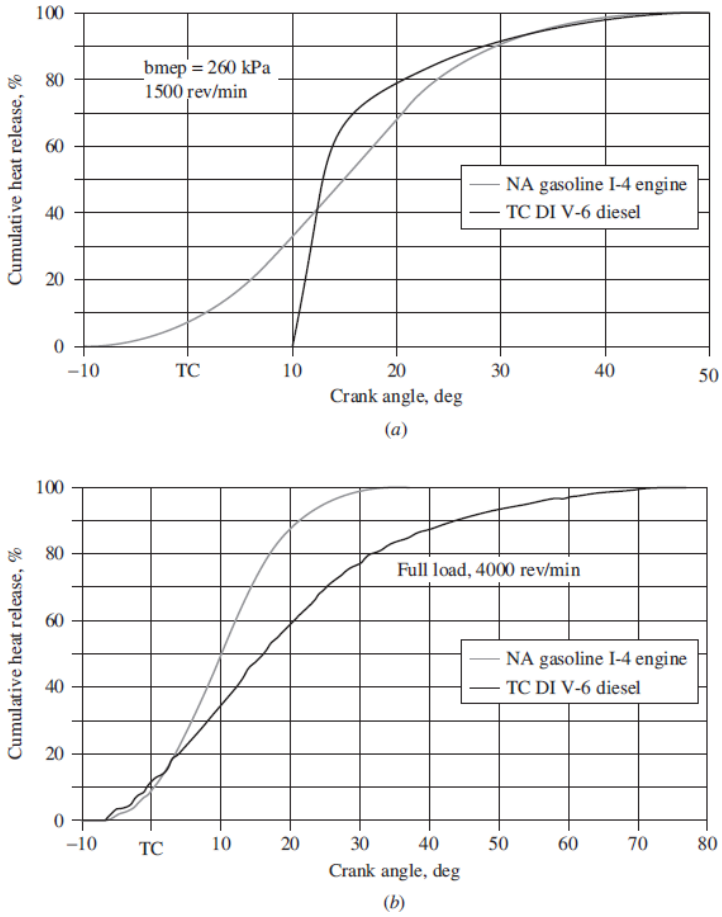
Combustion in the diesel engine is significantly different. The diesel operates unthrottled, so the airflow into the cylinder depends on engine speed. When operating turbocharged, in and above the mid-load region, the compressor generates boost (corresponding to the engine's load and speed) that increases the airflow into the engine. Fuel is injected in a relatively short pulse through several nozzle holes directly into the cylinder as each piston approaches TC. Partial entrainment and mixing of air into each vaporizing fuel spray results (after a short delay) in spontaneous ignition of the rich fuel-vapor/air mixture within each spray, rapidly releasing some of the fuel's chemical energy. Then, a diffusion flame develops around each spray and the main diffusion-flame phase of the combustion process occurs as "fuel" (the products of rich-mixture combustion, the first phase of the diesel's combustion process) diffuses from the spray interior into this diffusion flame surrounding the spray. Simultaneously, air diffuses into the flame from outside the spray. Combustion, the release of the fuel's chemical energy, occurs in the diffusion flame at close to stoichiometric conditions. Load (torque level) is controlled by the amount of fuel injected per cycle. (Since diesel engines operate lean, there is always enough air.) In a naturally-aspirated diesel, the airflow changes little as load is changed: in a turbocharged diesel, when the turbocharger is generating boost there is some feedback between engine load and compression boost level, and therefore airflow. At light loads, the turbocharger is largely ineffective and the overall engine fuel/air equivalence ratio is very lean: at maximum torque, the fuel/air equivalence ratio increases to approach 0.7, conditions just below the value of ϕ at which the black smoke combustion limit occurs. Thus the diesel's overall equivalence ratio increases steadily as load (torque) is increased from low to high levels. Combustion retard (in this case controlled by retarding the start of injection) is used to moderate the in-cylinder peak pressure level, exhaust gas temperature, and engine-out emissions.

Figure 15.1 illustrates these two different combustion processes (SI engine and diesel) at two operating conditions for these light-duty vehicle engines. The cumulative heat release, as a percent of the total injected fuel's chemical energy ($m_f Q_{HV}$), is plotted versus crank angle. Figure 15.1*a* compares these combustion profiles at a light-load (260 kPa bmep) and low speed (1500 rev/min). Figure 15.1*b* shows a similar comparison at full load and 4000 rev/min. At the light load, the diesel combustion process is initially very fast, and then slows down after about half the fuel has burned. The gasoline engine combustion profile exhibits a slower flame development process (some 15 degrees CA) and a comparable ending process (beyond 90% burned). The high load, higher speed comparison indicates that the gasoline-engine burning process shortens in terms of crank angle degrees. However, the burn duration in crank angle degrees ($\Delta\theta_{10-90\%}$) in gasoline engines varies only modestly across normal load and speed ranges, because the turbulent flame speed scales approximately with gas velocities which scale with engine speed via the piston motion. In the diesel engine, the amount of fuel injected at high load is about five times that at light load, and since engine speed is almost three times higher, the injection duration is much longer which is reflected in the significantly longer (in crank angle degrees) diesel burn profile. Note that while the diffusion-flame burning phase of the diesel combustion process is often described as *mixing controlled* (as it is), it does not scale as well with engine

© McGraw-Hill Education. All rights reserved. Any use is subject to the Terms of Use, Privacy Notice and copyright information.

speed as does the spark-ignition engine premixed flame propagation process. Thus diesel engine high-load torque becomes limited at a lower engine speed (4500 rev/min) than does gasoline engine torque (at some 6000 rev/min), due to the slower rate of increase in mixing and thus burning rate as speed increases in the diesel engine.

Figure 15.1 Heat release comparison: naturally-aspirated 2-liter four-cylinder SI gasoline engine and 3-liter V-6 turbocharged diesel engine. Upper figure (a): both engines are lightly loaded—bmep = 2.6 bar, 1500 rev/min. Lower figure (b): both engines at full load and 4000 rev/min.[5]



This combustion summary provides a useful introduction to the differences in performance and operating characteristics of these two types of internal combustion engines.

15.2.2. Characterizing Engine Performance

The practical performance parameters of interest are an engine's maximum power, the maximum torque available as a function of engine speed, and the engines specific fuel consumption. Power and torque are related by

$$\text{Power} = 2\pi \times \text{Torque} \times \text{Speed}$$

Power and torque depend on an engine's displaced cylinder volume. If the engine is turbocharged, they also depend on the air's boost pressure at entry to the engine's cylinders.[1]

In Chap. 2, a set of normalized and dimensionless performance and emissions parameters was defined to eliminate the effects of engine size. Power, torque, and fuel consumption were expressed in terms of these parameters (Secs. 2.4 and 2.8),

© McGraw-Hill Education. All rights reserved. Any use is subject to the Terms of Use, Privacy Notice and copyright information.

and the significance of these parameters over an engine's load and speed range was discussed (Sec. 2.15). The key normalized parameters are mean effective pressure, mep, (see Sec. 2.7) which is the work per cycle divided by the displaced volume,

$$\text{mep} = \frac{Pn_R}{V_d N} = \frac{2\pi n_R T}{V_d}$$

(15.1)

where n_R is the number of crank revolutions per power stroke (n_R = 2 for four-stroke cycle engines, and 1 for two-stroke cycle engines), and specific fuel consumption

$$\text{sfc} = \frac{\dot{m}_f}{P}$$

(15.2)

the fuel flow rate per unit power output. These parameters can have *brake* and net and gross *indicated* values. Torque—the turning moment the drive shaft provides—is a "brake" parameter, so bmep is effectively the engine's torque normalized by displaced volume: see Eq. (15.1). These normalized parameters allow the effect of engine size to be made explicit. The power P can be expressed as:

$$P = \text{mep}\, A_p \overline{S}_p / 4 \quad \text{(four-stroke cycle)}$$
$$P = \text{mep}\, A_p \overline{S}_p / 2 \quad \text{(two-stroke cycle)}$$

(15.3)

The torque T is given by

$$T = \text{mep}\, V_d / (4\pi) \quad \text{(four-stroke cycle)}$$
$$T = \text{mep}\, V_d / (2\pi) \quad \text{(two-stroke cycle)}$$

(15.4)

Thus for well-designed engines, where the maximum values of mean effective pressure and piston speed are either flow limited (in naturally-aspirated engines) or stress limited (in turbocharged engines), power is proportional to piston area and torque to displaced volume. Mean effective pressure can be expressed in terms of the dimensionless efficiencies defined in Chap. 2:

$$\text{mep} = \eta_f \eta_v Q_{\text{HV}} \rho_{a,i} \left(\frac{F}{A} \right)$$

(15.5)

for four-stroke cycle engines [Eq. (2.48)], and as

© McGraw-Hill Education. All rights reserved. Any use is subject to the Terms of Use, Privacy Notice and copyright information.

$$\text{mep} = \eta_f \eta_{\text{tr}} \Lambda Q_{\text{HV}} \rho_{a,i} \left(\frac{F}{A} \right)$$

(15.6)

for two-stroke cycle engines. The importance of high fuel conversion efficiency, breathing capacity, and intake air density is clear. Specific fuel consumption is related to fuel conversion efficiency by Eq. (2.24):

$$\text{sfc} = \frac{1}{\eta_f Q_{\text{HV}}}$$

(15.7)

These parameters have both brake and indicated values (see Secs. 2.3, 2.4, and 2.5). The difference between these two quantities is the engine's friction (and pumping) requirements, and their ratio is the mechanical efficiency η_m.

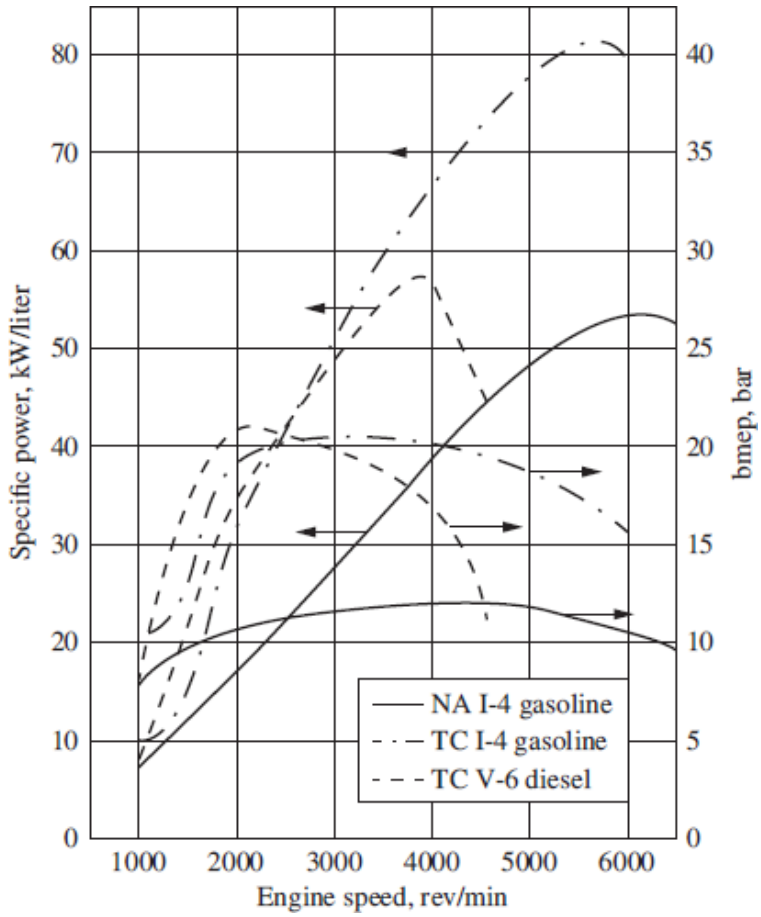
The relative importance of these parameters varies over an engine's operating speed and load range. The maximum or rated brake power (see Sec. 2.1) and the quantities such as bmep derived from it (see Sec. 2.7) define an engine's full potential. The maximum brake torque (and bmep derived from it) over the engine's speed range, indicates the ability of the designer to obtain a high airflow through the engine over the full speed range and use that air effectively. Then over the whole engine operating range, and most especially those parts of that range where the engine will operate for long periods of time, engine fuel consumption and efficiency, and engine emissions are important. Since the operating and emissions characteristics of gasoline spark-ignition engines and compression-ignition diesel engines are substantially different, each engine type is dealt with separately.

15.2.3. Torque, Power, and Mean Effective Pressure

Figure 15.2 shows the wide-open-throttle normalized torque (bmep) and specific power (kW/liter) behavior, as a function of speed, for a naturally-aspirated and a turbocharged gasoline engine, as well as a turbocharged high-speed DI diesel. (Since these are both normalized performance parameters, engine size is not a factor in this comparison.) For the reasons discussed above in Sec. 15.2.1, such smaller high-speed diesels operate over a narrower speed range than do gasoline engines: maximum power is realized at engine speeds of about 4500 rev/min (mean piston speeds of 13 m/s), where fuel-air mixing rates (in crank angle degrees) become too slow to achieve fast enough burning rates. The naturally-aspirated gasoline engine generates maximum power at around 6000 rev/min, at 17 m/s mean piston speed. Naturally-aspirated gasoline engines are operated up to the intake-flow choking point (see Sec. 6.2.5), to maximize the power realized. With turbocharging, engines are *down speeded*: maximum power is achieved at slightly lower speeds (5500 rev/min, 15 m/s) by increasing boost levels. InFig. 15.2, both of the turbocharged engines show rapidly rising torque levels as engine speed increases from about 1250 to 2000 rev/min. In naturally-aspirated gasoline engines, normalized torque levels are a factor of two or so lower: such NA engines realize a maximum bmep of 12 bar at about 4500 rev/min, rather than at about 2000 rev/min as with turbocharged engines. The gasoline engines at wide-open throttle operate at stoichiometric or up to about 20% fuel rich (for knock and exhaust gas temperature control, slightly higher power). Thus they fully utilize the air inducted into the cylinders. The maximum relative fueling rate for diesels is $\phi \leq 0.7$, so full air utilization is not achieved.

© McGraw-Hill Education. All rights reserved. Any use is subject to the Terms of Use, Privacy Notice and copyright information.

Figure 15.2 Full load bmep (bar) and specific power (kW/liter) versus engine speed for three types of internal combustion engines: (a) 2-liter I-4 naturally-aspirated gasoline SI engine; (b) 1.4-liter I-4 turbocharged gasoline engine;[6] (c) 3-liter V-6 turbocharged DI diesel engine.



Note that turbocharged engines normally use an *intercooler*, a charge air cooler, between the compressor and cylinder head. Reducing the air's temperature before it enters the cylinder has several important benefits. At a given compressor exit pressure, cooling the air increases its density. Also, lower intake air temperatures reduce the burned gas temperatures and thus the amount of NO_x formed within the engine's cylinders, and slow down the autoignition chemistry and thus delay the onset of knock constraints in gasoline engines.

The wide-open-throttle operating characteristics of an automobile spark-ignition engine are shown in Fig. 15.3. The brake power shown is the power the basic engine can provide, including the built-in engine accessories. The indicated (gross) power was obtained by adding the friction power to the brake power: it is the average rate of work transfer from the gases in the engine cylinders to the pistons during the compression and expansion strokes of the engine cycle (see Sec. 2.4). The indicated mean effective pressure shows a maximum in the engine's mid-speed range, just below 3000 rev/min. The shape of the indicated power curve follows from multiplying the imep curve by engine speed. Since the full-load indicated specific fuel consumption (and hence indicated fuel conversion efficiency) varies little over the full speed range, this variation of full-load imep and power with speed is primarily due to the variation in volumetric efficiency, η_v [see Eq. (15.5)].[2] Since friction mean effective pressure increases with increasing speed, friction power will increase even more rapidly. Hence mechanical efficiency decreases with increasing speed from a maximum of about 0.9 at low speed to 0.7 at 5000 rev/min. Thus bmep peaks at a lower speed than imep. The brake power shows a maximum at about 4300 rev/min in this older gasoline engine, increases in speed above this value result in a decrease in P_b. The indicated fuel conversion efficiency increases by about 10% from 0.31 to 0.34 over the speed range 1000 to 4000 rev/min, due primarily to the decreasing importance of heat transfer per cycle with increasing speed. For a turbocharged gasoline engine, the WOT imep and bmep values will be significantly higher, while the fmep only increases slightly. Thus the mechanical efficiency will be higher (an important benefit of turbocharging).

© McGraw-Hill Education. All rights reserved. Any use is subject to the Terms of Use, Privacy Notice and copyright information.

Figure 15.3 Gross indicated, brake, and friction power (P_i, P_b, P_f), indicated, brake, and friction mean effective pressure, indicated and brake-specific fuel consumption, and mechanical efficiency for a 3.8-liter six-cylinder naturally-aspirated automotive spark-ignition engine at wide-open throttle. Bore = 96.8 mm, stroke = 86 mm, r_c = 8.6.[7]

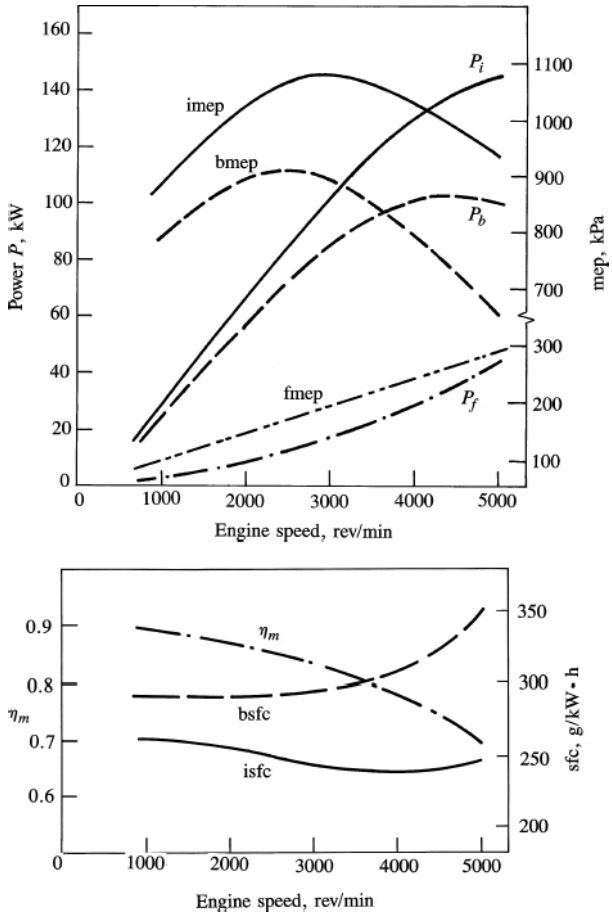
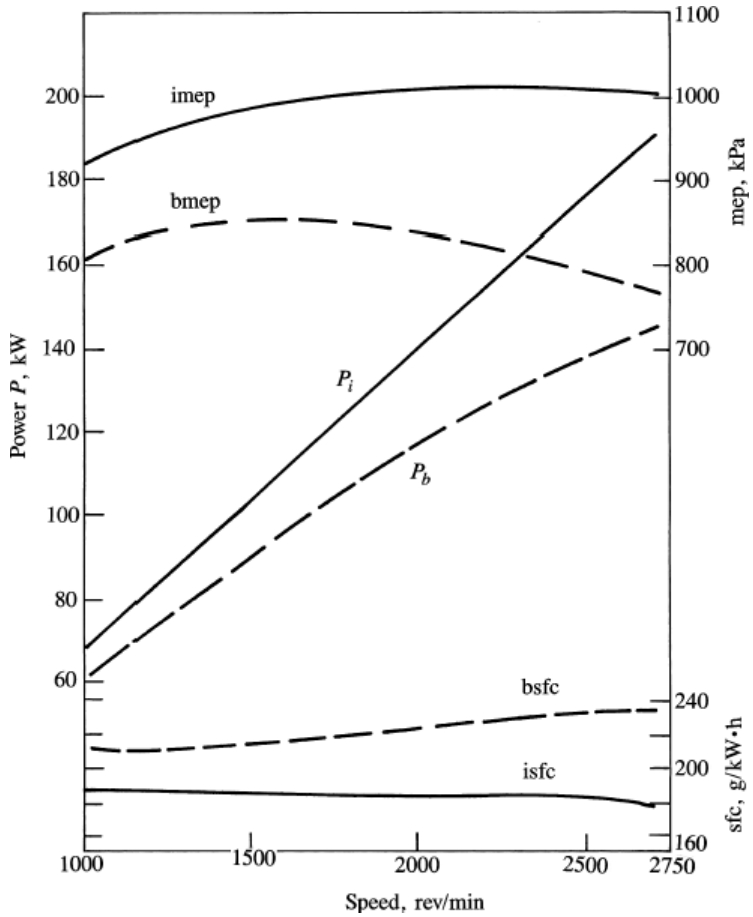


Figure 15.4 shows full-load indicated and brake power and mean effective pressure for naturally-aspirated DI diesel engine, as a function of speed. Except at high engine speeds, brake torque and mep vary only modestly with engine speed since the intake system of the diesel can have larger flow areas than the intake of SI engines with their throttle and intake-system fuel transport requirements. The part-load torque and bmep characteristics (at fixed amount of fuel injected per cycle) have a similar shape to the full-load characteristics in Fig. 15.2. The decrease in torque and bmep with increasing engine speed is due primarily to the increase in friction mep with speed (see Figs. 13.7, 13.11, and 13.12). Decreasing engine heat transfer per cycle and decreasing airflow rate, as speed increases, have modest additional impacts.

© McGraw-Hill Education. All rights reserved. Any use is subject to the Terms of Use, Privacy Notice and copyright information.

Figure 15.4 Gross indicated and brake power (P_i, P_b), mean effective pressure (imep, bmep), and specific fuel consumption (isfc, bsfc) for a 8.4-liter six-cylinder naturally-aspirated direct-injection diesel engine. Bore =115 mm, stroke = 135 mm, r_c=16[8].



15.2.4. Engine Performance Maps

One common way to present the operating characteristics of an internal combustion engine over its full load and speed range is to plot contours of constant brake-specific fuel consumption on a graph of torque (or brake mean effective pressure) versus engine speed. Such a plot is called an engine *performance map*. Operation of the engine, coupled to a dynamometer on a test stand, over its load and speed range, generates the torque and fuel flow-rate data from which a performance map is derived. Equations (15.1) and (15.2), also Eqs. (2.25), (2.26), and (2.28), relate bmep and bsfc to torque, $\dot{m}_f$, speed, and power. Figure 15.5 shows an example of such a performance map for a naturally-aspirated gasoline spark-ignition engine. The upper envelope of the map is the wide-open-throttle performance curve. Points below this curve define the part-load operating characteristics (realized by steadily closing the air-controlling throttle value). While details differ from one engine to another (and turbocharged engines have significantly higher maximum load versus speed curves; see Fig. 15.2), the overall shapes of these maps are remarkably similar. Performance maps are usually plotted with crankshaft rotational speed as the abscissa: when mean piston speed $(\overline{S}_p = 2LN)$ is used, the quantitative similarity of such maps for a given type of engine is more apparent.

© McGraw-Hill Education. All rights reserved. Any use is subject to the Terms of Use, Privacy Notice and copyright information.

Figure 15.5 Performance map for a naturally-aspirated gasoline SI engine: torque/bmep versus engine speed showing contours of constant bsfc (g/kW·h). 3-liter, V-6, four-valve per cylinder, port-fuel-injected engine, r_c = 10, maximum power 143 kW at 5200 rev/min, bore and stroke 88 and 83 mm, respectively.[9]

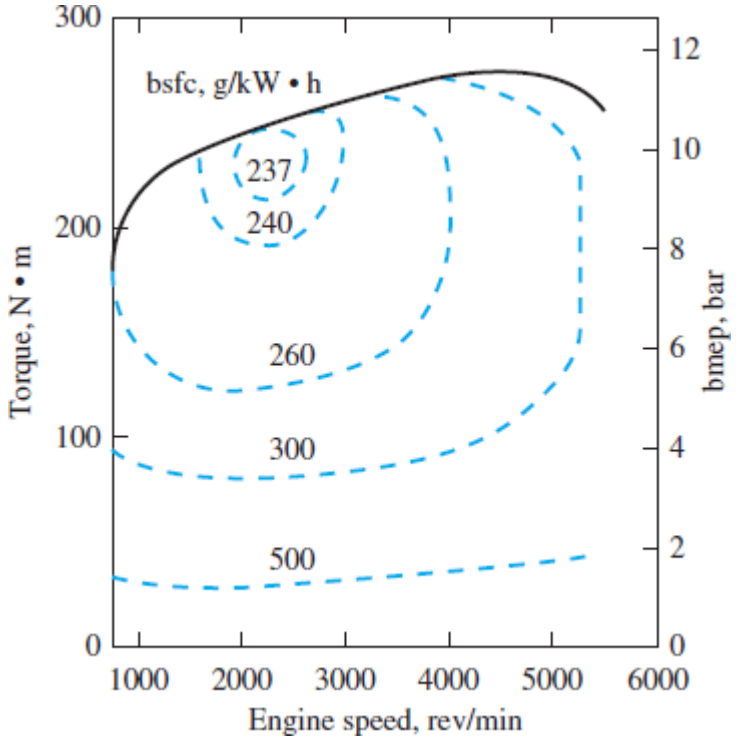
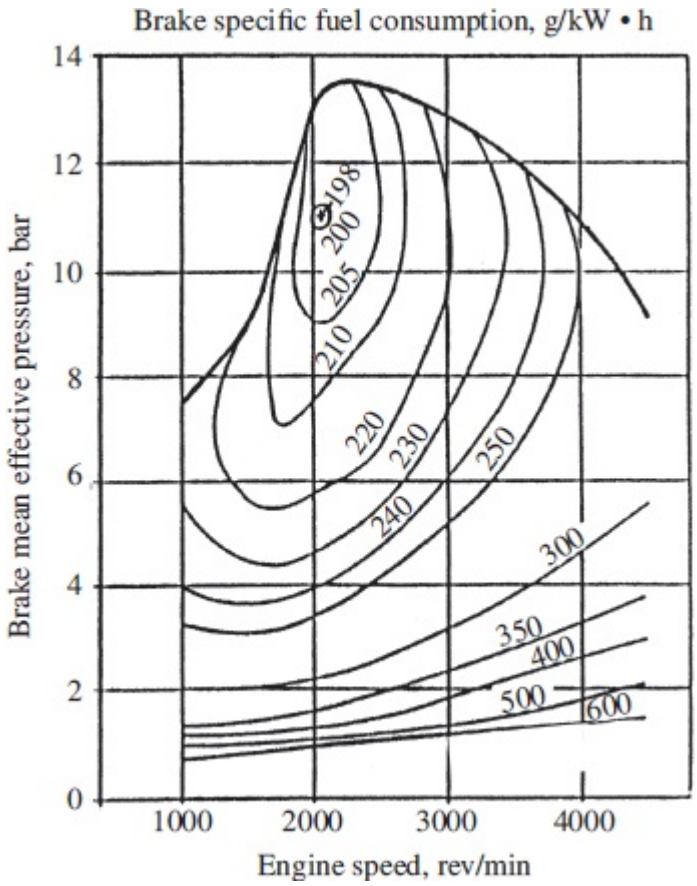


Figure 15.5 shows a performance map for a standard naturally-aspirated gasoline engine. The maximum torque (at about 4500 rev/min) corresponds to a bmep of 1200 kPa. The best bsfc value (in the upper left quadrant) of 237 g/kW·h corresponds to a brake fuel conversion efficiency of 35%. In the lower half of the map, the bsfc and efficiency worsens significantly. At a typical engine-in-vehicle light load (bmep about one-quarter the max. bmep and mid engine speed), bsfc is some 380 g/kW·h and $\eta_{f,\,b}$ is 22%.

Figure 15.6 shows a performance map for a turbocharged high-speed automotive diesel engine. The upper bound of the map, the maximum torque curve, has a shape typical of turbocharged engines: a rapid rise in torque/bmep from 1000 to 2000 rev/min; then depending of relative size of turbocharger and engine, approximately constant, declining or slightly rising maximum torque as the engine moves through the mid to high-speed range. The diesel's fuel consumptions are lower than for a (naturally-aspirated) gasoline engine (Fig. 15.5), and brake efficiencies are higher. The most efficient diesel operating conditions (high torque, low- to mid-speed) has bsfc values close to 200 g/kW·h and $\eta_{f,\,b}$ values of 42 to 44%. At typical automotive engine conditions (quarter maximum torque/bmep and mid-speed), the fuel consumption and efficiency worsen to some 260 g/kW·h and 33%, respectively.

© McGraw-Hill Education. All rights reserved. Any use is subject to the Terms of Use, Privacy Notice and copyright information.

Figure 15.6 Performance map for a turbocharged 2.5-liter DI 5-cylinder diesel engine: bmep versus engine speed, with brake-specific fuel consumption contours (g/kW·h). Torque, in excess of 240 N·m, available over a wide speed range (1500 to 3300 rev/min): maximum torque 265 N·m, maximum bmep = 13.5 bar at 2250 rev/min. Compression ratio = 21, bore and stroke 86 mm.[10]

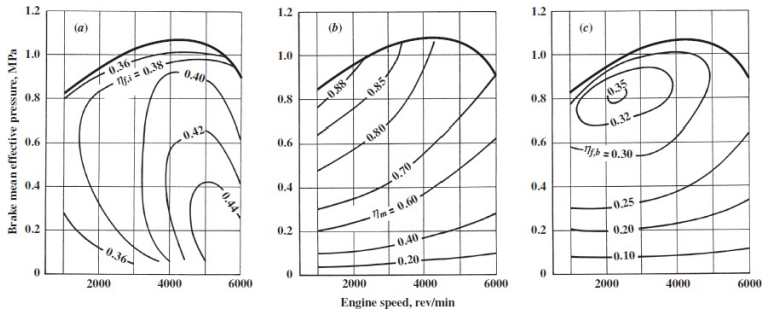


This comparison, naturally-aspirated gasoline to turbocharged diesel engine shows that at the most efficient operating conditions (high load, lower speed), the ratio of fuel consumptions, diesel:gasoline, is 0.8 to 0.85. At typical light load and low speed, this ratio is 0.65 to 0.7: that is, as load decreases, the diesel's efficiency advantage increases significantly. The reasons behind this difference between diesel and gasoline engines are the following. The diesel operates fuel-lean overall, and has a higher compression (in effect expansion) ratio: both of these directly impact engine fuel consumption and efficiency. Also, at light load, the naturally-aspirated gasoline engine is substantially throttled: the intake manifold pressure at this typically one-quarter maximum load point is about 0.5 bar (abs.). This adds significantly to engine friction (see Sec. 13.7).

The overall engine fuel consumption and efficiency behavior over such performance maps is explained by the set of three maps shown in Fig. 15.7. Each map shows lines of constant values of different efficiencies: (*a*) gross indicated fuel conversion efficiency, $\eta_{f,\,ig}$; (*b*) mechanical efficiency, η_m; (*c*) brake fuel conversion efficiency, $\eta_{f,\,b}$. For the gasoline engine (operating stoichiometric), the gross indicated fuel conversion efficiency is almost constant over the operating map (in the 35 to 40% range). The middle map (Fig. 15.7*b*) shows lines of constant mechanical efficiency (η_m = bmep/imep = 1 − fmep/imep). The mechanical efficiency is about 0.9 at high loads and low speeds. It decreases as speed is increased at constant bmep due to the rise in fmep with speed. Most importantly, at constant engine speed, η_m decreases markedly as load is decreased. Friction torque/fmep does not change that much with load [though in naturally-aspirated engines, where pumping work friction is included in total friction, the increase in pumping work as load decreases (see Fig. 13.30) does increase total friction some]. Thus as load decreases, friction becomes relatively much more important compared to the work delivered to the pistons (tfmep/imep increases substantially). At the one-quarter maximum torque, typical driving engine-torque requirement, mechanical efficiency for a naturally-aspirated gasoline engine is 0.5 to 0.6: at these conditions, almost half the work transferred to the engine's pistons is used to overcome engine friction. (At idle, η_m is zero, by definition.)

© McGraw-Hill Education. All rights reserved. Any use is subject to the Terms of Use, Privacy Notice and copyright information.

Figure 15.7 Three performance maps for a standard naturally-aspirated gasoline engine showing lines of (a) constant gross indicated fuel conversion efficiency, (b) constant mechanical efficiency, and (c) constant brake fuel conversion efficiency.[11]



This same logic is relevant to turbocharged engines, and diesel engines, with these additional factors. Turbocharging an engine raises its maximum bmep line by about a factor of two. It does not increase friction mep that much. Thus mechanical efficiency values do not decrease anywhere near as fast as load is decreased. If the maximum bmep is doubled, η_m at one-quarter maximum bmep would increase from a value of 0.6 in Fig. 15.7 to about 0.75. This would substantially increase the typical part-load brake-specific fuel consumption and efficiency. In diesels, one important additional factor is that as load decreases so does the engine's overall fuel-air equivalence ratio. Shifting to increasingly leaner mixtures leads to an increasing *indicated* fuel conversion efficiency.

A key question in the discussion of engine performance is engine size (and individual cylinder size). We have shown in this section that normalized performance parameters (which are size independent) are useful and instructive. In practice, engines are sized for specific tasks usually stated in terms of the maximum torque and power required. When comparing different types of engines where specific power and bmep vary, different engine displacements will be required to do the same practical task (stated in terms of the torque and power required). The example below goes through such a comparison: *downsizing* a turbocharged gasoline engine so it matches a larger naturally-aspirated engine.

Example

EXAMPLE 15.1

Determine the displacement of a turbocharged gasoline SI engine that matches the performance of a 5.0-liter naturally-aspirated engine that produces 270 kW (300 hp) brake power and 515 N·m (380 lb_f ft) torque.

The torque, brake mean effective pressure relationship is:

$$\text{bmep} = W_{\text{cycle,brake}}/V_d = 4\pi T/V_d$$

The following table gives the performance characteristics of the 5-liter NA engine and the matching 3.5-liter TC engine:

© McGraw-Hill Education. All rights reserved. Any use is subject to the Terms of Use, Privacy Notice and copyright information.

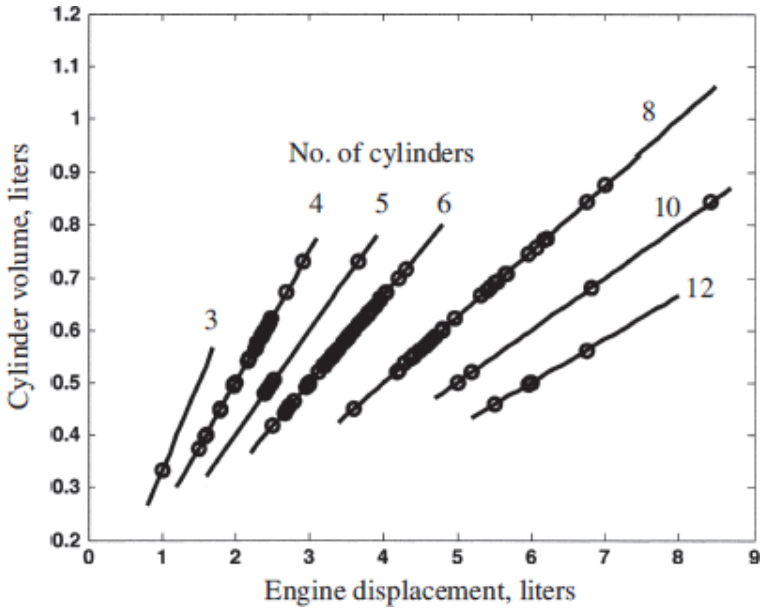
Performance parameter	Naturally-aspirated engine	Turbo engine
Displaced volume	5.0 L	3.5 L
Maximum power	270 kW	272 kW
Maximum torque	515 N·m	570 N·m
Maximum bmep	1294 kPa	2045 kPa
$^1/_4$ Maximum bmep	324 kPa	511 kPa
Total fmep	130 kPa	150 kPa
Mechanical efficiency	0.7	0.77
Brake fuel conversion efficiency	25%	28%

The end result: the TC engine due to its lower friction (in absolute and relative terms), at the same maximum power, gives higher torque at lower speed, and 10 to 15% better part-load fuel consumption and brake efficiency.

The maximum bmep levels realized in the different types of gasoline and diesel engines have been steadily increasing over time. This is due to improvements related to in engine breathing and combustion, increases in compression ratio, reductions in friction and, in turbocharged engines, increasing boost levels. Thus the engine displacement required to produce the same torque and power goes down. Engine sizes are moving downward to match this evolution in normalized engine performance with the practical performance requirements. As engine displacement is reduced, the number of cylinders and the size of those cylinders can be reduced. The geometric relationships between cylinder size, number of cylinders, and engine displacement are shown in Fig. 15.8. The lines for 3, 4, 5, 6, 8, 10, and 12-cylinder engines are purely geometric. The data[3] are for 2008 model year North American gasoline engines (almost all are naturally-aspirated). The range in cylinder volume is 330 cm^3 (three-cylinder, 1-liter engine) to 750 cm^3 (large, eight-cylinder engine). Average cylinder size in the United States is 500 to 600 cm^3; it will be about 25% less (400 to 450 cm^3) in most of the rest of the world.

© McGraw-Hill Education. All rights reserved. Any use is subject to the Terms of Use, Privacy Notice and copyright information.

Figure 15.8 *Cylinder volume as a function of engine size for 3, 4, 5, 6, 8, 10, and 12-cylinder engines. Data: 2008 model year North American light-duty vehicle gasoline engines.*[3]



[1] The basic dependence is on the air's density in the intake system. Since the air temperature (in kelvins) does not vary much, density and absolute pressure scale together: thus the manifold air pressure (MAP) is often used to characterize the boost level.

[2] The shape of the imep curve for this naturally-aspirated gasoline engine indicates that the intake manifold has not been tuned to significantly improve the engine's breathing capability in the mid- to high-speed range. See Fig. 6.12 and accompanying text.

© McGraw-Hill Education. All rights reserved. Any use is subject to the Terms of Use, Privacy Notice and copyright information.

15.3. OPERATING VARIABLES THAT AFFECT SI ENGINE PERFORMANCE, EFFICIENCY, AND EMISSIONS

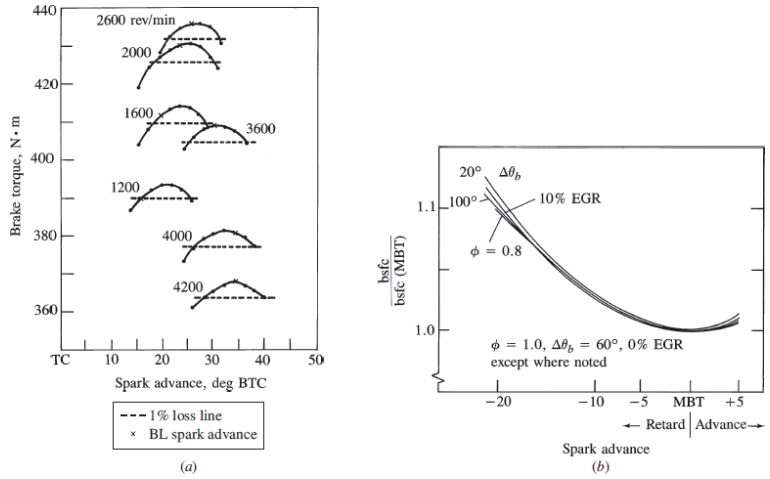
The major operating variables that affect spark-ignition engine performance, efficiency, and emissions at any given load and speed are: spark timing, fuel/air or air/fuel ratio relative to the stoichiometric value, and fraction of the exhaust gases that are recycled for NO_x emission control. Load is, of course, varied by varying the inlet manifold pressure. Both naturally-aspirated and turbocharged gasoline SI engines are in common use. In the former, the maximum manifold air pressure (MAP) is just below one atmosphere when the engine's throttle is fully open, and decreases as the throttle plate rotates toward the closed position. In turbocharged gasoline engines, the turbocharger compressor starts to provide boost as the throttle opens and the intake manifold pressure rises above atmospheric.[1] The effect of these variables will now be reviewed.

15.3.1. Spark Timing

Figure 9.5 and the accompanying text explain how variations in spark timing (and combustion phasing defined by the $\theta_{50\%}$ mass-fraction burned point), relative to top-center, affect the pressure development in the SI engine cylinder. Fundamentally, it is the phasing of the combustion process relative to the piston's motion that determines the amount of work transferred to the piston. If combustion starts too early in the cycle, the work transfer from the piston to the gases in the cylinder at the end of the compression stroke is too large; if combustion starts too late, the peak cylinder pressure is reduced and the expansion stroke work transfer from the gas to the piston decreases. Changes in combustion phasing, affect the relative importance of heat losses, also. There exists a particular spark timing which gives maximum engine torque at fixed speed, and mixture composition and flow rate. It is referred to as MBT—maximum brake torque—timing. This timing also gives maximum brake power and (except in boosted engines) the minimum brake-specific fuel consumption. Figure 15.9*a* shows the effect of spark advance variations on wide-open-throttle brake torque at selected speeds between 1200 and 4200 rev/min for a production eight-cylinder engine. At each speed, as spark is advanced from an initially retarded setting, torque rises to a maximum and then decreases. MBT timing depends on speed; as speed increases the spark must be advanced to maintain optimum timing because the duration of the combustion process in crank angle degrees increases. Optimum spark timing also depends on load. As intake manifold pressure and load are decreased, the spark timing must be further advanced to maintain optimum engine performance.

© McGraw-Hill Education. All rights reserved. Any use is subject to the Terms of Use, Privacy Notice and copyright information.

Figure 15.9 (a) Variation in brake torque with spark advance, eight-cylinder automotive spark-ignition engine at wide-open throttle, at engine speeds from 1200 to 4200 rev/min. One percent torque loss from MBT and spark advance for borderline (BL) knock are shown.[12] (b) Predicted variation in brake-specific fuel consumption (normalized by MBT value) with spark retard at several different part-load engine conditions.[13]



The maximum in each brake torque curve in Fig. 15.9*a* is relatively flat. Thus accurate determination of MBT timing is difficult, but is important because NO and HC emissions vary significantly with spark timing. In practice, to permit a more precise definition of spark timing, the spark is often retarded slightly to give a 1 or 2% reduction in torque from the maximum value.

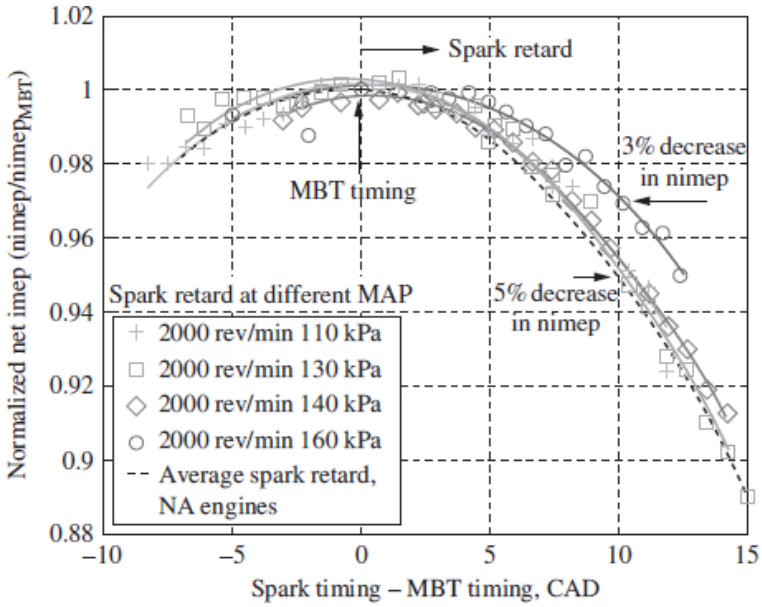
In Fig. 15.9*a* the mixture composition and flow rate were held constant at each engine speed. If the mixture flow rate is adjusted to maintain constant brake torque, the effect of spark timing variations on fuel consumption at constant engine load can be evaluated. Figure 15.9*b* shows results obtained with a computer simulation of the engine operating cycle.[13] The curves for several different part-load operating conditions and burn durations (from fast to slow) have been normalized, and fall essentially on top of each other.

The effects of spark retard on net imep, normalized by the maximum (MBT) combustion-timing value are shown in Fig. 9.16 for a wide range of *naturally-aspirated* engine data. When the abscissa is $\theta_{sp} - \theta_{sp,MBT}$ there is a common curve with some data variation: when the abscissa is $(\theta_{50\%} - \theta_{50\%,MBT})$ a tighter universal curve is obtained.[2]

Figure 15.10 shows data for a turbocharged gasoline engine at various boost levels. On the retard side of MBT timing, as boost levels rise, so do the normalized net imep values. This occurs because at constant λ, as combustion is retarded the exhaust energy increases. This increased exhaust energy/temperature drives the turbocharger more strongly, increasing the compressor airflow and outlet pressure. Thus the nimep decrease with spark retard under these (higher) boosted conditions is reduced. Note, however, that the fuel consumption does not benefit: the higher airflow (at constant stoichiometry) requires an increase in fuel flow, and with retarded combustion, the engine is less efficient.

© McGraw-Hill Education. All rights reserved. Any use is subject to the Terms of Use, Privacy Notice and copyright information.

Figure 15.10 Effect of spark retard from MBT spark timing on normalized net mean effective pressure, for several intake manifold pressures (absolute values), for naturally-aspirated and turbocharged SI engines, E25 fuel; 3 and 5% decrease from net imep at MBT timing indicated.[14]

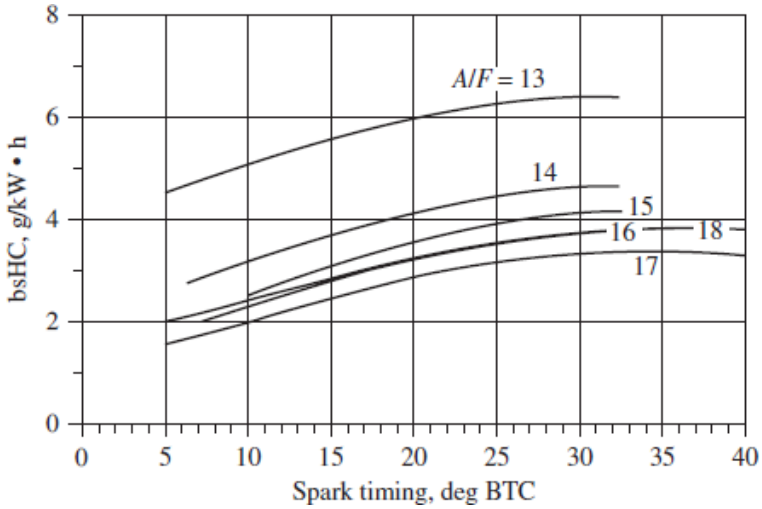


Spark timing affects the value of the peak cylinder pressure, and therefore affects peak unburned and burned gas temperatures (see Sec. 9.2.1). Retarding spark timing from the optimum reduces these variables. Retarded timing is used therefore for NO_x emission control (see Fig. 11.12 and accompanying text) and to avoid knock (see Sec. 9.6.1). The exhaust temperature is also affected by spark timing. Retarding timing from MBT increases late-expansion-stroke exhaust temperatures, so both engine efficiency and heat loss to the combustion chamber walls (see Fig. 12.12*b*) are decreased. Retarded timing may be used at engine idle to bring the ignition point closer to TC where conditions for avoiding misfire are more favorable.

Retarding spark reduces peak cylinder pressures, and thus peak burned gas temperatures so it impacts engine-out emissions. While the effect on CO emissions is small (see Sec. 11.3), retarding spark timing from MBT timing usefully reduces NO_x and HC emissions. Figure 11.12 shows the effect on NO_x: retarding spark 5 degrees CA from MBT timing reduces engine-out emissions by about 20% at stoichiometric light-load conditions. Retarded timing also reduces engine-out HC emissions, as shown in Fig. 15.11 for a range of *A/F*, rich to lean. The primary effect of spark retard on HC emissions is that it raises late-expansion-stroke in-cylinder and exhaust gas temperatures, and thus increases the amount of afterburning of HC left unburned at the end of the normal combustion process. The increase in exhaust gas temperature is a consequence of the reduced engine efficiency. Note that the exhaust gas temperature level impacts the light-off and steady-state catalyst temperature, and CO and HC oxidation efficiency.

© McGraw-Hill Education. All rights reserved. Any use is subject to the Terms of Use, Privacy Notice and copyright information.

Figure 15.11 Brake-specific hydrocarbon engine-out emissions for a 5-liter gasoline V-8 spark-ignition engine as a function of spark advance, for a range of A/F ratios. Stoichiometric A/F = 14.6. Operating conditions: bmep = 2.6 bar, speed = 1500 rev/min, without EGR.



15.3.2. Mixture Composition

The unburned mixture in the engine cylinder consists of fuel (normally vaporized), air, and burned gases. The burned gas fraction is the residual gas plus any recycled exhaust used for NO_x control. Mixture composition during combustion is most critical, since this determines the development of the combustion process which governs the engine's operating characteristics. While efforts are made to produce a uniform mixture within the cylinder, some nonuniformities remain (see Sec. 9.4.2). In a given cylinder, cycle-by-cycle variations in average charge composition exist. Also, within each cylinder in a given engine cycle, the fuel, air, EGR, and residual gas are not completely mixed, and composition nonuniformities across the charge may be significant.[3] These together produce variations in composition at the spark plug location (the critical region since the early stages of flame development influence the rest of the combustion process) which can be of order ±10% peak-to-peak. In addition, in multicylinder engines, the average air, fuel, and EGR flow rates to each cylinder are not identical. Typical cylinder-to-cylinder variations have standard deviations of ±5% of the mean for airflow rate and fuel flow rate (giving up to ±7% variation in the air/fuel ratio) for steady-state engine operation. EGR cylinder-to-cylinder flow rates may have higher variability. Under unsteady engine operating conditions these variations could be higher.

It is necessary to consider the effect of mixture composition changes on engine operating and emissions characteristics in two distinct regimes: (1) wide-open throttle (WOT) or full load and (2) part throttle or load. At WOT, the engine airflow is the maximum that the engine will induct.[4] At wide-open throttle, fuel flow can be varied, but airflow is set by engine design variables and speed. At part throttle, airflow, fuel flow, and EGR flow can be varied. Evaluation of mixture composition changes at part load are best done at fixed (brake) load and speed, that is, under conditions where the engine provides the desired torque level at the specified speed. To maintain torque (or bmep) constant as mixture composition is varied normally requires changes in throttle setting (and if EGR is varied, changes in EGR flow-control valve setting). This distinction between part-load comparisons at specified torque or bmep, rather than at constant throttle settings (which gives essentially constant airflow), is important because the pumping work component of engine friction will vary at constant engine load as mixture composition changes. At constant throttle setting and speed, the pumping work remains essentially unchanged.

15.3.2.1. Relative Air/Fuel or Equivalence Ratio

Mixture composition effects are usually discussed in terms of the air/fuel ratio (or fuel/air ratio) because in engine tests, the air and fuel flow rates to the engine can be measured directly and because the fuel system is designed to provide the

© McGraw-Hill Education. All rights reserved. Any use is subject to the Terms of Use, Privacy Notice and copyright information.

appropriate fuel flow for the actual airflow at each speed and load. However, the relative proportions of fuel and air can be stated more generally in terms of the fuel/air equivalence ratio ϕ [the actual fuel/air ratio normalized by dividing by the stoichiometric fuel/air ratio; see Eq. (3.8)] or the relative air/fuel ratio λ [see Eq. (3.9)]. The combustion characteristics of fuel-air mixtures and the properties of combustion products, which govern engine performance, efficiency, and emissions, correlate best for a wide range of fuels relative to the stoichiometric mixture proportions. Either the relative air/fuel ratio or the equivalence ratio can be used as the defining parameter: see Eq. (7.1). With gasoline engines, the relative air/fuel ratio λ is more commonly used.

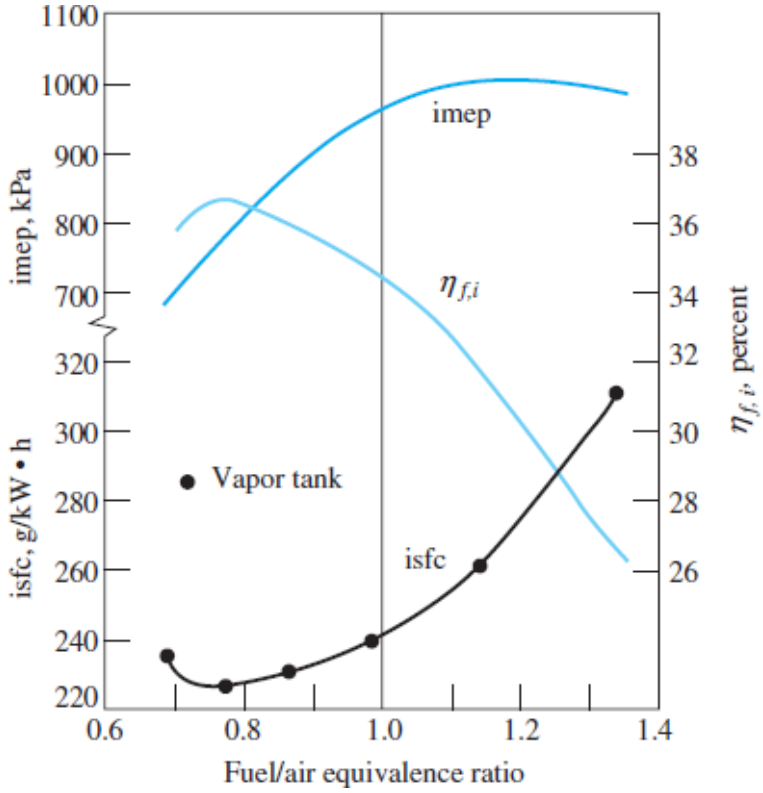
The theoretical basis for understanding the effect of changes in the equivalence ratio is the fuel-air cycle results in Figs. 5.9 and 5.10, where the indicated fuel conversion efficiency and mean effective pressure are shown as a function of the fuel/air equivalence ratio, ϕ. The mean effective pressure peaks slightly rich of stoichiometric, between $\phi = 1$ and 1.1. Due to dissociation at the high gas temperatures following combustion, molecular oxygen is present in the burned gases under stoichiometric conditions so some additional fuel can be added and partially burned. This increases the temperature and the number of moles of the burned gases in the cylinder. These effects increase the pressure to give increased power and mep. Fuel conversion efficiency decreases approximately as $1/\phi$, as the mixture is richened above stoichiometric ($\phi > 1$) due to the decreasing combustion efficiency associated with the richening mixture.

For mixtures lean of stoichiometric, the theoretical fuel conversion efficiency increases linearly as ϕ decreases below 1.0. Combustion of mixtures leaner than stoichiometric produces products at lower temperature, and with less dissociation of the triatomic molecules CO_2 and H_2O, and with excess oxygen and more nitrogen (both diatomic molecules). Thus the *fraction* of the chemical energy of the fuel which is released as sensible energy near TC is greater. As a consequence, a greater *fraction* of the fuel's energy is transferred as work to the piston during expansion, and the fraction of the fuel's available energy rejected to the exhaust system decreases since, with higher ratio of specific heats, γ the expansion stroke work as a fraction of the fuel's chemical energy increases (see Sec. 5.7). There is a discontinuity in the fuel conversion efficiency and imep curves at the stoichiometric point: the burned gas composition is significantly different on the rich and the lean sides of $\lambda = 1$.

Summarizing this behavior, Figure 15.12 shows gross indicated specific fuel consumption data for a six-cylinder spark-ignition engine at wide-open throttle and 1200 rev/min, along with values of gross indicated mean effective pressure and fuel conversion efficiency derived from the isfc data. In these engine tests, the fuel-air mixture was prepared with a heated vaporizing tank to ensure intake-mixture uniformity. Use of a fuel vaporizing and mixing tank removes any mixture nonuniformity and extends the lean misfire limit to about $\phi = 0.7, \lambda = 1.4$. However, $\eta_{f,i}$ starts to decrease before this point. The reasons are that cycle-to-cycle pressure variations and the total duration of the burning process increase as the mixture becomes leaner: both these factors degrade engine efficiency. Since the spark advance is set for the average cycle, increasing cycle-to-cycle dispersion produces increasing imep losses in "non-average" cycles due to non-optimum spark timing. The lengthening burn duration directly decreases efficiency, even in the absence of cyclic variations.

© McGraw-Hill Education. All rights reserved. Any use is subject to the Terms of Use, Privacy Notice and copyright information.

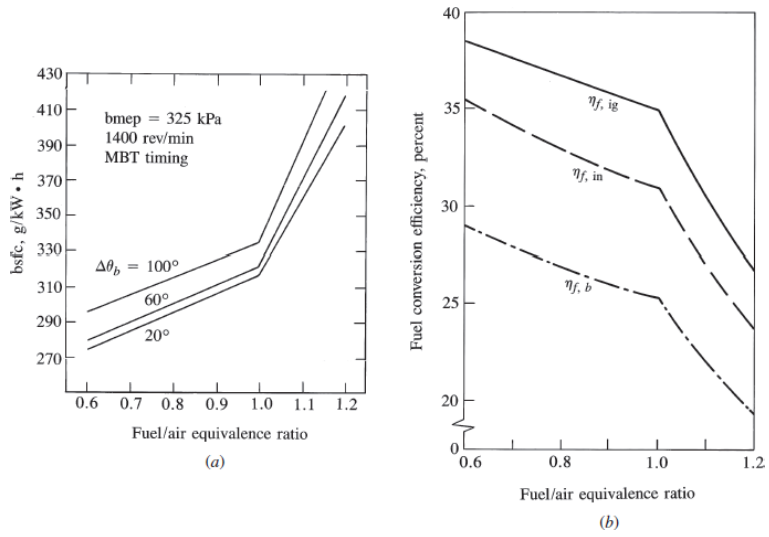
Figure 15.12 *Effect of the fuel/air equivalence ratio on indicated mean effective pressure, specific fuel consumption, and fuel conversion efficiency of a naturally-aspirated six-cylinder spark-ignition engine at wide-open throttle and 1200 rev/min. Data from a gasoline-fueled SI engine equipped with vapor tank.*[15]



Engine fuel consumption and efficiency well lean of stoichiometric depend strongly on the engine's combustion or burn rate. Figure 15.13*a* shows bsfc results obtained from a thermodynamic-based computer cycle simulation of the spark-ignition engine operating cycle (at 325 kPa bmep and 1400 rev/min).[13] The engine's fuel consumption depends on the combustion characteristics of the chamber. A slow-burning chamber ($\Delta\theta_b$ = 100°) shows much higher bsfc: more moderate burn rates (60°) significantly improve bsfc. Very fast burning chambers further improve bsfc but not by that much. As the mixture is leaned out from stoichiometric, the burn rate lengthens, but initially only slowly. Thus improvements in bsfc slow down, bsfc reaches a minimum, and then rises as burn duration increased at an accelerating rate.

© McGraw-Hill Education. All rights reserved. Any use is subject to the Terms of Use, Privacy Notice and copyright information.

Figure 15.13 (a) Effect of combustion-chamber burn rate on spark-ignition engine brake-specific fuel consumption; predictions from a thermodynamic-based computer simulation of engine cycle for 5.7-liter eight-cylinder engine at bmep of 325 kPa and 1400 rev/min with MBT spark timing. (b) Gross and net indicated, and brake, fuel conversion efficiencies (also predicted by a thermodynamic-based cycle simulation) at constant part-load bmep (325 kPa) and speed (1400 rev/min) for a fixed burn duration (0 to 100%, 60 degrees CA).[13]



At part load, as the air/fuel ratio is varied at constant brake load, the pumping work varies: this also contributes to the brake-specific fuel consumption and efficiency variation with equivalence ratio. Figure 15.13*b* shows the gross and net indicated fuel conversion efficiencies, and brake efficiency, as a function of equivalence ratio at a part-throttle constant load and speed point (325 kPa bmep and 1400 rev/min), again calculated using a thermodynamic-based computer simulation of the engine's operating cycle. The difference between the net and gross indicated curves illustrates the magnitude of the effect of the pumping work changes. As a naturally-aspirated engine is leaned out, the pumping work impact is reduced.

Note that engine data usually show a smooth transition between the rich and lean characteristics as the stoichiometric point is crossed, whereas the calculated sfc and efficiency characteristics show a discontinuity in slope. The difference is due to cylinder-to-cylinder and cycle-by-cycle mixture composition variations and to cycle-by-cycle cylinder pressure variations which exist (though to a lesser extent) even in the absence of these mixture variations. Averaging over these variations smooths out the theoretical discontinuity in slope at λ or ϕ = 1.0.

Relative air/fuel ratio effects on a spark-ignition engine's behavior over the full load and speed range have been explained above from the point of view of performance and efficiency. However, since engine-out emissions also depend on λ, emission control requirements may dictate a different engine calibration. The mixture requirements are usually discussed in relation to *steady* and to *transient* engine operation. Steady operation includes operation at a given speed and load over several engine cycles with a warmed-up engine. Transient operation includes engine starting, engine warm-up to steady-state temperatures, and changing rapidly from one engine load and speed to another. The mixture requirements of the engine as defined by the composition of the combustible mixture at the time of ignition, while they vary somewhat with speed and load, are essentially the same for all these operating modes.[5] However, the methods used to prepare the mixture prior to entry to the cylinder must be modified in the transient modes when liquid fuels are used, to allow for variations in the liquid fuel flow and fuel evaporation rate in the intake port and valve region as the airflow varies and as the pressure in the manifold, and port and valve and temperature change. The transient fuel metering requirements for adequate mixture preparation are discussed in Chap. 7.

The exhaust gas temperature varies with relative air/fuel. The exhaust gas temperature also varies continuously as the gas leaves the engine cylinder and flows through the exhaust port, and the manifold and pipe (see Sec. 6.5), so an appropriate definition of an average exhaust gas temperature should be used in quantifying this variation. However, time-averaged

© McGraw-Hill Education. All rights reserved. Any use is subject to the Terms of Use, Privacy Notice and copyright information.

thermocouple measurements from specific locations in the exhaust system can provide useful information on trends. Figure 14.10 shows examples of predictions of the enthalpy-averaged exhaust gas temperature at the exhaust port exit as a function of equivalence ratio compared with time-averaged measurements. The enthalpy-averaged temperature is defined by Eq. (6.22). These are typically 50 to 100 K higher than time-averaged measurements. The exhaust temperature peaks at the stoichiometric point and decreases as the mixture is richened and leaned on either side.

The relative air/fuel ratio is an important parameter controlling spark-ignition engine emissions. The critical factors affecting engine-out emissions, that are governed by the relative air/fuel ratio, are the oxygen concentration and the temperature of the burned gases. Excess oxygen is available in the burned gases lean of stoichiometric. The maximum burned gas temperatures occur slightly rich of stoichiometric at the beginning of the expansion stroke, and at the stoichiometric composition at the end of expansion and during the exhaust process. Figure 11.2 illustrates the general trends in engine-out emissions with equivalence ratio which have already been discussed. Of course, the behavior of the exhaust aftertreatment system largely controls the overall engine emissions. That behavior is influenced by the composition and temperature of the engine-out exhaust. (See Sec. 11.6.1.)

Historically, gasoline engines have been operated fuel rich at high loads. There are several reasons why. Air utilization is maximized, since all the oxygen is used up. Evaporation of the excess fuel provides additional charge cooling. The working fluid's ratio of specific heats, γ, is changed advantageously: during compression of the unburned mixture γ is lower so the temperature rise is less; during the burned gas expansion, γ is higher (less CO_2 and H_2O) so expansion stroke work is larger. With direct-injection, the evaporative cooling impact is significantly greater. Richer operation also reduces the exhaust gas temperature, which is important with turbocharged gasoline engines. However, for emissions control and fuel economy reasons, stoichiometric operation all the way up to wide-open throttle is to be preferred.

Figure 15.11 also shows the effect of variations in equivalence ratio, for rich through stoichiometric to lean mixtures, on unburned hydrocarbon emissions. For rich mixtures, engine-out HC emissions are significantly higher. This is primarily due to the lack of oxygen for afterburning of any unburned hydrocarbons that escape the primary combustion process, within the cylinder and the exhaust system. HC emissions decrease as the stoichiometric point is approached: increasing oxygen concentration and increasing expansion and exhaust stroke temperatures result in increasing HC burnup. For moderately lean mixtures, HC emission levels vary little with relative air/fuel ratio. Decreasing fuel concentration and increasing oxygen concentration essentially offset the effect of decreasing bulk gas temperatures. As the lean operating limit of the engine is approached, combustion quality deteriorates significantly and HC emissions start to rise again (e.g., *A/F*, 17 to 18) due to the occurrence of occasional partial-burning cycles. For still leaner mixtures, HC emissions rise more rapidly due to the increasing frequency of partial-burning cycles, and even the occurrence of completely misfiring cycles (see Sec. 9.4.3). The equivalence ratio at which partial-burning and misfiring cycles just start to appear depends on details of the engine combustion and fuel preparation systems, as well as the load and speed point.

The effect of equivalence ratio variations on CO emissions has already been explained in Sec. 11.3 (see Fig. 11.19). For rich mixtures, CO levels are high because complete oxidation of the fuel carbon to CO_2 is not possible due to insufficient oxygen. For lean mixtures, CO levels are approximately constant at a low level of about 0.5% or less.

The above discussion suggests that if an engine can be designed and operated so that its stable operating limit under the appropriate part-load conditions is sufficiently lean, excellent fuel consumption and substantial control of engine-out NO, HC, and CO emissions can be achieved. Such an approach requires good control of mixture preparation and a fast-burning combustion chamber design (see Sec. 15.4.1). However, this lean-engine approach is not compatible with the three-way catalyst system (see Sec. 11.6.3) which, with close-to-stoichiometric mixtures, achieves very substantial reductions in NO, HC, and CO emissions.

15.3.2.2. Exhaust Gas Recycle

Exhaust gas recycle (EGR) is the principal technique used for control of SI engine in-cylinder NO_x formation (see Sec. 11.2.3). A fraction of the exhaust gases are recycled through a control valve from the exhaust to the engine intake system. The

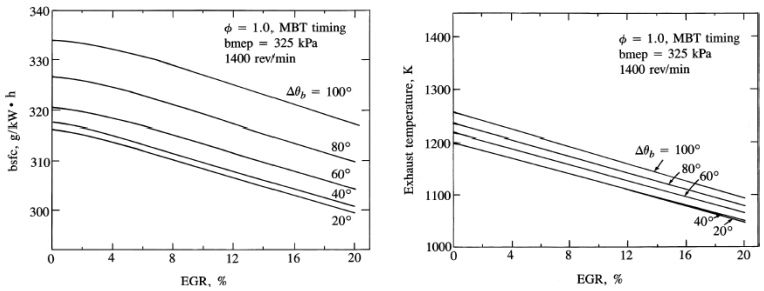
© McGraw-Hill Education. All rights reserved. Any use is subject to the Terms of Use, Privacy Notice and copyright information.

recycled exhaust gas is usually mixed with the intake air just downstream of the throttle valve. EGR acts, at part load, as an additional diluent in the unburned gas mixture, thereby reducing the peak burned gas temperatures and NO formation rates. Note that it is the total burned gas fraction in the unburned mixture in the cylinder that acts as a diluent. These burned gases are comprised of both residual gas from the previous cycle and exhaust gas recycled to the intake. As described in Sec. 6.4, the residual gas fraction is influenced by load and valve timing (especially the extent of valve overlap) and, to a lesser degree, by the air/fuel ratio and compression ratio. The total burned gas mass fraction is given by Eq. (4.3). Since the burned gases dilute the unburned mixture, the absolute temperature reached after combustion varies inversely with the burned gas mass fraction. Hence increasing the burned gas fraction reduces the rate of formation of NO emissions.

Figure 11.9 shows the effect on engine-out NO emissions of increasing the burned gas fraction by recycling exhaust gases to the intake system. Substantial reductions in NO concentrations are achieved with 10 to 25% EGR. However, EGR also reduces the combustion rate which makes stable combustion more difficult to achieve (see Sec. 9.4.3 and Fig. 9.36). The amount of EGR a particular combustion chamber will tolerate depends on its combustion characteristics, the engine speed and load, and the relative *A/F* ratio. EGR percentages in the 15 to 25 range are about the maximum amount of EGR a spark-ignition engine will tolerate under normal part-throttle conditions. Faster-burning engines will tolerate more EGR than slower-burning engines. Because of the decrease in burn rate and increase in cycle-by-cycle combustion variations, hydrocarbon emissions increase with increasing EGR, as shown in Fig. 11.31. At first, the increase in HC is modest and is due primarily to decreased HC burn-up due to lower expansion and exhaust stroke gas temperatures. The HC increase becomes more rapid as slow combustion, partial burning, and eventually misfire, in turn, occur with increasing frequency. EGR has no significant effect on engine CO emissions.

The effect of EGR on engine performance and efficiency, for mixtures with $\lambda \geq 1.0$, is similar to that of adding excess air. Both EGR and excess air dilute the unburned mixture. In practice, EGR is only used at part-throttle conditions, and since three-way catalysts are widely used where NO_x emission constraints are severe, greatest attention has been focused on dilution with EGR at $\lambda \approx 1.0$. Figure 15.14 shows the effect of increasing EGR on bsfc and enthalpy-mean exhaust temperature [defined by Eq. (6.22)] at constant bmep, predicted by using a thermodynamic-based computer simulation of the engine's operating cycle. Predictions made for different burn durations are shown, at MBT spark timing, for a stoichiometric mixture. At constant burn duration, bsfc and exhaust temperature decrease with increasing EGR. Only for very long combustion processes is the burn rate especially significant. This improvement in fuel consumption with increasing EGR is due to three factors: (1) reduced pumping work as EGR is increased at constant brake load (fuel and airflows remain almost constant; hence intake pressure increases); (2) reduced heat loss to the walls because the burned gas temperature is lower; and (3) decreased amount of dissociation in the lower temperature burned gases which allows more of the fuel's chemical energy to be converted to sensible energy near TC (the value of $\gamma = c_p/c_v$ is increased). These different effects are comparable in magnitude.

Figure 15.14 Effect of recycled exhaust gas on brake-specific fuel consumption and exhaust gas temperature at constant bmep and speed, stoichiometric mixture, and various burn durations (20 to 100°). Predictions from thermodynamic-based cycle simulation.[13]



Addition of EGR to the intake mixture lengthens both the flame development and propagation processes (and thus requires increasing spark advance to maintain the MBT timing requirement). Since faster-burning combustion chambers provide significant bsfc reductions until, approaching 15 to 20% EGR, the burn rate and combustion quality deteriorate much more

© McGraw-Hill Education. All rights reserved. Any use is subject to the Terms of Use, Privacy Notice and copyright information.

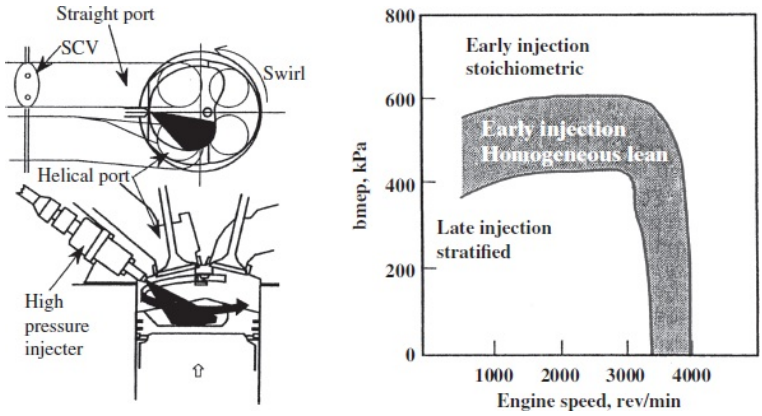
rapidly. For slower-burning combustion chambers, the tolerance to dilution with EGR is much less. The benefits of faster-burning combustion systems are discussed in Sec. 15.4.

15.3.2.3. Lean Operation and EGR

Lean operation of spark ignition engines has long been viewed as an attractive approach from the perspective of improved fuel consumption. It is primarily a part-load opportunity. At high load, lean operation does not fully utilize the air inducted into the engine cylinder: so maximum torque and power levels in naturally-aspirated engines of a given size are reduced. In turbocharged engines, this less-than-full intake air utilization could be offset by using higher compressor boost pressures. The advantages of lean operation are higher engine indicated efficiencies (lower fuel consumption) and, potentially, lower engine-out emissions (though this depends on the details). The disadvantages are primarily worse combustion quality (slower burn rates, higher cyclic variability), and the likely need for a highly effective lean NO_x catalyst (the very efficient three-way catalyst technology cannot be used with lean engine operation). Assessments of the potential benefits have been made. Of course, they depend on the base case assumed and what is held constant in such a comparison.

Both excess air (with lean operation) and EGR are diluents. They can be used separately, or they can be combined. One approach, extensively explored, is a DI gasoline engine that operates stratified (and very lean) at light load with some EGR, then homogeneous lean with EGR at mid-load, and stoichiometric at high load is illustrated on the performance map shown in Fig. 15.15. The EGR is added (in moderate amounts) to reduce peak burned gas temperatures, especially when stratified at lighter loads, when a "premixed" flame propagates from the spark plug, through the close-to-stoichiometric mixture around the plug.

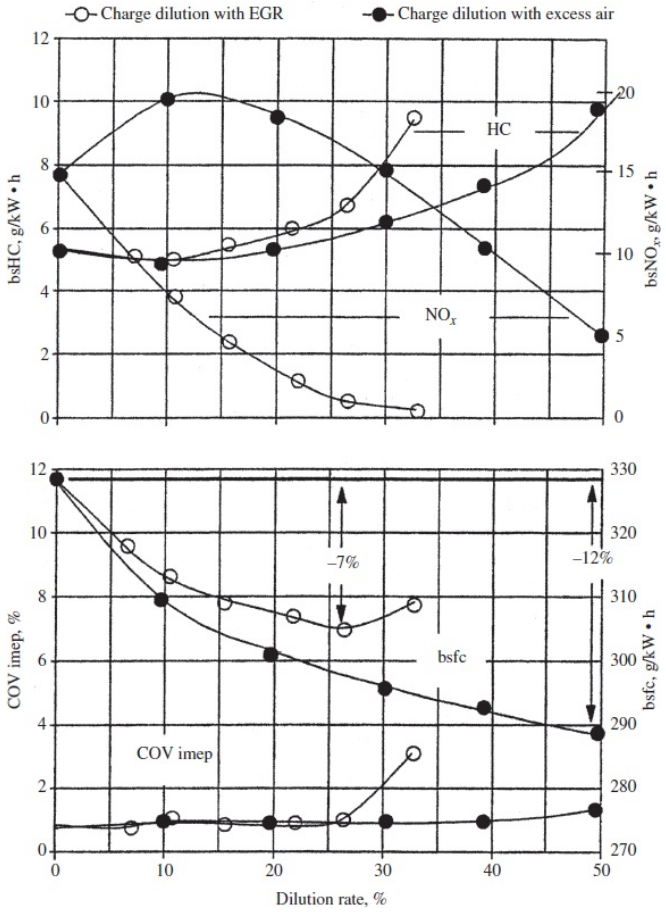
Figure 15.15 Illustrative performance map for a stratified DI gasoline engine showing the different regimes for lean stratified, lean homogeneous (both with EGR), and stoichiometric (higher load) regimes.[16]



The effects of increasing dilution with excess air, and with recycled exhaust with stoichiometric operation, on combustion stability, fuel consumption, and engine-out HC and NO_x emissions are shown in Fig. 15.16. EGR (open circles) is highly effective at reducing NO_x emissions: 15% EGR reduces NO_x by about a factor of 3. However, combustion stability (COV imep) worsens significantly at these steady state operating conditions as EGR levels move beyond 20%, and bsfc goes to a minimum. At the same combustion stability level (COV imep below 1%), lean operation out to 40% dilution with excess air gives significantly higher $bsNO_x$, slightly higher bsHC, but almost doubles the bsfc benefit (from about 6% to about 10%). Thus, at this 3-bar bmep light-load operating condition, the benefit of lean dilution relative to EGR dilution, at comparable combustion stability limits is an additional 6 or so percent lower bsfc. This example illustrates the approximate magnitude of the potential fuel consumption (and efficiency) benefit from lean gasoline engine operation.

© McGraw-Hill Education. All rights reserved. Any use is subject to the Terms of Use, Privacy Notice and copyright information.

Figure 15.16 Comparison of effect of charge dilution with excess air or with EGR, on gasoline engine combustion stability, bsNO$_x$ and bsHC emissions and bsfc: 2-liter four-valve I-4 engine, operated at 2000 rev/min and 2 bar bmep, with MBT spark timing. EGR data with stoichiometric operation.[17]

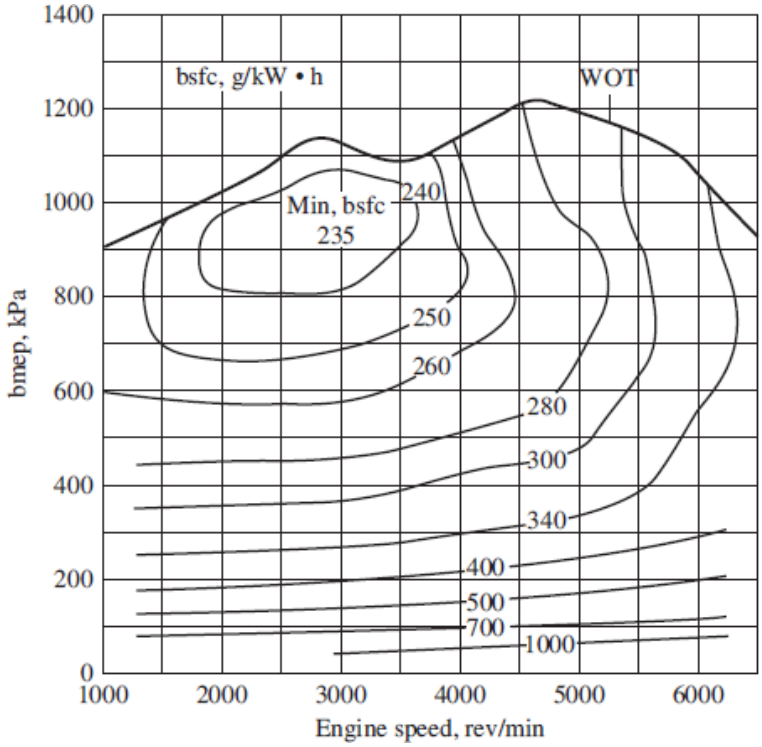


15.3.3. Load and Speed

The operating characteristics of an internal combustion engine over its full load and speed range are often plotted as lines of constant brake-specific fuel consumption on a graph of torque or brake mean effective pressure versus engine speed. Such *performance maps* have already been introduced in Sec. 15.2.3. Here we explore the specific effects of load and speed on the fuel consumption, efficiency and emissions of spark-ignition engines. While details differ from one engine to another, the overall shapes of these maps for gasoline engines are remarkably similar. Figure 15.17 shows the map for a 1.6-liter four-cylinder naturally-aspirated gasoline engine over its full load and speed range.

© McGraw-Hill Education. All rights reserved. Any use is subject to the Terms of Use, Privacy Notice and copyright information.

Figure 15.17 Performance map for 1.6-liter four-cylinder naturally-aspired SI engine showing contours of constant bsfc in grams per kilowatt-hour.[18]



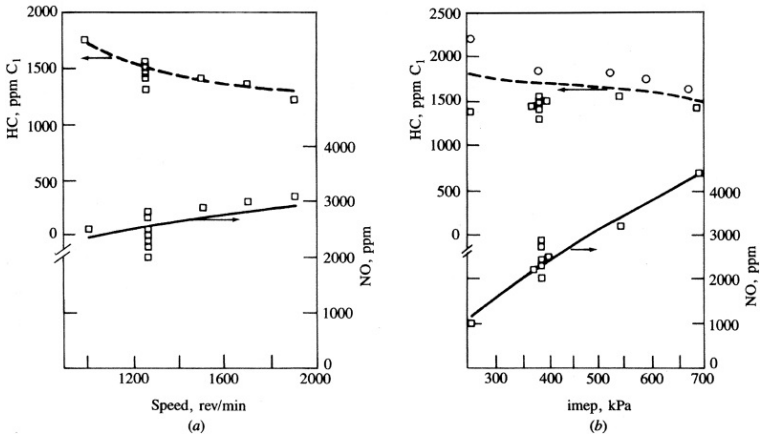
The wide-open-throttle bmep curve versus speed has the shape expected for a naturally-aspirated SI engine, with two tuning peaks (see Fig. 6.12). Maximum bmep (about 1200 kPa) occurs at 4500 rev/min; the minimum bsfc island is located at a lower speed, just below the WOT line. These map characteristics can be understood in terms of variations in volumetric efficiency η_v, gross indicated fuel conversion efficiency $\eta_{f,ig}$, and mechanical efficiency η_m, relative *A/F*, EGR (if used), and the importance of heat losses and friction, via Eqs. (15.5) and (15.7). The maximum bmep curve reflects the variation with speed of η_v, the decrease of η_m as
$\overline{S}_p$ increases, and the increase of $\eta_{f,ig}$ as
$\overline{S}_p$ increases due to decreasing importance of heat transfer per cycle.

The bsfc contour trends can be explained as follows. Starting at the minimum bsfc point, increasing speed at constant load increases bsfc due primarily to the increasing friction mep at higher speeds (which decreases η_m). While $\eta_{f,ig}$ increases modestly as speed increases, friction increases dominate. Decreasing speed at constant load increases bsfc due primarily to the increasing importance of heat transfer per cycle (which decreases $\eta_{f,ig}$). Friction also decreases, increasing η_m, but this is secondary. Any mixture enrichment required to maintain a sufficiently repeatable combustion process and avoid knock at low engine speeds contributes too. Increasing load at constant speed from the minimum bsfc point increases bsfc if mixture enrichment is used to increase torque as the engine becomes increasingly airflow limited, or to avoid knock. With or without such enrichment, spark retard worsens bsfc modestly, also. Decreasing load at constant speed increases bsfc due to the increased magnitude of friction (due to increased pumping work), the increased importance of friction mep relative to imep, and the increasing importance of heat transfer (which decreases $\eta_{f,ig}$).

The effects of speed and load variations on NO and HC emissions are shown in Fig. 15.18.[19] NO concentrations increase moderately with increasing speed at constant load. At lower loads, the proportional increase in NO is greater than at higher loads.[13] The residual gas fraction decreases as speed increases, this effect being greater at lower inlet manifold pressures (lighter loads): see Fig. 6.26. Also, the relative importance of heat transfer per cycle is less as speed increases (see Fig. 12.25), which would also be expected to increase NO concentrations. With increasing load (at constant speed), NO concentrations also increase. Again, as inlet manifold pressure and load increase, the residual gas fraction decreases (Fig. 6.26); also, the relative importance of heat transfer per cycle decreases with increasing load (Fig. 12.23).

© McGraw-Hill Education. All rights reserved. Any use is subject to the Terms of Use, Privacy Notice and copyright information.

Figure 15.18 Variation in spark-ignition engine HC and NO engine-out emissions with (a) engine speed at 330 kPa imep and (b) load (or imep) at 1250 rev/min. Relative air/fuel ratio = 1.1, MBT spark timing, r_c = 7.[19]

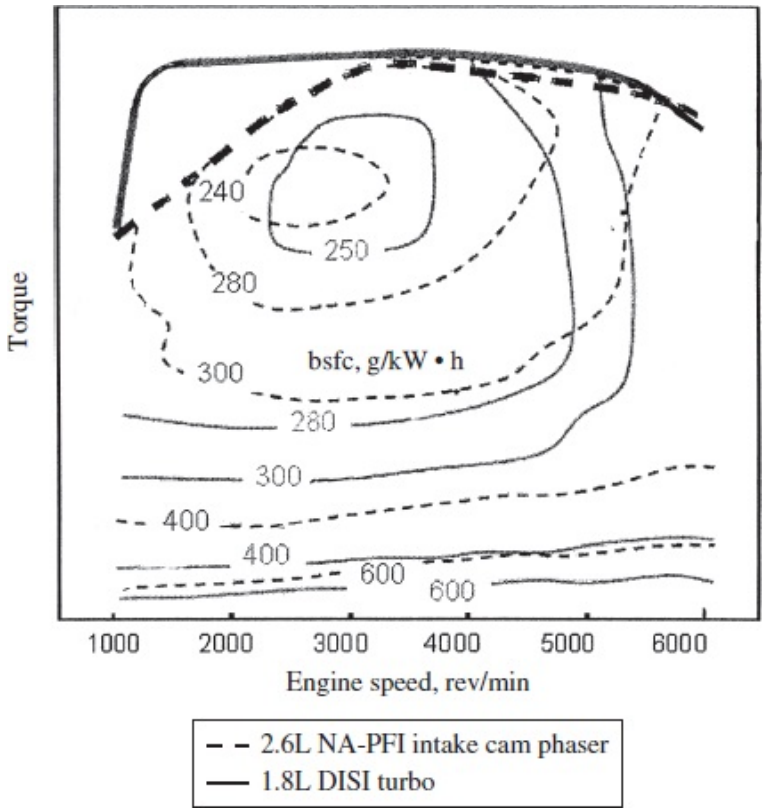


The hydrocarbon concentration trends with speed and load changes are the opposite of the NO concentration trends. As indicated in Table 11.8, speed and load are likely to affect several of the HC formation mechanisms such as the in-cylinder mixing of unburned hydrocarbons which escape normal combustion with the bulk gases, and the fraction of the in-cylinder HC which escape into the exhaust. If oxygen is available, oxidation of unburned hydrocarbons both within the cylinder and in the exhaust system will be significantly enhanced by increases in speed since the expansion stroke and exhaust process gas temperatures increase due to the reduced significance of heat transfer per cycle with increasing speed. This more than offsets the reduced residence time in the cylinder and in the exhaust. Measurements of the percent HC reacted in the exhaust port as a function of engine speed show the same proportional reduction as in the exhaust emissions data in Fig. 15.11.[20] The rationale behind the variation of HC with load is less clear. As load increases at constant speed, expansion and exhaust stroke temperatures increase, and the in-cylinder oxidation rate, if oxygen is available, will increase. However, as the exhaust gas flow rate increases, the residence time in critical sections of the exhaust system decreases and a reduction in exhaust port HC oxidation occurs.[21] The net trend is for the engine-out HC concentration to decrease modestly as load is increased.

We now compare turbocharged gasoline engine behavior with naturally-aspirated engine behavior. With a turbocharger, at higher loads when MAP increases above one bar, the density of the air entering the cylinder is increased, so imep will increase as given by Eq. (15.5). Thus, to replace a naturally-aspirated engine and provide the same torque, the turbocharged engine can be downsized—its displaced volume significantly decreased. Figure 15.19 compares the performance maps of a 1.8-liter turbocharged direct-injection spark-ignition (DISI) engine with a 2.6 liter V-6 naturally-aspirated port-fuel-injected (PFI) engine. Both have the same maximum torque (about 260 N·m), but different bmep values (TC DISI 1850 kPa, NA PFI 1200 kPa). Their low-speed torque levels, 1250 to 2500 rev/min, are significantly different.

© McGraw-Hill Education. All rights reserved. Any use is subject to the Terms of Use, Privacy Notice and copyright information.

Figure 15.19 Comparison of performance maps of a 2.6-liter naturally-aspirated port-fuel-injected gasoline V-6 engine (with cam phaser), and a 1.8-liter I-4 turbo direct-injection SI engine which have the same maximum torque and power. Wide-open-throttle lines (solid TC engine; dashed NA engine) match from about 3000 to 5500 rev/min. Lines of constant bsfc (g/kW·h) are shown (solid lines TC engine; dashed lines NA engine).[22]



The minimum bsfc of the turbo DISI engine is about 245 g/kW·h close to that of the naturally-aspirated engine (235 g/kW·h). However, when lightly loaded, at about one-quarter the maximum torque and 2000 rev/min, the TC engine has significantly lower bsfc (300 g/kW·h) than the larger-displacement NA engine (about 365 g/kW·h), an 18% reduction.

Several factors contribute to these differences, turbocharged (DI) versus naturally-aspirated (PFI). The compression ratios are similar: 10.5 for the DI turbocharged engine, 10.0 for the PFI NA engine. Turbocharging worsens the high load knock problem; direction-injection of fuel through evaporative cooling of the in-cylinder charge helps here. The biggest factor in this fuel consumption difference is the reduced impact of engine friction. The total friction mep values for the two types of engines are comparable: at part load, the NA engine has higher pumping mep, but the higher pressures (at the same torque) in the smaller displacement TC engine increases the mechanical friction mep, modestly. The much larger effect is the reduced size of the TC engine (downsized by 30%) which decreases the *magnitude* of the TC engine's friction *torque* by the same percentage. Since the bmep of the TC engine is increased by some 40% but the fmep changes little, the mechanical efficiency (η_m) increases significantly. The friction related benefits of turbocharging on part-load bsfc and efficiency, due to the major engine downsizing that usually occurs, are very significant.

Figure 15.20 shows the brake fuel conversion efficiency of a 2.0-liter 4-cylinder turbocharged DI gasoline engine, as a function of load at 2000 rev/min. Data for two fuels (for stoichiometric mixtures of each) are shown. Both the ethanol (E85) and the gasoline behaviors are essentially the same, with brake fuel conversion efficiencies at 2000 rev/min above 32% for bmep values above about 600 kPa. Efficiencies are still close to 30% for typical automotive part loads of about a quarter the maximum bmep. Note for these two fuels the brake efficiency contours on their performance maps are essentially the same. Both these fuels have high octane ratings, so engine performance at high output is not constrained by knock. Thus the performance map is essentially "fuel neutral" because the chemical energy content of their stoichiometric mixtures is almost

© McGraw-Hill Education. All rights reserved. Any use is subject to the Terms of Use, Privacy Notice and copyright information.

the same, and modest differences in their burn rates in these fast-burning engines (with optimized MBT spark timing) have little effect on engine efficiency. Note however that specific fuel consumption numbers (g/kW·h) for these two fuels are significantly different because the lower heating value, Q_{HV}, of E85 is only about 70% of gasoline's heating value![6] Thus, until knock onset occurs at high load, these performance maps for a given type of engine, expressed in brake fuel conversion efficiency at a given relative air/fuel ratio, are essentially independent of fuel.

Figure 15.20 Brake fuel conversion efficiency of a 2.0-liter four-cylinder turbocharged DI spark-ignition engine as a function of load (bmep) at 2000 rev/min with gasoline (RON 96) and with ethanol (E85).[23]

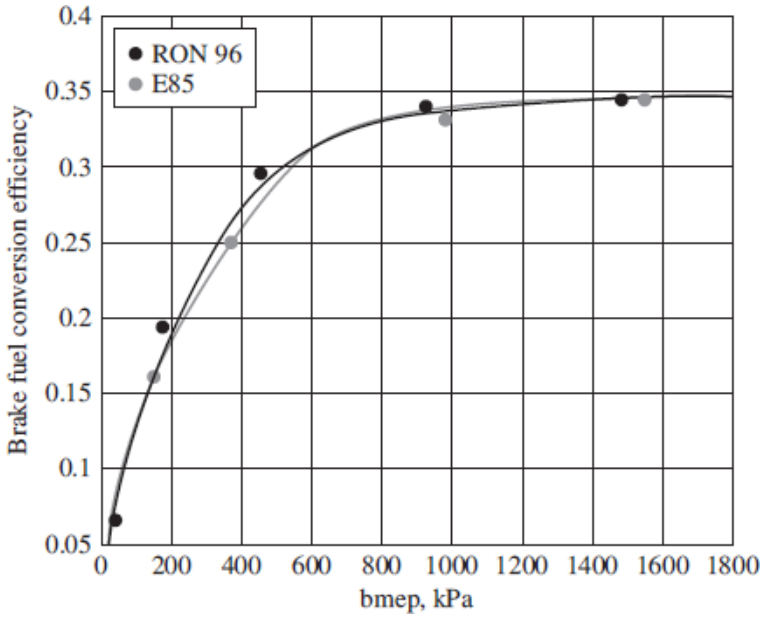
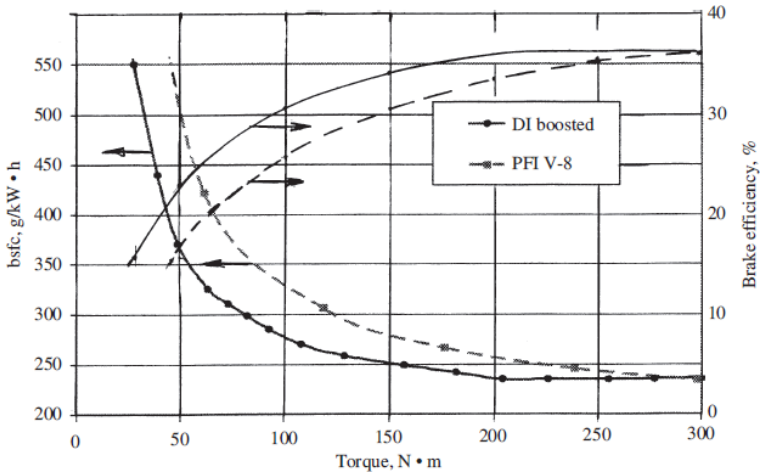


Figure 15.21 compares the bsfc and the brake fuel conversion efficiency of a DI turbocharged 3.56-liter V-6 gasoline engine, with a 10.5:1 compression ratio with a 5.7-liter V-8 naturally-aspirated PFI engine over the torque range of these engines, at 2000 rev/min, which produce comparable maximum power (DI boost 283 kW, PFI NA 298 kW) and torque (DI boost 560 N·m, PFI NA 536 N·m). The maximum bmep values for the two engines are 1980 and 1180 kPa, for the DI boost and PFI NA engines, respectively. Note that the brake efficiencies at full load are comparable (36%); however, the more rapid decline in brake efficiency (below about half maximum torque for the NA engine) is delayed significantly with the boosted engine.

© McGraw-Hill Education. All rights reserved. Any use is subject to the Terms of Use, Privacy Notice and copyright information.

Figure 15.21 Brake-specific fuel consumption and fuel conversion efficiency for a turbocharged and a naturally-aspirated gasoline engine, of comparable torque and power: 3.5-liter V-6 boosted DI TC engine and a 5.7-liter V-8 PFI NA engine. Their maximum power and torque are closely comparable. Stoichiometric operation at 2000 rev/min.[24]



Note that in turbocharged gasoline engines, maximum power and torque are often limited by maximum cylinder pressure constraints or knock. To implement these limits (since the exhaust gases contain plenty of thermal energy to drive the turbocharger to give really high boost), a turbine bypass valve or *wastegate* is employed to limit air compression in the compressor. Section 6.8.5 discusses engine/turbocharger matching and illustrates the total system configuration with a wastegate.

The above discussion illustrates how both the practical engine performance parameters (torque and power) and the normalized parameters (bmep, kW/liter, bsfc) need to be used together to explore and compare boosted gasoline engines (turbocharged and supercharged), and naturally-aspirate gasoline engines, with their different displaced volumes (for the same practical performance). It also indicates the value of calculating the important dimensionless engine efficiencies (gross and net indicated fuel-conversion efficiency, mechanical efficiency, and brake fuel-conversion efficiency) and using these efficiencies to explore the opportunities for improving engine efficiency and understanding engine performance opportunities and constraints, over the full performance map. It is useful in examining the role of individual engine variables on performance and efficiency to ask which of the various efficiencies (including volumetric efficiency) that particular variable impacts from a fundamental perspective. For example, compression ratio, which we examine next, directly affects the indicated work transfer to the piston and the indicated fuel conversion efficiency. Since it only modestly affects engine friction, so its impact on brake efficiency is not as direct.

15.3.4. Compression Ratio

The ideal cycle analysis in Chap. 5 showed that indicated fuel conversion efficiency increased continuously with compression ratio, according to Eq. (5.31). With $\gamma = 1.3$, this relation also matches closely the fuel-air cycle predictions with $\phi \approx 1.0$. However, in an actual engine other processes which influence engine performance and efficiency vary with changes in compression ratio: namely, combustion rate and stability, heat transfer, and friction. Over the load and speed range, the relative impact these processes have on power and efficiency varies also. Hence, the applicability of Eq. (5.31) is open to question. Also, while the geometric compression ratio (ratio of maximum to minimum cylinder volume) is well defined, the actual compression and expansion processes in engines depend on valve timing details and the importance of flow through the valves while they are opening or closing (which depends on engine speed). Of course, our ability to increase the compression ratio is limited by the octane quality of available fuels and knock (see Sec. 9.6.1).

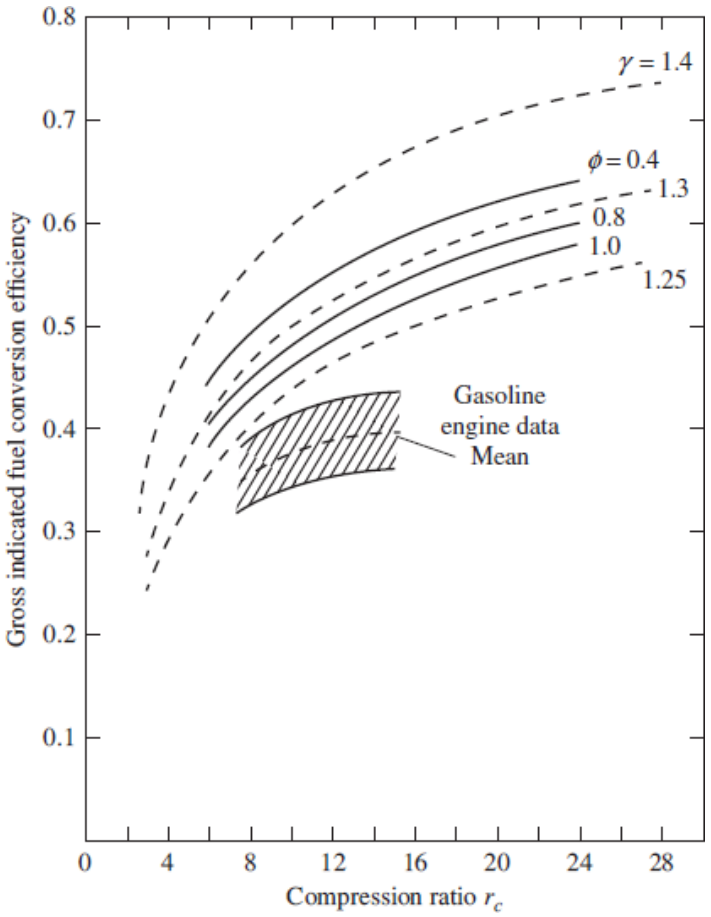
Note also that for this ideal cycle, the expansion ratio (TC to BC) equals the compression ratio. It is plausible that the term

© McGraw-Hill Education. All rights reserved. Any use is subject to the Terms of Use, Privacy Notice and copyright information.

compression ratio became standard because, long ago, poor quality fuels severely constrained the amount of compression that could be realized before knock occurred. However, the magnitude of the expansion-stroke work in this ideal cycle is about five times the compression-stroke work. So it is the *expansion ratio* and not the compression ratio that has the primary effect on engine efficiency. In actual engines the effective compression ratio and expansion ratio are not necessarily the same: they depend on intake-valve-closing and exhaust-valve-opening crank angles. Also, with modern engines, variable valve timing is a common feature. While the average intake valve closing is about 50 degrees after BC, and exhaust valve opening 55 degrees before BC, variations of some ±20 degrees about these mean values now occur. The terms *effective* compression and expansion ratio are often used to better define the actual engine's compression and expansion processes. These are defined by the cylinder volumes at intake valve closing and exhaust valve-opening crank angles, respectively.

Results from the ideal-gas constant-volume cycle and the fuel-air cycle for various compression ratios, specific heat ratios, and equivalence ratios are shown in Fig. 15.22. These results show that *indicated* fuel conversion efficiencies are expected to increase, though at a decreasing rate, with increasing compression ratio. However, analysis of extensive SI engine data shows a different behavior. There is a significant spread in the efficiency values across different engine designs and operating conditions and, as would be expected, the engine indicated efficiencies are lower than the ideal-cycle values by some 15%. In these several experiment studies, where compression ratio was changed in a given engine by decreasing the clearance height of the pistons (thus, at constant engine displaced volume), while efficiency increases with increasing compression ratio, it does so at a decreasing rate and reaches a maximum at a (geometric) compression ratio of about 15:1.

Figure 15.22 Gross indicated fuel conversion efficiency as a function of compression ratio for the ideal gas constant-volume cycle with different values of γ (dashed lines), the fuel-air cycle (see Sec. 5.5.1) for different values of ϕ (the fuel-air equivalence ratio), and the available modern gasoline SI engine data.[25]



© McGraw-Hill Education. All rights reserved. Any use is subject to the Terms of Use, Privacy Notice and copyright information.

That engine efficiency data are lower than the ideal cycle values, and at higher compression/expansion ratios have a different trend, should not be surprising. As this text has discussed, several "losses" contribute:

- Changing gas properties (the ratio of specific heats, γ) decreases with increasing temperature.
- The combustion process does not release all the fuel's chemical energy.
- Combustion, though fast, takes up a finite portion of the compression and expansion strokes.
- Significant heat loss from the burned gas reduces the gas pressure.
- The blowdown process when the exhaust valve opens before BC loses a fraction of the full expansion stroke work.

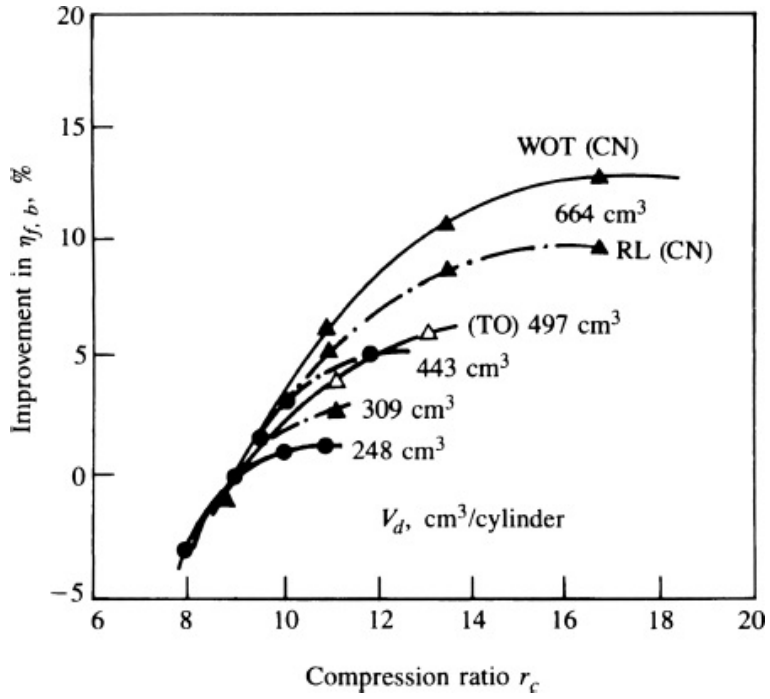
Note that the above losses occur over the compression and expansion strokes, and thus impact the gross indicated performance and efficiency of the engine. The net indicated output $\int pdV$ over the full four strokes of the cycle) additionally includes the pumping work (losses in a naturally-aspirated gasoline engine; a gain in a turbocharged gasoline engine operating with intake pressures above 1 bar). The brake performance and efficiency are additionally impacted by the magnitude of engine friction (its mechanical and accessory components: pumping work is included in the net indicated values).

Studies that have examined the effect of compression ratio on spark-ignition engine performance and efficiency over a wide range of compression ratios are limited. Figure 15.22 shows results from a recent broadly based analysis.[25]

An important question is the effect of compression ratio variations for different size engine cylinders. Improving engine performance and turbocharging/downsizing are prompting reductions in engine size. Figure 15.23 shows brake fuel-conversion efficiency data from engines of different cylinder volume. Both the compression ratio for maximum efficiency, and the value of maximum efficiency, depend on cylinder size. The wide-open-throttle and road-load data (top two curves[26]) confirm that the increase in efficiency with an increase in the compression ratio at part load apparently depends on the details of engine operation to a significant degree also. For the important compression ratio range of 9 to 11, this data set indicates that the relative efficiency improvement is between 1 and 3% per unit of compression ratio increase, depending on cylinder size and operating conditions. Naturally-aspirated gasoline engine cylinder sizes are about 500 cm^3 per cylinder (in 2015). Smaller turbocharged engines are becoming common (e.g., 1-liter three-cylinder engines with 333-cm^3-size cylinders).

© McGraw-Hill Education. All rights reserved. Any use is subject to the Terms of Use, Privacy Notice and copyright information.

Figure 15.23 Relative brake fuel conversion efficiency improvement with increasing compression ratio of spark-ignition engines of different displaced volume per cylinder: top curve at wide-open throttle, CN;[26] road load (RL), CN,[26] other curves at part throttle, MTJ;[27] TO.[28]



The exhaust temperature decreases as compression ratio and efficiency increase until the compression ratio corresponding to maximum efficiency is reached. It has also been shown that heat losses to the combustion chamber walls, as a fraction of the fuel's chemical energy, also decrease as the compression ratio and efficiency both increase.[26]

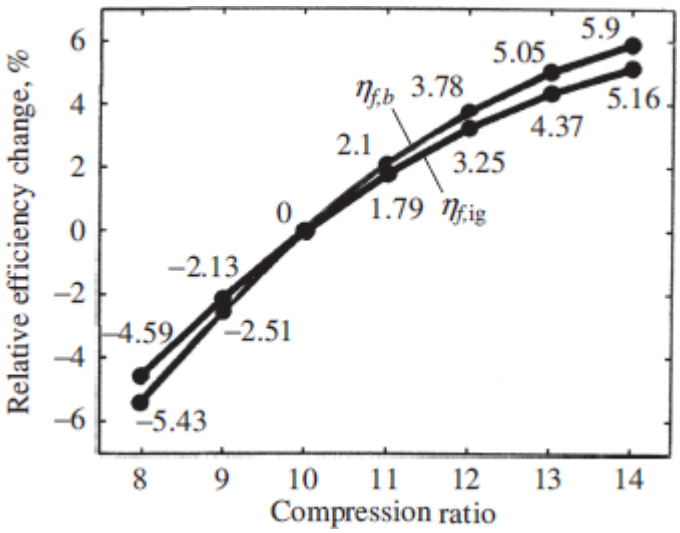
The effect of compression ratio changes on NO emissions is small. Some studies show a modest increase in specific NO emissions as the compression ratio increases at constant load and speed; other studies show a slight decrease. Increasing the compression ratio increases exhaust hydrocarbon emissions. Several trends could contribute: increased importance of crevice volumes at high r_c; lower gas temperatures during the latter part of the expansion stroke, thus producing less HC oxidation in the cylinder; decreasing residual gas fraction, thus increasing the fraction of in-cylinder HC exhausted; lower exhaust temperatures, hence less oxidation in the exhaust system.

The overall impact of increasing compression ratio on engine efficiency can be summarized as follows. Compression ratio values are currently about 10:1 for naturally-aspirated PFI gasoline engines, 9:1 for turbo PFI engines, and 10.5 for turbo DI engines. The higher pressures in turbocharged engines at high load make knock onset (autoignition of the fuel-air mixture ahead of the propagating flame) more likely. The cooling of the in-cylinder charge through evaporation of the direct-injected liquid gasoline spray delays knock onset and allows use of higher compression ratios. These compression ratio values have been steadily rising over time,[3] a trend that is expected to continue and is enabled by increasing use of variable intake valve closing, more uniform cylinder head cooling, and more sophisticated spark retard strategies based on better knock sensing and control.

Figure 15.24 shows the relative change in indicated and brake efficiency (expressed as a percentage) as a function of compression ratio, normalized to $r_c = 10$. The difference between the two curves (each an average of several data bases) is modest. (The changes in brake efficiency are slightly higher since the normalizing number—the brake efficiency at 10:1 compression ratio—is slightly lower.) The differences between these efficiencies at low (1 to 3 bar bmep), mid (4.5 to 7 bar bmep), and high (7.5 to 9.5 bar bmep) are also small. Overall, we see that at *constant engine displaced volume*, raising r_c from 10 to 11 gives a 2% efficiency improvement, from 12 to 13 a 1.3% improvement, and above 15:1 essentially no increase. Thus, future compression ratio increases offer decreasing benefits, with an upper limit at about 15:1.

© McGraw-Hill Education. All rights reserved. Any use is subject to the Terms of Use, Privacy Notice and copyright information.

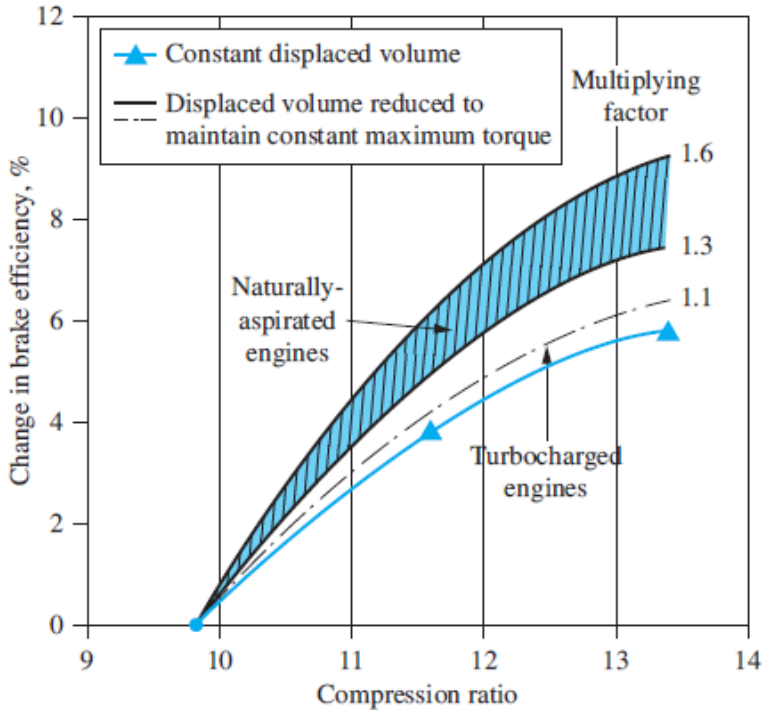
Figure 15.24 Average relative gross indicated and brake fuel conversion efficiency changes versus compression ratio, gasoline SI engines. Relative efficiency changes from unit compression ratio changes are noted (as percentages): r_c normalized at 10:1.[25]



However, as compression ratio is increased, so is the engine's maximum torque. Thus the engine's displacement can be reduced so the torque remains constant (as the higher-compression ratio engine does the same task). With engine downsizing, the benefits of raising compression ratio are significantly increased as shown in Fig. 15.25. Without engine downsizing, the increase in brake efficiency as r_c increases from 9.8 to 13.4 is close to 6% (close to the value, from a different study, in Fig. 15.24). With adjustments in engine size made to maintain constant maximum torque, the efficiency increase is higher. This constant torque comparison, with appropriate engine downsizing, is the comparison of greatest interest. Effectively, the benefits presented in Fig. 15.24 at constant engine displacement, for practical applications where downsizing would occur, understate the real potential.[29] The additional gain depends on whether the engine is naturally-aspirated or turbocharged. It also depends on the rate of change in efficiency with load at the bmep level at which this downsizing effect is being evaluated. At lighter loads, the multiplying factor (shown in Fig. 15.25) is higher: in the 1.3 to 1.6 range for naturally-aspirated gasoline engines. At higher loads, this enhancement factor is lower: it is about 1.1 for turbocharged gasoline engines.

© McGraw-Hill Education. All rights reserved. Any use is subject to the Terms of Use, Privacy Notice and copyright information.

Figure 15.25 *Estimated increase in light- to mid-load brake fuel-conversion efficiency of gasoline engines, with increasing compression ratio: bottom curve, at constant displaced volume; upper curves, with engine downsizing to maintain constant maximum engine torque. Efficiency benefit multiplying factor for naturally-aspirated and turbocharged engines shown on right. (Multiplying factor is change in efficiency with downsizing relative to change in efficiency at constant displaced volume.)*[29, 30]



[1] In this text we use *absolute* pressure levels (where zero is full vacuum). MAP values are sometimes given as *gauge* pressures: that is, relative to one atmosphere (≈ 1 bar).

[2] Note: this universal behavior between net indicated mep and combustion retard defined by $\theta_{50\%}$ mass fraction burned is expected. It is the indicated work transfer to the piston that combustion phasing controls and the midpoint of the burning process does effectively define the phasing of combustion relative to the piston position.

[3] This aspect of mixture nonuniformity is least well defined. Mixing of the fresh mixture (fuel, air, and EGR) with residual gas is likely to be incomplete (see Fig. 14.31), especially at light load when the residual gas fraction is highest. With intake-port fuel-injection systems, there is evidence of incomplete fuel-air mixing due to the fact that the airflow and fuel flow processes are not in phase. When the engine is cold, fuel distribution within the cylinder is known to be more nonuniform.

[4] EGR is normally zero at WOT, since maximum available torque is usually desired.

[5] Except during start-up and cold engine operation, when a significant part of the fuel within the cylinder can be in the liquid phase.

[6] With a given stoichiometry mixture of ethanol and air, the lower heating value of ethanol is offset by the higher *F/A* ratio required relative to gasoline, resulting in little difference in heating value per unit mass or volume of fuel vapor/air mixture.

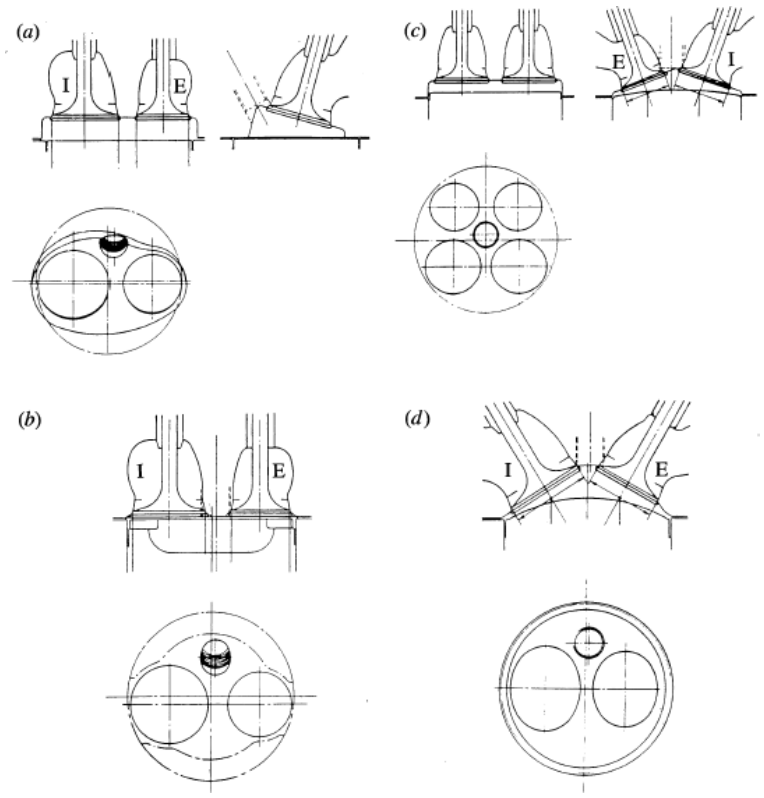
© McGraw-Hill Education. All rights reserved. Any use is subject to the Terms of Use, Privacy Notice and copyright information.

15.4. SI ENGINE COMBUSTION SYSTEM DESIGN

15.4.1. Objectives and Options

SI engine combustion-chamber design continues to evolve as requirements and our knowledge base changes. There are several options for cylinder head and piston crown shape, spark plug location, size and number of valves, and intake port design. Involved are questions such as chamber compactness, surface/volume ratio, flame travel length, how and where the fuel is injected, and use of swirl, tumble, and squish types of mixture motion. Figure 15.26 shows examples of several common combustion chamber shapes. A consensus has developed which favors faster-burning combustion-chamber designs. A chamber design where the fuel burning process takes place faster (i.e., occupies a shorter crank-angle interval at a given engine speed) produces a more robust and repeatable combustion process that provides emission control and efficiency gains simultaneously. A faster-burning chamber with its shorter burn time permits operation with substantially higher amounts of EGR, or with leaner mixtures, within the normal constraints of engine smoothness and response. Thus greater emissions control within the engine can be achieved and, at part load at this higher level of dilution, a faster-burning chamber shows an improvement in fuel consumption due to the reduced pumping work, reduced heat transfer (due to lower burned gas temperatures), and higher γ due to reduced temperatures and amount of dissociation in the burned gases.

Figure 15.26 Examples of different spark-ignition engine combustion chamber shapes: (a) bathtub and wedge; (b) bowl-in-piston; (c) four-valve pent roof; and (d) hemispherical.[31]



The major combustion chamber design objectives that relate to engine performance and emissions are:

- A fast combustion process, with low cycle-by-cycle variability, over the full engine operating range.
- High volumetric efficiency at wide-open throttle.

© McGraw-Hill Education. All rights reserved. Any use is subject to the Terms of Use, Privacy Notice and copyright information.

- Minimum heat loss to the combustion chamber walls.
- A low fuel-octane requirement.
- Low engine-out emission levels (especially when the engine is cold).

Many methods for producing "fast burn" have been proposed. These include ways of making the combustion chamber shape more compact, moving the spark plug to a more central location within the chamber, using two plugs, and increasing in-cylinder gas motion by creating a tumbling or swirling flow in the cylinder during the induction process.

A faster combustion process relative to slower burn-rate older engines does result in a direct engine efficiency gain, other factors being equal. The magnitude of this direct gain is relatively modest. Experimental studies of the effect of an increase in burn rate from slow to moderate on engine efficiency is significant: from moderate burn to fast burn at constant engine load, speed, and mixture composition, the burn rate effect is several percent but not more.[32] (From fast to very fast burn achieves a smaller percentage still.) Computer simulations of the engine operating cycle confirm these experimental observations: while a decrease in total burn duration from 100 to 60° does result in a 4% decrease in bsfc, a decrease in burn duration from 60 to 20° gives only a further 1.5% bsfc decrease.[13]

Of greater importance is the fact that the faster burn process is more robust and results in the engine being able to operate satisfactorily with much more EGR, or much leaner, or with greater spark retard, without a large deterioration in combustion quality. Faster burning chamber designs exhibit much less cycle-by-cycle variability. This ability to operate with greater dilution at part load while maintaining a short burn duration and low cycle-by-cycle combustion variability, permits greater control of NO_x within the engine with some 15% EGR without any substantial increase in HC emissions (see Fig. 11.31), or permits much leaner operation. In both cases the efficiency gain relative to moderate burn-rate engines, which must operate with less dilution, is sizeable.[33]

High volumetric efficiency is required to obtain the highest possible power density. The size and shape of the cylinder head affects the sizes of the valves that can be incorporated into the design. Effective valve open area, which depends on number of valves, valve diameter and lift, directly affects volumetric efficiency. Tumble and swirl are components in chamber designs that speed up the burning process and achieve greater combustion stability. Induction-generated tumble (see Sec. 8.4) is a particularly effective in-cylinder flow for increasing the burn rate. It results in higher turbulence inside the chamber during combustion thus increasing the rate of flame development and propagation. Generating tumble during the intake process does decrease volumetric efficiency.

Heat transfer to the combustion chamber walls has a significant impact on engine efficiency. It is affected by cylinder head and piston crown surface area, by the magnitude of in-cylinder gas velocities during combustion and expansion, by the gas temperatures and the wall temperatures. The heat-transfer implications of a combustion chamber should be included in the design process.

Knock effectively limits the maximum compression ratio that can be used in any combustion chamber; it therefore has a direct impact on efficiency. Knock is affected by most of the combustion chamber features discussed above. It is the hardest of all the constraints to incorporate into the design process because of its complexity.

Knowledge of the fundamentals of spark-ignition engine combustion, in-cylinder gas motion, and heat transfer has developed to the point where a rational procedure for evaluating these factors for optimum combustion chamber development and design can be defined. The next two sections develop this logic.

15.4.2. Factors That Control Combustion

Our understanding of the structure of the spark-ignition engine flame as it develops and propagates across the combustion chamber (see Secs. 9.3 and 9.4) allows us to relate the physical and chemical factors that control this process to the relevant

© McGraw-Hill Education. All rights reserved. Any use is subject to the Terms of Use, Privacy Notice and copyright information.

combustion system design and operating parameters. The following factors affect the flame development and propagation processes:

- *Geometry*. Combustion chamber shape and spark plug location.
- *Flow field characteristics*. Mean velocity, turbulence intensity, and characteristic turbulence length scale in the unburned mixture during the combustion process.
- *Unburned mixture composition and state.* Fuel, relative air/fuel ratio, burned gas fraction, mixture pressure and temperature.

Geometry primarily affects combustion through the flame-front surface area. It has a lesser effect on combustion development through its influence on in-cylinder motion. Geometric calculations (see Sec. 14.4.2), based on the assumption that the front surface of the flame can be modeled as a portion of a sphere centered at the spark plug, provide data on flame front area and the volume behind the flame front surface (the enflamed volume), contained within the combustion chamber, as a function of flame radius and piston position.

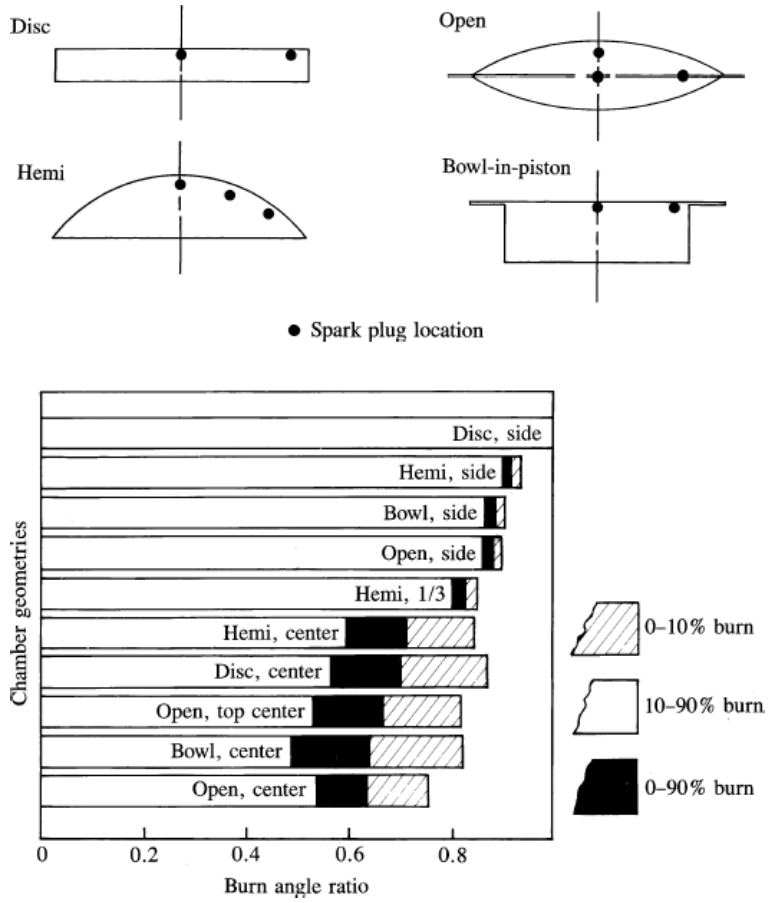
Flame area varies significantly from one chamber shape to another for a given enflamed volume. In the example shown inFig. 14.7, the bowl-in-piston chamber gives flame surface areas 30 to 45% larger than those for the disc chamber under equivalent conditions, around top center. Hemispherical and open or clamshell chambers showed gains of about 30% relative to the equivalent disc configuration. For a given chamber shape, flame area depends even more significantly on plug location. Figure 14.7 also shows that shifting the plug from a side to a center location for the bowl-in-piston chamber increased the peak flame area by 150%. For hemispherical and open chambers, the increases for a similar shift in plug location were 75 and 90%, respectively.[34]

Maps of flame area as a function of radius at different crank angle locations indicate the following pattern. For chamber geometries with side ignition, as flame radius increases the flame area first rises slowly, then remains approximately constant, and then decreases slowly to zero. In contrast, chambers with central ignition show, as flame radius increases, a rise in flame area to a peak during the major part of the flame travel followed by a rapid decrease as the flame encounters the chamber walls. Moving the plug location toward the center of the chamber produces a larger increase in flame front area than does making the chamber shape more compact (though this has a positive impact too).

The effect of chamber geometry on burn rate has been examined using thermodynamic-based engine cycle simulations with various types of combustion model (e.g., the type developed by Keck and coworkers; see Sec. 14.4.2). Figure 15.27 shows results from one such study.[34] The combustion characteristics of ten different chamber geometries were compared at fixed part-load engine operating conditions. The flame development and propagation phases were separated into 0 to 10% and 10 to 90% mass fraction burned times. These were then normalized by the equivalent burn times of the slowest burning chamber —the disc with side ignition. Chamber geometry has the greatest impact on the 10 to 90% burn time; its effect on 0 to 10% time is significant but substantially smaller. Total burn times can be reduced by between 20 and 30% by optimizing spark plug location—comparing worst to best location for each chamber shape. Comparing worst and best chamber shapes, total burn time with fixed plug location can be reduced by about 10%.

© McGraw-Hill Education. All rights reserved. Any use is subject to the Terms of Use, Privacy Notice and copyright information.

Figure 15.27 Comparison of burn angles (0 to 10% burned, 10 to 90% burned, 0 to 90% burned (see Fig. 9.15) for ten different spark-ignition engine combustion chamber geometries and spark plug locations. Burn angles are normalized by the burn duration angle for the slowest burning chamber: disc with side plug.[34]



Increased turbulence in the unburned mixture at the time of combustion increases the burning rate. Turbulence is usually increased by generating swirl during the induction process (see Sec. 8.3.2 and below). Cycle simulation studies[34] indicate that both the duration of the early stage of the burning process, and of the main stage, decrease when the turbulence levels during combustion are increased. The faster combustion process comes primarily from the higher turbulence intensity increasing the rate of flame propagation; however, the decreased characteristic turbulence scale that accompanies the increased turbulence is also significant since it results in a shorter characteristic burning time [see Eq. (14.38), and the accompanying text]. It is important to note that the fuel conversion efficiency of higher-turbulence chambers at the same operating conditions are not necessarily higher than for normal chambers, despite the faster burn rates, due to the higher heat transfer rates that accompanies the higher in-cylinder velocities. For example, predictions based on the combustion model defined by Eqs. (14.33) to (14.35), where the characteristic mixture convection speed u_T was increased by a factor of two, showed that the 0 to 10% and 10 to 90% burn durations decreased by about one-third. However, the indicated fuel conversion efficiency decreased by about 6% due to the predicted 15% increase in heat transfer per cycle.[34]

Mixture composition and state affect the burn rate through the dependence of laminar flame speed on temperature, pressure, fuel/air equivalence ratio, and burned gas fraction (residual gas and EGR): see Sec. 9.3.3 and Eqs. (14.33) to (14.35). Table 15.2 compares the burn durations for a stoichiometric mixture, a lean mixture with ϕ = 0.8, and a stoichiometric mixture with 20% EGR. The values of the laminar flame speed at the time of spark are also given (conditions at spark as well as composition are different in each case). The longer burn durations of the more dilute mixtures are clear. Note that EGR as a diluent has a much more deleterious effect on combustion than does air at these approximately equal levels of dilution.

© McGraw-Hill Education. All rights reserved. Any use is subject to the Terms of Use, Privacy Notice and copyright information.

Table 15.2 Effect of excess air and recycled exhaust on burn duration

λ	EGR, %	θ_s, deg	Burn durations, deg		S_L at θ_s, cm/s
			0–10%	10–90%	
1.0	0	340	22	17	75
1.25	0	336	26	21	52
1.0	20	324	31	28	23

400 cm^3 per cylinder displaced volume, 80 mm bore, compression ratio 8.5, disc chamber, center plug location. 1500 rev/min, stoichiometric operation, θ_S = spark timing (MBT), inlet pressure 0.5 atm, inlet temperature 350 K, S_L = laminar flame speed.[35]

All the above-described factors—flame geometry, fluid motion, and mixture composition—can vary cycle-by-cycle, and therefore contribute to combustion variability (see Sec. 9.4). Cyclic differences in gas motion in the vicinity of the spark plug result in differences in motion of the flame during its early stages of development. Differences in turbulence result in differences in the rates at which the initially smooth surface of the flame kernel becomes wrinkled and convoluted by the flow. Also, different initial flame center motions change the geometrical interaction of the flame front with the combustion chamber walls later in the flame propagation process. Differences in the amount of fuel, air, and EGR which enter each cylinder cycle-by-cycle, the nonuniformity in composition of the entering charge, and any incomplete mixing of that entering charge with the residual gases in the cylinder, also contribute to combustion variability. These composition nonuniformities lead to differences in the early stages of flame development. The variations in the amounts of fuel, air, and EGR that enter each cylinder cycle-by-cycle and in the uniformity of that mixture are factors over which the engine designer has some control.

A fast combustion process reduces cyclic combustion variability through the factors summarized inTable 15.3. With a faster burn, optimum spark timing is closer to top-center: mixture temperature and pressure at the time of spark are higher, so the laminar flame speed at the start of combustion is greater. This, combined with the higher turbulence of fast-burn combustion systems, results in faster flame kernel development. More rapid initial flame growth results in less variation in flame center motion during the critical flame-development phase. The resulting geometric variations in the flame front/chamber wall interaction are therefore reduced; this decreases the variations in burn rate that result from these geometric variations. Also, the faster burning process ends earlier in the expansion stroke. Thus the problem of occasional slow burning cycles, partial burning cycles, and eventually misfire, which occurs with dilute mixtures under normal burning conditions due to quenching of the combustion process as gas temperatures fall during expansion, is largely avoided (see Sec. 9.4.3).

© McGraw-Hill Education. All rights reserved. Any use is subject to the Terms of Use, Privacy Notice and copyright information.

Table 15.3 Causes of SI engine cycle-to-cycle combustion variations

Phases of combustion

1. Early flame development
2. Flame propagation
3. Late stage of burning

Factors affecting SI engine cycle-to-cycle variations

a. Spark energy deposition in gas (phase 1)
b. Flame kernel motion (phase 1)
c. Heat losses from kernel to spark plug (phase 1)
d. Local turbulence characteristics near plug (phase 1)
e. Local mixture composition near plug (phase 1)
f. Overall charge components – air, fuel, residual, EGR (phases 2, 3)
g. Average turbulence in the combustion chamber (phases 2, 3)
h. Large-scale features of the in-cylinder flow (phase 3)
i. Flame geometry interaction with the combustion chamber walls (phase 3)

15.4.3. Factors That Control Performance

15.4.3.1. Volumetric Efficiency

Combustion chamber shape affects volumetric efficiency through its constraints on maximum valve size and through the degree of tumble or swirl (if any) that the chamber and port designs produce to achieve the desired combustion characteristics. To obtain maximum performance and to reduce pumping losses, two intake valves (four-valve, three-valve cylinder heads), with the size of the valve heads as large as is practical. The valve sizes that can be accommodated depend on cylinder head layout. Table 6.1 lists the typical maximum valve sizes that can be accommodated into several common chamber shapes (see Fig. 15.26). The approximate mean piston speed at maximum power is a measure of the maximum airflow that each engine design can pump. Note that cylinder head configurations with inclined valve stems permit greater maximum airflow because, for a given bore, the valve and port open areas are larger. The four-valve pent-roof design, through its four valves and inclined valve stems, is the best of those listed since it accommodates the largest valve and port areas.

Table 15.4 illustrates the impact of the number of valves per cylinder (vpc), and fixed and variable valve timing, on the key engine performance parameters with results from a study of some 200 gasoline engines in the 2008 model year North American light-duty vehicles. The various configurations are listed in order of increasing airflow. With naturally-aspirated engines (the first four lines in Table 15.4), maximum bmep, $P_{b,\max}/V_d$ and $\overline{S}_p$ at $P_{b,\max}$ all increase as the cylinder-head intake flow resistances are decreased. With boosting (supercharging and turbocharging) output "jumps" significantly, and with turbocharging the maximum mean piston speed is reduced to limit the increasingly negative effect of engine friction at very high engine speed: additional boost can be used to offset this *downspeeding*.

© McGraw-Hill Education. All rights reserved. Any use is subject to the Terms of Use, Privacy Notice and copyright information.

Table 15.4 Normalized performance: 2008 North American engines[3]

Valve configuration, etc.	Number of engines, 203 total	Max. bmep (max torque), kPa	Specific power ($P_{b,max}/V_d$), kW/liter	bmep at max power, kPa	bmep at max power/max bmep	Max $\overline{S}_p$ at $P_{b,max}$, m/s
12 vpc	42	1082	42.9	970	0.90	15.8
3 vpc	7	1162	45.7	1018	0.88	17.2
4 vpc, fixed	47	1177	51.6	1039	0.88	17.3
4 vpc, variable	81	1230	56.9	1109	0.9	18.1
4 vpc, superch.	4	1734	75.6	1487	0.85	18.6
4 vpc, turboch.	22	1817	80.2	1688	0.93	16.9

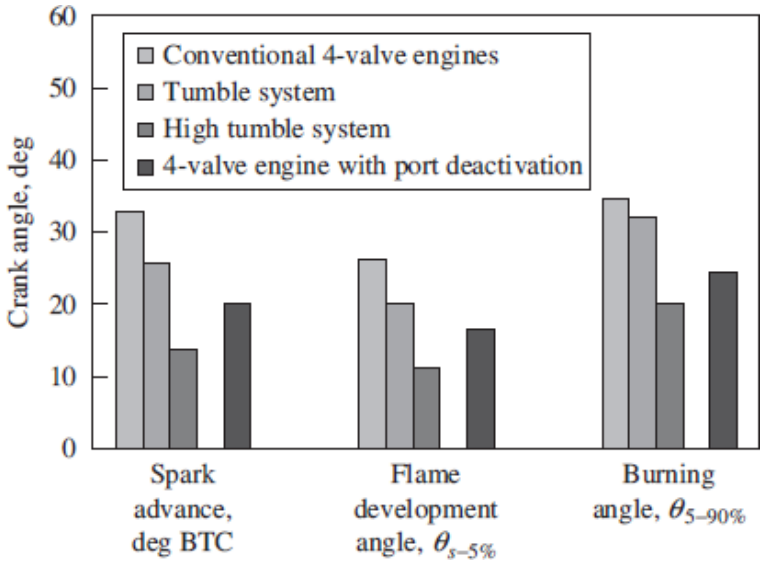
15.4.3.2. Tumble and Swirl

Moderate levels of *tumble* (or *swirl*) are used in gasoline SI engines to achieve fast-enough burn rates through realizing higher turbulence levels in the in-cylinder fluid (see Figs. 8.4 and 8.19). To achieve a tumbling in-cylinder flow, the cylinder head is designed with the intake port axes lowered so as to bring the airflow entering the cylinder largely past the top of the intake valve head and across the cylinder as shown in Fig. 8.19. As the piston moves down the cylinder, this flow moves downwards, then back across the cylinder and sets up the rotating flow illustrated. As the piston moves up after BC, this tumbling flow is "squashed" and breaks up during the compression stroke into first, smaller eddies, and then turbulence, in time to speed up the flame propagation process.

Typical impacts of tumble and swirl on spark-ignition engine's combustion characteristics are shown in Figure 15.28. Increasing the tumble ratio speeds up the burning process significantly: both the flame development angle ($\Delta\theta_{spark-5\%}$) and the burn duration ($\Delta\theta_{5-90\%}$) decrease. The port-deactivation swirl-generating system is intermediate in its impact between the medium and high tumble cases. This is in line with the broader assessment that moderate tumble is usually the appropriate choice to achieve stable SI engine combustion: it provides a fast-enough burn rate to realize most of the burn-rate efficiency benefits, while maintaining a relatively high flow coefficient at high speeds and loads. Typically, flame development and burning angles below about 20 and 25 degrees, respectively, are needed at these light-load low-speed conditions.

© McGraw-Hill Education. All rights reserved. Any use is subject to the Terms of Use, Privacy Notice and copyright information.

Figure 15.28 Influence of different types and levels of in-cylinder charge motion on SI engine flame development and propagation. Stoichiometric operation, at 3 bar bmep and 2000 rev/min. Conventional, four-valve pent roof combustion system (see Fig. 15.26): tumble systems ranged from tumble ratios of 3 to 6; port deactivation (see Fig. 8.28) generated a swirl ratio of about 2.[36]



As an alternative to tumble,*swirl* can be generated during the intake process through suitable port, valve, and head design. It requires either that the flow through the intake valve be directed tangentially into the cylinder so that gas flows through one side of the valve opening preferentially (e.g., through the use of masks to restrict flow at the mask location, or through the use of a tangentially-directed port, or a flow deflector in the port just upstream of the valve), or requires the use of a helical intake port that generates rotation of the flow about the valve stem before the air enters the cylinder. In either case the flow enters the cylinder with higher velocity than it would have in the absence of swirl: hence the pressure drop across the port and valve is increased, and the maximum airflow through the cylinder is reduced. Well-designed helical swirl-generating ports (see Sec. 8.3.2) appear to be the best way to create swirl. In gasoline engines geometric and production constraints often prevent the incorporation of such ports into the cylinder head design, and other swirl-generating methods must be used. The engine maximum-power penalty associated with generating significant swirl is of order 5%.

Since tumble or swirl is required at part-throttle operation when enhancement of the burn rate is most critical and is not usually needed at full throttle when the flow restriction penalty is most significant, induction systems with a modified passage for the part-throttle airflow are an attractive option. However, the gains in volumetric efficiency are offset by a higher cost due to the additional complexity in port and manifold of the double passage and the individual throttle valves required in each port for flow control.

In smaller-size DI diesel engines, swirl is intensified during compression with bowl-in-piston combustion chambers by decreasing the moment of inertia of the in-cylinder charge as the piston moves toward top-center, thereby increasing its angular velocity (see Sec. 8.3.3). An advantage here is that the swirl level generated during induction is less than would be required without the compression-produced radially inward motion of the charge. The impact of piston-motion generated radially-inward squish motion (see Sec. 8.5) on in-cylinder turbulence, and hence combustion, is complex. Chambers with significant squish are more compact; for this reason alone, they would be faster burning.

15.4.3.3. Heat Transfer

The convective heat transfer to the combustion chamber walls is described by equations of the form of Eq. (12.2). The heat-transfer coefficient is usually correlated by expressions of the form of Eq. (12.3), which relates the Nusselt, Reynolds, and Prandtl numbers (see Sec. 12.4). Thus combustion chamber surface area, and especially the surface area in contact with the

© McGraw-Hill Education. All rights reserved. Any use is subject to the Terms of Use, Privacy Notice and copyright information.

burned gases, is an important parameter. The in-cylinder gas velocity is also important: it influences the heat-transfer rate through the Reynolds number. Various characteristic velocities have been used in the Reynolds number to scale heat transfer: mean piston speed, mean in-cylinder gas velocity, turbulence intensity, either individually or in combination. Both of these variables, area and velocity, are affected by combustion chamber design.

Studies of engine performance using thermodynamic-based simulations of the engine's operating cycle (seeSec. 14.4) provide data that indicate the importance of changes in heat transfer. At part-throttle operating conditions, such simulation calculations show that a 10% change in combustion chamber heat losses results in a change of between 2 and 5% in brake-specific fuel consumption; an average fuel consumption (relative) change of about one-third the magnitude of the relative heat-transfer change (and of opposite sign) is an appropriate rule of thumb.[34,37] At wide-open throttle, the effect on mean effective pressure is comparable: a 10% change in heat transfer results in about a 3% change in bmep.

This impact of heat transfer on engine efficiency and performance underlines the importance of combustion chamber details that affect heat transfer. For the chamber shapes shown in Fig. 15.27, the total heat losses as a fraction of the fuel's energy, at fixed engine speed and intake conditions, were also calculated. Both chamber shape and spark plug location affect heat losses since together these govern the surface area of the hot burned gases in contact with the walls. The open and hemispherical chambers had least heat transfer. Geometries such as the bowl-in-piston which obviously have a higher surface area had about 10% higher heat transfer. The effect of shifting the plug from a side location to a center location depended on chamber shape. Open and bowl-in-piston chambers showed little change; the hemispherical chamber showed a 4% reduction. Given an overall chamber-shape choice, the details of the actual design are also important; it is easy to add substantial surface area with piston cutouts, plug bosses, cylinder head masking, and squish regions which can deteriorate chamber performance to a measurable degree.

Higher in-cylinder velocities affect heat-transfer rates through the Reynolds number term in the heat-transfer coefficient correlation. Tumble, swirl, and squish-generated flows increase in-cylinder gas velocities and will, therefore, increase heat-transfer rates.

15.4.4. Chamber Octane Requirement

The abnormal combustion phenomenon called knock limits a spark-ignition engine's compression ratio, and hence its performance and efficiency. The more fundamental aspects of knock are reviewed in Sec. 9.6.2. Knock occurs when the fuel-air end-gas mixture ahead of the flame ignites spontaneously prior to its being burned up by the normal flame-propagation process. The tendency to knock depends on engine design and operating variables which influence end-gas temperature, pressure, and time spent at high values of these two properties, before flame arrival.

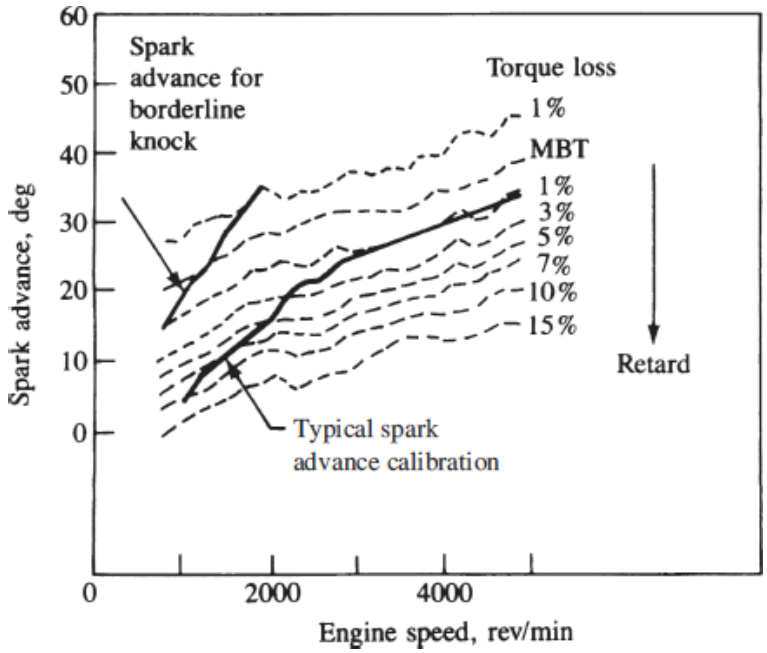
The presence or absence of knock in an engine also depends on the antiknock quality of the fuel, which is defined by the fuel's *octane number* (see Sec. 9.6.3). That parameter determines whether or not a fuel will knock in a given engine under given operating conditions: the higher the octane number, the higher the resistance to autoignition and knock. The *octane number requirement* of an engine is defined as the minimum fuel octane number that will resist knock throughout its speed and load range. The following factors affect an engine's octane requirement: (1) composition of the fuel; (2) chamber geometry and size; (3) charge motion; (4) spark-advance; (5) intake air, intake port and valve, and water jacket temperatures; (6) air/fuel ratio; and (7) ambient air conditions—pressure, temperature, and relative humidity—during the requirement determination.

The interaction between fuel octane rating and engine operating variables at higher loads, illustrated inFig. 15.29, shows the relation between spark advance, torque, and speed in an engine operating at wide-open throttle. The dashed lines, determined with a fuel of sufficiently high octane rating to avoid knock, show MBT timing as a function of speed, along with the spark-advance limits for constant specified percentage torque reductions. The upper solid line traces the spark advance for borderline knock with a particular commercial gasoline. To avoid knock onset with this fuel, the spark advance was set to lose 1% of engine torque at 800 rev/min, with the torque loss diminishing to zero at 1200 rev/min. Above that speed this particular fuel allows operation at MBT timing without knocking. The lower solid curve represents a typical spark-advance schedule at

© McGraw-Hill Education. All rights reserved. Any use is subject to the Terms of Use, Privacy Notice and copyright information.

WOT. It lies below the borderline knock advance (and results in an additional torque loss) for the following reasons. One is that different commercial gasolines with the same research octane number can respond differently to variations in engine operating conditions. Calibrating the engine (i.e., specifying the schedules for spark advance, *A/F*, and EGR) must be done with a sufficient margin to avoid objectionable knock with the normal range of commercial gasolines over the full operating conditions of the engine. A second reason is engine-to-engine production variability despite the close dimensional tolerances of modern production engineering. For example, the effective compression pressure in each cylinder of a multi-cylinder engine is not identical, due to geometric and ring-pack differences. The cylinder with the highest compression pressure is most knock-prone. Allowing for corresponding effects of cylinder-to-cylinder variations in *A/F*, EGR rates, and spark timing, it is obvious that for a given operating condition in a multi-cylinder engine, one cylinder is more likely to knock than the others. It is that cylinder which limits the spark advance.[1] A third reason for the discrepancy between actual spark-advance calibration and the knock limit for a given engine and fuel is the octane requirement increase associated with the buildup of deposits on the cylinder head and piston over extended mileage (see Sec. 9.6.3).

Figure 15.29 Relation between spark advance, speed, and torque loss for spark-ignition engine at wide-open throttle showing knock limit for a specific gasoline and typical spark-advance schedule that avoids knock problems.[38]



In the example shown, it was the problem of knock at lower engine speeds which required the calibrated spark advance to be retarded. Whether low-, medium-, or high-speed knock is the limiting factor in a particular engine depends on the sensitivity of the fuel (see Sec. 9.6.3), on engine design details, and on the engine's spark-advance requirements for MBT. The knock-limited spark advance determined from road octane rating tests can vary with engine speed and fuel sensitivity. While high sensitivity fuels usually show higher in-use octane index, at higher loads and speeds, in some engines, lower sensitivity fuels may resist knock better.

As Fig. 15.29 illustrates, spark retard from MBT spark timing is an effective way to delay the onset of knock, because it can immediately reduce the end-gas peak pressures and temperatures. Spark retard at low to mid engine speeds is built into the engine's calibration to prevent knock with the engine's specified fuel octane requirement. In turbocharged engines, at mid to high speed, this strategy is even more effective because the torque loss with a given spark retard from MBT is reduced (see Fig. 15.10). However, spark retard also results in an increase in engine exhaust gas temperature, which must not be allowed to exceed the maximum turbine intake gas temperature constraint.

As is well known, the octane requirement increases with increasing compression ratio. There are, however, differences in

© McGraw-Hill Education. All rights reserved. Any use is subject to the Terms of Use, Privacy Notice and copyright information.

octane requirement between different types of chamber at the same compression ratio. A critical dimension is the *flame travel distance*: the distance between the spark plug electrodes and the farthest combustion chamber wall. Thus spark plug location in the chamber and the cylinder bore are important factors: center plug locations are better; larger size cylinders are worse. Whether more turbulent modern combustion chambers effect octane requirement much is unclear: increased in-cylinder heat losses, and faster burn, have opposite effects on peak pressures. The latter phenomenon also decreases flame travel time. These effects (for a given size engine) do not appear to be that large.

Operating variables that affect the temperature or pressure time histories of the end-gas during combustion or the basic autoignition characteristics of the unburned fuel, air, residual mixture will also affect the engine's octane requirement. The most important additional variables which increase or decrease octane requirement in a consistent manner are listed in Table 15.5. Relative spark advance has a major impact on knock: since it is also easy to adjust, it is the engine variable most commonly used to control knock. Studies show that typically 0.5 to 1.0 RON reduction is achieved per degree of retard. Atmospheric conditions—pressure, temperature, and humidity—all affect the engine's octane number requirement. The fuel/air equivalence ratio affects the octane requirement of an engine. The highest requirement is for slightly rich mixtures: see Fig. 9.71. Increasing richness and leanness about this point decrease the octane requirement substantially.

Table 15.5 Engine conditions affecting octane number requirement

Octane number requirement goes *up* when:	Octane number requirement goes *down* when:
1. Ignition timing is advanced.	1. Ignition timing is retarded.
2. Air density rises due to a larger throttle opening or higher barometric pressure.	2. Engine is operated at higher altitudes or smaller throttle opening, or lower barometric pressure.
3. Humidity or moisture content of the air decreases.	3. Humidity of the air increases.
4. Intake air temperature is increased.	4. Intake air temperature is decreased.
5. Coolant temperature is increased.	5. Air/fuel ratio is richer or leaner than that producing maximum knock ($\lambda \approx 0.95$).
6. Antifreeze (glycol/water mixture) engine coolant is used.	6. Exhaust gas is recycled.
7. Engine load is increased.	7. Engine load is reduced.

In turbocharged engines the knock limit is more constraining, and the compression ratio is usually about one unit lower than an equivalent naturally-aspirated engine. Figure 15.28 illustrates how fuel octane requirement, intake air temperature relative fuel/air equivalence ratio, and compression ratio impact the knock-limited boost pressure in a turbocharged gasoline engine. All the above parameters have a significant impact. The case for an intercooler to cool the air charge prior to entry to the cylinder is clear, as is the importance of higher-octane fuel. As already mentioned, the evaporative charge cooling effect of direct fuel injection makes this injection technology especially attractive with turbocharged engines. The theoretical in-cylinder evaporative cooling impact of DI with a (hydrocarbon) gasoline is about 20 degrees C. Studies suggest that DI fueling systems relative to a port-fuel-injection system realize about 70% more of that limit in actual engines (i.e., about 14 deg C). Addition of ethanol to the fuel (U.S. gasolines usually contain close to 10% ethanol, E10), with its much higher heat of vaporization than gasoline, increases this evaporative cooling effect significantly. E10 provides about an additional 5 deg C of charge cooling.[39]

As engine load is decreased, the engine's octane requirement significantly decreases. Figure 15.31 shows this behavior: the Octane Number (RON) of the Primary Reference Fuel (PRF)[2] required to avoid knock, as a function of load (bmep), at three engine speeds. There are two distinct regimes: at higher loads (above about 800 kPa bmep) where the slope is modest; at lower loads (below about 600 kPa bmep) where the slope is much steeper. Clearly, much of the time in a given application, gasoline SI engines would be able to operate knock free with octane levels well below (of order 50 RON) what is needed to avoid knock at high loads (90 to 100 RON). Whether or not we will transition to matching more closely the fuel octane supplied to the engine with the actual engine's operating (and varying) octane requirement in the future is unclear. Currently, our

© McGraw-Hill Education. All rights reserved. Any use is subject to the Terms of Use, Privacy Notice and copyright information.

approach of using a given gasoline fuel, with a single high-octane rating (high enough to avoid knock at high engine load) over all engine loads and speeds is simpler and cost effective.

Figure 15.30 Dependence of turbocharged gasoline engine knock limits on: (a) charge pressure, temperature, and equivalence ratio ϕ, with r_c = 7, 2500 rev/min, MBT timing, 91 and 100 research octane number fuel; (b) charge pressure and compression ratio, without and with charge air cooling (to 60°C), 2500 rev/min, MBT timing, ϕ = 1.1, 100 RON fuel.[40]

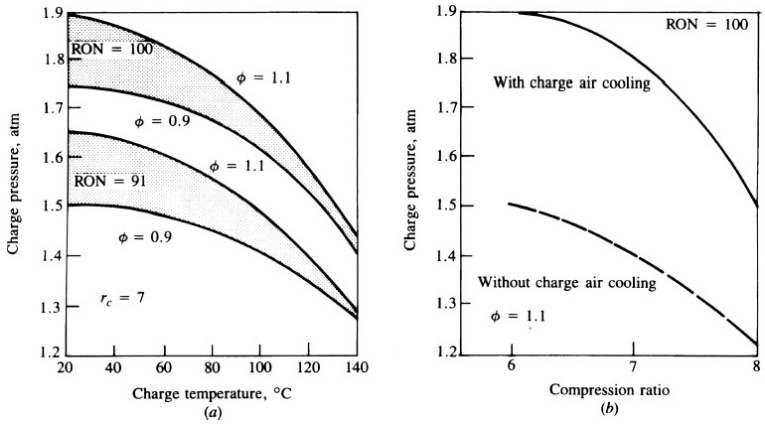
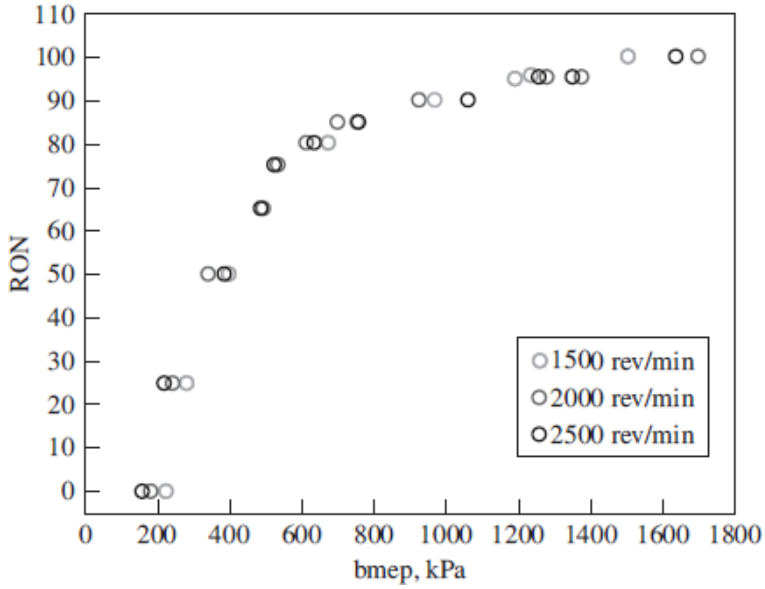


Figure 15.31 Octane requirement (primary reference fuels) as a function of engine load (bmep) for a 2-liter four-cylinder turbocharged gasoline SI engine, at 1500, 2000, and 2500 rev/min. Stoichiometric operation at MBT spark timing.[41]



Use of low-percentage ethanol gasoline blends (e.g., E5 in Europe, E10 in the U.S.) is allowing use of lower-octane base hydrocarbon gasolines which the ethanol upgrades. This ethanol octane blending benefit is illustrated in Fig. 9.70. Depending on the base gasoline composition and octane, 10% ethanol increases the base octane RON by some 3-7 octane numbers.

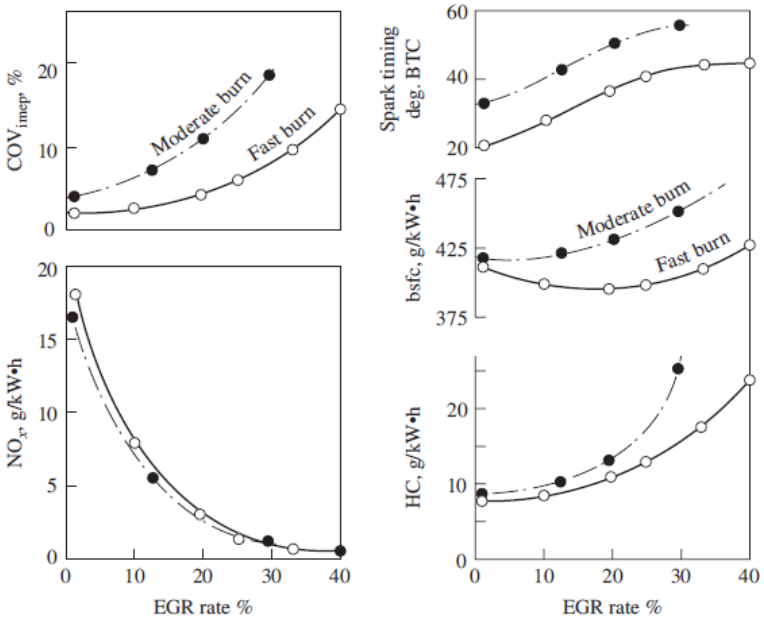
15.4.5. SI Engine Emissions

Fast-burn combustion systems allow use of substantial EGR (up to about 15%) to control engine-out NO_x emissions, improve bsfc, and hold the EGR-produced increase in HC emissions to modest levels. These benefits are illustrated in the set of graphs

© McGraw-Hill Education. All rights reserved. Any use is subject to the Terms of Use, Privacy Notice and copyright information.

in Fig. 15.32 where key combustion and emissions parameters are plotted against EGR rate, at constant engine operating conditions. MBT spark advance, coefficient of variation in imep (which defines the combustion cyclic variability), bsfc, and bsNO$_x$ and bsHC are plotted with increasing EGR for a moderate and fast-burn combustion system. The difference in burn rate is apparent from the MBT spark advance: the slower-burning combustion system requires 10 to 15 degrees more advance. One consequence of faster burn is less combustion variability, especially as dilution with EGR becomes significant. Acceptable COV of imep is a few percent, depending on load. The fast-burn system maintains such levels out to about 15% EGR. Substantial NO$_x$ reductions are realized as EGR increases, essentially independent of burn rate; but only the fast-burn system provides acceptable combustion stability. Also, the increase in HC emissions up to this EGR level is more modest.

Figure 15.32 Illustration of how a fast-burn combustion system extends the EGR tolerance limit, improves engine-out NO$_x$ and HC emissions, and fuel consumption, with acceptable combustion stability. Data for four-cylinder gasoline engine, stoichiometric operation, MBT spark timing, at 30 N·m torque, 1400 rev/min. COV, coefficient of variation in imep.[33]



Especially important is the impact of fast burn on fuel consumption. Increasing dilution of the fuel-air mixture with EGR has several benefits: (1) Lower burned gas temperatures (less dissociation), so higher expansion stroke γ; (2) lower heat loss to combustion chamber walls; (3) at the same engine part-load torque, intake system pressure is increased and pumping work decreases. All these effects are largely independent of burn rate. But increasing EGR slows down the burn rate which worsens fuel consumption. For a slower burning combustion system this negative burn-rate impact almost immediately offsets the three positive factors listed above, and then overshadows them. For the fast-burn system, this negative impact is much smaller and only becomes significant as EGR levels rise above about 15%. At that point, the fuel consumption benefit with fast burn relative to zero EGR is about 5%. This combined efficiency and emissions benefit with a fast-burn combustion system through use of significant EGR, while maintaining good combustion characteristics has been an important development.

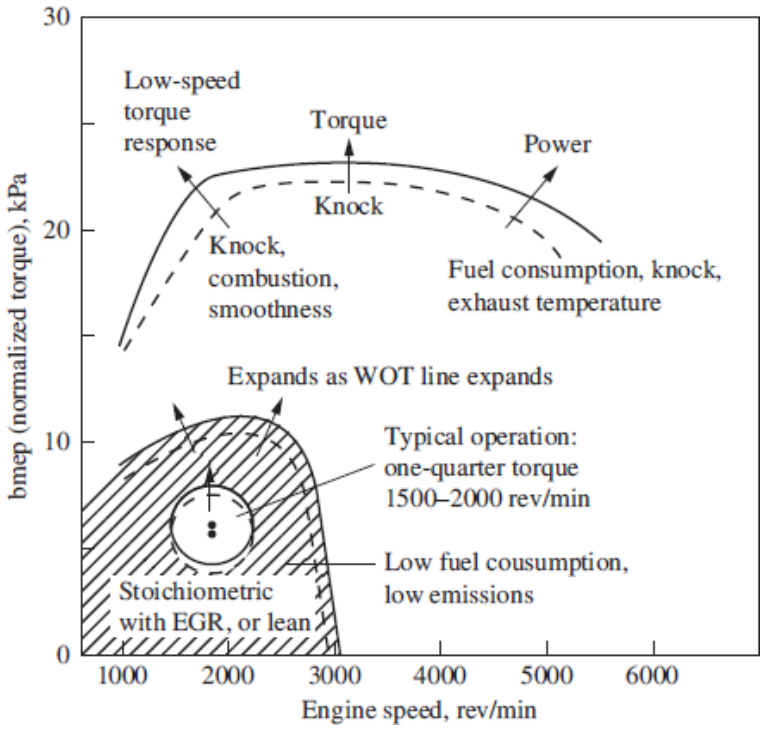
15.4.6. Optimization

Combustion system optimization is a core requirement for improving gasoline engine performance and efficiency, and reducing engine-out emissions. The objectives and challenges involved for a turbocharged SI engine (fueled with gasoline) are summarized on the performance map in Fig. 15.33. Two separate areas on the map (torque or bmep versus speed) are critical for automotive application: the wide-open-throttle curve; and the part-throttle lower load and speed shaded region shown

© McGraw-Hill Education. All rights reserved. Any use is subject to the Terms of Use, Privacy Notice and copyright information.

which, for this SI engine application is normally centered at one-quarter maximum torque and 1500 to 2000 rev/min (depending on cylinder size through $\overline{S}_p$, the mean piston speed).[3] Expanding the wide-open throttle "upward and outward" is clearly advantageous. Increasing engine output allows engine downsizing, which significantly improves part-load fuel consumption. For turbo engines, shifting the rising low speed torque boundary to lower speeds is especially important since it improves the response time of the engine to rapid throttle openings (decreasing the *turbo-lag* problem). Knock is a constraint at WOT: first at low speeds, then also at mid and higher speeds.

Figure 15.33 Opportunities for improvement, and the constraints, on a turbocharged gasoline-engine performance map in the key wide-open-throttle and part-load low-speed engine operating regimes. (Developed from Ref. 42.)



At a more detailed level, the following sequence of steps in a combustion chamber development process is most logical. First should come the selection of the best chamber geometry. Geometric optimization can result in substantial benefits and carries no significant penalties. Chamber geometry involves cylinder-head and piston-crown shape, and spark plug location. Open chambers such as the pent-roof or hemispherical cylinder head, with near central plug location, give close to the maximum flame front surface area (and hence a faster burn), have the lowest chamber surface area in contact with the burned gases (and therefore the lowest heat transfer), and have inclined valves which give high volumetric efficiency. Spark plug location close to the center of the chamber is especially important in obtaining a fast burn rate.

Following this first step, two problem areas may remain: the chamber may have a higher octane requirement than is desired, and the burn rate may not be fast enough to absorb the EGR or excess air dilution required at part load to meet the emissions and fuel consumption objectives. Positioning the spark plug as close as possible to the cylinder axis will have reduced the octane requirement for that particular chamber shape. Depending on chamber design details, some squish area could be introduced. However, the octane advantage of chamber designs which contain substantial squish is offset, at least in part, by their higher heat losses. For example, a unit compression ratio increase results in a 3% increase in efficiency at part load (with downsizing to hold torque constant). However, if the measures required to increase the compression ratio resulted in a 10% increase in heat transfer, engine efficiency would not improve.

The next step should be to reduce the cyclic variability in the combustion process to the maximum extent feasible, by

© McGraw-Hill Education. All rights reserved. Any use is subject to the Terms of Use, Privacy Notice and copyright information.

improving the uniformity of the in-cylinder fuel, air, and EGR mixture. Delivery of equal amounts of each of these constituents to each cylinder, provision for good mixing between constituents in the intake processes, and accurate control of mixture composition during engine transients are all especially important. So is achieving closely similar flow patterns within each engine cylinder during intake so as to obtain equal burn rates in all cylinders. Attention to these intake process and mixture preparation details will always improve engine operation and carries no performance penalties.

However, the burn rate may still not be fast enough, especially during the early stages of flame development, and cyclic variability may still be too high to meet the engine's operational goals. Then higher turbulence levels during combustion must be achieved. This is usually best done by creating a stronger tumbling flow during the induction process. The appropriate method for doing this will depend on any geometric manufacturing constraints and cost issues. With no geometric constraints, use of a four-valve cylinder head with low intake port axes, possibly with intake port throttling plates do direct the flow appropriately at light load are likely to have the lowest power penalties. It is especially important that only the minimum additional turbulence required to achieve the overall performance objectives be added at this stage. Higher than necessary gas velocities within the cylinder result in excessive heat losses and lower volumetric efficiency.

In summary, to meet the objectives of a fast, repeatable, and robust combustion process with high volumetric efficiency, low heat transfer, and acceptable octane requirement, combustion chamber development should proceed through the following steps.[35]

- Optimize the chamber geometry within the design constraints for maximum flame front area, minimum burned gas/chamber wall contact area, and largest intake valve size.
- Obtain additional reductions in the cyclic combustion variability by improving mixture distribution and uniformity and by creating flow patterns into each cylinder that are close to identical.
- Achieve any additional improvement in burn rate and cyclic variability required to meet objectives by increasing in-cylinder turbulence to the needed level. This is usually best done by creating tumble during the induction process.

[1] There is no assurance that the same cylinder will be the principal offender in all engines of the same model, nor in a given engine at all operating conditions.

[2] PRFs are isooctane/*n*-heptane mixtures: the number is the percent isooctane in the mixture. In the normal RON range (85 to 95 RON), the knock resistance of PRFs and gasolines with the same RON is closely comparable.

[3] Such a performance map for a naturally-aspirated gasoline engine would be similar. However, the wide-open-throttle torque curve would have a different shape and about half the bmep level (see Fig. 15.2). The part-load region where fuel consumption and emissions are critical would be comparable, again centered at about one-quarter the NA engine maximum torque level.

© McGraw-Hill Education. All rights reserved. Any use is subject to the Terms of Use, Privacy Notice and copyright information.

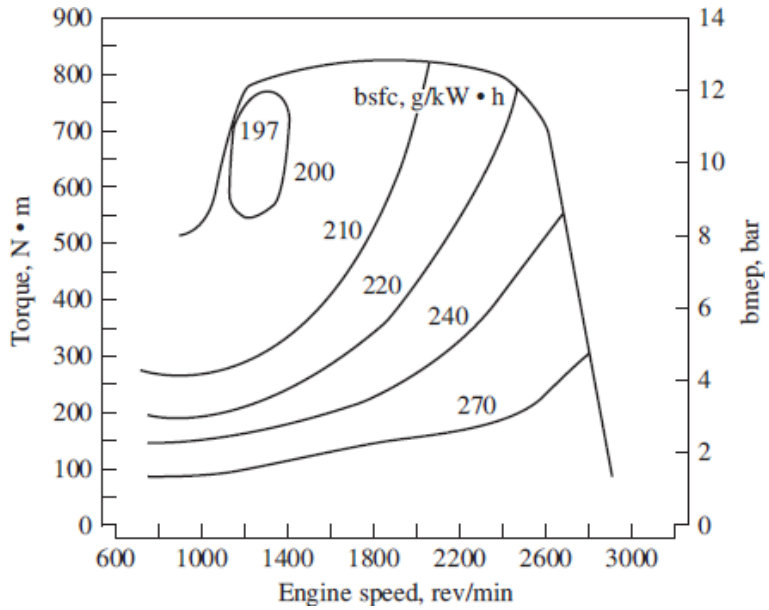
15.5. VARIABLES THAT AFFECT DIESEL ENGINE PERFORMANCE, EFFICIENCY, AND EMISSIONS

The performance characteristics of a turbocharged high-speed DI automotive diesel engine over the engine's load and speed range have already been introduced in Sec. 15.2.3. Here we examine diesel performance maps in more detail.

15.5.1. Load and Speed

As with SI engines, performance maps where bsfc contours are plotted on a graph of torque or bmep versus engine speed are commonly used to describe the effects of variations in load and speed. Figure 15.34 shows the performance map for a four-stroke cycle medium-swirl turbocharged and aftercooled truck DI diesel engine (similar to that in Fig. 1.31). Maximum rated power for this 8-liter displacement in-line six-cylinder engine is 188 kW at 2500 rev/min, maximum torque is close to 800 N·m at 1500 rev/min, minimum bsfc (at 1200 rev/min) is just below 200 g/kW·h. These practical parameters correspond to a brake mean effective pressure (bmep) of 1260 kPa and a brake fuel conversion efficiency of 42.5%. The gross indicated fuel conversion efficiency would be over 50%.

Figure 15.34 Performance map for an 8-liter in-line six-cylinder, turbocharged and aftercooled, DI diesel engine with a medium-swirl, central injection, multi-hole nozzle combustion system. Contours of constant bsfc in grams per kilowatt-hour are shown. Bore = 114 mm, stroke = 130 mm. r_c = 16.5.[43]



Turbocharged-diesel-engine performance maps are usually similar in shape. Torque and bmep rise rapidly as engine speed increases above about 1000 rev/min, then remain relatively flat through the mid-speed range to close to the rated speed at which maximum power is realized. Figure 15.6 shows the performance map of an automotive high-speed light-duty diesel of much smaller size that operates up to 4500 rev/min. The individual cylinder displaced volume of this 2.46-liter five-cylinder in-line engine (492 cm^3/cylinder) is much less than the cylinder size of the 8-liter medium-duty six-cylinder in-line engine of Fig. 15.34 (which is 1333 cm). For diesels such as the one illustrated in Fig. 15.34 maximum power occurs at mean piston speeds of 10 to 12 m/s: for the HSDI smaller diesel of Fig. 15.6 it occurs at 14 m/s.[10] The increase in bsfc from its minimum value with increasing speed at constant load is due to the increase in friction mep, partly offset by the effect on efficiency of

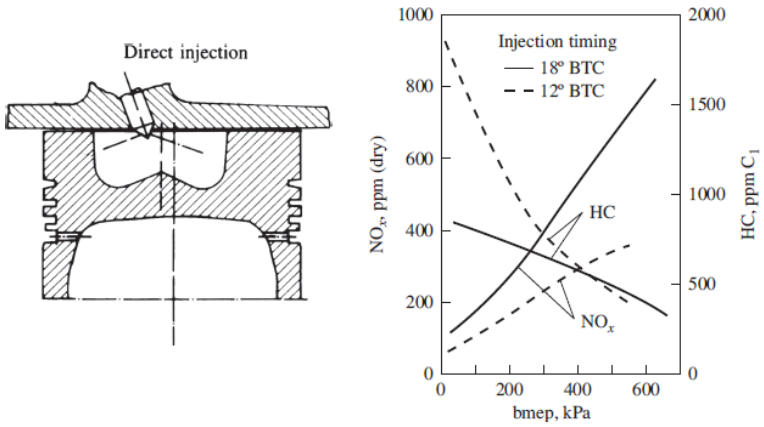
© McGraw-Hill Education. All rights reserved. Any use is subject to the Terms of Use, Privacy Notice and copyright information.

decreasing importance of heat losses per cycle. The increase in bsfc with decreasing load at constant speed is dominated by the decreasing mechanical efficiency as bmep is reduced. The indicated fuel conversion efficiency increase, as the fuel/air equivalence ratio is decreased, partly offsets this. The trends in bsfc when increasing load at constant speed and increasing speed at constant load from the minimum are modest. They are the net results of (1) the increase in mechanical efficiency and decrease in indicated fuel conversion efficiency as the load (and fuel/air equivalence ratio) increases and (2) decreasing indicated efficiency due to increasing importance of heat losses, and increasing mechanical efficiency, as the speed decreases. Note that the drop in efficiency (increase in bsfc) as load decreases is not that large (10%) until load drops below about one-third the maximum load. The significantly better part-load efficiency of the diesel relative to the gasoline engine is one of the diesels major advantages.

Diesel engine performance and efficiency are steadily improving. Use of higher boost levels in turbocharged diesels (4 bar or more) increases bmep levels above about 20 bar. Best brake fuel conversion efficiencies are rising through mid-40% levels.

Figure 15.35 shows the effect of load on engine-out NO_x and HC emissions for a naturally-aspirated DI diesel engine. For this DI engine NO_x concentrations rise steadily as the fuel/air ratio increases with increasing bmep at constant injection timing. The increasing quantity of fuel injected per cycle results in an increasing amount of close-to-stoichiometric diffusion-flame combustion near the peak pressure and temperature (see Sec. 11.2.4). The high HC at idle and light load are thought to result from fuel mixing to too lean an equivalence ratio to burn. If diesel engines are over-fueled at high load, HC emissions then rise rapidly. These HC mechanisms are described in Sec. 11.4.4. Injection timing affects NO_x and HC emissions significantly, as discussed in Sec. 15.5.3 below.

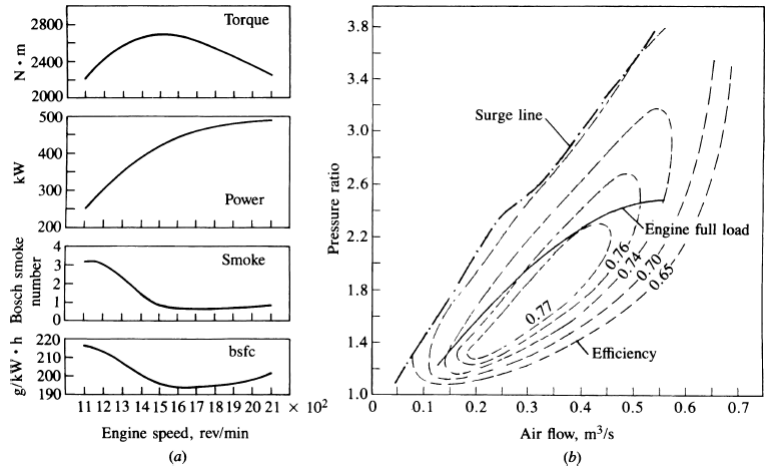
Figure 15.35 Effect of load on naturally-aspirated DI diesel engine-out NO_x and HC emissions at rated speed, with two injection timings. The direct-injection combustion system is shown. Six-cylinder, 5.9-liter displaced volume, engine: r_c = 17, rated speed = 2800 rev/min.[44]



With structurally rugged component design, aftercooled turbocharged medium-speed diesel engines with swirl can utilize higher boost and generate much higher bmep. Usually, wastegate control of boost level is no longer required. Figure 15.36 shows the performance characteristics of a V-8 diesel engine with its compressor map and full-load boost characteristic. This turbocharged intercooled engine achieves a maximum bmep of about 16 bar at the maximum torque (2700 N·m), and bsfc below 200 g/kW·h between the maximum torque speed and rated power. Boost pressure at full load increases continuously over the engine speed range. Maximum mean piston speed for this size TC engine is 10 m/s.

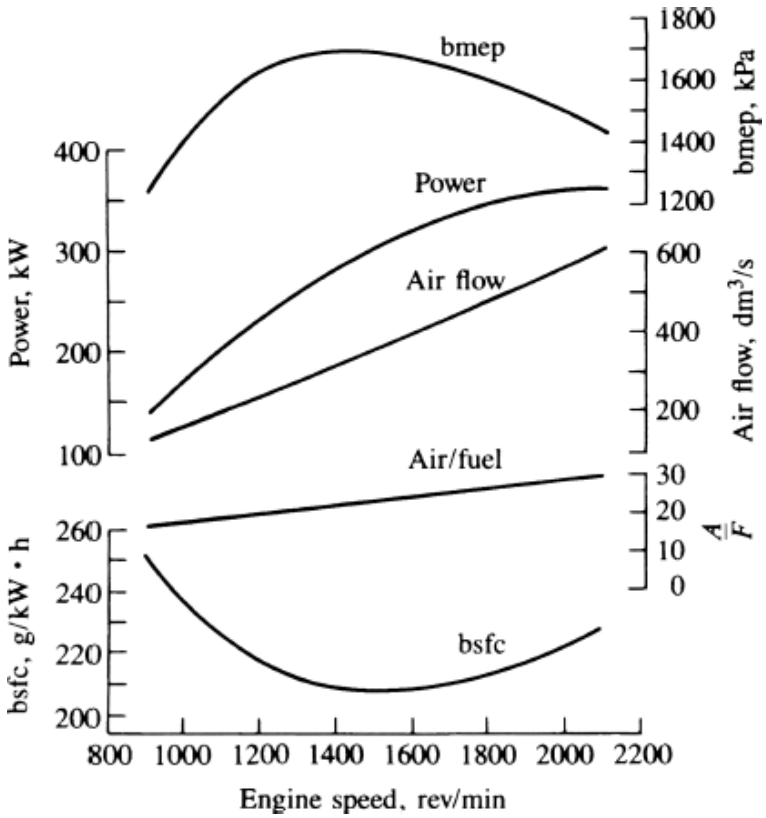
© McGraw-Hill Education. All rights reserved. Any use is subject to the Terms of Use, Privacy Notice and copyright information.

Figure 15.36 *Performance characteristics of medium-speed turbocharged aftercooled DI diesel engine: (a) torque, power, Bosch smoke number, and bsfc for V-12 cylinder 21.6-liter version; (b) compressor characteristics and engine full-load line for V-8 cylinder 14.4-liter version. Bore = 128 mm, stroke = 140 mm, r_c = 15.*[45]



Higher outputs can be obtained with two-stage turbocharged aftercooled diesel engines, the arrangement shown in Figs. 6.45*d* and *f*. The performance characteristics of such a high bmep (17.4 bar) six-cylinder engine of 14-liter displacement are shown in Fig. 15.37. The high airflow requires an overall pressure ratio of 3 at sea level ambient conditions (rising to 4 at 3658 m altitude). This was obtained at lower cost with two turbochargers in series than with a multistage single turbocharger. At rated conditions, the maximum cylinder pressure is 12.7 MPa and the maximum mean piston speed is 10.6 m/s.

Figure 15.37 *Operating characteristics of 14-liter six-cylinder two-stage turbocharged aftercooled quiescent-chamber DI diesel engine. Maximum bmep = 17.4 bar. Boost pressure ratio at rated power = 3. Bore = 140 mm, stroke = 152 mm.*[46]



© McGraw-Hill Education. All rights reserved. Any use is subject to the Terms of Use, Privacy Notice and copyright information.

Additional gains in efficiency with these heavy-duty automotive diesel engines can be achieved with turbocompounding: some of the available energy in the exhaust gases is captured in an additional turbine which is geared directly to the engine drive shaft. The above discussion indicates that typical turbocharged DI diesel engines achieve bsfc levels about 200 g/kW·h (brake fuel conversion efficiencies of over 40%). With the increased cylinder pressure capability, higher fuel-injection pressures, and lower-temperature aftercooling, lower bsfc can be achieved. With turbocompounding, bsfc values can be reduced another 5% to about 180 g/kW · h, or a brake efficiency of about 50%, at rated power.

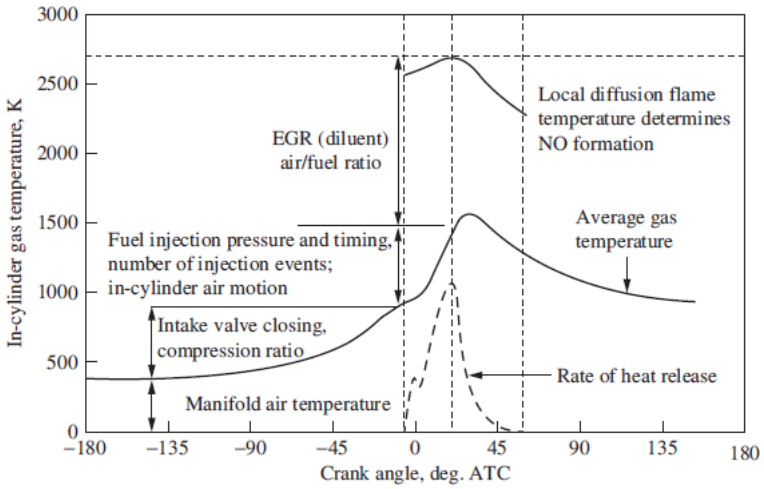
The largest four-stroke cycle DI diesel engines are used for marine propulsion. An example is the Sulzer 400-mm bore, 480-mm stroke engine which produces 640 kW per cylinder at 580 rev/min ($\overline{S}_p$ = 9.3 m/s). Very high bmep levels (22 bar) are achieved at maximum continuous rated power through progress in turbocharger design and engine improvements which allow higher maximum cylinder pressures. These, combined with optimization of gas exchange and combustion processes, achieve bsfc values of 185 to 190 g/kW · h (45 to 46% brake efficiency).[47]

Many diesel system concepts are being examined which promise even higher output and/or efficiency. Variable-geometry turbocharger-turbine nozzles are extensively used to increase utilization of the available exhaust-gas energy at lower engine speeds. Diesel engine systems can increase power through additional exhaust energy recovery in devices such as compounded turbines and exhaust-heated Rankine cycle and thermo-electric systems.

15.5.2. Combustion-System Design

As discussed in Sec. 10.2, a variety of combustion systems (combustion chamber shape, air motion, fuel injection and spray geometry) are used to obtain both low fuel consumption and pollutant emissions. Figure 10.1 shows the basic bowl-in-piston geometries, and the types of in-cylinder air motion that are used over the engine size range (bore 75 m to 150 mm). Figure 15.38 illustrates the combustion process in a medium-duty diesel engine, and identifies the critical combustion-system design features.

Figure 15.38 Important combustion-system design features: heat release rate and critical in-cylinder gas temperature profiles typical of a medium-duty diesel engine.[48]

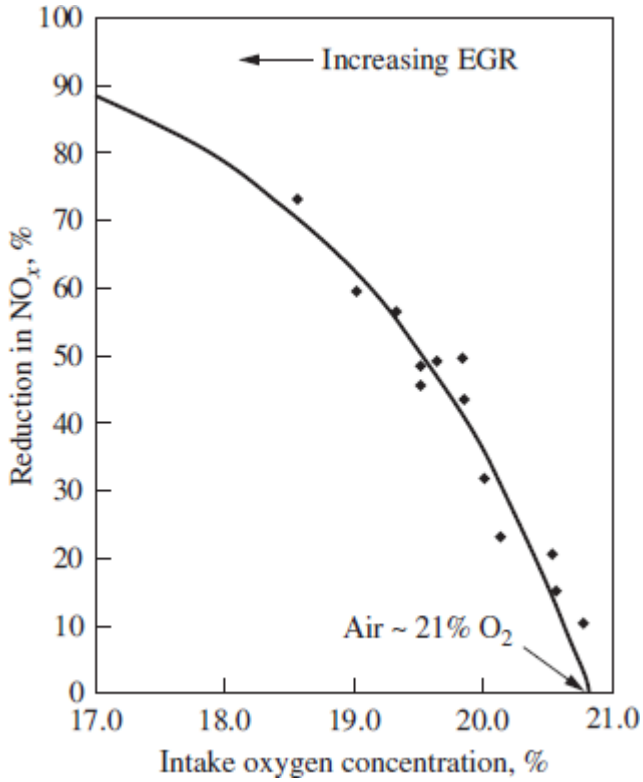


The high gas temperatures within the close-to-stoichiometric diffusion flames surrounding each fuel-rich spray (the main diesel combustion phase) is the primary NO formation region. These diffusion flame temperatures are much higher than the average in-cylinder gas temperatures. Recycled exhaust gas, at part load, is used to reduce diesel engine NO_x emissions. Note that since diesel engines operate with the airflow unthrottled, at part load the CO_2 and H_2O concentrations in exhaust gas are low; they are essentially proportional to the overall fuel/air ratio. Because of this, high EGR levels are required for significant

© McGraw-Hill Education. All rights reserved. Any use is subject to the Terms of Use, Privacy Notice and copyright information.

reductions in engine-out NO_x emissions. Figure 11.17*b* shows how NO_x concentrations decrease as a DI diesel engine inlet airflow is diluted at a constant fueling rate. The dilution can be expressed in terms of oxygen concentration in the mixture after dilution. Figure 15.39 shows how engine-out NO_x emissions decrease as the EGR increase decreases the intake oxygen concentration. The impacts of EGR are discussed more fully in Sec. 15.5.3.

Figure 15.39 Impact of increasing EGR (expressed through the corresponding decrease in oxygen concentration in the intake air and EGR mixture) on the reduction in engine-out NO_x emissions.[48]



As Fig. 15.38 indicates, fuel injection system pressure and fuel injection timing (relative to the timing that gives minimum bsfc) influence the heat release rate, and therefore maximum cylinder pressure. Also, with multiple injections (e.g., pilot injection), the rate-of-fuel-burning profile is affected. Mixing rates can be increased through use of swirl and optimized bowl-in-piston combustion chamber shapes, thus influencing the rate of chemical energy release. Finally, the amount of air compression (from about IVC to top center), and the intake air temperature, affect the mixture temperature just before combustion starts: this affects the mixture burning rate and the peak (diffusion flame) temperatures.

As engine size decreases and maximum engine speed increases, increasing amounts of air swirl within the cylinder are used in direct-injection diesel engines to achieve adequately fast fuel-air mixing rates (see Sec. 10.2.1). In these smaller-size engines, use of a bowl-in-piston combustion chamber (Figs. 10.1*b* and *c*) results in substantial swirl amplification at the end of the compression process (Sec. 8.3.3). Here, the impacts of varying air swirl on the performance and emissions characteristics of this type of DI engine are reviewed.

Swirl is used to increase the rate of air entrainment into the developing fuel sprays, and thus the fuel-air mixing rate. So one would expect the overall duration of the combustion process to shorten as swirl increases, and the emissions that depend on the local fuel/air equivalence ratio to be dependent on swirl level. The injection timing which gives minimum bsfc shifts toward TC as the swirl ratio increases due to the decreasing total combustion duration. For each combustion chamber design, there is an optimum swirl ratio for minimum bsfc: higher swirl levels continue to increase fuel-air mixing rates, but heat transfer increases also and eventually offsets the increased-mixing-rate gain. Particulate and CO emissions decrease as swirl increases due to more rapid fuel-air mixing and less-rich within-the-spray mixture. NO_x emissions increase with increasing

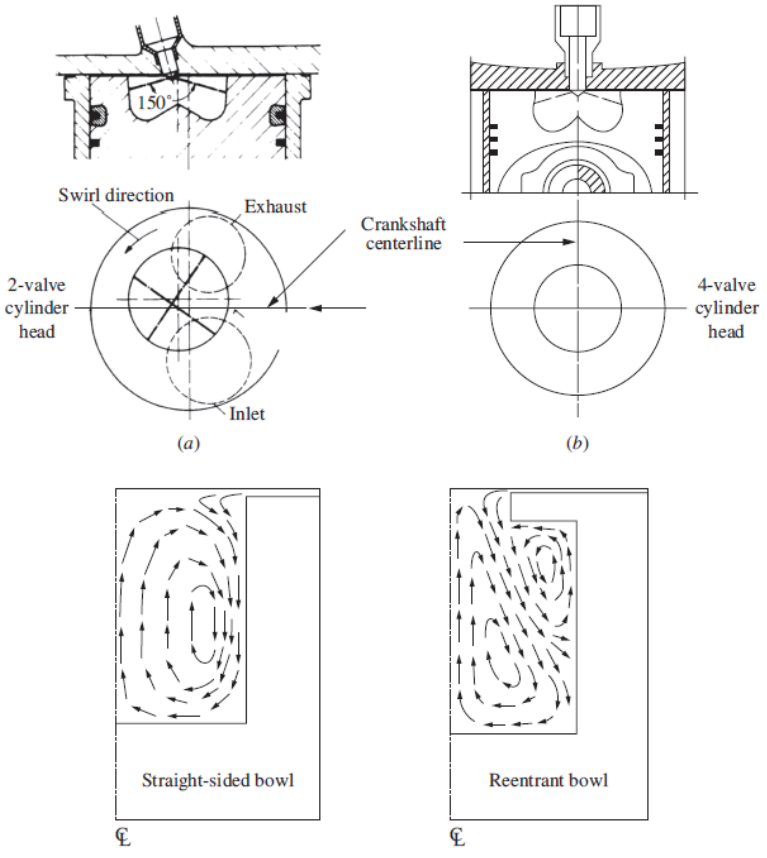
© McGraw-Hill Education. All rights reserved. Any use is subject to the Terms of Use, Privacy Notice and copyright information.

swirl. At constant injection timing, however, part of the increase is due to the effect of injection advance relative to the optimum timing due to the shorter combustion process.

In production engines, the various types of port design shown in Fig. 8.14 can be used to generate swirl during the induction process. Of these, the helical ports are most effective at producing relatively-uniform high swirl with the minimum loss in volumetric efficiency.

The geometry of the bowl-in-piston combustion chamber governs the extent to which induction-generated swirl is amplified during compression. The flow field in the bowl during fuel injection is also dependent on the interaction between this swirling flow and the squish motion which occurs as the top of the piston crown approaches the cylinder head (see Sec. 8.5). Two types of bowl-in-piston design for multihole fuel nozzle DI engines are shown in Fig. 15.40. Designs (e.g., Fig. 15.32*a*) used when really high mixing rates are not required have the bowl sides essentially parallel to the cylinder liner. Note that it may be necessary to offset the bowl axis from the cylinder axis and the injector nozzle hole locations from the bowl axis, due to the geometric constraints imposed by the valves. Smaller-size higher-speed designs use a reentrant bowl (Fig. 15.40*b*) to promote more rapid fuel-air mixing within the bowl. The squish-swirl interaction with highly reentrant bowl designs differs markedly from the interaction in nonreentrant bowls as shown by the two flow patterns set up in a diametral plane, at the bottom of the figure. With the straight-sided bowl, the swirling air entering the bowl flows down to the base of the bowl, then inward and upward in a toroidal motion. In reentrant bowls the swirling air entering the bowl spreads downward and outward into the undercut region, and then divides into a stream rising up the bowl sides and a stream flowing along the bowl base. Reentrant chambers produce higher swirl at the end of compression, and maintain a high swirl level further into the expansion stroke.[49] Reentrant chambers usually achieve lower HC and smoke emissions and slightly lower bsfc, especially at retarded injection timings.

Figure 15.40 Bowl-in-piston chamber designs for DI diesel engines with swirl: (a) straight-sided bowl; (b) reentrant bowl. Below, flow pattern set up in diametral plane by squish-swirl interaction in the straight-sided bowl and the reentrant bowl combustion chambers. See discussion in text.[44,49]



© McGraw-Hill Education. All rights reserved. Any use is subject to the Terms of Use, Privacy Notice and copyright information.

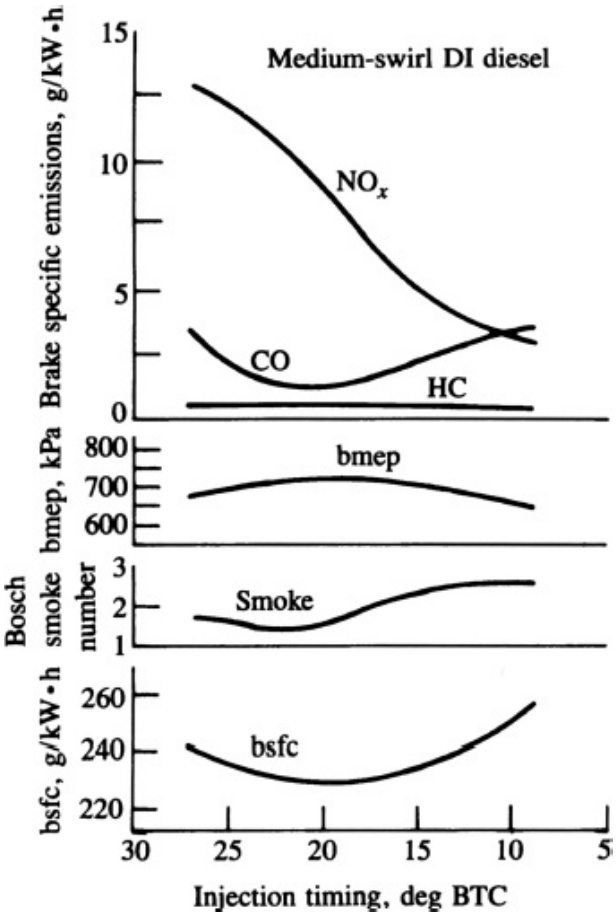
The airflow field within bowl-in-piston combustion chambers when fuel injection occurs is highly complex. However, certain generalizations hold: for example, reducing the bowl diameter at a constant compression ratio increases the swirl levels in the bowl at TC (see Sec. 8.3.3 and the accompanying text) which decreases smoke and increases NO_x, and HC emissions.[44] However, unraveling the squish-swirl interaction is challenging.

15.5.3. Fuel Injection and EGR

Fuel-injection timing essentially controls the crank angle at which combustion starts. While the state of the air into which the fuel is injected changes as injection timing is varied, and thus the ignition delay will vary, these effects are predictable (see Sec. 10.5.4). The fuel-injection rate, fuel nozzle design (including number of holes), the number of injections per cycle, and fuel-injection pressure all affect the characteristics of the diesel fuel spray and its mixing with air in the combustion chamber.

Figure 15.41 shows the effect on performance and emissions of varying injection timing, in a medium-swirl DI diesel engine at fixed speed and constant fuel delivery per cycle. The DI engine shows an optimum bsfc and bmep at a specific start of injection for a given injection duration. This optimum injection timing gives maximum brake torque, though the designation MBT timing is less commonly used with diesels than with SI engines.

Figure 15.41 Effect of start-of-injection timing on diesel engine performance and emissions: medium-swirl DI diesel engine with deep combustion bowl and four-hole injection nozzle, 2600 rev/min, fuel delivery 75 mm^3/cycle, fuel/air equivalence ratio 0.69.[44]



Injection timing variations have a strong effect on engine-out NO_x emissions for DI diesel engines. Retarded injection is commonly used to help control NO_x. It gives substantial reductions, initially with modest bsfc penalty. For DI engines, at high load, specific HC emissions are low and vary only modestly with injection timing. At lighter loads, HC emissions are higher

© McGraw-Hill Education. All rights reserved. Any use is subject to the Terms of Use, Privacy Notice and copyright information.

and increase as injection becomes significantly retarded from optimum. This trend is especially pronounced at idle. Retarding timing generally increases particulate emissions and smoke, though trends vary between different types and designs of diesel engine. Mass particulate emissions increase as injection is retarded.

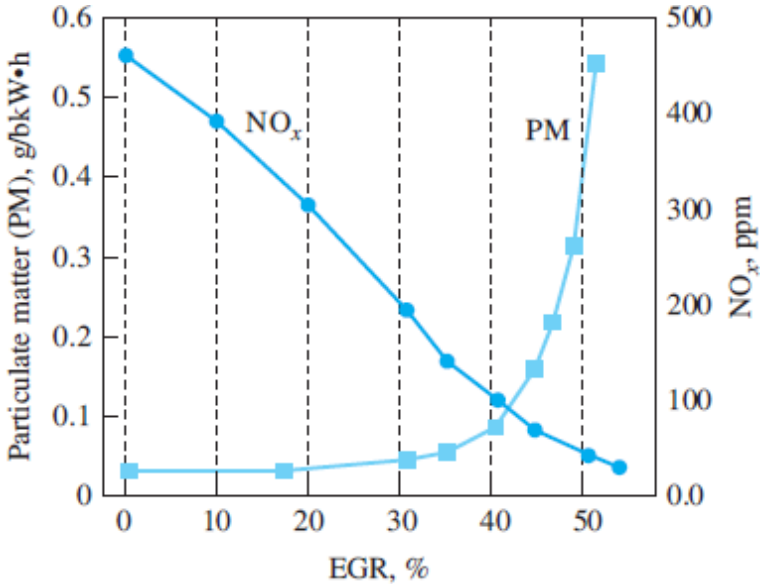
The injection rate depends on the fuel-injector nozzle open-area and injection pressure. Higher injection rates result in higher fuel-air mixing rates, and hence higher heat-release rates (see Sec. 10.6.3). For a given amount of fuel injected per cylinder per cycle, as the injection rate is increased the optimum injection timing moves closer to TC. The higher heat-release rates and shorter overall combustion process that result from the increased injection rate decrease the minimum bsfc at optimum injection timing; however, a limit to these benefits is eventually reached.

Increasing the injection rate increases NO_x emissions and decreases smoke and particulate emissions. The controlling physical process is the rate of fuel-air mixing in the combustion chamber so, at constant fuel injected per cylinder per cycle, both increased injection pressure at fixed nozzle orifice area (which reduces injection duration) and reduced nozzle area at fixed injection duration produce these trends.

A major factor is diesel NO_x control is use of exhaust gas cycle, EGR. The fundamentals of EGR's impact on emissions were reviewed in Sec. 11.2.4. The nitrogen, CO_2 and H_2O in the exhaust recycled into the intake air act as an additional diluent which reduces the burned gas temperatures by an amount in rough proportion to the diluent fraction. With the diesel's always lean operation
$(\phi \leq 0.7)$, the recycled exhaust gases can be thought of as air, mixed with a certain quantity of stoichiometric burned gases: the leaner the diesel's overall operation (the lighter the engine load), the smaller is the fraction of stoichiometric burned gas mixed with the air. Only the amount of stoichiometric burned gas (N_2, CO_2, and H_2O) acts as a "true" diluent: the "air component" in the EGR acts just like the intake air. Thus, the leaner the engine's operation, the higher must be the fraction of the overall exhaust recycled to achieve a given level of actual dilution of the intake mixture. Figure 11.17*b* illustrates this effect via EGR's impact on engine-out NO_x emissions.

EGR, at high levels, significantly increases particulate matter emissions (often referred to as smoke) which consists largely of soot particles. Figure 15.42 shows typical NO_x and PM emissions data as a function of EGR. The negative impact of EGR on PM is largely due to the reduced percentage of oxygen in the fuel-air mixture as exhaust gas is recycled (see Fig. 15.39). This both impacts the mixture within the sprays, where the soot is formed, and the diffusion flame temperature (see Fig. 15.38) where the soot is oxidized.

Figure 15.42 Typical response of engine-out brake-specific particulate (PM) emissions, and NO_x emissions (ppm), to EGR rate. Medium-duty DI diesel engine.[48]



© McGraw-Hill Education. All rights reserved. Any use is subject to the Terms of Use, Privacy Notice and copyright information.

This tradeoff between brake-specific particulate and NO_x engine-out emissions is well known, and for a given diesel engine configuration, is almost universal as injection timing and EGR levels are varied.

The engine designer's goal is obviously to achieve the best bsfc possible with emission levels low enough to satisfy the constraints imposed by emission standards. The variations in engine bsfc, NO_x, and particulate emissions described above involve tradeoffs that make achieving this goal especially difficult. As noted above, one tradeoff is between bsfc and engine-out $bsNO_x$. Injection retard from optimum injection timing decreases $bsNO_x$ at the expense of an increase in bsfc. A second important tradeoff is that between engine-out NO_x and particulate emissions, illustrated for a DI diesel engine in Fig. 15.42.

15.5.4. Overall System Behavior

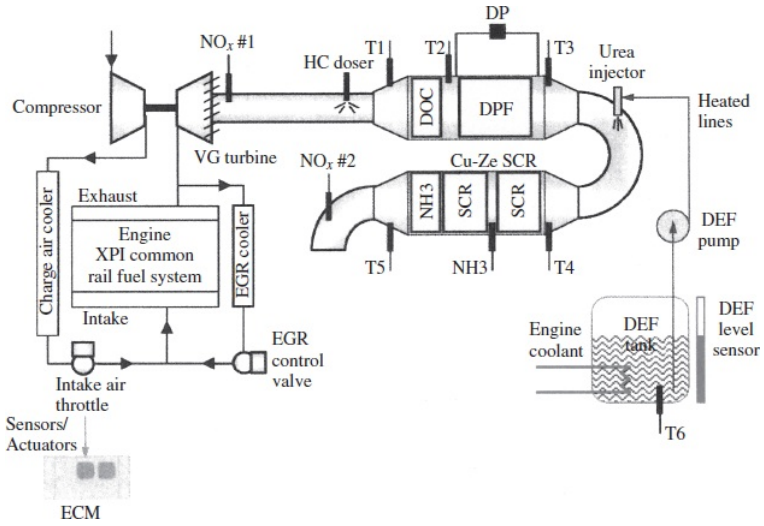
The factors that limit turbocharged diesel engine performance are different to those that limit turbocharged spark-ignition engines. The power output of naturally-aspirated diesel engines is limited by the maximum tolerable smoke emission levels, which occur at overall equivalence ratio values of about 0.7. Turbocharged diesel engine output is usually constrained by stress levels in critical mechanical components. These maximum stress levels limit the maximum cylinder pressure which can be tolerated under continuous operation, though the thermal loading of critical components can become limiting too. As boost pressure is raised, unless engine design and operating conditions are changed, the maximum pressures and thermal loadings will increase almost in proportion. In practice, the compression ratio utilized may need to be is reduced and the maximum fuel/air equivalence ratio must be reduced in turbocharged engines (relative to naturally-aspirated engines) to maintain peak pressures and thermal loadings at acceptable levels.

The different methods of supercharging internal combustion engines were reviewed in Sec. 6.8. Turbocharging and mechanical supercharging with a compressor are alternative methods of boosting the performance of diesel engines. The density of the charge air is the parameter that determines the amount of charge, and hence the torque. Aftercooling in a heat exchanger of the air coming out of the compressor is now standard: it increases the density of the air entering the engine and a lower air temperature reduces all temperatures within the cylinder, an important factor in determining engine-out NO_x emissions.

Figure 15.43 shows the layout of a typical current large-truck diesel engine: engine, turbocharger, controls, plus emissions aftertreatment system. The engine-out emissions, fuel consumption, tradeoff is handled through a charge air cooler (aftercooler) downstream of the turbocharger compressor, a cooled EGR system (high pressure EGR is extracted upstream of the variable nozzle geometry (VG) turbine, cooled, and fed into the intake air downstream of the air throttle which modulates the post-compressor air pressure so it is below the engine exhaust pressure),[1] and a multi-catalyst emissions-reduction aftertreatment system.

© McGraw-Hill Education. All rights reserved. Any use is subject to the Terms of Use, Privacy Notice and copyright information.

Figure 15.43 Turbocharged diesel, engine emissions controls, and aftertreatment system layout for heavy-duty truck application.[48]



This aftertreatment system consists of a diesel oxidation catalyst (DOC), a diesel particulate filter (DPF), urea to ammonia conversion catalyst (NH_3), and a selective catalytic reduction (SCR) catalyst (with two catalyst bricks). These operate as follows. The DOC oxidizes most of the NO in the exhaust to NO_2, which then burns up (oxidizes) the soot collected in the DPF at relatively low temperatures much of the time, through "passive regeneration." When higher exhaust gas temperatures are required, hydrocarbons are added upstream of the DOC as shown. Downstream of the DPF, urea ($CO(NH_2)_2$), the diesel emissions fluid (DEF), is injected, and in the hydrolysis catalyst produces ammonia, the reducing agent for the SCR system where NO and NO_2 are reduced to N_2 by reaction with NH_3. NO_x and NH_3 sensors and HC injection/dosing allow tight control of this multi-component aftertreatment system. The operation of these aftertreatment components is discussed in more detail in Sec. 11.6.

[1] An alternative to the high-pressure EGR system is a low-pressure system where EGR from downstream of the turbine is fed into the (atmospheric pressure) air entering the compressor.

© McGraw-Hill Education. All rights reserved. Any use is subject to the Terms of Use, Privacy Notice and copyright information.

15.6. TWO-STROKE CYCLE ENGINES

This section reviews the operating characteristics of the different types of two-stroke spark-ignition and compression-ignition engines. The effects of changes in the major design and operating variables on their operating characteristics are then related to the more fundamental engine processes such as scavenging, fluid flow, thermodynamics, combustion, heat transfer, and friction. The intent is to provide data on, and an explanation of, actual engine operation—performance, efficiency, and emissions.

15.6.1. Performance Parameters

The practical engine performance parameters of interest are power, torque, brake-specific fuel consumption, and emissions. Following the definitions in Chap. 2, the brake power and the torque of a reciprocating engine can be expressed in terms of the brake mean effective pressure (bmep) as follows:

$$P_b = \begin{cases} \text{bmep} \times A_p \overline{S}_p / 2 & (\text{for two-stroke cycle}) \\ \text{bmep} \times A_p \overline{S}_p / 4 & (\text{for four-stroke cycle}) \end{cases}$$

(15.8)

$$T = \begin{cases} \text{bmep} \times V_d / (2\pi) & (\text{for two-stroke cycle}) \\ \text{bmep} \times V_d / (4\pi) & (\text{for four-stroke cycle}) \end{cases}$$

(15.9)

Thus, for a well-designed engine, where the maximum values of bmep and mean piston speed are airflow (or stress) limited, power is proportional to piston area, and torque to displaced volume. Introducing the definitions of trapping efficiency and delivery ratio from Sec. 6.6.2, and of mechanical and fuel conversion efficiencies from Eqs. (2.24) and (2.29), bmep can be expressed in terms of other basic parameters as follows:

$$\text{bmep} = \eta_m \left(\eta_{\text{tr}} \Lambda\right) \eta_{f,i} \rho_{a,i} \frac{Q_{\text{HV}}}{\lambda (A/F)_s}$$

(15.10)

Equations (15.8) and (15.10) indicate that two-stroke engine power and torque depend on trapping efficiency and delivery ratio: for four-stroke engines, the product of the delivery ratio and trapping efficiency is replaced by the volumetric efficiency.

Brake-specific fuel consumption and normalized indicators of emissions levels have the same definitions and defining equations for both types of engines. Emission rates can also be normalized by the engine's power output (specific power), or by the fuel flow rate.

It is instructive to use typical numbers for full-load and part-load operation to compare the performance of equivalent two-stroke and four-stroke engines. For typical spark-ignition engines of the same displaced volume, at the same air/fuel ratio, the ratio of their maximum torques is given by

© McGraw-Hill Education. All rights reserved. Any use is subject to the Terms of Use, Privacy Notice and copyright information.

$$\frac{T_{2\text{-stroke}}}{T_{4\text{-stroke}}} = \frac{\left[\eta_m\left(\eta_{\text{tr}}\Lambda\right)\eta_{f,i}/2\right]_{2\text{-stroke}}}{\left[\eta_m\left(\eta_\nu\right)\eta_{f,i}/4\right]_{4\text{-stroke}}} \approx \frac{[0.85\times(0.8\times0.9)\times0.3/2]}{[0.8\times(0.95)\times0.34/4]} = 1.4$$

(15.11)

This is consistent with typical maximum bmep values of about 850 kPa for this type of two-stroke engine compared with the 1200 kPa value for a four-valve-per-cylinder modern four-stroke SI engine. This gives a torque ratio [Eq. (15.9)] of

$$\frac{T_{2\text{-stroke}}}{T_{4\text{-stroke}}} = \frac{2\times\text{bmep}_{2\text{-stroke}}}{\text{bmep}_{4\text{-stroke}}} \approx \frac{2\times850}{1200} = 1.4$$

(15.12)

Note that if the bmep of the two engines could be the same (not likely to occur in practice), then the torque ratio would be 2.0.

A comparison of maximum powers from these two different-cycle engines is less straightforward because the maximum power in the two-stroke depends strongly on the scavenging performance of the engine. This depends on the scavenging system, the design of the ports, and especially on the sophistication of the exhaust system and its tuning. For two-stroke SI engines the specific power can vary between about 30 and 80 kW/liter. With the upper value typical of high-performance motorcycle engines. High-performance naturally-aspirated four-stroke passenger car SI engines average about 50 to 60 kW/liter.

In a similar way, for equivalent engines at the same operating conditions, we can estimate the ratio of the brake-specific fuel consumptions to be

$$\frac{\text{bsfc}_{2\text{-stroke}}}{\text{bsfc}_{4\text{-stroke}}} = \frac{\left(\eta_m\eta_{f,i}\right)_{4\text{-stroke}}}{\left(\eta_m\eta_{f,i}\right)_{2\text{-stroke}}} \approx \frac{(0.6\times0.38)}{(0.75\times0.36)} = 0.85$$

(15.13)

Because the pumping losses under part-load conditions in two-stroke engines are smaller than in naturally-aspirated four-stroke engines, and the friction of the four-stroke's gas-exchange crank revolution is absent, the mechanical efficiency is higher. So, although the indicated fuel conversion efficiency of the two-stroke is somewhat lower, for the same fuel/air ratio and engine displaced volume, the brake-specific consumption at typical part-load operating conditions of a direct-injection two-stroke SI engine is lower than that of a standard modern four-stroke SI engine by about 15%. Note that if the two-stroke SI engine is carbureted or intake port-fuel-injected, this benefit essentially disappears due to fuel short-circuiting the cylinder.

15.6.2. Two-Stroke Gasoline SI Engines

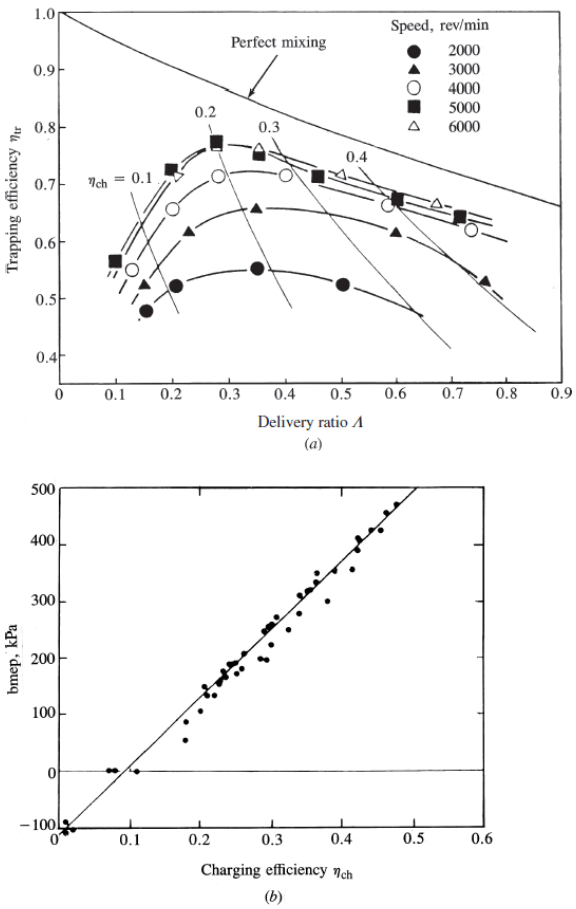
The two-stroke cycle spark-ignition engine in its standard form employs sealed crankcase induction and compression of the fresh charge prior to charge transfer, with compression and then spark ignition in the engine cylinder after charge transfer. The fresh mixture must be compressed to above exhaust system pressure, prior to entry to the cylinder, to achieve effective scavenging of the burned gases. Two-stroke cycle scavenging processes were discussed in Sec. 6.6. The two-stroke gasoline engine is an especially simple and light engine concept and finds its greatest use as a portable power source or on

© McGraw-Hill Education. All rights reserved. Any use is subject to the Terms of Use, Privacy Notice and copyright information.

motorcycles where these advantages are important. Its inherent weakness in its standard form is that the fresh fuel-air mixture which short-circuits the cylinder directly to the exhaust system during the scavenging process constitutes a significant fuel consumption penalty and results in excessive unburned hydrocarbon emissions.

This section reviews the performance characteristics of small crankcase compression two-stroke cycle SI engines. The performance characteristics (power and torque) of these engines depend on the extent to which the displaced volume is filled with fresh mixture, that is, the charging efficiency [Eq. (6.27)]. The fuel consumption will depend on both the trapping efficiency [Eq. (6.24)] and the charging efficiency. Figure 15.44*a* shows how the trapping efficiency η_{tr} varies with increasing delivery ratio Λ at several engine speeds for a two-cylinder 347-cm^3 displacement motorcycle crankcase compression engine. The delivery ratio increases from about 0.1 at idle conditions to 0.7 to 0.8 at wide-open throttle. Lines of constant charging efficiency η_{ch} [which equals $\Lambda\eta_{tr}$; see Eq. (6.28)]. Figure 15.44*b* shows bmep plotted against these charging efficiency values and the linear dependence on fresh charge mass retained is clear.

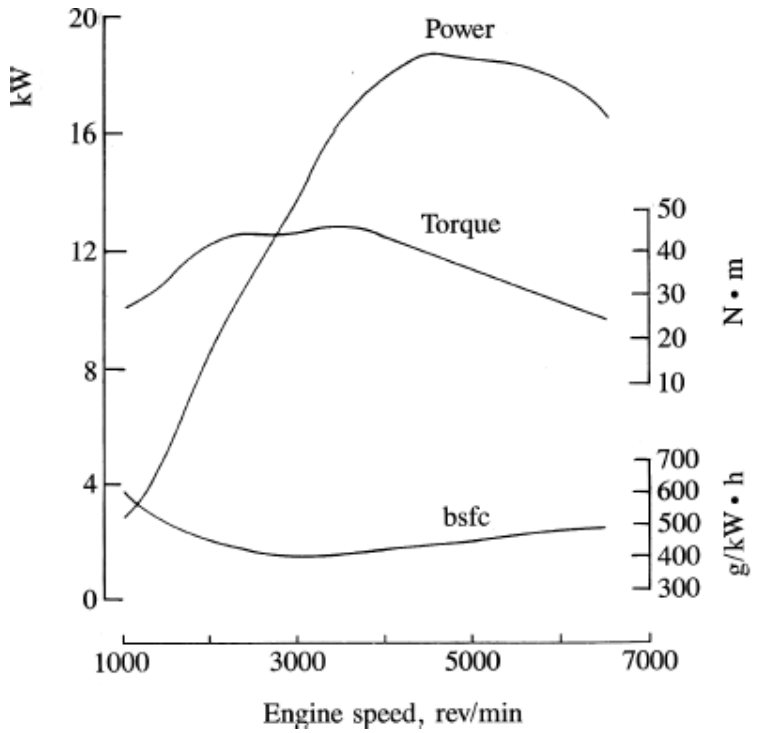
Figure 15.44 (a) Trapping and charging efficiencies as a function of the delivery ratio and (b) dependence of brake mean effective pressure on fresh-charge mass, defined by the charging efficiency. Two-cylinder 347-cm^3 displacement two-stroke cycle spark-ignition engine.[50]



Performance curves for a three-cylinder 450-cm^3 two-stroke cycle minicar engine are shown in Fig. 15.45. Maximum bmep is 640 kPa at about 4000 rev/min. Smaller motorcycle engines can achieve slightly higher maximum bmep at higher speeds (7000 rev/min). Fuel consumption at the maximum bmep point is about 400 g/kW·h. Average fuel consumption is usually one-and-a-half to two times that of an equivalent four-stroke cycle engine.

© McGraw-Hill Education. All rights reserved. Any use is subject to the Terms of Use, Privacy Notice and copyright information.

Figure 15.45 *Performance characteristics of a three-cylinder 450-cm^3 two-stroke cycle spark-ignition engine. Maximum bmep = 640 kPa. Bore = 58 mm, stroke = 56 mm.*[51]



CO emissions from two-stroke cycle engines vary primarily with the fuel/air equivalence ratio in a manner similar to that of four-stroke cycle engines (see Fig. 11.19). NO_x emissions are significantly lower than from four-stroke engines due to the high residual-gas fraction resulting from the low charging efficiency especially at light to mid loads. Unburned hydrocarbon emissions from carbureted or manifold fuel injected two-stroke engines are about five times as high as those of equivalent four-stroke engines due to fresh mixture short-circuiting the cylinder during scavenging. Exhaust mass hydrocarbon emissions vary approximately as $\Lambda(1 - \eta_{tr})\phi$, where ϕ is the fuel/air equivalence ratio.[50]

Table 15.6 compares the fuel consumption and emissions from a two-stroke and a four-stroke marine engine designed for similar applications. The fuel consumption and emissions data are weighted averages over different load and speed points. The two-stroke engine is inferior to the four-stroke engine in engine-out CO and HC levels, while superior in NO_x emissions. The first two are in part attributable to the engine lubrication approach used in this type of two-stroke engine: the piston ring and skirt in-cylinder lubricant is mixed with the fuel and introduced through the fuel system. Short-circuiting of the fuel through the exhaust ports during the scavenging process cannot be avoided with such fuel-air premixing, so high HC emissions and fuel consumption are unavoidable.

© McGraw-Hill Education. All rights reserved. Any use is subject to the Terms of Use, Privacy Notice and copyright information.

Table 15.6 Comparison between fuel consumption and exhaust gas composition of two- and four-stroke two-cylinder carbureted marine engines[52, 53]

Engine	Two-stroke OMC J10RCSE	Four-stroke Honda BF9.9A
Rated power (kW)	7.4 at 5000 rev/min	7.4 at 5000 rev/min
Displacement (cm^3)	216	280
Fuel/oil ratio	50:1	NA
Fuel consumption (g/kW·h)	910	550
CO (g/kW·h)	520 EI = 570	370 EI = 670
CO_2 (g/kW·h)	1300 EI = 1430	1050 EI = 1920
HC (g/kW·h)	240 EI = 260	32 EI = 58
NO_x (g/kW·h)	0.73 EI = 0.80	3.4 EI = 6.2

Because of its simple construction, compactness, high power-to-weight ratio, and low cost, small carbureted two-stroke cycle engines have been widely used for hand held equipment. As illustrated above, its most serious drawback is its high HC emission and low thermal efficiency due to short-circuiting of fuel to the exhaust port. This type of two-stroke engine, where the fuel and air are premixed really cannot meet the strict emissions limits now imposed.

Alternative two-stroke cycle spark-ignition engine approaches have been explored that largely avoid this major challenge. Several of these have been developed to the prototype stage. Table 15.7 summarizes three different concepts which we will briefly describe. Further details can be found in Ref. 52, along with engine layout drawings.

© McGraw-Hill Education. All rights reserved. Any use is subject to the Terms of Use, Privacy Notice and copyright information.

Table 15.7 Three different two-stroke cycle gasoline engine prototypes

	Orbital	Toyota	Honda (AR)
Engine type	DI, two-stroke	DI, two-stroke	DI, two-stroke
Scavenging flow	Cross-scavenged, ports	U-scavenged valves	Schnürle (loop)
Air compression	Crankcase	Supercharged, Roots blower	Crankcase
Fuel system	Air-assist, DI	High press. (10 MPa) liquid fuel, DI	Pneumatic (250 kPa), DI
Combustion	SI premixed flame	SI premixed flame	Active radical combustion
Displacement	1.2 dm^3 three-cylinder	804 cm^3 two-cylinder	402 cm^3 one-cylinder
Bore/stroke	81/78 mm	80/80 mm	80/80 mm
Max. power/speed	66 kW/5500 rev/min	47 kW/4000 rev/min	33 kW/6900 rev/min
Spec. P_b : bmep	55 kW/ℓ: 600 kPa	58 kW/ℓ: 877 kPa	82 kW/ℓ: 713 kPa
Compression ratio		8.5 (geometric)	6.1 (trapped)
$\overline{S}_p$ at $P_b$max.	14.3 m/s	10.7 m/s	18.4 m/s
Lubrication	Oil spray, dry sump	Wet oil sump	
Exhaust port/valve open/close	(port, w. throttle)	70° BBC/50° ABC (valve)	94° BBC/94° ABC (port, w. throttle)
Intake port/valve open/close		50° BBC/70° ABC (valve)	57° BBC/57° ABC
Fuel consumption	Reduced	Reduced	Much reduced
Emissions: HC	Factor ~ 5 less	Factor ~ 5 less	Much reduced
NO_x	Less	Factor ~ 2 less	Less
Source: Heywood and Sher[52]: 1990s prototype engines			

The three engine's listed in Table 15.7 utilize direct fuel injection into the cylinder. This obviously prevents loss of fuel through short circuiting during the scavenging process, an important improvement for both fuel consumption and HC emissions. Each uses a different form of direct fuel injection: air-assist (6 bar air pressure) to realize fine-spray atomization; high-pressure liquid fuel injection; lower pressure air-driven injection. While the Orbital two-stroke engine has a specific combustion-chamber design, its combustion process is similar to a fast-burn four-stroke SI engine combustion system. The Toyota, uniflow-scavenged valved (two intake and three exhaust valves, per cylinder) engine, is more highly boosted (and achieves the highest bmep at the quoted maximum power condition).

The Honda engine uses a different combustion process than normal spark-ignition flame initiation and propagation. By controlling the amount of hot residual gas trapped within the cylinder at the end of the scavenging process, the temperature of the fuel vapor, air, residual gas can be controlled at a high enough level for the charge to autoignite just after TC, releasing its chemical energy (rapidly, but not too rapidly) through a volume burning rather than flame propagation process. This novel two-stroke cycle combustion mode, first developed in Japan, is termed active-radical combustion (1979).[52, 54] The pressure

© McGraw-Hill Education. All rights reserved. Any use is subject to the Terms of Use, Privacy Notice and copyright information.

rise this spontaneous combustion process produced in two-stroke cycle engines can be readily controlled and is highly repeatable, cycle-by-cycle. A valve that controls the effective open area of the exhaust port is a key component in achieving the desired degree of control. This mode of operation works best up to about mid-load. It is a forerunner of the HCCI (homogeneous charge compression ignition) process now being explored and developed for four-stroke cycle engines (see Sec. 10.7.2). Note that these three examples of direct-injection two-stroke cycle gasoline engines are prototype concepts that have not yet been used in mass production.

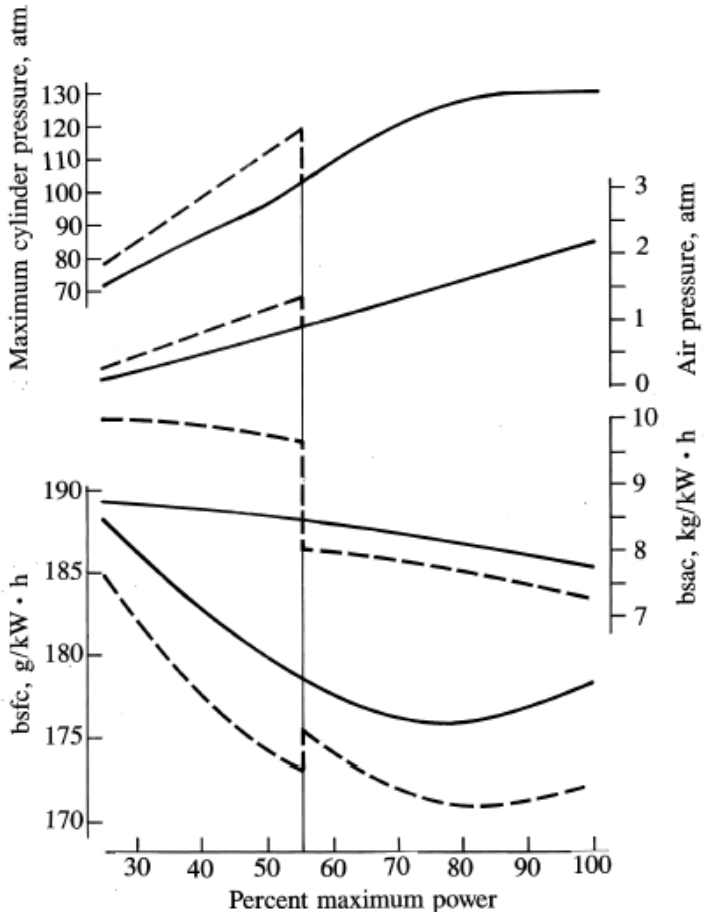
15.6.3. Two-Stroke Cycle CI Engines

Large marine diesel engines (0.4 to 1 m bore) utilize the two-stroke cycle. These low-speed engines with relatively few cylinders are well suited to marine propulsion since they are able to match the power/speed requirements of ships with simple direct-drive propeller arrangements. These engines are turbocharged to achieve high brake mean effective pressures and specific output. The largest of these engines can achieve brake fuel conversion efficiencies of up to 55%. An example of a large marine two-stroke engine is shown in Fig. 1.36. Over the past few decades, the output per cylinder of such engines has increased by a factor of more than two, and fuel consumption has decreased by 25%. These changes have been achieved by increasing the maximum firing pressure to about 15 MPa, and by refining critical engine processes such as fuel injection, combustion, supercharging, and scavenging. The uniflow-scavenging process is preferred to loop scavenging since it achieves higher scavenging efficiency at high stroke/bore ratios and allows increases in the expansion ratio.

The performance characteristics of a 580-mm bore Sulzer two-stroke marine diesel engine with a stroke/bore ratio of 2.9 are shown in Fig. 15.46. The solid lines show the standard turbocharged engine characteristics. The rated speed for the engine is 125 rev/min, corresponding to a maximum mean piston speed of 7.2 m/s. The rated bmep is 1.66 MPa. The minimum bsfc is 175 g/kW·h which equals a brake fuel conversion efficiency of 48%. For larger lower-speed engines, the efficiency is higher, above 50%. The dashed lines show how the performance of this engine can be improved by turbo-compounding. A proportion of the engine's exhaust flow, at loads higher than 50%, is diverted from the turbocharger inlet to a separate turbine coupled to the engine power takeoff gear via an epicyclic speed-reduction gear and hydraulic coupling. The additional power recovered in this manner from the engine exhaust flow improves bsfc by 5 or so g/kW·h. At part load, when the full exhaust flow passes through the turbocharger, an efficiency gain is also obtained, due to the higher scavenging pressure (and therefore increased cylinder pressure) obtained with the full exhaust flow.

© McGraw-Hill Education. All rights reserved. Any use is subject to the Terms of Use, Privacy Notice and copyright information.

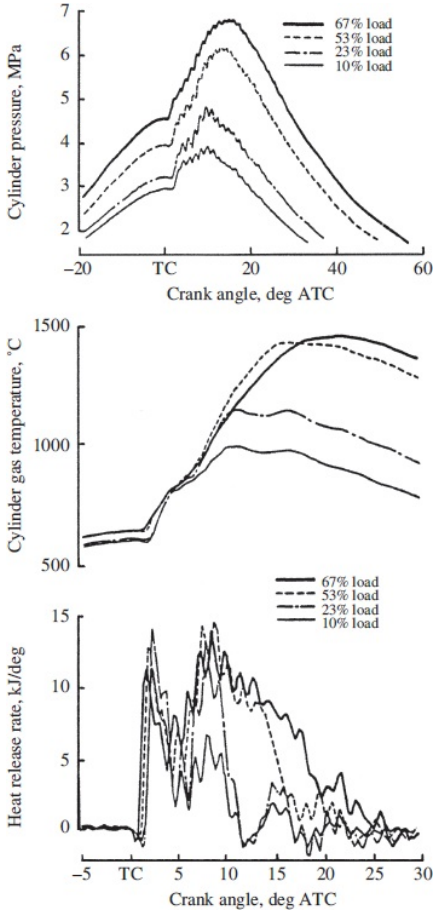
Figure 15.46 Performance characteristics of large marine two-stroke cycle uniflow-scavenged DI diesel engine. Bore = 580 mm, stroke/bore = 2.9, maximum rated speed = 125 rev/min (mean piston speed = 7.2 m/s), bmep (at rated power) = 1.66 MPa. Solid line: standard turbocharged configuration. Dashed lines: parallel turbocompounded configuration at greater than 50% load, bsac: brake-specific air consumption.[47]



The combustion characteristics of large-bore marine two-stroke diesel engines are shown in Fig. 15.47, at several different loads. The heat release rate profiles (bottom graph) lengthen as load increases: at the higher loads, the mixing-controlled diffusion flame phase of combustion becomes longer in duration and more dominant. Peak cylinder pressure and (average) in-cylinder gas pressure rise as load and overall fuel-air equivalence increases. Because diesels always run lean, *average* peak gas temperatures are substantially lower than burned-gas temperatures in SI engines. The integral of each heat-release-rate profile indicates the amount of fuel injected per cycle, at these different loads.

© McGraw-Hill Education. All rights reserved. Any use is subject to the Terms of Use, Privacy Notice and copyright information.

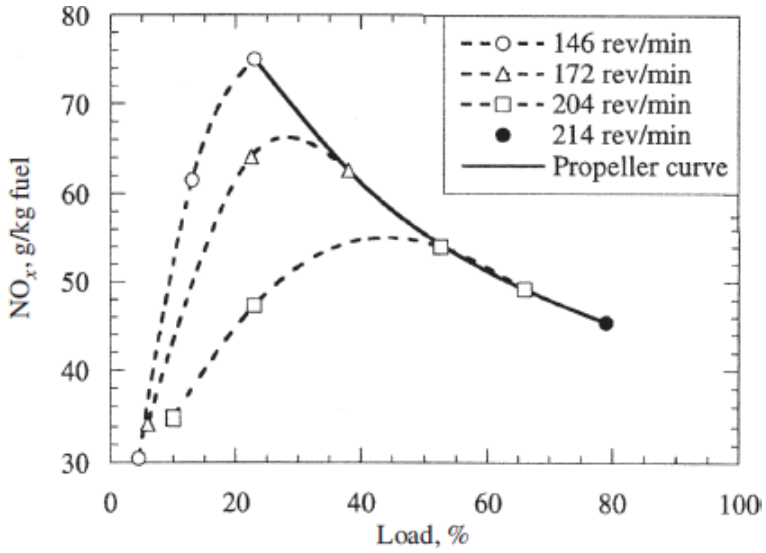
Figure 15.47 Combustion, characteristics of large-bore turbocharged two-stroke cycle uniflow-scavenged marine diesel engine. Bore = 450 mm, stroke = 750 mm. Maximum rated power is 2.8 MW, maximum bmep = 1.0.[55]



The NO_x emissions from large marine diesels (and when these engines are used for electricity generation) must be controlled. Engine-out NO_x emissions are of special concern. For the same large-bore diesel whose combustion details are shown in Fig. 15.47, Fig. 15.48 shows engine-out NO_x emissions as a function of load at different speeds. The engine here was used to drive the propeller in a large vessel (e.g., oil tanker) application. Here NO_x emission rate has been normalized by fuel flow rate (NO_x emission index is used). In absolute terms, the NO_x emission rate (gNO_x/h) goes up as load increases (as would be expected, ϕ is increasing). Relative to the fuel flow rate as EI_{NOx}, the NO_x goes down. Relative emissions are more challenging to interpret since, as load increases, the fuel/air equivalence ratio increases, airflow increases, and combustion duration lengthens.

© McGraw-Hill Education. All rights reserved. Any use is subject to the Terms of Use, Privacy Notice and copyright information.

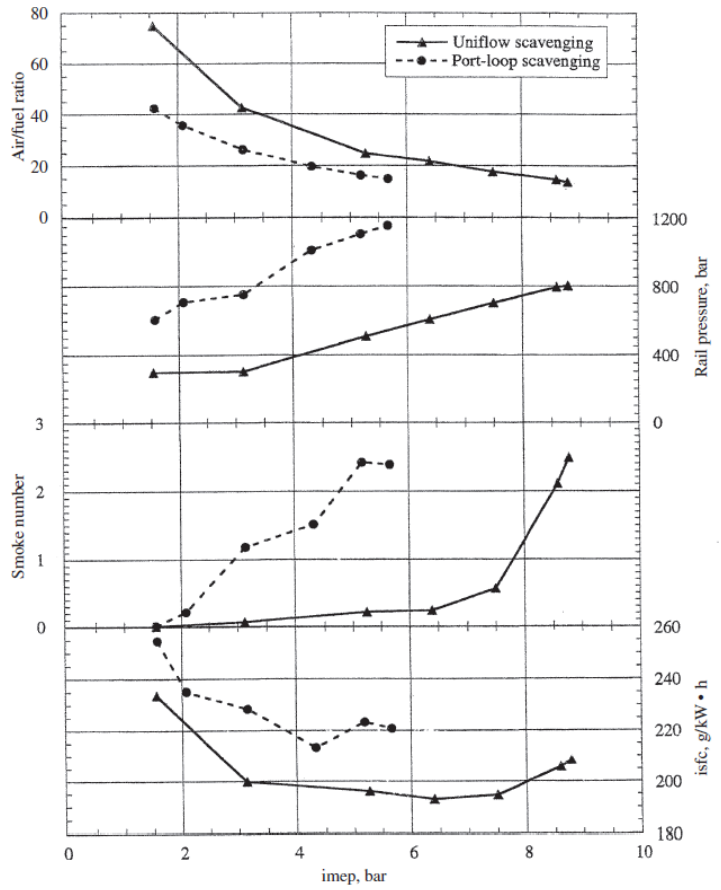
Figure 15.48 Effect of engine load and speed on engine-out NO_x emission index (with ppm in exhaust corrected to 13% oxygen): large-bore two-stroke marine diesel engine.[55]



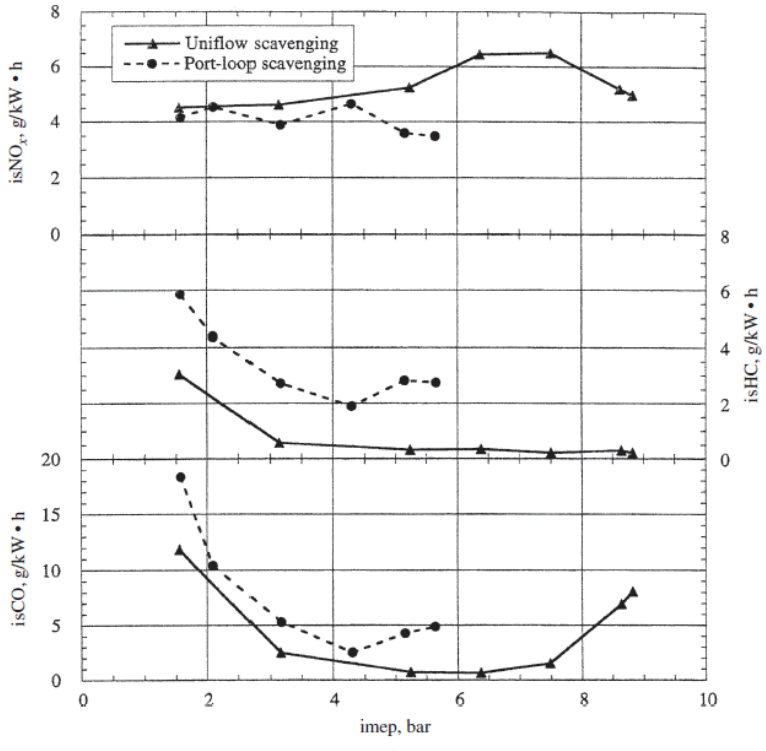
Two-stroke diesel engines of smaller size than these large-bore engines are used in several applications: rail, industrial, marine, and oil drilling. The performance and emissions characteristics of two turbocharged two-stroke DI diesel engines, one with a uniflow-scavenged, the other with a port loop-scavenged gas exchange process, with an 80-mm bore, at part load, are shown in Fig. 15.49. Such smaller two-stroke cycle DI diesel engines also compete with four-stroke cycle engines in the marine, industrial, and construction markets. Engine details are given in Table 15.7. The more effective scavenging process inherent in the uniflow scavenging flow design is apparent in the data shown in Fig. 15.49. For both engines, the air/fuel ratio decreases as load increases. The isHC emissions decrease, and the smoke number (SN) and isNO_x emissions both increase. The specific fuel consumption reaches a minimum at about 80% of the maximum load. The increase in isCO emissions when load decreases below 50% of its maximum value indicates that poor mixing is occurring within parts of the cylinder. With the port loop-scavenged engine, the SN exceeds a value of 1.0 at 300 kPA imep, and reaches the full load limit of 2.5 at about 500 kPa. With the uniflow-scavenged engine, the values of smoke number are significantly lower. As a consequence, lower fuel injection pressures can be utilized, and still achieve adequate fuel-air mixing rates. The fuel consumption for the ported loop-scavenged engine is 10% higher (in part due to its less favorable surface-to-volume ratio). The isNO_x emission levels are closely comparable.

Figure 15.49 (a) Part-load operating characteristics and (b) engine-out emissions characteristics, for a small-bore loop-scavenged and a uniflow-scavenged two-stroke diesel engine.[1] *Engine details in Table 15.8.*[52, 56]

© McGraw-Hill Education. All rights reserved. Any use is subject to the Terms of Use, Privacy Notice and copyright information.



(a)



(b)

© McGraw-Hill Education. All rights reserved. Any use is subject to the Terms of Use, Privacy Notice and copyright information.

Table 15.8 Daimler-Benz direct-injected two-stroke diesel engine comparison[52,56]

Engine type	Ported loop scavenging	Uniflow scavenging
Bore/stroke	80/70 mm	80/98 mm
Displacement, one cylinder	350 cm^3	493 cm^3
Combustion chamber	Bowl in cylinder head	Bowl in piston
Scavenging air	Crankcase compressed	External compressor

© McGraw-Hill Education. All rights reserved. Any use is subject to the Terms of Use, Privacy Notice and copyright information.

15.7. NOISE, VIBRATION, AND HARSHNESS

Noise, vibration, and harshness (NVH) is the phrase used to describe the audible and tactile disturbances that engines generate which are experienced by the operator, user, or bystander. In probably the most important application area, engines in vehicles, the engine, the source of the vibrational energy that creates these disturbances, couples with the vehicle structure leading to additional disturbances that vehicle occupants experience negatively. The mechanisms that generate these disturbances, and approaches that reduce their impacts, are the subject of this section. *Noise* is discussed in Sec. 15.7.1. The *dynamics* of the reciprocating engine's power transmitting components—pistons, connecting rods, and crankshaft, and the forces involved, are covered next (in Sec. 15.7.2), followed by a review of *balancing* issues in multi-cylinder engines (Sec. 15.7.3). Section 1.5 (Multi-cylinder Engines), Sec. 2.2 (Geometrical Relationships for Reciprocating Engines), and Sec. 2.3 (Forces in the Reciprocating Mechanism) provide important background material for these topics.

Harshness refers primarily to the audible impact of an overly fast engine combustion process. The rapid cylinder-pressure rise rate that this generates is "noisy" and unattractive to engine operators. It, therefore, needs to be controlled. Factors that control burn rates in spark-ignition engines (Chap. 9), and diesel engines (Chap. 10) have already been discussed. In gasoline engines, combustion system design (Sec. 15.4.6) embodies achieving "fast-enough" combustion at light to mid-load to achieve the desired efficiency and emissions benefits. However, the burn rate increases as engine load is increased (as the throttle is opened), so combustion harshness as wide-open-throttle operation is approached, may be a problem. Diesel engines inherently have a different burning profile (see Fig. 15.1), with a rapid initial burn rate and much slower later burn rate, with corresponding rates of pressure rise. This challenge becomes worse when the engine is cold, and the longer ignition delays result in more rapid initial burn rates still. Pre- or pilot injection helps here by reducing the duration of the delay, and thus the initial rate of pressure rise.

The overly rapid rise in pressure excites strong vibrations of the cylinder liner and head walls, thus radiating audible sound waves to the engine's surroundings.

15.7.1. Engine Noise

Noise is often defined as "unwanted sound." It is a significant problem with internal combustion engines, especially with diesel engines and small two-stroke gasoline engines. It is a difficult problem to resolve because effective noise suppression usually reduces engine power, increases engine bulk size and weight, and increases cost, all of which run counter to the competitive pressures in most engine markets. Noise is an extensive and well-defined field, with its own vocabulary and literature, which can separate it from more obvious aspects of engine operation. Increasingly, however, as noise limits on engines become more stringent, the reduction of engine noise must be integrated into a systems approach to engine design. While an extensive treatment of engine noise is beyond the scope of this book, in this section we develop enough of the fundamentals of the subject for the reader to be able to understand the sources of noise in internal combustion engines and the means available to reduce them. Additional details and more extensive reviews can be found in Annand and Roe,[57] Blair,[58] and the Bosch Automotive Handbook.[59]

15.7.1.1. Fundamentals and Definitions

Sound propagates through a medium as fluctuations in pressure. The frequency of these fluctuations determines the *pitch* of the sound. The human ear can detect frequencies from 20 Hz up to 15,000 to 20,000 Hz. A simple sinusoidal pressure oscillation produces a sound wave that is called a *pure tone*. Usually sound is composed of a fundamental frequency with smaller amplitude harmonics—simple multiples of this fundamental frequency. This mixture of frequencies gives the sound its "tone"; significant amplitude high-frequency components make sounds especially objectionable.

© McGraw-Hill Education. All rights reserved. Any use is subject to the Terms of Use, Privacy Notice and copyright information.

The pressure fluctuations generated by the noise source transfer energy outward through molecular collisions. The more energy transferred, the higher the sound level or volume. The *intensity of sound*, I (W/m^2), is defined as the energy transfer per unit time by the sound wave through unit area perpendicular to the wave propagation direction. It quantifies the actual energy flux associated with the sound wave. Usually, the effective sound pressure—the root-mean-square (rms) fluctuating pressure δp—is what is measured. For plane or spherical waves,

$$I = (\delta p)^2/(\rho a)$$

(15.14)

where ρ is the medium density [for ambient air,ρ = 1.184 kg/m^3 (0.0739 lbm/ft^3)] and a is the sound speed [given by $(\gamma RT)^{1/2}$, 346 m/s for air at 25°C]. With a localized noise source, the sound intensity I and the square of the rms fluctuating pressure $(\delta p)^2$ both fall off as the square of the distance from the source.

The range of sound intensities that humans can hear and tolerate is very large, from 10^{-12} W/m^2 to 1 W/m^2, so a logarithmic scale is used. The *sound intensity level* L_I is therefore defined as

$$L_I = 10 \log_{10}(I/I_0)$$

(15.15)

where I_0 is a chosen reference level. The unit of this relative intensity is the decibel (dB). Equation (15.15) can be expressed in terms of the sound pressure level L_p,

$$L_p = 10 \log_{10}[(\delta p)^2/(\delta p_0)^2] = 20 \log_{10}(\delta p/\delta p_0) \text{ dB}$$

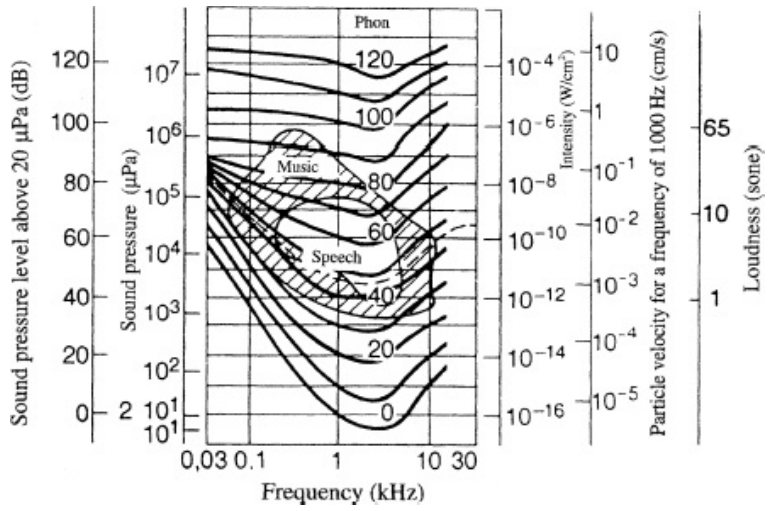
(15.16)

where δp_0 is the reference sound pressure level. The standard reference level corresponds to the threshold of hearing, where $I_0 = 10^{-12}$ W/m^2 and $\delta p_0 = 5 \times 10^{-5}$ Pa. Using Eqs. (15.14) to (15.16), a sound intensity of 1 W/m^2, which is the sound level at which the ear begins to feel pain, corresponds to a mean effective sound pressure of 20 Pa, and a sound pressure level of 120 dB.[52]

In the frequency range 500 to 5000 Hz, the ear responds almost logarithmically to sound intensity, so this logarithmic decibel scale is appropriate. However, sounds of different pitch or frequency perceived as equally loud do not have the same intensity. To provide a quantitative measure of subjective *loudness*, sound is said to have a loudness in *phons* equal to the intensity level of a pure tone of frequency 1 kHz that appears equally loud. Figure 15.50 shows how the actual intensity required to produce a certain sensation of loudness for an average listener varies with frequency. The weighting shown is known as the *A-weighting*, and corresponds to the ear's response at 40 phon. An A-weighting filter is normally applied automatically to noise-meter (a microphone that converts variations in pressure to variations in voltage) measurements and is designated dB(A). Note that the most irritating frequencies are between about 1 and 5 kHz, with increasingly higher sound pressure levels sounding equally loud as frequencies decrease and increase below and above this band, respectively.[52]

© McGraw-Hill Education. All rights reserved. Any use is subject to the Terms of Use, Privacy Notice and copyright information.

Figure 15.50 Objective (sound pressure level, in decibels) and subjective (A-weighted sound-meter curve, in phons) scales for noise curves of equal loudness level, as a function of frequency.[52, 59] (Courtesy Robert Bosch GmbH and SAE.)



With more than one source of sound, in nonreflecting surroundings and sufficiently distant from the sources, the combined effect is obtained by adding the absolute source intensities (the energy fluxes per unit area), as they are each planar sound waves. For example, with two sources of intensity I_1 and I_2, the combined intensity I_{12} is

$$I_{12} = I_1 + I_2$$

(15.17)

where, from Eq. (15.15),

$$I_1 = I_0 \text{antilog}_{10}(L_{I1}/10) \text{ and } I_2 - I_0 \text{antilog}_{10}(L_{I2}/10)$$

The resultant sound intensity level is given by

$$\begin{aligned} L_{I12} &= 10 \log_{10}(I_{12}/I_0) \\ &= 10 \log_{10}[\text{antilog}_{10}(L_{I1}/10) + \text{antilog}_1(L_{I2}/10)] \end{aligned}$$

(15.18)

If the two sources (1 and 2) are equal, Eq. (15.18) gives

$$\begin{aligned} L_{12} &= 10 \log_{10}[2 \text{antilog}_{10}(L_{I1}/10)] \\ &= 10[\log_{10}2 + (L_{I1}/10)] = L_{I1} + 3.01\,\text{dB} \end{aligned}$$

that is, doubling the intensity of sound increases the sound intensity level by 3 dB. If one source is substantially larger than the other, for example, the two sources are 100 dB and 90 dB, then the two sources together give

$$L_{I12} = 10 \log_{10}[\text{antilog}_{10}9] = 100.4\,\text{dB}$$

© McGraw-Hill Education. All rights reserved. Any use is subject to the Terms of Use, Privacy Notice and copyright information.

Here, the smaller source contributes little to the combined sound level.[52]

Two important consequences for reducing noise levels in engines follow from this review of noise fundamentals:[58]

- The loudest of the several sources of noise in an engine will be much the most important in determining the total sound pressure level. To reduce the noise emissions, that source must first be dealt with effectively.
- The higher frequency range (1 to 5 kHz) is much more objectionable to the human ear, at the same sound intensity level, than are lower frequencies. So treatment should focus first on this higher frequency range.
- When a major noise source varies with time and produces short intense pulses (e.g., a poorly muffled engine exhaust system at low speed), these are highly disagreeable and must be heavily damped by the noise treatment system.[57]

15.7.1.2. Sources of Engine Noise

There are three major sources of engine noise: the exhaust, the intake, and mechanical impacts and vibration. Exhaust noise is easiest to understand; its origin is the pressure waves set up in the exhaust system by each cylinder's exhaust blowdown process, and audible noise is generated as these waves enter the atmosphere. Intake noise is generated by the pressure waves set up by the periodic induction processes into each cylinder. Mechanically generated noise is generally lower than exhaust- and intake-generated noise. There are several sources. One is the rapid combustion-produced pressure rise that is transmitted through the block and cylinder-head walls to the atmosphere (often referred to as *harshness*). Another source is when the piston *slaps* against the cylinder liner, causing the block to vibrate. At close to TC piston position, the forces acting on the piston cause it to rock from one side of the liner to the other causing the block to vibrate. Mechanical noise also originates from the oscillating forces on the crankshaft bearings. The roller bearings sometimes used in the crankcase and valvetrain are noisier than standard lubricated plain bearings where the oil film damps out the mechanical vibration. In air-cooled engines, the cylinder and head cooling fins vibrate and produce noise. Liquid cooling of the engine damps out some of the vibrations the block and head structure would otherwise transmit. Gears and chain drives are also significant sources of mechanical noise.[57, 58]

In boosted engines, an additional noise source is the turbocharger. Constant-pressure turbocharger systems, where a gas reservoir upstream of the turbine is used to dampen the exhaust blow-down pressure pulses to improve overall turbine performance, are significantly quieter than the alternative impulse systems where the turbine is designed to take advantage of the exhaust pressure pulsations. In diesel engines, the high-pressure fuel-injection system is also a noise source.[52]

We now show some examples of engine noise levels and spectra. Noise level meters provide such information in several ways. One is to weight the sound pressure levels at different frequencies and then integrate to produce an overall sound intensity reading. The A-weighting mentioned earlier, which corresponds to the average ear's response at the 40-phon level, is usually used in engine and vehicle noise tests. However, knowledge of the noise spectral distribution is helpful when designing noise suppression systems.

Figure 15.51 compares the noise spectrums of equivalent four-stroke cycle and two-stroke cycle diesel engines. The sound pressure levels are highest in the 1 to 3 kHz range and decline significantly at higher and lower frequencies. The maximum noise levels are about 8 dB(A) lower for the two-stroke engine due to its shorter ignition delay (and hence slower initial combustion-generated rate of pressure rise), and the lower two-stroke engine peak pressures. The two-times-higher firing frequency of the two-stroke, at the same engine speed, also reduces mechanical vibration substantially, and the mechanical noise it generates.[60]

© McGraw-Hill Education. All rights reserved. Any use is subject to the Terms of Use, Privacy Notice and copyright information.

Figure 15.51 Engine noise spectra in dB(A) (the A-weighting corresponds to the ear's response at 40 phon) from two automotive diesel engines. Lower curve: 2.5-liter four-cylinder two-stroke supercharged CI engine producing 320 N·m of torque at 1800 rev/min and 100 kW at 3400 rev/min; bore/stroke 96/86 mm, r_c = 18. Upper curve: equivalent four-stroke cycle diesel engine.[60]

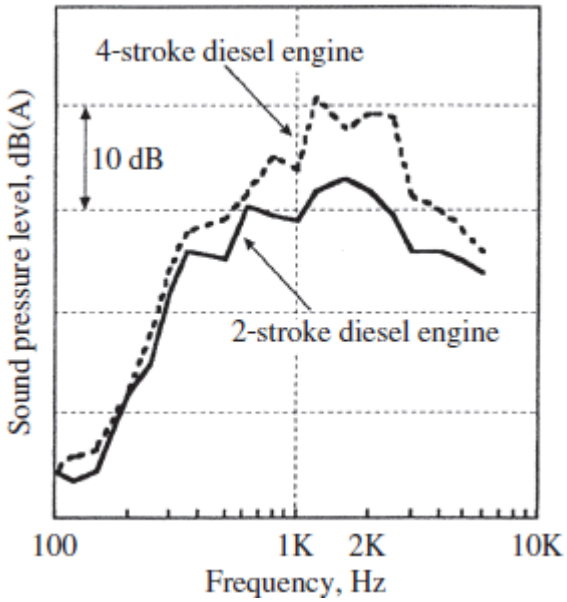
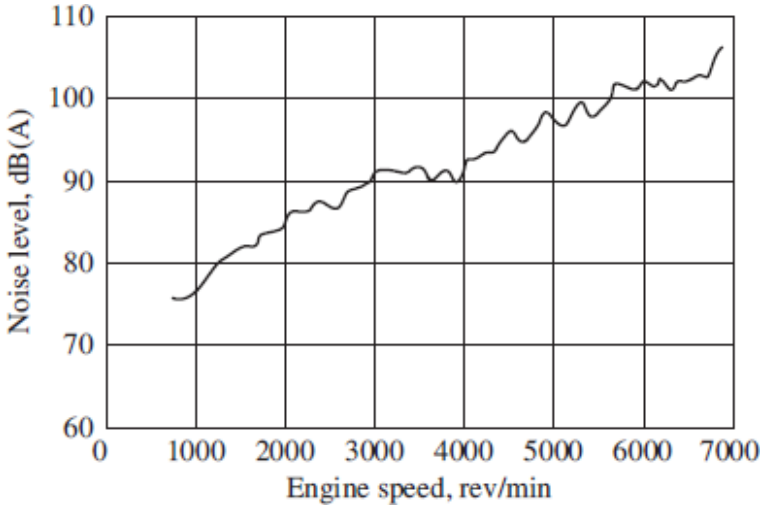


Figure 15.52 shows the noise level in dB(A) for a 4.5-liter V-8 naturally-aspirated gasoline engine, incorporating several noise reducing features, as a function of engine speed. Noise levels rise by some 30 dB(A) from low speed to high speed, which is typical for gasoline engines.[61]

Figure 15.52 Noise level in dB(A) at wide-open-throttle as a function of engine speed, for a 4.5-liter V-8 naturally-aspirated gasoline engine.[61]



15.7.1.3. Engine Noise Reduction

Ever increasing specific power, and changing requirements such as reduced vehicle weight, are demanding reductions in engine size and weight, and in fuel consumption. Increasing in-cylinder pressure levels and reducing engine weight, make achieving reductions in noise and vibration more important. The following are examples of engine enhancements that improve NVH characteristics.

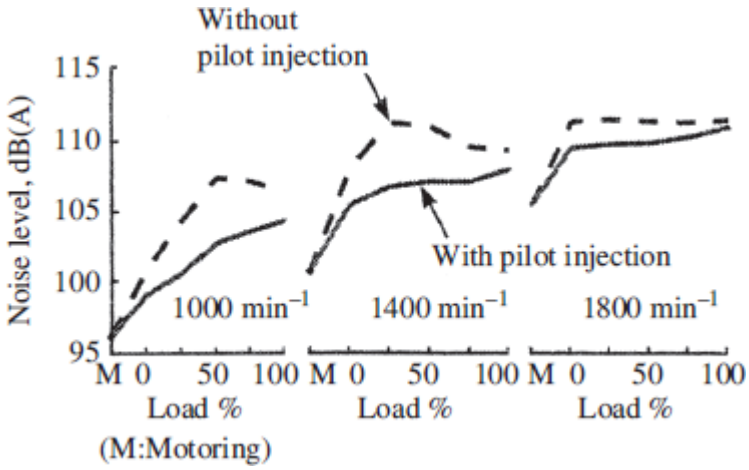
© McGraw-Hill Education. All rights reserved. Any use is subject to the Terms of Use, Privacy Notice and copyright information.

Stiffer block structures reduce vibration and sound radiation. A more rigid crankcase structure, larger crankshaft diameter with more rigid end bearings with a thinner oil film, reduce and damp crankshaft vibration. Lower noise-generating lighter smaller-pitch chain drives have been developed with smoother link and sprocket contract, with chain-driven accessories more rigidly mounted on the block, reduce noise generation. Soft mounted and stiffer oil pan and chain drive covers more effectively absorb the noise produced.

Simple two-stroke cycle gasoline engines are designed to be light and compact, so the engine surfaces radiate noise more easily, and the space available for noise suppression devices is limited. These small two-stroke engines usually employ a tuned exhaust, with a choked final outlet to maximize the power output. This exhaust system feature eases the task of designing a silencer-muffler with minimum impact on power. Also, due to its less effective filling of each cylinder with air, the two-stroke SI engine has lower peak cylinder pressures than the four-stroke. The resulting oscillating forces in major engine components are therefore lower and so is the mechanical noise they generate.

With diesel engines, these same opportunities are available. In addition, since the diesel's combustion process follows from the fuel injection strategy and rate (and in-cylinder air temperature and pressure at time of injection), opportunities exist to reduce the rapid rate of pressure rise that results in combustion harshness. Also, pre (or pilot) injection moderates the initial rapid-burning phase of diesel combustion and reduces its initial pressure rise rate. See Secs. 10.5.4 and 10.7.1. The attendant noise reductions are illustrated in Fig. 15.53 for a 19-liter V-8 turbocharged and intercooled diesel. The impact of pilot injection is greatest at below 50% load: also, in the frequency range 600 to 3000 Hz. Greatest benefits were realized with a small quantity of pilot-fuel (2 to 6 mm^3/injection) injected some 15 to 20 degrees before the main injection was initiated (main injection, 120 to 220 mm^3/injection).[62]

Figure 15.53 Noise reduction, dB(A), resulting from use of pilot injection in a 19-liter V-8 turbocharged DI diesel engine. Pilot fuel injection amount 2 to 6 mm^3/injection; main injection amount 120 to 220 mm^3/injection.[62]



In the large marine diesel application area where two-stroke cycle engines are often used, the major noise challenge is overall engine-room noise, which must be kept below 100 dB(A), measured at several locations at 2 to 3 m heights about 1 m from the engine's outer surface. The noise is primarily generated by individual engine components and their surfaces. Exhaust gas noise can be brought down by about 25 dB(A) to acceptable levels with large absorption silencers, which are especially effective at damping the higher frequencies.

15.7.1.4. Exhaust Noise

Exhaust noise is the result of pressure waves in the exhaust system exiting through its open end into the ambient air, and from vibration of the exhaust system surfaces caused by these pressure waves. Various muffler (silencer) technologies and exhaust system configurations have been developed to reduce exhaust noise. The selection of the appropriate approach, with

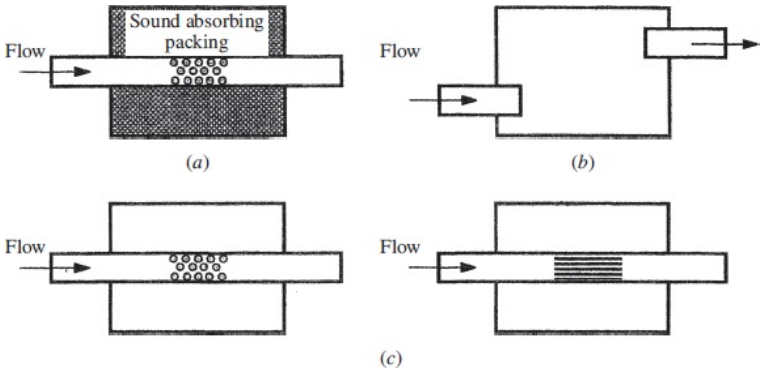
© McGraw-Hill Education. All rights reserved. Any use is subject to the Terms of Use, Privacy Notice and copyright information.

minimum impact on engine power levels, and its integration into the total exhaust system depend on the engine application (and space and weight constraints).

Mufflers take many forms, and more than one type may be used in a given exhaust system. Two basic principles are involved, absorption and reflection, and mufflers are divided into two types according to which principle is involved (although both absorption and reflection usually occur). Mufflers, together with the exhaust system, form an oscillator with natural resonance frequencies, so the location of the mufflers in the exhaust is critical. To avoid structure-borne noise (and provide thermal insulation) mufflers often have double walls and an insulating outer layer.[59]

Absorption mufflers (see Fig. 15.54) are constructed with one chamber filled with sound-deadening material through which the perforated exhaust pipe is passed. The absorbing material is usually long-fiber mineral wool with a bulk density of 120 to 150 g/liter. The level of muffling depends on the bulk density and sound-absorbing characteristics of the absorbing material, the muffler length, and material thickness. Damping takes place across a wide frequency band but only starts at higher frequencies (above about 1 kHz). Absorption mufflers are normally used as rear mufflers: they are the most frequently used design in large two-stroke diesels.[63]

Figure 15.54 (a) Absorption muffler element; (b) diffusing muffler element; (c) side-resonator muffler element.[57]



Reflection mufflers consist of chambers of varying dimensions connected together by pipes. The differences in cross sections of the pipes and the chambers, the dispersion of the exhaust gas flow, and the resonators formed by connecting pipes to chambers, all reduce the fraction of the incident pressure fluctuations transmitted. Diffusing mufflers or silencers (see Fig. 15.54*b*) absorb noise at frequencies other than those at which the expansion box will resonate. Side resonators (Fig.15.54*c*), where the flow connects with a separate closed chamber through holes or slits in the pipe wall, absorb noise at a specific frequency, such as the fundamental exhaust pulse frequency. The more chambers used, the more effective the muffler.[52]

Such reflection mufflers remove annoying components of the noise emitted by the exhaust through several different principles. The operation of the expansion box muffler in Fig. 15.54*b* can be explained as follows. The performance of an isolated muffler or silencer is often expressed as a *transmission loss*. Provided the relative amplitude of the pressure fluctuations is not too large, and the sound source is not affected by reflections from the muffler, the sound intensity at a given frequency is reduced by a fixed fraction. Thus, the intensity level is reduced by a fixed number of decibels. This reduction in decibels is the transmission loss. The transmission loss of a single pass through expansion box is a function only of the expansion area ratio $m = A_2/A_1$, and the ratio of the box length to the wavelength λ of the sound wave. The transmission loss T_{loss} is given by[57]

$$T_{\text{loss}} = 10 \log_{10} \left[1 + \frac{1}{4} \left(m - \frac{1}{m} \right)^2 \sin^2 \left(\frac{2\pi L}{\lambda} \right) \right] \text{dB}$$

(15.19)

© McGraw-Hill Education. All rights reserved. Any use is subject to the Terms of Use, Privacy Notice and copyright information.

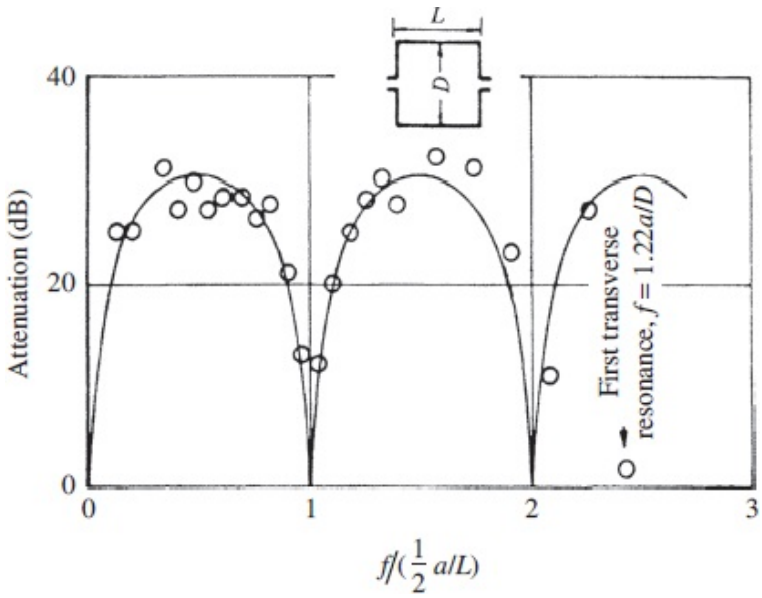
The box resonates whenever an integral number of half wavelengths just fits the length L [i.e., where $\lambda = 2L, L, 2L/3, L/2$, etc., at frequencies of $f = a(2L), a/L, 3a/(2L), 2a/L$, etc.]: the transmission loss then goes to zero. Between, it rises to a maximum value of

$$T_{\text{loss,max}} = 10 \log_{10} \left[\frac{1}{4} \left(m + \frac{1}{m} \right)^2 \right] \text{dB}$$

(15.20)

Experimental measurements show good agreement with theory until frequencies are reached where the box can resonate in a transverse or radial mode (see Fig. 15.55). For a box with circular cross-section, the first radial resonance occurs, as shown, at a frequency of $1.22a/D$.[57]

Figure 15.55 Transmission loss (attenuation) of an expansion box of circular cross-section showing pass bands at the first two longitudinal resonance frequencies, and the first transverse resonance.[57]



Pipes perforated with holes or slits connected to boxes, as used in side-resonator mufflers (see Fig. 15.54c), absorb strongly at the natural frequency of the box or side cavity. The transmission loss of a side-resonator element of volume V connected to a pipe of cross-sectional area A_p through an opening of conductivity K is given by

$$T_{\text{loss}} = 10 \log_{10} \left[1 + KV / \left\{ 2A_p \left(\frac{f}{f_n} - \frac{f_n}{f} \right) \right\}^2 \right] \text{dB}$$

(15.21)

The conductivity of the opening (which has the dimensions of length) is given approximately by

$$K = \pi r^2 / \left[l + (\pi/2) r \right]$$

(15.22)

© McGraw-Hill Education. All rights reserved. Any use is subject to the Terms of Use, Privacy Notice and copyright information.

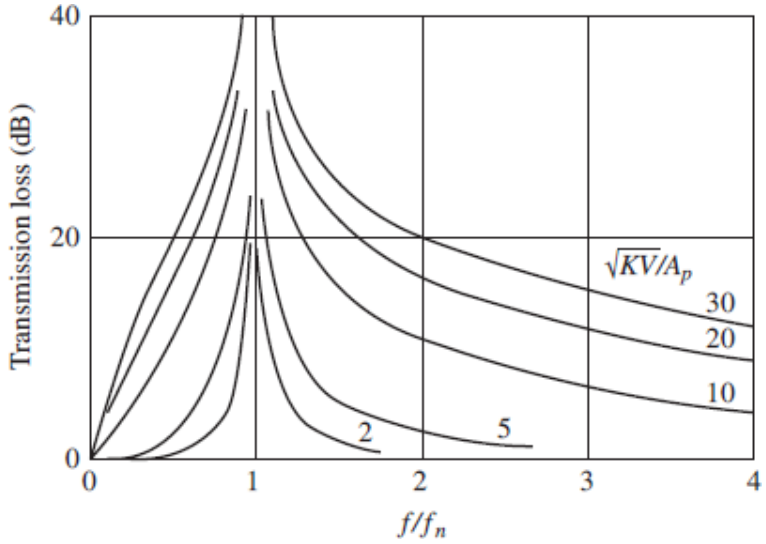
where r is the radius of the opening and l is the length of the pipe leading to the cavity (zero for a simple hole, when $K = 2r$). The resonant frequency f_n is

$$f_n = \frac{a}{2\pi}\sqrt{\frac{K}{V}}$$

(15.23)

The transmission loss is very high at and near the resonance frequency of the cavity. Away from this frequency, the loss depends on $\sqrt{KV}/A_p$, as shown in Fig.15.56. With high values of $\sqrt{KV}/A_p$, substantial transmission loss is achieved over a wide frequency range.[57]

Figure 15.56 Transmission loss of a simple side-resonator muffler element.[57]



Where there are several holes, the conductivity is the sum of the individual values. For a rectangular slit of length l and width b, in a sheet of thickness t, K is

$$K = bl/\left(t + 0.92k\sqrt{bl}\right)$$

(15.24)

where k decreases from 1.0 for $l = b$ to 0.6 at $l = 20b$. The attraction of side-cavity resonators is that the flow through the main pipe is virtually unimpeded.[57]

Practical mufflers are often combinations of more than one expansion box and/or side resonators so their operation is more complex than these simpler illustrations. The preceding transmission loss expressions are for a reflection-free muffler outlet. The open end of the tailpipe is not reflection free; an exiting pressure wave is reflected at an open-ended pipe as an equally strong rarefaction wave. Muffler location in the exhaust system is also important. The exhaust pipe upstream of the muffler can be thought of as an organ pipe with one end (the engine end) closed and one end open; the exhaust pipe downstream of the muffler has both ends open. Their resonant behavior will be different as a result. The design of exhaust systems, including their noise reducing features, is now done with unsteady one-dimensional gas-dynamic computer codes (see Sec. 14.3.4) as well as based on extensive empirical data.[52]

© McGraw-Hill Education. All rights reserved. Any use is subject to the Terms of Use, Privacy Notice and copyright information.

15.7.1.5. Intake Noise

Relative to exhaust noise, intake noise is surprisingly high, especially near wide-open throttle. Intake noise originates from the pulsating intake flow corresponding to individual cylinder filling events. Intake noise reduction is challenging because any flow restriction will reduce engine output. The basic induction pulse frequency is

$$f = n_c N\,(\mathrm{rev}/\mathrm{min})\,/60$$

(15.25)

where n_c is the number of cylinders. Intake noise reduction on small engines is usually accomplished with an expansion box silencer, which incorporates the air filter in its downstream end. The expansion box or cavity has a resonant frequency given by Eq. (15.23) where, because the entry duct is long in relation to its radius, the conductivity K is A_p/l [see Eq. (15.22)]. Intake flow losses limit the minimum value of A_p. The desired deep-toned sound requires the effective attenuation of the higher frequencies. This requires a low natural frequency for the resonator (where no attenuation will occur), requiring a high value for $V/K = lV$; it also requires a high value for $\sqrt{KV}/A_p$ [see Eq. (15.21)] or a large expansion-box cavity volume. In practice, the natural frequency is set at or below the frequency corresponding to the lowest engine speed at which high loads are produced, determined using Eq. (15.25); and using a box volume V between 10 and 20 $V_d\sqrt{n_c}$ where V_d is the displaced volume of each cylinder. The intake noise damping that such a system produces is zero at the resonant frequency of the cavity, and rises steadily to about 15 to 20 dB as frequency increases, before additional wave phenomena effectively limit further improvements.[59]

15.7.2. Reciprocating Mechanism Dynamics

Aspects of the motion of the internal combustion engine's reciprocating mechanism impact NVH and especially *vibration*. This linkage transmits the net pressure force acting on the piston, as it moves up and down the cylinder, through the oscillating motion of the connecting rod, to the rotating crankshaft (see Fig. 2.1). As explained in Sec. 2.3, the gas pressure forces (along with the other forces) acting on the piston generate a turning moment about the crankshaft axis (the torque), as indicated in Fig. 2.3. This time-varying torque (reduced by what is needed to overcome the engine's friction, Fig. 2.7), as a function of crank angle for an individual cylinder, is shown in Fig. 2.4. Thus each combustion event in each cylinder creates a torque pulse that is used to drive the engine's load.

Most engines are multi-cylinder engines for the reasons explained in Sec. 1.5. Then, the motions of the individual piston, connecting rod, and crank throw mechanism, with the appropriate crank angle phasing, are summed together. The major advantage, of course, is that more cylinders (and thus smaller displacement cylinders) results in more frequent and smaller torque pulses and thus smoother engine operation. An important downside is that the time-varying forces and the dynamics of the motions of the several piston/con rod combinations do not necessarily fully *balance*, resulting in oscillating net forces on engine components that can cause vibrations of the engine structure. In this section, we examine the dynamics of piston, connecting rod, and crankshaft behavior in multi-cylinder engines. In the following section (15.7.3), we apply the results of this analysis to the task of engine balancing.

At high engine speeds, the forces required to accelerate and decelerate the reciprocating mass (the piston assembly plus upper part of the connecting rod) become significant. These are termed *inertia forces* (mass × acceleration), and in multi-cylinder engines we want these forces to balance so that the net engine inertia force is zero. Unbalanced vertical or lateral inertia forces, if large enough, would cause the engine to vibrate, potentially exciting vibrations in the vehicle structure.

Following the analysis of Den Hartog,[64] the piston's displacement, given in exact form by Eq. (2.6), can be simplified for this

© McGraw-Hill Education. All rights reserved. Any use is subject to the Terms of Use, Privacy Notice and copyright information.

purpose by expanding the square-root term as a power series in 1/*R* (which is close to 0.3 for most engines), and retaining only the first term in that expansion. This yields the approximation for *c*, the piston clearance from its TC position,

$$\frac{c}{a} = \left(1 + \frac{1}{4R}\right) - \left(\cos\omega t + \frac{1}{4R}\cos 2\omega t\right)$$

(15.26)

where *R* = *l*/*a* (*l* is the con rod length, *a* the crank radius) and is between 3.0 and 3.5, ω is the crankshaft rotation rate in radians/s, and ωt equals the crank angle through which the crankshaft has turned at time *t*.

Differentiating once with respect to time gives the piston velocity (S_p); and differentiating twice, the acceleration (a_p), to obtain

$$S_p = a\omega\left(\sin\omega t + \frac{1}{2R}\sin 2\omega t\right)$$

(15.27)

$$a_p = a\omega^2\left(\cos\omega t + \frac{1}{R}\cos 2\omega t\right)$$

(15.28)

After multiplying by the piston mass, these expressions become the piston's vertical momentum and the inertia force, respectively. They consist of two terms, one varying with the same frequency as the crankshaft rotation and known as the *primary* or first-order term and the other varying at twice this frequency, known as the second-order term.[1] If the connecting rod is infinitely long, $R \to \infty$, and Eq. (15.28) indicates that the secondary term disappears and the piston executes harmonic motion. With normal connecting-rod lengths ($l \approx 3.5a$) the secondary term is significant.

The piston inertia force is given by the product $m_p a_p$. The piston mass is the mass of the piston, rings, piston pin, and upper portion of the connecting rod. Usually this con rod (reciprocating) mass is determined by replacing the actual connecting rod by two concentrated masses (one at each end of the rod at the bearing axes) so that the total rod mass remains unchanged, as does the location of its center of gravity.[2] The motion of the connecting rod is complex, with its top bearing axis moving up and down in a straight line and the bottom bearing axis moves in a circle. However, if the path of the center of gravity in this simple mass distribution model remains unchanged by this substitution, then the total inertia force on the rod is the same. In summary, the inertia force of the piston is

$$F_{p,i} = (m_p + m_{r,\mathrm{rec}})a_p$$

(15.29)

Typically, the reciprocating component of the connecting rod mass is close to one-third the total mass. Note, importantly, that the magnitude of the inertia force in Eq. (15.29), through the piston acceleration Eq. (15.28), increases as the square of engine speed. Thus, at 6000 rev/min it is 16 times its value at 1500 rev/min and is a dominant force. At low engine speeds, it is not nearly as important and is usually neglected.

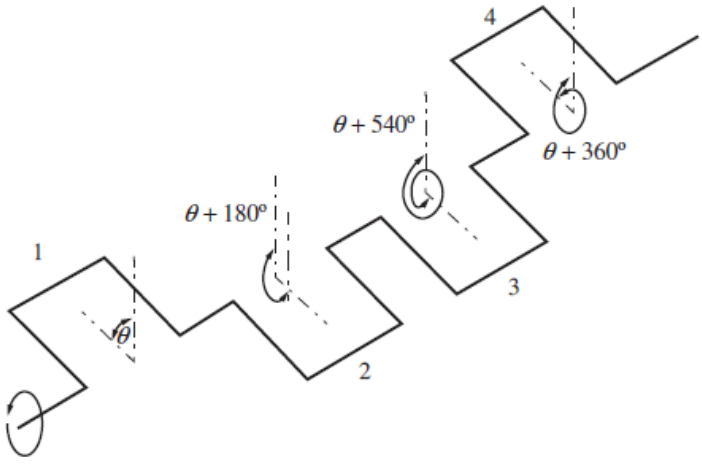
We illustrate the use of the above analysis by examining the primary and secondary components of the piston inertia force for an in-line four-cylinder engine. This multi-cylinder configuration is the easiest to understand because the reciprocating

© McGraw-Hill Education. All rights reserved. Any use is subject to the Terms of Use, Privacy Notice and copyright information.

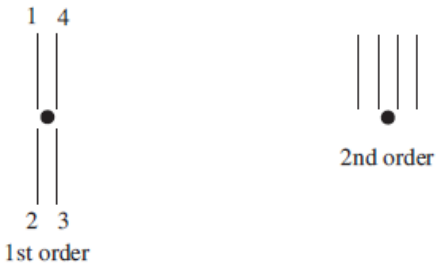
motions of each piston (in its own cylinder) are 180° apart.

Figure 15.57*a* shows, schematically, the positions of the four crank throws as the crankshaft rotates. If the crank angle position of the throw for cylinder number 1 is θ [which equals ωt in Eq. (15.28)], then for cylinders 2, 4, and 3, the throw angles at equivalent points in the operating cycle are (θ + 180), (θ + 360), (θ + 540) degrees, respectively, as shown.[3] Thus the cos(ωt) term in Eq. (15.28) for each of the pistons alternates in sign L: if θ is, say 45° CA, they are positive, negative, positive, negative. However, the cos(2ωt) term for each of the four pistons, with the angles now doubled, all have the same sign (again if θ is 45°, they are all positive). The combination of the individual piston first-order, and then second-order inertia forces for a given multi-cylinder engine geometry, when displayed in a star diagram, provides a useful visual representation of whether the engine is balanced or not. Figure 15.57*b* shows that the first-order (primary) inertia forces in the four-cylinder in-line engine balance. The second-order forces do not: with the same sign they all add to each other, as shown. This second-order inertia force is *out of balance*. To ensure smooth operation with four-cylinder in-line engines, balance shafts are frequently used to offset these (rotating) second-order out-of-balance inertia forces: see Sec. 15.7.3.

Figure 15.57 (a) Schematic showing phasing of crank throws and their individual cylinders and pistons in four-cylinder in-line engines. (b) Star diagram of first-order (primary) and second-order individual-piston reciprocating inertia forces. The first-order inertia forces balance; the second-order do not.



(*a*)



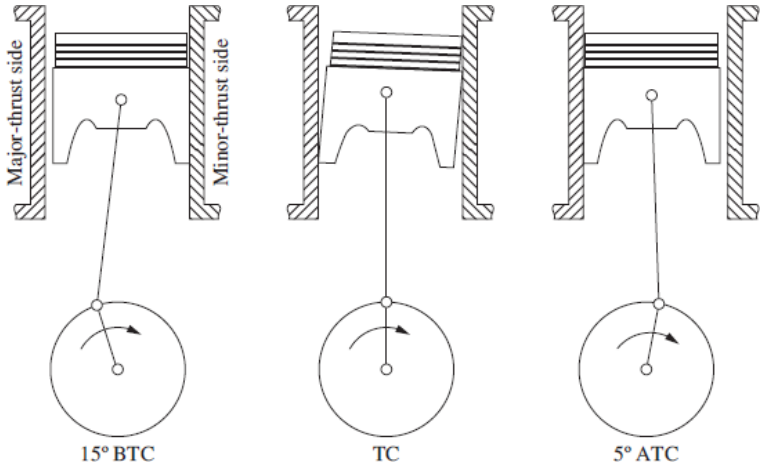
(*b*)

An additional dynamic feature of piston behavior that can generate noise and vibration is*piston slap*. As the piston moves through its top center position, due to the necessary clearance between the piston and liner the piston rotates slightly as it transitions from one side of the liner to the other, as shown in Fig. 15.58. During the compression stroke, the connecting rod reaction force pushes the piston to the right-hand side in Fig. 15.58 (the minor-thrust side); during the expansion power stroke, the connecting rod pushes the piston to the left, the major-thrust side. As this transition at TC occurs, the piston rotates as shown and then straightens up. The forces on the piston are high and increasing at this point in the cycle as

© McGraw-Hill Education. All rights reserved. Any use is subject to the Terms of Use, Privacy Notice and copyright information.

combustion proceeds. If the piston "slaps" the major-thrust side hard, liner vibration and noise can result. In Sec. 2.2 we explained that the piston pin axis is usually offset by 1.5% of the bore toward the major-thrust side of the liner to reduce this impact by initiating this piston transition from the minor-thrust side of the liner earlier when the forces on the piston are lower. As indicated in the figure, this transition then starts some 15 degrees before TC and ends at 5 degrees after TC.

Figure 15.58 Piston motion from one side of the liner to the other side, just before TC, during the early part of combustion. With piston-pin offset, transition occurs earlier than TC so piston slap is reduced.[65]



15.7.3. Engine Balancing

The time-varying forces involved in the reciprocating engine mechanism result from:

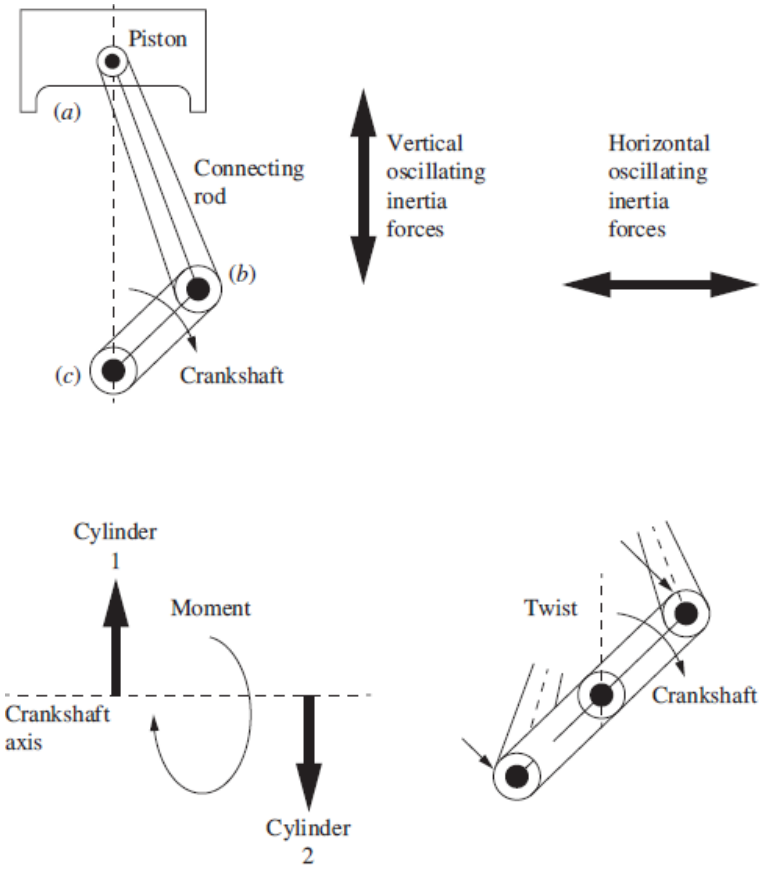
- Oscillating masses (pistons, top portion of the connecting rods)
- Rotating masses (crankshaft, connecting rod big ends)
- Periodic forces (cylinder pressure)

As discussed above, at higher engine speeds the forces associated with accelerating and decelerating these masses (called inertia forces—mass times acceleration) are significant. In multi-cylinder engines, we want to "balance" these inertia forces so that the net force on the crankshaft is zero. Unbalanced forces cause the engine to vibrate, exciting vibrations in the vehicle.

Figure 15.59 illustrates these phenomena: vertical (axial) and horizontal (transverse) oscillating inertia forces acting on each piston; moments (in multi-cylinder engines) tending to rock the crankshaft; twisting crankshaft moments due to unequal forces on the crank throws.

© McGraw-Hill Education. All rights reserved. Any use is subject to the Terms of Use, Privacy Notice and copyright information.

Figure 15.59 Schematics illustrating the oscillating inertia forces along (vertical) and transverse to (horizontal) the cylinder axis for each piston assembly. Also shown, are the moments tending to rock or twist the crankshaft which result from the different magnitude and the separation of the forces imposed by the motion of the pistons and connecting rods, in multi-cylinder engines.

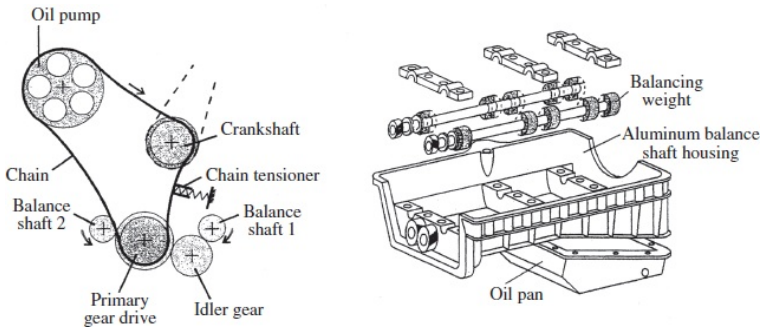


Rotating masses are the easiest to balance: counterweights are used to oppose the centrifugal force: for example, appropriate counterweights can readily offset the rotating inertia of the crank throws and connecting rod big end. Oscillating masses generate forces that vary responsively: to first order at the crankshaft angular speed, and at double that speed at the second order. Balancing can be achieved by using compensating unbalanced systems rotating at the appropriate speed and direction.

In the four-cylinder in-line engine discussed in the previous section, the first-order inertial forces balance. The out-of-balance second-order inertial forces can be offset using two identical auxiliary shafts rotating at double the rate of the crankshaft, in opposite directions. Balancing weights of appropriate mass are attached to these shafts as shown in Fig. 15.60. The two shafts are driven by the crankshaft at double the crankshaft rotation rate, with an idler gear to reverse the rotation direction of one of the shafts. The vertical inertia forces that these eccentric balance weights generate exactly offset the vertical components of the second-order inertia forces of the four pistons. The transverse component of the inertia force that each of the rotating balance weight shafts create cancel out since the shafts rotate in opposite directions. Thus the inertia forces in a four-cylinder in-line engine, *with* counter-rotating balance shafts become fully balanced.

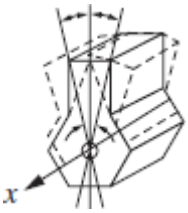
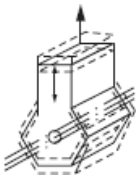
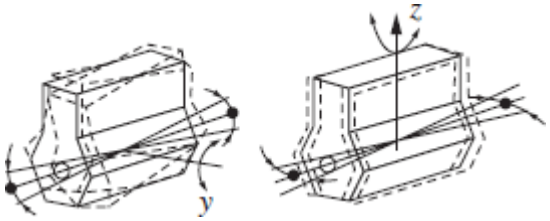
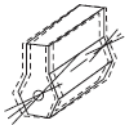
© McGraw-Hill Education. All rights reserved. Any use is subject to the Terms of Use, Privacy Notice and copyright information.

Figure 15.60 Example of balance shaft system for a four-cylinder in-line gasoline engine showing balancing weight and shaft positions, and gear drive mechanism.[66]



The inertial forces of a multi-cylinder engine result from the superposition of each individual piston-in-cylinder system, according to the crankshaft throw arrangement. Also, free moments are created as a result of the cylinder-to-cylinder spacing. Table 15.9 diagrams and summarizes the possible transverse and longitudinal titling moments, and axial free inertia forces and the vibration modes, that can result in multi-cylinder engines.

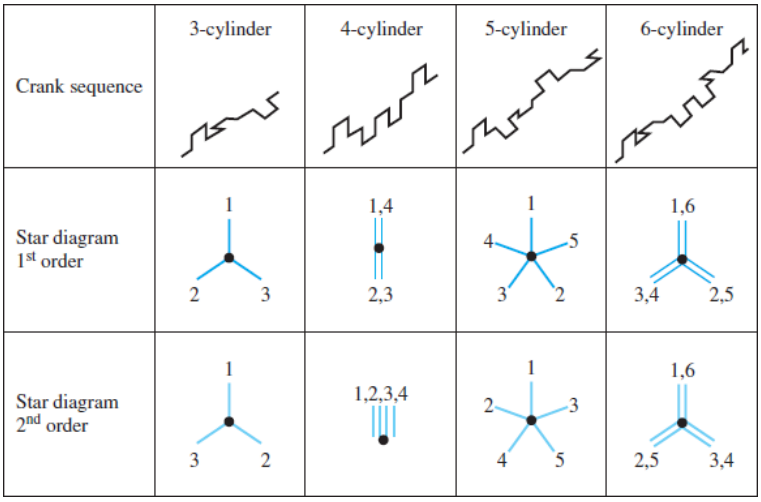
Table 15.9 Transverse and longitudinal titling moments, and axial free-inertia forces, and modes of vibrations, in multi-cylinder engines

Forces and moments at the engine				
Modes of vibration	Oscillating torque about cylinder axis: Engine transverse titling moment	Free reciprocating axial inertia force	Free inertial moment: Longitudinal tilting moment about the *y* (transverse) axis; pitching moment about the *z* (vertical) axis, also rolling moment	Internal flexing/ twisting moment
Developed from Bosch Automotive Handbook.[59]				

The mutual balancing of the inertial forces is one of the factors that determine the choice of an engine's number of cylinders and layout. The inertial forces are balanced if the common center of gravity for all moving crankshaft assembly components lies at the crankshaft's midpoint: that is, if the crankshaft is symmetrical when viewed from the front.[59] Figure 15.61 shows the crank arrangements and the star diagrams for the first- and second-order inertia forces for in-line engines, three through six-cylinders. All are balanced to first order (the diagrams are symmetric). All except the four-cylinder in-line engine (as discussed above) are balanced at second order.

© McGraw-Hill Education. All rights reserved. Any use is subject to the Terms of Use, Privacy Notice and copyright information.

Figure 15.61 Crank arrangements and star diagrams for first- and second-order components of the reciprocating inertia (free) forces, for three- through six-cylinder in-line engines.[59]



Thus, three-cylinder engine (inertia) forces are balanced to first and second order; first- and second-order moments are not. Four-cylinder in-line engines are first-order balanced, but unbalanced in their second-order free forces. Horizontally-opposed four-cylinder engines are balanced, except for second-order moments. Five cylinder engines are balanced in terms of free forces, but not in free moments. Six-cylinder in-line engines are fully balanced (and are often chosen for their smooth operation). V-6 engines (with 60° and 90° vee angles) are balanced in terms of inertia forces, but not free moments. Opposed six-cylinder engines (with 6 crank throws) are fully balanced. Eight-cylinder 90° V engines inertia forces are balanced to first and second order; free moments are not. Vee-12 engines are fully balanced. Additional details can be found in the Bosch Automotive Handbook.[59]

[1] Note that in the expansion of the square root term in Eq. (2.6), in a series in $1/R$, the third and higher order terms were omitted because they are small.

[2] This division of connecting rod mass into two distinct masses is an appropriate procedure for determining the inertia *forces*. However, it is not exact for determining the moments of these forces.

[3] Note that the firing order for a four-cylinder in-line engine is cylinder 1, 2, 4, 3 or 1, 3, 4, 2.

© McGraw-Hill Education. All rights reserved. Any use is subject to the Terms of Use, Privacy Notice and copyright information.

15.8. ENGINE PERFORMANCE AND FUELS SUMMARY

15.8.1.1. Engines

This chapter has described the major performance characteristics of the spark-ignition and the compression-ignition (diesel) engine, and has highlighted overall trends. Note that engine performance and efficiency are steadily improving over time, and emissions levels continue to be reduced. There are many different engine configurations and uses, and for each of these there are differences in design and operating characteristics. Nonetheless, our discussion of representative values of the various performance parameters for the more important types of internal combustion engines can be summarized as follows:

1. Within a given category of engines (e.g., naturally-aspirated four-stroke SI engines) the performance characteristics such as values of maximum bmep (at the maximum torque), specific power and $\overline{S}_p$ (at maximum rated power), and best bsfc (at lower engine speeds and close to wide-open throttle) are closely comparable.
2. Within an engine category where the range in engine size is substantial, there is an increase in maximum bmep and a decrease in minimum bsfc as size increases due to the decreasing relative importance of friction and heat loss per cycle.
3. The higher maximum bmep of gasoline-fueled SI engines compared to equivalent diesels results from the close-to-stoichiometric operation of the former at wide-open throttle.
4. The effect of supercharging or turbocharging, by boosting inlet air density by increasing intake air pressure, increases maximum bmep and specific power values substantially. Air compression *with after-cooling* gives further increases in bmep relative to turbocharging without after-cooling, at the same manifold air pressure level. The maximum bmep of turbocharged SI engines is limited by allowable maximum pressures, and the onset of knock. The maximum bmep of turbocharged compression-ignition engines is stress-limited. The larger CI engines are designed to accept higher maximum cylinder pressures, and hence can utilize higher boost levels.
5. Two-stroke cycle gasoline spark-ignition engines have significantly lower bmep and higher bsfc than equivalent four-stroke cycle SI engines.
6. The best efficiency values of modern automotive high-speed (turbocharged) DI diesel engines are about 15 to 20% higher than for naturally-aspirated gasoline engines. However, the diesel has a greater advantage at lower loads due to its low pumping work and much leaner air/fuel ratios. Brake fuel conversion efficiencies at about one-quarter maximum load, and lower engine speeds, are 30 to 40% higher.
7. The maximum bmep and best brake fuel conversion efficiency of DI diesel engines used over the size range, 80 cm to 1 m bore, steadily improve with increasing cylinder size. This is due to the reduced impacts of friction and heat loss per cycle, the latter enabling higher maximum cylinder pressure (thus achieving higher air boost levels): additionally, the output and efficiency of these larger engines can be usefully increased through turbo-compounding.

15.8.1.2. Fuels

This text has been largely focused on internal combustion engines operating with petroleum-based fuels, gasoline (or petrol) and diesel. These fuels currently dominate in engine use due to their being liquids with high inherent energy density, each extracted separately from multicomponent crude oil so their average characteristics can be controlled to match the fuel requirement of each type of engine (gasoline for SI, or diesel for CI). The current costs of these fuels (the combined extraction, processing, and delivery costs) make them in an overall sense the most attractive available options for engine users. However, they contain some 85% carbon (by mass) and are thus a major source of CO_2 (the key greenhouse gas emission).

© McGraw-Hill Education. All rights reserved. Any use is subject to the Terms of Use, Privacy Notice and copyright information.

Several alternatives are in limited use or being explored for use in transportation: natural gas (NG), liquid petroleum gas (LPG), ethanol, methanol, biodiesel; so is electricity. On a global scale, use of these alternatives is, as yet, modest.[4]

Since diesel fuel demand is growing faster than is gasoline demand worldwide, the use of petrol/gasoline in diesel-type engines, with a compression-ignition combustion process (achieved spontaneously, or with pilot diesel-fuel injection), is being explored as a way to better balance the demand for these two fuels. This represents one of the more promising opportunities for new Reaction-Controlled Compression-Ignition combustion modes (see Sec. 10.7.2).

Natural gas is used in spark-ignition engines, at moderate levels in a few countries where major tax incentives create an attractive market. It is obviously a gaseous and not a liquid fuel. Its combustion characteristics are not that different from gasoline. It is also used in large spark-ignition engines as an alternative to diesel. It has a higher knock resistance than gasoline but displaces significant air (some 10% in a stoichiometric mixture). On-board fuel storage in-vehicles is either as high-pressure gas, or liquefied in cryogenic tanks; both exact a significant cost, space and energy consumption penalty. Liquid petroleum gas, which is extracted along with natural gas, is used in limited amounts: at moderate pressures it can be stored as a liquid. The cost of gasoline/petrol SI engine conversions (or dual fuel systems with petrol) is high.

The alcohols, ethanol and methanol, have been introduced as supplements to gasoline. For example, ethanol is used in E10 (10%) blends with gasoline in the United States. It is largely produced from corn (in the U.S.) and sugar cane (Brazil). It has a significantly higher octane rating than gasolines (greater resistance to knock), and blending at these levels upgrades the base gasoline. Methanol offers similar benefits to those of ethanol, and is being used at modest levels in China. Both these alcohols have attractive characteristics, but also negatives: lower energy density relative to hydrocarbon fuels (ethanol some 70%, methanol about 50%); separation from gasoline-alcohol mixtures when water is present, toxicity. Currently, ethanol and methanol costs are higher than gasoline (per unit of energy). Future prospects and biomass supply constraints are uncertain. The full life-cycle greenhouse gas emissions impacts of ethanol and methanol are still being debated. Biodiesel (see Sec. 10.5.5) is also being used at the few percent level. Blended at this level with petroleum-based diesel fuel, its benefits and drawbacks are modest.

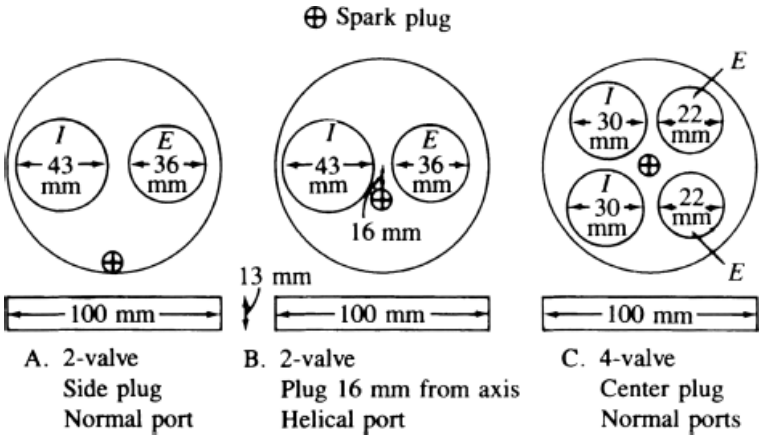
Use of electricity in plug-in-hybrid and battery electric propulsion systems is occurring. The potential for much larger-scale use of electricity is unclear: issues of relative costs, driving range (for EVs), supply-system recharging capabilities and recharging time, emissions from electricity generation, are as yet unresolved.

Overall, alternatives to petroleum-based gasoline and diesel face a challenging set of tasks. These mainstream fuels dominate a vast fuel production and supply system. If the alternative fuel is not readily compatible with this system, which long experience has honed to a high level of effectiveness and low cost, then establishing and growing a convenient-to-use and widely based alternative is a really challenging task.[4]

© McGraw-Hill Education. All rights reserved. Any use is subject to the Terms of Use, Privacy Notice and copyright information.

15.9. PROBLEMS

15.1. The schematics show three different four-stroke cycle spark-ignition engine combustion chambers. A and B are two-valve engines, C is a four-valve engine (two inlet valves which open simultaneously, two exhaust valves). Dimensions in millimeters are indicated. A and C have normal inlet ports and do not generate any swirl, B has a helical inlet port and generates substantial swirl. Spark plug locations are indicated. All three engines operate at the same speed (3000 rev/min), with the same inlet mixture composition, temperature, and pressure, and have the same displaced volume.



a. Rank the chambers 1, 2, 3 in the order of their volumetric efficiency (1 = highest η_v).

b. Rank the chambers in order (1, 2, 3) of their flame frontal area (1 = highest) when the mass fraction burned is about 0.2 and the piston is at TC.

c. Given this relative flame front area ranking, discuss whether the ranking by mass burning rate dm_b/dt will be different from the flame area ranking.

d. Briefly discuss the knock implications of these three chamber designs. Which is likely to have the worst knock problem?

15.2. Figures 15.5 and 15.6 show the variation in brake-specific fuel consumption (bsfc) for a port-fuel-injected automobile spark-ignition (SI) engine and a high-speed automobile DI diesel as a function of load and speed, respectively. From these graphs determine, and then plot, brake fuel conversion efficiency: (1) as a function of speed at *full load* and (2) as a function of load at a mid-speed of 2500 rev/min. Both engines are naturally aspirated. Assume the engine details are:

	Compression ratio	Equivalence ratio range	Displacement, dm^3
Diesel	22	0.3–0.75	2.5
SI engine	9	1.0–1.2	3.0

a. List the major engine design and operating variables that determine brake fuel conversion efficiency.

b. Explain briefly the reasons for the shapes of the curves you have plotted and the relative relationship of the diesel and SI engine curves.

c. At 2500 rev/min, estimate which engine will give the higher maximum brake power.

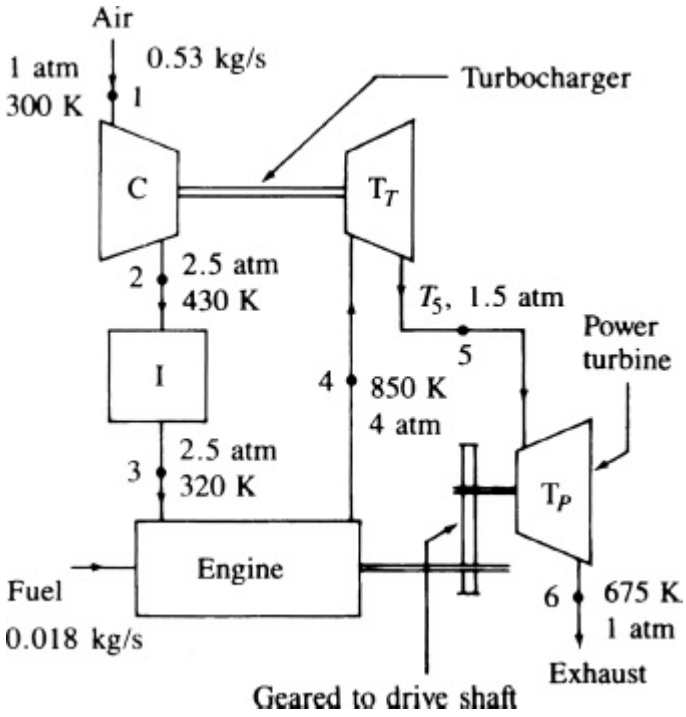
© McGraw-Hill Education. All rights reserved. Any use is subject to the Terms of Use, Privacy Notice and copyright information.

15.3. The diesel system shown in the figure consists of a multi-cylinder reciprocating DI diesel engine, a turbocharger (with a compressor C and turbine T_T mechanically connected to each other), an intercooler (I), and a power turbine (T_P) which is geared to the engine drive shaft. The gas and fuel flow paths and the gas states at the numbered points are shown. You can assume that the specific heat at constant pressure c_p of the gas throughout the entire system is 1.2 kJ/kg·K and $\gamma = c_p/c_v = 1.333$. The engine operates at 1900 rev/min. The fuel has a lower heating value of 42 MJ/kg of fuel.

a. What is the power (in kilowatts) which the turbocharger turbine (T_T) must produce? What is the gas temperature at the exit to the turbocharger turbine?

b. What is the power turbine power output?

c. The heat losses in the engine are 15% of the fuel's chemical energy $\left(\dot{m}_f Q_{\mathrm{LHV}}\right)$. Find the engine power output, the total system power output, and the total system brake fuel conversion efficiency (friction effects in the engine and power turbine are internal to these devices and do not need to be explicitly evaluated).



15.4. The graph shows how the brake power and specific fuel consumption of a four-stroke cycle single-cylinder spark-ignition engine vary with the fuel/air equivalence ratio at wide-open throttle. It also shows how the following efficiencies vary with equivalence ratio:

The volumetric efficiency: η_v

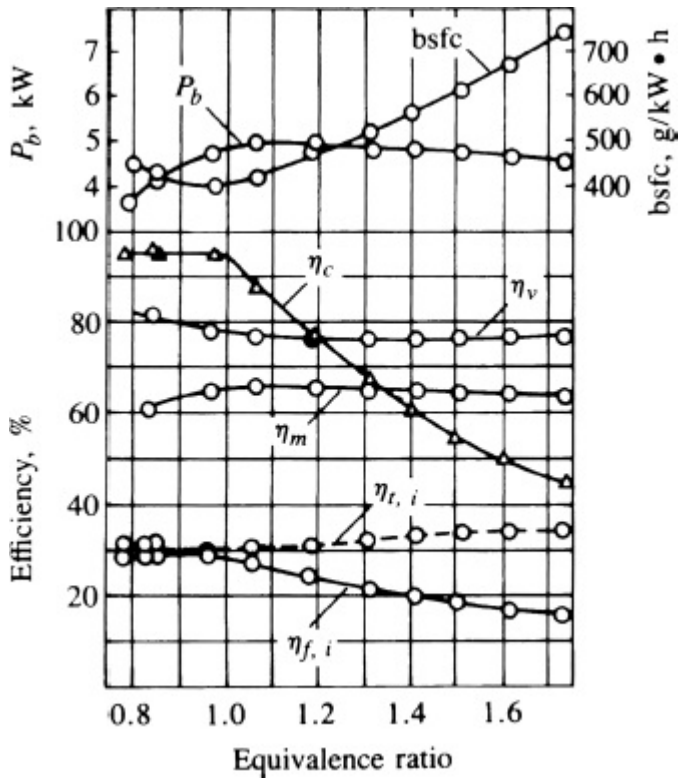
The mechanical efficiency: η_m

The combustion efficiency: η_c

The indicated fuel conversion efficiency: $\eta_{f,i}$

The indicated thermal conversion efficiency: $\eta_{t,i}$

© McGraw-Hill Education. All rights reserved. Any use is subject to the Terms of Use, Privacy Notice and copyright information.



a. Derive a relation between the variables $\eta_{f,i}$, η_c, and $\eta_{t,i}$.

b. Derive an equation which relates the brake power p_b to η_v, η_m, η_c, $\eta_{t,i}$ and any other engine and fuel parameters required.

c. Explain briefly why the variations of η_v, η_m, η_c, $\eta_{f,i}$, $\eta_{t,i}$ with equivalence ratio in the figure have the form shown (e.g., why the parameter is approximately constant, or has a maximum/minimum, or decreases/increases with increasing richness or leanness, etc.).

15.5. Automobile spark-ignition engines employ "fast-burn technology" to achieve an improvement in fuel consumption and reductions in hydrocarbon (HC) and oxides of nitrogen (NOJ emissions. This question asks you to explain the experimental data which shows that faster-burning combustion chambers do provide these benefits relative to more moderate burn-rate chambers.

a. Figure 9.36*b* shows the effect of increasing the percent of the exhaust gas recycled to the intake (for NO_x control) in a moderate burn-rate engine at constant speed and load, stoichiometric air/fuel ratio, with timing adjusted for MBT at each condition. COV_{imep} is the standard deviation in imep divided by the average imep, in percent. The different types of combustion are: *misfire*, *partial burn*, *slow burn*, *normal burn*, defined in Sec. 9.4.3. Frequency is percent of cycles in each of these categories. Use your knowledge of the spark-ignition engine flame-propagation process and HC emission mechanism to explain these trends in COV_{imep}, HC, and frequency as EGR is increased.

b. This fast-burn combustion chamber uses two spark plugs and generates swirl inside the chamber by placing a vane in the inlet port to direct the air to enter the chamber tangentially. The swirl angular velocity in the cylinder at the end of intake is six times the crankshaft angular velocity. There is no swirl in the moderate burn-rate chamber which has a single spark plug and a relatively quiescent in-cylinder flow. The table shows spark timing, average time of peak pressure, average flame-development angle (0 to 10% mass burned) and rapid burning period (10 to 90% mass burned) for these two engines. Figure 15.32 shows how the operating and emission characteristics of the fast burn and moderate burn-rate engines change as percent EGR is increased. Explain the reasons for the differences in these trends in COV_{imep}, bsfc (brake-specific fuel consumption), and HC, and similarity in NO_x. The operating conditions are held constant at the same values as before.

© McGraw-Hill Education. All rights reserved. Any use is subject to the Terms of Use, Privacy Notice and copyright information.

	Fast burn	Moderate burn	
Spark timing	18°	35°	BTC
Crank angle for average p_{max}	15°	16°	ATC
0–10% burned	24°	35°	
10–90% burned	20°	35°	

15.6. Two alternative fuels, methanol and hydrogen, are being studied as potential future spark-ignition engine fuels which might replace gasoline (modeled by isooctane C_8H_{18}). The table gives some of the relevant properties of these fuels.

a. For each fuel calculate the energy content per unit volume (in joules per cubic meter) of a stoichiometric mixture of fuel vapor and air at 1 atm and 350 K. The universal gas constant is 8314 J/kmol·K. What implications can you draw from these numbers regarding the maximum power output of an engine of fixed geometry operating with these fuels with stoichiometric mixtures?

b. The octane rating of each fuel, and hence the knock-limited compression ratio of an engine optimized for each fuel, is different. Estimate the ratio of the maximum indicated mean effective pressure for methanol- and hydrogen-fueled engines to that of the gasoline-fueled engine, allowing for energy density effects at intake (at 1 atm and 350 K), at the knock-limited compression ratio for each fuel, for stoichiometric mixtures. You can assume that the fuel-air cycle results (scaled by 0.85) for isooctane apply also for methanol and hydrogen cycles to a good approximation, when the energy density is the same.

c. The lean operating limit for the three fuels is different as indicated. Estimate the ratio of indicated fuel conversion efficiency for methanol and hydrogen at their lean limit and knock-limited compression ratio, relative to gasoline at its lean limit and knock-limited compression ratio, at the same inlet pressure (0.5 atm). Under these conditions, rank the fuel-engine combinations in order of decreasing power output.

	Gasoline (isooctane), C_8H_{18}	Methanol, CH_3OH	Hydrogen, H_2
Stoichiometric *F/A*	0.066	0.155	0.0292
Lower heating value, MJ/kg	44.4	20.0	120.1
Molecular weight of fuel	114	32	2
Molecular weight of stoichiometric mixture	30.3	29.4	21
Research octane number	95	106	~90
Knock-limited compression ratio	9	12	8
Equivalence ratio at lean misfire limit	0.9	0.8	0.6

15.7. A four-stroke cycle naturally-aspirated direct-injection diesel is being developed to provide 200 kW of power at the engine's maximum rated speed. Using information available in Chaps. 2, 5, and 15, on typical values of critical engine operating parameters at maximum power and speed for good engine designs, estimate the following:

a. The displaced volume, the compression ratio, the number of cylinders, the cylinder bore and stroke, and the maximum rated speed of an appropriate engine design that would provide this maximum power.

© McGraw-Hill Education. All rights reserved. Any use is subject to the Terms of Use, Privacy Notice and copyright information.

b. The brake-specific fuel consumption of this engine design at the maximum power operating point.

c. The approximate increase in brake power that would result if the engine was turbocharged to an air boost level of 3 bar.

15.8. Natural gas (which is close to 100% methane, CH_4) is being considered as a spark-ignition engine fuel. The properties of methane and gasoline (assume the same properties as isooctane) and the engine details for each fuel are summarized below (ϕ is the fuel/air equivalence ratio).

	Natural gas	Gasoline
Composition	CH_4	C_8H_{18}
Heating value, MJ/kg	50.0	44.3
Research octane number	120	94
Compression ratio	14	8
Displaced volume, dm^3	2	2
Lean misfire limit	$\phi = 0.5$	$\phi = 0.8$
Part-load equivalence ratio	$\phi = 0.6$	$\phi = 0.9$
Full-load equivalence ratio	$\phi = 1.1$	$\phi = 1.2$

As indicated in the table, the displaced volume of the engine is unchanged when the conversion for natural gas is made; however, the clearance height is reduced to increase the compression ratio.

a. Estimate the ratio of the volumetric efficiency of the engine operating on natural gas to the volumetric efficiency with gasoline, at wide-open throttle and 2000 rev/min, with both fuels in the gaseous state.

b. Estimate the ratio of the maximum indicated power of the engine operating with natural gas to the maximum power of the gasoline engine.

c. Estimate the ratio of the gross indicated fuel conversion efficiency of the natural gas engine to that of the gasoline engine, at the part-load conditions given.

d. Explain whether the NO, CO, and hydrocarbon specific emissions (grams of pollutant per hour, per unit indicated power) at part-load conditions of the natural gas engine will be higher, about the same, or lower than the NO, CO, and HC emissions from the gasoline engine. Explain briefly why.

You can assume that the fuel-air cycle results derived for isooctane-air mixtures are also appropriate for methane-air mixtures.

15.9. For four-stroke cycle direct-injection diesel engines:

a. Show from the definition of mean effective pressure that

$$\text{bmep} \propto \eta_m \eta_{f,i} \eta_v \rho_{a,i} (F/A)$$

where bmep = brake mean effective pressure

η_m = mechanical efficiency

© McGraw-Hill Education. All rights reserved. Any use is subject to the Terms of Use, Privacy Notice and copyright information.

$\eta_{f,i}$ = indicated fuel conversion efficiency

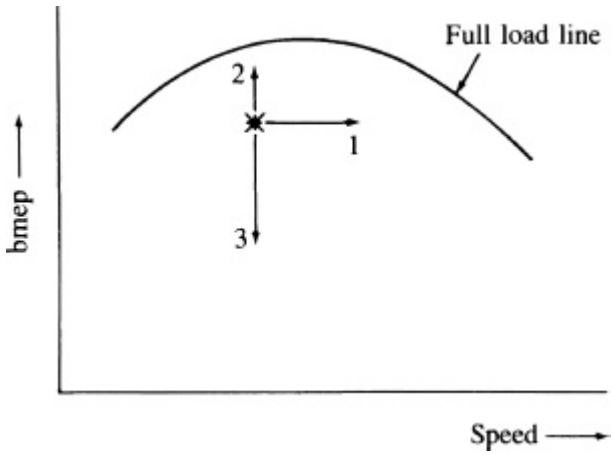
η_v = volumetric efficiency

$\rho_{a,i}$ = density of air in the intake manifold

F/A = fuel/air ratio

b. Sketch carefully proportioned qualitative graphs of η_m, $\eta_{f,i}$, η_v, $\rho_{a,i}$ and $(F/A)/(F/A)_{stoich}$ versus speed N at full load, and explain the reasons for the shapes of the curves. Then explain why the maximum bmep versus speed curve has the shape shown in the figure below.

c. The minimum brake-specific fuel consumption point is indicated by the asterisk (*) in the figure (see Fig. 15.34). Explain why brake-specific fuel consumption *increases* with (1) increasing speed, (2) increasing bmep, (3) decreasing bmep, from the best efficiency/bsfc point.



15.10. Figure 15.7 shows three performance maps for a 2-liter naturally-aspirated gasoline-fueled spark-ignition engine, with two valves per cylinder and standard fixed valve timing. Each performance map has bmep (w_e) as the vertical axis (1 kJ/liter = 1000 kPa), and engine speed as the horizontal axis. The upper curve is the wide-open-throttle bmep. Graph (*a*) shows lines of constant (gross) indicated fuel conversion efficiency. Graph (*b*) shows lines of constant mechanical efficiency. Graph (*c*) shows lines of constant brake fuel conversion efficiency.

i. Explain what processes and what variables affect (a) the gross indicated fuel conversation efficiency and gross imep; (b) the mechanical efficiency; and (c) the brake fuel conversion efficiency and bmep.

Note, as an example, that engine heat transfer is a process, and engine speed is a variable. Also, only list processes and variables where engine fundamentals show they have a significant direct role. For example, engine heat transfer affects indicated performance directly, and affects brake performance only indirectly through its impact on indicated performance. A complete and well-explained list will be required to get good marks.

ii. This is a standard production gasoline engine, as described above. Suggest specific improvements and changes in engine design and how the engine is operated, that you judge to be feasible, for a new production engine that will improve the maximum bmep, and the brake fuel conversion efficiency at 0.26 kJ/dm^3 (260 kPa) and 1500 rev/min, significantly. The engine will be naturally-aspirated. Provide approximate percentage improvements in each of the areas where you indicate improvements can be made, and combine these to indicate the percentage improvements in maximum bmep and part-load brake fuel conversion efficiency overall that you judge could be achieved. Explain your logic clearly.

15.11. You are in the Environmental Affairs Department of the City of Cambridge, MA, and your task is to compare the CO_2 emissions per mile of travel from a natural-gas-fueled spark-ignition engine bus and an equivalent diesel engine bus. Both buses must achieve low air pollutant emissions as well. Both engines are turbocharged and intercooled and have comparable outputs.

© McGraw-Hill Education. All rights reserved. Any use is subject to the Terms of Use, Privacy Notice and copyright information.

The diesel bus engine has a compression ratio of 16, operates on average with an overall fuel-air equivalence ratio of 0.4, and an intake manifold pressure of 1.5 bar (150 kPa). The exhaust pressure is essentially the same as the intake pressure, 1.5 bar. The engine's mechanical efficiency at these conditions is 0.7. A particulate trap and selective catalytic reduction NO_x catalyst with urea as a reducing agent reduce air pollutant emissions to acceptable levels. These exhaust emission treatment systems increase the average engine bsfc by 6%. The diesel fuel is a low sulfur fuel with a formula $(CH_{1.8})_n$.

The natural-gas-fueled engine has a compression ratio of 12. The natural gas is injected into the engine's intake so natural gas displaces air (see Fig. 6.5). The engine operates stoichiometric, and at the average driving conditions the intake pressure is 0.8 bar (80 kPa) and exhaust pressure is 1.05 bar (105 kPa). The mechanical and accessory friction mean effective pressure is the same as in the diesel engine. This engine uses a three-way catalyst to reduce emissions with no fuel consumption penalty. Natural gas is 90% CH_4 and 10% C_2H_6 in molar proportions, so its H:C ratio is less than methane's value of 4.

The lower heating value for diesel fuel is 43.2 MJ/kg fuel, and for natural gas is 45 MJ/kg fuel.

a. Estimate the bsfc of these two engines at their stated operating conditions.

b. Determine the ratio of CO_2 emissions from the natural gas engine to CO_2 emissions from the diesel, each at its average operating conditions (which give closely comparable engine and hence vehicle performance). Useful units would be brake-specific emissions, g CO_2/MJ or g CO_2/kW·h.

15.12. One promising approach to improving the part-load efficiency of a spark-ignition engine is to deactivate half of the cylinders. For example, an eight-cylinder engine at part load operates with the intake and exhaust valves on four of the cylinders closed through the complete four-stroke cycle, while the other four cylinders operate with normal valve timing. The throttle must be more open in this cylinder-deactivated mode to produce the same torque that the eight cylinders operating normally at light load would produce.

a. Using the fuel-air constant-volume-combustion cycle as your model, draw three side-by-side carefully proportioned (qualitative) cylinder-pressure *p* versus cylinder volume *V* diagrams for one cylinder of: (i) the eight-cylinder engine operating normally with an intake pressure of 45 kPa (0.45 bar); (ii) the four firing cylinders in the deactivated engine operating mode; (iii) the four deactivated cylinders. Identify the maximum and minimum volumes on the *V* axis, the exhaust and intake pressures relative to atmospheric pressure, and the relative (qualitative) magnitudes of the end of compression pressure and maximum pressure in each of the three diagrams. Note that the intake and exhaust valves are deactivated immediately following the intake stroke. Briefly explain your diagrams.

b. A 4-liter displacement, V-8 engine, must generate a brake torque of 80 N·m at this light-load condition. The mechanical rubbing plus accessory friction means effective pressure is 120 kPa and is the same for all cylinders (both those operating normally and those that are deactivated). Determine the imep in each cylinder when all 8-cylinders are operating, and the imep and intake manifold pressure of the four firing cylinders in the deactivated mode. The engine operates at stoichiometric and the compression ratio is 10.

c. The intent of cylinder deactivation is to increase the brake fuel conversion efficiency at part-load conditions like those in (*a*) and (*b*) above. Calculate the ratio of the brake fuel conversion efficiency of the engine in (*b*) in its cylinder deactivated mode to the brake fuel conversion efficiency in its normal all-eight-cylinders firing mode.

Note: Standard definitions of mean effective pressures assume all cylinders are firing. Fuel-air cycle results when multiplied by 0.85 also apply to normally firing real engine cylinders. When half the cylinders are firing and half are deactivated, appropriate adjustments must be made in how these standard definitions and results are used.

15.13. For a 1.6-liter four-cylinder engine, with compression ratio of 9.1, we would like to get a sense of the forces the piston experiences. Assume that bore is equal to the stroke, the connecting rod length is 132 mm, the ratio of connecting rod length to crank radius is 3.5, and the effective piston reciprocating mass is 0.57 kg (this includes the piston mass and

© McGraw-Hill Education. All rights reserved. Any use is subject to the Terms of Use, Privacy Notice and copyright information.

a portion of the connecting rod mass). The crankcase pressure is 100 kPa. A typical fired pressure trace at high load is shown below.

Hint: A good approximation to the piston acceleration is

$$\ddot{s} = 2\pi^2 N^2 L \cdot \left(\cos\theta + \frac{1}{R}\cos 2\theta\right).$$

In this equation N = engine speed, L = stroke, θ = crank angle, measured from top center, R = ratio of connecting rod length to crank radius.

a. Draw a free-body diagram of the piston. (A free-body diagram shows a body "free" from its surroundings with all of the forces and moments that act on it.)

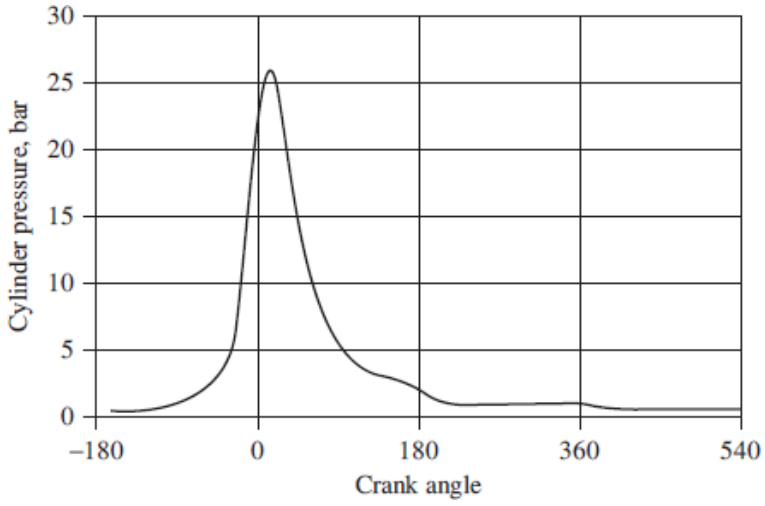
b. For engine speeds of 1000 rev/min and 6000 rev/min, estimate the maximum inertial force (mass × acceleration) and pressure force on the piston.

   We also want to examine the effect of the number of engine cylinders on the output of the engine. Instead of four cylinders with a total displaced volume of 1.6 liters, consider a single larger cylinder with the same displaced volume.

c. Determine the ratio of maximum power outputs produced by these engines.

d. Determine the ratio of maximum torques produced by these engines.

e. Briefly describe the other factors that make the four-cylinder design much more attractive than the single-cylinder design.



© McGraw-Hill Education. All rights reserved. Any use is subject to the Terms of Use, Privacy Notice and copyright information.

15.10. REFERENCES

1. Yasuda, M., and Maruyama, H.: "A New 1.6-liter Twin-Cam 16-Valve Nissan Engine," SAE paper 910677, 1991.
2. Chon, D. M., and Heywood, J. B.: "Performance Scaling of Spark-Ignition Engines: Correlation and Historical Analysis of Production Engine Data," SAE paper 2000-01-0565, in *Modeling for SI Engine*, SP-1511, SAE, 2000.
3. Heywood, J. B., and Welling, O. Z.: "Trends in Performance Characteristics of Modern Automobile SI and Diesel Engines," SAE paper 2009-01-1892, *SAE Int. J. Engines*, vol. 2, no. 1, pp. 1650–1662, 2009.
4. Heywood, J. B., MacKenzie, D., et al.: *On the Road Toward 2050: Potential for Substantial Reductions in Light-Duty Vehicle Energy Use and Greenhouse Gas Emissions*, MIT Energy Initiative Report, November 2015.
5. Fulton, B., and Belaire, R.: personal communication, 2005.
6. Pirelli, M., DiCaprio, F., and Torella, E.: "Fun to Drive and Fuel Economy: The New 1.4 16v Turbo Gasoline Engine from FIAT," SAE paper 2007-24-0062, 2007.
7. Armstrong, D. L., and Stirrat, G. F.: "Ford's 1982 3.8L V6 Engine," SAE paper 820112,1982.
8. Okino, M., Okada, K., and Abe, M.: "Isuzu New 8.4L Diesel Engine," SAE paper 850258, 1985.
9. Noguchi, T., Kuramoto, A., Kono, T., and Kawakita, T.: "New Light Weight 3-liter V6 Toyota Engine with High Output Torque, Good Fuel Economy and Low Exhaust Emission Levels," SAE paper 950805, 1995.
10. Stock, D., and Bauder, R.: "The New Audi 5-Cylinder Turbo Diesel Engine," SAE paper 900648, 1990.
11. Gruden, D., Küper, P. F., and Porsche, F.: "Heat Balance of Modern Passenger Car SI Engine," in *Heat and Mass Transfer in Gasoline and Diesel Engines*, D. B. Spalding and N. H. Afgan (eds), Hemisphere Publishing Corporation (member of the Taylor & Francis Group), 1989.
12. *General Motors Automotive Engine Test Code For Four Cycle Spark Ignition Engines*, 6th ed., General Motors Corp., Detroit, 1975.
13. Heywood, J. B., Higgins, J. M., Watts, P. A., and Tabaczynski, R. J.: "Development and Use of a Cycle Simulation to Predict SI Engine Efficiency and NO_x Emissions," SAE paper 790291, 1979.
14. Jo, Y. S.: "More Effective Use of Octane in a Turbocharged Gasoline Engine: Combustion, Knock, Octane, Efficiency, and Fuel Economy," Ph.D. Thesis, Mechanical Engineering Department, MIT, Cambridge, MA, January 2016.
15. Robison, J. A., and Brehob, W. M.: "The Influence of Improved Mixture Quality on Engine Exhaust Emissions and Performance," *J. Air Pollution Control Ass.*, vol. 17, no. 7, pp. 446–453, July 1967.
16. Harada, J., Tomita, T., Mizuno, H., Mashiki, Z., and Ito, Y.: "Development of Direct Injection Gasoline Engine," SAE paper 970540, 1997.
17. Bandel, W., Fraidl, G. K., Mikulic, L. A., Quissek, F., and Carstensen, H.: "Investigation of Mixture Preparation and Charge Motion Effects on the Combustion of Fast-Burn Gasoline Engines," SAE paper 890160, 1989.
18. Regueiro, A.: "DaimlerChrysler's New 1.6L Multi-Valve 4-Cylinder Engine Series," SAE paper 2001-01-0330, 2001.
19. Lavoie, G. A., and Blumberg, P. N.: "A Fundamental Model for Predicting Fuel Consumption, NO_x and HC Emissions of a Conventional Spark-Ignited Engine," *Combust. Sci. Technol.*, vol. 21, pp. 225–258, 1980.
20. Caton, J. A., Heywood, J. B., and Mendillo, J. V.: "Hydrocarbon Oxidation in a Spark-Ignition Engine Exhaust Port," *Combust. Sci. Technol.*, vol. 37, nos. 3 and 4, pp. 153–169, 1984.

© McGraw-Hill Education. All rights reserved. Any use is subject to the Terms of Use, Privacy Notice and copyright information.

21. Caton, J. A., and Heywood, J. B.: "Models for Heat Transfer, Mixing and Hydrocarbon Oxidation in an Exhaust Port of a Spark-Ignited Engine," SAE paper 800290, 1980.
22. Kleeberg, H., Tomazic, D., Lang, O., and Habermann, K.: "Future Potential and Development Methods for High Output Turbocharged Direct Injected Gasoline Engines," SAE paper 2006-01-0046, 2006.
23. Jo, Y. S., Lewis, R., Bromberg, L., and Heywood, J. B.: "Performance Maps of Turbocharged SI Engines with Gasoline-Ethanol Blends: Torque, Efficiency, Compression Ratio, Knock Limits, and Octane," SAE paper 2014-01-1206, 2014.
24. Woldring, D., Landenfeld, T., and Christie, M.: "DI Boost: Application of High Performance Gasoline Direct Injection Concept," SAE paper 2007-01-1410, 2007.
25. Smith, P., Heywood, J. B., and Cheng, W. K.: "Effects of Compression Ratio on Spark-Ignition Engine Efficiency," SAE paper 2014-01-2599, 2014.
26. Caris, D. F., and Nelson, E. E.: "A New Look at High Compression Engines,"*SAE Trans.*, vol. 67, pp. 112–124, 1959.
27. Muranaka, S., Takagi, Y., and Ishida, T.: "Factors Limiting the Improvement in Thermal Efficiency of S.I. Engine at Higher Compression Ratio," SAE paper 870548, 1987.
28. Thring, R. H., and Overington, M. T.: "Gasoline Engine Combustion—The High Ratio Compact Chamber," SAE paper 820166, *SAE Trans.*, vol. 91, 1982.
29. Leone, T. G., et al.: "The Effect of Compression Ratio, Fuel Octane Rating, and Ethanol Content on Spark-Ignition Engine Efficiency," *Env. Sci. & Technol.*, vol. 49, no. 18, pp. 10778–10789, 2015.
30. Gerty, M. D., and Heywood, J.B.: "An Investigation of Gasoline Engine Knock-Limited Performance and the Effects of Hydrogen Enhancement," SAE paper 2006-01-0228, in *SI Combustion and Direct Injection SI Engine Technology*, SP-2016, SAE, 2006.
31. Barnes-Moss, H. W.: "A Designers Viewpoint," paper C343/73, in *Proceedings of Conference on Passenger Car Engines*, pp. 133–147, Institution of Mechanical Engineers, Conference Publication 19, London, 1973.
32. Thring, R. H.: "The Effects of Varying Combustion Rate in Spark Ignited Engines," SAE paper 790387, 1979.
33. Harada, M., Kadota, T., and Sugiyama, Y.: "Nissan NAPS-Z Engine Realizes Better Fuel Economy and Low NO_x Emission," SAE paper 810010, 1981.
34. Poulos, S. G., and Heywood, J. B.: "The Effect of Chamber Geometry on Spark-Ignition Engine Combustion," SAE paper 830334, *SAE Trans.*, vol. 92, 1983.
35. Heywood, J. B.: "Combustion Chamber Design for Optimum Spark-Ignition Engine Performance,"*Int. J. Vehicle Des.*, vol. 5, no. 3, pp. 336–357, 1984.
36. Endres, H., Neuber, H., and Wurms, R., "Influence of Swirl and Tumble on Economy and Emissions of Multi Valve SI Engines," SAE paper 920516, 1992.
37. Novak, J. M., and Blumberg, P. N.: "Parametric Simulation of Significant Design and Operating Alternatives Affecting the Fuel Economy and Emissions of Spark-Ignited Engines," SAE paper 780943, *SAE Trans.*, vol. 87, 1978.
38. Amann, C. A.: "Control of the Homogeneous-Charge Passenger-Car Engine: Defining the Problem," SAE paper 801440, 1980.
39. Kasseris, E., and Heywood, J. B.: "Charge Cooling Effects on Knock Limits in SI DI Engines Using Gasoline/Ethanol Blends: Part 1—Quantifying Charge Cooling," SAE paper 2012-01-1275, 2012.
40. Hiereth, H., and Withalm, G.: "Some Special Features of the Turbocharged Gasoline Engine," SAE paper 790207, 1979.

© McGraw-Hill Education. All rights reserved. Any use is subject to the Terms of Use, Privacy Notice and copyright information.

41. Jo, Y. S., Blomberg, L., and Heywood, J. B.: "Octane Requirement of a Turbocharged Spark Ignition Engine in Various Driving Cycles," SAE paper 2016-01-0831, 2016.
42. Schwarz, C., Schüremannm, E., Durst, B., Fischer, J., and Witt, A.: "Potentials of the Spray-Guided BMW DI Combustion System," SAE paper 2006-01-1265, 2006.
43. Mano, T., Kawasaki, T., and Miyakawa, K.: "Development of Low Fuel Consumption, High Durability, and Low Emissions J-Series Engines," SAE paper 1999-01-0830, 1999.
44. Pischinger, R., and Cartellieri, W.: "Combustion System Parameters and Their Effect upon Diesel Engine Exhaust Emissions," SAE paper 720756, *SAE Trans.*, vol. 81, 1972.
45. Schittler, M.: "MWM TBD 234 Compact High-Output Engines for Installation in Heavy Equipment and Military Vehicles," SAE paper 850257, 1985.
46. Robinson, R. H., and Schnapp, J. P.: "Cummins NTC-475 Series Turbocharged Engine," SAE paper 820982, 1982.
47. Lustgarten, G. A.: "The Latest Sulzer Marine Diesel Engine Technology," SAE paper 851219, 1985.
48. Stanton, D. W.: "Systematic Development of Highly Efficient and Clean Engines to Meet Future Commercial Vehicle Greenhouse Gas Regulations," SAE paper 2013-01-2421, Buckendale Lecture, *SAE Int. J. Engines*, vol. 6, issue 3, 2013.
49. Arcoumanis, C., Bicen, A. F., and Whitelaw, J. H.: "Squish and Swirl-Squish Interaction in Motored Model Engines,"*ASME Trans., J. Fluids Engng*, vol. 105, pp. 105–112, 1983.
50. Tsuchiya, K., and Hirano, S.: "Characteristics of 2-Stroke Motorcycle Exhaust HC Emission and Effects of Air-Fuel Ratio and Ignition Timing," SAE paper 750908, 1975.
51. Uchiyama, H., Chiku, T., and Sayo, S.: "Emission Control of Two-Stroke Automobile Engine," SAE paper 770766,*SAE Trans.*, vol. 86, 1977.
52. Heywood, J. B., and Sher, E.: *The Two-Stroke Cycle Engine: Its Development, Operation, and Design*, Taylor and Francis, Philadelphia, and SAE, Warrendale, PA, 1999.
53. Barton, P. J., and Fearn, J.: "Study of Two and Four Stroke Outboard Marine Engine Exhaust Emissions Using a Total Dilution Sampling System," SAE paper 972740, 1997.
54. Onishi, S., Jo, H. S., Shoda, K., Jo, P. D., and Kato, S.: "Active Thermo-Atmospheric Combustion (ATAC)—A New Combustion Process for Internal Combustion Engines," SAE paper 790501, *SAE Trans.*, vol. 88, 1979.
55. Maeda, K., Yasunari, M., Hikasa, S., and Mirishita, S.: "Characteristics and Reduction Methods of NO_x Emission from Two-Stroke Marine Diesel Engine," *Bull. M.E.S.J.*, vol. 22, no. 1, pp. 1–7, 1994.
56. Abthoff, J., Duvinage, F., Hardt, T., Kramer, M., and Paule, M.: "The Two-Stroke DI Diesel Engine with Common Rail Injection for Passenger Car Application," SAE paper 981032, 1998.
57. Annand, W. J. D., and Roe, G. E.: *Gas Flow in the Internal Combustion Engine*, G.T. Foulis, Yeovil, U.K., 1994.
58. Blair, G. P.: *Design and Simulation of Two-Stroke Engines*, SAE, Warrendale, PA, 1996.
59. Bosch, R., *Automotive Handbook*, 8th edition, Robert Bosch GmbH and SAE, 2011.
60. Nomura, K., and Nakamura, N.: "Development of a New Two-Stroke Engine with Poppet Valves: Toyota S-2 Engine," in*A New Generation of Two-Stroke Engines for the Future?* P. Duret (ed.), Proceedings of the International Seminar, Nov. 29–30, Rueil-Malmaison, France, Editions Technip, Paris, 1993.
61. Okuzumi, T., et al.: "Development of New High-Performance Nissan V8 Engine," SAE paper 2001-01-0329, 2001.
62. Fujino, Y., Itabashi, K, Kamikubo, H., and Takami, K.: "New Mitsubishi V8 19-liter Turbocharged and Intercooled Diesel Engine," SAE paper 971673, 1997.

© McGraw-Hill Education. All rights reserved. Any use is subject to the Terms of Use, Privacy Notice and copyright information.

63. MAN B&W, *Engines and the Environment-Noise*, MAN B&W Diesel A/S, Copenhagen, Denmark, 1989.

64. Den Hartog, J. P.: *Mechanical Vibrations*, McGraw-Hill, New York, 1947.

65. Amann, A. C.: "Engineering the Spark-Ignition Engine—The Piston-Rings-Cylinder Wall Interface," SAE paper 885056, 1988.

66. Huegen, S., Warren, G., Menne, R., Wolschendorf, J., Schwaderlapp, M., and Schoenherr, C.: "A New 2.3L DOHC Engine with Balance Shaft Housing—Steps of Refinement and Optimization," SAE paper 970921, 1997.

© McGraw-Hill Education. All rights reserved. Any use is subject to the Terms of Use, Privacy Notice and copyright information.

A. Unit Conversion Factors

A.0. APPENDIX PRELIMINARIES

This table provides conversion factors for common units of measure for physical quantities to the International System (SI) units. The conversion factors are presented in two ways: columns 2 and 3 give the conversion to the base or derived SI unit with the conversion factor as a number between one and ten with six or fewer decimal places, followed by the power of ten that the number must be multiplied by to obtain the correct value; columns 4 and 5 provide conversion to a recommended multiple or submultiple of the SI unit with the conversion factor given as a four-digit number between 0.1 and 1000.

1 To convert from	2 To	3 Multiply by	4 To	5 Multiply by
Area				
foot^2	m^2	$9.290\,304 \times 10^{-2}$	cm^2	929.0
inch^2	m^2	$6.451\,600 \times 10^{-4}$	cm^2	6.452
Energy, heat, and work				
Btu (International Table)	J	$1.055\,056 \times 10^{3}$	kJ	1.055
calorie (thermochemical)	J	$4.184\,000 \times 10^{0}$	J	4.184
erg	J	$1.000\,000 \times 10^{-7}$	μJ	0.1000
foot pound-force (ft · lbf)	J	$1.355\,818 \times 10^{0}$	J	1.356
horsepower-hour (hp · h)	J	$2.684\,520 \times 10^{6}$	MJ	2.685
kilowatt-hour (kW · h)	J	$3.600\,000 \times 10^{6}$	MJ	3.600
meter kilogram-force (m · kgf)	J	$9.806\,650 \times 10^{0}$	J	9.807
Energy (specific, specific heat)				
Btu (IT)/lb	J/kg	$2.326\,000 \times 10^{3}$	kJ/kg	2.326
Btu (IT)/lb · °F	J/kg · K	$4.186\,800 \times 10^{3}$	kJ/kg · K	4.187
calorie (thermo.)/g	J/kg	$4.184\,000 \times 10^{3}$	kJ/kg	4.184
calorie (thermo.)/g · °C	J/kg · K	$4.184\,000 \times 10^{3}$	kJ/kg · K	4.184
Force				
dyne	N	$1.000\,000 \times 10^{-5}$	μN	10.00

© McGraw-Hill Education. All rights reserved. Any use is subject to the Terms of Use, Privacy Notice and copyright information.

1 To convert from	2 To	3 Multiply by	4 To	5 Multiply by
kilogram-force	N	$9.806\,650 \times 10^{0}$	N	9.807
pound-force	N	$4.448\,222 \times 10^{0}$	N	4.448
Force per unit length (includes surface tension)				
dyne/centimeter	N/m	$1.000\,000 \times 10^{-3}$	mN/m	1.000
pound-force/inch	N/m	$1.751\,268 \times 10^{2}$	N/m	175.1
pound-force/foot	N/m	$1.459\,390 \times 10^{1}$	N/m	14.59
Fuel consumption (economy)				
pound/horsepower-hour	kg/J	$1.689\,660 \times 10^{-7}$	g/kW · h	608.3
gram/kilowatt-hour	kg/J	$2.777\,778 \times 10^{-10}$	μg/J	0.2778
mile/gallon (U.S.)	m/m^3	$4.251\,437 \times 10^{5}$	km/dm^3	0.4251
mile/gallon (Imp.)	m/m^3	$3.540\,060 \times 10^{5}$	km/dm^3	0.3540
Heat flux (includes thermal conductivity)				
Btu (IT) · in/h · ft^2 · °F	W/m · K	$1.442\,279 \times 10^{-1}$	W/m · K	0.1442
Btu (IT)/ft^2	J/m^2	$1.135\,653 \times 10^{4}$	kJ/m^2	11.36
Btu (IT)/h · ft^2 · °F	$W/m^2 \cdot K$	$5.678\,263 \times 10^{0}$	$W/m^2 \cdot K$	5.678
calorie (thermo.)/cm^2	J/m^2	$4.184\,000 \times 10^{4}$	kJ/m^2	41.84
Length				
foot	m	$3.048\,000 \times 10^{-1}$	m	0.3048
inch	m	$2.540\,000 \times 10^{-2}$	mm	25.40
micron	m	$1.000\,000 \times 10^{-6}$	μm	1.000
mile	m	$1.609\,344 \times 10^{3}$	km	1.609
Mass				
ounce	kg	$2.834\,952 \times 10^{-2}$	g	28.35
pound	kg	$4.535\,924 \times 10^{-1}$	kg	0.4536
ton (long or Imp., 2240 lb)	kg	$1.016\,047 \times 10^{3}$	Mg	1.016
ton (short, 2000 lb)	kg	$9.071\,847 \times 10^{2}$	Mg	0.9072

© McGraw-Hill Education. All rights reserved. Any use is subject to the Terms of Use, Privacy Notice and copyright information.

1 To convert from	2 To	3 Multiply by	4 To	5 Multiply by
tonne (metric)	kg	$1.000\,000 \times 10^{3}$	Mg	1.000
Mass per unit time (flow)				
pound/second	kg/s	$4.535\,924 \times 10^{-1}$	kg/s	0.4536
pound/minute	kg/s	$7.559\,873 \times 10^{-3}$	g/s	7.560
pound/hour	kg/s	$1.259\,979 \times 10^{-4}$	g/s	0.1260
Mass per unit volume				
gram/gallon (U.S.)	kg/m^3	$2.641\,724 \times 10^{-1}$	g/dm^3	0.2642
pound/foot^3	kg/m^3	$1.601\,846 \times 10^{1}$	kg/m^3	16.02
pound/inch^3	kg/m^3	$2.767\,990 \times 10^{4}$	kg/dm^3	27.68
pound/gallon (Imp.)	kg/m^3	$9.977\,644 \times 10^{1}$	kg/dm^3	0.0998
pound/gallon (U.S.)	kg/m^3	$1.198\,264 \times 10^{2}$	kg/dm^3	0.1198
Power, heat flow				
Btu (IT)/hour	W	$2.930\,711 \times 10^{-1}$	W	0.2931
horsepower (550 ft · lbf/s)	W	$7.456\,999 \times 10^{2}$	kW	0.7457
horsepower (metric, CV, PS)	W	$7.354\,99 \times 10^{2}$	kW	0.7355
Pressure, stress (force per unit area)				
atmosphere (normal, 760 torr)	Pa	$1.013\,250 \times 10^{5}$	kPa	101.3
inch of mercury (60°F)	Pa	$3.376\,85 \times 10^{3}$	kPa	3.377
kilogram-force/centimeter^2	Pa	$9.806\,650 \times 10^{4}$	kPa	98.07
mm of mercury, 0°C (torr)	Pa	$1.333\,224 \times 10^{2}$	Pa	133.3
pound-force/foot^2	Pa	$4.788\,026 \times 10^{1}$	Pa	47.88
pound-force/inch^2 (psi)	Pa	$6.894\,757 \times 10^{3}$	kPa	6.895
Temperature interval				
degree Celsius	K	$1.000\,000 \times 10^{0}$		
degree Fahrenheit	K	$5.555\,556 \times 10^{-1}$	K	0.5556
Temperature				

© McGraw-Hill Education. All rights reserved. Any use is subject to the Terms of Use, Privacy Notice and copyright information.

1 To convert from	2 To	3 Multiply by	4 To	5 Multiply by
temperature (°C)	K	°C + 273.15		
temperature (°F)	K	(°F + 459.67)/1.80	°C	(°F − 32)/1.80
Torque				
kilogram-force meter	N · m	$9.806\,650 \times 10^{0}$	N · m	9.807
pound-force foot	N · m	$1.355\,818 \times 10^{0}$	N · m	1.356
Velocity				
foot/second	m/s	$3.048\,000 \times 10^{-1}$	m/s	0.3048
kilometer/hour	m/s	$2.777\,778 \times 10^{-1}$	m/s	0.2778
mile/hour	m/s	$4.470\,400 \times 10^{-1}$	km/h	1.609
Viscosity				
centipoise	Pa · s	$1.000\,000 \times 10^{-3}$	mPa · s	1.000
centistoke	m^2/s	$1.000\,000 \times 10^{-6}$	mm^2/s	1.000
poise	Pa · s	$1.000\,000 \times 10^{-1}$	Pa · s	0.1000
stoke	m^2/s	$1.000\,000 \times 10^{-4}$	mm^2/s	100.0
Volume				
barrel (42 U.S. gallon)	m^3	$1.589\,873 \times 10^{-1}$	m^3	0.1590
$foot^3$	m^3	$2.831\,685 \times 10^{-2}$	dm^3	28.32
gallon (Imp.)	m^3	$4.546\,092 \times 10^{-3}$	dm^3	4.546
gallon (U.S.)	m^3	$3.785\,412 \times 10^{-3}$	dm^3	3.785
$inch^3$	m^3	$1.638\,706 \times 10^{-5}$	cm^3	16.39
liter	m^3	$1.000\,000 \times 10^{-3}$	dm^3	1.000
Volume per unit time				
$foot^3$/minute (cfm)	m^3/s	$4.719\,474 \times 10^{-4}$	dm^3/s	0.4719
$foot^3$/second	m^3/s	$2.831\,685 \times 10^{-2}$	dm^3/s	28.32
gallon (U.S.)/minute (gpm)	m^3/s	$6.309\,020 \times 10^{-5}$	cm^3/s	63.09

© McGraw-Hill Education. All rights reserved. Any use is subject to the Terms of Use, Privacy Notice and copyright information.

1	2	3	4	5
To convert from	To	Multiply by	To	Multiply by

Notes:

1. Derived units such as that for torque (newton · meter, N · m) are written with a period between each component unit for clarity. In practice, the period is often omitted.
2. Derived from Mobil Technical Bulletin *SI Units, The Modern Metric System.* Copyright Mobil Oil Corporation, 1974. Sections reproduced courtesy Mobil Oil Corporation.

© McGraw-Hill Education. All rights reserved. Any use is subject to the Terms of Use, Privacy Notice and copyright information.

B. Ideal Gas Relationships

B.0. APPENDIX PRELIMINARIES

IDEAL GAS LAW

THE MOLE

THERMODYNAMIC PROPERTIES

MIXTURES OF IDEAL GASES

B. IDEAL GAS LAW

The gas species which make up the working fluids in internal combustion engines (e.g., oxygen, nitrogen, carbon dioxide, etc.) can usually be treated as ideal gases. This appendix reviews the relationships between the thermodynamic properties of ideal gases.

The pressure *p*, specific volume *v*, and absolute temperature *T* of an ideal gas are related by the ideal gas law

$$pv = RT$$

(B.1)

For each gas species, *R* is a constant (the gas constant). It is different for each gas and is given by

$$R = \frac{\tilde{R}}{M}$$

(B.2)

where
$\tilde{R}$ is the universal gas constant (for all ideal gases) and *M* is the molecular weight of the gas. Since *v* is given by *V*/*m*, where *V* is the volume of a mass of gas *m*, Eq. (B.1) can be rewritten as

$$pV = mRT = \frac{m\tilde{R}T}{M}$$

(B.3)

B. THE MOLE

It is convenient to introduce a mass unit based on the molecular structure of matter, the mole:

> The mole is the amount of substance which contains as many molecules as there are carbon atoms in 12 grams of carbon-

© McGraw-Hill Education. All rights reserved. Any use is subject to the Terms of Use, Privacy Notice and copyright information.

12.[1]

Thus, the number of moles *n* of gas is given by

$$n = \frac{m}{M}$$

(B.4)

and Eq. (B.3) becomes

$$pV = n\tilde{R}T \quad \text{or} \quad p = \rho RT$$

(B.5)

Values for the universal gas constant in different units are given in Table B.1. In the SI system, the value is 8314.3 J/kmol · K. The density of dry air at standard conditions (101.33 kPa and 25°C) is 1.184 kg/m^3.

Table B.1 Values of universal gas constant
$\tilde{R}$

8314.3 J/kmol · K
8.3143 J/mol · K
1.9859 Btu/lb-mole · °R
1543.3 ft · lbf/lb-mole · °R

B. THERMODYNAMIC PROPERTIES

It follows from Eq. (B.1) that the internal energy *u*[2] of an ideal gas is a function of temperature only:

$$u = u(T)$$

(B.6)

Since the enthalpy *h* is given by *u* + *pv*, it follows also that

$$h = h(T)$$

(B.7)

The specific heats at constant volume and constant pressure of an ideal gas, c_v and c_p, respectively, are defined by

$$c_v = \left(\frac{\partial u}{\partial T}\right)_v = \frac{du}{dT}$$

© McGraw-Hill Education. All rights reserved. Any use is subject to the Terms of Use, Privacy Notice and copyright information.

(B.8)

$$c_p = \left(\frac{\partial h}{\partial T}\right)_p = \frac{dh}{dT}$$

(B.9)

From Eq. (B.1) it follows that

$$c_p - c_v = R$$

(B.10)

The ratio of specific heats, γ, is a useful quantity:

$$\gamma = \frac{c_p}{c_v}$$

(B.11)

An *additional* restrictive assumption is often made that the specific heats are constants. This is not a necessary part of the ideal gas relationships.

In general, the internal energy and enthalpy of an ideal gas at a temperature T relative to its internal energy and enthalpy at some reference temperature T_0 are given by

$$u = u_0 + \int_{T_0}^{T} c_v(T)\, dT$$

(B.12)

and

$$h = h_0 + \int_{T_0}^{T} c_p(T)\, dT$$

(B.13)

The entropy at T, v, and p, relative to the entropy at some reference state T_0, v_0, p_0, can be obtained from the relationships

$$ds = \frac{c_v}{T}dT + R\frac{dv}{v} = \frac{c_p}{T}dT - R\frac{dp}{p}$$

(B.14)

which integrate to give

© McGraw-Hill Education. All rights reserved. Any use is subject to the Terms of Use, Privacy Notice and copyright information.

$$s = s_0 + \int_{T_0}^{T} \frac{c_v}{T} dT + R \ln \frac{v}{v_0}$$

(B.15*a*)

and

$$s = s_0 + \int_{T_0}^{T} \frac{c_p}{T} dT - R \ln \frac{p}{p_0}$$

(B.15*b*)

The properties *u*, *h*, and *s* can be evaluated on a per unit mass or per mole basis. On a mass basis, c_v, c_p, and *R* would have the units J/kg · K (Btu/lbm · °R); on a mole basis, *u*, *h*, and *s* are replaced by
$\tilde{u}$,
$\tilde{h}$, and
$\tilde{s}$. *R* is then the universal gas constant
$\tilde{R}$, c_v and c_p are replaced by
$\tilde{c}_v$ and
$\tilde{c}_p$, and
$\tilde{c}_v, \tilde{c}_p$, and
$\tilde{R}$ would have the units J/kmol · K (Btu/lb-mol · °R).

B. MIXTURES OF IDEAL GASES

The working fluids in engines are mixtures of gases. The composition of a mixture of ideal gases can be expressed in terms of the following properties of each component:

Partial pressure p_i. The pressure each component would exert if it alone occupied the volume of the mixture at the temperature of the mixture.

Parts by volume V_i/V. The fraction of the total mixture volume each component would occupy if separated from the mixture, at the mixture temperature and pressure.

Mass fraction x_i. The mass of each component m_i, divided by the total mass of mixture *m*.

Mole fraction
$\tilde{x}_i$. The number of moles of each component n_i, divided by the total number of moles of mixture *n*.

From Eq. (B.5) it follows that

$$\frac{p_i}{p} = \frac{V_i}{V} = x_i \frac{M}{M_i} = \tilde{x}_i$$

(B.16)

The thermodynamic properties of mixtures of ideal gases can be computed from the following relationships:

Molecular weight

© McGraw-Hill Education. All rights reserved. Any use is subject to the Terms of Use, Privacy Notice and copyright information.

$$M = \frac{1}{n}\sum_i n_i M_i = \sum_i \tilde{x}_i M_i$$

(B.17)

Internal energy, enthalpy, and entropy

On a mass basis:

$$u = \sum_i x_i u_i \quad h = \sum_i x_i h_i \quad s = \sum_i x_i s_i$$

(B.18*a*, *b*, *c*)

On a mole basis:

$$\tilde{u} = \sum_i \tilde{x}_i \tilde{u}_i \quad \tilde{h} = \sum_i \tilde{x}_i \tilde{h}_i \quad \tilde{s} = \sum_i \tilde{x}_i \tilde{s}_i$$

(B.19*a*, *b*, *c*)

[1] This is the SI system definition of the mole; it was formerly called the gram-mole. The kilogram-mole (kmol) is also used; it is 1000 times as large as the mole.

[2] The symbol *u* will be used for internal energy per unit mass, $\tilde{u}$ for internal energy per mole, and *U* for internal energy of a previously defined system of mass *m*. Similar notation will be used for enthalpy, entropy, and specific heats, per unit mass and per mole.

© McGraw-Hill Education. All rights reserved. Any use is subject to the Terms of Use, Privacy Notice and copyright information.

C. Equations for Fluid Flow through a Restriction

C.0. APPENDIX PRELIMINARIES

LIQUID FLOW

GAS FLOW

REFERENCES

In many parts of the engine cycle, fluid flows through a restriction or reduction in flow area. Real flows of this nature are usually related to an equivalent ideal flow. The equivalent ideal flow is the steady adiabatic reversible (frictionless) flow of an ideal fluid through a duct of identical geometry and dimensions. For a real fluid flow, the departures from the ideal assumptions listed above are taken into account by introducing a flow coefficient or discharge coefficient C_D, where

$$C_D = \frac{\text{actual mass flow}}{\text{ideal mass flow}}$$

Alternatively, the flow or discharge coefficient can be defined in terms of an effective cross-sectional area of the duct and a reference area. The reference area A_R is usually taken as the minimum cross-sectional area. The effective area of the flow restriction A_E is then the cross-sectional area of the throat of a frictionless nozzle which would pass the measured mass flow between a large upstream reservoir at the upstream stagnation pressure and a large downstream reservoir at the downstream measured static pressure. Thus

$$C_D = \frac{A_E}{A_R}$$

C. LIQUID FLOW

Consider the flow of a liquid through an orifice as shown in Fig. C.1. For the ideal flow, Bernoulli's equation can be written

$$p_1 + \rho\frac{V_1^2}{2} = p_2 + \rho\frac{V_2^2}{2}$$

For an incompressible flow, continuity gives $V_1A_1 = V_2A_2$ and the ideal mass flow rate through an orifice is given by

$$\dot{m}_{\text{ideal}} = A_2\left[\frac{2\rho\,(p_1 - p_2)}{1 - (A_2/A_1)^2}\right]^{1/2}$$

(C.1)

The real mass flow rate is obtained by introducing the discharge coefficient:

© McGraw-Hill Education. All rights reserved. Any use is subject to the Terms of Use, Privacy Notice and copyright information.

$$\dot{m}_{\text{real}} = C_D A_2 \left[\frac{2\rho (p_1 - p_2)}{1 - (A_2/A_1)^2} \right]^{1/2}$$

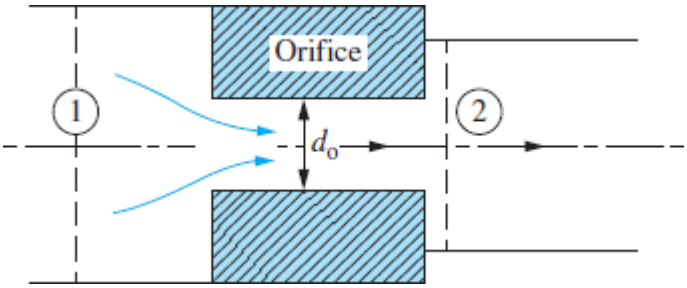
(C.2)

The discharge coefficient is a function of orifice dimensions, shape and surface roughness, mass flow rate, and fluid properties (density, surface tension, and viscosity). The use of the orifice Reynolds number

$$\text{Re}_o = \frac{\rho V_2 D_2}{\mu} = \frac{V_2 D_2}{\nu}$$

along with orifice diameter ratio d_o/D_2, are correlating parameters for C_D, accounting for the effects of *m* over-dot, Greek *Rho*, Greek *Nu*, d_o, and D_2, to a good approximation.[1]

Figure C.1 Schematic of liquid flow through orifice.



C. GAS FLOW

Consider the flow of an ideal gas with constant specific heats through the duct shown in Fig. C.2. For the *ideal flow*, the stagnation temperature and pressure, T_0 and p_0, are related to the conditions at other locations in the duct by the steady flow energy equation

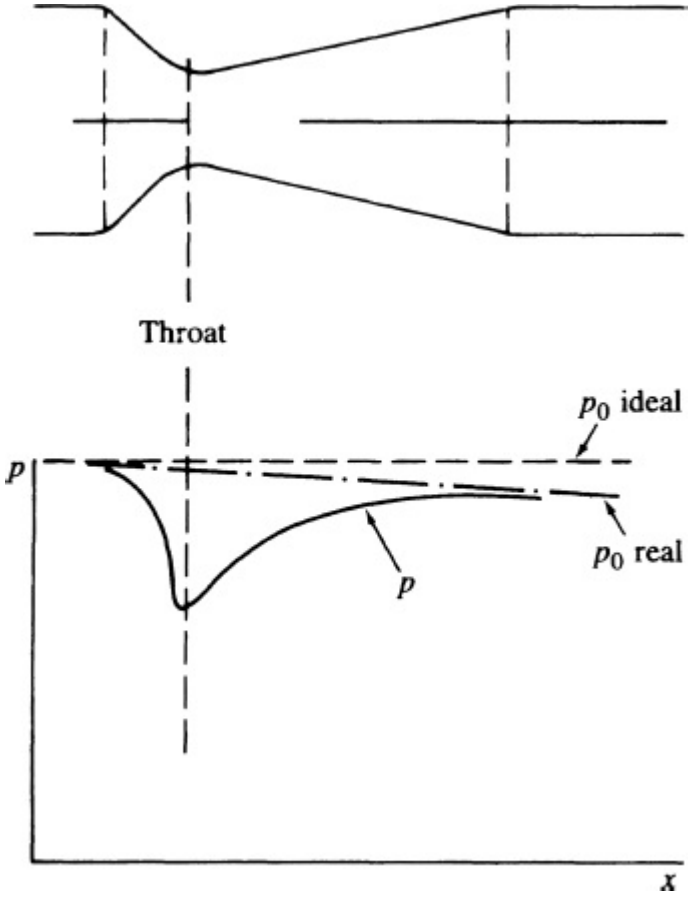
$$T_0 = T + \frac{V^2}{2c_p}$$

and the isentropic relation

$$\left(\frac{T}{T_0}\right) = \left(\frac{p}{p_0}\right)^{(\gamma-1)/\gamma}$$

© McGraw-Hill Education. All rights reserved. Any use is subject to the Terms of Use, Privacy Notice and copyright information.

Figure C.2 *Pressure distribution for gas flow through a nozzle.*



By introducing the Mach number $M = V/a$, where a is the sound speed $(= \sqrt{\gamma RT})$, the following equations are obtained:

$$\frac{T_0}{T} = 1 + \frac{\gamma - 1}{2} M^2 \tag{C.3}$$

$$\frac{p_0}{p} = \left(1 + \frac{\gamma - 1}{2} M^2\right)^{\gamma/(\gamma-1)} \tag{C.4}$$

The mass flow rate $\dot{m}$ is

$$\dot{m} = \rho A V$$

With the ideal gas law and the above relations for p and T, this can be rearranged as

© McGraw-Hill Education. All rights reserved. Any use is subject to the Terms of Use, Privacy Notice and copyright information.

$$\frac{\dot{m}_{\text{ideal}}\sqrt{\gamma RT_0}}{Ap_0} = \gamma M\left(1+\frac{\gamma-1}{2}M^2\right)^{-(\gamma+1)/2(\gamma-1)}$$

(C.5)

or

$$\frac{\dot{m}_{\text{ideal}}\sqrt{\gamma RT_0}}{Ap_0} = \gamma\left(\frac{p}{p_0}\right)^{1/\gamma}\left\{\frac{2}{\gamma-1}\left[1-\left(\frac{p}{p_0}\right)^{(\gamma-1)/\gamma}\right]\right\}^{1/2}$$

(C.6)

For given values of p_0 and T_0, the maximum mass flow occurs when the velocity at the minimum area or throat equals the velocity of sound. This condition is called choked or critical flow. When the flow is choked the pressure at the throat, p_T, is related to the stagnation pressure p_0 as follows:

$$\frac{p_T}{p_0} = \left(\frac{2}{\gamma+1}\right)^{\gamma/(\gamma-1)}$$

This ratio is called the critical pressure ratio. For (p_T/p_0) less than or equal to the critical pressure ratio,

$$\frac{\dot{m}_{\text{ideal}}\sqrt{\gamma RT_0}}{A_T p_0} = \gamma\left(\frac{2}{\gamma+1}\right)^{(\gamma+1)/2(\gamma-1)}$$

(C.7)

The critical pressure ratio is 0.528 for $\gamma = 1.4$ and 0.546 for $\gamma = 1.3$.

For a real gas flow, the discharge coefficient is introduced. Then, for sub-critical flow, the real mass flow rate is given in terms of conditions at the minimum area or throat by

$$\dot{m}_{\text{real}} = \frac{C_D A_T p_0}{\sqrt{RT_0}}\left(\frac{p_T}{p_0}\right)^{1/\gamma}\left\{\frac{2\gamma}{\gamma-1}\left[1-\left(\frac{p_T}{p_0}\right)^{(\gamma-1)/\gamma}\right]\right\}^{1/2}$$

(C.8)

For a choked flow,

$$\dot{m}_{\text{real}} = \frac{C_D A_T p_0}{\sqrt{RT_0}}\gamma^{1/2}\left(\frac{2}{\gamma+1}\right)^{(\gamma+1)/2(\gamma-1)}$$

(C.9)

Equation (C.8) can be rearranged in the form of Eq. (C.2) (with $A_2 \ll A_1$) as

© McGraw-Hill Education. All rights reserved. Any use is subject to the Terms of Use, Privacy Notice and copyright information.

$$\dot{m}_{\text{real}} = C_D A_R [2\rho_0 (p_0 - p_T)]^{1/2} \Phi$$

(C.10)

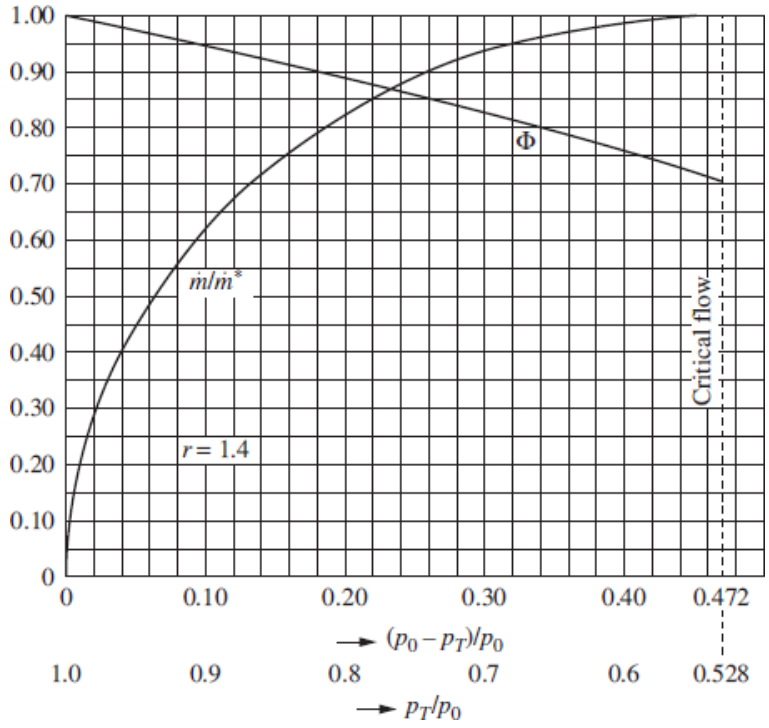
where Φ is given by

$$\Phi = \left\{ \frac{[\gamma/(\gamma-1)]\left[(p_T/p_0)^{2/\gamma} - (p_T/p_0)^{(\gamma+1)/\gamma}\right]}{1 - p_T/p_0} \right\}^{1/2}$$

(C.11)

Figure C.3 shows the variation of Φ and $(\dot{m}/\dot{m}^*)_{\text{ideal}}$ with $(p_0 - p_T)/p_0$.
$\dot{m}^*$ is the mass flow rate through the restriction under choked flow conditions (when the Mach number at the throat is unity). For flow rates less than about 60% of the choked flow, the effects of compressibility on the mass flow rate are less than 5%.

Figure C.3 Relative mass flow rate $\dot{m}/\dot{m}^*$ and compressible flow function Φ [Eq. (C.11)] as function of nozzle or restriction pressure ratio for ideal gas with γ = 1.4. (From Taylor.[2])



Flow coefficients are determined experimentally and are a function of the shape of the passage, the Reynolds number and Mach number of the flow, and the gas properties. For a Mach number at the throat less than about 0.7 and for passages of similar shape, the flow coefficient is essentially a function of Reynolds number only.

Orifice plates are frequently used to measure gas flow rates. Standard methods for determining flows through orifice plates can be found in Ref. 3.

© McGraw-Hill Education. All rights reserved. Any use is subject to the Terms of Use, Privacy Notice and copyright information.

C. REFERENCES

1. White, F. M.: *Fluid Mechanics*, 4th edition, McGraw-Hill, New York, 1999.
2. Taylor, C. F.: *The Internal Combustion Engine in Theory and Practice*, vol. I, p. 506, MIT Press, Cambridge, MA, 1966.
3. *Marks' Standard Handbook for Mechanical Engineers*, 8th ed., McGraw-Hill, New York, 1978.

© McGraw-Hill Education. All rights reserved. Any use is subject to the Terms of Use, Privacy Notice and copyright information.

D. Data on Working Fluids

D.0. APPENDIX PRELIMINARIES

Table D.1 Thermodynamic properties of air at low density†

			Ψ	Φ			c_p	c_v	
T, K	h, kJ/kg	u, kJ/kg	kJ/(kg · K)		p_r	v_r	kJ/(kg · K)		γ
250	409.9	338.1	4.4505	7.6603	38.81	1849.0	1.003	0.715	1.401
275	435.0	356.0	4.5187	7.7559	54.14	1458.0	1.003	0.716	1.401
300	460.1	374.0	4.5811	7.8432	73.39	1173.0	1.004	0.717	1.400
325	485.2	391.9	4.6385	7.9236	97.13	960.6	1.006	0.718	1.400
350	510.4	409.9	4.6919	7.9982	125.9	797.8	1.007	0.720	1.399
375	535.6	427.9	4.7416	8.0678	160.5	670.8	1.010	0.723	1.397
400	560.8	446.0	4.7884	8.1330	201.4	570.0	1.013	0.725	1.396
425	586.2	464.2	4.8324	8.1945	249.6	488.9	1.016	0.729	1.394
450	611.6	482.5	4.8742	8.2527	305.6	422.7	1.020	0.733	1.392
475	637.2	500.8	4.9139	8.3079	370.4	368.1	1.024	0.737	1.390
500	662.8	519.3	4.9518	8.3606	445.0	322.6	1.028	0.741	1.387
525	688.6	537.9	4.9881	8.4109	530.2	284.3	1.033	0.746	1.385
550	714.5	556.6	5.0229	8.4590	627.1	251.8	1.039	0.752	1.382
575	740.5	575.5	5.0565	8.5053	736.8	224.0	1.044	0.757	1.379
600	766.7	594.5	5.0888	8.5499	860.6	200.1	1.050	0.763	1.376
625	793.0	613.6	5.1201	8.5929	999.5	179.5	1.056	0.768	1.374
650	819.5	632.9	5.1503	8.6344	1155.0	161.5	1.061	0.774	1.371
675	846.1	652.3	5.1796	8.6745	1329.0	145.9	1.067	0.780	1.368
700	872.9	671.9	5.2081	8.7135	1521.0	132.1	1.073	0.786	1.365
725	899.8	691.7	5.2358	8.7512	1735.0	119.9	1.079	0.792	1.362
750	926.8	711.5	5.2628	8.7879	1972.0	109.2	1.085	0.798	1.360

© McGraw-Hill Education. All rights reserved. Any use is subject to the Terms of Use, Privacy Notice and copyright information.

			Ψ	Φ			c	c	
T, K	h, kJ/kg	u, kJ/kg	kJ/(kg · K)		p	v	kJ/(kg · K)		γ
775	954.0	731.6	5.2891	8.8236	2233.0	99.63	1.091	0.804	1.357
800	981.4	751.7	5.3147	8.8584	2520.0	91.12	1.097	0.810	1.354
825	1008.9	772.1	5.3397	8.8922	2836.0	83.52	1.103	0.816	1.352
850	1036.5	792.5	5.3641	8.9252	3181.0	76.71	1.108	0.821	1.350
875	1064.3	813.1	5.3880	8.9574	3559.0	70.58	1.114	0.827	1.347
900	1092.2	833.8	5.4114	8.9889	3971.0	65.07	1.119	0.832	1.345
925	1120.2	854.7	5.4342	9.0196	4419.0	60.08	1.124	0.837	1.343
950	1148.4	875.7	5.4566	9.0496	4907.0	55.58	1.129	0.842	1.341
975	1176.7	896.8	5.4786	9.0790	5436.0	51.49	1.134	0.847	1.339
1000	1205.1	918.1	5.5001	9.1078	6009.0	47.77	1.139	0.852	1.337
1025	1233.7	939.4	5.5212	9.1360	6629.0	44.39	1.144	0.856	1.335
1050	1262.3	960.9	5.5419	9.1636	7299.0	41.30	1.148	0.861	1.333
1075	1291.1	982.5	5.5622	9.1907	8020.0	38.48	1.152	0.865	1.332
1100	1319.9	1004.1	5.5821	9.2172	8797.0	35.90	1.157	0.870	1.330
1125	1348.9	1025.9	5.6017	9.2432	9632.0	33.53	1.161	0.874	1.329
1150	1378.0	1047.8	5.6209	9.2688	10529.0	31.35	1.165	0.878	1.327
1175	1407.1	1069.8	5.6399	9.2939	11490.0	29.36	1.168	0.881	1.326
1200	1436.4	1091.9	5.6585	9.3185	12520.0	27.51	1.172	0.885	1.324

†Abstracted with permission from *Thermodynamic Properties in SI* (Graphs, Tables, and Computational Equations for Forty Substances), by W. C. Reynolds, published by the Department of Mechanical Engineering, Stanford University, Stanford, CA 94305, 1979.

© McGraw-Hill Education. All rights reserved. Any use is subject to the Terms of Use, Privacy Notice and copyright information.

Table D.2 Standard enthalpy of formation and molecular weight of species

Species	Formula	Molecular weight, g/mole	State†	$\Delta\tilde{h}_f^\circ$ MJ/kmol	$\Delta\tilde{h}_f^\circ$ kcal/mol
Oxygen	O_2	32.00	gas	0	0
Nitrogen	N_2	28.01	gas	0	0
Carbon	C	12.011	solid	0	0
Carbon monoxide	CO	28.01	gas	−110.5	−26.42
Carbon dioxide	CO_2	44.01	gas	−393.5	−94.05
Hydrogen	H_2	2.016	gas	0	0
Water	H_2O	18.02	gas	−241.8	−57.80
Water	H_2O	18.02	liquid	−285.8	−68.32
Methane	CH_4	16.04	gas	−74.9	−17.89
Propane	C_3H_8	44.10	gas	−103.8	−24.82
Isooctane	C_8H_{18}	114.23	gas	−224.1	−53.57
Isooctane	C_8H_{18}	114.23	liquid	−259.28	−61.97
Cetane	$C_{16}H_{34}$	226.44	liquid	−454.5	−108.6
Methyl alcohol	CH_3OH	32.04	gas	−201.2	−48.08
Methyl alcohol	CH_3OH	32.04	liquid	−238.6	−57.02
Ethyl alcohol	C_2H_5OH	46.07	gas	−234.6	−56.08
Ethyl alcohol	C_2H_5OH	46.07	liquid	−277.0	−66.20

†At 298.15 K (25°C) and 1 atm.

Table D.3 Enthalpy of C, CO, CO_2, H_2, H_2O, N_2, O_2

	$\tilde{h}^\circ(T) - \tilde{h}^\circ(298.15)$, kcal/mol						
T (K)	C	CO	CO_2	H_2	H_2O	N_2	O_2
298	0.000	0.000	0.000	0.000	0.000	0.000	0.000
300	0.004	0.013	0.016	0.013	0.015	0.013	0.013
400	0.250	0.711	0.958	0.707	0.825	0.710	0.724
500	0.569	1.417	1.987	1.406	1.654	1.413	1.455

© McGraw-Hill Education. All rights reserved. Any use is subject to the Terms of Use, Privacy Notice and copyright information.

T (K)	C	CO	CO	H	H O	N	O
600	0.947	2.137	3.087	2.106	2.509	2.125	2.210
700	1.372	2.873	4.245	2.808	3.390	2.853	2.988
800	1.831	3.627	5.453	3.514	4.300	3.596	3.786
900	2.318	4.397	6.702	4.226	5.240	4.355	4.600
1000	2.824	5.183	7.984	4.944	6.209	5.129	5.427
1100	3.347	5.983	9.296	5.670	7.210	5.917	6.266
1200	3.883	6.794	10.632	6.404	8.240	6.718	7.114
1300	4.432	7.616	11.988	7.148	9.298	7.529	7.971
1400	4.988	8.446	13.362	7.902	10.384	8.350	8.835
1500	5.552	9.285	14.750	8.668	11.495	9.179	9.706
1600	6.122	10.130	16.152	9.446	12.630	10.015	10.583
1700	6.696	10.980	17.565	10.233	13.787	10.858	11.465
1800	7.275	11.836	18.987	11.030	14.964	11.707	12.354
1900	7.857	12.697	20.418	11.836	16.160	12.560	13.249
2000	8.442	13.561	21.857	12.651	17.373	13.418	14.149
2100	9.029	14.430	23.303	13.475	18.602	14.280	15.054
2200	9.620	15.301	24.755	14.307	19.846	15.146	15.966
2300	10.212	16.175	26.212	15.146	21.103	16.015	16.882
2400	10.807	17.052	27.674	15.993	22.372	16.886	17.804
2500	11.403	17.931	29.141	16.848	23.653	17.761	18.732
2600	12.002	18.813	30.613	17.708	24.945	18.638	19.664
2700	12.602	19.696	32.088	18.575	26.246	19.517	20.602
2800	13.203	20.582	33.567	19.448	27.556	20.398	21.545
2900	13.807	21.469	35.049	20.326	28.875	21.280	22.493
3000	14.412	22.357	36.535	21.210	30.201	22.165	23.446

Source: JANAF Thermochemical Tables, National Bureau of Standards Publication NSRDS-NBS37, 1971.

© McGraw-Hill Education. All rights reserved. Any use is subject to the Terms of Use, Privacy Notice and copyright information.

T (K)	C	CO	CO	H	H O	N	O

Table D.4 Data on fuel properties

Fuel	Formula (phase)[a]	Molecular weight	Specific gravity (density,[b] kg/dm^3)	Heat of vaporization, kJ/kg[c]	Specific heat		Higher heating value, MJ/kg	Lower heating value, MJ/kg	LHV of stoich. mixture, MJ/kg[d]	$(A/F)_s$	$(F/A)_s$	Fuel octane rating	
					Liquid, kJ/kg · K	Vapor c_p, kJ/kg · K						RON	MON
Practical fuels[e]													
Gasoline	$C_nH_{1.87n}$(l)	~100	0.72–0.78	350	2.4	~1.7	46.3	43.0	2.76	14.6	0.0685	91–99	82–89
E10 gasoline	$C_nH_{1.94n}O_{0.043n}$(l)	~100	~0.75	400	2.4	~1.7	44.5	41.5	2.82	13.7	0.0730	96[e]	85[e]
Light diesel	$C_nH_{1.8n}$(l)	~170	0.78–0.84	270	2.2	~1.7	46.1	43.2	2.79	14.5	0.0690	—	—
Heavy diesel	$C_nH_{1.7n}$(l)	~200	0.82–0.88	230	1.9	~1.7	45.5	42.8	2.85	14.4	0.0697	—	—
Natural gas	$C_nH_{3.8n}N_{0.1n}$(g)	~18	(~0.79)	—	—	~2	50	45	2.9	15.7[f]	0.0637	—	—
Pure hydrocarbons													
Methane	CH_4(g)	16.04	(0.72)	509	0.63	2.2	55.5	50.0	2.72	17.23	0.0580	120	120
Propane	C_3H_8(g)	44.10	0.51 (2.0)	426	2.5	1.6	50.4	46.4	2.75	15.67	0.0638	112	97
Isooctane	C_8H_{18}(l)	114.23	0.692	308	2.1	1.63	47.8	44.3	2.75	15.13	0.0661	100	100
Cetane	$C_{16}H_{34}$(l)	226.44	0.773	358	2.2	1.6	47.3	44.0	2.78	14.82	0.0675	—	—
Benzene	C_6H_6(l)	78.11	0.879	433	1.72	1.1	41.9	40.2	2.82	13.27	0.0753	125	115
Toluene	C_7H_8(l)	92.14	0.867	412	1.68	1.1	42.5	40.6	2.79	13.50	0.0741	120	109
Alcohols													

© McGraw-Hill Education. All rights reserved. Any use is subject to the Terms of Use, Privacy Notice and copyright information.

Fuel	Formula (phase)	Molecular weight	Specific gravity (density, kg/dm)	Heat of vaporization, kJ/kg	Specific heat		Higher heating value, MJ/kg	Lower heating value, MJ/kg	LHV of stoich. mixture, MJ/kg	(*A/F*)	(*F/A*)	Fuel octane rating	
					Liquid, kJ/kg · K	Vapor c, kJ/kg · K						RON	MON
Methanol	CH_4O(l)	32.04	0.792	1100	2.6	1.72	22.7	20.0	2.68	6.47	0.155	109	89
Ethanol	C_2H_6O(l)	46.07	0.785	900	2.5	1.93	29.7	26.9	2.69	9.00	0.111	109	90
Other fuels													
Carbon	C(s)	12.01	~2	—	—	—	33.8	33.8	2.70	11.51	0.0869	—	—
Carbon monoxide	CO(g)	28.01	(1.25)	—	—	1.05	10.1	10.1	2.91	2.467	0.405	106	—
Hydrogen	H_2(g)	2.015	(0.090)	—	—	1.44	142.0	120.0	3.40	34.3	0.0292	120–140	—

[a](l) liquid phase; (g) gaseous phase; (s) solid phase.

[b]Density in kg/m^3 at 0°C and 1 atm.

[c]At 1 atm and 25°C for liquid fuels; at 1 atm and boiling temperature for gaseous fuels.

[d]Between 3.5 and 3.7 MJ/m^3.

[e]10% ethanol adds some 2–5 octane numbers: so RON and MON depend on rating of base gasoline.

[f]$(A/F)_s$ influenced by N_2 and CO_2 content.

RON, research octane number; MON, motor octane number.

Sources:

E. M. Goodger, *Hydrocarbon Fuels: Production, Properties and Performance of Liquids and Gases*, Macmillan, London, 1975.

C. F. Taylor, *The Internal Combustion Engine in Theory and Practice*, vol. I, MIT Press, 1966.

J. W. Rose and J. R. Cooper (eds.), *Technical Data on Fuel*, 7th ed., British National Committee, World Energy Conference, London, 1977.

J. C. Guibet, *Fuels and Engines: Technology—Energy—Environment*, vols. 1 and 2, Editions TECHNIP, Paris, 1999.

J. A. Topinka, M. D. Gerty, J. B. Heywood, and J. C. Keck, "Knock Behavior of a Lean-Burn, H_2 and CO Enhanced, SI Gasoline Engine Concept," SAE paper 2004-01-0975, 2004.

J. E. Anderson, U. Kramer, S. A. Mueller, and T. J. Wellington, "Octane Numbers of Ethanol- and Methanol-Gasoline Blends Estimated from Molar Concentrations," *Energy & Fuels*, vol. 24, pp. 6576–6585, 2010.

© McGraw-Hill Education. All rights reserved. Any use is subject to the Terms of Use, Privacy Notice and copyright information.